



Universität Hamburg

DER FORSCHUNG | DER LEHRE | DER BILDUNG

Shaping the Future:

Surface-Modified Cellulose Nanofibrils (CNFs) for Multifunctional 3D-Printable Hybrid Materials

Fluorescent labeling of CNFs for Morphology Studies
and Development of CNF-based hybrid Materials with
Inorganic Nanoparticles

A Cumulative Dissertation

For the Degree of *Doctor rerum naturalium* (Dr. rer. nat.)

at the Faculty of Mathematics, Informatics, and Natural Sciences

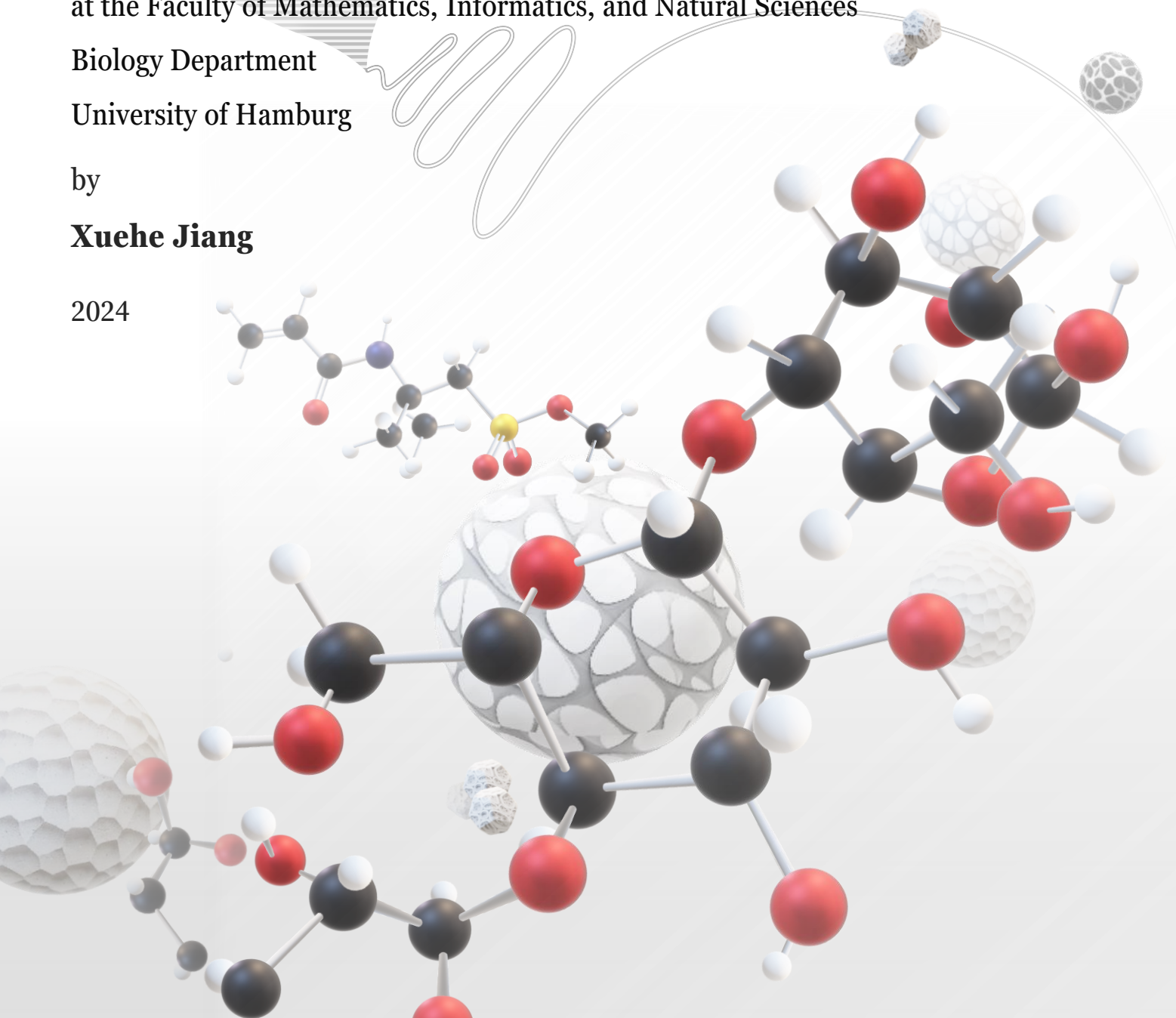
Biology Department

University of Hamburg

by

Xuehe Jiang

2024



Reviewers:

Prof. Dr. Bodo Saake
University of Hamburg

Prof. Dr. Ming-Guo Ma
Beijing Forestry University

Oral defense committee:

Prof. Dr. Bodo Saake

Prof. Dr. Ming-Guo Ma

Prof. Dr. Elisabeth Magel

Prof. Dr. Linnea Hesse

Prof. Dr. Stephan V. Roth

Date of disputation: 08.04.2025

Declaration on oath

Eidesstattliche Versicherung:

Hiermit versichere ich an Eides statt, die vorliegende Dissertationsschrift selbst verfasst und keine anderen als die angegebenen Hilfsmittel und Quellen benutzt zu haben.

Sofern im Zuge der Erstellung der vorliegenden Dissertationsschrift generative Künstliche Intelligenz (gKI) basierte elektronische Hilfsmittel verwendet wurden, versichere ich, dass meine eigene Leistung im Vordergrund stand und dass eine vollständige Dokumentation aller verwendeten Hilfsmittel gemäß der Guten wissenschaftlichen Praxis vorliegt. Ich trage die Verantwortung für eventuell durch die gKI generierte fehlerhafte oder verzerrte Inhalte, fehlerhafte Referenzen, Verstöße gegen das Datenschutz- und Urheberrecht oder Plagiate.

Affidavit:

I hereby declare and affirm that this doctoral dissertation is my own work and that I have not used any aids and sources other than those indicated.

If electronic resources based on generative artificial intelligence (gAI) were used in the course of writing this dissertation, I confirm that my own work was the main and value-adding contribution and that complete documentation of all resources used is available in accordance with good scientific practice. I am responsible for any erroneous or distorted content, incorrect references, violations of data protection and copyright law or plagiarism that may have been generated by the gAI.

Hamburg, den 19.07.2024

Unterschrift:

A handwritten signature in black ink, appearing to be 'F. J. ...', written over a light blue horizontal line.

Acknowledgements

Everything began with an excursion during my master study. In a cozy local restaurant in the Netherlands, I found myself sitting face-to-face with Prof. Bodo Saake. When I mentioned my interest in doing a study project in wood chemistry, he responded with warmth, "Of course. There are plenty of possible projects. You are very welcome." I cannot thank him enough for his encouragement and opening up many opportunities.

Later, Prof. Saake recommended a project that perfectly aligned with my bachelor background. That's how I met Dr. Benedikt Mietner, my supervisor for that study project and now a cherished colleague. He made that one-month study project so engaging that even the long daily commute to Barsbüttel during the dark German winter became totally bearable :)

During that time, I also met Dr. Julien Navarro, who later became my supervisor for my master thesis and doctoral study. I recall that during my master thesis, I would write him weekly lab reports that felt like "dear diary" entries. I am deeply grateful to Julien for offering me this PhD position, providing a cheerful ending to my master study and a perfect extension into my doctoral journey.

I feel really lucky to work with such wonderful colleagues- Feras, Enguerrand, Dhanya- who are not only supportive at work but also great friends outside of it. I've also enjoyed great times with other doctoral students, like Maï, Frederik, Yue, and Carol... We work hard and party hard together.

"Many hands make light work," and I want to thank all my collaborators in various projects: Prof. Stephan Roth from DESY, Dr. Rajesh Komban, and Dr. Christoph Gimmler from Fraunhofer... Special thanks as well to Anna, Birte, Bernhard, and everyone who made the facilities at our institute easily accessible.

I am grateful to my loved ones who welcome me home every day, no matter how tough the day has been, and to my two little "monsters" always trying to help me type on the keyboard, adding a bit of "fun" to writing.

Lastly, a huge thank you to Prof. Ming-Guo Ma, who was a major support during my bachelor thesis and now serves as one of the examiners of this dissertation. It feels like a perfect full circle.

There are still so many people I want to thank.

Keep calm and carry on.

Contents

| | |
|--|------|
| Acknowledgements | iv |
| Abbreviations..... | viii |
| List of publications and summary of the contribution | xii |
| Abstract | 1 |
| Zusammenfassung | 4 |
| 1 Introduction..... | 7 |
| 1.1 Cellulose and nanocellulose..... | 7 |
| 1.1.1 Nanocellulose | 10 |
| 1.1.2 Production of cellulose nanofibrils | 15 |
| 1.1.3 Properties and characterization of cellulose nanofibrils | 26 |
| 1.1.4 Surface modification of nanocellulose..... | 34 |
| 1.2 Single electron transfer surface-initiated controlled radical polymerization (SET-LRP)..... | 43 |
| 1.2.1 Mechanism..... | 43 |
| 1.2.2 Monomers..... | 45 |
| 1.2.3 Solvents..... | 46 |
| 1.2.4 Catalyst system of Cu ⁰ -mediated LRP | 47 |
| 1.2.5 Post-modification..... | 49 |
| 1.3 Emerging applications of cellulose nanofibrils | 52 |
| 1.3.1 CNFs as rheology modifiers | 52 |
| 1.3.2 CNFs loaded with inorganic nanoparticles | 55 |
| 1.4 Objectives and outline of this thesis | 58 |
| 2 Extraction, surface modification and morphology study of CNFs | 60 |
| 2.1 Introduction..... | 61 |
| 2.2 Results and discussion..... | 65 |
| 2.2.1 Production of CNFs..... | 65 |
| 2.2.2 Solvent exchange, chemical conversion and surface modification of CNFs with poly-SA..... | 67 |
| 2.2.3 Surface initiated SET-LRP: growth of random copolymer poly-DEGEEA and poly-TMSPgA on CNFs (DEG-TMSPgA-CNF) and its post-treatment..... | 73 |

| | |
|---|-----|
| 2.2.4 Click chemistry azide-alkyne cycloaddition of alkyne-modified CNFs and various fluorescent azide dyes | 78 |
| 2.2.5 Morphology study of modified CNFs and their embeddings in PVA..... | 82 |
| 2.3 Conclusion | 91 |
| 2.4 Materials and methods | 93 |
| 2.4.1 Materials..... | 93 |
| 2.4.2 Experimental section..... | 93 |
| 2.4.3 Characterization | 97 |
| 3 Syntheses, characterizations and applications of CNF-based hybrids with rare-earth-based nanoparticles..... | 100 |
| 3.1 Introduction..... | 101 |
| 3.1.1 Lanthanide-doped upconversion nanoparticles (UCNPs) | 103 |
| 3.1.2 Gadolinium nanoparticles (Gd NPs) | 106 |
| 3.1.3 CNFs as an innovative pool for biomedical applications..... | 108 |
| 3.2 Results and discussion..... | 111 |
| 3.2.1 Surface modification of UCNPs | 111 |
| 3.2.2 Surface modification of GdF ₃ nanoparticles (GdF ₃ NPs)..... | 115 |
| 3.2.3 Surface-initiated radical polymerization and <i>in situ</i> cross-linking | 116 |
| 3.2.4 Ultrasmall- and wide-angle X-ray scattering (USAX/WAXS) measurements of CNF-based hybrids | 126 |
| 3.2.5 Performance and application potential of CNF-based hybrids..... | 135 |
| 3.3 Conclusion | 148 |
| 3.4 Materials and methods | 150 |
| 3.4.1 Materials..... | 150 |
| 3.4.2 Experimental section..... | 150 |
| 3.4.3 Characterization | 153 |
| 4 General conclusions and perspectives..... | 156 |
| References..... | 161 |
| Table of figures and schemes..... | 192 |
| List of tables..... | 199 |
| Journal publications | 200 |

Abbreviations

$^1\text{H-NMR}$ — Proton Nuclear Magnetic Resonance

2D — 2 Dimension

3D — 3 Dimension

Achol — Acetic Acid

AF 488 — Azide Fluor 488 Dye

AFM — Atomic Force Microscopy

AGU — Anhydroglucose Unit

AM — Additive Manufacturing

AMPS — 2-Acrylamido-2-Methyl-1-Propanesulfonic Acid

AS — Accessible Fibril Surface

ATRP — Atom Transfer Radical Polymerization

ATTO 633 — Azide ATTO 633 Dye

BNC — Bacterial-based Nanocellulose

CA — Contrast Agent

CCD — Charge-Coupled Device

CDI — 1,1'-Carbonyl diimidazole

CF — Cellulose Fiber

CLSM — Confocal Laser Scanning Microscopy

CMLE — Classical Likelihood Estimation

CNC — Cellulose Nanocrystal

CNF — Cellulose Nanofibril

CNF-MI — Cellulose Nanofibril-based Macroinitiator

CNM — Cellulose Nanomaterial

CP-MAS — ^{13}C Cross-Polarization Magic Angle Spinning

CuAAC — Cu^{I} -Catalyzed Azide-Alkyne Cycloaddition

DEGEEA — Di(Ethylene-Glycol)-2-Ethylhexyl Ether Acrylate

DEG-PgA-CNF — Random Polymer of Di(Ethylene-Glycol)-2-Ethylhexyl Ether Acrylate and Propargyl Acrylate grafted Cellulose Nanofibrils

DEG-TMSPgA-CNF — Random Polymer of Di(Ethylene-Glycol)-2-Ethylhexyl Ether Acrylate and Trimethylsilyl Propargyl Acrylate grafted Cellulose Nanofibrils

DIW — Direct Ink Writing

DLS — Dynamic Light Scattering

DMF — Dimethylformamide

DMSO — Dimethyl Sulfoxide

DP — Degree of Polymerization

EbiB — Ethyl 2-Bromo-2-Methyl Propionate

ECF — Elemental Chlorine-Free

EOR — Enhanced Oil Recovery

ETU — Energy-Transfer Upconversion

FE-SEM — Field Emission Scanning Electron Microscopy

FT-IR — Fourier-Transform Infrared Spectroscopy

Gd NP — Gadolinium Nanoparticle

GdF₃ NP — Gadolinium Fluoride Nanoparticle

HFIPA — 1,1,1,3,3,3-Hexafluoroisopropyl Acrylate

HPH — High-Pressure Homogenization

IAS — Inaccessible Fibril Surface

LA — Lauryl Acrylate

LFAD — Lateral Fibril Aggregation Dimension

LFD — Lateral Fibril Dimension

Me₆-TREN — Tris[2-(dimethylamino)ethyl]amine

MONP — Metal Oxide Nanoparticle

MP1 — Micrococcin P1

MRI — Magnetic Resonance Imaging

MRSA — Methicillin-Resistant *S. aureus*

M_w — Average Molecular Weight

NC — Nanocellulose

NIR — Near-Infrared

NMR — Nuclear Magnetic Resonance

NP — Nanoparticle

OA — Oleic Acid

OEOMEA — Oligo (Ethylene Oxide) Methyl Ether Acrylate

PCr — Paracrystalline

PDA — 11-Phosphoundecyl Acrylate

PgA — Propargyl Acrylate

PMDTA — N,N,N',N'',N''-Pentamethyldiethylenetriamine

PSA-CNF — Polymer Stearyl Acrylate grafted Cellulose Nanofibrils

PSF — Point Spread Function

PVA — Polyvinyl Alcohol

RE — Rare Earth

RENP — Rare-Earth-based Nanoparticle

ROP — Ring-Opening Polymerization

SA — Stearyl Acrylate

SANS — Small-Angle Neutron Scattering

SAXS — Small-Angle X-Ray Scattering

sd — Simple Dried

SEM — Scanning Electron Microscopy

SET-LRP — Single-Electron Transfer Controlled Radical Polymerization

SIP — Surface-Initiated Polymerization

SPAD — Single-Photon Avalanche Diode

STED — Stimulated Emission Depletion

T_1 — Longitudinal Relaxation

T_2 — Transverse Relaxation

TAPPI — Technical Association of the Pulp and Paper Industry

TBAF — Tetra-n-Butylammonium Fluoride
TEA — Triethylamine
TEM — Transmission Electron Microscopy
TEMPO — 2,2,6,6-Tetramethylpiperidine-1-Oxyl
TGA — Thermogravimetric Analysis
TFE — 2,2,2-trifluoroethanol
TFP — 2,2,3,3-tetrafluoropropanol
THF — Tetrahydrofuran
TMSPgA — Trimethylsilyl Propargyl Acrylate
TREN — Tris(2-Aminoethyl)amine
UCNP — Upconversion Nanoparticle
UV — Ultraviolet
WAXS — Wide-Angle X-Ray Scattering
XRD — X-Ray Diffraction

List of publications and summary of the contribution

--- Publications included in this thesis ---

- I. Xuehe Jiang, J. Benedikt Mietner, Julien R. G. Navarro
A Combination of Surface-Initiated Controlled Radical Polymerization (SET-LRP) and Click-Chemistry for the Chemical Modification and Fluorescent Labeling of Cellulose Nanofibrils: STED Super-Resolution Imaging of a Single Fibril and a Single Fibril Embedded in a Composite
Cellulose, 2023, 30, 2929–2950
 - Idea and plan
 - Operation of experiments and analyses, including FT-IR, UV-Vis Spectroscopy
 - Data analyses and interpretation
 - Summarize results and write the manuscript

- II. Xuehe Jiang, J. Benedikt Mietner, Constantin Harder, Rajesh Kombar, Shouzheng Chen, Christian Strelow, Uta Sazama, Michael Fröba, Christoph Gimmler, Peter Müller-Buschbaum, Stephan V. Roth, and Julien R. G. Navarro
3D Printable Hybrid Gel Made of Polymer Surface-Modified Cellulose Nanofibrils Prepared by Surface-Initiated Controlled Radical Polymerization (SI-SET-LRP) and Upconversion Luminescent Nanoparticles
ACS Appl. Mater. Interfaces, 2023, 15, 4, 5687–5700
 - Idea and plan
 - Operation of experiments and analyses, including FT-IR, rheology measurements
 - Data analyses and interpretation
 - Summarize results and write the manuscript

III. Xuehe Jiang, J. Benedikt Mietner, Dhanya Raveendran, Kirill V. Ovchinnikov, Benedikt Sochor, Susanne Mueller, Philipp Boehm-Sturm, Frédéric Lerouge, Frédéric Chaput, Pavel Gurikov, Stephan V. Roth, and Julien R. G. Navarro

Multifunctional Cellulose Nanofibrils–GdF₃ Nanoparticles Hybrid Gel and Its Potential Uses for Drug Delivery and Magnetic Resonance Imaging

ACS Appl. Nano Mater., 2023, 6, 22, 21182–21193

- Idea and plan
- Operation of experiments and analyses, including FT-IR, rheology measurements
- Data analyses and interpretation
- Summarize results and write the manuscript

Reprints were made with permission from the respective publishers.

--- Publications not included in this thesis ---

I. J. Benedikt Mietner, Xuehe Jiang, Ulrica Edlund, Bodo Saake and Julien R. G. Navarro
3D printing of a bio-based ink made of cross-linked cellulose nanofibrils with various metal cations

Sci Rep, 2021, 11, 6461

- Operation of experiments and analyses, including FT-IR, rheology measurements
- Data analyses and interpretation

Signature of the doctoral candidate



Signature of the supervisor



Abstract

Cellulose nanofibrils (CNFs) are well-known biodegradable, renewable, and biocompatible materials that can be extracted from lignocellulosic materials via various chemical, mechanical, or enzymatic processes. Typically, CNFs obtained by mechanical processes are in aqueous media, generating viscous dispersion. The abundant numbers of hydroxy groups on their surface are a double-edged sword when utilizing CNFs: while those functions lead to some drawbacks such as hygroscopic character, instability in many organic solvents, strong interfibrillar hydrogen interactions (leading to fibril aggregation), they can also participate in many chemical modifications through specific reactions.

This thesis presents a surface modification pathway for CNFs, beginning with their conversion into CNF-based macroinitiators (CNF-MI) in a single step, followed by a Cu⁰-mediated radical polymerization (SET-LRP) to graft polymers onto the CNF surface. The introduction of polymers onto their surface allows to change the properties and the behavior of the CNF drastically. By carefully selecting the appropriate monomers, CNF can be adapted and is suitable for many applications.

In the first study, a combination of SET-LRP and a subsequent Cu^I-catalyzed azide-alkyne click chemistry (CuAAC) was employed to functionalize the CNFs, together creating a versatile multifunctional platform for various applications. CNFs were grafted with some random copolymers made of di(ethylene glycol) ethyl ether acrylate (DEGEEA) and acrylic acid 3-trimethylsilyl-prop-2-ynyl ester (TMSPgA) via SET-LRP. TMSPgA was for the introduction of luminescent dyes on the CNF surface via CuAAC, while DEGEEA enhanced the stability of the CNFs in selected solvents (DMSO&H₂O) and acted as a spacer between neighbor luminescent dyes by spacing the reactive clickable monomers.

With the successful fluorescent labeling of modified CNFs, we were able to employ confocal laser scanning microscopy (CLSM) and stimulated emission depletion (STED) microscopy to observe the modified CNFs directly. The study explored the behaviors of CNFs dried from DMSO, and single fibrils, fibril networks, bundles, and clusters could be observed/imaged. Finally, the distribution and morphology of the modified CNFs embedded in a polyvinyl alcohol (PVA) composite (approximately 10 μm thick) were

revealed. This morphology observation, which could not be realized with traditional electron microscopy techniques (SEM, AFM), was possible with the STED.

The second study expanded on the surface modification approach by *in situ* cross-link CNFs with inorganic particles, specifically upconversion nanoparticles (UCNPs) and gadolinium fluoride nanoparticles (GdF₃ NPs). To do this, we explored various surface modification approaches to adapt those NPs to our established surface modification routine for CNFs.

For UCNPs, a two-step ligand exchange strategy was exploited to replace oleic acid (OA) with 2-acrylamido-2-methyl-1-propanesulfonic acid (AMPS), making them suitable for SET-LRP. While GdF₃ NPs, initially stabilized by citric acid in H₂O, were directly surface-modified with 11-phosphoundecyl acrylate (PDA).

In the syntheses of both CNF-based hybrids via SET-LRP, the monomer stearyl acrylate (SA) and the modified nanoparticles were used to surface-modify the CNF. By grafting SA onto CNF surfaces (PSA-CNF), the inter-fibrillar hydrogen bond effect in CNFs decreased, creating CNF individual species that form highly stable suspensions in toluene and could even be redispersible in toluene from a dried state. In addition, PSA-modified CNF gels exhibited favorable rheological properties suitable for 3D gel printing.

For the CNF-based hybrids with UCNPs, the imparted UCNPs preserved their optical characteristics in the CNF matrix, as detected by a confocal microscope and corroborated by emission spectra. The measurement of the confocal microscope revealed the 3D distribution of the UCNPs and individual CNFs inside the network.

Furthermore, Small-Angle X-ray scattering (SAXS) analysis revealed intriguing structural changes in CNFs induced by the cross-linked UCNPs. The SAXS analysis of the CNF-based hybrids revealed a reduced agglomeration compared to the unmodified CNFs and resulted in a higher-ordered arrangement of the cross-linked UCNPs.

For the CNF-based hybrids with GdF₃ NPs, the magnetic resonance imaging (MRI) active properties of GdF₃ NPs were preserved in the gel. MRI relaxivity measurements at 7T demonstrated the potential of this hybrid gel as a novel MRI contrast agent.

USAXS/WAXS measurements confirmed the presence of GdF₃ NPs throughout the sample, displaying a chain-like and disordered arrangement within the modified CNF matrix. GdF₃ NPs were found to be more individually distributed and spaced at larger distances compared with UCNPs, which tended to form spherical aggregates, spreading over relatively shorter distances.

Additionally, the encapsulation of bacteriocin MP1 demonstrated the potential of modified CNF-based hybrid materials with antimicrobial activity. Antimicrobial tests confirmed the effective antimicrobial activity and sustained drug release of the dried CNF-based hybrid gel containing MP1 against the Methicillin-resistant *S. aureus* (MRSA) strain, indicating its potential as a skin wound dressing with customizable size and shape.

Zusammenfassung

Cellulose-Nanofibrillen, kurz CNF, sind biologische und biokompatible Materialien, welche aus erneuerbaren lignocellulosehaltigen Materialien durch unterschiedliche chemische, mechanische oder enzymatische Prozesse gewonnen werden können. CNF, welche durch mechanische Prozesse gewonnen werden, befinden sich typischerweise in wässrigen Medien, und liegen dort als viskose Dispersion vor. Die Oberfläche von CNF ist mit einer Vielzahl an Hydroxygruppen bestückt, was unterschiedliche Folgen hat. Einerseits führen diese zu Nachteilen wie hygroskopischen Eigenschaften, Instabilität in vielen organischen Lösungsmitteln und starken interfibrillären Wasserstoffbindungen, welche wiederum zu einer Aggregation der Fibrillen führen kann. Der große Vorteil ist jedoch, dass über diese Hydroxygruppen zahlreiche chemische Modifikationen ermöglicht werden.

In dieser Arbeit wird eine Oberflächenmodifizierungsstrategie für CNF vorgestellt, bei welcher zuerst CNF in einen CNF-basierten Makroinitiator (CNF-MI) umgewandelt wird und anschließend eine Cu⁰-vermittelte radikalische Polymerisation (SET-LRP) durchgeführt wird. Letztere dient der Pfropfung von Polymeren auf die CNF. Im Anschluss kann eine Cu^I-katalysierte Azid-Alkin-Click-Chemie (CuAAC) eingesetzt werden, um die CNF weiter zu funktionalisieren. Durch diese Kombination zweier chemischer Modifizierungen ergibt sich eine vielseitige multifunktionale Plattform für diverse Anwendungen.

Im Rahmen einer ersten Studie wurden CNF mit zufälligen Copolymeren aus Di(ethylenglykol)ethyletheracrylat (DEGEEA) und Acrylsäure-3-trimethylsilylprop-2-ynylester (TMSPgA) über SET-LRP funktionalisiert. TMSPgA diente dazu, lumineszierende Farbstoffe über CuAAC auf der CNF-Oberfläche zu binden, während DEGEEA die Stabilität der CNF in ausgewählten Lösungsmitteln (DMSO und H₂O) erhöhte und als Abstandshalter zwischen benachbarten lumineszierenden Farbstoffen fungierte, indem es die reaktiven clickbaren Monomere voneinander trennte.

Die erfolgreiche Fluoreszenzmarkierung der modifizierten CNF ermöglichte die direkte Beobachtung der modifizierten CNF mittels konfokaler Laser-Scanning-Mikroskopie (CLSM) und Mikroskopie mit stimulierter Emissionsverarmung (STED). Gegenstand der

Studie war das Verhalten von aus Dimethylsulfoxid getrockneten CNF, einschließlich einzelner Fibrillen, Fibrillennetzwerke, Fibrillenbündel und -cluster. Auch die Verteilung und Morphologie der in einen Polyvinylalkohol-Komposit (ca. 10 μm dick) eingebetteten modifizierten CNF konnte schließlich aufgeklärt werden. Die Beobachtung dieser Morphologie war mit herkömmlichen Methoden der Elektronenmikroskopie, wie beispielsweise dem Rasterelektronenmikroskop (SEM) oder dem Rasterkraftmikroskop (AFM), unmöglich und wurde durch den Einsatz des STED durchgeführt.

Im Rahmen einer zweiten Studie wurde der Ansatz der Oberflächenmodifizierung erweitert, indem die CNF *in situ* mit anorganischen Partikeln vernetzt wurden, insbesondere mit *Upconversion*-Nanopartikeln (UCNP) und Gadoliniumfluorid-Nanopartikeln (GdF_3 NP). Zu diesem Zweck wurden verschiedene Ansätze zur Oberflächenmodifikation untersucht, um diese Nanopartikel in unsere etablierte Oberflächenmodifikationsroutine für CNF zu integrieren. Für UCNP wurde eine zweistufige Ligandenaustauschstrategie angewandt, um Ölsäure (OA) durch 2-Acrylamido-2-methyl-1-propansulfonsäure (AMPS) zu ersetzen, wodurch sie für SET-LRP geeignet wurden. GdF_3 NP, die ursprünglich mit Zitronensäure in H_2O stabilisiert wurden, wurden direkt mit 11-Phosphonoundecylacrylat (PDA) oberflächenmodifiziert.

Die Synthese der beiden CNF-basierten Hybride mittels SET-LRP erfolgte unter Verwendung des Monomers Stearylacrylat (SA) zur Oberflächenmodifizierung von CNF. Durch die Aufpfropfung von poly-SA auf die Oberfläche von CNF (PSA-CNF) konnte der Effekt der interfibrillären Wasserstoffbrückenbindungen in CNF verringert werden. Dies resultierte in CNF-Spezies, die in Toluol hochstabile Suspensionen bilden und im getrockneten Zustand in Toluol redispergierbar sind. Des Weiteren wiesen die PSA-modifizierten CNF-Gele 3D-druckgeeignete rheologische Eigenschaften auf.

Bei den CNF-Hybriden mit UCNP wurden die eingebrachten UCNP in der CNF-Matrix nachgewiesen. Dies wurde durch konfokale Mikroskopie festgestellt und durch Emissionsspektren bestätigt. Die Messungen des konfokalen Mikroskops zeigten die 3D-Verteilung der UCNP und einzelner CNF innerhalb des Netzwerks.

Darüber hinaus zeigte die SAXS-Analyse, dass die vernetzten UCNP eine Veränderung der CNF-Struktur hervorriefen. Diese ging von einer abgeflachten Struktur über in eine

kugelförmige Struktur. Die Agglomeration der PSA-CNF wurde im Verlauf des Prozesses ebenfalls verringert. Der 3D-Druckprozess führte zu einer weiter reduzierten Agglomeration sowie einer erhöhten Ordnung der vernetzten UCNP.

Für die CNF-basierten Hybride mit GdF₃ NP zeigte die Magnetresonanztomographie (MRT), dass die aktiven Eigenschaften der GdF₃ NP im Gel erhalten blieben. MRT-Relaxivitätsmessungen bei 7 T zeigten das Potenzial dieses Hybridgels als neuartiges MRT-Kontrastmittel.

Die Ergebnisse der USAXS/WAXS-Messungen belegen die Präsenz der GdF₃ NP innerhalb der gesamten Probe. Dabei zeigt die modifizierte CNF-Matrix eine kettenartige und ungeordnete Anordnung dieser NP. Die Verteilung der GdF₃ NP war weniger dicht, und die Abstände zwischen den einzelnen Partikeln waren größer als bei den UCNP, die in kugelförmigen Aggregaten organisiert waren, deren räumliche Verteilung über einen kurzen Bereich erfolgte.

Des Weiteren wurde das Potenzial Hybridmaterialien mit antimikrobieller Aktivität durch die Verkapselung des Bakteriocins MP1 aufgezeigt. Die durchgeführten antimikrobiellen Tests bestätigten die wirksame antimikrobielle Aktivität sowie die anhaltende Wirkstofffreisetzung des getrockneten Hybridgels auf CNF-Basis, welches das Bakteriocin MP1 gegen den Methicillin-resistenten *S. aureus*-Stamm (MRSA) enthielt. Dies deutet auf das Potenzial des CNF Hybridgels als Hautwundverband mit anpassbarer Größe und Form hin.

1 Introduction

1.1 Cellulose and nanocellulose

Cellulose is the most abundant biopolymer found in biomass and can be extracted from numerous resources, such as plants, algae, and agricultural wastes or produced by certain types of bacteria¹. It presents several advantages, such as being renewable, biodegradable, non-toxic, and it could be an ideal replacement for fossil fuel resources in the near future².

The building block of the unbranched cellulose homopolymer chain consists of a repeated unit of β -D-glucopyranose molecules, also known as anhydroglucose units (AGUs) (Figure 1. 1). Each AGU unit is rotated by 180° with respect to its neighbors, along the chain axis, and connected together through a chemical bond known as the glycosidic linkage³. The combination of two AGUs is defined as the anhydrocellobiose. Each AGU repeating unit has six carbon atoms with three hydroxy groups located at the C2, C3, and C6 atoms. The cellulose polymer has two types of chemical groups located at each of chain ends: (i) a closed ring structure, with an original C4-OH group at the C4 atom, which constitutes a non-reducing end; (ii) an opened ring structure with an original C1-OH group, with a reversible equilibrium between an aliphatic structure that bears an aldehyde group and a cyclic hemiacetal (Figure 1. 1).

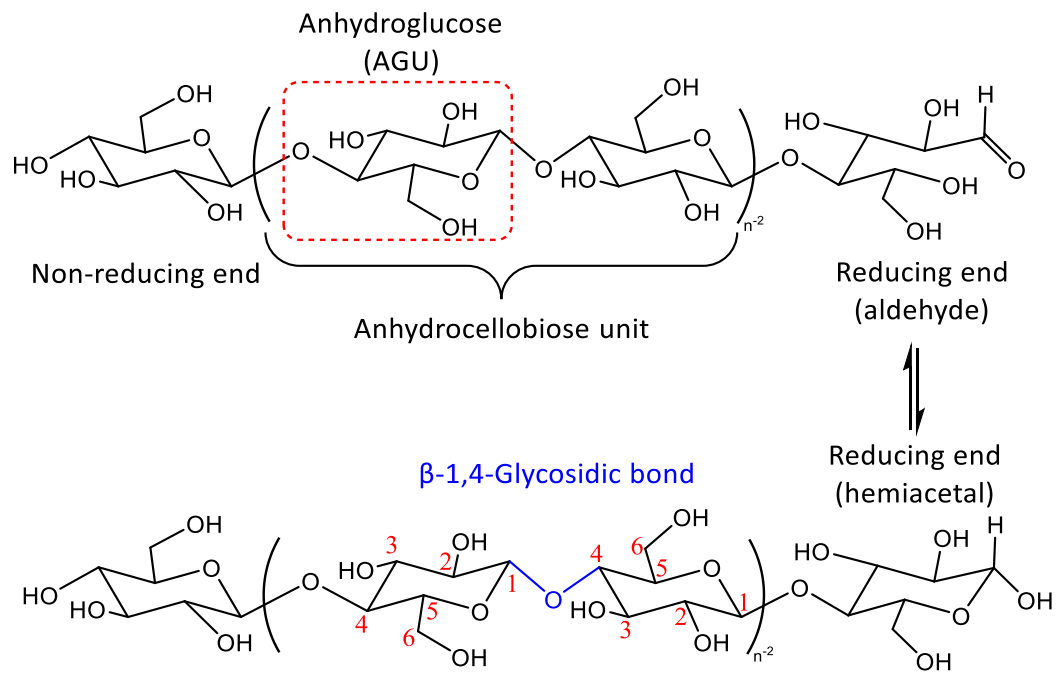


Figure 1. 1 Structure of cellulose molecule, representing the anhydrocellulose unit as the repeating structural, showing the non-reducing end and the reversible equilibrium between hemiacetal and aldehyde groups at the reducing end. The numbering system for carbon atoms in anhydroglucose is indicated in red, and the β -1,4 linkage is indicated in blue.

The large amount of hydroxy groups on the polymer backbone creates strong inter-and intra-molecular interactions through hydrogen bonds (Figure 1. 2). The intra-chain hydrogen bonding induces the high axial stiffness of the linear cellulose polymer, while the inter-chain hydrogen bonding creates a link between the adjacent polymers - forming a 2D sheet.

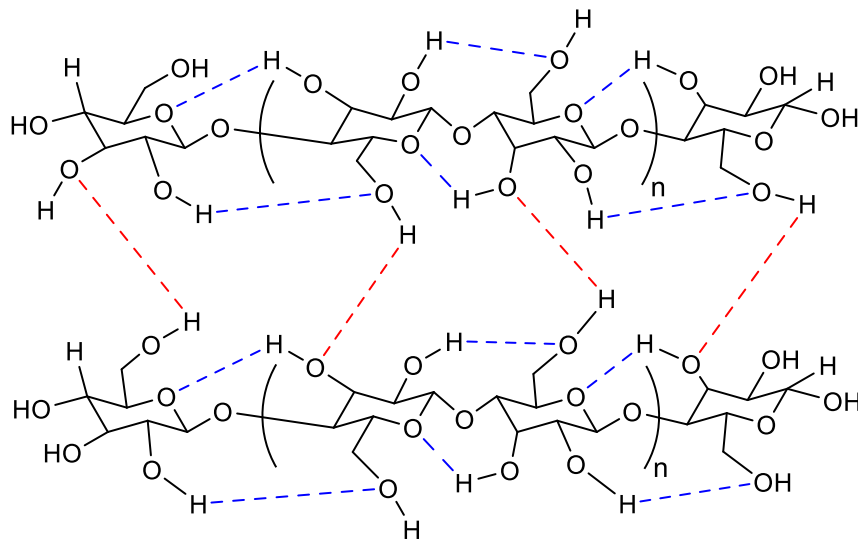


Figure 1. 2 Inter-and intra-molecular hydrogen bonding network in cellulose.

Cellulose is a semi-crystalline polymer that contains both crystalline and amorphous regions. The crystalline domains consist of highly ordered cellulose chains, which are stabilized by extensive intermolecular and intramolecular hydrogen bonds, as well as by Van der Waals forces. The amorphous regions of polymer chains exhibit a lower density and are characterized by twists and torsions. These structural disruptions interfere with the orderly arrangement of the polymer, thereby enhancing its chemical accessibility⁴.

The crystallinity highly depends on the origin and extraction procedures of cellulose fibers. In general, crystalline domains are more resistant to chemical, mechanical, and enzymatic treatments than the amorphous regions.

In conclusion, the intra- and intermolecular interactions and the surface hydroxy groups within cellulose endow it with characteristic properties such as hydrophilicity, degradability, chirality and chemical accessibility, depending not only on its chain length and molecular structure but also on its hierarchical order.

Lately, various forms of cellulose, such as with different crystallites in nano scales, have gained increasing attention due to their specific chemical and physical properties⁵. The following sections will introduce different types of nanocellulose, especially cellulose nanofibrils, and dig into the methods for their production, modification, characterization, and potential applications.

1.1.1 Nanocellulose

The term “nanocellulose” (NC) refers to a cellulosic particle type that usually has at least one dimension - width or length - on the nanometer scale. These particles keep the key cellulose properties, including hydrophilicity, extensive chemical-modification capability, and the ability to form versatile semi-crystalline fiber morphologies.

Nanocelluloses can be classified into different forms based on their sources, preparation methods, and dimensions.

Considering the sources, NC can be categorized into plant-derived nanocellulose and bacterial-based nanocellulose (BNC) (Figure 1. 3)⁶. Plant-derived nanocellulose is more prevalent compared to BNCs as they are obtained through the mechanical disintegration of cellulose fibers into the nanoscale structure, a method known as the top-down approach, whereas BNC is produced through a bottom-up process wherein nanofibrils are built up from low molecular weight sugars by *Gluconacetobacter* bacteria strains.

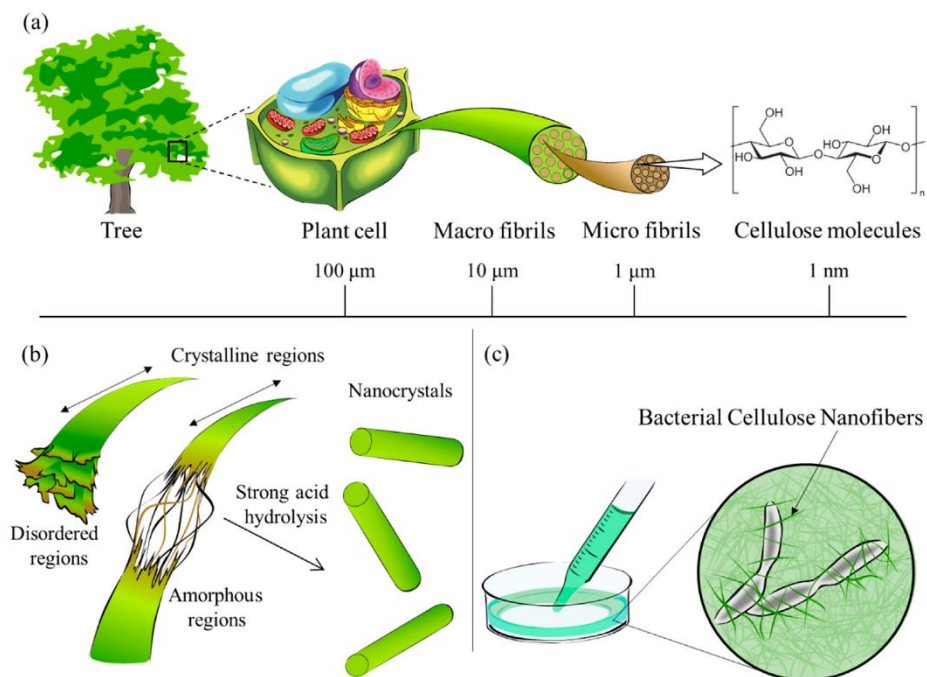


Figure 1. 3 (a) Cellulose contained in plants or trees has a hierarchical structure from the meter to the nanometer scale; (b) schematic diagram of the reaction between cellulose and strong acid to obtain nanocellulose; (c) bionanocellulose cultured from cellulose-synthesizing bacteria⁷. Copyright 2020 Nanomaterials, with permission of MDPI.

BNC is derived from biochemically activated dextrose within bacterial bodies through a cellulose-synthesizing complex associated with the surface pores of bacterial cells⁸. Typically, BNC has a typical diameter ranging from 20 to 100 nm and a length greater than 10 μm . In addition, BNC is composed of pure cellulose, free from functional groups, such as carbonyl groups, as well as other polymers like hemicellulose and lignin. These characteristics make them particularly advantageous for biomedical applications^{9,10}.

According to the standardization of cellulose nanomaterials definitions established by the Technical Association of the Pulp and Paper Industry (TAPPI), cellulose nanomaterials can be divided into nanostructured materials and nano-objects based on their dimensions (Figure 1. 4). The nanostructured materials are categorized into cellulose microcrystals and cellulose microfibrils. However, the cellulose nanofibers are sub-grouped into: (a) cellulose nanofibrils (CNFs), previously known as nanofibrillated cellulose or microfibrillated cellulose and (b) cellulose nanocrystals (CNCs), previously known as cellulose whiskers.

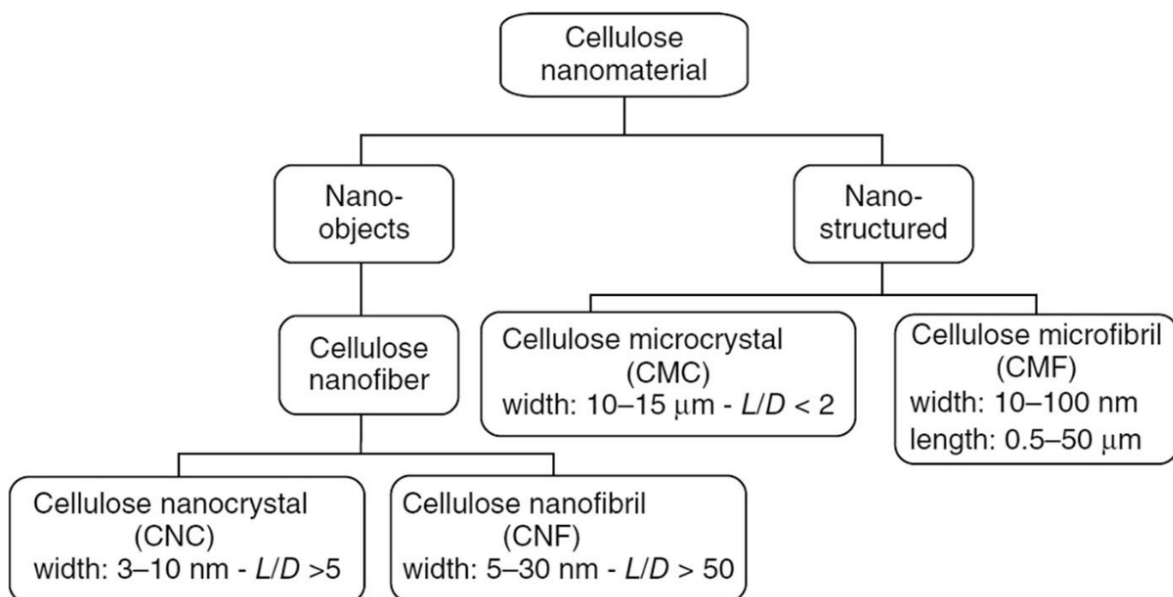


Figure 1. 4 Standard terms for cellulose nanomaterials (TAPPI WI 3021)¹¹. Copyright 2018 Cellulose, with permission of Springer Nature. This figure is adapted from Mariano *et al.*¹², Copyright 2014 Journal of Polymer Science Part B: Polymer Physics, with permission of John Wiley and Sons.

1.1.1.a Cellulose nanocrystals (CNCs)

The extraction of CNCs from cellulosic materials can be divided into two main categories (Figure 1.5). Firstly, the raw material is pretreated to isolate the cellulosic pulp by entirely or partially removing the matrix materials, such as hemicellulose and lignin, from wood and plants. The second stage involves a controlled chemical treatment, typically hydrolysis, to remove the amorphous regions of the cellulose polymer.

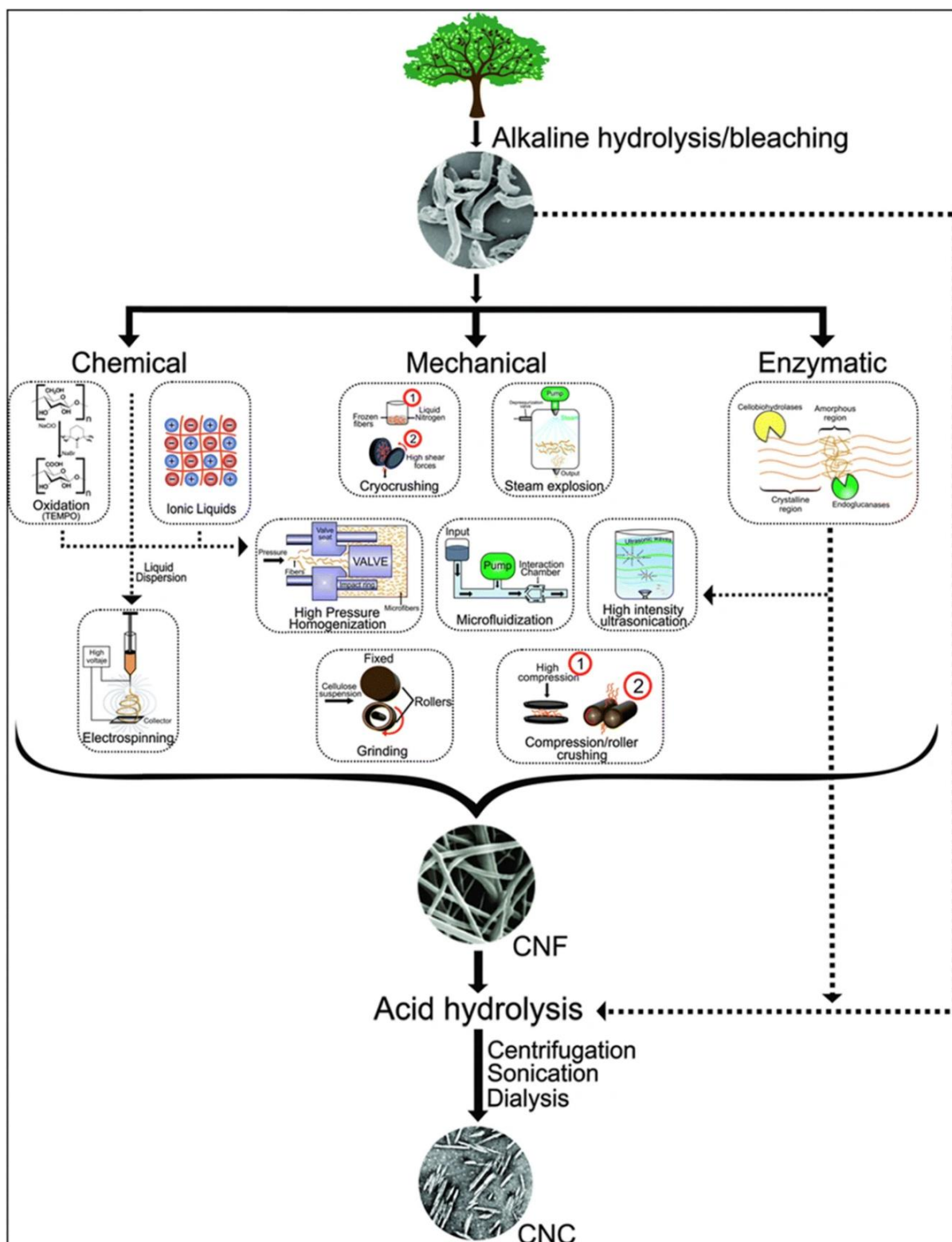


Figure 1. 5 Schematic illustrations of recent processes to produce CNFs and CNCs from lignocellulosic materials¹³. Copyright 2015 Cellulose - Fundamental Aspects and Current Trends, with permission of InTech.

CNCs can also be directly extracted from CNFs via acid hydrolysis¹⁴. Owing to the stability of the resulting suspensions, acid hydrolysis is still a common choice to treat purified cellulosic materials^{15,16}. Hydrochloric and sulfuric acids are the two commonly used acids for CNC extraction, resulting in different surface characteristics of CNCs. Particles are, however, more negatively charged with H₂SO₄ than HCl, as H₂SO₄ can functionalize glucose units with sulfate ester groups; the repulsive forces created by those charged groups render CNCs with a higher dispersibility and stability in water¹⁷.

The obtained CNCs have high crystallinity and exhibit rod-like shapes (Figure 1. 11 d-f) with relatively limited flexibility as they do not contain amorphous regions. The dimensions, morphologies, and crystallinity degree of CNCs depend on the source of the cellulosic material, the production conditions, and the experimental techniques. In addition, since the cleaving of cellulose chains via acid hydrolysis occurs randomly, the dimensions of CNCs are not uniform. For instance, CNCs obtained from cotton have a width of 5-10 nm and a length of 100-200 nm¹⁸. CNCs from softwood pulp, upon the acid-to-pulp ratio and time of hydrolysis, have widths of 4-5 nm and lengths ranging from 100-160 nm¹⁹. Studies have reported that CNCs derived from tunicate and bacterial cellulose generally have larger dimensions than those obtained from wood and cotton. This is due to the higher crystallinity of tunicate and bacterial cellulose, resulting in lower cleaving of amorphous domains and, therefore, larger nanocrystals^{20,21}.

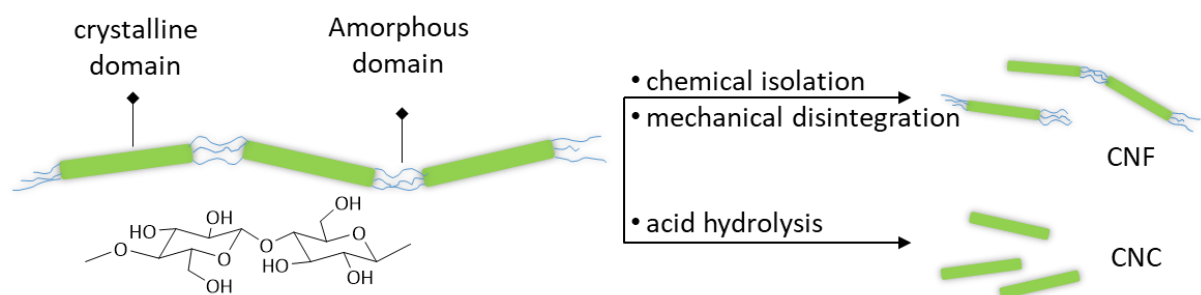


Figure 1. 6 The crystalline and amorphous structures of cellulose.

1.1.1.b Cellulose nanofibrils (CNFs)

The production of cellulose nanofibrils dates back to the 80s, according to Turbak *et al.*²² and Herrick *et al.*²³. They produced a gel-like cellulosic material by passing softwood pulp through a mechanical refiner and a high-pressure homogenizer. When subjected to high shearing forces, the resulting CNFs exhibit strongly entangled networks encompassing

crystalline and amorphous domains. Typically, CNFs (Figure 1. 12) defibrillated through mechanical treatments have a width of 5-30 nm and a length of several micrometers²⁴. An in-depth review of CNF production is presented in the following section.

1.1.2 Production of cellulose nanofibrils

Cellulose from wood and plants is combined with hemicellulose and lignin. In general, for CNF production, the raw material undergoes several cooking and bleaching treatments, similar to those in the papermaking industry. The isolated cellulosic materials are sequentially broken down into microscale to nanoscale objects by combinations of different operations, typically mechanical disintegration process, enzymatic or chemical treatments (Figure 1. 7).

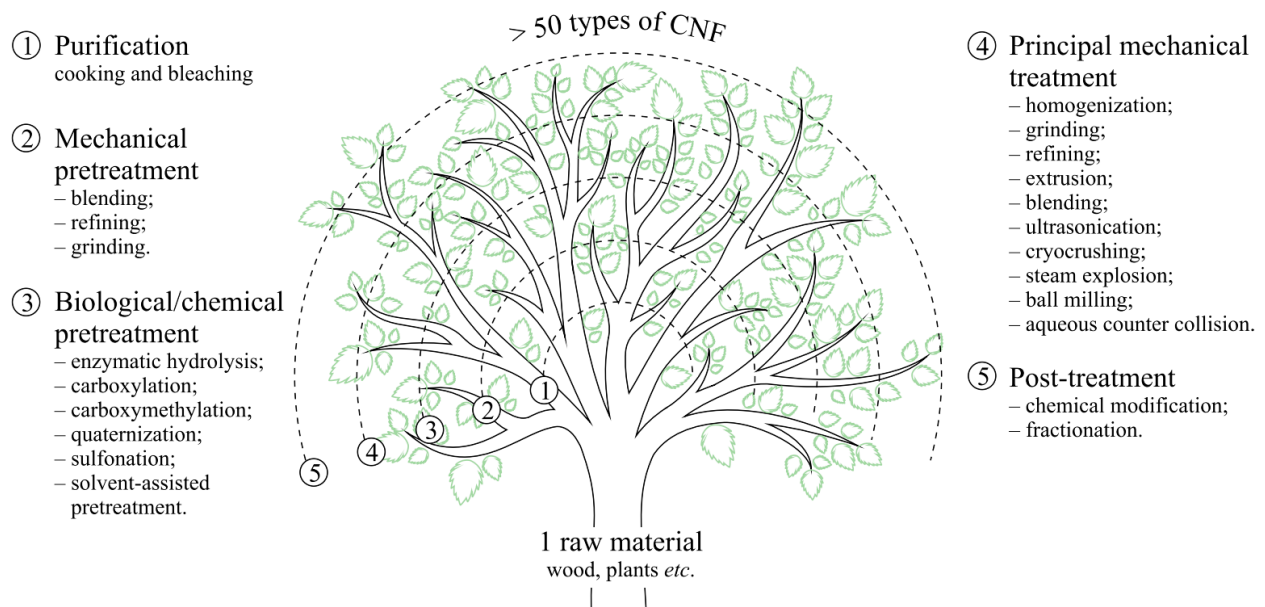


Figure 1. 7 Schematic diagram of CNF production². Copyright 2016 Industrial Crops and Products, with permission of Elsevier.

1.1.2.a Mechanical disintegration

To delaminate the nanofibrils successfully, it is essential to surpass the interfibrillar hydrogen bonding energy of cellulose rather than merely cutting the fibrils. CNFs are commonly produced in an aqueous medium that loosens the interfibrillar hydrogen bonds. Mechanical methods can be employed to break down dry cellulose pulp into small fragments, but this often results in fiber shredding instead of elementary fibril

delamination, which leads to CNFs with low DP, crystallinity, and aspect ratio, consequently leading to poor mechanical properties of products.

Mechanical treatments are usually employed for industry production of CNFs due to their high efficiency in delaminating fiber cell walls and isolating CNFs, as well as their suitability for up-scaling²⁵. There are three commonly used techniques: high-pressure homogenization, micro-fluidization, and micro-grinding.

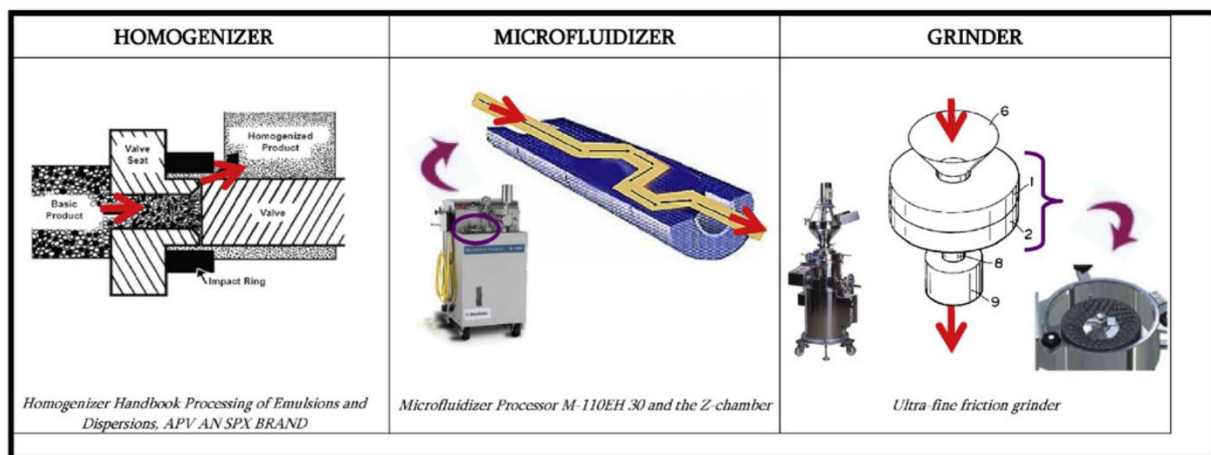


Figure 1. 8 The most applied mechanical treatment processes used in fabricating CNFs are the homogenizer, the microfluidizer and the grinder²⁶. Copyright 2012 Carbohydrate Polymers, with permission of Elsevier.

High-pressure homogenization (HPH) is the first and widely used method for producing CNFs from wood-based fibers^{22,23}. The strong mechanical shearing, combined with the high pressure, initiates the fibrillation of fibers. A cellulose slurry enters a spring-loaded valve area at high pressure and low velocity (Figure 1. 8). The pressure is applied when the valve shifts between the impact head and the passage head repetitively. Meanwhile, the fibers are subjected to a rapid pressure drop with high shear and impact forces generated in the microsized zone and disintegrated into CNFs. The homogenized fibers are directed towards the impact ring, where they stay at sufficient pressure for moving to the subsequent stage.

The application of these forces results in a significant degree of micro-defibrillation of cellulose fibers. Cellulose fibrillation can be extended to multiple homogenization cycles as well as various levels of pressure. As the pressure increases, so does the disruption

efficiency per pass through the equipment. This process is also scalable and operates continuously. The downside of this technique is the substantial energy consumption (over 25 MWh·t⁻¹) and the clogging issue, particularly at the in-line valves²⁷.

Microfluidizers are an alternative to high-pressure homogenizers. Other than homogenizers that operate at a steady pressure, microfluidizers maintain a consistent shear rate. The cellulose aqueous suspension is passed through narrow chambers with a specific geometry, such as a Z or Y shape (Figure 1. 9), and an orifice width ranging from 100-400 μm under high pressure. This generates strong shear forces and promotes cellulose fibrillation as the suspension collides with the channel walls. At the end of the process, a heat exchanger cools down the product stream to ambient temperature. To improve the degree of fibrillation, the process can be repeated multiple times, and chambers of varying sizes can be utilized.

Moreover, the absence of in-line moving parts in this process lowers the probability of clogging. However, to prevent clogging by long fibers, it is necessary to pre-treat the cellulose suspension. Despite its potential, the high energy consumption of up to 70 MWh·t⁻¹ has been a significant obstacle to its commercial viability for an extended period^{28,29}.

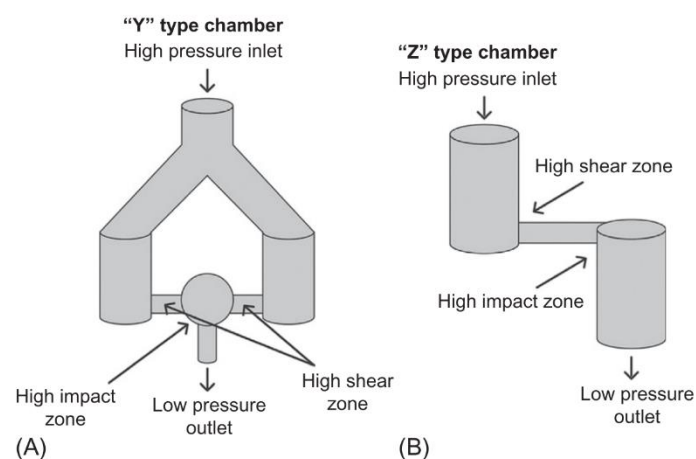


Figure 1. 9 (A) Y-type interaction chamber and (B) Z-type interaction chamber³⁰. Copyright 2018 Nanoemulsions, with permission of Elsevier.

The grinding process involves forcing cellulose slurries through a gap between a static and a rotating grindstone at around 1500 rpm (Figure 1. 8). This generates shearing

forces that break down cell wall structures and hydrogen bonds, liberating nanofibers in a multilayered structure. The degree of fibrillation depends on several factors, such as the gap between the two discs, the disc channel morphology, and the number of passes through the grinder. Micro-grinding does not suffer from clogging problems and is considered less energy-intensive than the two previous methods²⁹. However, frequent disk maintenance and replacement are the primary drawbacks of this technique due to rapid wear-out.

Apart from homogenization and grinding methods, various other processing techniques, such as refining³¹, extrusion^{32,33}, cryocrushing^{34,35}, and ultrasonification^{36,37} are currently being developed. These methods aim to isolate and refine CNFs further and enhance their properties.

1.1.2.b Pre-treatment for CNF production

Two common issues have plagued the manufacturing of CNFs from wood pulp: (i) clogging, when the pulp is pumped through high-pressure fluidizers/homogenizers; (ii) substantial energy consumption, mainly due to multiple passes through the disintegration device to achieve efficient delamination of cell walls. This energy is necessary to overcome the interfibrillar hydrogen bonds and liberate CNFs. As a result, the development of less energy-intensive disintegration methods has become a top priority for securing the industrialization of CNF production. Pre-treatments have been employed to tackle this issue.

To reduce the energy required for fibrillation, various approaches have been suggested to obtain less rigid and cohesive fibers. Three alternatives have been proposed: mechanical, chemical and enzymatic pre-treatments.

Mechanical pre-treatment

Mechanical pre-treatment methods are employed to pre-fibrillate cellulose fibers and reduce their size to facilitate disintegration. Mechanical refining is often applied before homogenization to promote defibrillation and decrease energy consumption. Various methods, such as manual cutting³⁸, disc refiners³⁹, PFI mills⁴⁰, and Valley beaters⁴¹, have been reported for CNF production. On a laboratory scale, the PFI mill and Valley beater

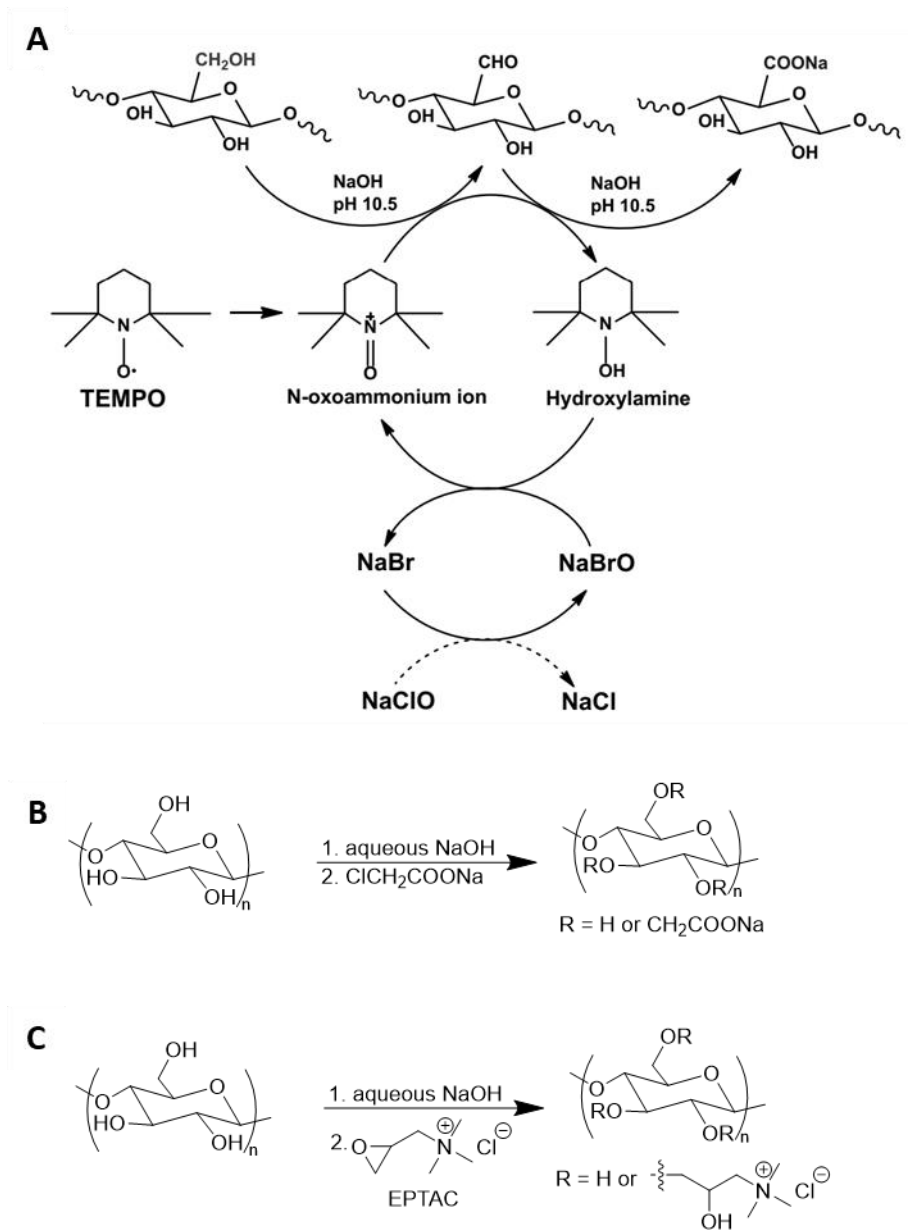
are frequently employed for pulp refining^{38,39,42}. The PFI mill, while it consumes a significant amount of energy, is considered a low-intensity refiner that processes pulps between an inner roll and an outer bedplate; conversely, the Valley beater requires larger pulp samples and has a longer operating time²³.

The beating process involves looping the pulps around a wall and forcing them between a rotor and a loaded bed plate. During the refining process, repeated cyclic stresses are subjected to cellulose fibers to peel off external cell walls and expose the secondary layer for sequential fibrillation, e.g., homogenization^{23,43}. However, mechanical refining can also damage the microfibril structure by reducing the polymer molecular mass and its crystallinity degree.

However, the energy consumption of these methods leads to increased manufacturing costs for CNFs. For instance, it was reported that the effective energy consumption in a Valley beater for bleached eucalyptus and bleached pine was about 0.482 and 0.578 MWh·t⁻¹, respectively, with a total beating time of 1 h. In addition, a 3 h beating process produced cellulose microfiber with a diameter of 0.24 μm from cellulose fibers with a diameter of 30 μm consumed about 2 MWh·t⁻¹^{29,44}. Similarly, a PFI mill required an estimated energy consumption of up to 2.7 MWh·t⁻¹ to generate cellulose microfibrils with a diameter of 1.3 μm from bleached softwood kraft pulp with a diameter of 13 μm⁴⁵. Therefore, the development of low-energy mechanical pre-treatment techniques can help reduce the overall energy consumption for CNF production. Furthermore, these mechanical pre-treatment processes produce wet cellulose precursors, which can be challenging to store and handle due to their large volume.

Chemical pre-treatment

A more promising approach for facilitating the extraction of CNFs involves the use of chemical treatments, such as 2,2,6,6-Tetramethylpiperidine-1-oxyl (TEMPO)-mediated oxidation, carboxymethylation, and quaternization (Scheme 1. 1).



Scheme 1. 1 Chemical pre-treatments of CNF productions: (A) TEMPO-mediated oxidation, adapted from ref ⁴⁶, Copyright 2019 Cellulose, with permission of Springer Nature. (B) carboxymethylation, (C) quaternization.

TEMPO-mediated oxidation is a well-studied chemical pre-treatment method used in the production of CNFs. The pioneering work of Saito *et al.*⁴⁷ demonstrated the efficacy of this technique in releasing CNFs from never-dried cellulose fibers and facilitating low-energy mechanical disintegration of oxidized fibers in aqueous suspensions. The oxidation reaction is typically carried out at room temperature for several hours on cellulose fibers from diverse sources, such as wood pulp, cotton linters, tunicate and bacterial cellulose⁴⁸.

The mechanically disintegrated CNFs, pretreated with TEMPO-mediated oxidation, have a uniform width of 3-5 nm and can be easily separated into individual nanofibrils⁴⁹.

The basic principle of TEMPO-mediated oxidation involves using the nitrosonium ion ($+N=O$), which is generated *in situ* through the reaction of TEMPO radical with the oxidants to oxidize the hydroxy groups of the cellulose fibers (Scheme 1. 1 A). In an aqueous environment, TEMPO catalyzes the conversion of C6 primary alcohols to carboxylate (COO^-) functionalities in the presence of a primary oxidizing agent, e.g., sodium hypochlorite ($NaOCl$).

Compared to the energy usage of a high-pressure homogenizer, TEMPO-mediated oxidation pre-treatment was shown to decrease the consumption dramatically by a factor of more than 100⁵⁰. Several benefits have been demonstrated in using TEMPO-mediated oxidation for the delamination process, such as:

- (a) negatively charged carboxyl groups are induced to create repulsive forces between cellulose fibers, which loosens the cohesion of microfibrils;
- (b) the oxidation makes the inner cell wall more accessible and prone to fibrillation by loosening the primary cell wall;
- (c) TEMPO oxidation increases the hydration and swelling of cellulose fibers, which increases their flexibility and also enhances the accessibility of crystalline domains;
- (d) chain scission in the amorphous region due to oxidation creates defects within the cell wall, facilitating delamination.

However, there are also some drawbacks associated with this process, such as the difficulty of upscaling the reaction to an industrial level, the potential environmental impact of chemical reagents used, and possible economic limitations related to large-scale production.

The carboxymethylation process is another commonly used chemical pre-treatment. This process increases the anionic charges on cellulose surfaces by inducing carboxyl groups, which was first applied to CNF production by Wågberg *et al.*⁵¹. Carboxymethylation,

through the Williamson reaction, is a simple and cost-effective method that involves activating fibers with alkali hydroxide, typically with sodium hydroxide, followed by treatment with monochloroacetic acid to introduce carboxymethyl groups (Scheme 1. 1 B).

Introducing charged groups to cellulose fibers enhances their delamination by creating repulsive electrostatic forces between fibers. Additionally, carboxymethylation leads to fiber swelling, and carboxymethyl groups should be in the form of their sodium salts to maximize the swelling of cellulose fibers²⁴. This leaves the highly charged fibers, thus making them more accessible to liberate. It was reported that with the carboxymethylation pre-treatment, the energy consumption of homogenization can be significantly reduced from 27 MWh·t⁻¹ to 0.5 MWh·t⁻¹⁵¹. Moreover, cellulose nanofibrils with a diameter of 5-10 nm were successfully obtained with only one pass through a high-pressure fluidizer^{52,53}.

Additional chemical pre-treatments can be carried out on cellulose fibers to modify their surface charge and improve their disintegration process. For example, carboxylation^{49,54} and sulfonation⁵⁵ can be used to introduce strong anionic groups onto the surface of the fibers, while quaternization^{56,57} can cationize the surface. By modifying the surface charge in these ways, the fibers are made to repel each other electrostatically, which in turn weakens the hydrogen bonding and van der Waals interactions between them. This makes the pulp disintegration process easier and more efficient.

Chemical pre-treatment methods have some significant drawbacks. Firstly, they require various chemicals and organic solvents, which can harm the environment and pose health risks. As mentioned above, TEMPO oxidation and carboxymethylation use sodium hypochlorite or sodium chlorite and toxic halocarbon reactants, respectively. It is reported that CNFs produced via the carboxymethylation route have the highest environmental impacts due to the large use of solvents made from crude oil⁵⁸. Moreover, the introduction of functional groups like carboxyl and carboxymethyl groups can decrease the thermal stability of cellulose due to decarbonization^{59,60}. Additionally, CNFs produced by these methods are typically more hydrophilic, which may limit their applications in nonpolar media⁶¹.

Enzymatic pre-treatment

Enzymatic pre-treatment has gained attention in the production of CNFs owing to its potential to mitigate certain drawbacks of chemical pre-treatment. This approach offers the promise of reducing environmental impact, as well as cutting down on the chemical and energy expenses required for subsequent mechanical disintegration processes. As an emerging method, enzymatic hydrolysis presents several advantages over mineral acid hydrolysis by avoiding the generation of toxic residues. Operating under mild thermal and pressure conditions, enzymatic hydrolysis stands out as a less energy-intensive process.

Enzymatic methods do not alter cellulose substantially, primarily targeting the amorphous regions of cellulose fibers using cellulases⁶². Cellulases are a group of enzymes that catalyze the hydrolysis of cellulose, breaking down the complex polysaccharide into simpler sugars. Commercial cellulases are the most widely used enzymes for this purpose, comprising three main groups (Figure 1. 10):

- (a) endoglucanases, which cleave randomly at internal amorphous sites within the cellulose polysaccharide chain, yielding oligosaccharides of varying lengths and thereby creating new chain ends;
- (b) cellobiohydrolases (or exoglucanases), which act on reducing or nonreducing ends, creating cellobiose or glucose; they can also act on microcrystalline cellulose, peeling cellulose chains from the microcrystalline structure;
- (c) glucosidases, which break down soluble cellodextrins and cellobiose into glucose⁶³.

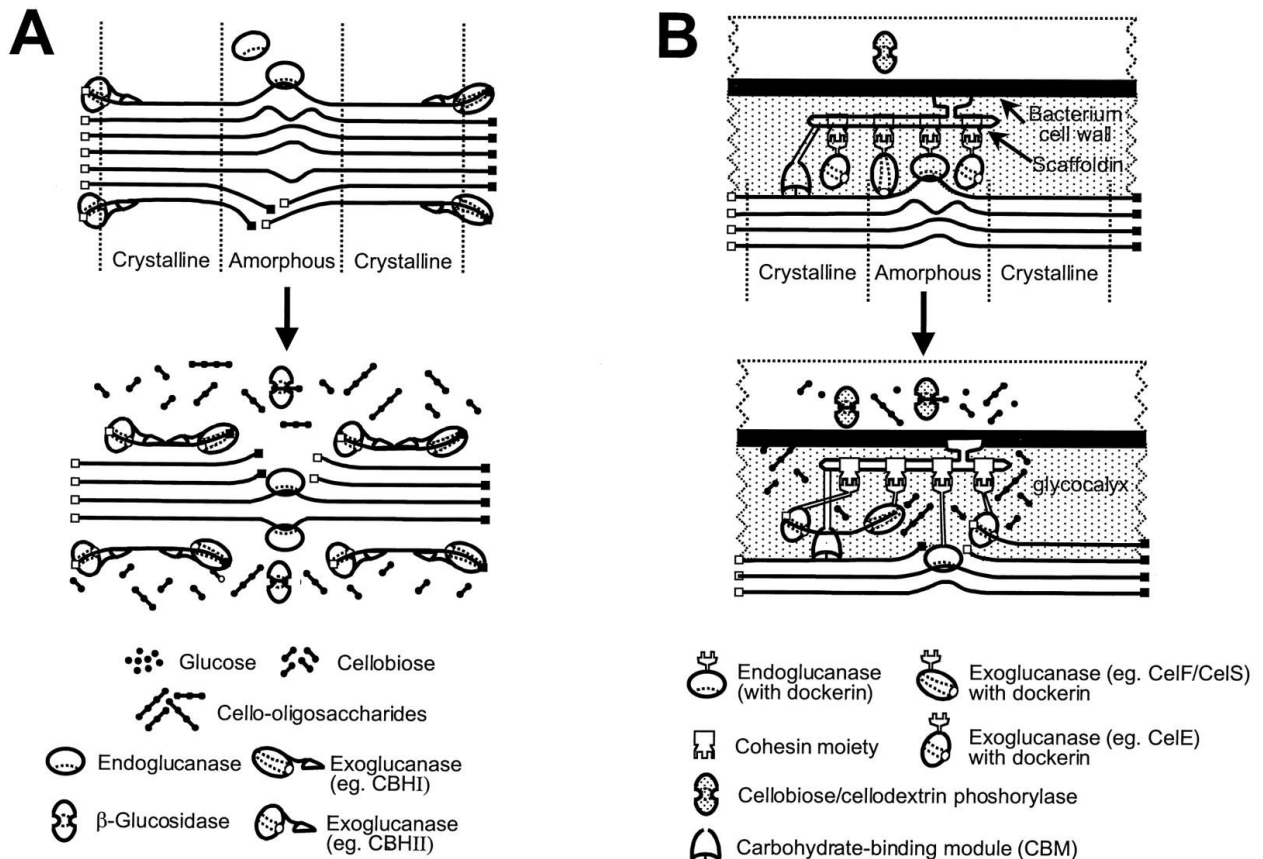


Figure 1.10 Schematic illustration of the hydrolysis of amorphous and microcrystalline cellulose by (A) noncomplexed and (B) complexed cellulase systems. The solid squares represent reducing ends, and the open squares represent nonreducing ends⁶³. Copyright 1997 Microbiology and molecular biology reviews: MMBR, with permission of American Society for Microbiology.

A study compared CNF production using a high-pressure homogenizer with and without prior enzymatic pre-treatment using endoglucanases⁶⁴. It revealed that enzymatic hydrolysis significantly enhanced the homogeneity of the resulting products. Mechanical disintegration alone encountered severe blockage issues during homogenization, leading to inadequately homogeneous materials. Moreover, milder enzymatic hydrolysis facilitated a higher aspect ratio, resulting in a stronger gel network compared to more aggressive acid hydrolysis. Additionally, pre-treatment with low concentrations of endoglucanase facilitated the disintegration of wood pulp into cellulosic nanofibers while preserving molecular weight and fiber length⁶⁵.

However, enzymatic pre-treatment may incur higher costs due to the use of expensive enzymes, potentially elevating the overall cost of CNF production. It also requires careful control of reaction conditions, such as pH, temperature, and reaction time, to ensure

optimal enzyme activity and prevent enzyme deactivation or substrate degradation. Furthermore, the enzymatic pre-treatment process is typically slower than chemical pre-treatment, potentially limiting production scale and throughput. Lastly, enzymatic pre-treatment may not be universally applicable to all cellulose sources and may require optimization for each specific source.

1.1.2.c Post-treatment

Despite the array of pre-treatment methods available, the utilization of post-treatment techniques in CNF production remains relatively limited. The objectives of the two treatments are distinct: while pre-treatments target reducing energy consumption during CNF production, post-treatments are geared towards enhancing CNF properties or improving their compatibility for specific applications. To extend the usage of CNFs in further applications, it is important not to overlook the intrinsic deficiencies of CNFs. One of the main challenges brought by the surface hydroxy groups is poor dispersibility in water and most organic solvents and irreversible agglomeration after drying, also known as hornification⁶⁶. This occurs due to the strong hydrogen bonds between adjacent cellulose molecules, causing the cellulosic fibrillar strands to lose their flexibility and conformability.

Post-treatments can be categorized into physical and chemical modifications. Physical treatments involve the use of thermal and mechanical methods to adjust CNF concentration or solvent, including techniques such as filtration, freeze-drying, centrifugation, solvent exchange, or the incorporation of various additives.

Chemical modifications, on the other hand, include molecular substitution or polymer grafting, aiming to impart new properties to CNF with or preserve their intrinsic characteristics. These modifications may, for instance, enhance the compatibility of CNF with nonpolar solvents and polymeric matrices in composite applications or prepare solvent-redispersible CNFs. The focus of this work lies in exploring chemical modification strategies, which will be discussed in detail later on.

1.1.3 Properties and characterization of cellulose nanofibrils

As previously mentioned, CNFs possess several nano-specific properties that distinguish them from traditional cellulosic materials. These properties encompass their diminutive size, with diameters ranging from three to several hundred nanometers, as well as their high aspect ratio and extensive specific surface area. However, achieving unambiguous characterization of CNF poses challenges due to their heterogeneous nature and considerable variability arising from different raw materials, pre-treatments, and processing methods. For instance, Young's modulus of CNF can vary widely, spanning from 13 to 180 GPa, depending on these factors⁶⁷. Given that CNF consists of fibers, fibrils, and fibril aggregates with varying dimensions and a high degree of entanglement, comprehensive characterization cannot be accomplished through a single method. Instead, a combination of methods that operate on several dimensional scales is required.

In a review by Kangas *et al.*⁶⁸, various characterization methods were evaluated, leading to the conclusion that the most effective combination for assessing the fundamental properties of CNF includes microscopic examination to observe the appearance, morphology, and size of CNF fibrils, apparent viscosity measurement as a rapid means of evaluating rheological properties, and transmittance measurement to analyze particle/fibril size distribution. They emphasized that visual analysis via light and electron microscopy remains the primary characterization method that should always be incorporated in CNF evaluation despite its drawbacks, such as being time-consuming and reliant on subjective assessment of small areas from a larger sample⁶⁸.

1.1.3.a Morphology

Various characterization techniques can be employed to determine the shape and size of CNFs. Recent research by Mao *et al.*⁶⁹ investigated the use of scattering techniques, such as small-angle neutron scattering (SANS), small-angle X-ray scattering (SAXS), and dynamic light scattering (DLS). While SANS and SAXS provided consistent information regarding particle cross-section and revealed the crystalline structure of cellulose down to the exact atomic positions of the polymers in the unit cell, they could not provide length measurements and a full understanding of the structure and assembly of nanocellulose

fibrils. Moreover, DLS data only offered apparent sizes without actual length and diameter values⁷⁰.

Microscopic techniques at varying magnifications are essential for examining the appearance, morphology, dimensions, and shapes of NC. Optical microscopy offers a quick overview of the fibrillated material, including its appearance and homogeneity. Microscopy techniques such as scanning-, transmission electron microscopies (SEM and TEM) and atomic force microscopy (AFM) are better suited for size and morphology determination due to their high resolution.

AFM works by moving a sharp tip over the sample surface and measuring the interaction forces between the tip and the surface to provide a high-resolution topographic image with good thickness resolution capable of imaging at the nanometer scale. AFM can offer quantitative information on the height, diameter and roughness of surface NC. However, the measurement is time-consuming and limited to surface imaging, thus having poor lateral resolution, hindering length measurements. Additionally, AFM specimen preparation is challenging due to the irregular shape and polydisperse nature of NC, often requiring manual or semi-automated microscopy analyses to ensure accurate statistical analysis⁷¹.

SEM, on the other hand, scans a focused beam of electrons across the sample surface, and the interaction between the electrons and the sample generates various signals to create an image. When employed with field emission electron source (FESEM), it is advantageous for studying the morphology of NC due to its high-resolution imaging capabilities, versatility in sample analysis, and real-time observation, such as fibril arrangement, dimensions and distribution, providing valuable insights into cellulose structure at the micro- and nanoscale. However, the limitations of FESEM include the need for sample coating, which can potentially introduce artifacts, as well as a limited depth of field and resolution constraints, impacting the accurate quantification of surface features and the visualization of cellulose nanostructures. Cryo-SEM is a specialized technique that combines SEM with cryogenic sample preparation methods, allowing for the imaging of samples in a frozen-hydrated state. In Cryo-SEM, the sample is rapidly frozen, preserving its native structure and preventing artifacts associated with conventional sample preparation techniques, such as dehydration or distortion.

In TEM, a beam of electrons is transmitted through a thin specimen, facilitating imaging of the internal structure and morphology of Ns with the highest resolution among all three techniques introduced. TEM allows for rapid analysis of NCs in solution or embedded in soft matter. However, the challenge of low contrast in TEM images of NC hampers their adequate morphological characterization and size determination. To address this, uranyl acetate staining, a widely adopted methodology in the biological field, has been applied to the analysis of cellulose-based nanomaterials⁷²⁻⁷⁴. Nevertheless, issues such as particle aggregation and grid conditions have resulted in poor-quality images and unreliable size measurements⁷⁵. To overcome these challenges, efforts have been directed towards developing improved sample preparation methods for TEM imaging. Da Silva *et al.*⁷⁵ presented a protocol for cost-effective and readily available guidelines to enhance TEM imaging by modifying the standard uranyl acetate protocol and aspect ratio calculation of cellulose-based nanomaterials.

Depending on the source of cellulose and the production method, CNFs exhibit similar morphologies but vary in dimensions. For example, Yang *et al.*⁷⁶ used TEM to study NC isolated from corn husks via various methods. They reported that acid-hydrolyzed nanocellulose had an average diameter of 26.9 ± 3.35 nm and an average length of 162 ± 35.9 nm, while TEMPO-NC and ultrasonicated NC exhibited interconnected webs with slender nanofibrils. The average diameter of TEMPO-NC and ultrasonicated NC are 10.48 ± 1.83 nm and 20.14 ± 4.32 nm, respectively, with lengths ranging from several hundred nanometers to micrometers.

Figure 1. 11 presents overview images of three different nanocellulose systems- wood CNF (w-CNF), wood CNC (w-CNC) and bacterial CNC (b-CNC)- acquired via AFM, Cryo-SEM and TEM⁷⁷. Notably, w-CNFs exhibit a relatively consistent cross-section with a narrower width range compared to w-CNC and b-CNC. While w-CNFs display plenty of bends, the CNC samples appear rather straight. In contrast to w-CNC, the b-CNC sample has longer lengths ranging from 1-5 μ m and irregular widths spanning 10-50 nm⁷⁷.

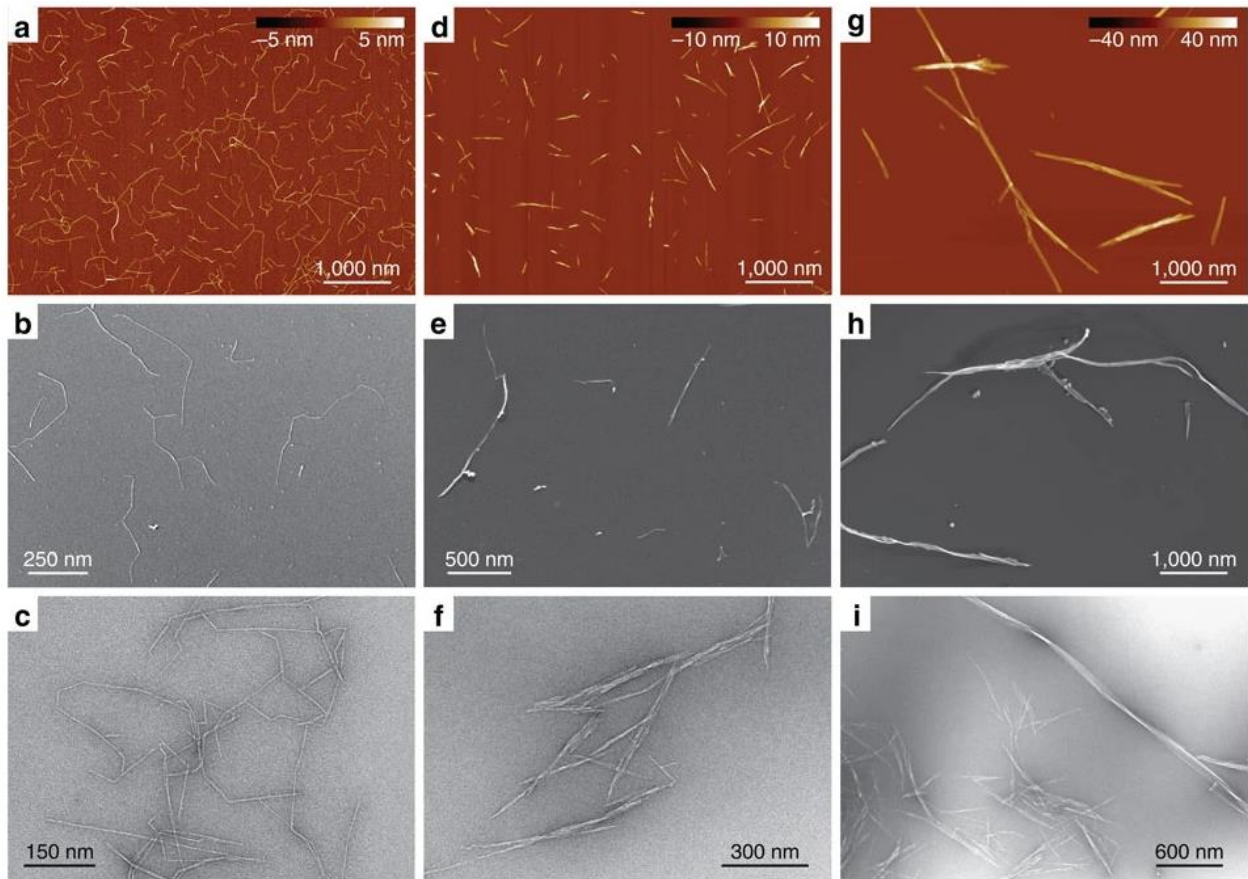


Figure 1. 11 Overview microscopic images of NC: (a-c) TEMPO-mediated oxidized w-CNF, (d-f) w-CNC and (g-i) b-CNC samples via AFM (a,d,g) Cryo-SEM (b,e,h) and TEM (c,f, i). All AFM images have the same magnification in order to provide a direct comparison between nanocellulose particles⁷⁷. Copyright 2015 Nature Communications, with permission of Springer Nature.

CNFs produced through mechanical disintegration with enzymatic pre-treatment typically exhibit greater thickness, length and highly entangled flocculated structure compared to those obtained via chemical pre-treatments (Figure 1. 12)⁷⁸. Chemical pre-treatment yields CNFs have lower lateral dimensions, and reduced length, which are usually well dispersed and more colloidally stable, although some microstructural physical entanglements may persist⁷⁸.

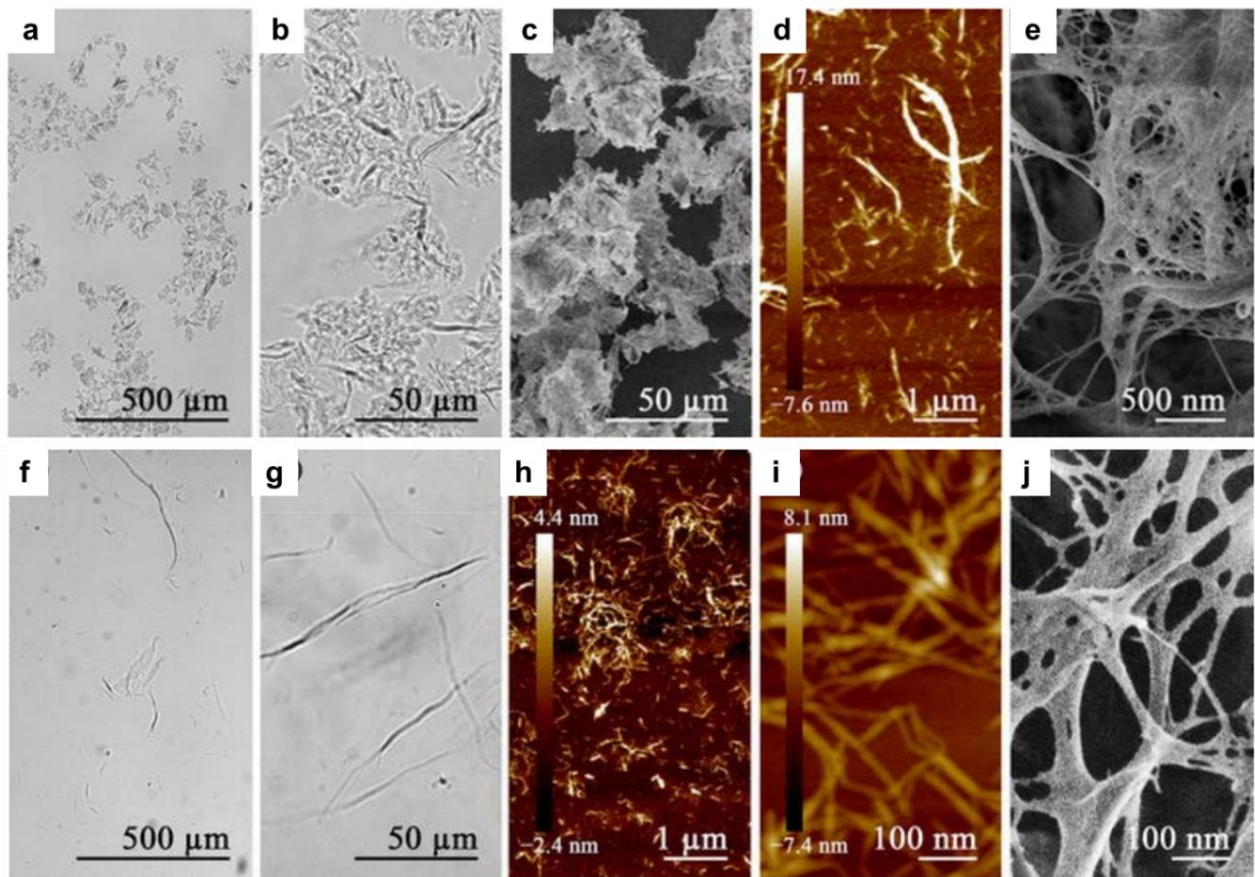


Figure 1. 12 Microscopic images of CNFs with enzymatic pre-treatment (a-e) and with chemical pre-treatment (f-j): (a, b, f, g) optical microscopy; (c, e, j) FE-SEM and (d, h, i) AFM height images. Adapted with permission from ref⁷⁸. Copyright 2014 Journal of Materials Science, with permission of Springer Nature.

Additionally, all types of CNFs may contain non-fibrillated residual fiber fragments. Mechanical fibrillation results in nanofibrils comprising bundles of elementary and microfibrils, whereas chemically pretreated CNFs have smaller and more uniform thicknesses attributed to individual elementary fibrils⁷⁹. Both cellulose crystalline and amorphous domains are presented within these elementary fibrils, suggesting complex polymer chains traversing multiple crystalline and amorphous regions.

1.1.3.b Rheological behaviors of CNF suspensions

As previously mentioned, CNFs exhibit particularly high specific area flexibility and contain a high amount of hydroxy groups. These attributes profoundly influence their interactions, primarily within suspensions. These colloidal suspensions consist of highly anisotropic fibrous entities, which, even at minimal concentrations, tend to form

entangled aggregates. Over time, these aggregates evolve into interconnected three-dimensional networks, exhibiting exponentially increasing strength. Consequently, these networks give rise to complex rheological responses.

The rheological properties of CNF were first studied by Herrick *et al.*²³, who unveiled their pseudoplastic (shear-thinning) and gel-forming behavior. They observed that CNF suspensions exhibit network formation even at low solids contents (2 wt%)²³. Rheological measurements have since been extensively employed to characterize nanocellulose and monitor its behavior during preparation and processing.

Despite the utility of rheological principles, challenges persist in their application to CNF materials due to incomplete knowledge of their structures and complex surface chemistry, making accurate modeling difficult. Factors influencing the rheological properties of nanocellulose-containing suspensions can be broadly categorized into two main areas⁸⁰. Firstly, morphology, encompassing fibril size, shape, length, diameter, fibrillation, and network structure, plays a crucial role. Secondly, surface-chemical composition is another key differentiator, which affects surface charge and can be influenced by treatment processes during material preparation, such as electrostatic or ionic charge and hydrophilic or hydrophobic nature.

The strength of CNF networks is heavily influenced by the type of pre-treatment and the extent of mechanical fibrillation applied during CNF production. Chemically pretreated CNF suspensions usually exhibit stronger network properties compared to those obtained through enzymatic hydrolysis or purely mechanical fibrillation at equivalent concentrations⁸¹. This difference arises from the higher specific surface area of chemically pretreated CNFs, leading to an increased degree of entanglements within the network structure despite the presence of strong electrostatic repulsion between the nanofibrils. Moreover, when compared to CNCs, which are rigid rod-like particles, CNFs form stronger networks at similar concentrations due to their higher aspect ratio and their capability to form physically entangled structures comprising flexible nanofibrils (Figure 1. 13).

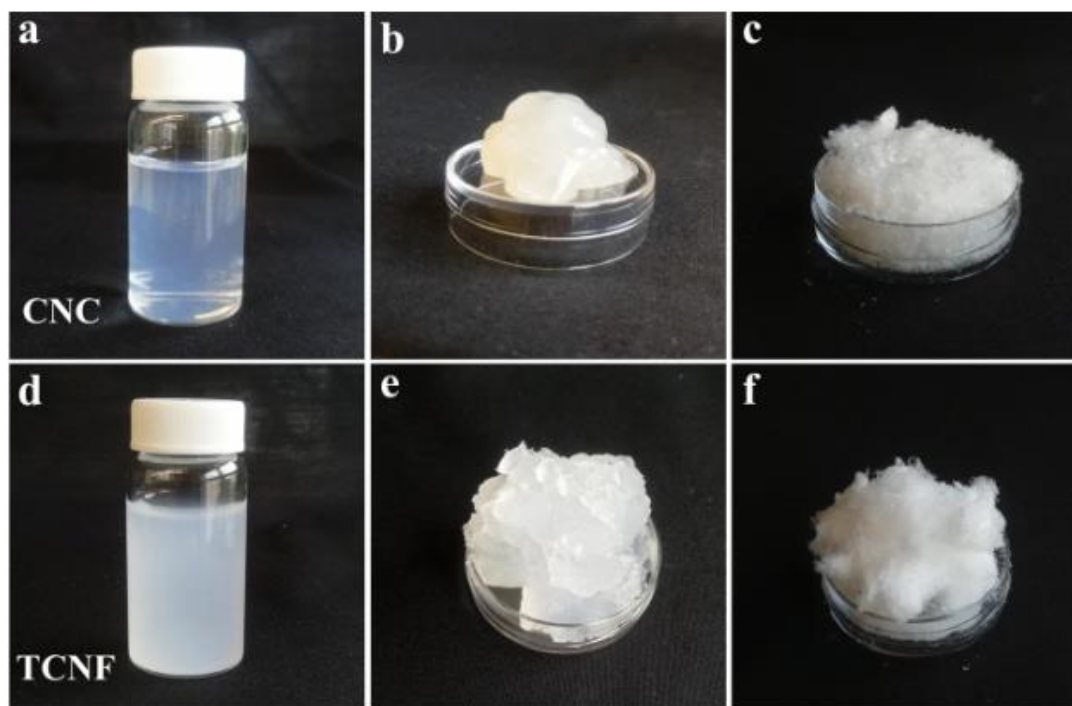


Figure 1. 13 Photographs of NC: (a) 1.0 wt% CNC suspension, (b) 10.0 wt% CNC hydrogel, (c) freeze-dried CNC, (d) 2.0 wt% TEMPO-CNF suspension, (e) 10.0 wt% TEMPO-CNF hydrogel, (f) freeze-dried TEMPO-CNF. Adapted from ref ⁸². Copyright 2022 Cellulose, with permission of Springer Nature.

Regardless of the production conditions, all types of CNF suspensions possess shear-thinning behavior, wherein their viscosity decreases as the shear rate increases⁸³. They also display thixotropic properties, whereby their viscosity decreases under a steady shear rate, reaching equilibrium, and then returns to the original level when the shear rate decreases to zero. As a result, due to significant time dependencies, measurements should be conducted under steady-state flow conditions⁸⁰. Shear flow measurements serve as a valuable tool for characterizing the degree of fibrillation, similar to linear viscoelastic measurements. Many studies have shown that the viscosity of CNF suspensions increases with higher mechanical fibrillation levels or chemical pre-treatment, such as TEMPO-mediated oxidation⁸⁰.

Oscillatory shear measurements are commonly employed to explore the linear viscoelastic properties of CNF structures. These measurements typically involve conducting oscillatory strain sweeps and frequency sweeps to identify the linear viscoelastic regions (Figure 1. 14). Within this linear region, CNF suspensions usually manifest stable storage (G') and loss (G'') moduli, which remain unaffected by the applied

strain at a fixed frequency. This method can facilitate a precise evaluation of the dynamic mechanical behavior of CNF networks and their reaction to applied strains across varying frequencies.

Moreover, a nonlinear region emerges beyond a critical strain, where both G' and G'' decline due to the structural breakdown of CNF networks under significant deformation. The critical strain value is widely employed to compare the structural stability of different samples.

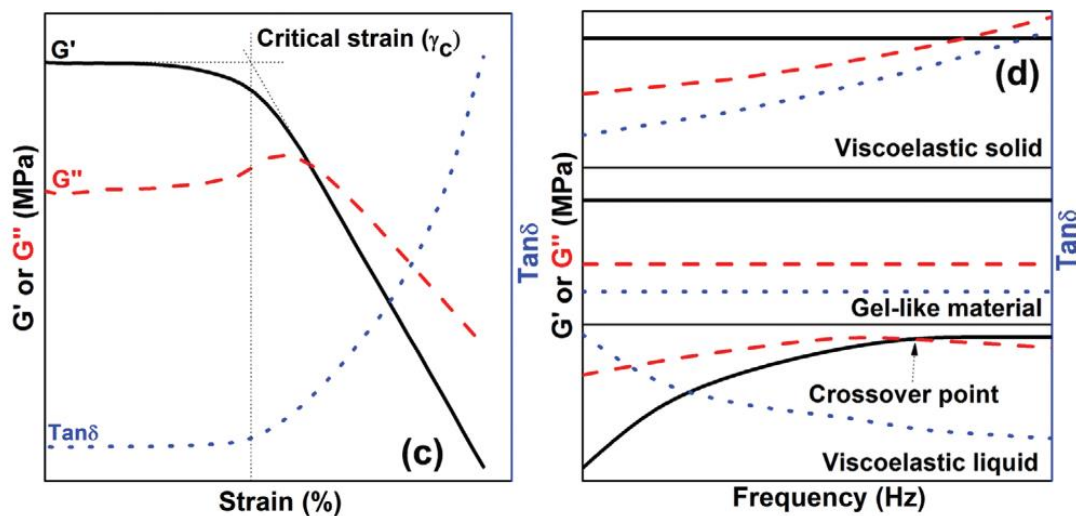


Figure 1.14 Viscoelasticity curves as functions of strain (C) and frequency (D). The black solid lines, red dashed lines and blue dotted lines represent storage (G') and loss (G'') modulus and $\tan \delta$ (G'/G''), respectively. The configuration of the frequency sweep curve varies based on the characteristics of viscoelastic materials. In solid viscoelastic materials, G'' follows a linear trend, while G' remains frequency-independent. Conversely, in gel-like materials, both G' and G'' exhibit frequency independence. On the other hand, for viscoelastic liquids, both G'' and G' gradually rise with increasing frequency. Adapted with permission from ref ⁸⁴. Copyright 2021 Advanced Materials, with permission of John Wiley and Sons.

The unique rheological characteristics of CNFs render them highly suitable for a variety of applications, such as serving as rheology modifiers and being utilized in additive manufacturing. Efforts have been undertaken to control and alter the rheology of CNF suspensions across various fluids by incorporating them with other bio-additives or utilizing surface modification/extraction techniques. These efforts will be discussed in the subsequent section.

1.1.4 Surface modification of nanocellulose

One prominent feature of the CNF is the abundance of polar hydroxy groups presenting on their surface, which induces high hydrophilicity and strong interfibrillar hydrogen interactions. Those hydroxy groups also lead to certain limitations. CNFs exhibit a hygroscopic behavior and lack a distinct melting point, which can impact their processability. Furthermore, their inherent hydrophilicity renders them insoluble/unstable in water and most organic solvents, posing challenges to their dispersion and utilization in various applications.

Conversely, surface modification of nanocellulose heavily relies on the presence of hydroxy groups, which play crucial roles in both chemical and physical transformations. Each AGU has three available surface hydroxy groups (Figure 1. 1): the primary C6-OH and two secondary C2-OH and C3-OH, each having specific reactivity. Although all three hydroxy groups are theoretically accessible at the surface of CNFs, the C6-OH is typically presumed to have the highest activity, while the other two hydroxy groups have lower activity^{85,86}. Experimental evidence has shown that the reactivity of the C3-OH group is particularly limited due to steric effects and intrachain hydrogen bonding^{87,88}.

In addition to those reactive sites, CNFs possess a high specific surface area to volume ratio due to their nanostructure, providing many C6 positions for potential modification. Consequently, there has been significant interest in surface modification of CNFs to address their intrinsic drawbacks and unleash their potential in a broader array of applications.

Figure 1. 15 provides an overview of commonly employed surface modification approaches of NC, including chemical, physical and enzymatic routes.

Physical surface functionalization techniques for NC encompass a variety of methods, including plasma treatment, ultrasonic treatment, irradiation, and surface fibrillation⁵. One promising avenue of research involves blending NC with drug entities and subjecting the mixture to surface defibrillation. This process alters the morphology of NC and yields a novel matrix system characterized by a densely interconnected fiber network, thereby enhancing its versatility and potential for a wide range of applications⁸⁹.

In addition to physical techniques, enzymes can also be utilized to modify the surface of NC. There are two primary approaches for utilizing enzymes for NC functionalization⁹⁰:

(i) direct modification, in which the enzyme comes into direct contact with NC as substrate, including phosphorylation via hexokinase⁹¹, oxidation via galactose oxidase⁹², and enzymatic acylation⁹³.

(ii) indirect enzyme-mediated modification, in which enzymes facilitate the NC functionalization reactions, including click chemistry^{94,95}, *in situ* polymerization⁹⁶ and grafting of active molecules⁹⁷.

The use of enzymes for NC functionalization presents both advantages and disadvantages. Enzymes, being environmentally friendly, exhibit specificity in targeting particular functional groups on the cellulose surface and operate under mild reaction conditions, thereby preserving the integrity of NC properties. Their versatility allows for a wide range of functionalization strategies, and their biocompatibility makes them suitable for various biomedical applications. However, limitations such as restricted substrate specificity and longer reaction times compared to chemical methods exist. Additionally, enzymes can be costly to produce or obtain, and their reactions may require longer timeframes compared to chemical processes. Ensuring the stability and scalability of enzyme-modified NC for industrial production also poses significant challenges. In Figure 1. 15, a schematic representation of the most commonly used surface modification routes of nanocellulose is shown.

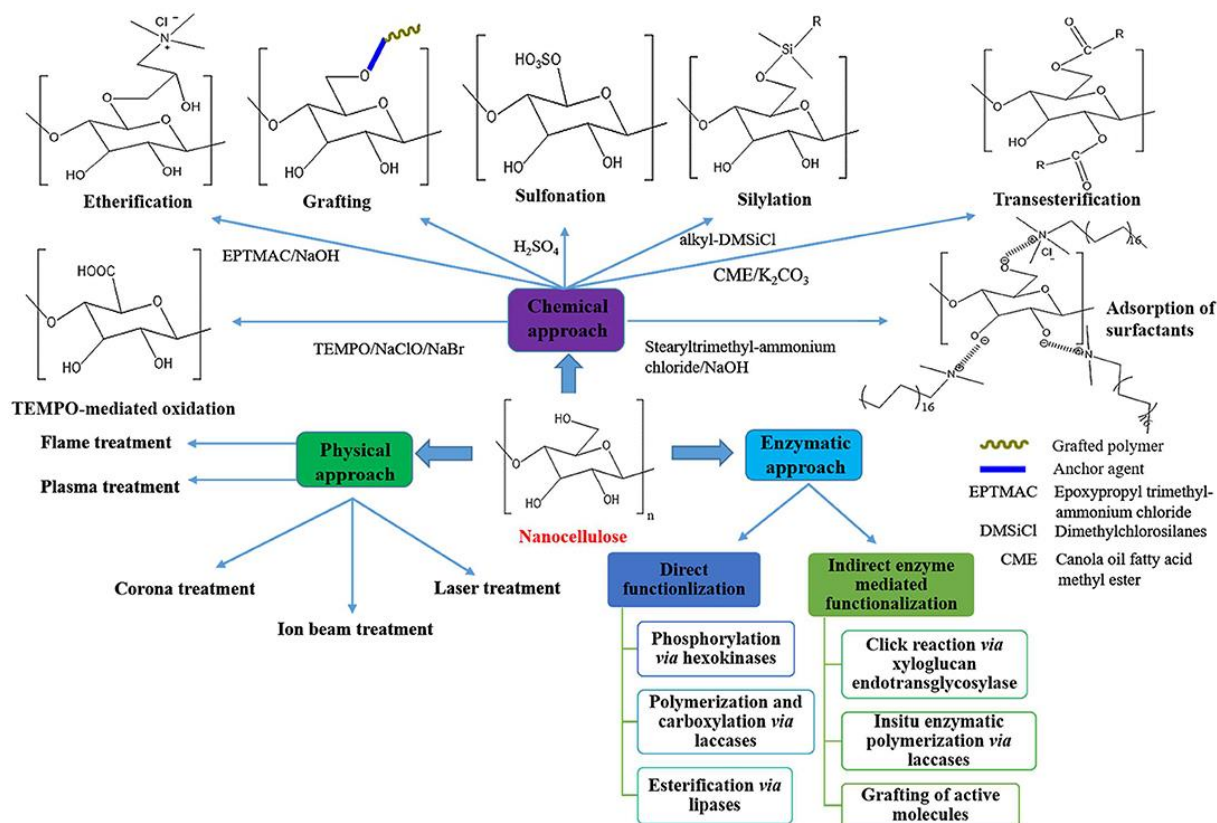


Figure 1. 15 Schematic representation of the most commonly used surface modification routes of nanocellulose⁵. Copyright 2020 Sec. Polymer Chemistry, with permission of Frontiers Chemistry.

1.1.4.a Surface chemical modification

The surface of CNFs can be tailored using surfactants, polyelectrolytes or oppositely charged entities. Surfactants are usually amphiphilic organic compounds containing both hydrophobic groups and hydrophilic groups. For example, CNFs pretreated with TEMPO-mediated oxidation bear various contents of carboxyl groups, which can be modified with a cationic surfactant^{98,99}. Bertsch *et al.*¹⁰⁰ explored the adsorption and interfacial structure of NC at the fluid interface, highlighting the distinct interfacial structures and adsorption characteristics of native hydrophilic and hydrophobized surfaces of CNFs. Adsorption of NC at oil-water interfaces facilitates the formation of stable and biocompatible Pickering emulsions.

Furthermore, the layer-by-layer self-assembly technique is another potent approach to customize CNF properties by depositing different materials onto their surfaces. Sequential layer deposition exploits electrostatic interactions, hydrogen bonds, or van der Waals forces to connect with either polyelectrolytes or neutral biopolymers¹⁰¹.

CNFs are characterized by the presence of a primary hydroxy group, enabling direct functionalization through reactions with various functional groups. These reactions can yield a variety of alternative surface chemistries, as illustrated in Figure 1. 16. Generally, they can be divided into four categories¹⁰²:

(a) substitution of hydroxy groups with small molecules (indicated with red arrows);

(b) polymer grafting based on the “grafting to” strategy with different coupling agents (indicated with blue arrows);

(c) polymer grafting based on the “grafting from” approach with a radical polymerization (indicated with yellow arrows) involving ring-opening polymerization, atom transfer radical polymerization and single-electron transfer living radical polymerization.

(d) polymer grafting strategy known as “grafting-through”, which could be considered an intermediate approach between the “grafting onto” and “grafting from” strategies.

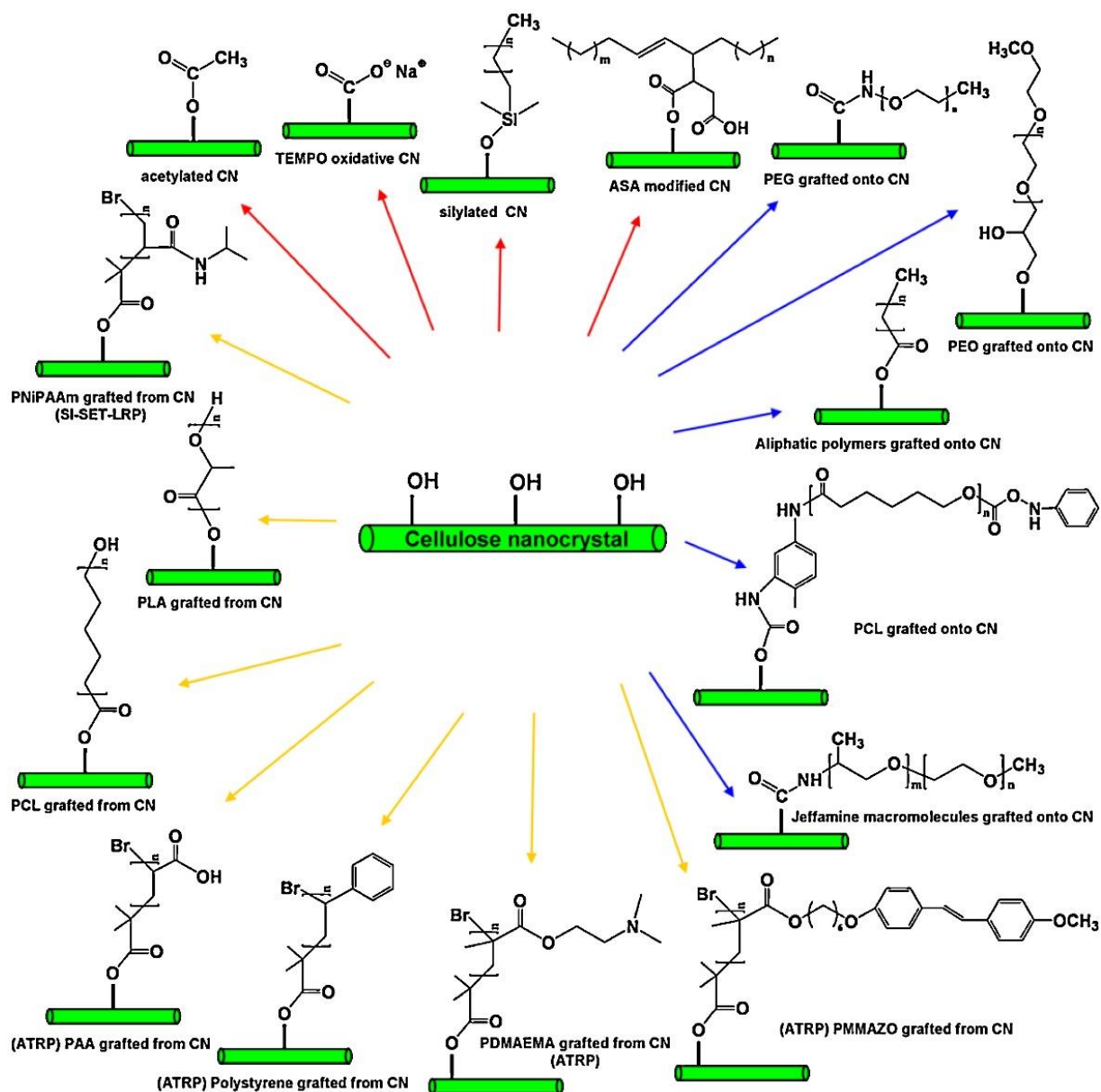


Figure 1.16 Common surface covalent chemical modifications of cellulose nanocrystals¹⁰². Red arrows: substitution of hydroxy groups with small molecules; blue arrows: “grafting to” strategy; yellow arrows: “grafting from” approach. Copyright 2012 Nanoscale, with permission of RSC Pub.

Small molecule substitution

The substitution of hydroxy groups with small molecules has been sought to change their chemistry and endow CNFs with new properties (Figure 1.17). Chemical reactions, such as sulfonation, acetylation, esterification, silane treatments, and carboxylation, which interact with hydroxy groups, are commonly employed for the surface modification of CNFs.

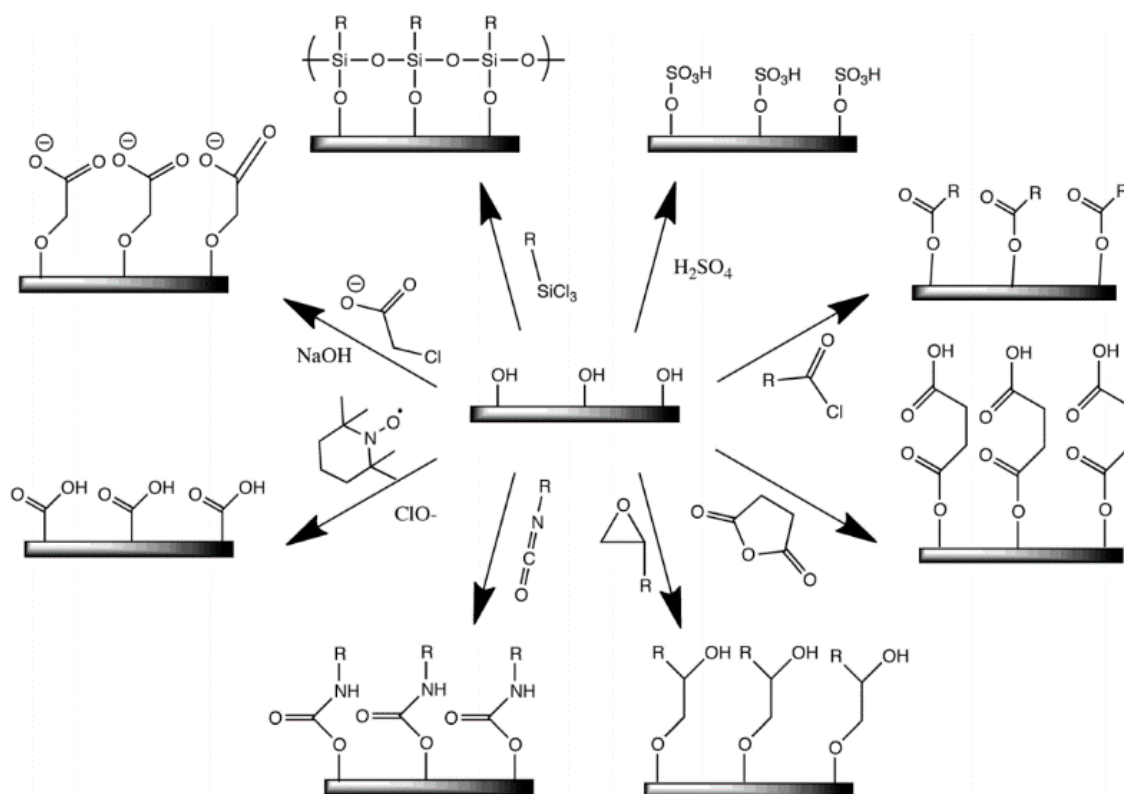


Figure 1. 17 Surface modification of CNFs through “traditional” chemical reaction¹⁰³. Copyright 2011 Chemical Society reviews, with permission of ROYAL SOCIETY OF CHEMISTRY, ETC.

Broadly, sulfonation results in the formation of sulfate esters and imparts negatively charged surfaces to cellulose. Acetylation introduces an acetyl functional group $\text{CH}_3\text{-C(=O)-}$ onto the surface of cellulose. Esterification involves the creation of ester functional groups (O-C=O) on the surface of cellulose through the condensation of a carboxylic acid with the cellulosic hydroxy groups. Silane treatments create a silylated layer on the surface of CNFs. The well-known TEMPO-mediated oxidation reaction allows the introduction of carboxylate groups (-COO^-) on the CNF surface. These anionic surface CNFs obtained through TEMPO-mediated oxidation can be readily modified with cationic surfactants. For example, cellulose-based hydrogels can be prepared via metal-ion-induced ionic crosslinking of CNFs, where the choice of cations can fine-tune the rheological properties of the hydrogels¹⁰⁴.

However, despite the introduction of those small molecules, a generic challenge persists. Due to the relatively low degree of substitution on the CNF surface, the properties of the modified CNFs remain slightly unchanged. These modified CNFs still exhibit high

hydrophilicity, low miscibility with low or non-polar solvents, a tendency for inter-fibril agglomeration, moisture absorption, and poor interfacial compatibility with conventional composites.

Polymer grafting

As previously discussed, the covalent attachment of low molecular weight molecules poses limitations to the use and advancement of CNFs. Therefore, transitioning towards grafting polymerizations onto CNFs represents a pivotal solution to overcome these challenges, as it allows for the attachment of numerous monomers using a single CNF anchoring point.

Polymer grafting onto the CNF surface can be achieved via three main approaches: “grafting to”, “grafting from”, and “grafting through” (Figure 1. 18).

In the “grafting to” approach, pre-formed polymers are covalently attached to the cellulosic nanomaterials¹⁰⁵. The chain end of the pre-formed polymer reacts with the functional groups on the cellulose surface. While this method may encounter challenges such as sterical hindrance, a significant advantage lies in the precise control over resulting material properties, as the molecular weight of the attached polymers can be fully characterized prior to grafting¹⁰⁶.

The “grafting from” approach, also known as surface-initiated polymerization (SIP), involves immobilizing reactive moieties onto the surface, initiating monomer propagation¹⁰⁷. Unlike “grafting to”, this method offers greater efficiency due to reduced steric hindrance of monomer diffusion and yields higher grafting densities. Examples include ring-opening polymerization (ROP)¹⁰⁸, atom transfer radical polymerization (ATRP)¹⁰⁹, and single-electron transfer controlled radical polymerization (SET-LRP)¹¹⁰, enabling precise control over chemical composition, graft length and topology of cellulose-based hybrid materials.

The “grafting through” strategy serves as an intermediate approach involving a macromolecule formed via solution polymerization in the presence of a surface with functionalized groups that participate in polymerization. This technique offers the advantage of integration with other polymerization methods, allowing for one-pot

synthesis, with living polymerization offering superior control over grafted chain structures¹¹¹.

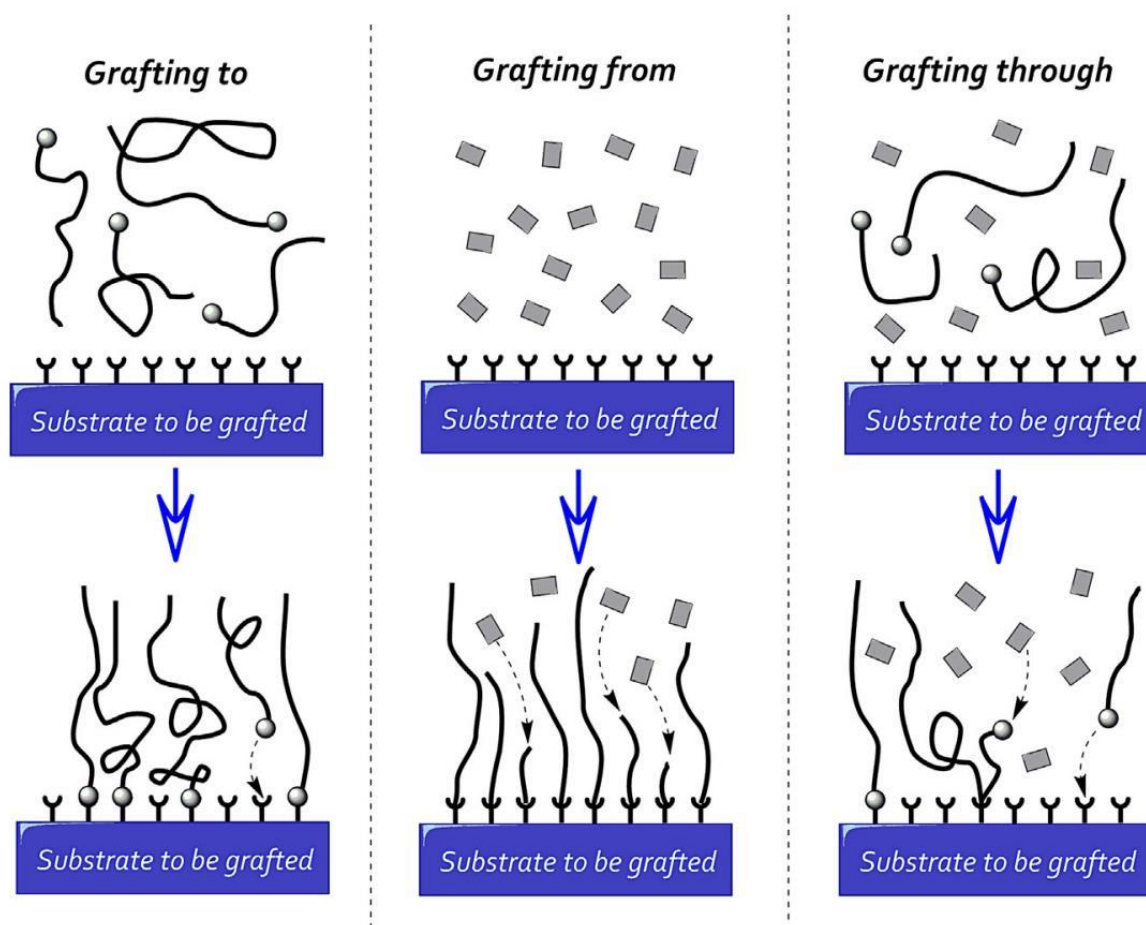


Figure 1. 18 Schematic illustrations of surface modification approaches: (A) the “grafting to”, (B) the “grafting from”, and (C) the “grafting through”¹⁰⁵. Copyright 2016 Multifunctional Polymeric Nanocomposites Based on Cellulosic Reinforcements, with permission of Elsevier.

To conclude, each grafting approach offers unique advantages and challenges. The “grafting to” method provides controlled and predictable material properties but may be limited by steric hindrance during the later grafting process. The “grafting from” method, in contrast, achieves higher grafting densities and reduces steric hindrance issues, making it suitable for yielding higher grafting densities. However, it requires careful initiation and propagation control. The “grafting through” approach balances these aspects by permitting integration with various polymerization techniques and allowing one-pot synthesis, although ensuring efficient participation of functionalized groups during

polymerization can be challenging. Overall, the choice of grafting method depends on the specific polymer design and application requirements.

The versatility of surface modification strategies holds promise for enhancing properties and expanding the application domains of resulting materials across various fields. These fields include but are not limited to packaging¹¹², composites¹¹³, selective adsorption¹¹⁴, optoelectronics¹¹⁵, biomedicine¹¹⁶, and catalysis¹¹⁷. Through tailored surface modifications, modified CNFs can meet the specific requirements of each application, unlocking their full potential in a wide range of industries and technologies.

1.2 Single electron transfer surface-initiated controlled radical polymerization (SET-LRP)

Percec *et al.*¹¹⁸ first introduced Cu⁰-mediated SET-LRP, which enabled the rapid synthesis of “ultrahigh molecular weight polymers” using functional monomers containing electron-withdrawing groups, such as acrylates and methacrylates, all at ambient temperature (Figure 1. 19). The reaction was conducted in polar media, facilitating the disproportionation of Cu^I into Cu⁰ and Cu^{II} species in the presence of specific disproportionation ligands. The initial activation was proposed to occur via Cu⁰-mediated (source: Cu wire, Cu powder, or Cu particles) single electron transfer to the electron acceptor alkyl halide. Remarkably, this synthesis facilitated the production of high molecular weight polymers (M_n ~ 1 400 000 g/mol) within just a few hours without the need for any purification steps¹¹⁸.

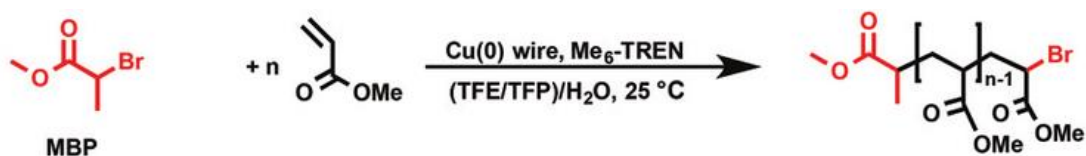


Figure 1. 19 Cu⁰-mediated SET-LRP of methyl acrylate in binary mixtures of 2,2,2-trifluoroethanol (TFE) and 2,2,3,3-tetrafluoropropanol (TFP) with water in the presence of the ligand Me₆-Tren¹¹⁹. Adapted with ref¹¹⁹. Copyright 2018 Polymer Chemistry, with permission of Royal Society of Chemistry.

1.2.1 Mechanism

SET-LRP is driven by the disproportionation of Cu^I into Cu⁰ and Cu^{II}. Figure 1. 20 illustrates this cyclical process, wherein the polymer chain lengthens as the disproportionation of Cu^I continuously regenerates the copper (Cu⁰) catalyst.

The notations Cu⁰, Cu^IX/L, and Cu^{II}X₂/L represent all the unionized Cu species, all Cu species in the oxidation state (+1 and +2) either bonded to a halide (X) or attached to a ligand (L). The notations P_n-X, P_n[•], and P_n-P_n represent the deactivated polymers bonded to a halide, the activated polymer, and the undesired terminated polymer chain, respectively, while M represents an individual monomer unit.

At the beginning of the polymerization, the copper catalyst (Cu^0 , the electron donor) transfers a single electron to the acceptor alkyl halide (initiator at first, then later the dormant propagation species $\text{P}_n\text{-X}$), generating the Cu^{I} species and activates the propagating radical P_n^\bullet . The rapid disproportionation of Cu^{I} regulates the concentrations of initiating species (Cu^0) and deactivating species ($\text{Cu}^{\text{II}}\text{X}_2/\text{L}$) required for the reversible termination step (P_n^\bullet to $\text{P}_n\text{-X}$). Both the activation and deactivation of the polymer renew the Cu^{I} species in the system, allowing the disproportionation reaction to occur repeatedly in both cycles of activation and deactivation.

In addition, the deprotonation of Cu^{I} species is promoted not only through the presence of the ligand (as mentioned earlier) but also by the solvent. In this scenario, sufficient deactivators in the medium suppress the chance of a possible unwanted termination (terminated polymer chain, $\text{P}_n\text{-P}_n$) due to potential free-radical cross-reactions.

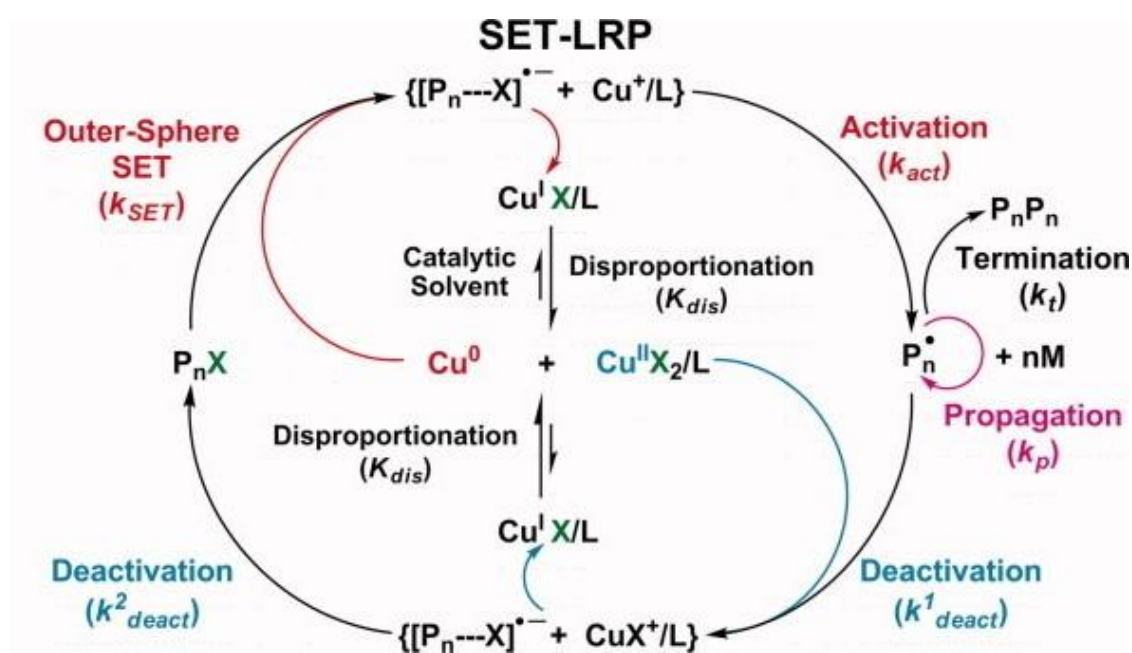


Figure 1. 20 Schematic illustration of SET-LRP reaction mechanism¹²⁰. Copyright 2007 Journal of Polymer Science Part A: Polymer Chemistry, with permission of John Wiley and Sons.

The chain length is significantly influenced by the rates of activation (K_{act}) and deactivation (K_{deact}). With the constant propagation (K_p) and steady propagation radicals achieved by the balanced rate of K_{act} and K_{deact} , the reaction exhibits first-order kinetics with respect to monomer concentration. Initiation occurs early in the polymerization process, leading to a constant number of propagative radicals (P_n^\bullet) over time, resulting in

predictable polymerization behavior. The number average molecular weight (M_n) is directly proportional to monomer conversion, defining SET polymerization as a form of controlled radical polymerization.

The distinctive features of SET-LRP make it a powerful synthetic tool for designing complex macromolecular structures while maintaining precise control over key parameters such as degree of polymerization, compositions, functionalities, and topologies.

However, the SET-LRP mechanism can be complex due to its responsiveness to various environmental factors, including solvent polarity, nature and concentration of ligands, and the ability to stabilize Cu^0 colloidal particles. Moreover, the reactivity of nascent Cu^0 is self-controlled by the extent of disproportionation influenced by the combination of solvent and ligand. Therefore, careful selection of reaction conditions and functional initiators is crucial to produce well-defined copolymers and polymers with complex architectures.

1.2.2 Monomers

A wide range of monomers, including acrylates¹²¹⁻¹²⁵, methacrylates¹²⁶⁻¹²⁸, acrylamides^{129,130}, and methacrylamide¹³¹, can be effectively polymerized using SET-LRP. Acrylates, particularly methyl acrylate, have been the most extensively studied for optimizing reaction conditions. Monomers with long alkyl side chains, for example, lauryl acrylate (LA)¹³², and semifluorinated acrylates (e.g. 1,1,1,3,3,3-hexafluoroisopropyl acrylate (HFIPA))¹³³, have also been reported to be compatible with the technique. Monomers containing more complex water-soluble side groups, such as sugars¹³⁴, di(ethylene-glycol)-2-ethylhexyl ether acrylate (DEGEEA)¹³⁵, oligo (ethylene oxide) methyl ether acrylate (OEOMEA)¹³⁶, have also been successfully polymerized to adjust the aqueous solubility of the final polymers (Figure 1. 21).

leading to decreased participation in the activation process and an increase in the concentration of Cu^IX/L with conversion. Insufficient disproportionation results in propagating radicals being inadequately deactivated by Cu^{II}X₂/L. Consequently, extensive bimolecular termination (terminated polymer chain, P_n-P_n) occurs to offset the inhibited disproportionation, leading to low end-halide functionality.

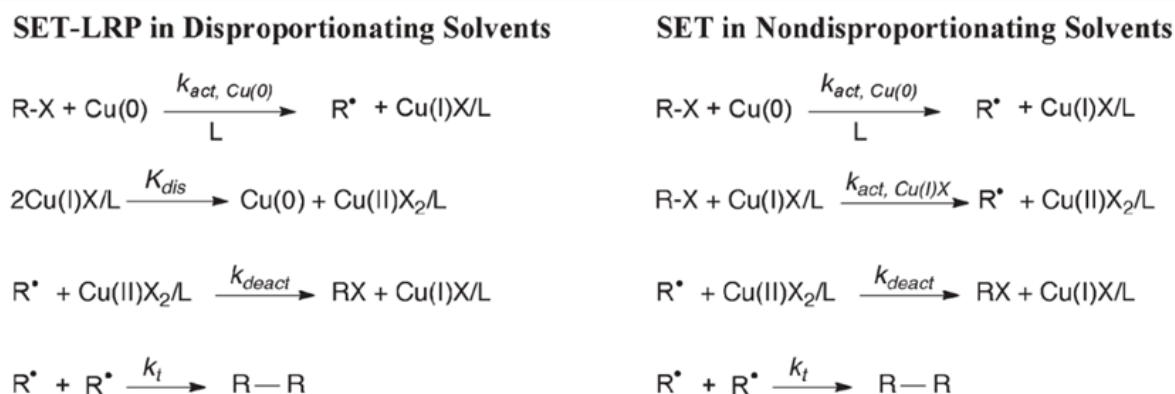


Figure 1. 22 Kinetic models for SET-LRP in the presence and absence of disproportionation. Adapted with permission from ref¹⁴⁹. Copyright 2011 Journal of Polymer Science Part A: Polymer Chemistry, with permission of John Wiley and Sons.

In addition, binary mixtures of non-polar solvents with disproportionating solvents will still yield efficient SET-LRP^{144,150,151}. This allows for the technique to be applied using a wider range of solvents and solvent mixtures.

1.2.4 Catalyst system of Cu⁰-mediated LRP

The catalyst in Cu⁰-mediated SET-LRP is a combination of metal and ligand, with copper being the most widely employed catalyst. Levere *et al.*¹⁵² interrupted SET-LRP experiments of methyl acrylate in DMSO by removing the Cu⁰ catalyst to determine the role of Cu⁰ in the activation of polymerization. Their finding suggested that Cu⁰ or “nascent” Cu⁰ (produced *in situ* during the deactivation process) primarily acts as the activator of the initiator, whereas only a limited activation contribution occurs by CuBr, as CuBr undergoes rapid disproportionation¹⁵².

When Cu powder is employed as the catalyst, perfect or near-perfect end-group fidelity can be maintained throughout the polymerization^{153,154}. However, the use of Cu particles presents challenges as the particle size directly impacts the polymerization conditions.

Studies have shown that reducing the Cu particle size (from 425 to 0.05 μm) while maintaining a constant concentration in the reaction medium leads to a significant increase in the propagation rate and faster polymerization reaction (13 min instead of 90 min)^{155,156}.

Despite these advantages, the use of Cu powder has become less common over the past year, with Cu wire gaining popularity. Cu wire offers several advantages over Cu powder, including better control over the molecular weight distributions, enhanced predictability, easier tuning of reaction rate, and recyclability^{138,157-159}. However, it should be noted that Cu wire may take longer to interact with the monomer and initiator to mediate SET-LRP in an aqueous system¹⁶⁰.

N-containing ligands have been found to be effective in promoting the disproportionation of Cu^{I} into Cu^0 and Cu^{II} in the catalytic system¹⁶¹. However, even small changes in ligand concentration can negatively affect the end-group fidelity of the polymer chain, necessitating careful optimization of reaction conditions¹⁶². Figure 1. 23 displays the structures of some N-containing ligands, with $\text{Me}_6\text{-TREN}$ being one of the most widely used and highly recommended for the polymerization of acrylates and methacrylates¹⁶³⁻¹⁶⁵. PMDETA and tris(2-aminoethyl)amine (TREN) are also good commercially available alternatives^{153,166}. TREN has been used as a replacement for $\text{Me}_6\text{-Tren}$ in Cu^0 -catalyzed SET-LRP of acrylates and methacrylates, as it is less expensive (206 € per 100 mL for 96 % from Sigma-Aldrich) than $\text{Me}_6\text{-Tren}$ (185 € per 1 ml for 97 % from Sigma-Aldrich) and has been found to mediate the reaction efficiently¹⁶⁷.

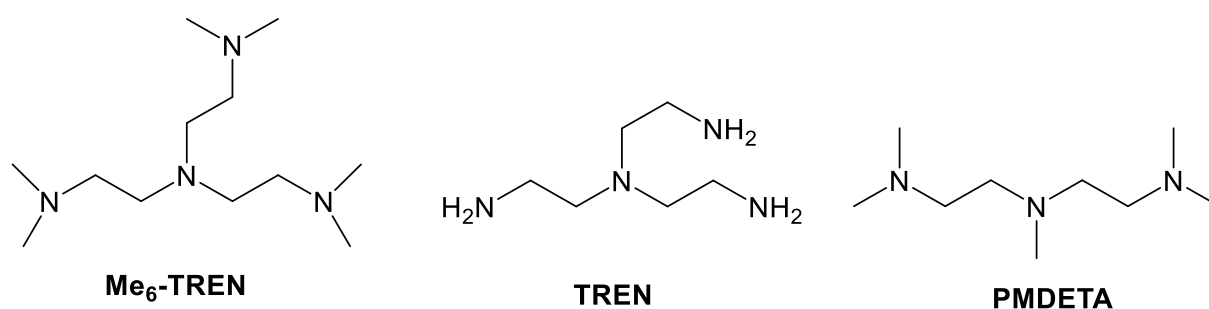


Figure 1. 23 Molecule structures of N-containing ligands: $\text{Me}_6\text{-TREN}$, TREN, PMDETA.

1.2.5 Post-modification

Post-modification reactions offer a valuable approach when grafting di-functional reactants onto the CNF surface. This method allows for the installation of a diverse array of functionalities onto the reactive scaffold, which may be incompatible or not readily inducible during the initial modification stage.

The end-functionality group of the polymers prepared by SET-LRP can serve as macroinitiators for copolymer synthesis or precipitate in varieties of post-modifications. The halogen, the typical functional end group, can be substituted to induce complex structures, as shown in Figure 1. 24. For thio-bromo coupling, bromo-amine induces different polymer architectures. Moreover, polymers can be coupled together to form novel structures using radical coupling chemistries such as atom transfer radical coupling and atom transfer nitroxide radical coupling.

Indirect post-modification approaches can also be used, such as replacing the end-halide with an azide followed by attaching alkyne-functionalized polymers or through methanethiosulfonate-mediated thiol-ene and thiol-disulfide exchange reactions.

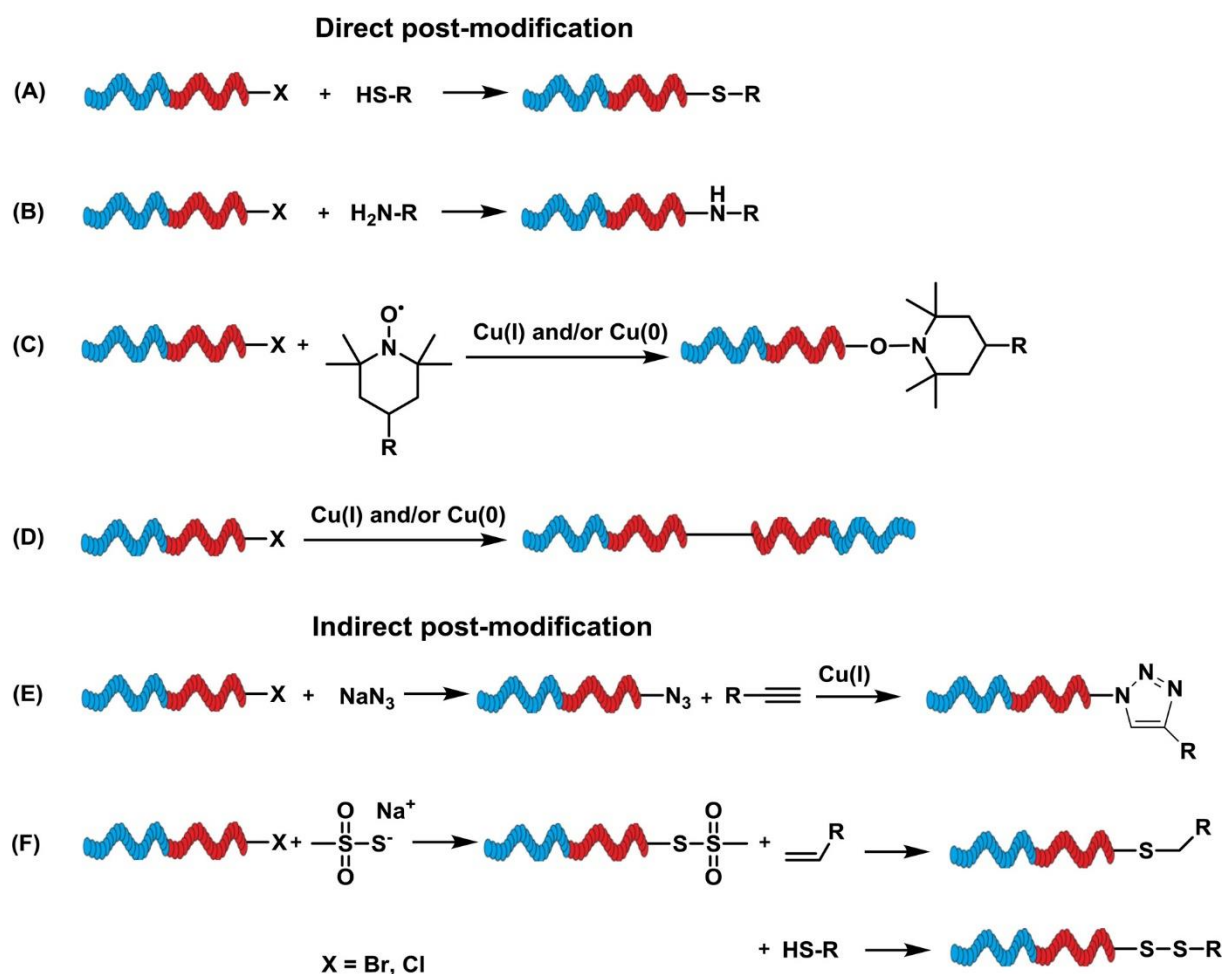


Figure 1. 24 Schematic illustrations of several post-modification methods¹⁶⁸. Copyright 2015 American Chemical Society.

In addition, post-modification of the polymers can be achieved through the polymerization of monomers containing reactive functionality in the initial step. This straightforward approach allows for the introduction of desirable amounts of azido- or alkyne-groups, which can subsequently participate in efficient click-type modifications with complementary alkyne or azido-functionalized species. This versatile approach extends beyond simple end-group substitutions.

“Click chemistry” refers to modular reactions characterized by high yield and in-offensive by-products¹⁶⁹. They are conducted under simple synthetic conditions, allowing for efficient solvent removal and straightforward product isolation. Notable examples include the Diels–Alder cycloaddition^{170,171} and the thiol-ene reaction^{172,173}, along with the Cu^I-catalyzed azide-alkyne cycloaddition (CuAAC).

CuAAC has been widely explored under various experimental conditions since its discovery^{174,175}, highlighting its robustness and compatibility with diverse functional groups, solvents, and additives regardless of its source catalyst. Importantly, biomolecules retain their bioactivity during CuAAC, rendering them valuable for numerous biomedical applications¹⁷⁶⁻¹⁸⁰. Over the years, the popularity of this reaction has grown, leading to the commercial availability of a large library of starting compounds, which has made it very attractive to the scientific community^{181,182}.

1.3 Emerging applications of cellulose nanofibrils

Cellulose stands as a fundamental building block in various everyday materials like paper, cardboard, and textiles derived from plant sources such as cotton or flax. Its versatility also extends to the production of fibers, films, and cellulose derivatives¹⁸³. With remarkable mechanical strength, reinforcing capabilities, and biodegradability at the nanoscale, cellulose emerges as an ideal selection for diverse applications.

1.3.1 CNFs as rheology modifiers

The diversity in cellulosic sources and production methods contributes to the varied morphology and surface chemistry of CNFs, which directly impacts the rheology of CNF suspensions. CNFs have proven to be effective rheological modifiers with customizable viscosity and viscoelastic properties. They exhibit high viscosity at rest, significant shear-thinning behavior, favorable thixotropic properties, excellent water retention capacities, and remarkable emulsion stabilization abilities. These rheological characteristics suggest that CNFs may be well-suited for a range of specific applications (Figure 1. 25).

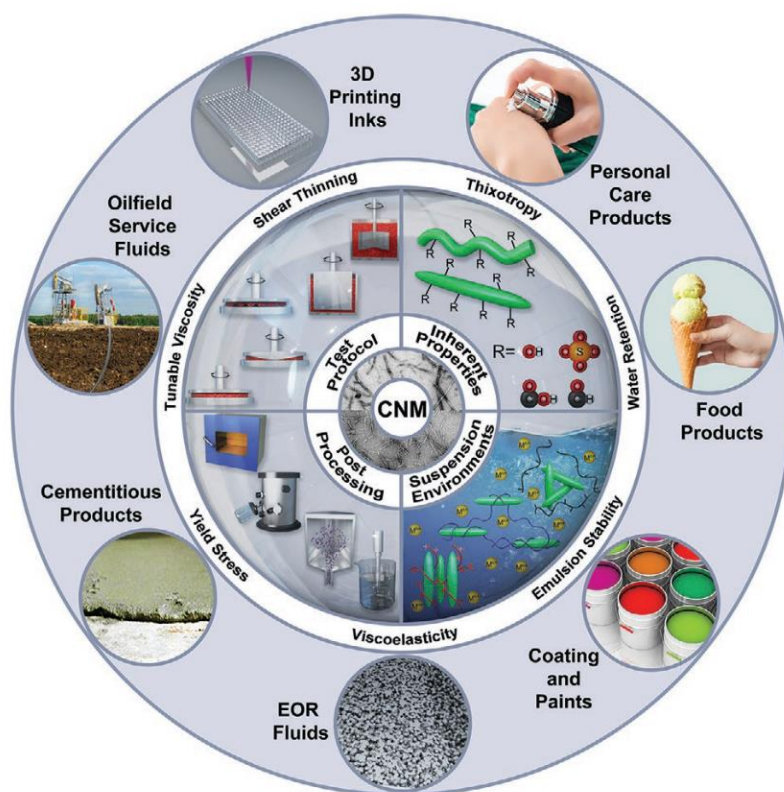


Figure 1. 25 An overview of key factors in cellulose nanomaterial rheology and their influence on its emerging applications⁸⁴. Copyright 2021 Advanced Materials, with permission of John Wiley and Sons.

These rheological characteristics make CNFs well-suited for specific applications. For instance, CNFs have the potential to serve as additives, replacing other natural and synthetic co-binders in paper coating formulations¹⁸⁴. This is due to their thixotropic behavior, which is advantageous in situations where the mixture must flow readily initially but thicken or immobilize once the flow stops. Additionally, the water-holding tendency of CNFs is also beneficial in paper coating formulations as it prevents the formation of crumbs on coating blades from water-binding gel-forming components, thus ensuring smooth coating¹⁸⁵.

In the realm of additive manufacturing (AM), also known as 3D printing, direct ink writing (DIW), a subset of material extrusion AM, is particularly relevant for CNFs. The rheological properties of inks are crucial for DIW, impacting printability and shape fidelity. As shown in Figure 1. 26, an ideal DIW ink should exhibit shear-thinning capability, which allows it to flow smoothly through small deposition nozzles under shear stress. Additionally, it needs to have sufficient zero-shear viscosity and high yield stress to maintain the

structural stability of printed constructs, preventing them from deforming or collapsing under their own weight. Moreover, superior thixotropic properties are desirable, facilitating rapid recovery in viscoelastic properties after printing.

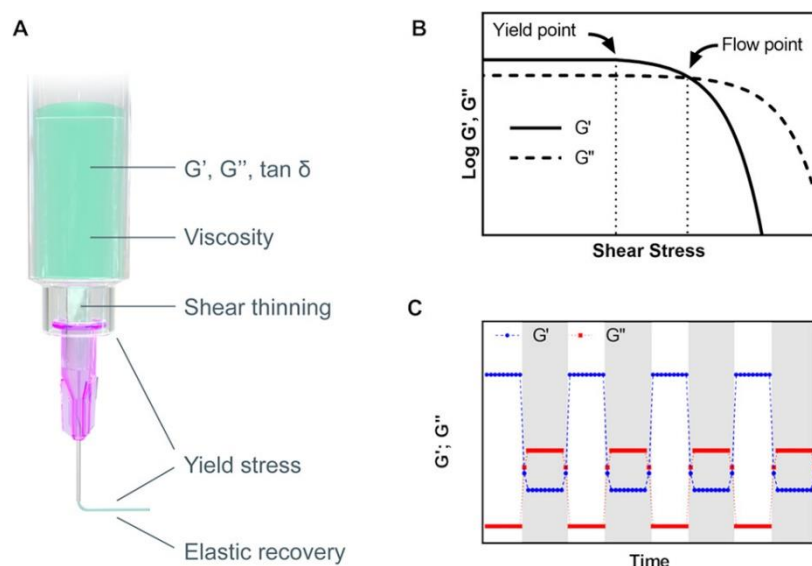


Figure 1. 26 Ideal rheological properties of a DIW ink for good printability and shape retention. (A) The interplay of rheological properties in extrusion-based printing. (B) The amplitude sweep for a viscoelastic material is represented as a function of the shear stress, showing the yield point as the limit of the linear viscoelastic range and the flow point where the viscous modulus G'' surpasses the elastic modulus G' , indicating the onset of flow. (C) Elastic recovery test, where G' (blue) and G'' (red) are measured under low deformation (white time interval) and high deformation (gray time interval)¹⁸⁶. Copyright 2020 American Chemical Society.

CNF-based gels meet these requirements, emerging as promising candidates serving as novel inks or rheological modifiers in multi-component ink formulations for 3D printing structural constructs. Efforts have been devoted to fine-tuning the rheology of CNF suspensions in various fluids through blending with other bio-additives or employing surface modification/extraction techniques. A comprehensive review by Rana *et al.*⁸⁰ underscored the distinctive rheological qualities of CNFs, elucidating their significant value across a spectrum of applications. These applications include the formulation of bioinks (Figure 1. 27) for printing 3D electronic and biomedical¹⁸⁷⁻¹⁸⁹, as well as advancements in tissue engineering¹⁹⁰⁻¹⁹².

ability to leverage the distinct features and complementary properties of both constituents.

Currently, the deposition of metal nanoparticles onto nanocellulose is primarily achieved through physical adsorption and chemical reduction synthesis. A wide range of metal NPs, including noble, non-noble metals, such as gold, silver, nickel, platinum, copper, and iron, as well as metal oxides, such as zinc oxide, titanium dioxide, copper oxide, have been successfully loaded or assembled onto CNFs. These cellulose-based hybrids with NPs have been extensively investigated for various applications, including catalysis, biomedicine, and electronic devices (Figure 1. 28).

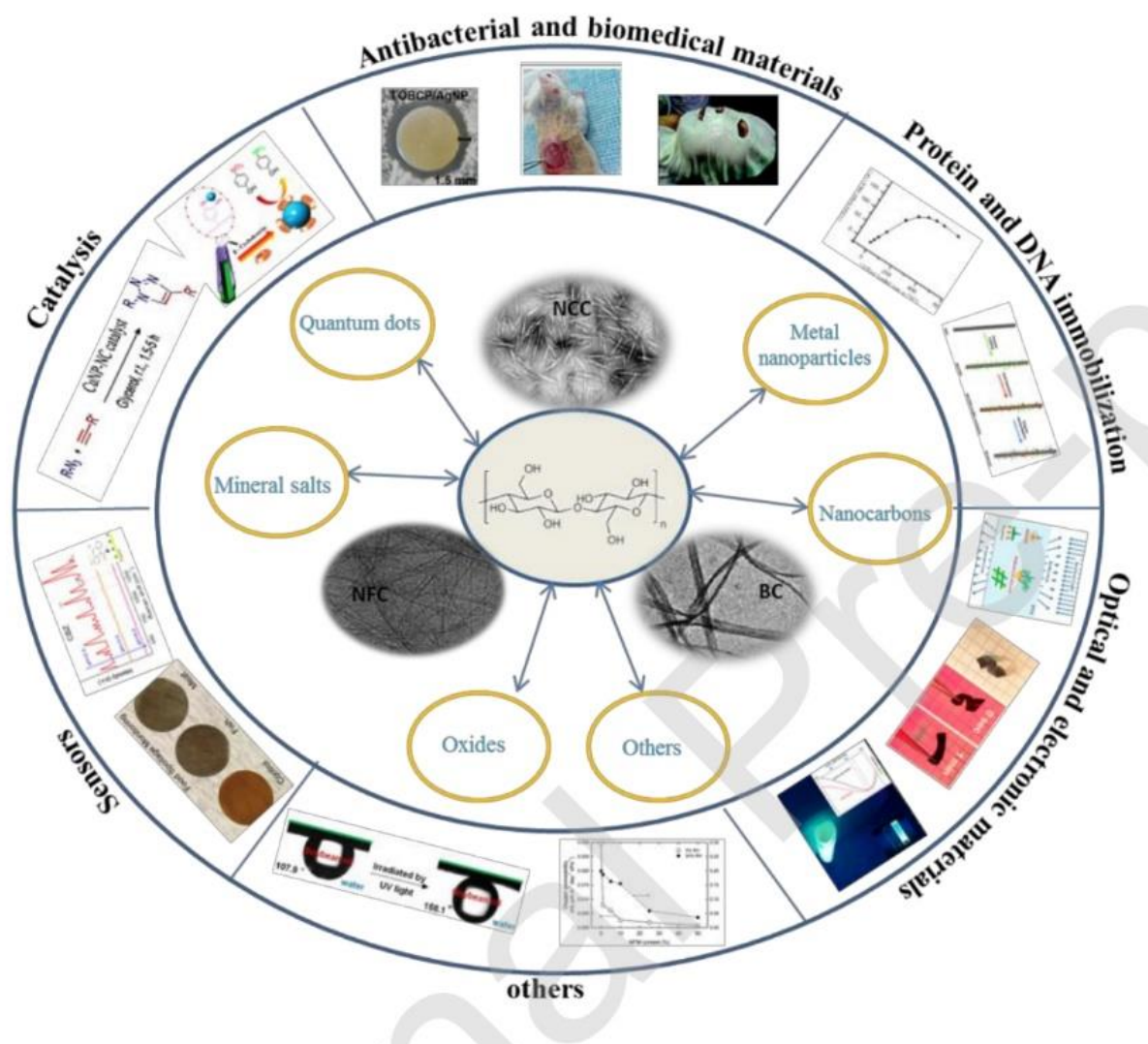


Figure 1. 28 An overview of the applications of nanocellulose-based hybrid materials with inorganic nanoparticles²⁰². Copyright 2020 Carbohydrate Polymers, with permission of Elsevier.

For example, Madivoli *et al.*²⁰³ reported a TEMPO-oxidized CNF composite embedded with silver NPs, which exhibited antimicrobial properties. This composite can be utilized in wound dressings and packaging materials to inhibit microbial growth *in vivo*. Alle *et al.*²⁰⁴ developed a spontaneous method for integrating gold NPs onto CNFs. This hybrid composite was further processed into a paper strip, which functions as a biosensor for detecting H₂O₂ and cholesterol, indicating its significant potential for disease diagnosis applications²⁰⁴.

Farooq *et al.*²⁰⁵ reviewed the latest advancements in the synthesis of nanocellulose-zinc oxide hybrid nanocomposites, highlighting their excellent mechanical, UV-barrier capabilities and antibacterial properties. These composites hold promise for applications in food packaging, biochemistry, and the cosmetics industry. Zeng *et al.*²⁰⁶ developed a series of CNF-based hybrid aerogels embedded with conducting nanomaterials (transition-metal carbide), demonstrating superior mechanical flexibility, strength, tunable electrical properties, and potential for low-cost terahertz device development. Oprea *et al.*²⁰⁷ provided an overview of nanocellulose hybrids with metal oxide nanoparticles (MONPs) in biomedical applications. MONPs, such as ZnO, TiO₂, CuO, MgO or Fe₃O₄, are incorporated to introduce antibacterial and magnetic functionalities to CNFs, with CNFs serving as a support material offering flexibility and high surface area for MONPs impregnation²⁰⁷.

1.4 Objectives and outline of this thesis

To broaden the application potential of CNFs, the intrinsic deficiencies of CNFs cannot be neglected. One of the main challenges arises from the surface hydroxy groups, which induce high hydrophilicity and strong interfibrillar hydrogen interactions, resulting in poor dispersibility in water and most organic solvents, as well as irreversible agglomeration after drying. Consequently, the cellulosic fibrillar strands lose their flexibility and conformability. However, hydroxy functions are also the primary reactive moieties of CNFs.

As introduced previously, conventional methods involving the substitution of hydroxy groups with small molecules suffer from low substitution degrees and are limited to the CNF surface. Grafting polymers onto the surfaces of CNFs has become a widely favored approach. The extended polymer chains function as "spacers," significantly diminishing hydrogen bonding effects. This modification enhances interactions with the surrounding solvent molecules, thereby improving the dispersibility of the CNFs.

This thesis comprises two interconnected studies with distinct objectives.

The first study (Chapter 2) focuses on the development of a multifunctional platform made of CNFs adaptable to various applications, and morphology study of CNFs, CNFs grafted with polymers and their embedding in a matrix.

The specific objectives of this study were to:

- 1) Produce CNFs from dried elemental chlorine-free (ECF) bleached kraft pulp using grinding and a microfluidizer.
- 2) Convert CNFs into CNF-based macroinitiators.
- 3) Graft polymers onto CNFs surface via Cu⁰-mediated radical polymerization (SET-LRP). The monomers comprise a di(ethylene glycol) ethyl ether acrylate (DEGEEA) and a protected alkyne monomer (acrylic acid 3-trimethylsilyl-prop-2-ynyl ester, TMSPgA).
- 4) Label polymer-grafted CNFs with different luminescent dyes via post-modification through Cu^I-catalyzed azide-alkyne click chemistry (CuAAC).

5) Morphology study of CNFs during the production process, CNFs grafted with polymers and their embedding in a matrix by SEM, confocal laser scanning microscopy (CLSM) and stimulated emission depletion (STED) microscopy.

The second study (Chapter 3) continues the surface modification approach and attempts to *in situ* cross-link CNFs with inorganic particles, specifically upconversion nanoparticles (UCNPs) and gadolinium fluoride nanoparticles (GdF₃ NPs). The objectives were to:

- 1) Surface-modify NPs for adapting the current surface modification strategy of CNFs.
- 2) Characterize surface-modified CNFs cross-linked with UCNPs and GdF₃ NPs, respectively.
- 3) Discuss the properties and potential applications of these novel CNF-based hybrid materials.

Chapter 4 concludes the thesis, summarizing the findings and providing insights and future prospects for surface-modified CNFs.

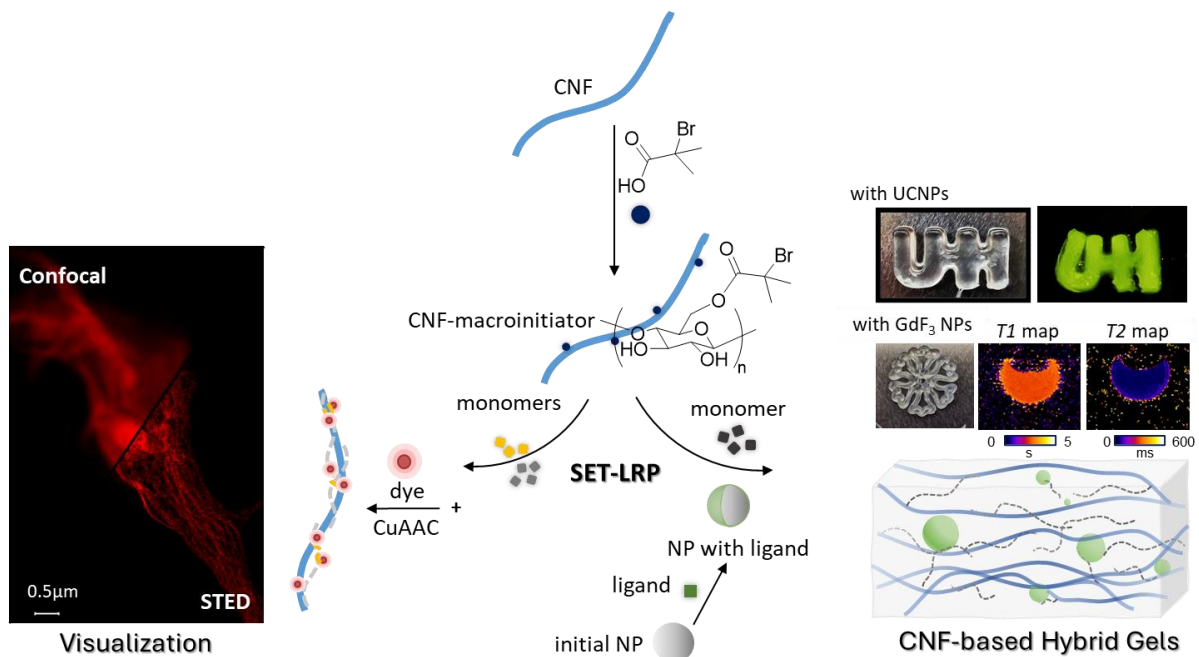


Figure 1.29 Graphical overview of the studies.

2 Extraction, surface modification and morphology study of CNFs

The content in this chapter (except Caption 2.2.1, Figure 2.7-2.8, and Table 2.1) has been published and adapted from:

(1) Jiang, X.; Mietner, J. B.; Navarro, J. R. G. A Combination of Surface-Initiated Controlled Radical Polymerization (SET-LRP) and Click-Chemistry for the Chemical Modification and Fluorescent Labeling of Cellulose Nanofibrils: STED Super-Resolution Imaging of a Single Fibril and a Single Fibril Embedd. *Cellulose* 2023, No. 0123456789. <https://doi.org/10.1007/s10570-022-04983-y>.

Reproduced with permission from Springer Nature.

2.1 Introduction

The interest in using CNFs as fillers or reinforcing agents in bio-based composite applications has constantly increased over the last decade due to their numerous advantages, such as their relatively low cost, extraction feasibility from numerous renewable resources, indicating high abundance and global availability, and their excellent mechanical properties¹⁰³. Over the last few years, various research groups have focused their efforts on developing composites reinforced with wood flour, cellulose fibers, or cellulose nanofibrils²⁰⁸⁻²¹⁰. They aimed to enhance the understanding of the filler-matrix compatibility, the interaction at their interface, and morphological/dimensional aspects, such as homogeneous dispersion and orientation of the filler in the matrix.

Although SEM and AFM have been extensively employed for imaging and localizing cellulose fibrils/fibers in the host matrix, the challenge of elucidating how and where CNFs organize themselves within a polymer matrix persists. The direct observation of single-buried CNFs in composite remains significantly challenging.

In this chapter, we aimed to address the challenge of revealing the morphology of CNFs embedded in a polymer matrix (bio-based composites) in a non-destructive manner. To achieve this, we first obtained CNFs from elemental chlorine-free (ECF) bleached kraft pulp through grinding and the use of a microfluidizer; subsequently, we developed a surface chemistry modification protocol for CNFs. It began with converting the CNFs into a CNF-based macroinitiator (CNF-MI). Following this conversion, we employed a synthesis route that combined SET-LRP and Cu^I-catalyzed azide-alkyne click chemistry (CuAAC) to both graft polymers onto the CNFs and label them with fluorescent dyes for visualization purposes (Figure 2. 1).

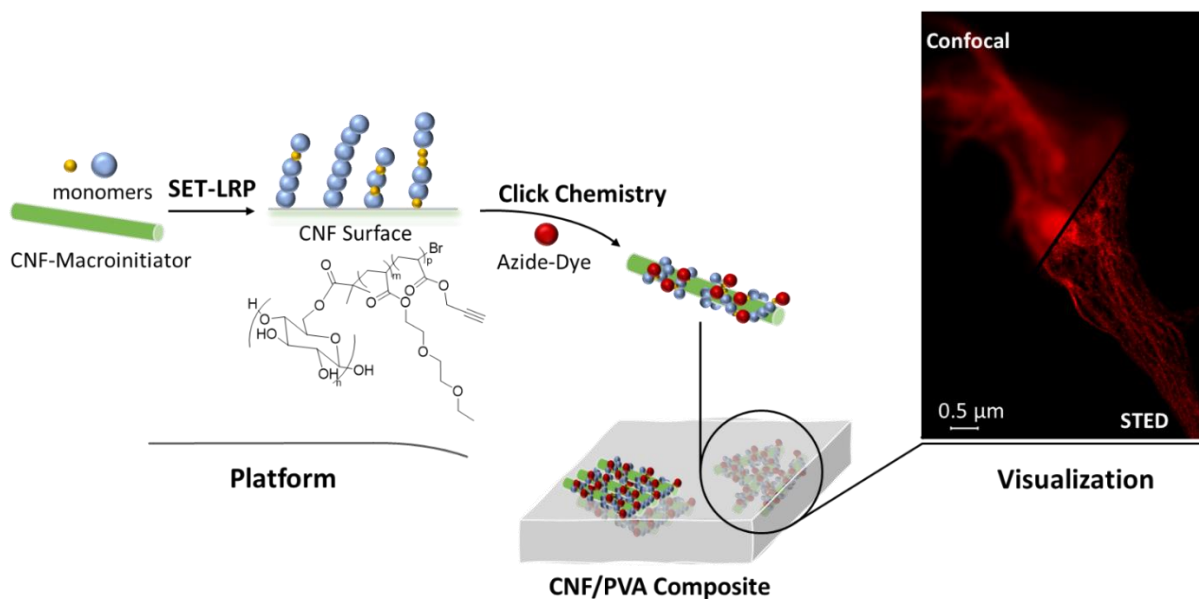


Figure 2. 1 Graphical overview of the Chapter 2.

SET-LRP, as introduced in the previous chapter, is widely regarded as a powerful and adaptable technique for synthesizing acrylate polymers with precise functionalities. In this chapter, we focused on two specific monomers: di(ethylene glycol) ethyl ether acrylate (DEGEEA) and acrylic acid 3-trimethylsilyl-prop-2-ynyl ester (TMSPgA). TMSPgA was used to attach luminescent dyes to the CNF surface through CuAAC, while DEGEEA served to enhance CNF stability in selected solvents (DMSO and H₂O) and acted as a spacer reactive clickable monomer to ensure proper separation of luminescent dyes.

Following this, the post-modification reaction - CuAAC - was employed to label surface-modified CNFs with various fluorescent dyes, specifically azide fluor 488 dye (AF 488) and azide ATTO 633 (Figure 2. 2). Those dyes are suitable for imaging with confocal laser scanning microscopy (CLSM) and/or stimulated emission depletion (STED) microscopy. We investigated the behavior of CNFs dried from DMSO, examining single fibrils, fibril networks, bundles, and clusters. The distribution and morphology of the modified CNFs, embedded in a PVA composite with an approximate thickness of 10 μm, were revealed through a wide field microscope and CLSM/STED microscopes.

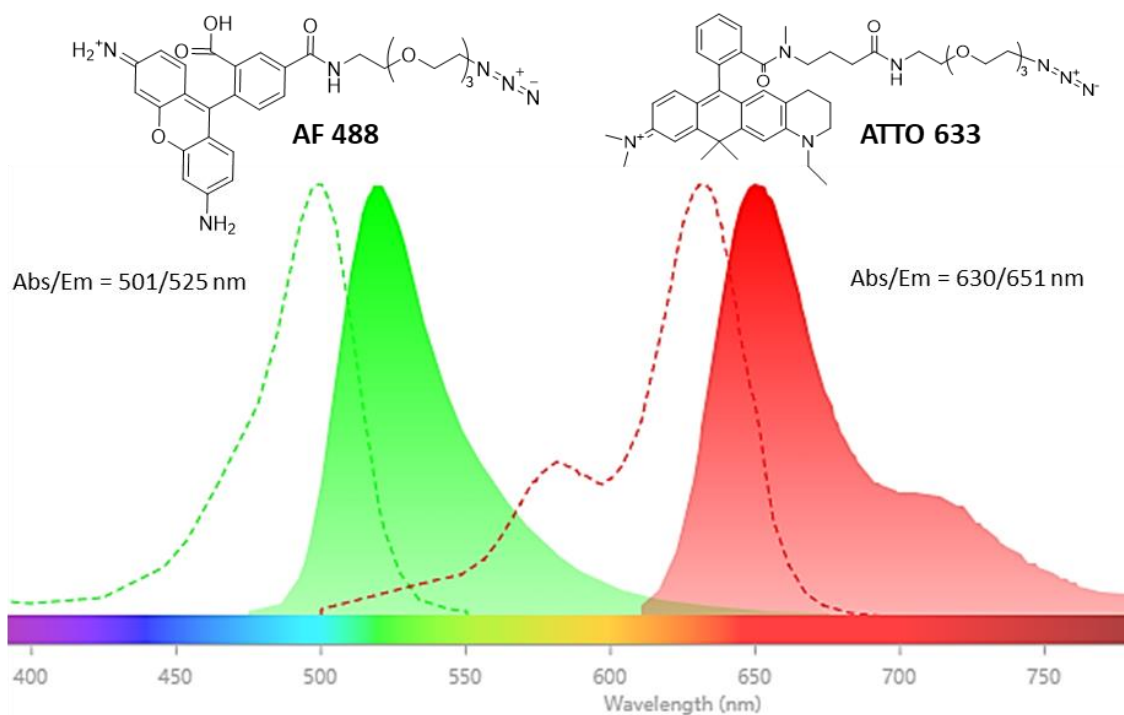


Figure 2. 2 Chemical structure and spectral properties of AF 488 and ATTO 633. The spectra are obtained from Fluorescence SpectraViewer, ThermoFischer Scientific²¹¹.

Furthermore, the morphology of CNFs throughout the production process, CNFs grafted with polymers and their embedding in a host matrix, was studied using SEM and STED microscopy,

STED microscopy, one of the light-based super-resolution microscopy techniques, has been developed to overcome the diffraction limit of light microscopy^{212,213}. In STED microscopy, a depletion laser beam is superimposed on the excitation laser beam. This overlapping pattern forces excited fluorophores to return to their ground state in predefined regions, thereby reducing the amount of spontaneous fluorescence emission (Figure 2. 3)²¹⁴. As a result, the effective point spread function is lower than the diffraction limit, thus achieving a high resolution down to 20 nm²¹⁵. It has proven versatile in biological research²¹⁶⁻²¹⁸ and nanoscale materials²¹⁹⁻²²¹, enabling living-cell imaging^{222,223}, 3D imaging, as well as fast imaging²²⁴. Another advantage of STED is deep imaging. By minimizing specimen-induced spherical aberration, STED microscopy can achieve a resolution of 60 to 80 nm, even at depths of up to 120 μm within scattering biological tissue²²⁵. However, to effectively characterize CNFs using STED microscopy,

specific luminescent dyes must be labeled on the CNFs. Fortunately, there is a wide variety of commercially available fluorophores that are well-suited for this purpose.

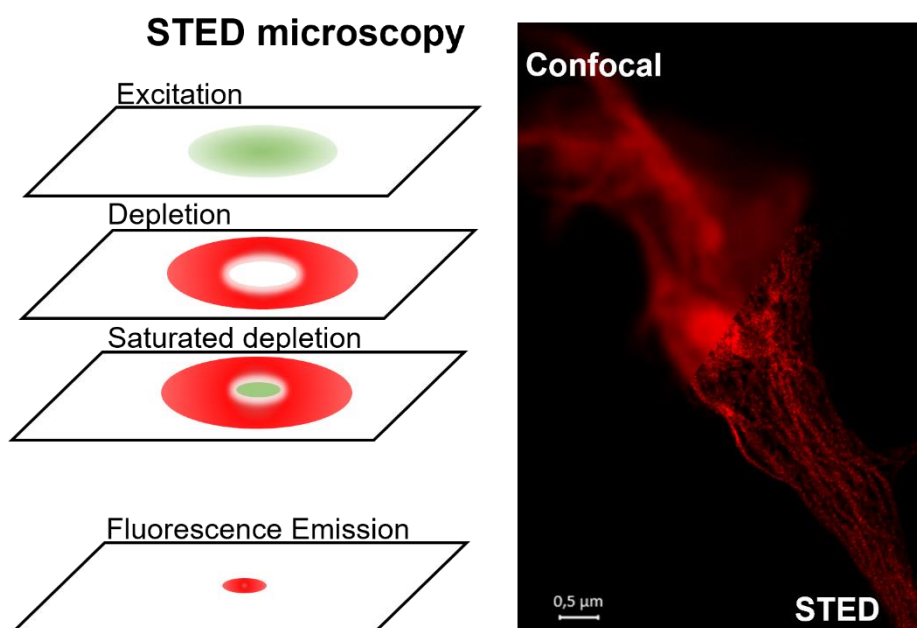


Figure 2.3 Left: illustration of stimulated emission depletion (STED) microscopy²¹⁴. Copyright 2010 Cell, with permission of Elsevier. Right: comparison of confocal laser scanning microscopy and STED microscopy images of modified cellulose nanofibrils labeled with a fluorescent dye.

The labeling of CNMs with fluorescent dyes is particularly valuable for biomedical and sensor applications^{226–230}. Fluorescently tagged CNFs are also employed in studies related to nanotoxicology and therapeutics^{231,232}. Schyrr *et al.*²³³ prepared CNF/PVA nanocomposites with a high concentration of fluorescent sensor motifs using thiol-ene click reactions. Navarro *et al.*²³⁴ modified CNFs with methyl acrylate and acrylic acid N-hydroxysuccinimide ester, enabling the labeling of a fluorescent probe (Lucifer yellow derivative) through an amidation reaction. Goodge *et al.*²³⁵ functionalized biotin-CNF membranes with the substitution of alkyne groups and fluorescently tagged azide-biotin conjugate via CuAAC. Recently, a method to label CNFs with fluorescence using a triazine linker and click chemistry also has been reported²³⁶. In all these examples, the labeling process involved specific chemical reactions where certain precursors were sequentially introduced, followed by one or two click chemistry reactions.

2.2 Results and discussion

2.2.1 Production of CNFs

CNFs were obtained from dry kraft pulp via a series of mechanical disintegration steps. SEM images in Figure 2. 4 illustrate the progression of cellulose morphology through each stage of mechanical disintegration. Upon grinding, cellulose fibers exhibit reduced aggregation, leading to the liberation of cellulose fibrils (CFs) and fragmentation into smaller entities. Fiber shredding phenomena are primarily observed at this stage.

Subsequently, the cellulose aqueous suspension underwent microfluidization under consistent shear rates. Initially, it traversed a chamber pair with orifice widths of 400 μm and 200 μm successively, subject to a pressure of 15 000 Psi, repeated twice. This was followed by passing through another chamber pair with orifice widths of 200 μm and 100 μm successively, subjected to a pressure of 25 000 Psi, repeated four times. The intermediate product from the first chamber pair (Figure 2. 4 C&D) exhibited significantly reduced dimensions and enhanced separation compared to the post-grinding stage. After undergoing microfluidization through the smaller chamber pair twice, the number of CF aggregates further decreased, but with some heterogeneity (Figure 2. 4 E&F). Subsequent delamination processes, repeated twice, yielded CNFs with improved homogeneity (Figure 2. 4 G&H). The application of high pressure and strong shear forces facilitated precise geometrical control of the fibrils. The yield of CNFs from the kraft pulp was then calculated to be 50 %.

The data obtained from optical fiber analysis through FiberLab aligns with the observations from SEM images (Figure 2. 5). At the post-grinding stage, the distribution of cellulose fiber lengths primarily clustered in the range of 0.20-1.20 mm (83.3 %) and then significantly transitioned to the range of 0.00-0.20 mm (52.7 %) following exposure to the microfluidizer. Subsequently, after completion of the entire microfluidization process, the distribution was further concentrated in the range of 0.00-0.20 mm (90.3 %). Similarly, the width distribution exhibited a consistent trend towards lower values as mechanical disintegration progressed.

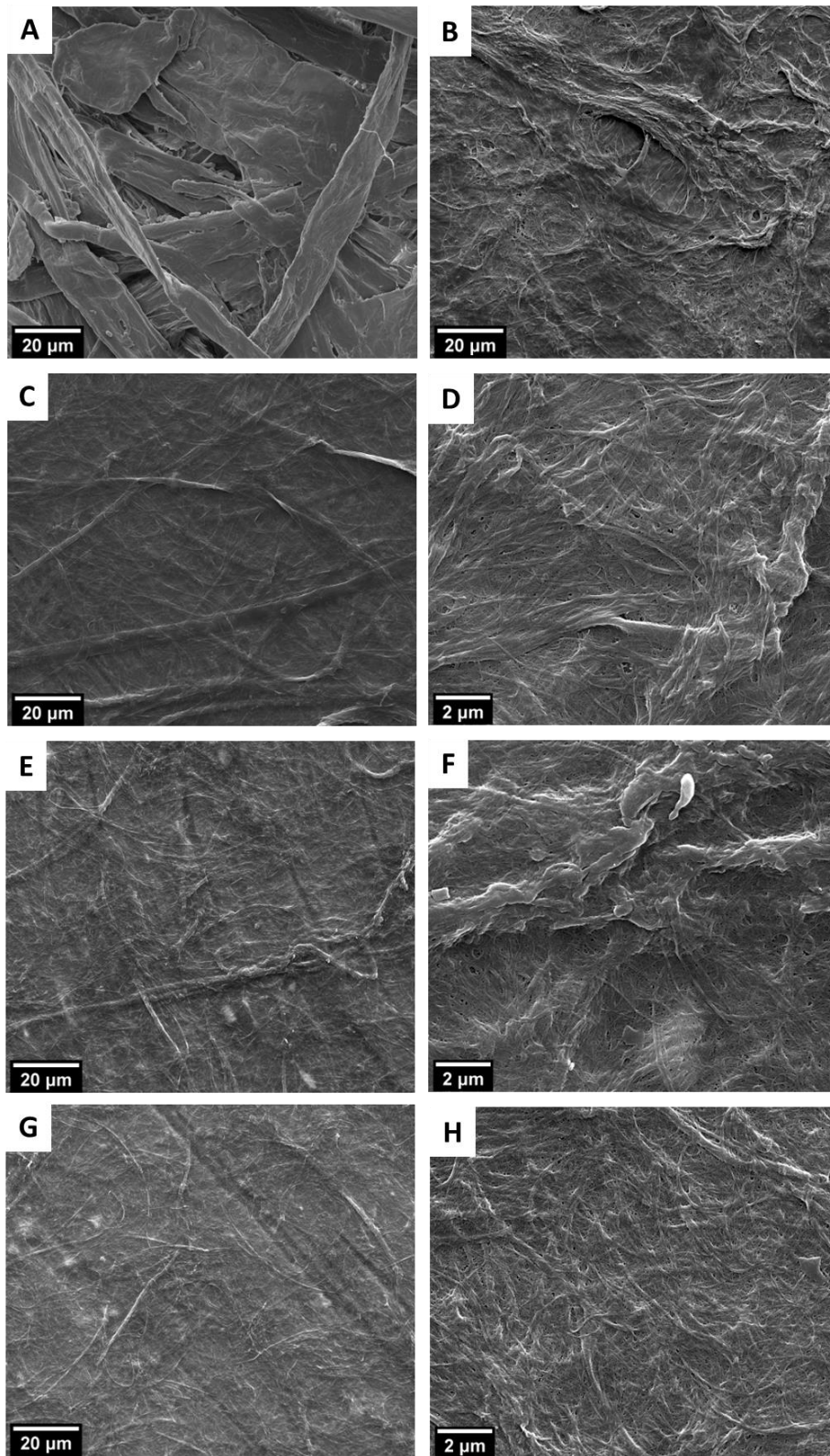


Figure 2. 4 SEM images of cellulose from each stage of mechanical disintegration steps: (A) initial kraft pulp, (B) cellulose fibers after grinding, (C)&(D) CFs underwent microfluidizer 2 times with 400 μm and 200 μm chambers, (E)&(F) CFs underwent microfluidizer 2 times with 200 μm and 100 μm chambers, (G)&(H) final CNFs underwent microfluidizer 4 times with 200 μm and 100 μm chambers.

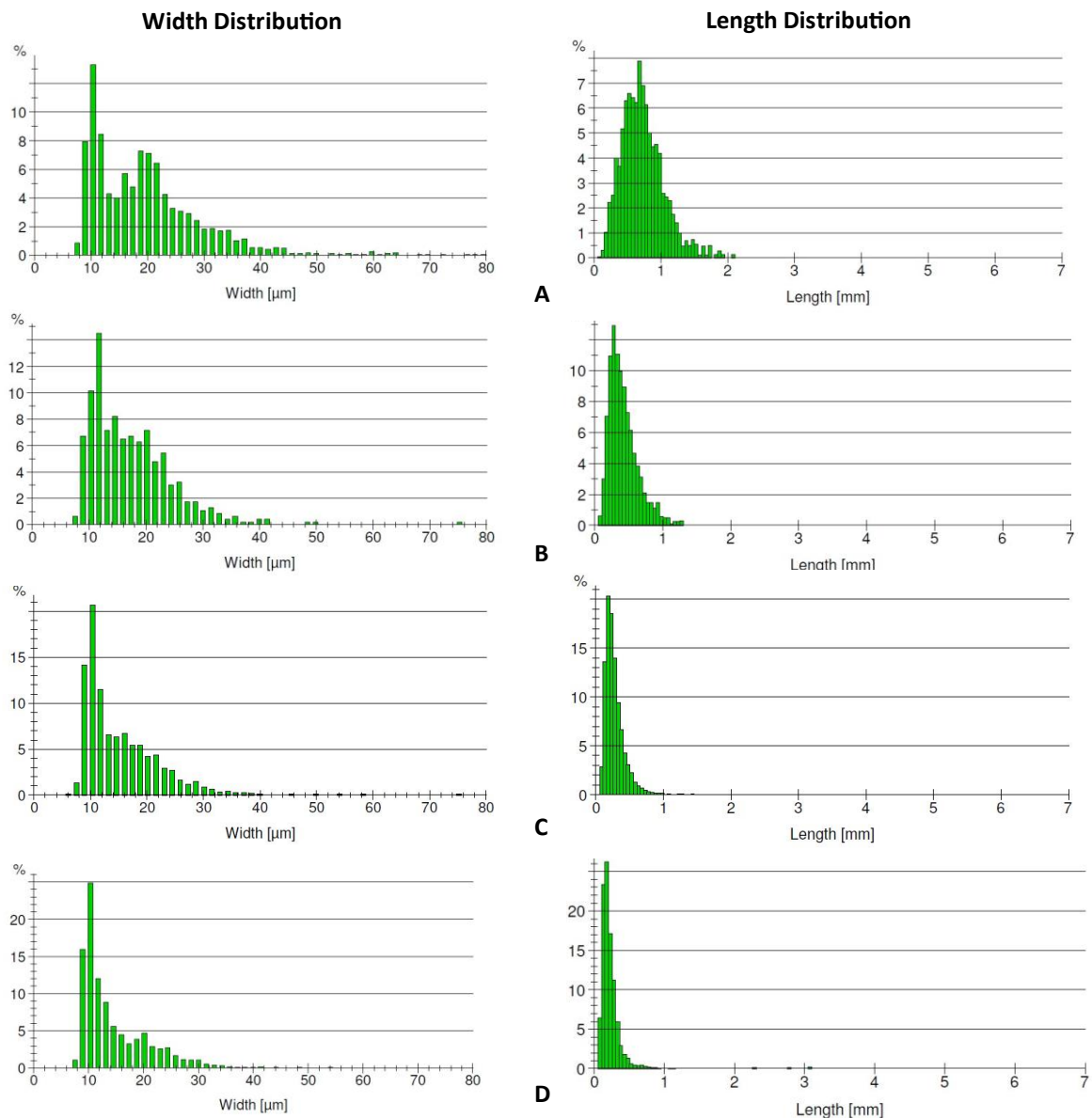
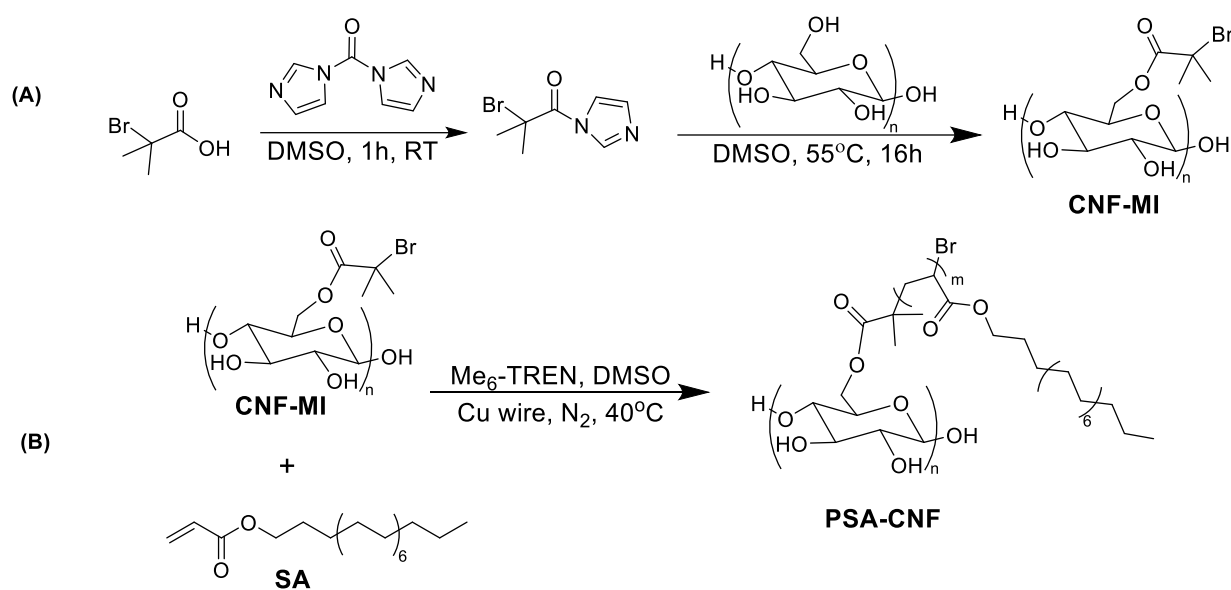


Figure 2. 5 Width- (left row) and length (right row) distribution diagrams of (A) cellulose fibers after grinding, (B) CFs underwent microfluidizer 2 times with 400 μm and 200 μm chambers, (C) CFs underwent microfluidizer 2 times with 200 μm and 100 μm chambers, (D) final CNFs underwent microfluidizer 4 times with 200 μm and 100 μm chambers. * The values of CFs&CNFs may exceed the resolution of FiberLab (length: 50 μm , width: 1 μm).

2.2.2 Solvent exchange, chemical conversion and surface modification of CNFs with poly-SA

The process began with the solvent exchange of the unmodified pristine CNFs, which were first suspended in water, and then an appropriate amount of DMSO was slowly added. This exchange procedure is an exothermic process due to the water-DMSO interaction and

the hydrogen bonding formation between the CNFs and the DMSO²³⁷. Subsequently, the CNFs suspended in DMSO underwent surface modification to yield CNF-MI via an esterification reaction between the hydroxy groups of the CNF and the 2-bromo-2-methylpropionic acid in DMSO. The immobilization of the initiator onto CNFs occurred in a one-step process, enabling subsequent polymer growth via SET-LRP directly from the CNF surface using the macroinitiator unit as an anchoring point. This surface-initiated polymerization offers a pathway for fully tuning and optimizing CNF properties. The chemical conversion is illustrated in Scheme 2. 1.



Scheme 2. 1 Synthesis of the CNF-based macroinitiator (CNF-MI) and PSA-CNF.

The polymerization was conducted in a mixture of DMSO and toluene because the CNF-MI is only stable in DMSO, whereas the monomer SA is only soluble in toluene, and the addition of toluene to the CNF-MI/DMSO suspension did not destabilize the nanocellulose suspension. During the controlled radical polymerization of SA to form PSA-CNF, phase separation was observed. White floccules were observed after 1 h of the reaction and accumulated in the upper phase when the reaction ended, which predominantly consisted of PSA-CNF. The lower DMSO-rich phase displayed a green to blueish color, indicating the primary presence of Cu-ligand complexes, also containing unreacted monomer SA, catalyst, and Me₆-TREN. Similar phasic separation was observed during the SET-LRP of the SA homopolymerization.

The successful chemical conversion and surface modification were confirmed with FT-IR spectroscopy (Figure 2. 6). The FT-IR spectrum of unmodified CNFs exhibited characteristic cellulose absorption bands at 3320 cm^{-1} (O-H), 2950 and 2895 cm^{-1} (C-H), 1430 cm^{-1} (C-H), and 1161 cm^{-1} (C-O-C). Following the chemical conversion, the spectrum of the CNF-MI induced a distinct band at 1733 cm^{-1} , attributed to C=O stretching from the ester group, confirming the introduction of ester functionalities. Furthermore, the spectrum of PSA-CNF displayed not only the unaltered characteristic bands of cellulose but also additional peaks at 2917 and 2850 cm^{-1} (C-H), 1733 cm^{-1} (C=O), 1467 cm^{-1} (C-H) and 1162 cm^{-1} (C-O-C). These new bands indicate the successful grafting of polymer chains, evidenced by the presence of ester groups and an increased number of methylene groups in the main and side chains of each graft repeating unit.

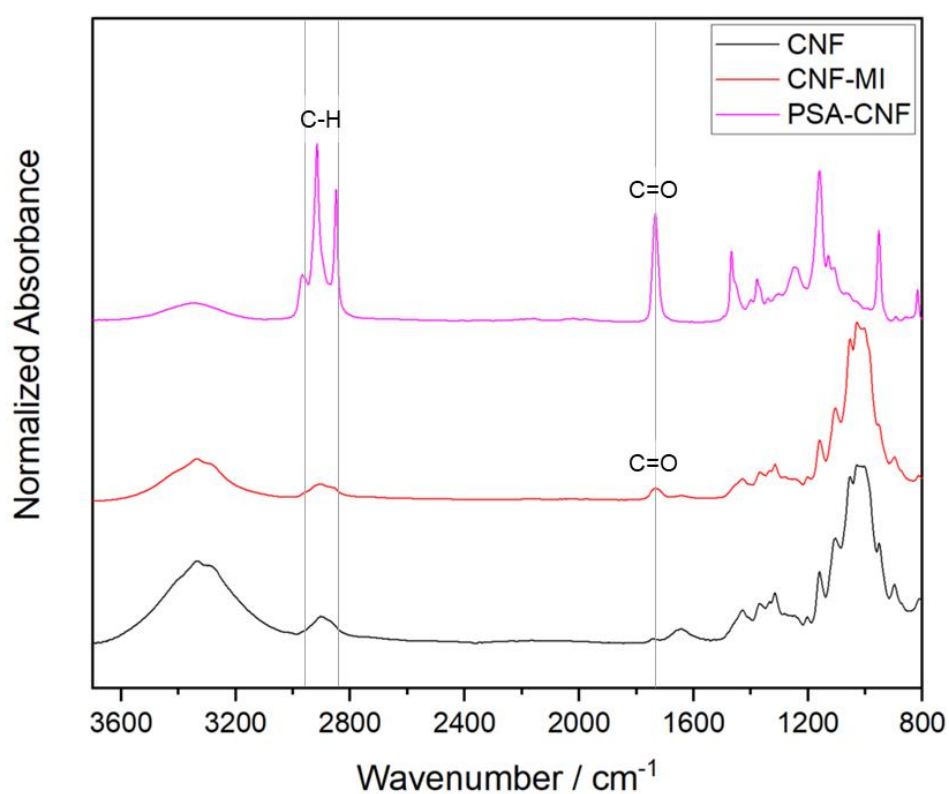


Figure 2. 6 FT-IR spectra of pristine CNF (black), CNF-MI (red) and PSA-CNF (pink).

The ^{13}C cross-polarization magic angle spinning (CP-MAS) NMR spectra of unmodified CNFs, CNF-MI and PSA-CNF are presented in Figure 2. 7. The pristine CNFs have the characteristic NMR signals for cellulose at 105 ppm (C1, glycosidic bonds), 84 ppm

(C4am), 72 ppm (C2, C3, C5), 62 ppm (C6am) for surface sites, and at 89 ppm (C4cr), 76 ppm (C2, C3, C5), 65 ppm (C6cr) for the crystalline fibril interior²³⁸. Spectral deconvolution revealed a significant proportion of hemicellulose (Figure 2. 7 b, orange signals), approximately 15 % molar, which may potentially participate in chemical reactions and consequently impact the conversion rate of CNFs.

Based on the commonly accepted 'core-shell' model, the supramolecular organization of CNFs can be characterized by three parameters: the crystallinity index, lateral fibril dimension (LFD), and lateral fibril aggregate dimension (LFAD), illustrated in Figure 2. 7 b. These parameters allow tracking potential modifications of CNFs induced by different grafting processes. As summarized in Table 2. 1 , the crystallinity of CNF-MI decreases slightly, from 32 % to 27 %, suggesting that the chemical conversion did occur to CNFs. Conversely, in the PSA-CNF sample, the crystallinity significantly increases to 54 %, suggesting degradation of amorphous cellulose. This change correlates with a reduction in the molar proportion of hemicellulose to 7 %.

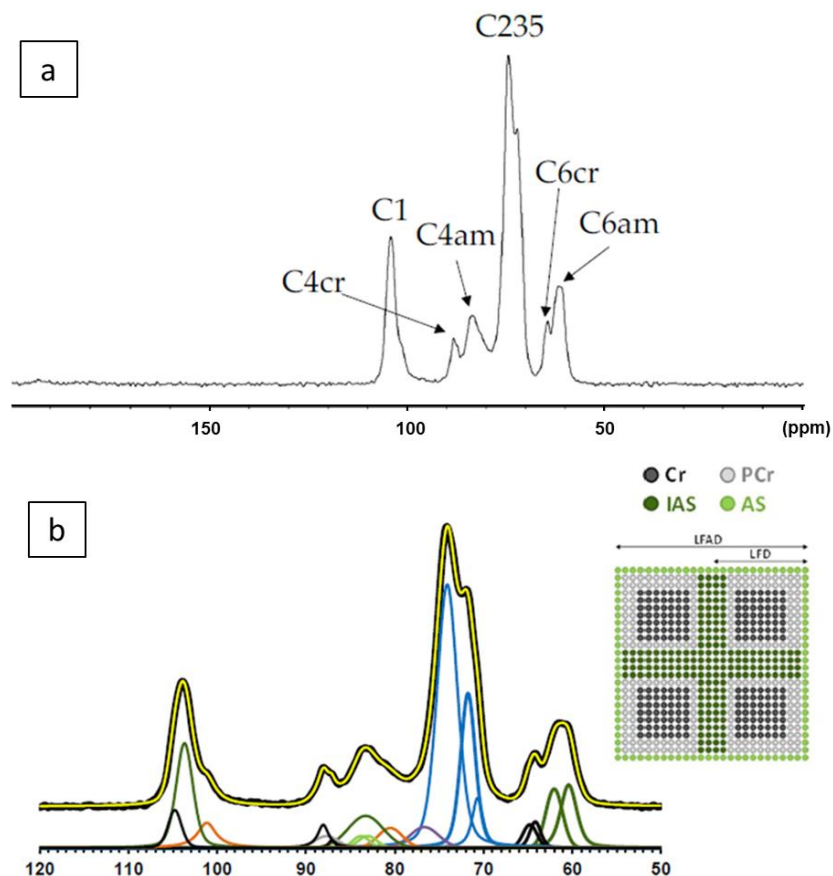


Figure 2. 7 (a) ^{13}C CP-MAS spectrum of CNF sample (b) Deconvolution of 50-120 ppm region. The upper black line corresponds to experimental data. The yellow line corresponds to the sum of individual peaks resulting from the spectral deconvolution. Two signals from hemicelluloses are indicated in orange. Deconvolution of C4 region with crystalline forms Cr ($I\beta$) and Cr ($I\alpha+\beta$) (black), paracrystalline form (PCr) (grey), accessible fibril surfaces (AS) (green), and inaccessible fibril surface (IAS) (dark green).

Table 2. 1 Various parameters for the supramolecular organization of CNFs.

| | CNF | CNF-MI | PSA-CNF |
|---------------------|------|--------|---------|
| Crystallinity index | 32 % | 27 % | 54 % |
| LFD / nm | 2.6 | 2.4 | 4.3 |
| LAFD / nm | 5.2 | 3.9 | n.c. |

Grafting rates were calculated by dividing the signal integral associated with 1 carbon atom from the polymer graft by all signals related to the C4 of cellulose. Note that the signal observed at approximately 39.5 ppm, visible almost exclusively in multiCP spectra, corresponds to residual DMSO and not to a part of the grafts.

For CNF-MI, grafting rates were found to be relatively low at 1.1 %. The CP-MAS spectrum subtracted from the multiCP spectrum provides an estimate of the mobile part of the sample. As shown in Figure 2. 8, CNF-MI exhibits a more significant mobile cellulose component than CNFs and the PSA-CNF sample, which is consistent with a reduction in the crystallinity of CNFs.

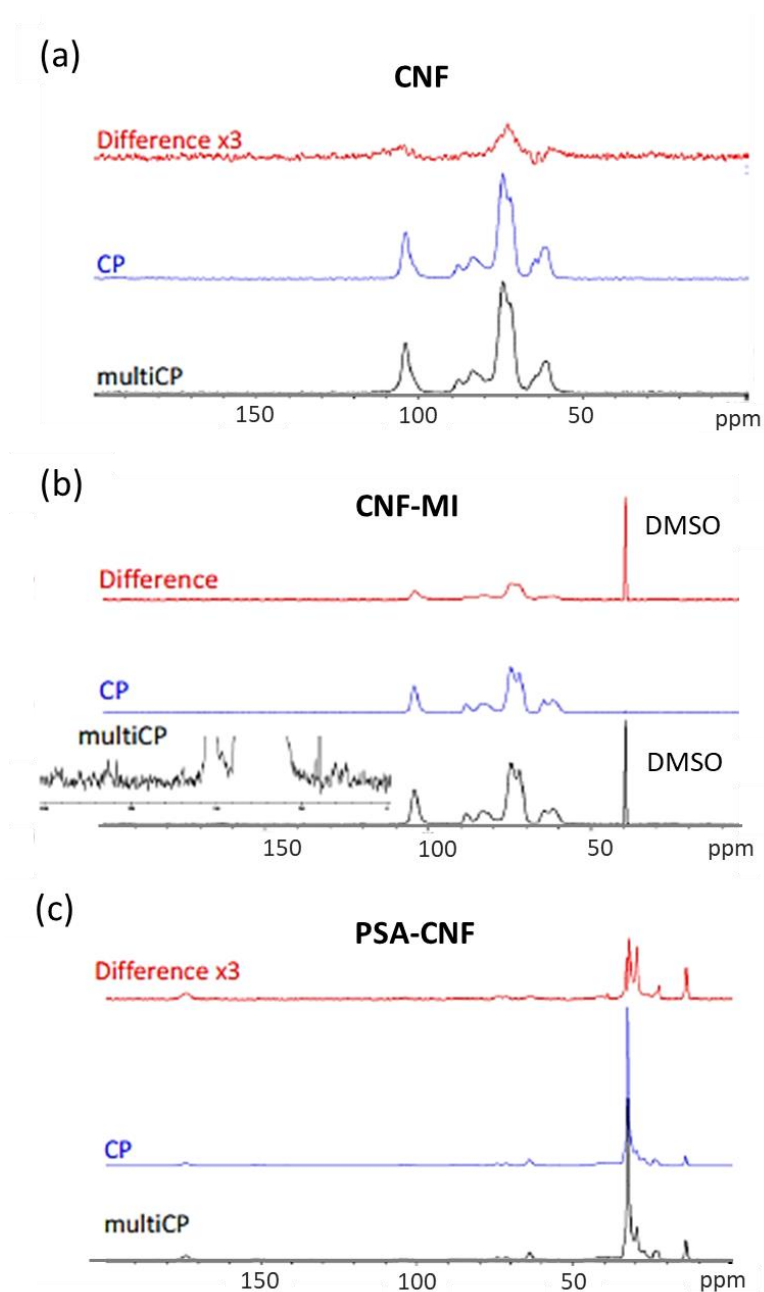


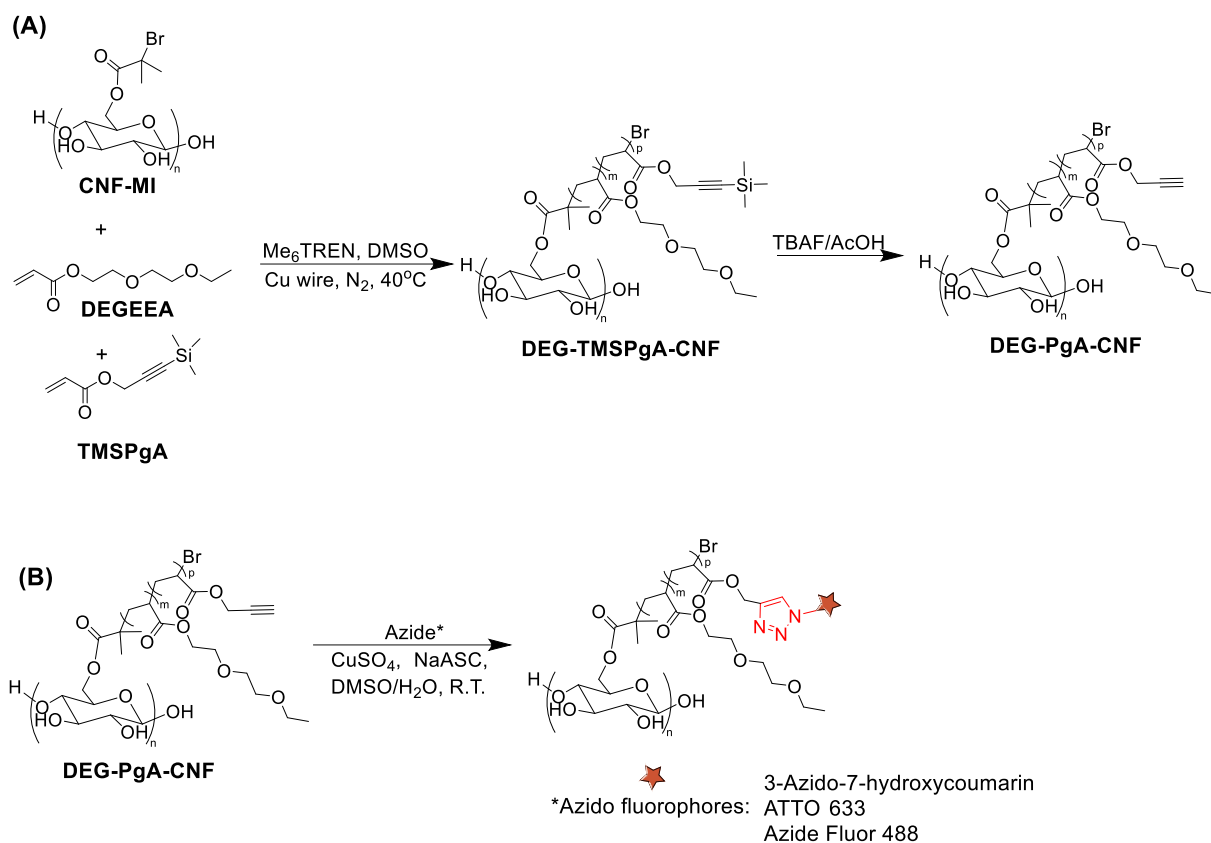
Figure 2. 8 ^{13}C CP-MAS spectra (blue), ^{13}C multiCP spectra (black) and the difference between these spectra (red) of (a) CNF, (b) CNF-MI and (c) PSA-CNF.

It is important to mention that the PSA-CNF sample was synthesized in toluene, which has a CH₃ function, therefore making the grafting calculation obsolete since it was based on this chemical function. To enhance accuracy, the calculation was carried out with the signal at approximately 175 ppm, associated with two esterified carbons; this analysis determined the molar percentage of PSA on CNFs to be 187 %. Combining this with the grafting rate of CNF-MI (1.1 %), the molar percentage of PSA-CNF on each AGU is thus determined to be 170 %. The average molecular weight (M_w) of each graft is calculated to be 55 165 g/mol.

In summary, the successful conversion of CNFs to CNF-MI and their subsequent surface modification with PSA via SET-LRP have been effectively confirmed by combining the results from FT-IR and ¹³C CP-MAS NMR.

2.2.3 Surface initiated SET-LRP: growth of random copolymer poly-DEGEEA and poly-TMSPgA on CNFs (DEG-TMSPgA-CNF) and its post-treatment

Given that the chemical conversion and surface-initiated grafting polymerization pathway have been successfully demonstrated, we now extend it to a more complex scenario. The current objective is to initiate the growth of random copolymers made of di(ethylene glycol) ethyl ether acrylate (DEGEEA) and an alkyne-functionalized monomer in the presence of CNF-MI. The SET-LRP of these two monomers was conducted in the presence of a Cu wire and ligand Me₆-TREN (Scheme 2. 2 A).



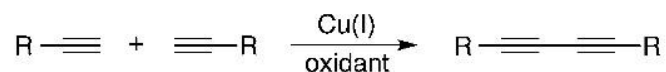
Scheme 2. 2 General chemical strategy for the immobilization of fluorescent dye onto the CNF. (A) di(ethylene glycol) ethyl ether acrylate (DEGEAA) and the protected alkyne acrylate (TMSPgA) grafted onto the CNFs via surface-initiated SET-LRP, followed by the sequential deprotection of trimethylsilyl groups; (B) Cu-catalyzed azide-alkyne cycloaddition between alkyne-induced CNFs and the azido-chromophores.

In the preliminary experiments, we attempted to initiate the SET-LRP of unprotected propargyl acrylate. Unfortunately, the modification of CNFs was not achieved through this polymerization technique. Several undesirable side reactions involving the alkyne functionalities transpired under Cu-catalyzed radical polymerization conditions. Notably, the terminal alkyne groups are not completely inert under the conditions typically employed in Cu-catalyzed radical polymerizations and are susceptible to various side reactions (Figure 2. 9).

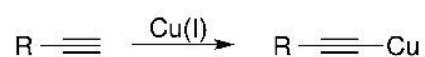
One of the primary unintended reactions was oxidative coupling, commonly referred to as Glaser coupling²³⁹. This side reaction is likely to occur due to the oxidation of Cu^I to Cu^{II} during the polymerization process. Moreover, Glaser coupling may also occur in the presence of deprotected alkyne groups during an open-air CuAAC coupling, whether an

additional Cu^I catalyst is still employed. Thus, employing excess reducing agents or conducting the reaction under an inert atmosphere was considered.

A) oxidative coupling



B) cuprous acetylide formation



C) radical addition



D) radical chain transfer

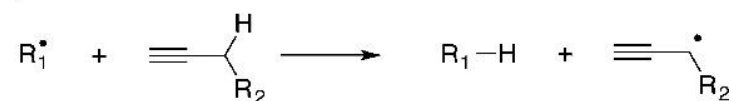


Figure 2. 9 Schematic illustration of side reactions of terminal alkynes under radical polymerizations²³⁹. Copyright 2015 Macromolecules, with permission of American Chemical Society.

In this study, we implemented a protection/deprotection methodology for the alkyne groups to prevent undesired side reactions during the copolymerization process. Firstly, trimethylsilyl propargyl acrylate (TMSPgA) was synthesized via the esterification reaction of acryloyl chloride and 3-(trimethylsilyl) propargyl alcohol. Following the protection step, both monomers TMSPgA and DEGEEA were copolymerized onto the CNF surface to form DEG-TMSPgA-CNF. In the final step, the TMS protecting group was removed and deprotected using a tetra-n-butylammonium fluoride (TBAF) in tetrahydrofuran (THF), with acetic acid (AcOH) as a buffering agent. This approach successfully produced deprotected alkyne-functionalized CNF groups, as illustrated in Scheme 2. 2 B.

The efficiency of the co-grafting polymerization of DEGEAA and TMSPgA onto CNFs was first evaluated with FT-IR spectroscopy (Figure 2. 10). The spectra of DEG-TMSPgA-CNF and DEG-PgA-CNF exhibit a significant increase in the carbonyl band at 1733 cm^{-1} , indicating a substantial increase in the number of ester groups per polymer repeating unit compared to the CNF-MI spectra. Additionally, the bands observed at 1250 cm^{-1} and 700 cm^{-1} are attributed to trimethylsilyl groups (TMS, $\text{Si}(\text{C}-\text{H}_3)$) from the TMS-protected alkynes. This confirmed that the trimethylsilyl group remained intact, with no cleavage occurring during or after the surface-initiated polymerization onto CNFs.

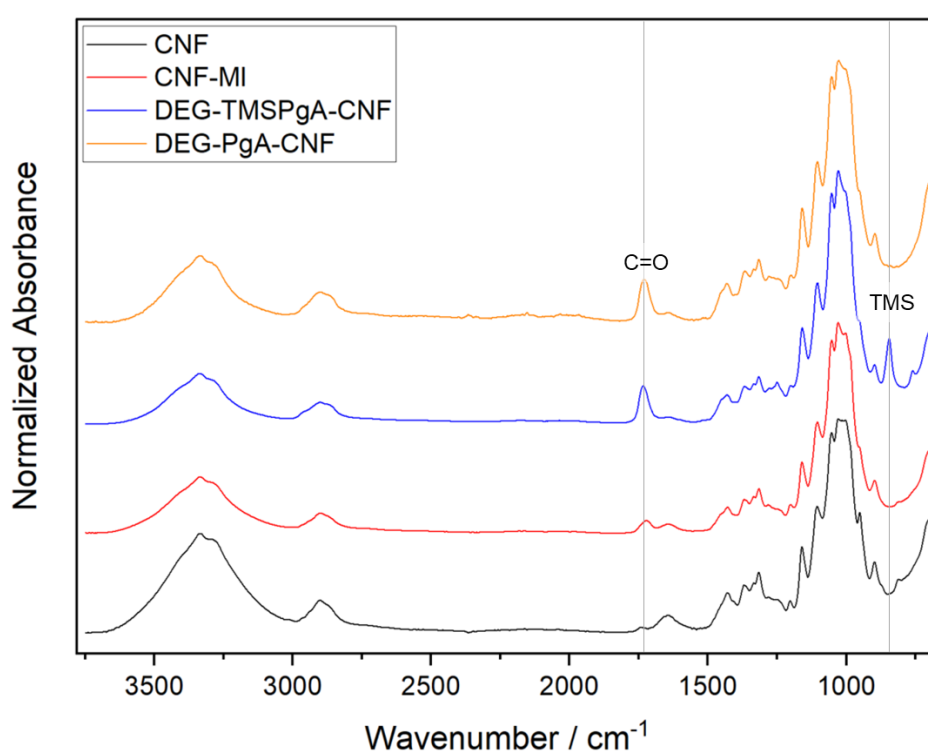


Figure 2. 10 FT-IR spectra of the pridine CNF (black), CNF-MI (red), DEG-TMSPgA-CNF (protected alkyne, blue), DEG-PgA-CNF (deprotected alkyne, yellow).

Following the deprotection step, which involves removing the TMS groups from the CNF surface, the absorption bands at 1250 cm^{-1} and 700 cm^{-1} disappear from the FT-IR spectra, while the carbonyl signals remain unchanged. Unfortunately, detecting the alkyne groups on CNFs is more challenging, as they are difficult to distinguish from the background in the spectrum clearly.

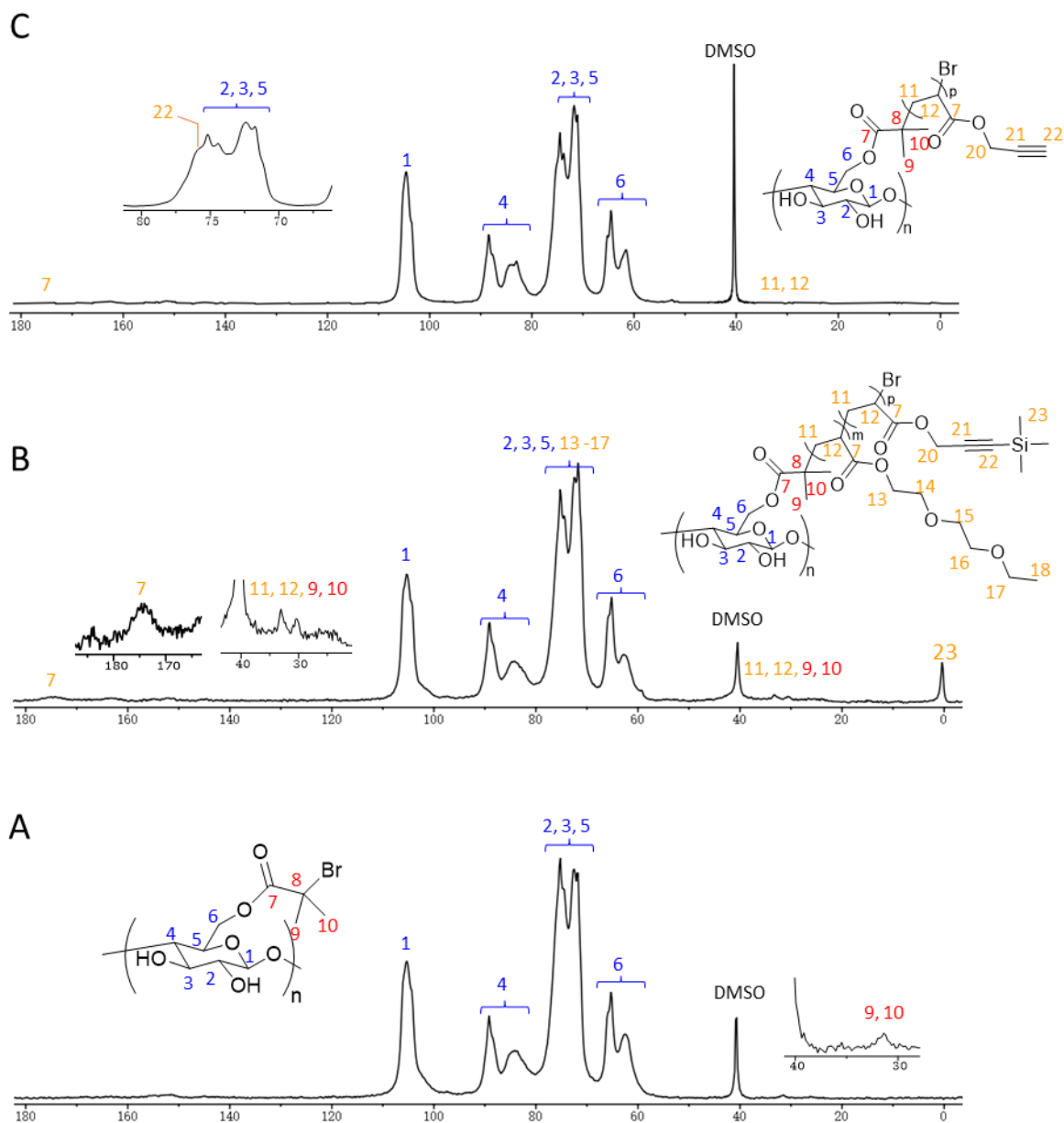


Figure 2. 11 ^{13}C CP-MAS NMR spectra of (a) CNF-MI, (b) DEG-TMSPgA-CNF, (c) DEG-PgA-CNF.

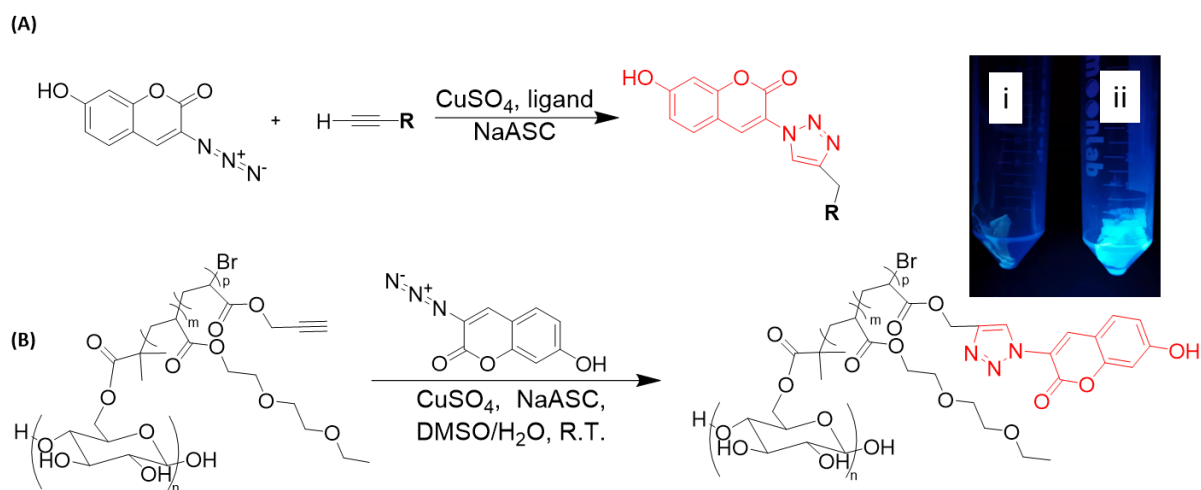
We further enhanced our characterization using solid-state CP-MAS ^{13}C NMR, with the spectra presented in Figure 2. 11. The results align with those obtained from FT-IR. In addition to the characteristic signals of CNFs, an additional signal located at 175 ppm (C7) was observed, corresponding to the carbonyl bonds and the accumulated ester groups of the polymer repeating units. The peak at 0 ppm (C23) corresponds to the TMS-protecting group. Following the deprotection step, the TMS groups disappeared, and a new signal at 76 ppm (C22), appearing as a broad peak overlapping with CNFs (C4), was detected and attributed to the deprotected alkyne groups.

2.2.4 Click chemistry azide-alkyne cycloaddition of alkyne-modified CNFs and various fluorescent azide dyes

2.2.4.a The proof of the presence of alkyne functions via click chemistry with 3-azido-7-hydroxycoumarin

As previously discussed, the grafting of DEGEEA and TMSPgA onto CNFs through SET-LRP was successful. Nevertheless, the direct visualization of alkyne functionalities on CNFs proved challenging, necessitating confirmation via a combination of two characterization techniques. To ensure the presence of the alkyne function onto CNFs, we conducted a test click reaction using DEG-PgA-CNF and 3-azido-7-hydroxycoumarin in a DMSO/H₂O mixture (Scheme 2. 3). An essential aspect of this experiment relies on the fluorescence feature of 3-azido-7-hydroxycoumarin, which can be revealed only when the dye forms a 1,2,3-triazole linkage with an alkyne group through CuAAC; otherwise, the fluorescence remains quenched (Scheme 2. 3 A).

Shortly after initiating the reaction, the CNF suspension became highly fluorescent. Following several purification steps, the luminescent CNFs were collected (Scheme 2. 3 B (ii)). This click reaction was also performed with unmodified CNFs and CNF-MI under identical conditions to serve as controls. In both control cases, the suspensions did not show any fluorescence under UV light, indicating no cycloaddition reaction occurred due to the absence of alkyne functionalities.



Scheme 2.3 (A) Fluorescence feature of 3-azido-7-hydroxycoumarin, used to investigate reaction conditions before using the expensive biomolecule or cargo reagent(s); (B) CuAAC reaction of DEG-PgA-CNF and 3-azido-7-hydroxycoumarin: (i) DEG-PgA-CNF before the reaction, (ii) after the reaction with the fluorescence of 3-azido-7-hydroxycoumarin.

Despite the successful attachment of functional molecules to CNF surfaces, determining the precise number of reagents remains challenging, particularly in estimating the exact quantity necessary for complete surface coverage. In our experimental setup, the reagents for CuAAC were calculated based on the assumption of 100 % chemical conversion in SET-LRP and the subsequent deprotection, equating to 1 μmol of alkyne groups in 0.4 mg of dry DEG-PgA-CNF. 2 equivalents of azide were used for each alkyne group to ensure rapid reaction kinetics, given the relatively low alkyne concentration; the concentration of the Cu catalyst was controlled at 250 μM for efficient cycloaddition.

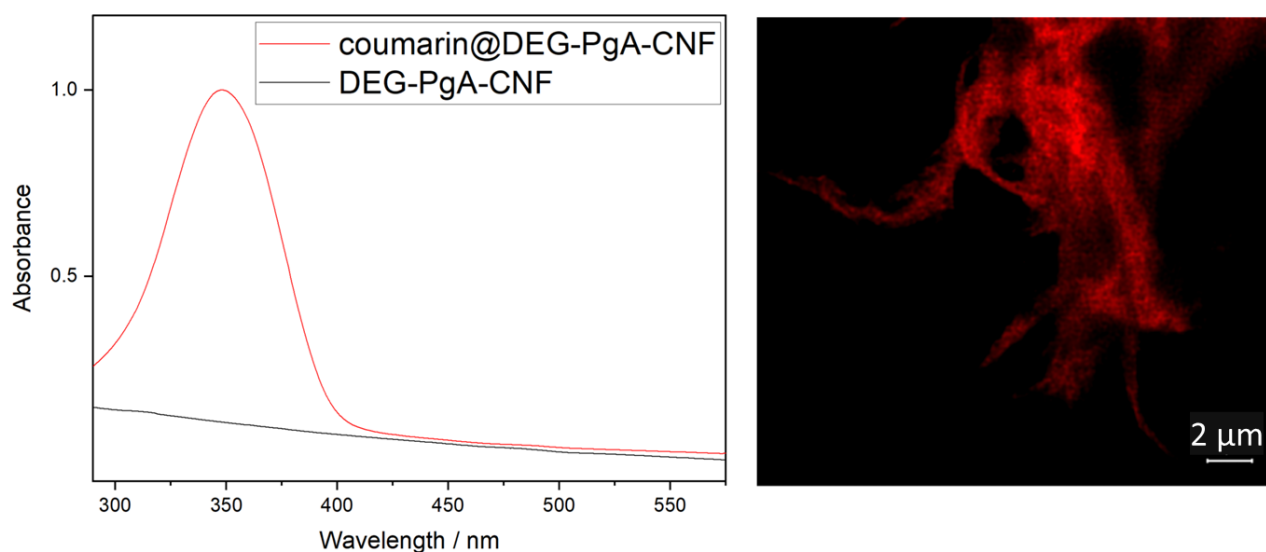


Figure 2. 12 Left: UV-Vis spectra of DEG-PgA-CNF (black) and coumarin@DEG-PgA-CNF (red); right: confocal scanning laser microscopy imaging of coumarin derivate labeled on the polymer modified CNFs (fluorescence image obtained at an excitation wavelength of 488 nm, red color).

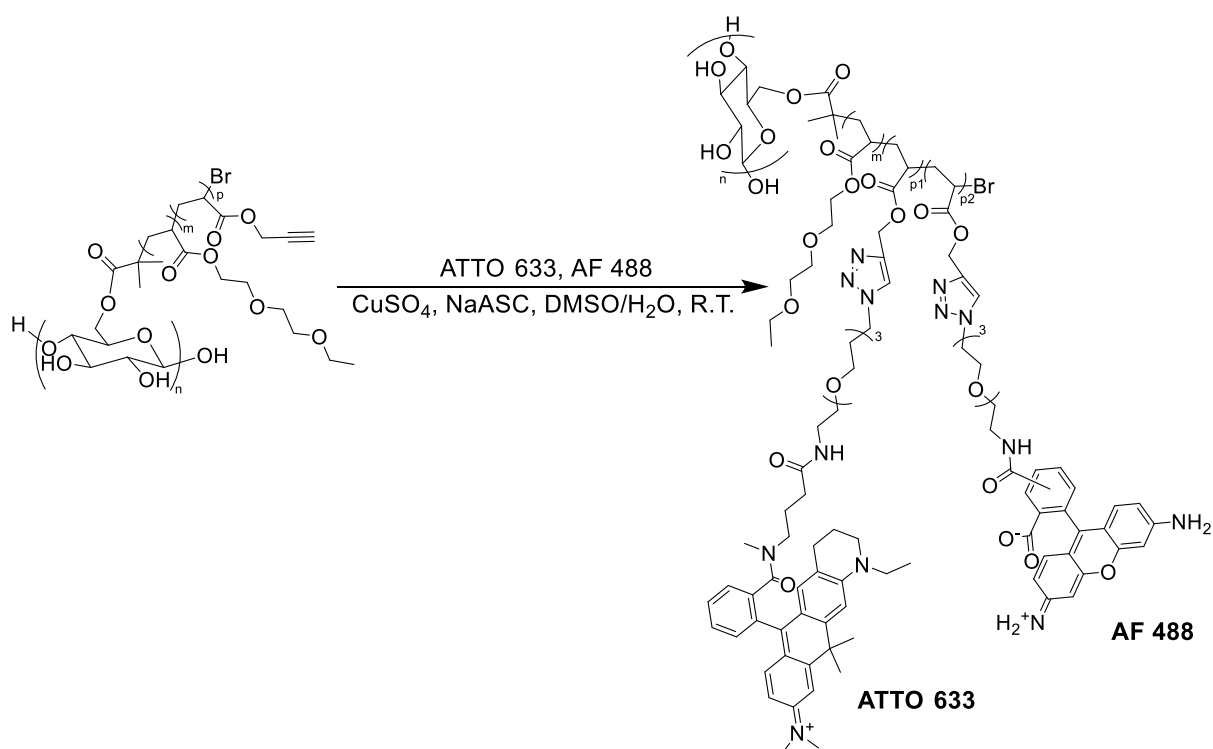
Initial characterization was performed using UV-Vis spectroscopy; the resulting spectra (Figure 2. 12, left) showed a strong absorption band at 350 nm in the luminescent CNFs, in contrast to the spectra of DEG-PgA-CNF, which displayed no distinct absorption bands in the visible range. This result confirms the successful grafting of the coumarin azide dye onto the alkyne-functionalized CNFs through CuAAC.

Further imaging by confocal laser scanning microscopy (CLSM) revealed fluorescent spots uniformly distributed along the CNF surface, indicating a homogeneous decoration of the fibrils with the fluorescent dye (Figure 2. 12, Right). This visualization not only confirms the presence of alkyne functionalities but also demonstrates the effectiveness of the surface modification strategy.

2.2.4.b Fluorescence labeling of DEG-PgA-CNF via click chemistry with ATTO 633 and AF 488

As detailed earlier, successful attachment of a fluorescent coumarin dye derivative to CNFs was achieved using a CuAAC, providing a foundation for further functional modifications. Building upon this success, our objective shifted towards labeling CNFs with specific dyes to facilitate single-molecule studies using stimulated emission

depletion (STED) microscopy. For this purpose, two distinct fluorescent dyes, ATTO 633 and AF 488, were conjugated onto CNFs as depicted in Scheme 2. 4.



Scheme 2. 4 Preparation of luminescent cellulose nanofibrils: labeling of the two dyes ATTO 633 and AF 488 onto DEG-PgA-CNF through click chemistry.

The first dye, AF 488, with absorption and emission wavelengths (Abs/Em) of 501/525 nm, was chosen for its bright green fluorescence. This dye is extensively utilized in confocal microscopy due to its robustness and provides excellent spectral separation from ATTO 633. Its primary purpose in this study was to facilitate easy localization of CNFs under the microscope.

The second dye, ATTO 633, exhibits red fluorescence with Abs/Em wavelengths of 630/657 nm. This dye is particularly advantageous for STED microscopy because of its high quantum yield and photo-stability, which are essential attributes for accurate and detailed imaging at the molecular level.

Two separate batches of fluorescent CNFs were prepared: one batch labeled with both dyes (AF 488 and ATTO 633), referred to as AF 488&ATTO 633@DEG-PgA-CNF, and

another batch labeled solely with ATTO 633, referred to as ATTO 633@DEG-PgA-CNF, as exposed in Scheme 2. 4. The dual-labeled and singly-labeled CNFs are intended to address different aspects of the microscopy and labeling study, enabling a comprehensive analysis of CNF behavior under various imaging conditions.

2.2.5 Morphology study of modified CNFs and their embeddings in PVA

As previously mentioned, STED microscopy, when combined with suitable dyes and optical schemes, can achieve exceptionally high resolution, as illustrated in Figure 2. 3. To process the images, we employed a deconvolution method using a standard algorithm to prevent over-deconvolution, along with a modeled point spread function (PSF) specific to our experiment. This PSF was validated using 40 nm beads that exhibit excitation and emission within the same wavelength ranges as our fibrils.

Accordingly, the CNFs, modified and labeled with specialized fluorescent dyes or integrated into a composite material, are ideally suited for exploration using this high-resolution technique. Samples were prepared with DEG-PgA-CNF labeled with both AF 488 and ATTO 633 (AF 488&ATTO 633@DEG-PgA-CNF) or solely with ATTO 633 (ATTO 633@DEG-PgA-CNF) in a 0.5 wt% DMSO suspension to ensure the detection of isolated modified CNFs and optimal signal clarity against a clean background under microscopic observation.

We hypothesized two possible morphologies of the grafted polymer chains on the CNF surfaces: either extending away from (Figure 2. 13, M1) or wrapping around the CNFs (Figure 2. 13, M2). These morphologies correspond to the observed fluorescent patterns, either spreading along or encircling the CNFs.

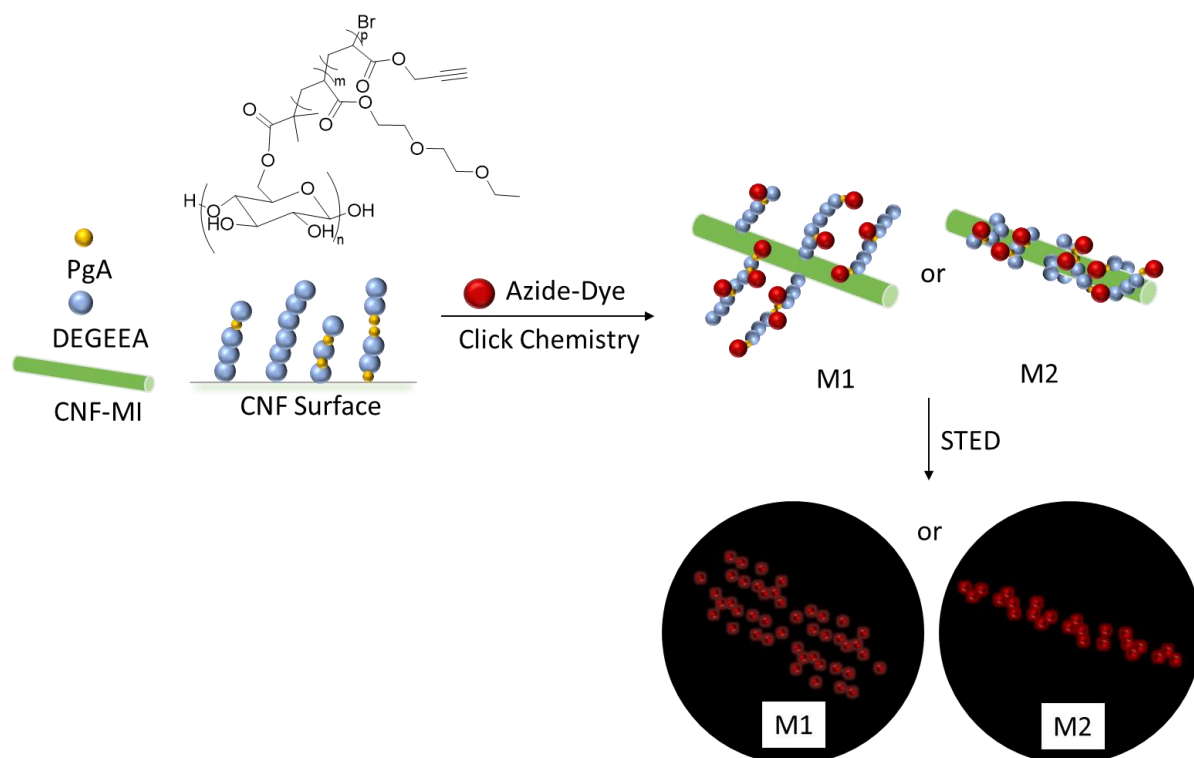


Figure 2. 13 Schematic illustration of labeling fluorescent dyes on CNF surfaces and hypothetical morphologies of modified CNFs.

2.2.5.a STED & high-resolution imaging of modified single CNFs

Figure 2. 14 presents a series of deconvolved STED images, where fluorophores appear as red dots configured into spaghetti-like shapes. In Figure 2. 14 (a), for instance, the fibrils display a continuous fluorescent strip measuring 56 nm in width and 9 μm in length, dimensions typical of CNFs processed mechanically. Notably, the fluorescent strip exhibits a periodic pattern of luminescent red dots interspersed with non-fluorescent (black) spaces, potentially indicating either grafted di(ethylene) glycol chains, unmodified alkyne functions or unmodified CNF surfaces due to the low grafting rate, as described previously. As mentioned earlier, excess azide dyes were employed strategically to maximize the functionalization efficiency of the alkyne groups.

This periodical interval phenomenon was consistent across all imaged CNFs and samples. Detailed analysis of the polymeric-modified CNF morphology confirmed that the grafted polymer chains predominantly wrap around the CNF surfaces (Figure 2. 13, M2). The spatial arrangement of the fluorophores primarily reflects the intrinsic dimensions and morphology of CNFs rather than the disposition of the grafted polymer.

Further observations were made regarding the interactions between various CNF nanostructures. Figure 2. 14 (b) provides an overview of the representative CNFs with different interfibrillar structures, as observable via STED microscopy. These interfibrillar structures can be categorized into three types: homogeneous networks (Figure 2. 14, c), fibril bundles (Figure 2. 14, d), and clusters (Figure 2. 14, e). A homogeneous network consists of individual fibrils spaced no more than 0.5 μm apart; a fibril bundle comprises multiple aligned fibrils separated by approximately 50 nm; and a cluster encompasses entangled fibrils or bundles with minimal gaps below 10 nm.

For optimal dispersion of CNFs in solvents such as DMSO to create a stable suspension, monomers with extended hydrophilic groups like oligo(ethylene glycol) are considered for the CNF surface modification. These long hydrophilic groups effectively interact with the solvent molecules (DMSO & H_2O), thereby reducing interfibrillar interactions.

Lastly, it is important to note that for a given chromophore, the intensity of the fluorescent signal is directly proportional to the concentration of the fluorophore. In some instances, this can indicate an inhomogeneous dispersion of CNFs, with dense dye aggregations potentially leading to fluorescence signal saturation and rendering STED measurements infeasible.

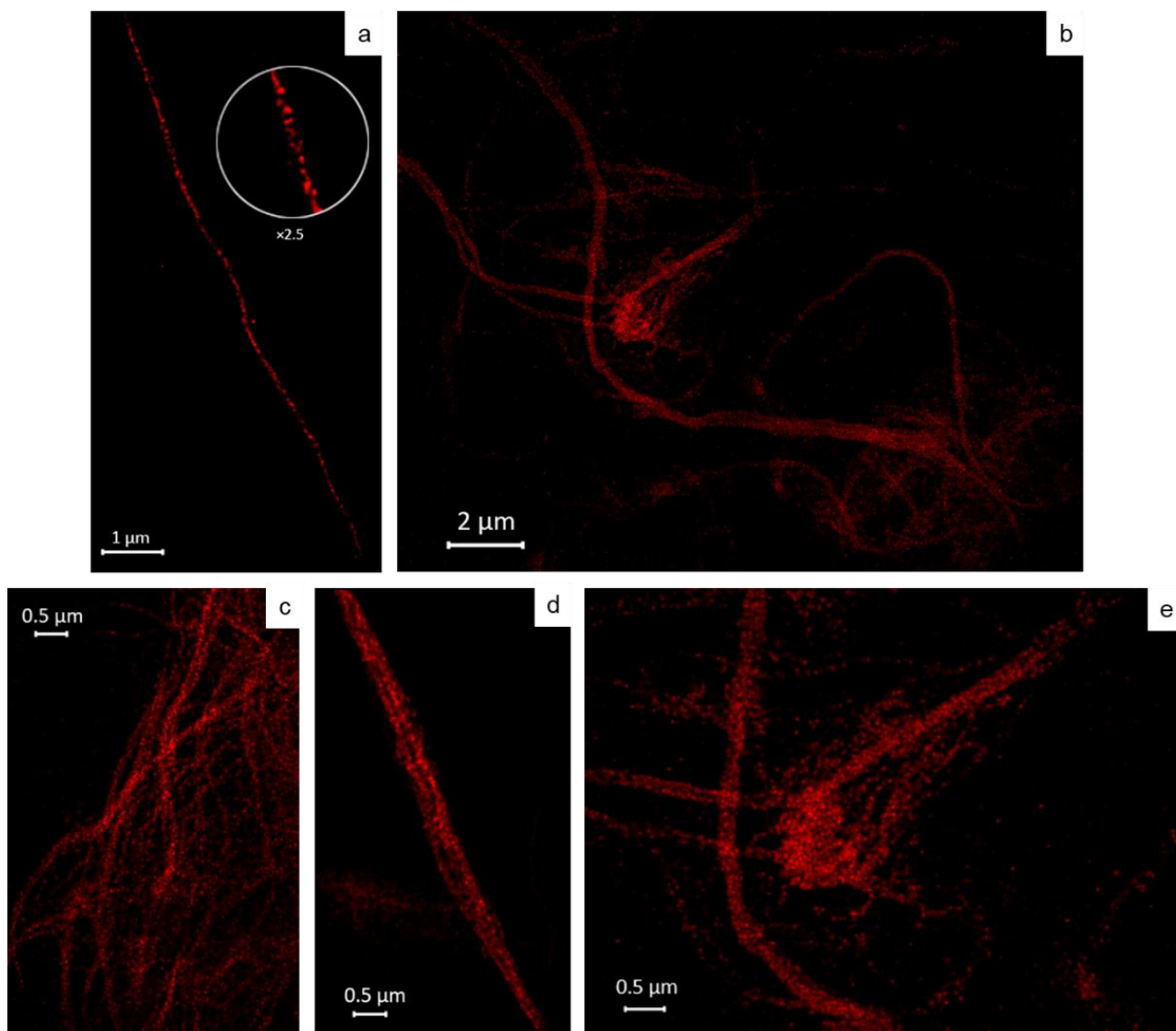


Figure 2. 14 Deconvolved STED images of modified CNFs: (a) isolated fibril, (b) dispersion state of fibrils, (c) fibril network, (d) fibril bundle, (e) cluster.

2.2.5.b STED & high-resolution imaging of modified CNFs in PVA

As previously noted, traditional methods for investigating the morphology of CNFs within composites, such as AFM, SEM and TEM, often struggle to differentiate between CNFs and the surrounding matrix materials. For example, Figure 2. 15 (a) illustrates a FESEM image of a modified CNF/PVA composite where the CNFs are indistinguishable as they are completely embedded within the matrix. However, the application of STED microscopy, especially when combined with fluorescent labeling, significantly enhances the visualization of CNFs, revealing not only their morphology but also their spatial arrangement within the PVA matrix (Figure 2. 15, b).

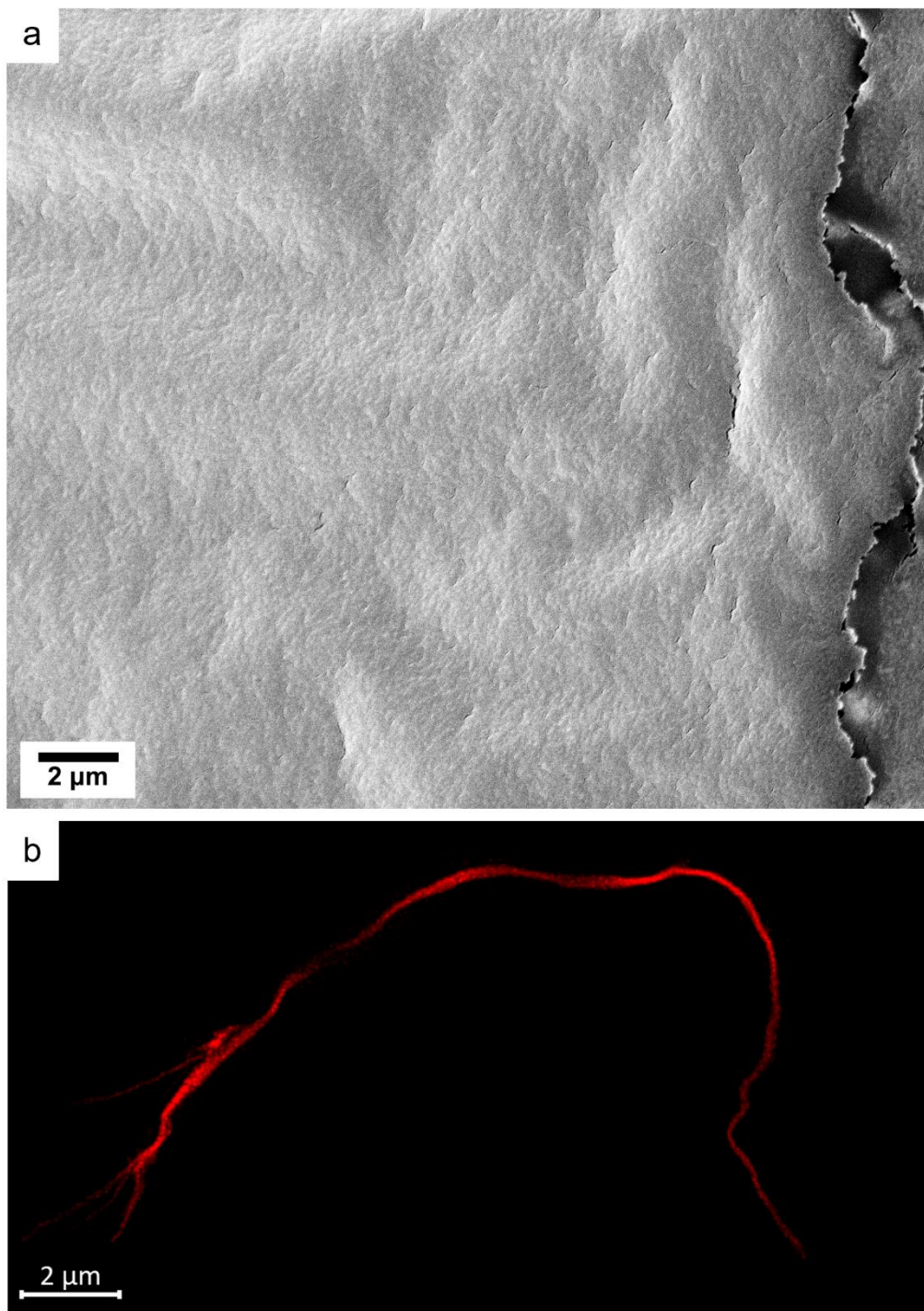


Figure 2. 15 (a) FESEM image of fibrils/PVA composite, (b) STED image of fibrils in PVA.

Our initial investigations utilized STED microscopy to image isolated CNF nanostructures. We then extended this approach to explore the morphology of CNFs embedded in a PVA composite using a combination of CLSM and STED microscopy (Figure 2. 16). CLSM is beneficial for its ability to illuminate the entire specimen quickly and locate all chromophores simultaneously. By integrating CLSM with STED microscopy, we were able

to clearly identify and analyze the distribution of fluorescently labeled CNFs (AF 488&ATTO 633@DEG-PgA-CNF and ATTO 633@DEG-PgA-CNF) throughout the three-dimensional PVA matrix (Figure 2. 16, b).

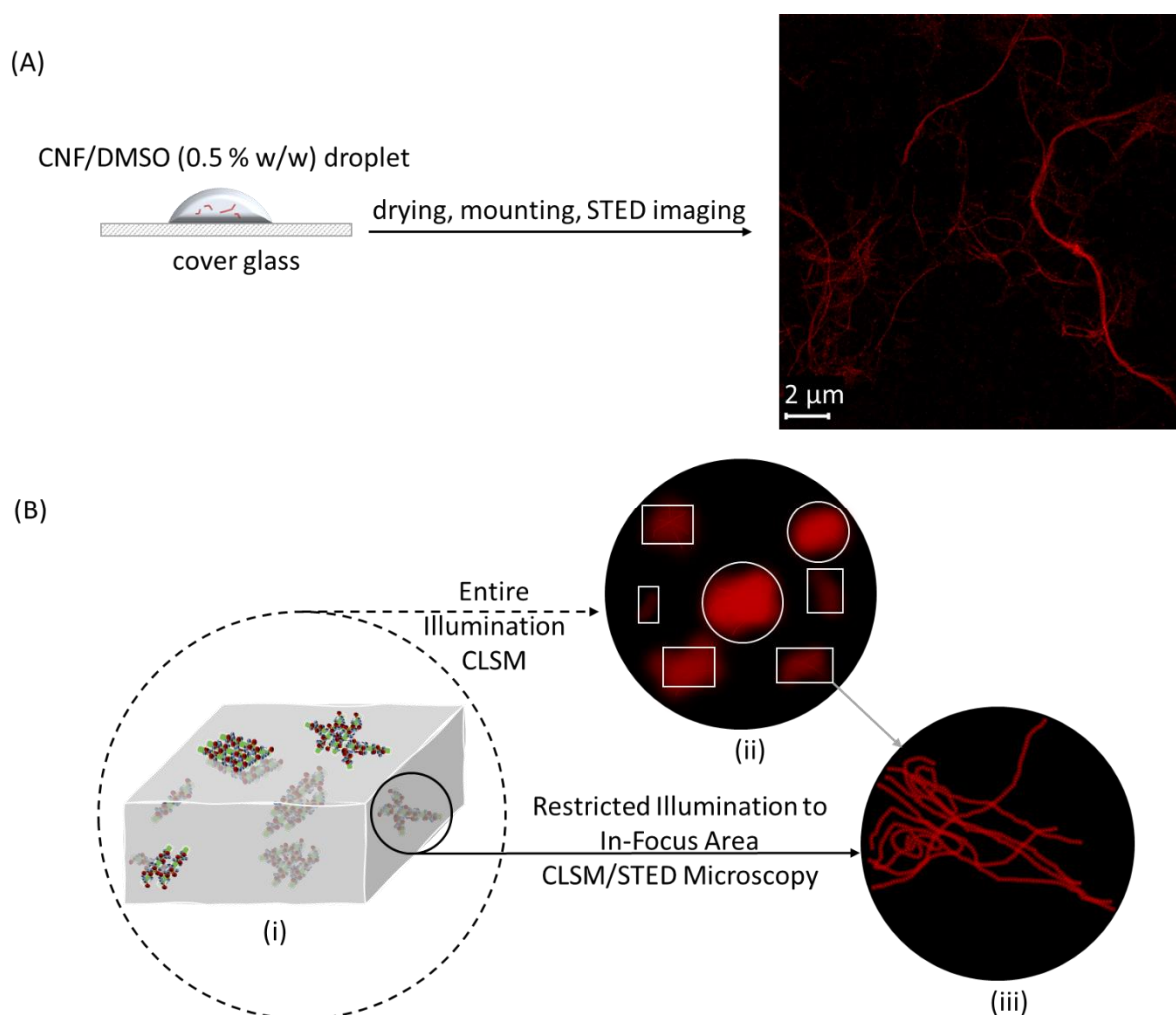


Figure 2. 16 Schematic illustrations of (a) STED imaging of fibrils dried from DMSO, (b) detecting distribution and morphology of modified CNFs within a PVA composite: (i) a model showcasing modified CNFs in PVA, (ii) a concept map overview depicting modified CNFs in PVA with "in-focus" regions highlighted in circles and "out-of-focus" regions in rectangles, (iii) a conceptual image illustrating the focused structure of modified CNFs within the PVA matrix.

When observed in a previous STED study, fibrils were deposited directly on a cover glass via solvent evaporation, positioning all fibrils within the same focal plane (Figure 2. 16, a). But now, within the PVA matrix approximately 10 μm thick, CNFs are distributed three-dimensionally, leading to potential dispersion or aggregation at varying depths. This results in CNFs appearing sharply on the "in-focus" plane or as blurry spots depending on the "out-of-focus" plane (Figure 2. 16, b).

The distribution and localization of the CNFs within the PVA matrix were first studied using the CSLM, providing a broad overview of the composite structure (Figure 2. 17, a b). Interestingly, although both dyes served specifically within our samples, we observed distinct behaviors when the CNFs were incorporated into the PVA matrix. In the CNFs labeled with both AF 488 and ATTO 633, large aggregates ranging from 50-100 μm were observed in Figure 2. 17 a; these aggregates exhibited chromophore density so high that they caused complete signal saturation and could not be further analyzed by STED microscopy.

Conversely, the sample containing only ATTO 633@DEG-PgA-CNF demonstrated much smaller aggregates when first observed under CSLM (Figure 2. 17, b). Subsequent STED analysis revealed distinct interfibrillar structures and fibril networks with clear spacing between each fibril. Further detailed structures within the ATTO 633@DEG-PgA-CNF aggregates were disclosed, illustrating a relatively homogeneous network of fibrils tightly associated within the PVA, with maximum inter-fibril distances of about 0.2 μm (Figure 2. 17, c-e).

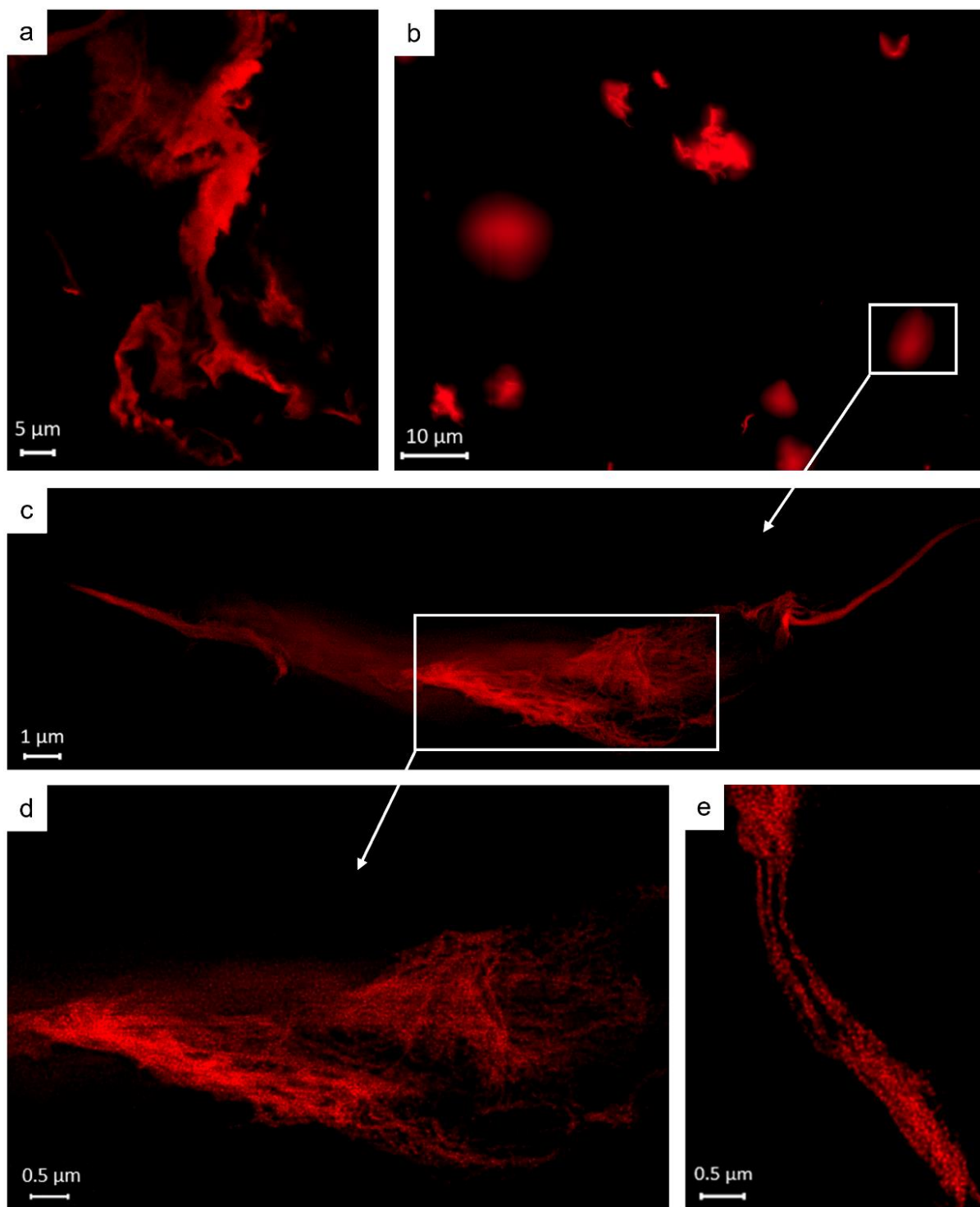


Figure 2. 17 STED images of modified CNFs (0.5 wt%) in PVA (10 wt%): (a) deconvolved confocal image of a cluster of AF 488&ATTO 633@DEG-PgA-CNF, (b) map overview of ATTO 633@DEG-PgA-CNF in PVA matrix, (c) deconvolved STED image of a cluster of ATTO 633@DEG-PgA-CNF, (d) intrafibrillar network, (e) single fibrils from a bundle.

Through STED microscopy, the modified CNFs embedded in a PVA composite are finally exposed. When compared to traditional grey-scale FESEM images, such as that shown in

Figure 2. 18, which displays an outer-face aggregate of ATTO 633@DEG-PgA-CNF with a buried deeper structure, STED microscopy significantly enhanced our understanding of fibril morphology within composites.

In summary, STED microscopy has proven to be an exceptional tool for the detailed study of fibril morphology, affirming its superior performance over conventional microscopic techniques in discerning detailed structural differences in composite materials.

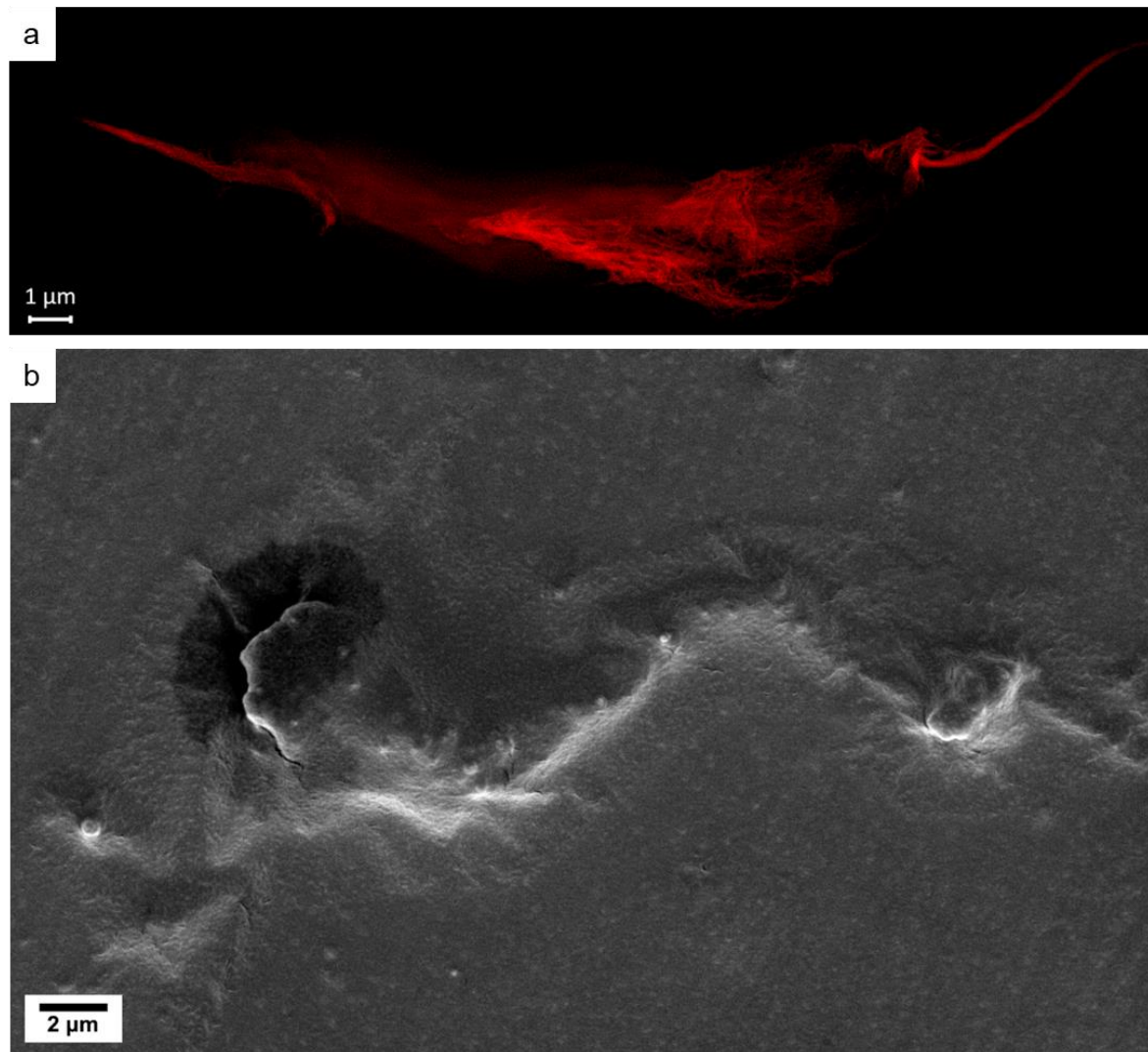


Figure 2. 18 ATTO 633@DEG-PgA-CNF in a PVA matrix: (a) STED image, (b) FESEM image.

2.3 Conclusion

The extraction of CNFs from ECF-bleached kraft pulp was accomplished through a series of mechanical disintegrations. We employed SEM and optical fiber analysis through FiberLab to monitor the morphology and dimensions of cellulose as the production process advanced. Initially, fiber shredding was predominantly observed during the grinding stage, which resulted in the liberation of CFs and their fragmentation into smaller entities. Subsequent repetitions of microfluidization under high pressure and high shear forces enhanced the homogeneity of the CNFs.

To surface-modify the CNFs, we devised a tunable strategy combining Cu⁰-mediated radical polymerization and CuAAC. FT-IR and solid-state ¹³C NMR confirmed the successful synthesis of CNF-MI and the initiation of random copolymer growth on CNF surfaces via SET-LRP. The effectiveness of induced terminal alkyne groups was proven by the restored fluorescence of 3-azido-7-hydroxycoumarin through CuAAC. This versatile strategy could be adapted to modify CNFs with desired properties for applications in a broad scope. This adaptable strategy has the potential to custom-tailor CNFs with specific properties for a wide range of applications. Nonetheless, the method's main drawback is the relatively high cost of synthesizing TMSTgA and the extensive use of protection/deprotection strategies.

The novelty of this study lies in the morphology investigation of modified CNFs using CLSM and STED microscopy. These techniques also enabled nondestructive visualization of the modified CNFs within a PVA composite.

The deconvolved STED images revealed that the grafted polymer chains closely enveloped the CNFs, hence highlighting their dimensions. Measurements of multiple specimens revealed widths ranging from 56 nm to 68 nm, and lengths extending several micrometers, aligning with the typical dimensions of CNFs produced through mechanical treatment. The study also examined the behaviors of CNFs dried from DMSO, including individual fibrils, fibril networks, bundles, and clusters.

Finally, the distribution and morphology of modified CNFs embedded in a PVA composite with a thickness of approximately 10 μm were revealed using a combination of a widefield

microscope and CLSM/STED microscopes. Additionally, we were able to adjust the compatibility of the modified CNFs within the matrix by varying the clickable entity/precursor, significantly altering the adhesion of the CNFs within the composite matrix. These modifications, which are typically undetectable using traditional electron microscopy techniques like SEM and AFM, were successfully captured with STED microscopy. This demonstrates the superior capability of STED microscopy in resolving fine structural details within composite materials.

2.4 Materials and methods

2.4.1 Materials

1,1'-carbonyldiimidazole (CDI, 98 %), 3-(Trimethylsilyl)propargyl alcohol (98 %) were purchased from abcr. Dimethyl sulfoxide (DMSO, ≥ 99 %), imidazole (≥ 99 %), anhydrous diethyl ether (99 %), acryloyl chloride (96 %), tris[2-(dimethylamino)ethyl]amine (Me₆-TREN, 98 %), copper(II) sulfate pentahydrate (CuSO₄·5H₂O, ≥ 99 %), L-ascorbic acid sodium salt (NaASC, 99 %), poly(vinyl alcohol) (PVA, 98-99 %), Cu wire (diameter 0.812 mm, 99.9 %) were purchased from Alfa Aesar. 2-bromo-2-methyl-propionic acid (98 %), di(ethylene glycol) ethyl ether acrylate (DEGEEA, 90 %), hydroquinone (99 %), triethylamine (TEA, 99 %), sodium carbonate (Na₂CO₃, 99.5 %), hydrogen chloride solution (0.1 M), tetrahydrofuran (THF, 99.9 %) and azide fluor 488 (AF 488, ≥ 90 %) were purchased from Sigma-Aldrich. Acetone (99.90 %) was purchased from BCD-Chemie. Acetic acid (AcOH, 99 %) was purchased from Chemsolute. Ethyl 2-bromo-2-methyl propionate (EBiB, 98 %) was purchased from Fisher. Tetrabutylammonium fluoride (TBAF, 1 M in THF) and 3-azido-7-hydroxycoumarin were purchased from TCI Chemical. ATTO 633 was purchased from ATTO-TEC GmbH.

DI water (0.055 μ S/cm) was used for the solvent-exchange procedure and synthesis.

All the monomers for grafting polymerization were passed through a basic alumina column to remove inhibitors.

2.4.2 Experimental section

2.4.2.a Production of CNFs

As a source of dry cellulose, elemental chlorine-free (ECF) bleached softwood kraft pulp was supplied by MERCER Stendal GmbH, Germany. The Northern bleached softwood kraft pulp, composed of 30 - 60 % pine and 40 - 70 % spruce, was PFI-milled at 23 °C with 50 % relative humidity. For the initial step, 10 g dry cellulose pulp was shredded into small parts and distributed into the grinding elements of a Herzog grinding machine. After

adding 212 ml, the grinding vessel was secured into the planetary mill and processed for 6 min. To determine the grind rate, the resulting suspension was diluted to 0.24 % (w/v) using 4.2 l water. From this dilution, 835 ml fiber suspension was transferred into a Schopper-Riegler measuring vessel and topped up to 1000 ml with water. The degree of grinding was determined to be 75 SR° using the SCHOPPER-RIEGLER method (DIN EN ISO 5267-1).

To mechanically disintegrate the cellulose fibers into CNFs, a Microfluidizer (M-110EH-30 Microfluidics) from Indexcorp was employed. The fiber suspension first passed through two chambers with orifice widths of 400 µm and 200 µm width under a pressure of 15 000 Psi twice. Subsequently, the suspension was processed through two thinner chambers with orifice widths of 200 µm and 100 µm successively under the pressure of 25 000 Psi four times.

Finally, the CNF suspension was concentrated by centrifugation at 6000 rpm for 45 min using a centrifuge (Sorvall LYNX 6000) from Thermo SCIENTIFIC. A portion of the CNFs was then dried overnight at 60 °C to determine the solid content.

2.4.2.b Solvent exchange procedure

10 g of the CNF aqueous gel (2 wt%) were first suspended in 80 ml of water. Following this, DMSO (150 ml) was gradually added to the aqueous mixture while stirring continuously for 2 h. The resulting suspension was finally collected and subjected to centrifugation (6000 rpm, 20 min). The supernatants were removed and replaced with fresh DMSO. The centrifugation process was repeated four times. To assess the solid content, a portion of the CNF gel was dried overnight at 50 °C.

2.4.2.c Synthesis of the CNF-Based macroinitiator (CNF-MI)

The CNF gel, which had been solvent-exchanged in DMSO (10 g, 1.0 wt%), was suspended in DMSO (100 ml). The temperature was then increased to 55 °C., and imidazole (3 g, 44 mmol) was added to the suspension. To degas the mixture, nitrogen was continually purged throughout the process. Separately, 2-bromo-2-methyl propionic acid (4 g, 24 mmol) was dissolved in DMSO (60 ml) and purged with nitrogen for 10 min. Then CDI (4 g, 24 mmol) was slowly added while stirring at room temperature until it was fully

dissolved and gas production ceased. This prepared solution was then gradually introduced into the CNF suspension. The reaction proceeded under a nitrogen atmosphere overnight at 55 °C. To purify the modified CNF, the mixture underwent sequential washing with DMSO (30 ml) and centrifugation (6000 rpm, 30 min). The purification process was repeated eight times. A certain amount of CNF-MI gel was dried under 50 °C overnight to determine the solid content.

2.4.2.d Synthesis of acrylic acid 3-trimethylsilyl-prop-2-ynyl ester (TMSPgA)

3-(Trimethylsilyl) propargyl alcohol (5 g, 39 mmol), TEA (7.61 ml), and hydroquinone (30 mg, 0.3 mmol) were dissolved in anhydrous diethyl ether (50 ml) and cooled in an ice-water bath. A solution of acryloyl chloride (3.80 ml) in diethyl ether (20 ml) was added dropwise over 30 min. The reaction mixture was kept in an inert nitrogen atmosphere, stirred in the ice bath for 1 h, and then allowed to warm to room temperature and stirred overnight. The final product was obtained by extracting the mixture with a Na₂CO₃ solution (1 M aq., 3×100 ml) and then evaporating the collected organic phase using a rotary evaporator.

2.4.2.e Synthesis of polymer SA onto CNFs (PSA-CNF) via SET-LRP

A Cu wire (diameter=1 mm, length=6 cm) was first immersed in a concentrated HCl solution for 10 min, then rinsed with acetone and dried prior to use. Meanwhile, CNF-MI (4.0 g, 1.0 wt%) was suspended in DMSO (30 ml). SA (5 g, 15.4 mmol) dissolved in toluene (15 ml) was added into the suspension. The HCl-treated Cu wire was then added to the mixture, which was degassed by purging with nitrogen for 10 min. Once the temperature was raised to 40 °C, the Me₆-TREN ligand (200 μl, 10 vol% in DMSO) was added, initiating the reaction that continued overnight under a nitrogen atmosphere. The product was collected by centrifugation (6000 rpm, 30 min), redissolved in toluene (15 ml) then precipitated in isopropanol (50 ml). These purification steps were repeated four times.

The synthesis of homopolymer SA was also carried out for testing according to the description above, except that EBiB was employed as a sacrificial initiator instead of CNF-MI at a [M]₀/[I]₀/[L]₀ ratio of 100/1/0.2.

2.4.2.f Synthesis of random copolymer of DEGEEA and TMSPgA onto CNFs (DEG-TMSPgA-CNF) via SET-LRP

The polymerization procedure of DEG-TMSPgA-CNF was carried out similarly according to the description above, except that the monomers DEGEEA (1.71 ml, 9.24 mmol) and TMSPgA (1.12 g, 6.16 mmol) were added directly in the suspension, and toluene was not used. The copolymerization of statistical copolymer DEG-TMSPgA-CNF (DEGEEA:TMSPgA=6:4) was carried out in one pot. The modified CNF was purified by sequential washing with DMSO (30 ml) and centrifugation (6000 rpm, 30 min). The purification process was repeated four times.

The synthesis of statistical copolymer DEGEEA and TMSPgA (DEGEEA:TMSPgA=6:4) was also carried out for testing according to the description above, except that EBiB was employed as a sacrificial initiator instead of CNF-MI at a $[M]_0/[I]_0/[L]_0$ ratio of 100/1/0.2.

2.4.2.g Deprotection of trimethyl Silyl (TMS) protected polymers

The TMS-protected polymer (DEG-TMSPgA-CNF 2.9 g, 6.16 mmol TMS groups in theory) was first suspended in THF (72 ml), to which acetic acid (0.7 ml, 12.32 mmol, 2 equiv. mol/mol to TMS groups) was added. The suspension was purged with nitrogen and cooled to -20 °C. Subsequently, a 1 M solution of TBAF·3H₂O in THF (12.32 mmol, 2 equiv. mol/mol to the TMS groups) was slowly added. The mixture was stirred at -20 °C for 30 min before warming to room temperature overnight. The resulting deprotected polymer was purified through sequential washing with THF (50 ml) followed by centrifugation (6000 rpm, 30 min). This purification step was repeated four times.

2.4.2.h General procedure of CuAAC click reaction

A suspension of an alkyne-containing composite (TMS-deprotected CNFs, DEG-PgA-CNF 4 mg dry, 10 μmol alkyne groups in theory) in DMSO (1.6 ml) was combined with a solution of 3-azido-7-hydroxycoumarin in DMSO (4 ml, 5 mM, 2 equiv. mol/mol to alkyne groups) under a nitrogen atmosphere. Separately, a solution of CuSO₄ (0.075 ml, 20 mM aq., 0.15 equiv. mol/mol to alkyne groups) and sodium ascorbate (0.3 ml, 100 mM aq., 3 equiv. mol/mol to alkyne groups) was deoxygenated and then transferred in the suspension. The resulting mixture was covered with aluminum foil and stirred in a

nitrogen atmosphere at room temperature for 24 h. The product was purified by sequential washing with DMSO (5 ml) and centrifugation (6000 rpm, 30 min). This purification process was repeated four times.

The same procedure was performed for labeling DEG-PgA-CNF with fluorescent dyes AF 488 and ATTO 633, respectively, with the exception that 0.5 mg azide dye was used for 1 g DEG-PgA-CNF (1 wt%).

2.4.2.i Blending of PVA with modified CNFs

Two PVA/DMSO solution concentrations were prepared: 5 % and 10 %. PVA was dissolved in DMSO at 80 °C with continuous stirring and then cooled down to room temperature. Afterwards, the suspension of modified CNFs, containing different dyes in DMSO, was thoroughly mixed into each PVA/DMSO solution. This ensured that the final concentration of modified CNFs in each solution was consistently 0.5 wt%.

2.4.3 Characterization

Fourier transform infrared spectroscopy (FT-IR) with an attenuated total reflection was performed using a Bruker Vector 33 spectrometer. The collected spectra represented an average of 60 scans over the spectral region of 3600-550 cm^{-1} , with a spectral resolution of 4 cm^{-1} .

Ultraviolet-visible (UV-Vis) spectroscopy was performed with a Lambda 65 UV-VIS Spectrometer. Absorption spectra in DMSO were measured from 380 to 900 nm, with a resolution of 1 nm, using a 10 mm quartz cuvette.

Proton nuclear magnetic resonance ($^1\text{H-NMR}$) measurements were carried out on a Bruker Avance-III spectrometer HD 400MHz at 400 MHz at room temperature. Samples were dissolved in chloroform-d and placed in NMR tubes.

The micromolecular structure of CNFs and the grafting rate of CNF-MI and PSA-CNF were monitored using a Bruker NEO Ascend 400 WB spectrometer equipped with a cross-polarization magic angle spinning (CPMAS) 4 mm double H/X probe. The spectra were recorded with an accumulation of 2000 scans and a rotation speed of 12 kHz. The spectra

were processed with line broadening at -10 Hz, coupled with a Gaussian multiplication factor of 0.1. Quantitative analysis of the spectra was performed using Peakfit v4.12. Prior to analysis, the samples were hydrated by the addition of 21.9 +/- 0.7 % by mass of ultrapure water. Two acquisitions were performed on each sample: ¹³C CPMAS spectrum, providing signals associated with the rigid portions of the sample, characterizing the supramolecular organization of CNF; ¹³C multiCPMAS spectrum, providing signals from the entire sample and ensuring the quantitiveness of signals from different molecules.

¹³C NMR spectra in Figure 2. 11 were obtained using a Bruker 500 Avance III HD spectrometer. The spectra were acquired at Larmor frequencies of at Larmor frequencies of 125 MHz for ¹³C and 500 MHz for ¹H, respectively. The samples were packed in 4 mm zirconia rotors for magic angle spinning at a rate of 8 kHz. ¹³C CP MAS NMR spectra were recorded with a ¹³C nutation frequency of 10 kHz and a contact time of 1.5 ms. All spectra were produced by Fourier transforming the free induction decays (FIDs), with chemical shifts referenced to neat tetramethylsilane (TMS).

The dimensions of cellulose were evaluated using the fiber image analyzer FiberLab from Kajaani. To ensure an optimal measurement speed of 50-70 particles per second (psc/s), cellulose samples were prepared at various concentrations in water.

The morphology of cellulose fibers, fibrils, modified CNFs, and their embeddings in PVA was examined using ultra-high-resolution field emission scanning electron microscopy (FE-SEM) of the Hitachi S-800. Dried samples were affixed to sample supports with carbon tape and coated with a 5 nm layer of Pd/Pt with a Cressington 208HR under an inert atmosphere.

Super-resolution imaging through Stimulated Emission Depletion Microscopy (STED) was performed on 1.5H fixed coverslips using a STEDYCON scanner equipped with 488, 561 and 640 nm excitation lasers, along with a 775 nm STED laser (all pulsed) (Abberior Instruments GmbH, Göttingen, Germany). The STEDYCON was connected to a Zeiss Axio-imager Z2 with a 100x/1.46 NA oil immersion Apochromat objective. Depletion power was set to achieve a resolution of 40 nm, with the pinhole set at 50 nm and the sampling rate fixed at 20 nm/px. The samples were dried on cover glasses under vacuum and mounted on slide glasses using Abberior MOUNT embedding media.

Deconvolution and post-processing were done by the software Huygens Essential and Zeiss Zen. We applied iterative CMLE (Classical Likelihood Estimation) deconvolution with a maximum of 30 iterations to prevent over-deconvolution using the Huygens Professional software package. This algorithm is well-validated and considered a standard approach in deconvolution. The software package includes a module to estimate the point spread function (PSF) specifically for STEDYCON scanners fitted with a 1.46 NA lens. Additionally, the theoretical PSF was adjusted to align with the experimental PSF closely, providing the software with detailed input parameters such as pixel size (sampling), refractive index mismatch, imaging depth, wavelength, projected pinhole radius, and STED saturation factor.

3 Syntheses, characterizations and applications of CNF-based hybrids with rare-earth-based nanoparticles

The content in this chapter (except Figure 3.4) has been published and adapted from:

(1) Jiang, X.; Mietner, J. B.; Harder, C.; Komban, R.; Chen, S.; Strelow, C.; Sazama, U.; Fröba, M.; Gimmler, C.; Müller-Buschbaum, P.; Roth, S. V.; Navarro, J. R. G. 3D Printable Hybrid Gel Made of Polymer Surface-Modified Cellulose Nanofibrils Prepared by Surface-Initiated Controlled Radical Polymerization (SI-SET-LRP) and Upconversion Luminescent Nanoparticles. *ACS Appl. Mater. Interfaces* 2023, 15 (4), 5687–5700. <https://doi.org/10.1021/acsami.2c20775>.

(2) Jiang, X.; Mietner, J. B.; Raveendran, D.; Ovchinnikov, K. V.; Sochor, B.; Mueller, S.; Boehm-Sturm, P.; Lerouge, F.; Chaput, F.; Gurikov, P.; Roth, S. V.; Navarro, J. R. G. Multifunctional Cellulose Nanofibrils–GdF₃ Nanoparticles Hybrid Gel and Its Potential Uses for Drug Delivery and Magnetic Resonance Imaging. *ACS Appl. Nano Mater.* 2023, 6 (22), 21182–21193. <https://doi.org/10.1021/acsanm.3c04272>.

Reproduced with permission from the American Chemical Society.

3.1 Introduction

Rare earth (RE) elements, encompassing a group of 17 elements, including scandium, yttrium, and 15 lanthanides (La-Lu), are important in functional materials. These elements are characterized by many similar physical and chemical properties, which can be attributed to their similar ground-state electronic configurations, and often occur together in geological deposits²⁴⁰.

Rare-earth-based nanoparticles (RENPs) are garnering increased interest across multiple fields due to their unique optical, electrical, magnetic, and chemical properties²⁴¹⁻²⁴⁴. Their applications span healthcare^{245,246}, optical sensing²⁴⁷, catalysis²⁴⁸ as well as technology involving optical three-dimensional displays²⁴⁹ and information storage²⁵⁰. A comprehensive review by Zheng *et al.*²⁵¹ summarizes the recent development of RENPs (Figure 3. 1), highlighting their unique properties and recent progress in the strategic design, including core-shell structures, spatially confined doping strategies, and organic-inorganic hybrid nanocomposites²⁵¹.

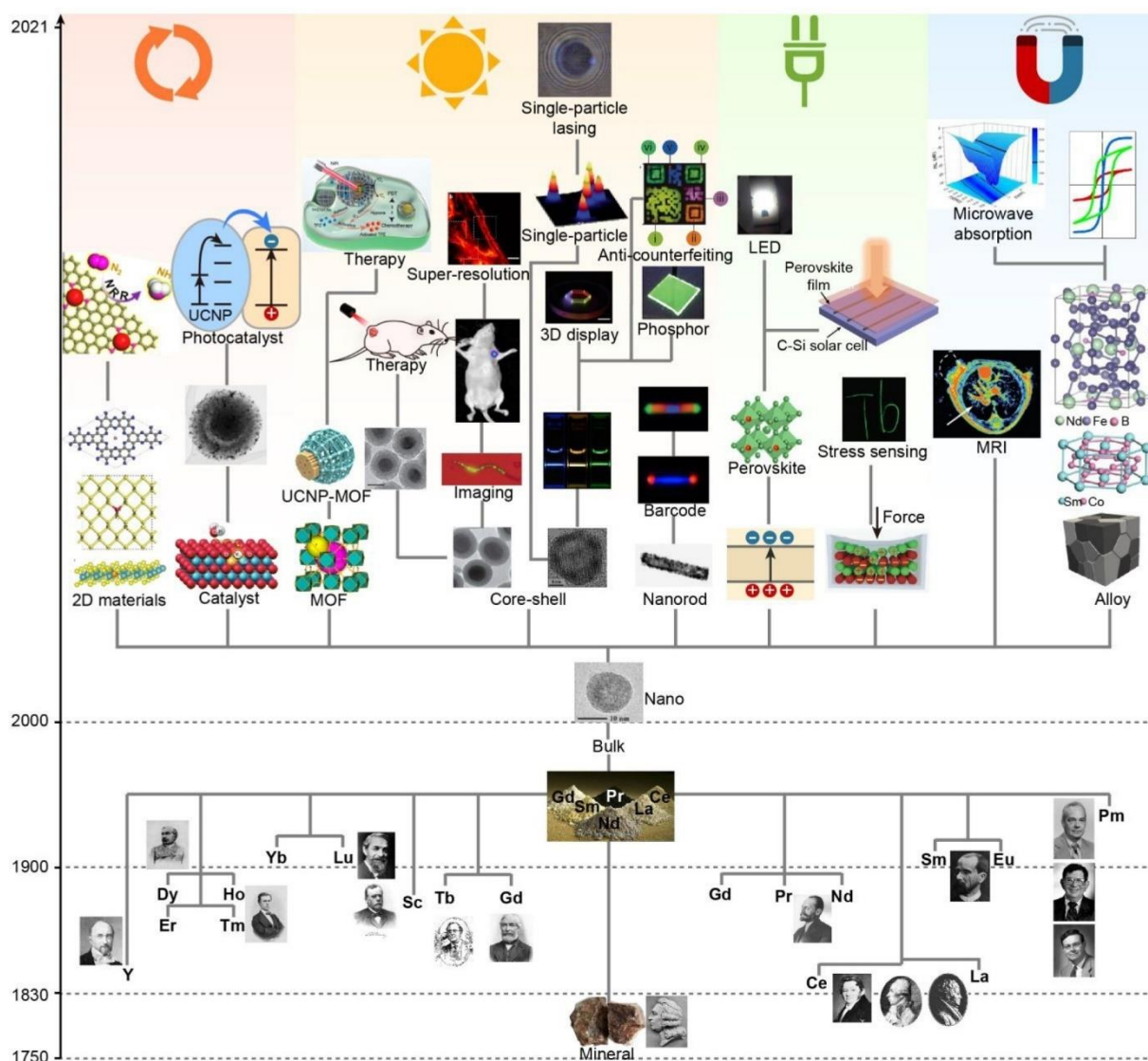


Figure 3. 1 The history, development and application of rare-earth-based nanomaterials²⁵¹. Copyright 2022 Chemical Reviews, with permission of American Chemical Society.

This chapter will primarily explore two specific types of RENPs that exhibit unique characteristics, which, when coupled with CNFs, introduce novel properties to the composites. It will provide a brief overview of the intrinsic properties of those NPs - including their optical, magnetic, and chemical behaviors - to understand their potential capabilities better. Additionally, the potential for modifying their surface chemistry to enhance their interaction with CNFs will be discussed. The goal of this study is to develop CNF-based hybrid gel materials that leverage the combined properties of CNFs and NPs for advanced applications.

3.1.1 Lanthanide-doped upconversion nanoparticles (UCNPs)

The history of upconversion (UC) started from a novel concept of nonlinear optics first proposed by physicist Nicolaas Bloembergen in 1959²⁵². He began investigating UC with a device called an infrared quantum counter and introduced the phenomenon of photon upconversion, where high-energy luminescent emission is achieved through the sequential absorption of two or more low-energy photons²⁵². This initiated a wave of research aimed at expanding the family of UC materials.

A significant advancement was made by François Auzel in 1966²⁵³, who observed the visible emission under near-infrared (NIR) excitation using Yb³⁺ to sensitize Er³⁺ and Tm³⁺. Auzel's work, along with his recollections and discussions on efficient upconversion processes, provided valuable insights into the early development of this field²⁵³. Soon after, the Yb³⁺-Ho³⁺ couple was also found to emit upconverting green emissions²⁵⁴. In the early stages, the development of photon upconversion led to the creation of devices known as upconverters, which could turn NIR light into UV or visible light and stimulated a few applications in laser and optical technologies^{255,256}.

In recent years, lanthanide-doped upconversion nanoparticles (UCNPs) are fluorescent nanoparticles that have gained significant interest due to their unique luminescence properties²⁵⁷. Unlike semiconductor quantum dots, where luminescence strongly correlates with particle size, the luminescence of UCNPs is less affected by size but rather by the energy transfers between the RE ions they contain. Additionally, unlike the conventional luminescence process (known as the Stokes shift process) that involves the excitation of electrons from the ground state to a higher energy state through the absorption of high-energy photons, the luminescence in UCNPs involves an anti-Stokes process. This process relies on the sequential absorption of multiple low-energy photons, facilitating the accumulation of energy through long-lived excited states. These energy transfers are crucial in determining the efficiency and color of the emitted light in UCNPs²⁵⁸.

Lanthanide-doped UCNPs can emit light through three main mechanisms²⁵²: excited-state absorption, energy-transfer upconversion (ETU), and photon avalanche. Among these, ETU is the most common and efficient method, especially when UCNPs are co-doped with

sensitizer and activator ions²⁵⁸. During ETU, the sensitizer ion absorbs a photon, exciting it from the ground state to a higher energy state. This energy is then transferred to the activator ion, which upon receiving enough energy, emits light as it returns to a lower energy state.

Figure 3. 2 illustrates the energy-level diagrams and energy transfer pathways for pairs of Yb³⁺-Er³⁺, Yb³⁺-Ho³⁺, and Yb³⁺-Tm³⁺ ions. The number of photons involved in the upconversion processes is determined using I-P curves, which plot the intensity of upconversion emission against excitation power density.

The upconversion properties of UCNPs doped with Yb³⁺ and Er³⁺ have been extensively studied. When excited with a 980 nm laser, Yb³⁺ ions absorb energy and transition from the ²F_{7/2} to the ²F_{5/2} energy level. These excited ions then transfer energy through multiple transitions to neighboring Er³⁺ ions. The upward transitions of Er³⁺ ions subsequently lead to the emission of light in the green (²H_{11/2} → ⁴I_{15/2}, 525 nm; ⁴S_{3/2} → ⁴I_{15/2}, 545 nm), red (⁴F_{9/2} → ⁴I_{15/2}, 655 nm), and violet (²H_{9/2} → ⁴I_{15/2}, 415 nm) region (Figure 3. 2). The green and red emissions result from two-photon upconversion processes, whereas the violet emissions occur via a three-photon process.

Similarly, Yb³⁺-Ho³⁺ doped UCNPs can emit two-photon green (⁵F₄, ⁵S₂ → ⁵I₈, 545 nm) and red (⁵F₅ → ⁵I₈, 650 nm) light. These UCNPs also show a weak blue emission (⁵F₃ → ⁵I₈, 485 nm) from a different energy transition. In contrast, Yb³⁺-Tm³⁺ doped UCNPs involve more complex multi-photon processes due to the distinct energy levels of Tm³⁺ ions, which reduce nonradiative energy loss. These complexes can exhibit two-photon red (³F₃ → ³H₆, 695 nm), NIR emissions (³H₄ → ³H₆, 800 nm), three-photon blue (¹G₄ → ³H₆, 475 nm), four-photon blue (¹D₂ → ³F₄, 450 nm) and UV (¹D₂ → ³H₆, 365 nm), along with five-photon UV emission (¹I₆ → ³F₄, 345 nm; ¹I₆ → ³H₆, 290 nm).

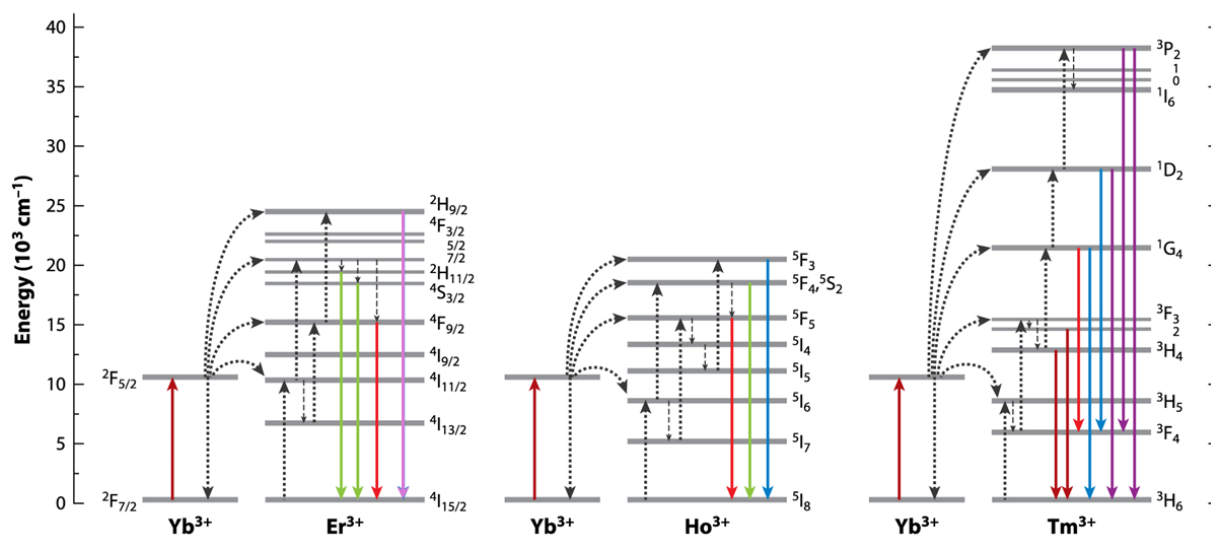


Figure 3. 2 Energy-level diagrams and proposed UC energy transfer pathways in the Yb³⁺-Er³⁺, Yb³⁺-Ho³⁺, and Yb³⁺-Tm³⁺ pairs. Adapted with permission from ref ²⁵⁷. Copyright 2015 Annual Review of Physical Chemistry, with permission of Annual Reviews, Inc.

Thanks to their specific NIR excitation capabilities, UCNPs can achieve excellent penetration depth in biosystems without causing background autofluorescence, an advantage that has facilitated their widespread use in the biomedical sector²⁵⁹. Their nonlinear optical properties, specifically absorbing NIR photons and emitting light in the visible and UV spectra, have facilitated breakthroughs in biomedical fields^{258,260}, such as biological imaging^{261,262}, biological detection^{263,264}, and therapeutics²⁶⁵. Furthermore, the integration of luminescent nanoparticles in cellulose as a photonic/bio hybrid is also an active area of research. Previously, upconverting photonic cellulose composite films displaying chiral nematic order were successfully created by co-assembling cellulose nanocrystals with UCNPs²⁶⁶. In addition, UCNPs are chemically stable, potentially possess good biocompatibility, and exhibit high photostability, unperturbed by the laser excitation power and exposure time²⁵⁸.

UCNPs synthesized in organic solvents are typically capped with hydrophobic ligands, such as oleate or oleylamine ligands²⁶⁷. To facilitate subsequent processes like SET-LRP polymerization, it is crucial to modify the surface of NPs by incorporating a polymerizable, reactive group. Introducing an acrylate function on the outer shell of the NPs is necessary for this purpose. Thus, surface modifications must be performed before these NPs can be effectively utilized in hydrophilic or aqueous environments.

A straightforward and versatile method for replacing the original ligand with a specific species involves a ligand exchange procedure. This method allows for precise control of the distance between the new ligand and the luminescent particle²⁶⁷. Dong *et al.*²⁶⁸ presented a comprehensive approach for ligand exchange in NPs using nitrosyl tetrafluoroborate (NOBF₄) (Figure 3. 3). This method facilitates sequential surface modification and phase transfer across a broad range of NPs, including iron oxide NPs, titanium oxide nanorods, and NaYF₄ nanoplates, ultimately allowing them to be functionalized with a diverse array of new protective ligands²⁶⁸.

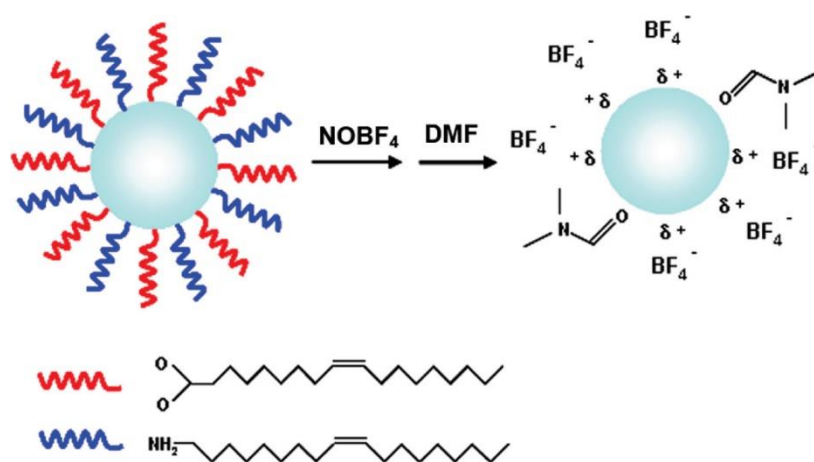


Figure 3. 3 Schematic illustration of the ligand-exchange process with NOBF₄²⁶⁸. Copyright 2011 Journal of the American Chemical Society, with permission of American Chemical Society.

Based on this, we explored a 2-step strategy to surface-modify UCNPs by replacing the original oleic ligands with molecules containing acrylate functions. These modified UCNPs with surface ligands can, therefore, participate in the surface-initiated radical polymerization, serving as cross-linking agents to create networks of modified nanofibrils *in situ* (Figure 3. 4). This modification endows the CNFs with new properties, such as enhanced rheological performance and NIR absorption.

3.1.2 Gadolinium nanoparticles (Gd NPs)

Gadolinium (Gd), another rare-earth element from the lanthanide series, is widely used as a positive contrast agent (CA) in magnetic resonance imaging (MRI) systems²⁶⁹. MRI CAs can enhance visibility and image quality by increasing the contrast of specific tissues or organs during an MRI scan, thereby boosting diagnostic accuracy. The main source of

image contrast in MRI stems from the differences in the relaxation times of tissues interacting with the CA. These relaxation times measure how quickly hydrogen nuclei return to their equilibrium state after being disturbed by a radiofrequency pulse in the scanner. They are affected by the molecular environment of the hydrogen atoms within the tissue, which is predominantly related to the tissue's water and fat content *in vivo*²⁷⁰. Relaxation in MRI happens through two distinct processes, known as longitudinal (T_1) and transverse (T_2) relaxation²⁷¹. T_1 relaxation time indicates how rapidly the net magnetization vector returns to its equilibrium state along the direction of the main static magnetic field. T_2 relaxation, on the other hand, describes the gradual dephasing of spinning dipoles, causing a decay in magnetization within the transverse plane. The accelerated relaxations manifest as signal enhancement on T_1 -weighted MR images and signal reduction on T_2 -weighted MR images²⁷².

Paramagnetic gadolinium (III) ions (Gd^{3+}) chelated complexes are widely used as CAs in MRI²⁷³. However, conventional Gd-chelates have certain limitations, such as a lack of diagnostic specificity and the potential toxicity from the unintended release of free Gd ions²⁷⁴. To address these issues and minimize the release of Gd^{3+} ions *in vivo*, researchers have suggested using Gd-based NPs. Various Gd-based NPs, including Gd_2O_3 ^{275,276}, $GdPO_4$ ^{277,278}, and $Gd(OH)_3$ ²⁷⁹, have been explored; and gadolinium fluorides (GdF_3) or GdF_3 NPs doped with luminescent lanthanides, such as Eu^{272,280}, Tb^{280,281} and Er²⁸², have gained significant interest due to their high relaxivity values. In addition, recent studies have emphasized their non-toxicity and good biocompatibility²⁸². Notably, GdF_3 NPs also present a distinct advantage over other Gd-based inorganic nanoparticles due to their chemical versatility, allowing easy tailoring of surface properties through both cations and anions²⁸³.

Over the past few decades, considerable effort has been directed toward synthesizing Gd NPs with diverse dimensions and compositions^{284–287}. There is also a growing interest in optimizing the surface properties of Gd NPs, including coating with macromolecules, to their contrast capabilities^{288–290}. Our research made the first attempt to couple Gd NPs with cellulose nanomaterials, aiming to develop a novel contrast agent that combines the MRI-active magnetic properties of Gd NPs with the biocompatibility of CNFs.

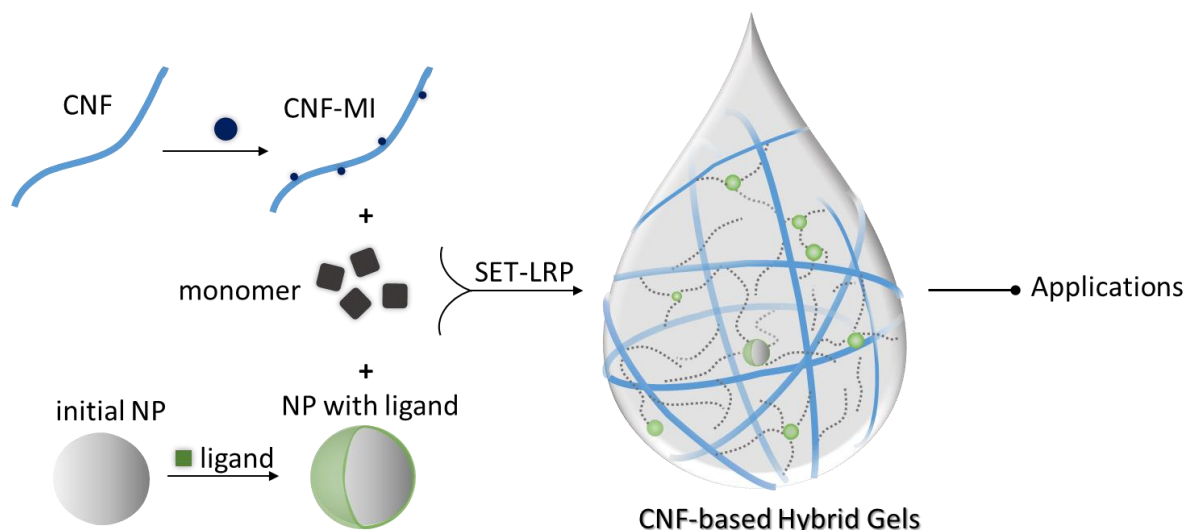


Figure 3. 4 Schematic illustration of synthesis route of CNF-based hybrid gels.

In this project, we used SET-LRP to cross-link surface-modified Gd NPs into CNFs (Figure 3. 4). The surface chemistry of Gd NPs was modified with the ligand 11-Phosphoundecyl acrylate, enabling their participation in the polymerization process and their function as a cross-linking agent, creating sophisticated networks in modified nanofibrils.

Moreover, our conception is not only to develop a novel MRI contrast agent of Gd NPs and CNF hybrid but also to fully explore the potential of CNF-based hybrid gels and identify more applications in the field of biomedicine. As a whole, we aim to produce a multifunctional hybrid gel based on CNFs suitable for a variety of versatile applications.

3.1.3 CNFs as an innovative pool for biomedical applications

In recent years, there has been a global surge in the use of nanocellulose in biomedical applications, including drug delivery systems^{89,232,291}, wound dressing²⁹²⁻²⁹⁴, and scaffolds²⁹⁵⁻²⁹⁷, etc., along with the assistance of the coupling of multidisciplinary fields such as biology, and chemistry²⁹⁸. Durand *et al.*²⁹⁹ on the applications of nanocellulose in the biomedical field, focusing on health and toxicology aspects. In general, CNFs are found to be cytocompatible and mostly not non-toxic to human health, additionally supporting cell proliferation and migration^{300,301}.

Kolakovic *et al.*³⁰² were pioneers in using CNFs for drug delivery, producing a CNF-based film capable of encapsulating and delivering drugs at concentrations of 20-40 %. Their

studies demonstrated a prolonged drug release period of up to 3 months, with the release kinetics dependent on the specific drug used. These findings suggest that CNFs are well-suited for controlled release applications and can effectively manage poorly water-soluble drugs for sustained release³⁰². In a more recent study, Taher *et al.*³⁰³ developed nanocellulose composites incorporating honey for antimicrobial wound dressings. The drug release from these composites followed first-order kinetics and provided a continuous release period, proving effective in treating chronic wounds³⁰³.

Additionally, the characteristic features of CNFs can be significantly modified through surface treatments to create custom polymers suited for various biomedical applications. The surface hydroxy groups of CNFs are available for numerous chemical modifications. Rai *et al.*¹¹⁶ provided an in-depth look at the recent advancements in the synthesis, fabrication, and processing of cellulose nanomaterials, highlighting strategic chemical modification methods to customize their properties for specific biomedical uses.

Furthermore, bacteriocins, a group of natural antimicrobial peptides, have emerged as promising alternatives to antibiotics for both food preservation and the treatment of infectious diseases in livestock and humans^{304,305}. These peptides are particularly appealing due to their minimal toxicity and protein-based nature, offering a solution to the growing issue of drug-resistant pathogens. Bacteriocins are produced by bacteria to hinder the growth of other bacterial strains in the competition for nutrients and habitats³⁰⁶. They represent a potent class of natural antibacterial compounds, showing effectiveness against various Gram-positive pathogens³⁰⁷. This effectiveness extends to antibiotic-resistant strains, including MRSA, vancomycin-resistant enterococci and penicillin-resistant *Streptococcus pneumoniae*³⁰⁸.

In conclusion, cellulose nanomaterials, with their versatile properties, provide an innovative foundation for biomaterial development. We, therefore, presented the development of a gel that serves multiple purposes: it can be used as ink for 3D gel-printing, acts as a novel hybrid contrast agent incorporating MRI-active magnetic GdF₃ NPs, and functions as an antimicrobial medium by encapsulating bacteriocins(Figure 3. 5).

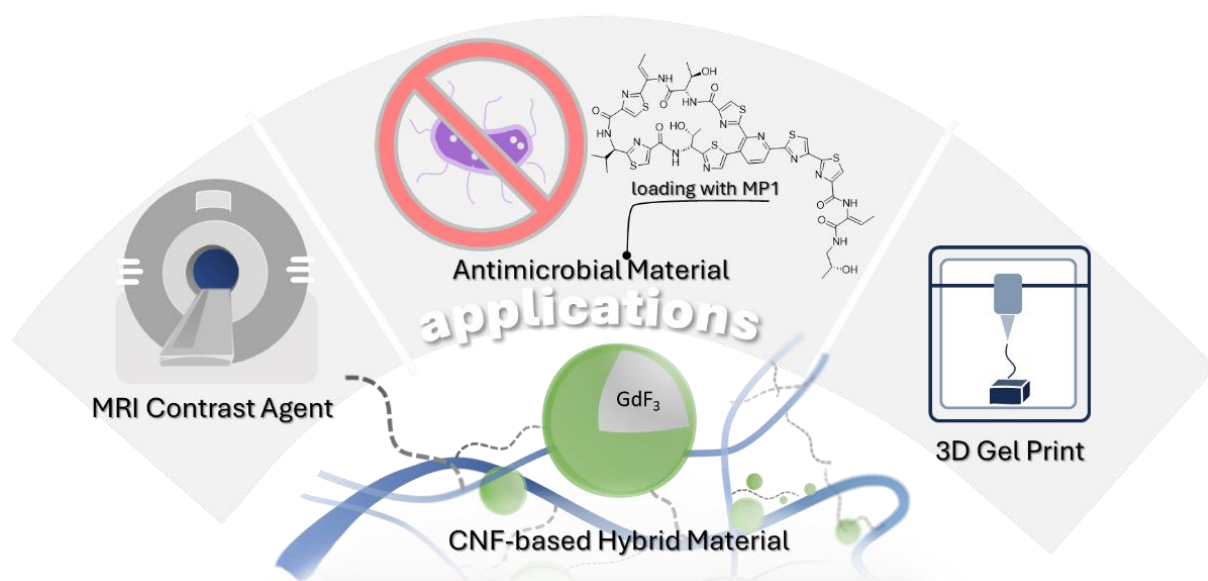


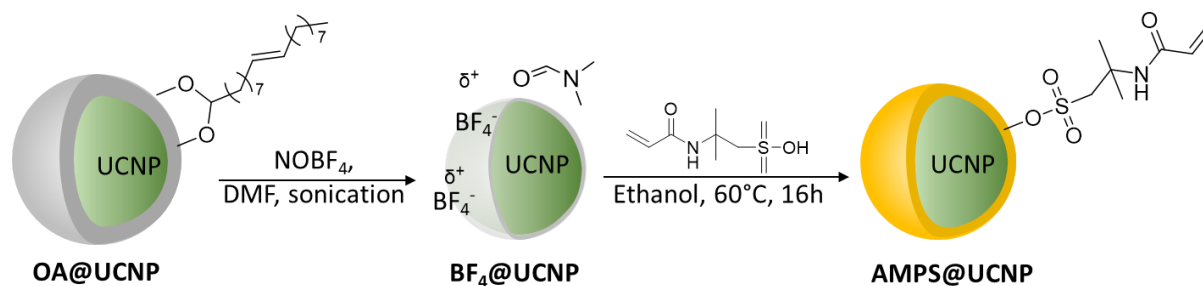
Figure 3. 5 CNF-based hybrid materials as an innovative pool for biomaterial development³⁰⁹.

To achieve this, a surface-initiated radical polymerization (SET-LRP) was employed to graft polymers from CNFs surfaces and cross-linked surface-modified GdF₃ *in situ*, ultimately encapsulating bacteriocins. Specifically, by grafting stearyl acrylate onto CNF surfaces, the inter-fibrillar hydrogen bond effect in CNFs decreased. This modification not only created CNF species that form highly stable suspensions in toluene but also allowed these modified CNFs to be redispersed in toluene from a dried state without any hornification as in pristine CNF. Moreover, this alteration enhanced the encapsulation efficiency of hydrophobic biomolecules within the CNFs. In order to evaluate the impact of the fabrication process on the nanostructure of the hybrid materials, we applied ultrasmall- and wide-angle X-ray scattering (USAX/WAXS) measurements, which allowed us to disentangle the nanostructural changes of different materials induced by the composite formation³¹⁰.

3.2 Results and discussion

3.2.1 Surface modification of UCNPs

We implemented a two-step ligand exchange method to modify the surfaces of UCNPs, aiming to attach acrylate functions on UCNP surfaces, thereby enabling their involvement in subsequent living radical polymerization processes (Scheme 3. 1).



Scheme 3. 1 Two-step ligand exchange of UCNPs.

The first step involved removing the oleate ligand from the surfaces of UCNP using NOBF_4 treatment (Scheme 3. 1). Initially, the UCNPs were capped with oleic acid (OA@UCNP), allowing them to be fully suspended in toluene. The sterically stabilized OA@UCNP s were also fully redispersible in nonpolar solvents, such as cyclohexane. The addition of NOBF_4 led to the phase transfer of UCNPs from cyclohexane to dimethylformamide (DMF), resulting in the formation of $\text{BF}_4@UCNP$, which can also be redispersed in DMF .

For the second step of ligand exchange, 2-acrylamido-2-methyl-1-propanesulfonic acid (AMPS) was used to functionalize the UCNPs, followed by a modified procedure from a previous report¹²². $\text{BF}_4@UCNP$ was then suspended in ethanol, and a large excess of ligands AMPS was added to the suspension to replace BF_4^- .

The characterization of the NPs via FT-IR spectroscopy confirmed the successful ligand exchange strategy, as evidenced by the changes in the spectra (Figure 3. 6). The OA capping agent was identified with signals localized at $2800\text{-}3000\text{ cm}^{-1}$ (C-H) and $1500\text{-}1600\text{ cm}^{-1}$ (COO). Conversely, those bands were absent in the spectrum of $\text{BF}_4@UCNP$. After the initial treatment, a new band emerged at 1073 cm^{-1} , consistent with the presence of BF_4^- . An additional band at approximately 1650 cm^{-1} corresponded to the C=O of the

DMF solvent. These results indicate a successful replacement of the OA capping agent with inorganic BF_4^- .

After the second ligand exchange step, the spectrum of AMPS@UCNP (Figure 3. 6) displays characteristic bands at 1090 cm^{-1} (symmetric stretching $\text{S}=\text{O}$), 1190 cm^{-1} (asymmetric stretching $\text{S}=\text{O}$), 1556 cm^{-1} ($\text{C}=\text{C}$), 1672 cm^{-1} ($\text{N}-\text{C}=\text{O}$) and 1120 cm^{-1} ($\text{C}-\text{N}$). This indicates that the surface of UCNP has been successfully functionalized with AMPS, making it suitable for further grafting polymerization onto CNFs.

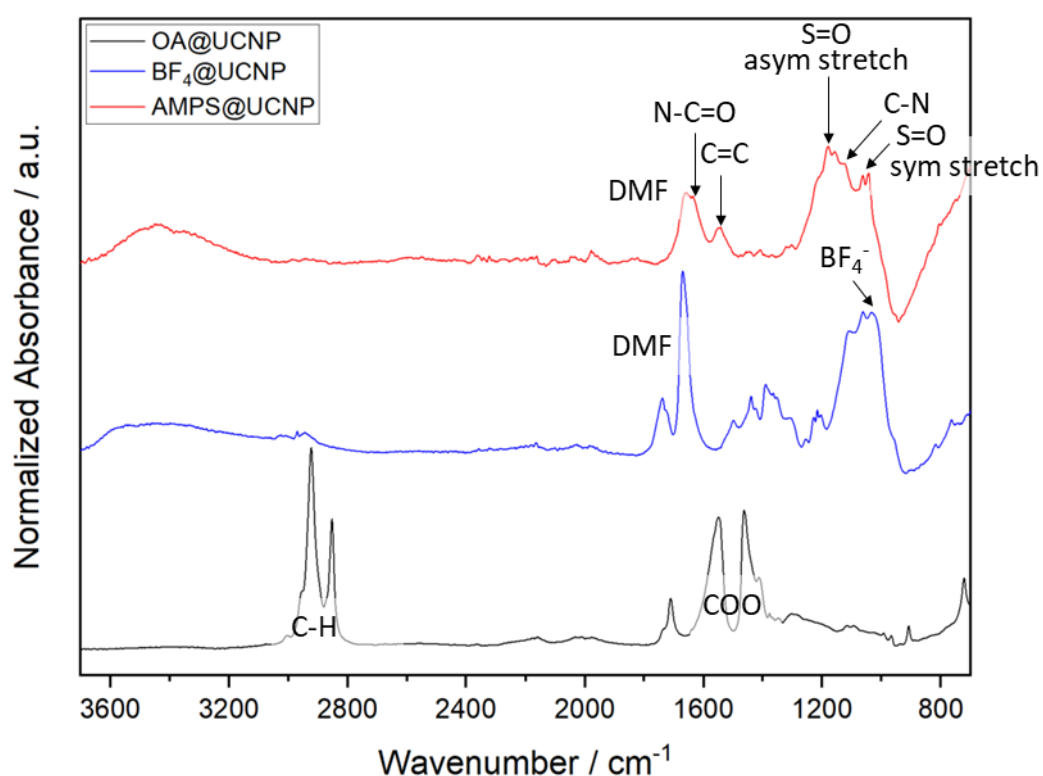


Figure 3. 6 FT-IR spectra of OA@UCNP (black), BF_4^- @UCNP (blue), and AMPS@UCNP (red).

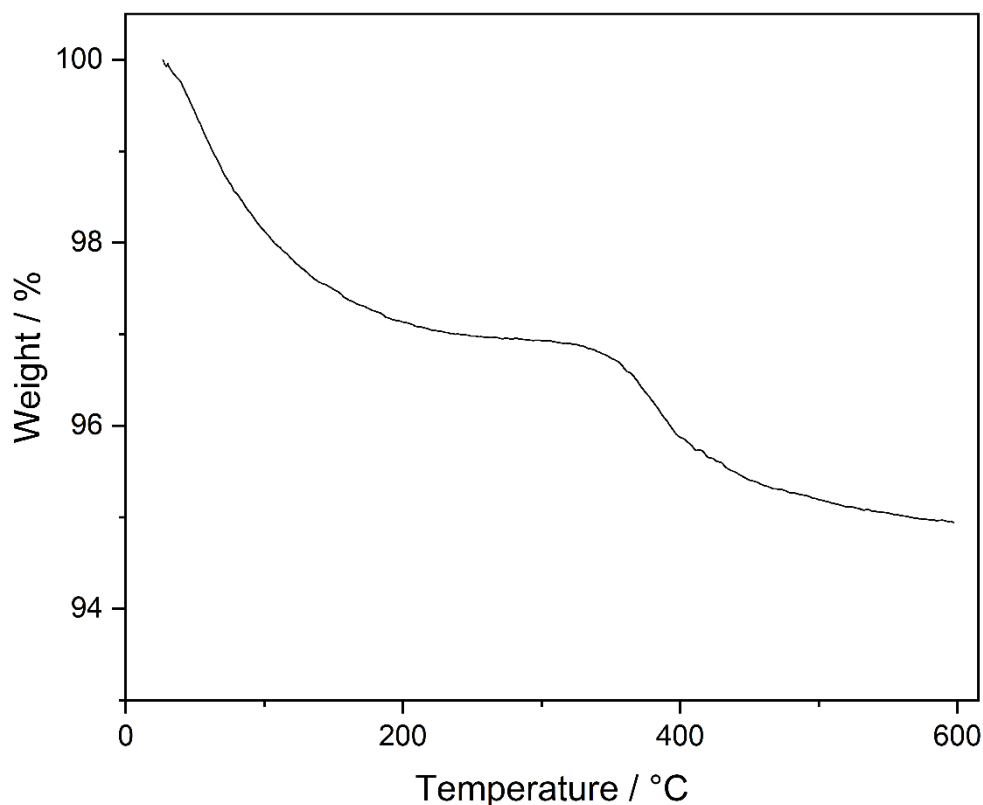


Figure 3. 7 TGA curve of AMPS@UCNP.

The surface-modified UCNP was further analyzed using thermal gravimetric analysis. Figure 3. 7 shows a two-step weight loss, totaling 5.06 % when AMPS@UCNP was heated beyond 500 °C. The first weight loss was attributed to the evaporation of the absorbed solvent, while the second weight loss of 1.8 % corresponded to the decomposition of surface ligands.

The surface coverage (φ , molecules/nm²) of AMPS@UCNP was then calculated using the following equations:

$$\varphi = \frac{N_{AMPS}}{S}$$

(1)

where N_{AMPS} is the number of the ligand AMPS, S is the total surface area of AMPS@UCNP.

$$N_{AMPS} = n_{AMPS} \cdot N_A$$

(2)

$$n_{AMPS} = \frac{m_{AMPS}}{M_{AMPS}}$$

(3)

where n_{AMPS} is the molar of AMPS, calculated by the weight of AMPS and the molar mass of AMPS ($M_{AMPS}=207.24$ g/mol), N_A is the Avogadro constant.

$$S = N_{UCNP} \cdot S_{UCNP}$$

(4)

$$N_{UCNP} = \frac{m_t}{m_{UCNP}}$$

(5)

$$m_{UCNP} = \rho_{UCNP} \cdot V_{UCNP}$$

(6)

$$V_{UCNP} = \frac{4}{3} \pi r_{UCNP}^3$$

(7)

$$S_{UCNP} = 4 \pi r_{UCNP}^2$$

(8)

Where N_{UCNP} is the number of UCNPs, S_{UCNP} is the surface area of a single UCNP, m_t is the net weight of UCNPs, which is 94.94 % determined by TGA. The weight of a single UCNP (m_{UCNP}) is calculated by the density of a single UCNP ($\rho_{UCNP}=4.452 \times 10^{-21}$ g/nm³) and the volume of a single UCNP (V_{UCNP}). The prepared UCNPs showed a low aspect ratio; therefore, we approximate their shape as spheres ($r_{UCNP}=9$ nm) for the ligand density calculation.

$$\varphi = \frac{\rho_{UCNP} \cdot r_{UCNP} \cdot m_{AMPS} \cdot N_A}{3 \cdot m_t \cdot M_{AMPS}}$$

(9)

By applying equations (2)-(8) to eq. (1), the ligand density can be described as eq. (9). Therefore, we can estimate that the ligand density of AMPS@UCNP is 0.7 AMPS/nm².

The surface coverage (φ , molecules/nm²) of AMPS@UCNP was then calculated, and the ligand density of AMPS@UCNP is 0.7 AMPS/nm².

3.2.2 Surface modification of GdF₃ nanoparticles (GdF₃ NPs)

The initial GdF₃ NPs, stabilized with citric acid (GdF₃:cit), were fully dispersed in H₂O. To introduce acrylic functionalities for polymerization, the surface of GdF₃ NPs underwent modification with 11-phosphonoundecyl acrylate (PDA). The transformation in surface chemistry was tracked using FT-IR measurements (Figure 3. 8). After surface modification, the spectrum in Figure 3. 8 revealed new signals indicative of the presence of phosphonate groups on GdF₃ NPs. These were evidenced by the bands at 1058 cm⁻¹ (P-O) and 945 cm⁻¹ (P-OH), 1225 cm⁻¹ (P=O), 1560 cm⁻¹ (C=C), 2950 and 2895 cm⁻¹ (C-H), 1733 cm⁻¹ (C=O).

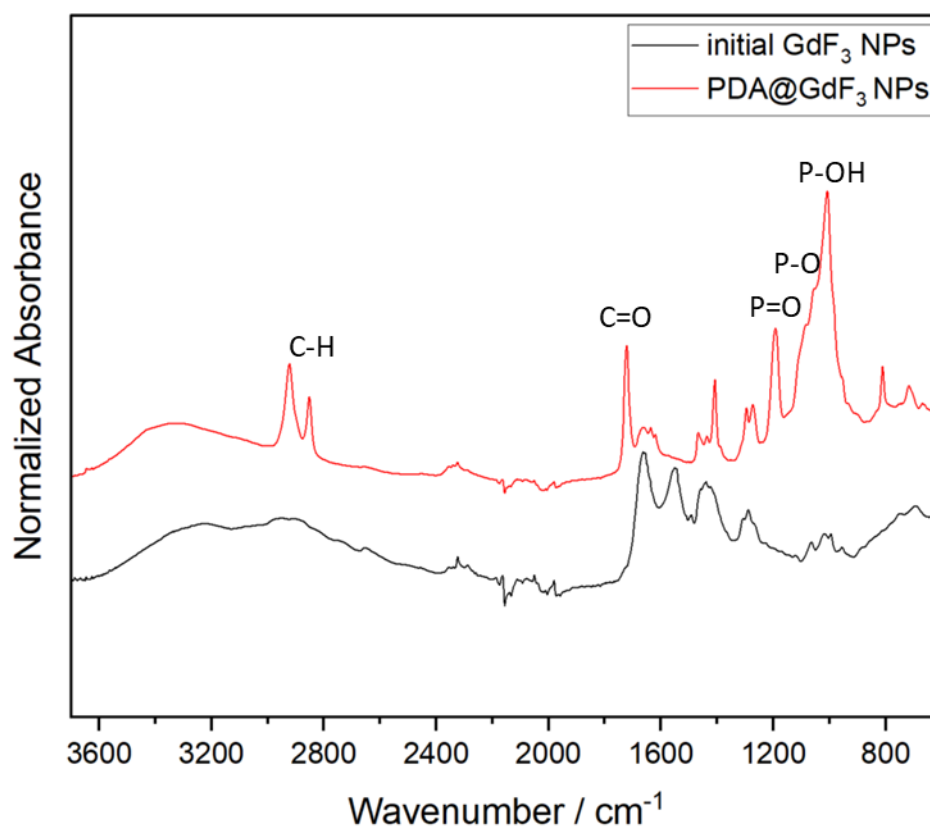


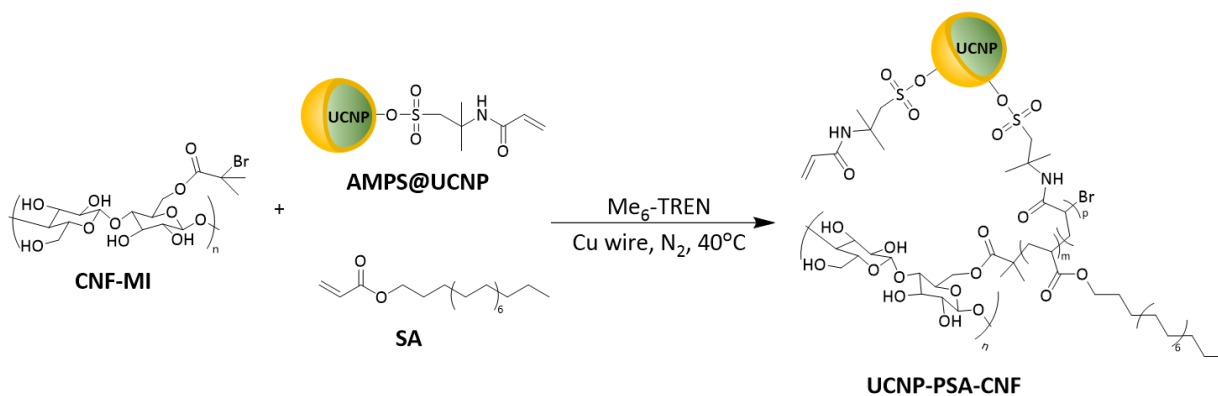
Figure 3. 8 . FT-IR spectra of dried initial GdF_3 NPs (black) and dried $PDA@GdF_3$ (red).

3.2.3 Surface-initiated radical polymerization and *in situ* cross-linking

CNFs were chemically converted into CNF-MI previously, to anchor the alkyl bromide on their surface to enable monomers to graft from it. The monomer stearyl acrylate was used in both CNF-based hybrids, respectively, since it is well investigated and for controlling parameters. Also, PSA-CNF can be fully (re)dispersed in toluene (after drying). The synthesis and characterization of CNF-MI and PSA-CNF are discussed in the previous chapter.

3.2.3.a Synthesis and characterization of CNF-based hybrid with UCNP (UCNP-PSA-CNF)

Finally, we conducted the surface-initiated controlled radical polymerization of SA and AMPS@UCNP with CNF-MI, resulting in the hybrid CNF material (UCNP-PSA-CNF), as illustrated in Scheme 3. 2. For comparison, we also carried out the polymerization without the incorporation of NPs, resulting in the formation of PSA-CNF.



Scheme 3. 2 Grafting polymerization and *in situ* cross-linking of CNF-MI with SA and UCNPs via SET-LRP.

The polymerization was carried out in a DMSO/toluene mixture to ensure a homogeneous condition. This was necessary because both CNF-MI and AMPS@UCNP were stable in DMSO, whereas SA exhibited poor solubility in DMSO but was highly soluble in toluene. As the polymerization proceeded, a significant number of white floccules appeared rapidly (in 10 min) due to the low solubility of the grafted PSA units in the solvent system.

The grafting polymerization onto CNF surfaces was investigated using FT-IR (Figure 3. 9) for both UCNP-PSA-CNF and PSA-CNF samples. In addition to the characteristic bands of CNFs, the spectrum of UCNP-PSA-CNF matched that of PSA-CNF, which was detailed in the previous chapter. This confirms the successful grafting of PSA onto CNFs. However, identifying UCNP cross-linked in modified CNF via FT-IR remains challenging, as the characteristic absorption bands of AMPS@UCNP overlap with those of PSA and CNFs.

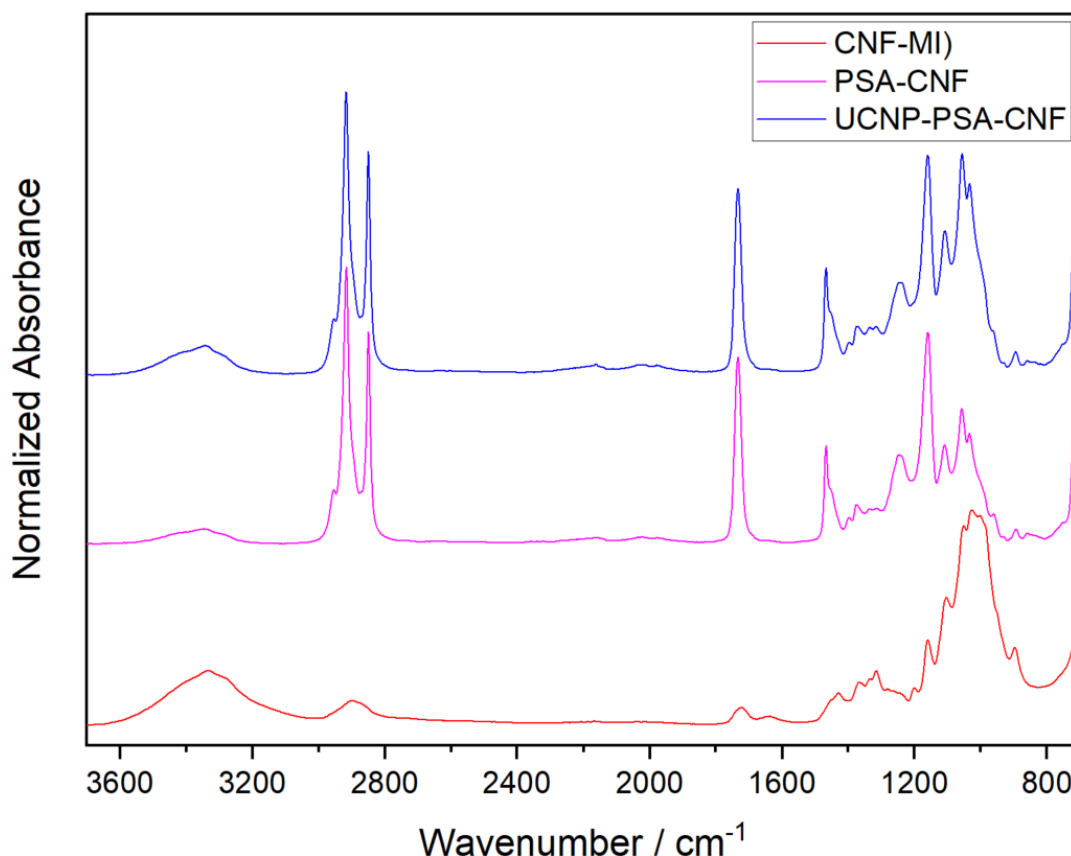


Figure 3. 9 FT-IR spectra of CNF-MI (red), PSA-CNF (pink) and UCNP-PSA-CNF (blue).

As previously mentioned, lanthanide ions possess abundant energy levels and transitions, granting them unique photophysical properties. For instance, they can absorb near-infrared (NIR) light and emit visible or ultraviolet light when exposed to a continuous-wave or pulsed laser, even with low power density at room temperature³¹¹. In our system (NaYF₄:Yb,Er/NaYF₄), Er³⁺ ions function as activators due to their ladder-like intermediate energy levels, while co-doped Yb³⁺ ions serve as sensitizers since they only possess a simple energy transition and higher absorptivity of NIR, enabling them to transfer energy to the neighboring activator (Figure 3. 10 A).

Emission spectra of the OA@UCNP, AMPS@UCNP and UCNP-PSA-CNF in toluene are recorded at $\lambda_{\text{ex}}=980$ nm and presented in Figure 3. 10 B. Characteristic emission signals from Er³⁺ ions are evident in all three spectra. The emission bands at 525 nm and 545 nm, responsible for the green color emission, correspond to the $^2\text{H}_{11/2}, ^4\text{S}_{3/2} \rightarrow ^4\text{I}_{15/2}$ transitions, respectively. The peak at 650 nm is attributed to $^4\text{F}_{9/2} \rightarrow ^4\text{I}_{15/2}$. As expected, the optical

properties of UCNP remain unchanged with AMPS@UCNP and its incorporation into the CNF matrix, evidenced by identical fingerprint emission lines from Er^{3+} in both spectra.

The additive mixture of spectral colors is represented in the chromaticity diagram (CIE 1931). All luminescent species, including the UCNP-PSA-CNF gel, were positioned in the green zone (Figure 3. 10 C). This result aligns with the visible green light emitted from the entire area of the UCNP-PSA-CNF gel when excited by a 980 nm laser diode (Figure 3. 10 D).

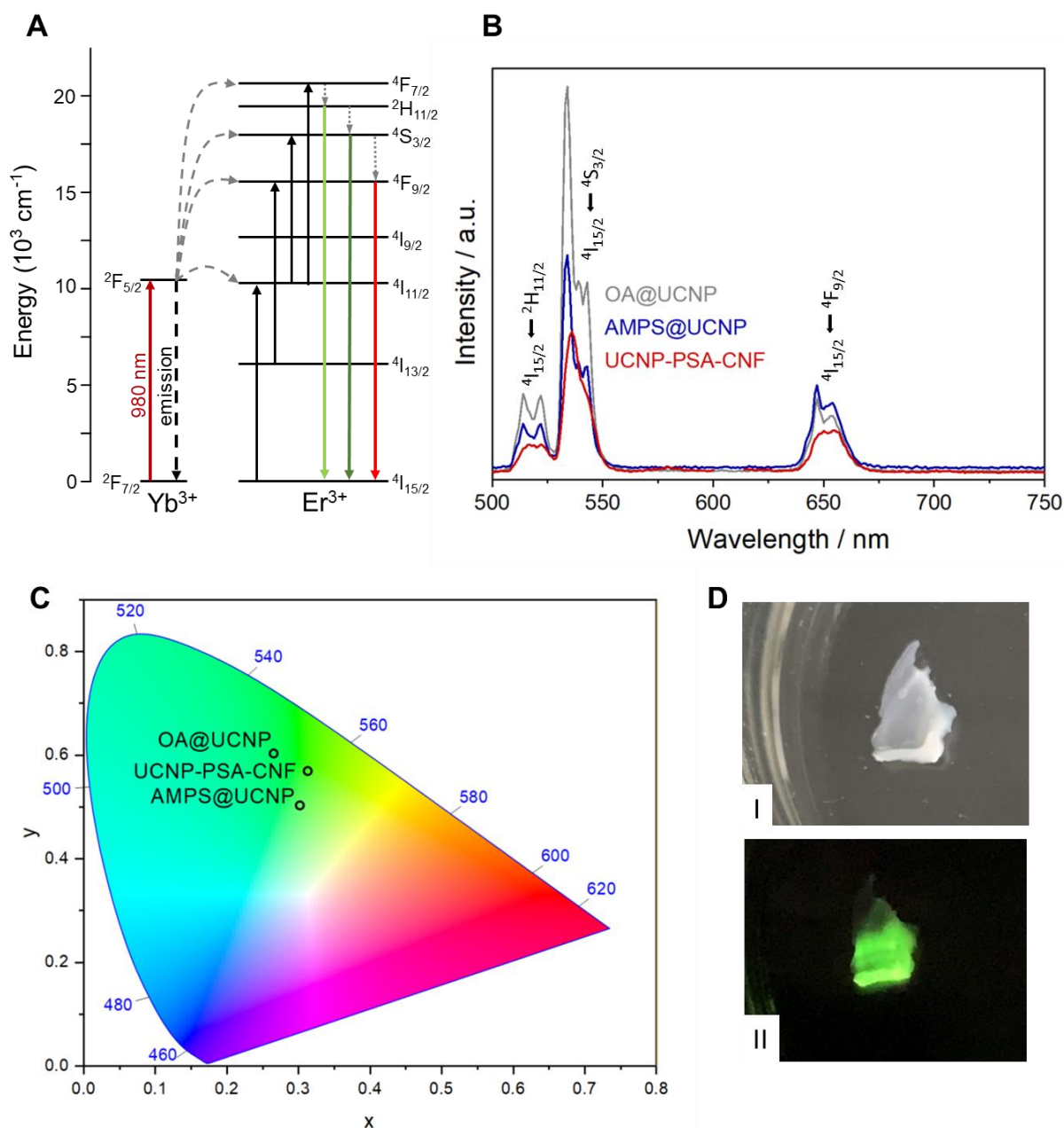


Figure 3. 10 (A) Schematic illustration of upconversion mechanism of UCNPs doped with Yb^{3+} - Er^{3+} ; (B) emission spectra of OA@UCNP (grey), AMPS@UCNP (blue) and UCNP-PSA-CNF (red);(C) the corresponding CIE 1931 chromaticity diagram (D) UCNP-PSA-CNF gel under (I) daylight, (II) 980 nm laser diode excitation.

To assess the thermal stability and quantify the amount of UCNP coupled to CNFs, thermogravimetric analysis (TGA) and sequential X-ray diffraction (XRD) of UCNP-PSA-CNF were conducted. The results are depicted in Figure 3. 11. The observed weight loss of UCNP-PSA-CNF from room temperature to 200 °C was mainly due to solvent evaporation. The decomposition of PSA-CNF started at 350 °C, whereas UCNP-PSA-CNF

maintained thermal stability up to 400 °C. The incorporation of UCNPs contributed to a higher residual content of 4.9 % compared to PSA-CNF.

The crystalline nature of the residual UCNP-PSA-CNF was examined by XRD (Figure 3. 11). Although the XRD pattern of the residue exhibits relatively weak signals, likely due to its low quantity, it nonetheless indicates crystallinity. The diffraction signals correspond predominantly to the high-temperature cubic phase of NaYF₄ (PDF#06-0432)^{312,313}, confirming the presence of UCNPs.

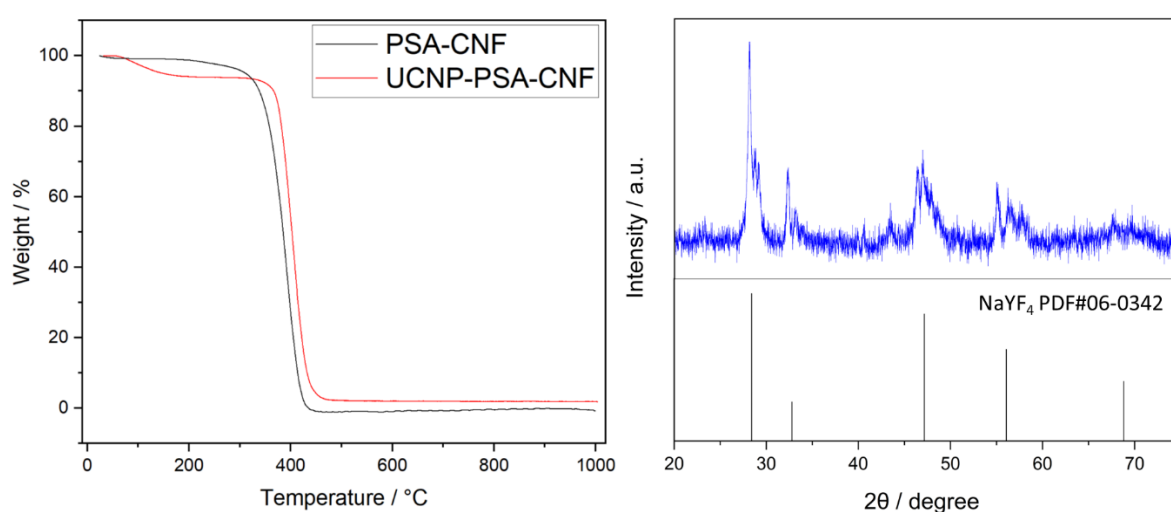


Figure 3. 11 Left: TGA of PSA-CNF (black), UCNP-PSA-CNF (red); right: XRD patterns of UCNPs as residue from TGA and the standard data of NaYF₄ (PDF#06-0432).

TEM was employed to examine the UCNPs and their cross-linked CNF gels, which were dried at ambient temperature. The TEM images of OA@UCNP, AMPS@UCNP, and UCNP-PSA-CNF are shown in Figure 3. 12.

The TEM image of OA@UCNP (Figure 3. 12 A) displays highly monodisperse individual nanoparticles with an average size of approximately 18 nm with a slightly elongated shape. In Figure 3. 12 B, AMPS@UCNP exhibits a similar size and hexagonal structure, consistent with the XRD results. Besides, the single crystalline morphology is also shown with a lattice distance of approximately 0.5 nm.

The TEM images of UCNP-PSA-CNF Figure 3. 12 C-E) show that modified UCNPs were surrounded by a sphere of AMPS ligand/PSA and coupled on the surface of CNF through them.

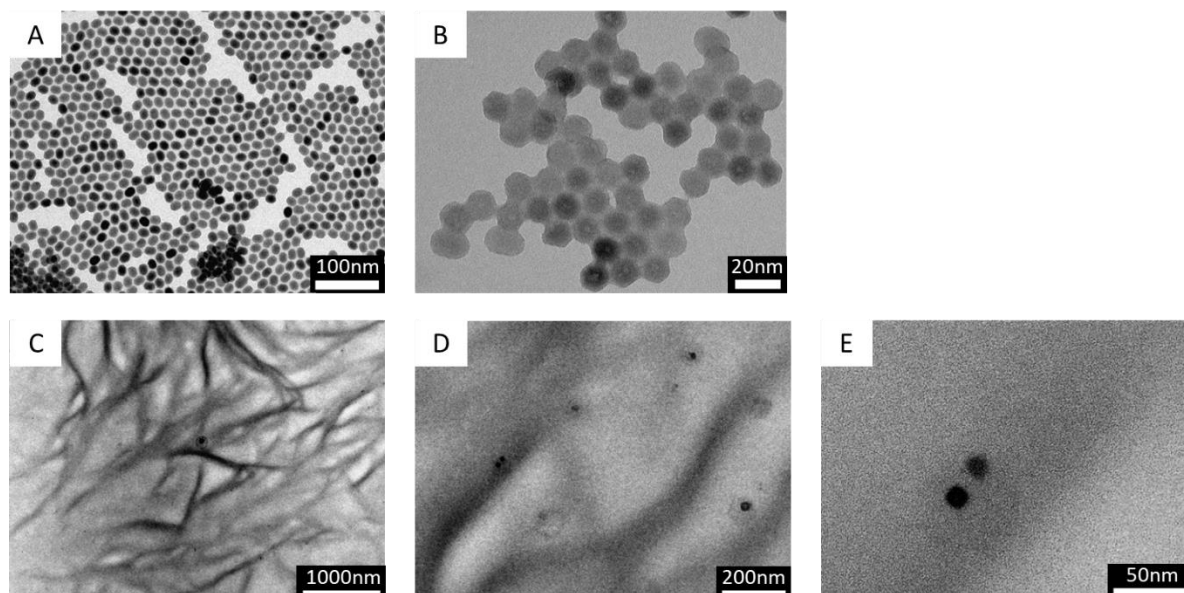
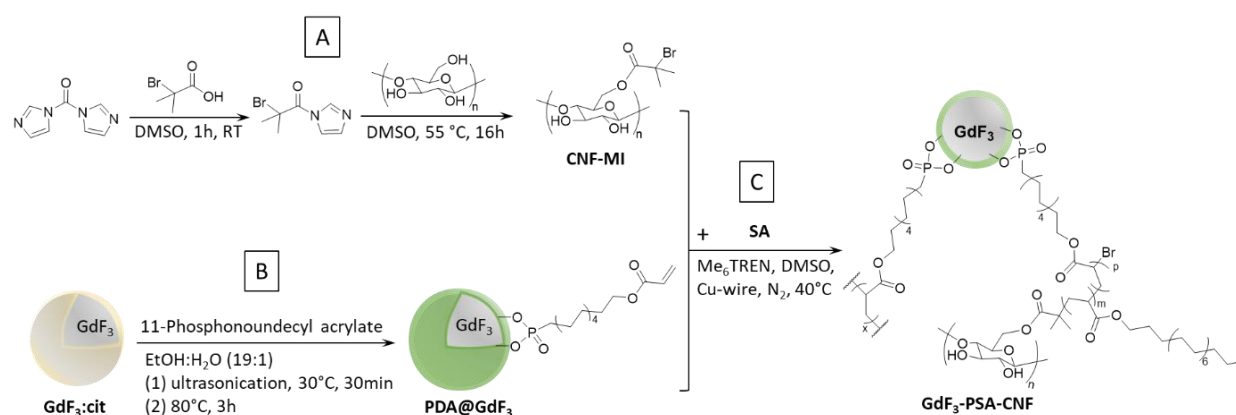


Figure 3. 12 TEM images of (A) OA@UCNP, (B) AMPS@UCNP, (C)-(E) UCNP-PSA-CNF.

3.2.3.b Synthesis and characterization of CNF-based hybrid with GdF₃ NPs (GdF₃-PSA-CNF)

Scheme 3.3 illustrates the overall synthesis strategy for GdF₃-PSA-CNF material. Similarly, surface-modified GdF₃ (PDA@GdF₃) was polymerized along with the monomer SA on CNF surfaces through surface-initiated controlled radical polymerization, resulting in the hybrid CNF material, namely GdF₃-PSA-CNF.



Scheme 3. 3 (A) Chemical conversion of CNFs to CNF-MI; (B) surface modification of GdF₃ NPs with PDA; (C) polymerization and *in situ* cross-linking of CNF-MI with SA and PDA@ GdF₃ via SET-LRP.

The result was analyzed with FT-IR (Figure 3. 13). The spectrum of GdF₃-PSA-CNF was identical to that of PSA-CNF, as discussed in the previous chapter, confirming the successful grafting of PSA onto the CNFs. However, identifying the signal from the GdF₃ cross-linked in modified CNFs remains challenging. This is because the characteristic absorption bands of PSA and CNF overlap with those of PDA@ GdF₃.

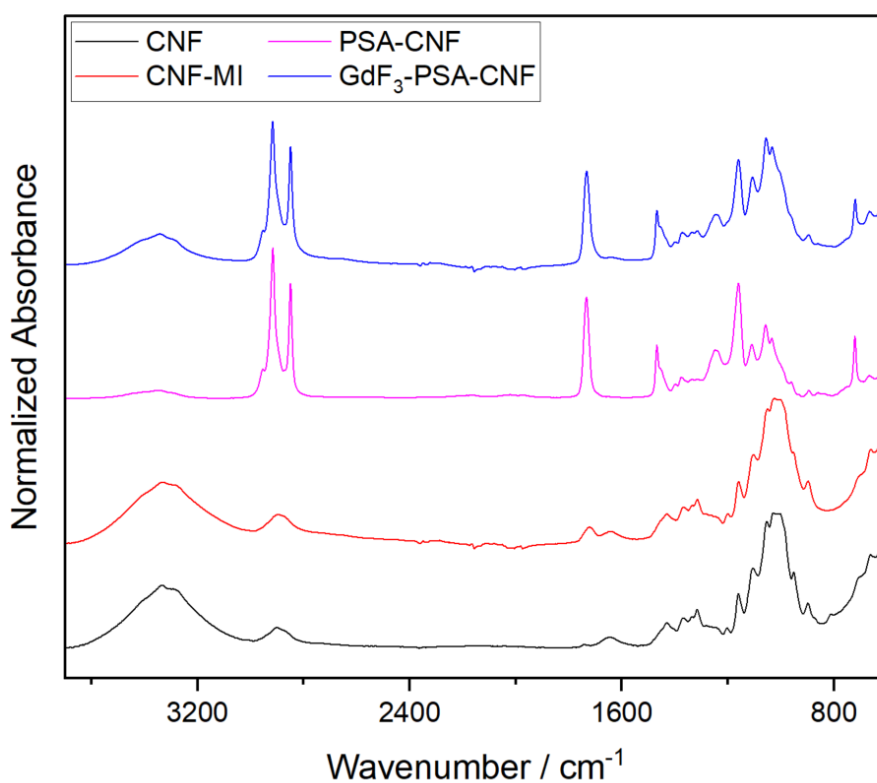


Figure 3. 13 FT-IR spectra of initial CNF (black), CNF-MI (red), PSA-CNF (pink), and GdF₃-PSA-CNF (blue).

TGA measurement was conducted to characterize the thermal stability and quantify the amount of GdF₃ NPs coupled to the CNFs. The result is provided in Figure 3. 14. The decomposition of GdF₃-PSA-CNF started at 200 °C, which is slightly lower than PSA-CNF at 225 °C. However, the presence of GdF₃ NPs resulted in a higher residual content of 3.4 % compared to PSA-CNF, indicating the successful incorporation of GdF₃ NPs.

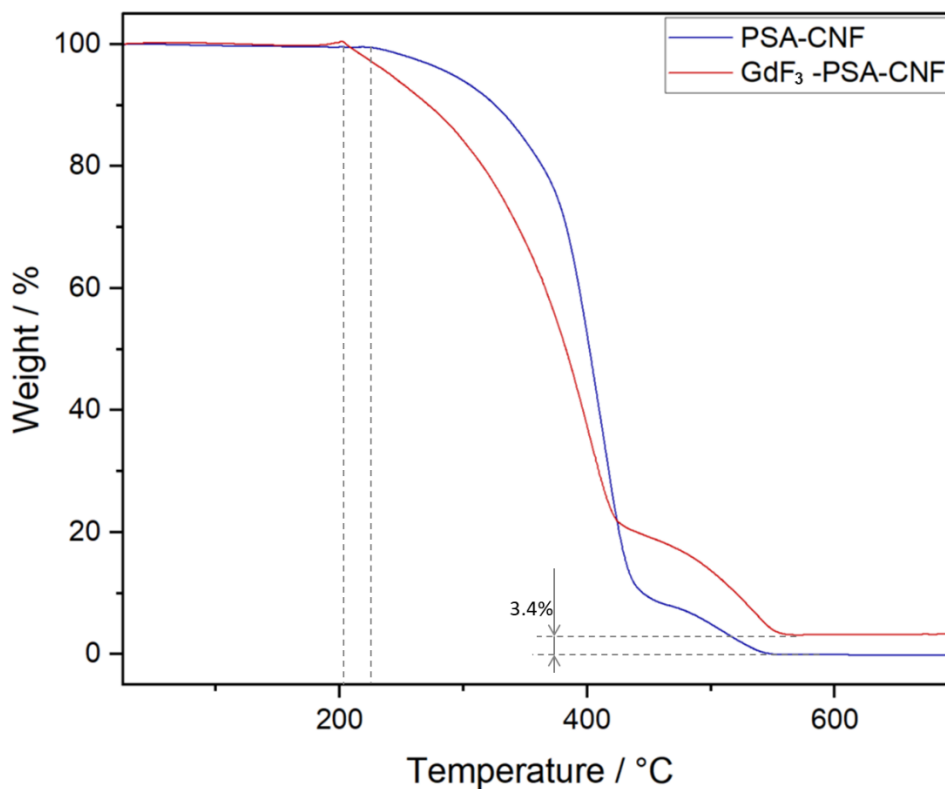


Figure 3. 14 Thermogravimetric analysis of PSA-CNF (blue), GdF₃-PSA-CNF (red).

SEM was employed to examine GdF₃ cross-linked CNF gel prints, which were subjected to two different drying techniques: freeze drying and supercritical CO₂ drying (Figure 3. 15).

The freeze-dried gel (Figure 3. 15 A, C, E) exhibited a rougher and uneven surface, possibly attributed to structural disruptions caused by the transition from solid to gas phases during the freeze-drying process. In contrast, the gel dried using supercritical CO₂ (Figure 3. 15 B, D, F) displays a significantly smoother surface, which can be attributed to the absence of any phase boundary during supercritical drying, thereby preserving the gel structure more effectively. Additionally, a cluster observed in Figure 3. 15 F could potentially represent aggregates of cross-linked GdF₃ NPs.

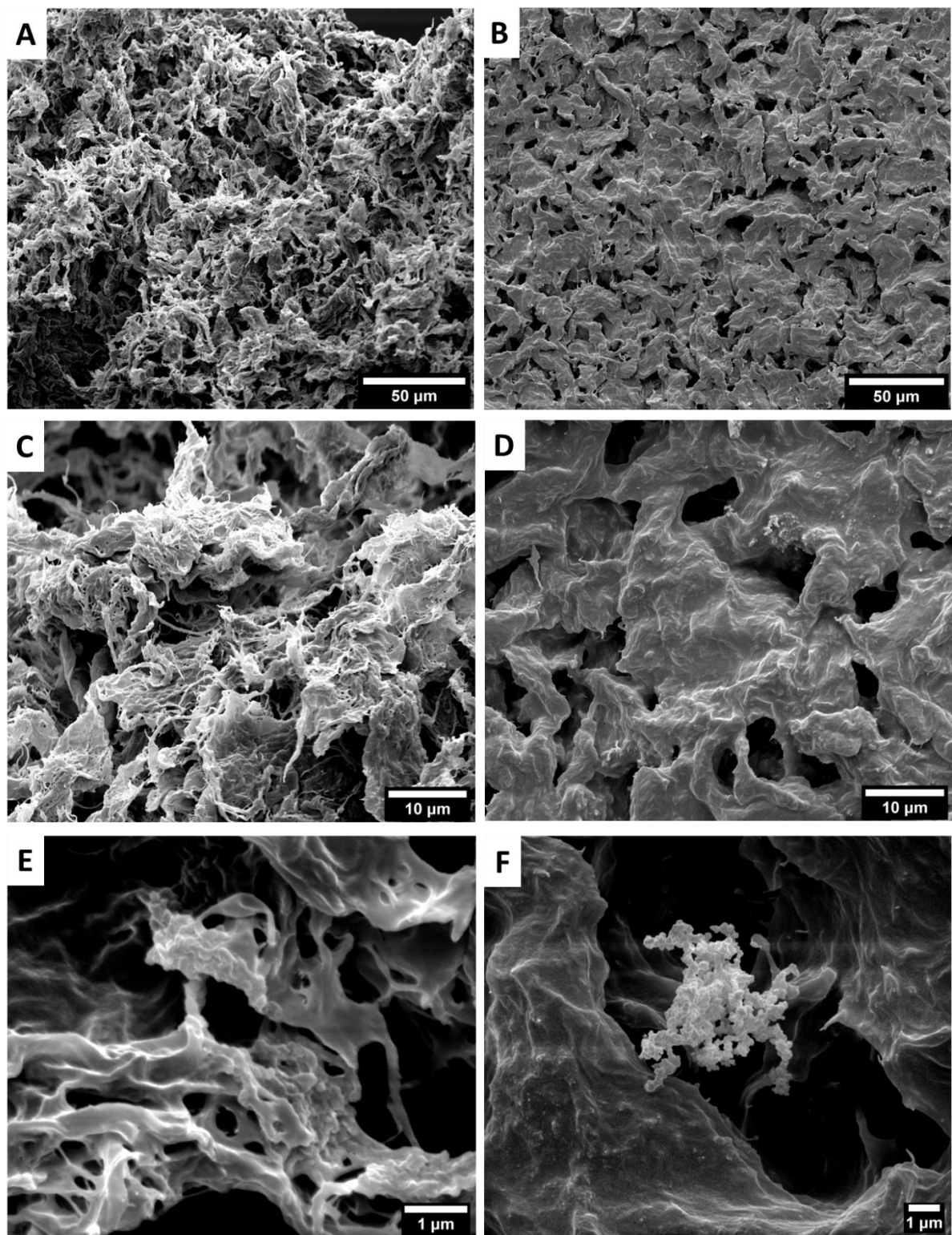


Figure 3. 15 SEM images of GdF₃-PSA-CNF: (A, C, E) freeze dried, (B, D, F) supercritical CO₂ dried.

3.2.4 Ultrasmall- and wide-angle X-ray scattering (USAX/WAXS) measurements of CNF-based hybrids

A series of USAX/WAXS measurements were performed to deepen our understanding of the structure of modified CNFs cross-linked with NPs.

USAXS allows for retrieving nanostructural data with high statistical relevance, providing detailed insights into the material at the nanoscale. Meanwhile, WAXS enables the detection and analysis of crystalline structures within the samples, thereby complementing the USAXS data and offering a more comprehensive overview of the material's architecture.

3.2.4 a UCNP-PSA-CNF

USAXS experiments were conducted to characterize the original UCNPs, the pristine CNF, “simply dried” (annotated as “sd”) and 3D-printed (annotated as “3D”) gels of PSA-CNF and UCNP-PSA-CNF. All data were background corrected. The two-dimensional (2D) SAXS pattern is shown in Figure 3. 16 for completeness. In detail, Figure 3. 16 A-C illustrates the pristine CNF, the simply dried PSA-CNF composite, and the 3D-printed composite, respectively. Figure 3. 16 F displays the SAXS pattern of UCNPs without any matrix.

These four SAXS patterns help to disentangle the contributions from CNFs, PSA, and UCNPs in both simply dried (Figure 3. 16 E) and 3D-printed (Figure 3. 16 D) composites. By employing the methodology developed in reference³¹⁴ for complex multicomponent systems, this approach makes it possible to identify fabrication-induced changes in the nanostructure and the interactions among the various materials within the full composite. For instance, SAXS measurements reveal that the PSA component exhibits detectable changes.

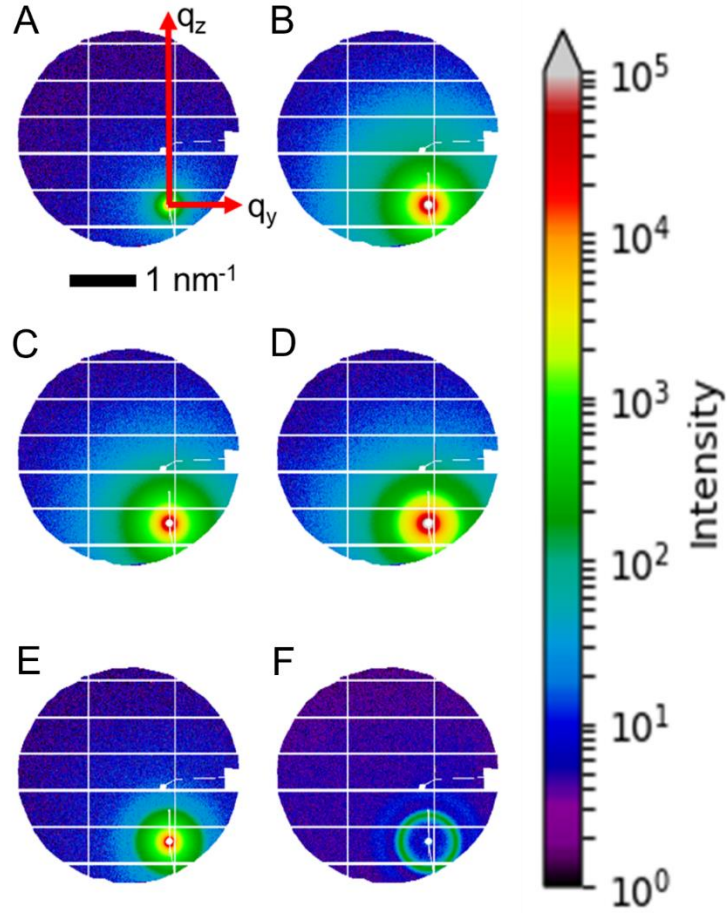


Figure 3. 16 Background-corrected 2D-SAXS data of (A) pristine CNF, (B) PSA-CNF-sd (simply dried), (C) PSA-CNF-3D (3D printed), (D) UCNP-PSA-CNF-3D, (E) UCNP-PSA-CNF-sd, (F) original UCNPs on Kapton. White lines indicate the masked areas. The logarithmic intensity scale for all SAXS patterns is displayed on the right side. The reciprocal space coordinate system with a scale bar is presented in (A).

To analyze the SAXS data for the CNF, we modified the model from Guccini *et al.*³¹⁵, incorporating the Guinier-Porod model from Hammouda³¹⁶.

$$I(q) = A_1 \cdot F(q) + A_2 \exp\left(-\frac{(q - q_0)^2}{2\sigma^2}\right) + A_3 \cdot \frac{1}{1 + q^2\xi^2} + B$$

(10)

$$F(q) = \frac{G}{q^s} \exp\left(-qR_g^2/(3-s)\right) \text{ for } q \leq q_1$$

(11)

$$F(q) = \frac{D}{q^m} \text{ for } q \geq q_1$$

(12)

q denotes the wavevector transfer, q_0 and σ denote the maximum and standard deviation of the Gaussian function. $A_{1,2,3}$ are scale factors. B denotes the background. ξ denotes the correlation length of polymer chains. G , D are scale factors, s indicates the shape of particles, e.g., $s=0$ a sphere. R_g denotes the Guinier radius, m the Porod exponent. q_1 denotes the cross-over point between Guinier and Porod region. For $q_1=0 \text{ nm}^{-1}$ and $q_0=0 \text{ nm}^{-1}$, one retains the functional form of Guccini *et al.*³¹⁵ $1/\sigma$ is then interpreted as the characteristic size of an entangled region³¹⁷. To analyze the UCNP data without CNF, a sum of four Gaussian was used to determine the length scales.

For modeling the UCNP data with CNF and PSA, we assumed that the UCNPs were arranged in a close-packed structure. Due to the existence of a long and short axis, we assumed two paracrystalline lattices with a spherical NP shape each (radius=long/short axis) and used eq. (10) with $A_3=0$ for the CNF and PSA contribution.

One-dimensional (1D) SAXS curves $I(q)$ were calculated by integrating the full 2D SAXS pattern over the full azimuth (Figure 3. 18 & Figure 3. 25).

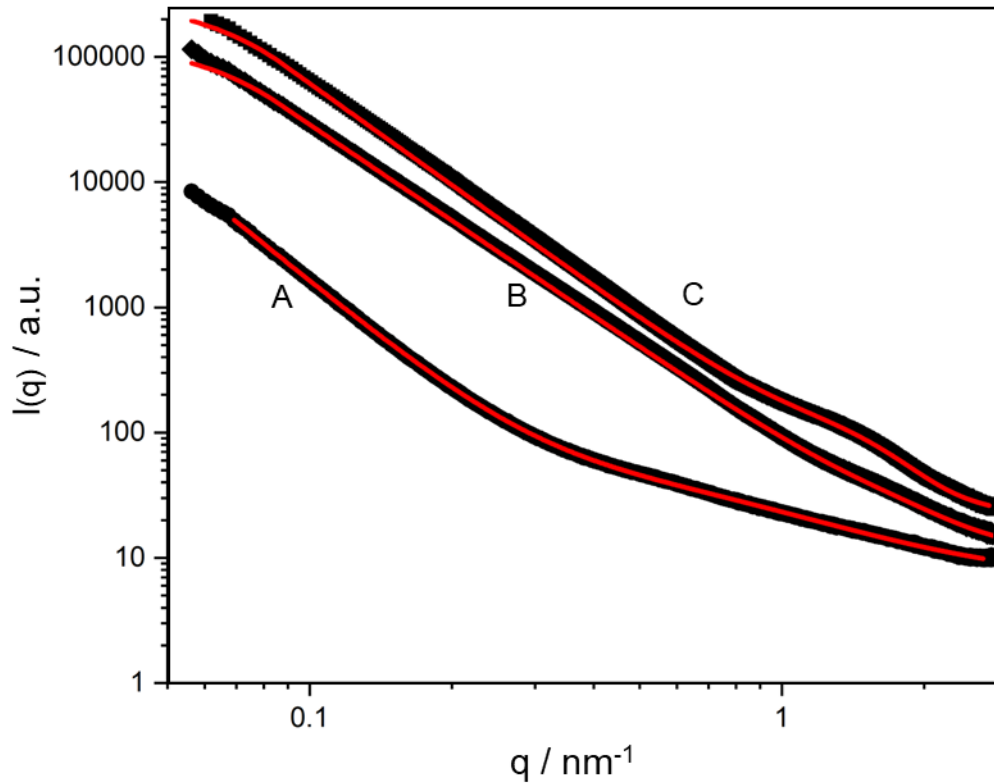


Figure 3. 17 1D-SAXS curves and corresponding fits: (A) the pristine CNF, (B) PSA-CNF-3D, (C) PSA-CNF-sd. The corresponding fits are presented in red color. Curves are shifted for clarity.

The pristine CNF exhibits a structure with a Guinier radius (R_g) of 14.9 ± 1 nm with the shape of a sphere ($s=0$), which is interpreted as a large bundle of CNFs. The slope of $m=3.08$ suggests the presence of rough 3D structures. In addition, a correlation length of polymer chains (ξ) of 1.2 ± 0.1 nm shows a short-range correlation length similar to the literature³¹⁵. The Gaussian in eq. (10) shows no contribution.

The addition of PSA results in a noticeable structural change. For both PSA-CNF-sd and PSA-CNF-3D, R_g changes to $R_g=23 \pm 3$ nm with $s=2.7$ and $s=2.55$, indicating more oblate structures. The CNF matrix is a porous system. Large values of R_g for pristine CNFs correlate to large bundles or agglomerations of CNFs, as stated above, while the smaller values of R_g are consistent with smaller agglomerates³¹⁸ or voids filled by PSA³¹⁹. Figure 3. 12 C-E shows CNF within a similar size range.

In addition, the contribution of the Ornstein-Zernike correlation length ξ is negligible, and a new broad structure appears around 1.1 nm^{-1} for sd samples and 1.5 nm^{-1} for 3D samples. This broad structure, represented by a Gaussian, corresponds to real space length scales of around 4-6 nm and is interpreted as polymer globules (PSA). In the case of the 3D-printed hybrid materials, the contribution of the PSA additive is significantly reduced by 90 %.

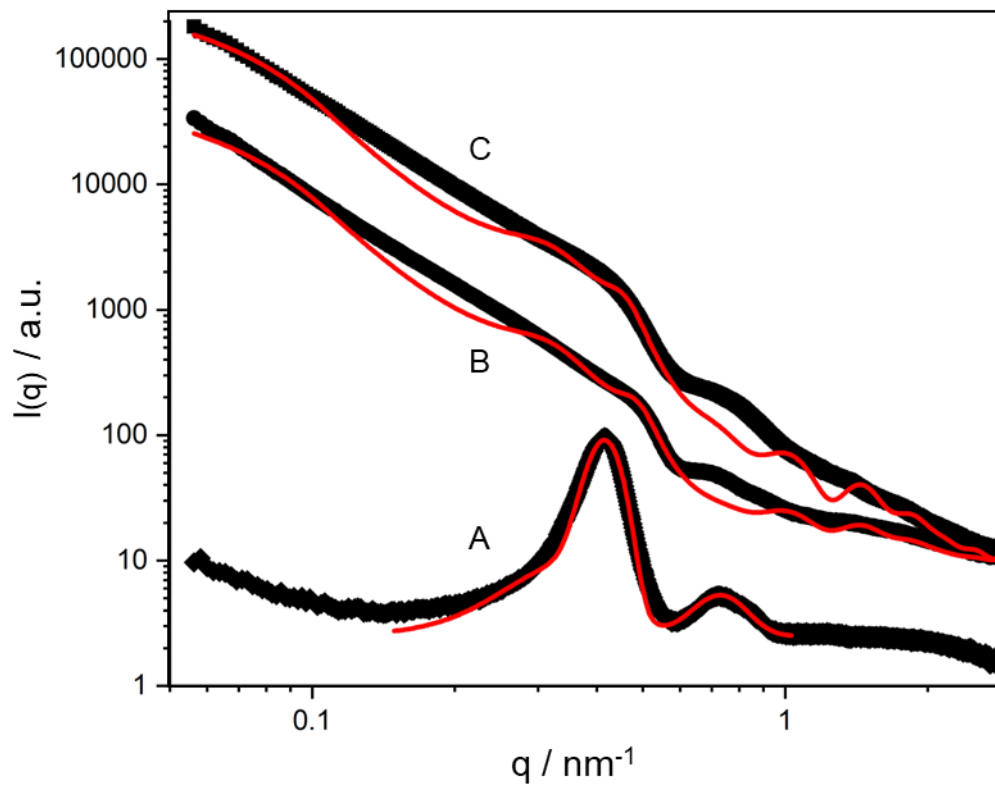


Figure 3. 18 1D-SAXS curves and corresponding fits: (A) OA@UCNPs, (B) UCNP-PSA-CNF-sd, (C) UCNP-PSA-CNF-3D. The corresponding fits are presented in red color. Curves are shifted for clarity.

In Figure 3. 18, we present the 1D-SAXS curves along with the fits derived from the simplified composite model (eq. (10)-(12)). This model effectively reproduces the curve progression $I(q)$, thus allowing for disentangling the contribution of CNFs, UCNPs, and PSA. The sample containing UCNPs shows four major structural features with corresponding q -values of $0.35 \pm 0.05 \text{ nm}^{-1}$, $0.415 \pm 0.001 \text{ nm}^{-1}$, $0.72 \pm 0.02 \text{ nm}^{-1}$ and $0.82 \pm 0.04 \text{ nm}^{-1}$, which correspond to distances of $18 \pm 3 \text{ nm}$, $15.13 \pm 0.03 \text{ nm}$,

8.7 ± 0.2 nm, 7.7 ± 0.4 nm, respectively. Given the elongated shape of the UCNPs, these length scales are interpreted as the distance of stacked UCNPs along the long axis, the short axis and higher orders.

The fraction of the short-axis paracrystalline sub-lattice compared to the long-axis paracrystalline sub-lattice is approximately 87 % for UCNP-PSA-CNF-sd and 92 % for UCNP-PSA-CNF-3D. In the case of UCNP-PSA-CNF-sd, the nearest-neighbor distance is $d_{nn,sd,s}=12.6 \pm 0.2$ nm and for UCNP-PSA-CNF-3D, $d_{nn,3d,s}=13.5 \pm 0.2$ nm. It implies a slightly distorted lattice of UCNP-PSA-CNF-3D. However, the long-axis-sublattice stays constant: $d_{nn,sd,l}=d_{nn,3d,l}=18$ nm and is thus unaffected by the deposition method. Interestingly, for both sublattices, the disorder of the paracrystalline lattices is in both cases 0.3 for the long-axis sublattice $d_{nn,sd/3d,s}$ and 0.2 for the short-axis sublattice $d_{nn,sd,s}$.

The UCNP-PSA-CNF displays distinct regions in its SAXS pattern (Figure 3. 18). At $q < 0.2$ nm⁻¹, the SAXS pattern is primarily influenced by CNFs, whereas at $q > 0.3$ nm⁻¹, it is dominated by the arrangement of UCNPs. Several peaks emerge at $q \geq 0.6$ nm⁻¹, which can be effectively modeled using two paracrystalline structure factors and an approximated spherical shape with different radii for the two lattices. Interestingly, in the 3D-printed samples, the influence of the PSA structure is significantly reduced by 50 %, which is indicated by the steeper slope after 1 nm⁻¹.

In both cases (sd, 3D), the UCNP-PSA-CNF shows a structure with $R_g=23 \pm 3$ nm, $s=0$, and a Porod constant of $m=4$, suggesting a rearrangement into more spherical structures, which is consistent with recent studies on voids in CNF films³¹⁹⁻³²². Consequently, the cross-linked UCNPs induce a structural transformation in the CNF matrix from an oblate structure ($m=2.7$ for sd and $m=2.55$ for 3D) to a more spherical geometry.

Overall, the SAXS results suggest a reduced agglomeration of UCNP-PSA-CNF. In addition, the UCNP-PSA-CNF-sd shows a more compact arrangement of UCNPs along the short axis, while the UCNP-PSA-CNF-3D shows a slightly increased distance between these particles. These findings indicate that the different deposition methods, sd and 3D, result in distinct phase separations: the 3D-printed sample exhibits reduced polymer agglomeration. The reduction in polymer agglomerates in the 3D-printed sample might account for the increased spacing between stacked UCNPs.

3.2.4 b GdF₃-PSA-CNF

The samples of GdF₃ NPs cross-linked CNFs included “simply dried” without 3D printing (annotated as “sd”, as reference), 3D-printed (annotated as “3D/piece”) gels, and a single layer of 3d-printed gel (annotated as “3D/1L”) of GdF₃-PSA-CNF. All data underwent background correction, as explained in the previous section.

In this study, we employed a simplified model compared to eq.(10) in the previous work. The model is described by the eq.(13):

$$I(q) = A_1 \cdot F(q) + A_2 \exp\left(-\frac{(q - q_0)^2}{2\sigma^2}\right) + B$$

(13)

where A_1 and A_2 denote scale factors, $F(q)$ denotes the Guinier-Porod-model from Hammouda³²³, B denotes the background. q_0 and σ are the maximum and standard deviation of the Gaussian function.

The results of the USAXS measurements are presented in Figure 3. 19 and summarized in Table 3. 1. The stacking distance of NPs is observed to be 12 nm, which aligns well with a stacking arrangement along the short axis of the GdF₃ NPs. The shape coefficient (s) is approximately 2, and the Porod coefficient (m) falls within the range of 2.5 to 3. These values suggest the presence of 1D structures and ellipsoidal shapes in the Porod region. This observation is consistent with our previous research on UCNPs cross-linked CNFs³²⁴, suggesting the presence of CNF structures and rough voids. Furthermore, voids with a Guinier radius approximately in the range of 230-260 Å were identified. Notably, in this study, the influence of NP scattering appears to be minimized.

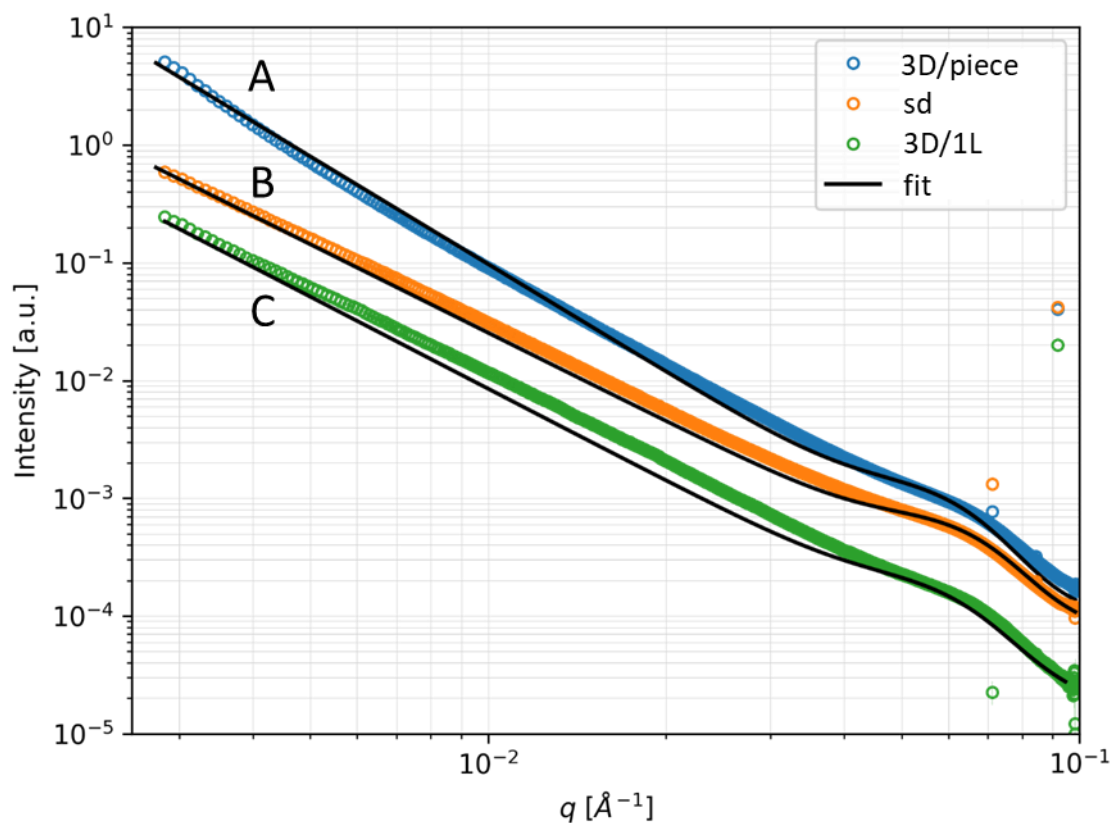


Figure 3. 19 USAXS data of (A) 3D-printed gel (blue), (B) simply dried sample (orange), and (C) a single layer of 3D-printed gel (green). The fitted lines are black.

The GdF_3 NPs cross-linked in modified CNFs exhibit a more chain-like and disordered arrangement compared to the configuration observed in UCNP-PSA-CNF (Figure 3. 20). This is evident from the absence of a second-order peak in the range $0.06\text{-}0.1 \text{ \AA}^{-1}$. A predominant stacking along the long axis is indicated by a GdF_3 NPs distance of around 12 nm, as detailed in Table 3. 1. Using the Debye Scherrer equation³²⁵, we estimate the domain size to be $395 \pm 25 \text{ \AA}$, which approximates $40 \pm 3 \text{ nm}$. This estimation suggests that each domain contains only a few GdF_3 NPs.

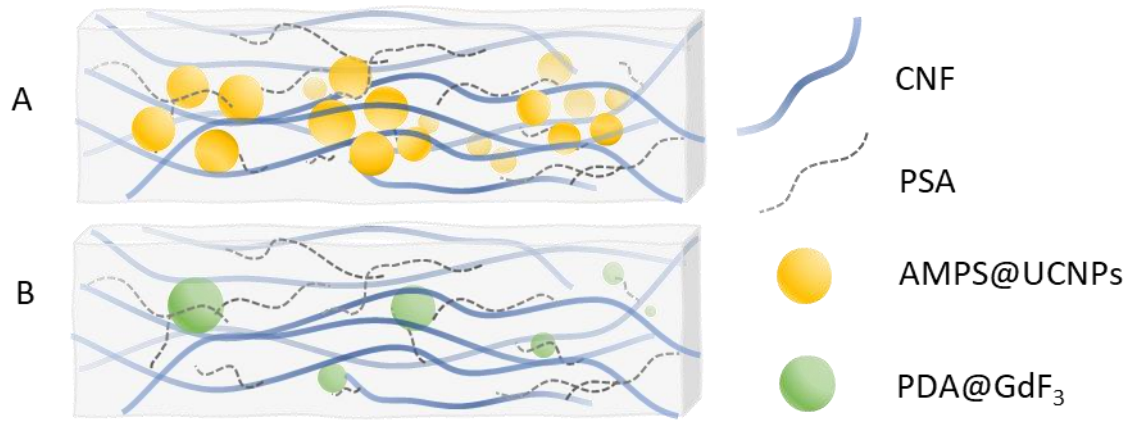


Figure 3. 20 Schematic illustration of stacking and distribution of (A) UCNPs and (B) GdF₃ NPs within modified CNFs.

Table 3. 1 R_g denotes the Guinier radius, s the shape parameter and m the Porod coefficient. D is the stacking distance of the nanoparticles, calculated as $D = 2\pi/q_0$.

| Sample | $R_g / \text{\AA}$ | s | m | $q_0 / \text{\AA}^{-1}$ | $D / \text{\AA}$ | $\sigma / \text{\AA}^{-1}$ |
|----------|--------------------|------|------|-------------------------|------------------|----------------------------|
| 3D/1L | 230 ± 30 | 2.02 | 2.6 | 0.053 ± 0.002 | 119 ± 5 | 0.015 ± 0.001 |
| 3D/piece | 257 ± 30 | 2 | 3.04 | 0.051 ± 0.002 | 123 ± 5 | 0.015 ± 0.001 |
| sd | 230 ± 30 | 2 | 2.5 | 0.055 ± 0.003 | 114 ± 6 | 0.15 ± 0.001 |

The WAXS data are presented in Figure 3. 21. For fitting, the following model was used:

$$I(q) = \sum_{j=1}^3 G_j \exp\left(-\frac{(q - q_j)^2}{2\sigma_j^2}\right) + \sum_{j=1}^2 L_j / \left(1 + ((q - q_j)/(w_j/2))^2\right) + BG$$

(14)

where q_j denotes the peak positions of Gaussian and Lorentzian functions, s_j and w_j their corresponding standard deviation and widths. BG is the background. G_j and L_j denote the amplitudes.

All the curves exhibit a similar pattern (Figure 3. 21). The peak observed at around 1.5\AA^{-1} corresponds to CNFs, while the peak around 2.75\AA^{-1} corresponds to amorphous PSA. The peaks detected at around 3.25\AA^{-1} indicate the arrangement of GdF₃ NPs. These peaks have a Lorentz function width of 0.08\AA^{-1} , yielding a coherent scattering size of 71\AA , which aligns well with the diameter range of GdF₃ NPs. Additionally, the observed peaks

correspond to the (131) and (230) lattice planes³²⁶, confirming the presence of GdF₃ NPs throughout the sample.

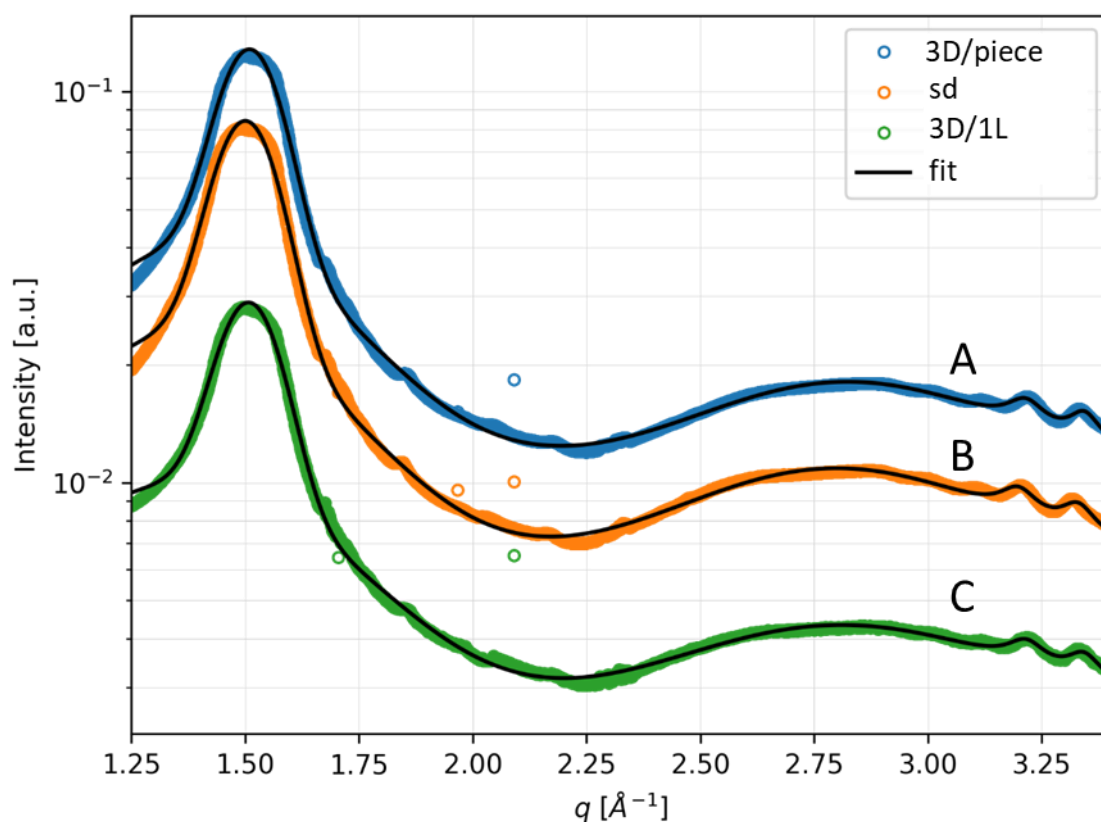


Figure 3. 21. WAXS data of (A) 3D-printed gel (blue), (B) simply dried sample (orange), and (C) a single layer of 3D-printed gel (green). The fitting lines are black.

3.2.5 Performance and application potential of CNF-based hybrids

3.2.5.a CNF-based hybrids with UCNP

Rheology and 3D-printing performance of UCNP-PSA-CNF gel

As mentioned previously, the physical and mechanical properties of CNF gels have been extensively studied^{327,328}. Also, in one of our previous studies, we evaluated the physical properties of CNFs and modified CNF gels using rheological measurements, demonstrating that the cross-linked network enhanced the yield stress and viscoelasticity of the CNF gels¹²². Building on this, we measured key rheological parameters and compared them with those of the UCNP cross-linked CNF gel. Ultimately, we aimed to use the UCNP cross-linked CNF gel for 3D printing.

It is important to note that both samples, UCNP-PSA-CNF and PSA-CNF, can be fully (re)dispersed in toluene after drying (Figure 3. 22). Therefore, gel samples for rheology measurements were prepared with a fixed solid content of 20 % by redispersing modified CNF species in toluene. The results of the rheology measurements are presented in Figure 3. 23.



Figure 3. 22 A suspension of dried UCNP-PSA-CNF redispersed in toluene.

The viscoelastic moduli (Figure 3. 23 A) were measured as a function of oscillatory frequency within the range of 0.1 and 1000 rad/s. It is clear that both CNF gels consistently exhibit a higher storage modulus (G') compared to the loss modulus (G''), indicating that these CNF gels maintain gel-like properties throughout the applied angular frequency range. Generally, the UCNP cross-linked CNF gel exhibited higher viscoelastic moduli values than the PSA-CNF gel. Additionally, the ratio of the loss modulus to the storage modulus (G''/G'), known as loss tangent, was below 0.35 for UCNP-PSA-CNF gel, while PSA-CNF gel reached a maximum value of 0.42. This suggests that UCNP-PSA-CNF has a better elastic behavior, likely due to the cross-linked UCNP with surface ligand forming a more highly entangled network compared to the non-cross-linked CNF gel.

The yield stress test (Figure 3. 23 B) displayed enhanced physical and mechanical properties. The viscosity and strain versus shear stress curves illustrate the different responses of UCNP-PSA-CNF and PSA-CNF to external forces. As shear stress increased, the viscosity of UCNP-PSA-CNF sharply dropped while maintaining better shape retention. This finding is consistent with the earlier observation that UCNP-PSA-CNF exhibits improved flow and shape-retention properties, leading to higher yield stress.

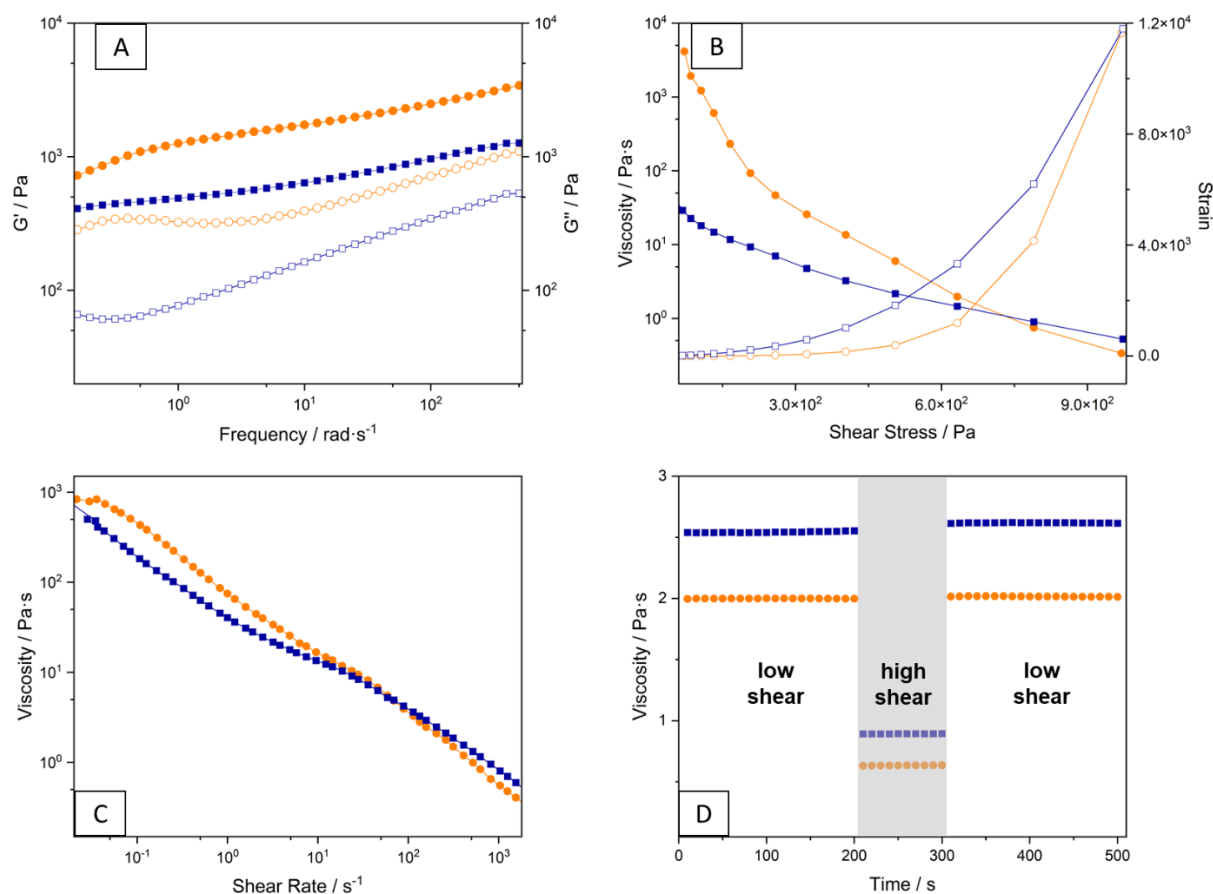


Figure 3. 23 Rheology measurements of CNF-based gels: (A) viscoelastic moduli, (B) yield stress, (C) shear-thinning, (D) shear recovery. The blue square represents PSA-CNF, and the orange circle represents UCNP-PSA-CNF; the solid shape refers to the left Y-axis, and the hollow shape refers to the right Y-axis.

Figure 3. 23 C illustrates the shear-thinning behavior of CNF gels. The zero-shear viscosity of UCNP-PSA-CNF gel, which was initially higher, dropped significantly as the shear rate increased, ultimately reaching a lower value than that of the PSA-CNF. This indicates that the UCNP-PSA-CNF gel can be extruded more easily while maintaining good initial shape retention. The molecular mechanisms behind this behavior likely involve the disentanglement and orientation of grafted PSA and CNFs along the shear flow, which is also influenced by the solvent³²⁹.

The transition of elastic shape retention and fluid-like flow was monitored by measuring the recovery of the viscosity at different shear rates. In Figure 3. 23 D, the white area shows the viscosity of CNF gels at a low shear rate of 200 s^{-1} , while the grey area shows the viscosity at a higher shear rate of 1000 s^{-1} . Due to the shear-thinning behavior, the

viscosity of UCNP-PSA-CNF is lower than PSA-CNF at shear rates above 100 s^{-1} . Both UCNP-PSA-CNF and PSA-CNF gels exhibited rapid transition over time and showed optimal shear recovery. Thus, these CNF gels are promising for high-resolution 3D gel-printing applications.

Overall, both PSA-CNF gel and UCNP-PSA-CNF gel possess rheological properties that make them suitable for 3D gel-printing applications. Moreover, the UCNP-PSA-CNF gel exhibits higher viscosity and enhanced flow and shape-retention properties due to the cross-linked UCNP network.

In the final step, the UCNP-PSA-CNF gel (20 wt%) was applied as ink for 3D printing, resulting in several complex structures. The theoretical models and the 3D prints under daylight or 980 nm laser diode excitation are shown in Figure 3. 24.

The 3D gel structure was reproducibly printed and closely matched the corresponding design model, with a deposition pressure of 20 KPa, a nozzle size of 0.59 mm, and a print speed of 10 mm/s. However, slight deformation occurred later due to excessive solvent evaporation from prints under ambient temperature. Thanks to the unique optical property of UCNP, the 3D prints emitted green light when irradiated with a 980 nm laser diode. It should be noted that the green color is homogeneously distributed throughout the entire 3D-printed object.



Figure 3. 24 3D models and prints under daylight and 980 nm laser diodes.

UCNP-PSA-CNF as fluorescence markers

To further demonstrate the potential of UCNPs as fluorescence markers, a 3D-printed cube of UCNP-PSA-CNF gel was examined using a custom-built confocal microscope (Figure 3. 25). A 980 nm laser diode excited a specific region of the 3D print with the excitation focused on a defined sample volume using an objective lens. The emitted light, collected by the objective, was filtered through a 750 nm short-pass before being directed to the detectors. The sample was mounted on an XYZ piezo stage, which enabled point-by-point scanning across the desired region in all three dimensions.

Figure 3. 25 B illustrates six confocal slices at varying depths within the sample, recorded using the SPAD. Strongly localized intensity maxima were detected at different lateral positions and sample depths. Analysis of these light maxima with a spectrometer and CCD

camera revealed the characteristic emission spectra of UCNPs (Figure 3. 25 C). Aside from the peak marked with an asterisk (*) representing the second harmonic of the excitation laser, the recorded signals matched the known emission spectra of UCNPs, confirming the presence of UCNPs coupled with CNFs.

A detailed examination of the slice at $Z=58 \mu\text{m}$ (Figure 3. 25 D) revealed highly localized emission maxima with diameters of just a few microns, indicating small regions consisting of only a few UCNPs. These localized regions correspond to the specific binding sites of UCNPs on the individual CNFs. It is important to note that the beam quality of the used laser does not allow for the formation of a diffraction-limited 3D laser spot. Therefore, the resolution of our experimental setup is lower compared to conventional confocal microscopes, suggesting that the emission of UCNPs should be localized even stronger.

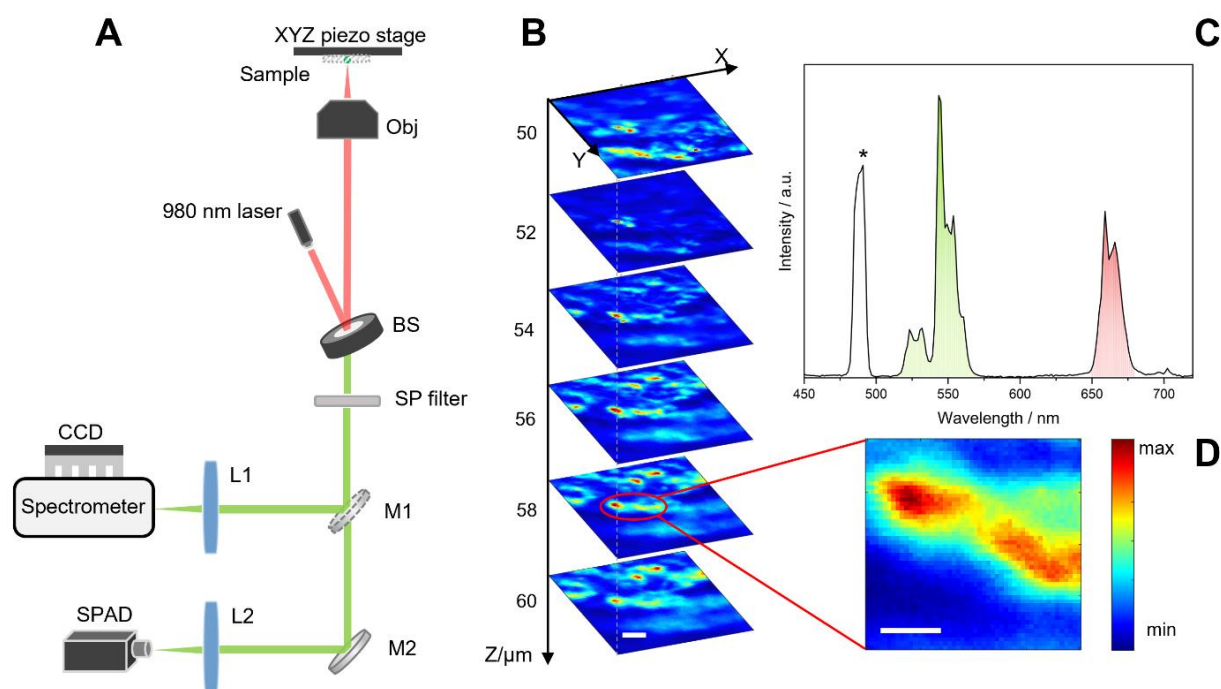


Figure 3. 25 (A) Layout of the custom-built confocal microscope: BS, 90/10 beamsplitter; Obj, an objective lens with a numerical aperture of 0.7; SP filter, short-pass 750 nm filter; M1&M2, (flip) mirror; L1&L2, lenses; CCD, charge-coupled device; SPAD, single-photon avalanche diode; (B) confocal maps at different depths of the sample; scale bar: $10 \mu\text{m}$; (C) typical emission spectrum under 980 nm irradiation; scale bars: $10 \mu\text{m}$; (D) zoomed-in image at the focus plane $Z=58 \mu\text{m}$; intensity is scaled between global min-max.

Furthermore, we observed the alignment of signals in wire-like structures extending laterally across all confocal slices, suggesting that the observed 3D distribution is attributable to the modified CNFs.

These measurements principally demonstrate that 3D confocal microscopy of UCNPs within CNF networks is feasible and represents a significant initial step towards identifying the 3D distribution of UCNPs and individual CNFs within the network. However, enhancing the beam profile of the laser source could further improve the accuracy and resolution of these measurements.

3.2.5.b CNF-based hybrids with GdF₃ NPs

Rheology and 3D-printing performance of GdF₃-PSA-CNF gel

In this study, we measured the key rheological parameters, such as viscose flow, yield stress, and shape retention properties, of GdF₃-PSA-CNF gels and attempted to use the gel to 3D-print models.

For the rheology measurement, the gel sample had a solid content of 10 %. The results of the rheology measurements are displayed in Figure 3. 26.

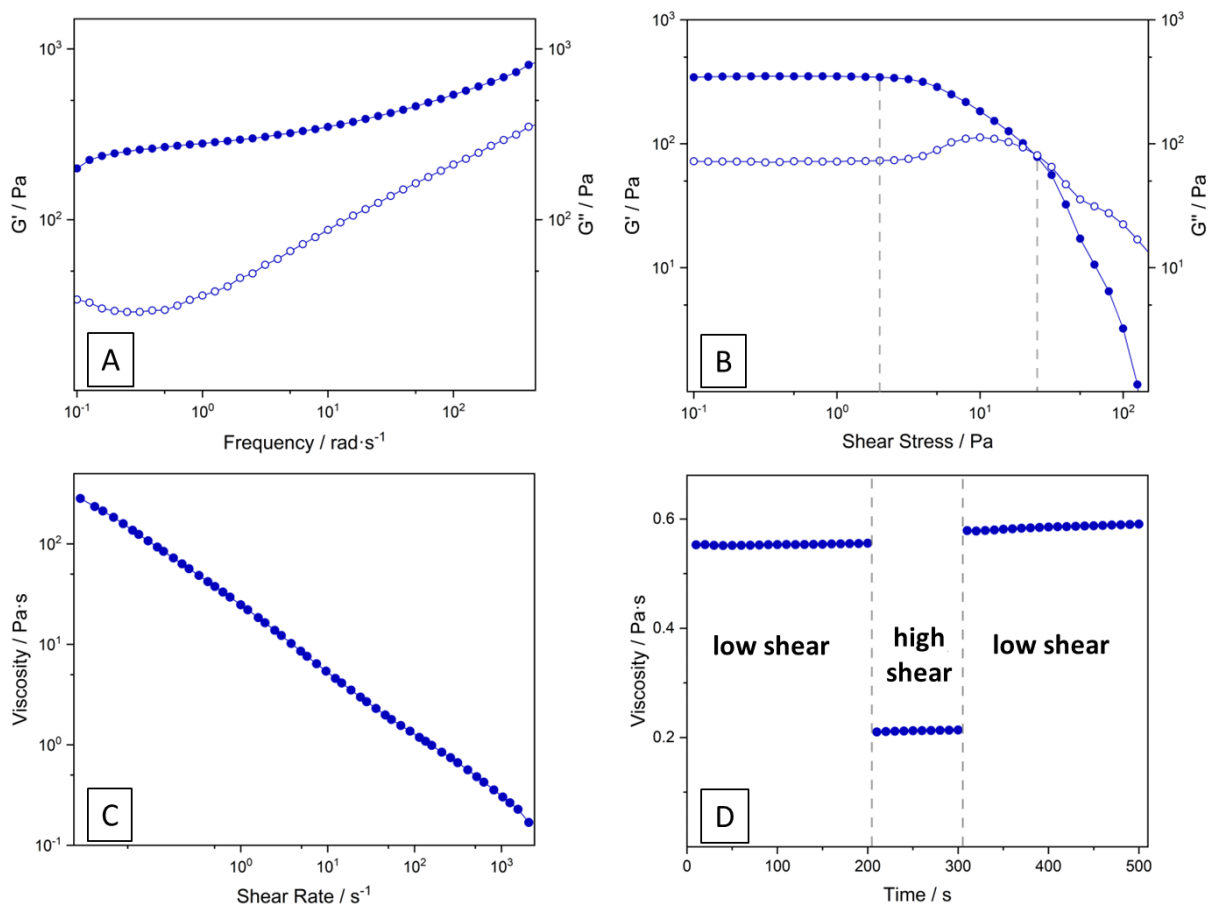


Figure 3. 26. Rheology measurements of GdF₃-PSA-CNF gels: (A) viscoelastic moduli, (B) amplitude sweep, (C) shear-thinning, (D) shear recovery. The solid circle refers to the left Y-axis; the hollow circle refers to the right Y-axis.

In the oscillatory rheology experiment, the viscoelastic moduli were measured over oscillatory frequency from 0.1 to 1000 rad/s. Figure 3. 26 A shows that G' consistently exceeded G'' , confirming that the GdF₃-PSA-CNF gel exhibited gel-like behavior across all tested frequencies and demonstrated good shape retention properties.

In another typical experiment (Figure 3. 26 B), G' and G'' were measured with increasing oscillatory stress at a fixed frequency of 6.28 rad/s. Initially, G' remained higher than G'' , indicating a predominantly solid-like elastic response within a lower stress range. At certain deformation amplitudes, the gel entered the non-linear viscoelastic range and ultimately reached the flow point where G' and G'' intersected, signifying a transition to a liquid, viscous state. Interestingly, the G'' curve shows a peak before decreasing. The

increasing G'' value can be explained by the increased deformation energy due to the changes in the intramolecular interaction of the gel.

Additionally, GdF_3 -PSA-CNF gel also possesses shear-thinning behavior (Figure 3. 26 C). With increasing shear forces, the viscosity of GdF_3 -PSA-CNF gel significantly declined. This *non-Newtonian* fluid behavior combined with good initial shape preservation indicates that the gel is suitable for extrusion-based 3D printing. Following extrusion, a rise in viscosity was expected with the reducing shear rate, aiding in maintaining the printed shape. To observe this, viscosity recovery measurements under varying shear rates were conducted. In Figure 3. 26 D, the GdF_3 -PSA-CNF gel exhibited a rapid transition between elastic shape retention and fluid-like flow over time intervals, showing nearly optimal shear recovery.

To conclude, the GdF_3 -PSA-CNF gel displays a rheological profile supporting good 3D printability. We utilized a gel with a concentration of 10 wt% to 3D print several models at a speed of 10 mm/s through a 0.45 mm nozzle controlled by a 20 KPa deposition pressure. The resulting 3D structures were consistently reproducible. The theoretical models and the 3D prints are shown in Figure 3. 27. The prints in toluene directly underwent supercritical drying and successfully maintained their shape with minimal shrinkage (Figure 3. 28).



Figure 3. 27. 3D models and 3D prints obtained using the GdF_3 -PSA-CNF gels.



Figure 3. 28 3D prints before (upper) and after (down) supercritical drying.

Measurements of relaxivities at 7T and magnetic resonance imaging (MRI)

By employing SET-LRP, we have successfully cross-linked GdF₃ NPs onto CNFs. Our next objective is to assess the MRI activity imparted to the CNF-based gel by the inclusion of GdF₃ NPs.

Figure 3. 29 presents ¹H MRI relaxation time mapping, showing significantly reduced T_1 and T_2 relaxation times, which indicates enhanced relaxivity of GdF₃-PSA-CNF (1 wt% in toluene) compared to toluene control. This demonstrates that GdF₃-PSA-CNF functions effectively as a contrast agent.

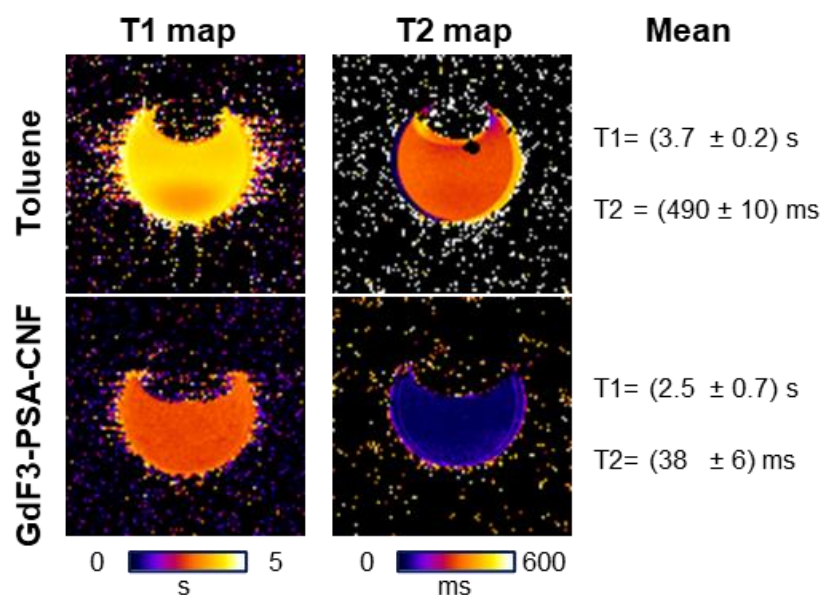


Figure 3. 29. ^1H MRI of toluene control (upper row) and $\text{GdF}_3\text{-PSA-CNF}$ suspension in toluene (1 wt%, lower row).

For the agar-embedded $\text{GdF}_3\text{-CNF}$ suspension in H_2O (1 wt%), we observed a paramagnetic transverse relaxation effect, marked by a moderate decrease in T_2 from (51.0±0.3) ms to (18±9) ms. Interestingly, there was a significant reduction in T_1 from (2.33±0.02) s to (0.6±0.2) s, suggesting direct water exchange with the Gd in addition to long-range paramagnetic relaxation. The gel appeared hypointense due to the reduced T_2 relaxation time. The presence of GdF_3 seemed to induce a blooming effect, where the paramagnetic effect extends beyond the sample into the surrounding agarose. Although a hyperintensity on T_1 -weighted images indicates strong water exchange with the Gd atoms, this was not observed under standard MRI scan parameters for T_1 -weighted imaging (Figure 3. 30).

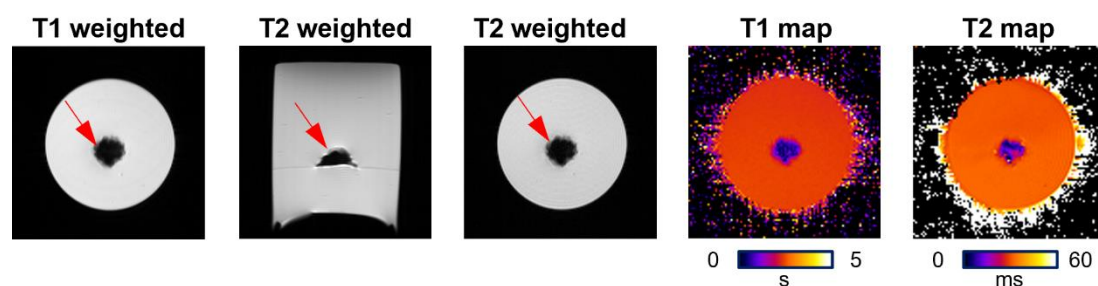
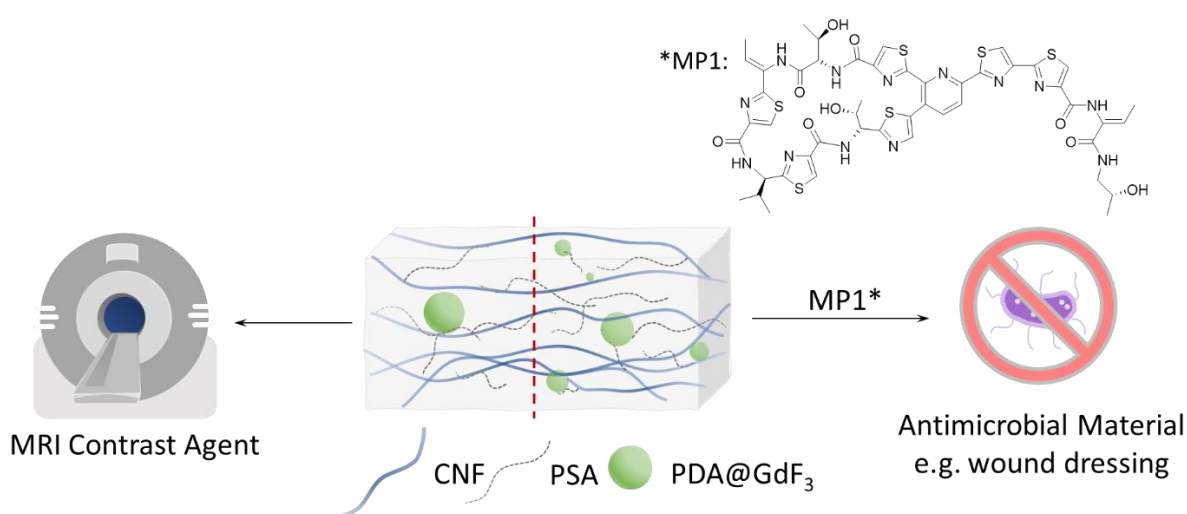


Figure 3. 30. ^1H MRI of $\text{GdF}_3\text{-CNF}$ suspension in H_2O (1 wt%) embedded in control gel (2 wt% agar in 1× phosphate buffered saline). The arrows indicate the gel, which appears hypointense

compared to the surrounding agarose control. This hypointensity can be attributed to transverse relaxation enhancement, resulting in a lower T_2 relaxation time.

CNF-hybrid gel loaded with bacteriocin as a skin wound dressing candidate

As mentioned earlier, our goal is to develop a versatile hybrid gel based on CNFs, designed to serve various purposes as an innovation pool (Scheme 3. 4). Therefore, we attempted to introduce bacteriocin micrococcin P1 (MP1) to the gel to act as an antimicrobial agent. Previous studies have demonstrated that MP1 is effective against the multiresistant MRSA strain ATCC 33591-lux (Perkin Elmer, Waltham, MA)^{330,331}.



Scheme 3. 4 Concept: CNF-based hybrid gels serve different purposes.

In this study, we incorporated MP1 (1 mg/ml) into the GdF₃-PSA-CNF gel prints to evaluate its antimicrobial activity against MRSA. Both freeze-dried and simply dried CNF-based gels containing MP1 showed effective antimicrobial activity against the MRSA strain, even after being stored at room temperature for 7 days. Each group of samples was tested three times, consistently yielding the same results, as shown in Figure 3. 31. This suggests that the modified CNF-based gels are promising candidates for skin wound dressings capable of sustained release of hydrophobic drugs within the wound area. Moreover, the favorable rheology and printability of this gel allow for the customization of wound dressing size and shape to match specific wound dimensions.

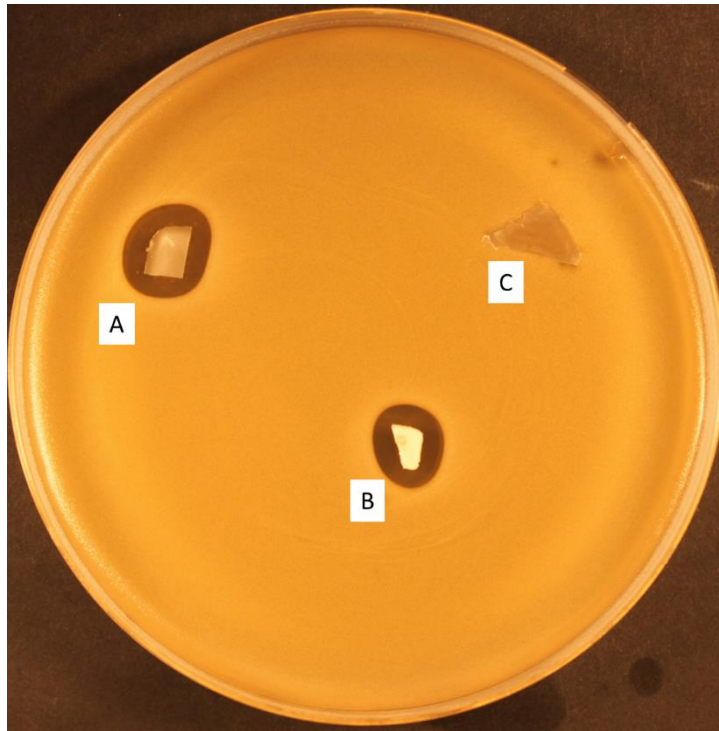


Figure 3. 31 Antimicrobial test against MRSA ATCC 33591-lux in vitro: (A) simply dried print, (B) freeze-dried print, (C) blank sample (negative control).

3.3 Conclusion

In this chapter, we explored various surface modification approaches to adapt NPs to our established surface modification strategy for CNFs. We successfully demonstrated the *in situ* cross-linking of CNFs with inorganic particles, specifically UCNPs and GdF₃ NPs.

For UCNPs, we employed a two-step strategy to replace the initial ligand, oleic acid, with a polymerizable small molecule ligand (AMPS). The first step involved ligand exchange using NOBF₄, which achieved phase transfer and complete removal of oleic acid, as confirmed by FT-IR spectroscopy. In the second step, AMPS was attached to the UCNPs, facilitating their sequential coupling on CNF-MI with SA via SET-LRP, as evidenced by TGA, XRD, and microscopic measurements.

Furthermore, SAXS analysis revealed significant structural transformations induced by the cross-linked UCNPs. The modified CNF structure evolved from an oblate form to a more spherical configuration, exhibiting decreased aggregation of PSA-grafted CNFs. The 3D printing process further minimized aggregation, resulting in a more ordered structure of the cross-linked UCNPs.

Moreover, integrating AMPS@UCNP into the CNF matrix preserved the optical characteristics of the UCNPs, as detected by a custom-built confocal microscope and confirmed through emission spectra. Confocal microscopy provided an initial visualization of the 3D distribution of UCNPs and individual CNFs within the network.

This CNF-based hybrid gel exhibited rheological properties that are ideal for 3D gel-printing, aided by the enhanced cross-linked network due to the UCNPs and their surface ligands. Consequently, this hybrid material shows great promise for applications in security inks, additive manufacturing, optical/photonic technologies, and biomedical fields.

For GdF₃ NPs, we first modified their surfaces with the ligand PDA, as verified by FT-IR, and successfully incorporated them into the SET-LRP of CNFs along with the monomer SA. The final composite was characterized using FT-IR, TGA, and SEM.

The GdF₃-PSA-CNF gel (10 wt%) exhibited rheological characteristics suitable for 3D gel printing via pneumatic extrusion. Structural investigations, both pre- and post-3D printing, using USAXS/WAXS measurements confirmed the uniform distribution of GdF₃ NPs throughout the sample, showing a chain-like and disorganized arrangement within the CNF matrix. An interesting observation was the different distribution and arrangement of GdF₃ NPs and UCNPs within the hybrid gels. GdF₃ NPs were more individually spaced and distributed at greater distances, whereas UCNPs tended to form spherical clusters over shorter distances.

The hybrid gel maintained the MRI activity of GdF₃ NPs. MRI relaxivity measurements at 7T represent a significant step toward employing this modified CNF-based hybrid gel as an MRI contrast agent.

Furthermore, the concept of hybrid CNF-based materials with antimicrobial properties was successfully demonstrated. Antimicrobial tests showed that the dried CNF-based hybrid gel containing MP1 effectively inhibited the MRSA strain, with sustained drug release, making it a promising candidate for customizable skin wound dressings.

3.4 Materials and methods

3.4.1 Materials

1,1'-carbonyldiimidazole (CDI), 2-bromo-2-methyl-propionic acid (98 %), imidazole (≥ 99 %), stearyl acrylate (SA, 97 %), 11-phosphonoundecyl acrylate (PDA), 2-acrylamido-2-methyl-1-propanesulfonic acid (AMPS, 99 %), N,N-dimethylformamid (DMF, 99.8 %), chloroform (≥ 99.5 %), cyclohexane (≥ 99 %), nitrosyltetrafluoroborat (NOBF_4 , 95 %), isopropanol (≥ 99.5 %), ethanol (98 %) and toluene were purchased from Sigma-Aldrich. Tris[2-(dimethylamino)ethyl]amine ($\text{Me}_6\text{-TREN}$) and dimethyl sulfoxide (DMSO, ≥ 99 %) were purchased from Alfa Aesar. Copper wire (diameter 1 mm) was purchased from Fisher.

The rare-earth-doped upconversion nanoparticles (UCNP, $\text{NaYF}_4\text{:Yb,Er/NaYF}_4$) were capped with oleic acid and received as a dispersion (180 mg/ml) in toluene from the *Fraunhofer Institute for Applied Polymer Research (IAP) - Center for Applied Nanotechnology (CAN)*.

The Gadolinium (III)-fluoride ($\text{Gd}_{0.9}\text{Tb}_{0.1}\text{F}_3$) nanoparticles were received as a dispersion (460 mg/ml) in water from *Laboratoire de Chimie, ENS de Lyon*. The GdF_3 nanoparticles have an average size of about 10 nm with a slightly elongated spheroids shape³³².

DI water (0.055 $\mu\text{S/cm}$) was used for all procedures and syntheses.

The monomer used for grafting polymerization was purified by passing through a basic alumina column as a toluene solution to remove inhibitors.

3.4.2 Experimental section

The previous chapter describes the general procedure for producing CNFs, the solvent exchange of CNFs and the synthesis of CNF-MI.

3.4.2.a Surface modification of UCNPs

We employed a two-step ligand exchange method to modify the surface of UCNPs²⁶⁸. More specifically, 55 μl of oleic acid-capped UCNPs (OA@UCNP) in toluene (180 mg/ml) was

diluted to 10 mg/ml using cyclohexane. Next, 1 ml DMF was added, resulting in a biphasic system with cyclohexane in the upper layer containing OA@UCNP and DMF in the lower layer. Subsequently, 10 mg nitrosonium tetrafluoroborate (NOBF_4 , 0.086 mmol) was added, and the mixture was sonicated for 30 min. This process caused the UCNPs to transfer from cyclohexane to DMF, resulting in $\text{BF}_4\text{@UCNP}$.

The UCNPs in DMF were subsequently collected by adding excessive chloroform (10 ml) and centrifuging at 20 000 rpm for 20 min. The resulting pellet ($\text{BF}_4\text{@UCNP}$) was redispersed in DMF, followed by chloroform addition and another round of centrifugation. This purification process was repeated three times.

The secondary ligand exchange involved modifying the UCNPs with AMPS. The $\text{BF}_4\text{@UCNP}$ was suspended in 1 ml ethanol and combined with a solution of AMPS (200 mg, 0.97 mmol) in 4 ml ethanol. The suspension was heated to 60 °C and stirred vigorously overnight. After cooling to room temperature, the surface-modified UCNPs (AMPS@UCNP) were collected and purified by centrifugation (15 000 rpm, 20 min) in ethanol three times.

3.4.2.b Surface modification of GdNPs

A solvent mixture of 95:5 (v/v) ethanol/ H_2O was used for surface modification. 25 mg 11-phosphonoundecyl acrylate (0.082 mmol) was dissolved in 4 ml solvent. This solution was then added to a pre-dispersed GdF_3 suspension (50 mg/2.18 ml). The mixture was ultrasonicated at 30-40 °C for 20 min and stirred at 80 °C for 3 h. The surface-modified nanoparticles (PDA@GdF_3) were collected by centrifugation (10 000 rpm, 5 min) in ethanol, and the process was repeated three times for purification.

3.4.2.c General procedure for SET-LRP grafting of CNF and nanoparticles

AMPS@UCNP and PDA@GdF_3 were applied in this synthesis, respectively.

The CNF-MI (4 g, 1 wt%) and surface-modified nanoparticles (10 mg) were suspended in DMSO (30 ml). Separately, SA (5 g, 15.4 mmol) was dissolved in toluene (15 ml) and added to the suspension. A copper wire (diameter=1 mm, length=6 cm) was pre-treated with HCl solution (37 %), rinsed with water and acetone, and then added to the

suspension. The system was degassed by purging with nitrogen for 10 min and heated to 40 °C. The reaction started with the addition of Me₆-TREN (200 µl, 0.75 mmol, 10 vol% in DMSO) and proceeded overnight under a nitrogen atmosphere. The resulting solid gel was collected by removing the reaction liquid, redissolved in toluene (15 ml) and subsequently precipitated in isopropanol (15 ml). This purification process was repeated four times by centrifugation (6 000 rpm, 1 h) in a toluene/isopropanol (1:1) mixture (30 ml).

3.4.2.d 3D gel-printing of CNF-based gels

A CELLINK INKREDIBLE 3D bioprinter was used in this study, employing pneumatic extrusion. A disposable syringe was loaded with our printable gel and connected to the printing cartridge via a female-female Luer lock adaptor. The printability was fine-tuned by adjusting the inflow air rate through the fixed nozzle to ensure stable and precise layer deposition.

For the UCNP-PSA-CNF gel, a 0.59 mm diameter conical nozzle was used, while the GdF₃-PSA-CNF gel was printed with a 0.45 mm diameter conical nozzle. Both gels were extruded under an applied pressure range of 20-25 kPa. The 3D models were designed in Tinkercad and converted into g-code using PrusaSlicer.

3.4.2.e Bacteriocin loading on CNF-based gels

The thiopeptide bacteriocin micrococcin P1 (MP1) was used in this study. The separation and purification of MP1 were carried out as previously described³³¹. The 3D-printed cuboids (1×1×0.5 cm) of GdF₃-PSA-CNF gel were either freeze-dried or air-dried at ambient temperature. 1 mg MP1 dissolved in DMSO (1 mg/ml) was slowly applied onto each cuboid and allowed to dry overnight.

3.4.2.f Procedure for supercritical CO₂ drying

The toluene-based sample gels were placed into a high-pressure autoclave with a 3.9 l capacity and dried using supercritical CO₂ at 40 °C and 100 bar pressure for 5 h. The continuous CO₂ flow rate was maintained at 30 g/min. After the drying process was complete, the pressure in the autoclave was gradually reduced at a rate of 2 bar/min.

3.4.3 Characterization

FT-IR spectroscopy was conducted on a Bruker Vector 33 spectrometer. All spectra were averaged over 60 scans in the spectral region of 3600-550 cm^{-1} , with a spectral resolution of 4 cm^{-1} .

X-ray diffraction (XRD) analysis was performed using a PANalytical X'PERT Pro diffractometer with a $\text{Cu K}\alpha$ X-ray source (wavelength 0.154 nm). Samples were prepared by depositing 50 μl of the stable colloidal dispersion containing nanocrystals directly onto a Si wafer and allowing it to dry.

Thermogravimetric analysis (TGA) was performed on Netzsch STA 409 with a TG sample holder. Approximately 20 mg of each sample was heated under a nitrogen atmosphere up to 1000 $^{\circ}\text{C}$ at a flow rate of 50 ml/min and a heating rate of 5 $^{\circ}\text{C}/\text{min}$ and then held at this temperature for 1 h. Blank measurements (without a sample) were conducted under identical conditions to correct for balance drift. TGA of AMPS@UCNP was measured in a NETZSCH TG 209F1 under a nitrogen atmosphere with a heating rate of 20 K/min.

Rheology tests were monitored using a TA Instrument AR 2000ex with the Advantage Software v5.8.2. All materials were tested with a 40 mm parallel-plate setup and 500 μm gap distance at room temperature. A shear stress ramp ranging from 0.01 to 1000 Pa was applied, and rotational shear-viscosity measurements were performed in flow mode with shear rates ranging from 0.01 to 1000 s^{-1} . For frequency sweep tests, measurements were taken between 0.1 and 100 rad/s. A strain sweep was performed at an angular frequency of 6.28 rad/s to ensure the measurements in the linear viscoelastic region. Rotational recovery measurements were carried out to evaluate the material recovery behavior by applying a low shear rate of 100 s^{-1} for 200 s, followed by a high shear rate at 1000 s^{-1} for 100 s, and then returning to a low shear rate of 100 s^{-1} for an additional 200 s.

An ultra-high-resolution field emission scanning electron microscope (Quanta FEG Type 250, FEI Electron Optics SN: D9122, Netherlands) was utilized to observe modified CNFs. The samples were examined at an acceleration voltage of 7 kV under high vacuum conditions using an Everhart-Thornley Detector. Prior to imaging, samples were mounted

on stubs with carbon tape and coated with a 5 nm gold layer in an inert atmosphere using a BIORAD SC510 sputtering machine.

Transmission electron microscopy (TEM) images were captured using a JEOL JEM-1011 operating at 100 kV. 10 μ l of the diluted colloidal solution was dried on a carbon-coated copper grid. Emission spectra were obtained using a PTI fluorospectrometer (Horiba) coupled with a 980 nm IR laser. The samples, consisting of 3 ml of dispersed UCNP, UCNP-PSA-CNF in toluene, and AMPS@UCNP in DMSO, were taken in quartz cuvettes for analysis.

The microscopic fluorescence images and spectra were acquired with a custom-built confocal laser scanning setup. A 980 nm diode laser pointer (15 mW at the sample) was used as an excitation source, focusing through a Mitutoyo NIR APO 100X HR objective (Obj., 480-1800 nm, N.A.=0.7) and a 92/8 beam splitter (BS). The laser was focused on the sample placed on an XYZ-piezo stage with a 100 μ m range in all three dimensions. A 750 nm short-pass filter blocked the scattered laser light. The emitted light from the sample was collected from the same objective and routed to one of two detection units using a moveable mirror (M1): the upconversion signal was either focused by a lens (L1) into a spectrograph with a charge-coupled device (CCD) camera for spectral information or by another lens (L2) directly onto the 50 microns sized active area of a single-photon avalanche diode (SPAD) for fast and sensitive confocal imaging via single-photon counting. The small SPAD detector effectively acts as a pinhole, preventing light collected from outside the diffraction-limited volume from reaching the active area.

Ultrasmall- and wide-angle X-ray scattering (USAX/WAXS) were performed at beamline P03, PETRA III, DESY, Hamburg³³³. For samples containing UCNPs, a 25 μ m beam size was used with a wavelength of $\lambda=0.105$ nm and a sample-to-detector distance (SDD) of 3901 mm. For samples containing GdF₃ NPs, a 30 μ m beam size with $\lambda=0.105$ nm was used, with SDD(USAXS)=9500 mm and SDD(WAXS)=211 mm. The detectors used were a PILATUS 2M with a pixel size of 172 μ m (Dectris GmbH, Switzerland) for USAXS and a LAMBDA 9M with a pixel size of 55 μ m (X-spectrum GmbH, Germany) were used. Samples were scanned over a 2 \times 2 mm² area with a 0.1 mm step size and an acquisition time of 1 s to prevent beam damage. All collected images were summed and radially integrated to obtain intensity $I(q)$ as a function of wavevector transfer q .

For antimicrobial activity testing, the MRSA strain ATCC 33591-lux (Perkin Elmer, Waltham, MA) was cultivated in brain heart infusion (BHI) broth (Oxoid, United Kingdom) overnight at 37 °C under aerobic conditions without shaking. The strain originated from the parental strain *S. aureus* ATCC 33591, a clinical MRSA strain isolated from Elmhurst Hospital in New York, NY, USA³³⁴. Agar plate assay and MP1 purification followed previously described procedures³³¹.

4 General conclusions and perspectives

This thesis comprises two distinct studies that share a common CNF modification approach, each addressing different application fields for CNFs.

Chapter 1 introduced the basics of cellulose and its nanoscale variants, detailing the production and pre/post-treatment processes of CNFs. It elucidated their characterization and properties and reviewed some common surface modification approaches and emerging applications, particularly emphasizing using CNFs as rheology modifiers in additive manufacturing and components in hybrid materials with inorganic nanoparticles for biomedicine and electronic devices.

Additionally, Chapter 1 discussed some limitations associated with the surface modification of CNFs using small molecules, and the limitations of some common microscopic techniques for morphology studies of CNFs, particularly when embedded in a composite. To address the first limitation, we developed a versatile surface modification route for CNFs. This process involved first chemically converting CNFs into CNF-MI and then grafting polymers onto them via SET-LRP. Various monomers were successfully grafted onto CNFs, requiring only minor adjustments in reaction conditions to accommodate different monomer characteristics. For example, different solvent systems were employed: a toluene/DMSO mixture for SA and DMSO alone for DEGEEA. The properties of the modified CNFs varied depending on the grafted polymers. For example, DEGEEA-CNF formed stable suspensions in DMSO, while PSA-CNFs solidified in DMSO but fully dispersed in toluene.

However, while the thesis has demonstrated the feasibility and potential of surface-modified CNFs via SET-LRP, some facts cannot be overlooked and remain challenging. One issue is the large amount of organic solvent waste generated during the process. During the solvent-exchange procedure, excessive DMSO (ca. 400 ml for 10 g CNF aqueous gel at 2 wt%) was used to ensure the complete replacement of H₂O. For the purification of CNF-MI, washing with DMSO (ca. 350 ml for 0.1 g CNF-MI) was repeated eight times.

The use of DMSO is crucial for maintaining the stability of CNF suspensions and ensuring the success of the modifications. There are three main reasons: first, initial CNFs,

produced through mechanical processes and obtained in aqueous suspension, can only remain stably suspended in DMSO; second, CDI, used to facilitate the esterification of CNFs, is highly prone to hydrolysis in the presence of water; third, the ligand Me₆-TREN, employed in SET-LRP procedure, requires a H₂O-free environment to maintain its preferred geometry for disproportionation of Cu^I.

Another challenge is the scalability of the process. In a standard synthesis of PSA-CNF, the obtained amount of dried PSA-CNF remains in the milligram scale, and the yield from CNF-MI (4 g, 1 wt%) is approximately 30 %. Scaling up the process resulted in more time-consuming purification procedures, adding complexity and making it difficult to produce larger quantities efficiently.

The second objective of Chapter 2, which was to reveal the morphology and configuration of modified CNFs within a matrix, was realized via CLSM and STED microscopy. In order to visualize the modified CNFs under these high-resolution microscopes, the CNFs were first labeled with some special luminescent dyes. This was achieved by combining SET-LRP and a post-modification step using the click chemistry - CuAAC. The morphology of single fibrils and their embedding within a matrix was observed vividly under the CLSM and STED microscope, appearing in the forms of fibril bundles, aggregates, and homogeneous networks.

However, despite offering a promising approach for a multifunctional platform of CNFs and a novel method for studying CNF morphology, the process incurred a high cost due to the synthesis of the protected alkyne monomer necessary for compatibility with SET-LRP. This monomer's synthesis is required to enable the attachment of azide-functionalized fluorescent dyes via CuAAC, which adds to the complexity and expense of the modification pathway. These factors, therefore, hinder the broader application of this combined modification strategy.

Our focus then shifted to extending the use of the established surface modification route to CNF-based hybrid materials incorporating inorganic nanoparticles. Thanks to the support of our collaborators, we had access to rare-earth-based nanoparticles, such as UCNPs and GdF₃ NPs, and succeeded in integrating their unique properties into CNFs using our methods. The major challenge was modifying the surface chemistry of these

nanoparticles to adapt to the CNF modification process. Different approaches, such as ligand exchange and direct surface modification, were employed on the received initial nanoparticles. Subsequently, the CNFs were cross-linked with the nanoparticles *in situ* via SET-LRP.

The successful adaptation and the properties of these hybrid materials were confirmed and evaluated with various characterization methods. The incorporation of UCNPs and GdF₃ NPs preserved their distinct properties within the modified CNFs, showcasing significant potential for advanced applications. For example, CNF-based hybrids with UCNPs showed potential in optical technologies, such as biomarkers and security inks, and the hybrids with GdF₃ NPs hold potential as novel MRI contrast agents.

Furthermore, those modified CNFs cross-linked with NPs showed outstanding rheological properties suitable for 3D gel printing. When loaded with antimicrobial molecules, these hybrid materials show promising potential as wound dressings featuring sustained drug release and customizable shapes via 3D gel printing.

An ongoing project at our lab focuses on developing wound dressings made of CNF-based gels with customizable shapes and dimensions, offering better flexibility to adhere well to the skin (Figure 4. 1). The CNF-based gel will be 3D-printed into specific shapes on Tegaderm™ film and applied directly to the mouse skin. This involves tailoring the CNFs by grafting with polymers that are not only compatible with biomolecules but also make the modified CNFs 3D-printable, providing sufficient flexibility and elasticity in the dried state.

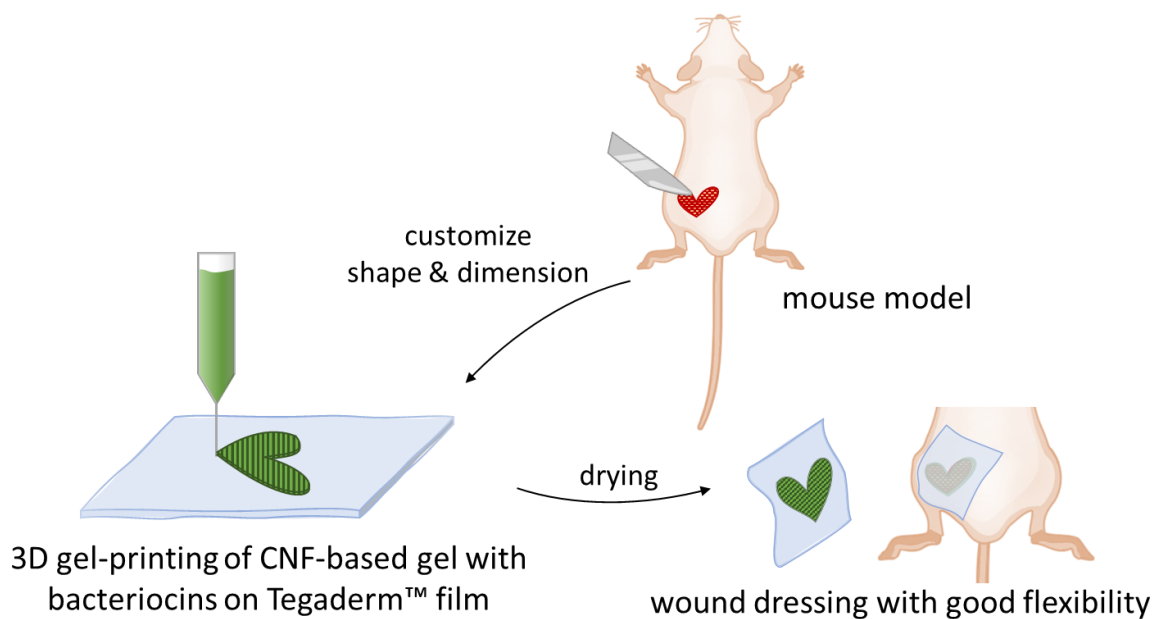


Figure 4. 1 Concept of wound dressing made of CNF-based hybrid gels with customizable shapes and dimensions and drug slow-releasing feature.

Moreover, the long-term stability and durability of the CNF-based hybrid materials require further study. Evaluating the performance of these materials under various environmental conditions, including exposure to moisture, temperature fluctuations, and mechanical stress, is crucial for assessing their applicability in real-world scenarios. Additionally, given the public concern about the potential leaching of inorganic nanoparticles and harmful effects on humans, *in vivo* studies are essential to understand the health risks involved fully. Understanding the biocompatibility and potential toxicity of these materials is critical for ensuring their safe use in medical applications. Research focusing on these aspects is key to reducing any adverse effects and adopting CNF-based hybrid materials in medical settings.

Another ongoing project involves studying the structural changes of 3D-printed CNF-based hybrid gels under deformation using an integrated X-ray beam simultaneously. As illustrated in Figure 4. 2, CNF-based gels are printed in specific shapes with different layer orientations: either parallel to or perpendicular to the longitudinal axis. An X-ray beam is directed through the sample, and a detector captures the resulting diffraction patterns. This setup allows for real-time detection of microstructural changes during tensile loading. At the end of the tensile test, the total elongation at break is measured, providing

insights into the mechanical behavior and internal structural evolution of the CNF-based hybrid gels under deformation.

The objective is to understand how the cross-linked CNF layers interact with each other under stress. This will provide valuable information about the 3D printing process, how the layers in the printed object are assembled, and how they react under strain, including failure modes such as crazing and debonding. Ultimately, this knowledge could help in optimizing the fabrication and performance of CNF-based materials for various applications.

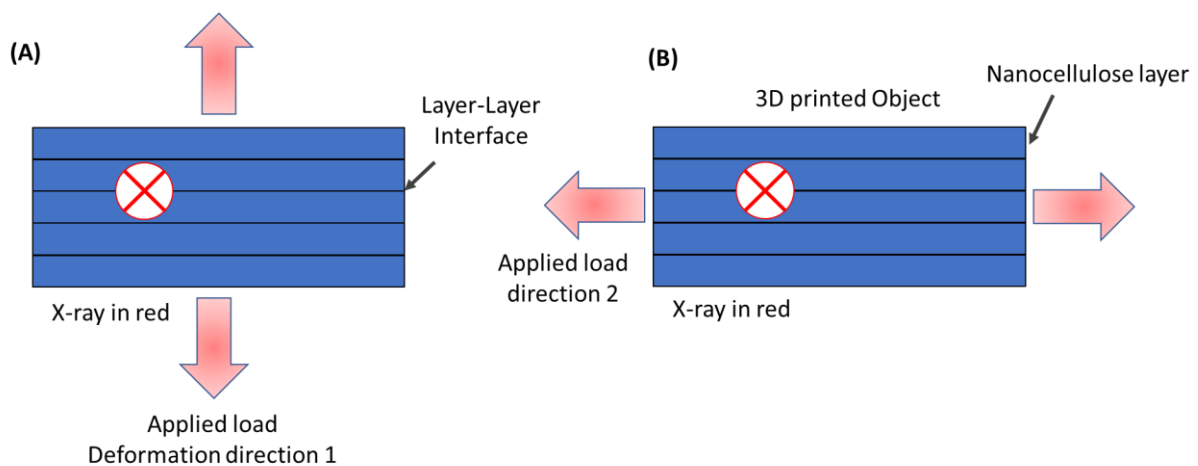


Figure 4. 2 Schematic illustration of tensile testing of 3D-printed CNF objects with X-ray beam detecting structural changes: (A) force applied perpendicular to the layer interface, (B) stretching along the layer interface.

Continued research in the domain of CNF-based hybrid materials calls for interdisciplinary collaboration. Combining expertise from various fields, including chemistry, biology, materials science and engineering, will help develop innovative CNF-based hybrid materials that meet specific application standards and performance criteria. In the future, working with regulatory bodies to set guidelines and standards for the safe production and application of CNF-based hybrid materials will ensure their smooth integration into commercial products.

References

- (1) Varshney, V. K.; Naithani, S. "Chemical Functionalization of Cellulose Derived from Nonconventional Sources". In *Cellulose Fibers: Bio- and Nano-Polymer Composites*; Springer Berlin Heidelberg: Berlin, Heidelberg, 2011; pp 43–60. DOI: 10.1007/978-3-642-17370-7_2.
- (2) Nechyporchuk, O.; Belgacem, M. N.; Bras, J. "Production of Cellulose Nanofibrils: A Review of Recent Advances". *Ind. Crops Prod.* 2016, 93, 2–25. DOI: 10.1016/j.indcrop.2016.02.016.
- (3) Gopi, S.; Balakrishnan, P.; Chandradhara, D.; Poovathankandy, D.; Thomas, S. "General Scenarios of Cellulose and Its Use in the Biomedical Field". *Mater. Today Chem.* 2019, 13, 59–78. DOI: 10.1016/j.mtchem.2019.04.012.
- (4) Estela, R.; Luis, J. "Hydrolysis of Biomass Mediated by Cellulases for the Production of Sugars". In *Sustainable Degradation of Lignocellulosic Biomass - Techniques, Applications and Commercialization*; InTech, 2013. DOI: 10.5772/53719.
- (5) Trache, D.; Tarchoun, A. F.; Derradji, M.; Hamidon, T. S.; Masruchin, N.; Brosse, N.; Hussin, M. H. "Nanocellulose: From Fundamentals to Advanced Applications". *Front. Chem.* 2020, 8 (May). DOI: 10.3389/fchem.2020.00392.
- (6) Thakur, V.; Guleria, A.; Kumar, S.; Sharma, S.; Singh, K. "Recent Advances in Nanocellulose Processing, Functionalization and Applications: A Review". In *Materials Advances*; Royal Society of Chemistry, 2021; Vol. 2, pp 1872–1895. DOI: 10.1039/D1MA00049G.
- (7) Miyashiro, D.; Hamano, R.; Umemura, K. "A Review of Applications Using Mixed Materials of Cellulose, Nanocellulose and Carbon Nanotubes". *Nanomaterials* 2020, 10 (2), 186. DOI: 10.3390/nano10020186.
- (8) Trache, D. "Nanocellulose as a Promising Sustainable Material for Biomedical Applications". *AIMS Mater. Sci.* 2018, 5 (2), 201–205. DOI: 10.3934/matensci.2018.2.201.
- (9) Ullah, H.; Wahid, F.; Santos, H. A.; Khan, T. *Advances in Biomedical and Pharmaceutical Applications of Functional Bacterial Cellulose-Based Nanocomposites*; Elsevier Ltd., 2016; Vol. 150. DOI: 10.1016/j.carbpol.2016.05.029.
- (10) Jozala, A. F.; Lencastre-novaes, L. C. De; Lopes, A. M.; Santos-ebinuma, V. D. C.; Mazzola, P. G.; Pessoa-jr, A. "Bacterial Nanocellulose Production and Application : A 10-Year Overview". 2016, 2063–2072. DOI: 10.1007/s00253-015-7243-4.
- (11) Kargarzadeh, H.; Mariano, M.; Gopakumar, D.; Ahmad, I.; Thomas, S.; Dufresne, A.; Huang, J.; Lin, N. "Advances in Cellulose Nanomaterials". *Cellulose* 2018, 25 (4), 2151–2189. DOI: 10.1007/s10570-018-1723-5.

- (12) Mariano, M.; El Kissi, N.; Dufresne, A. "Cellulose Nanocrystals and Related Nanocomposites: Review of Some Properties and Challenges". *J. Polym. Sci. Part B Polym. Phys.* 2014, *52* (12), 791–806. DOI: 10.1002/polb.23490.
- (13) Rojas, J.; Bedoya, M.; Ciro, Y. "Current Trends in the Production of Cellulose Nanoparticles and Nanocomposites for Biomedical Applications". In *Cellulose - Fundamental Aspects and Current Trends*; InTech, 2015. DOI: 10.5772/61334.
- (14) Mokhena, T. C.; John, M. J. *Cellulose Nanomaterials: New Generation Materials for Solving Global Issues*; Springer Netherlands, 2020; Vol. 27. DOI: 10.1007/s10570-019-02889-w.
- (15) Calvino, C.; Macke, N.; Kato, R.; Rowan, S. J. "Development, Processing and Applications of Bio-Sourced Cellulose Nanocrystal Composites". *Prog. Polym. Sci.* 2020, *103*, 101221. DOI: 10.1016/j.progpolymsci.2020.101221.
- (16) Brinchi, L.; Cotana, F.; Fortunati, E.; Kenny, J. M. "Production of Nanocrystalline Cellulose from Lignocellulosic Biomass: Technology and Applications". *Carbohydr. Polym.* 2013, *94* (1), 154–169. DOI: 10.1016/j.carbpol.2013.01.033.
- (17) Dong, X. M.; Revol, J. F.; Gray, D. G. "Effect of Microcrystallite Preparation Conditions on the Formation of Colloid Crystals of Cellulose". *Cellulose* 1998, *5* (1), 19–32. DOI: 10.1023/A:1009260511939.
- (18) Araki, J.; Wada, M.; Kuga, S. "Steric Stabilization of a Cellulose Microcrystal Suspension by Poly (Ethylene Glycol) Grafting". 2001, No. 17, 21–27.
- (19) Beck-Candanedo, S.; Roman, M.; Gray, D. G. "Effect of Reaction Conditions on the Properties and Behavior of Wood Cellulose Nanocrystal Suspensions". *Biomacromolecules* 2005, *6* (2), 1048–1054. DOI: 10.1021/bm049300p.
- (20) Lima, M. M. D. S.; Wong, J. T.; Paillet, M.; Borsali, R.; Pecora, R. "Translational and Rotational Dynamics of Rodlike". 2003, No. 23, 24–29.
- (21) Patel, D. K.; Dutta, S. D.; Lim, K. T. "Nanocellulose-Based Polymer Hybrids and Their Emerging Applications in Biomedical Engineering and Water Purification". *RSC Advances*. Royal Society of Chemistry 2019, pp 19143–19162. DOI: 10.1039/c9ra03261d.
- (22) Turbak, A. F.; Snyder, F. W.; Sandberg, K. R. "Microfibrillated Cellulose, a New Cellulose Product: Properties, Uses, and Commercial Potential". In *Applied Polymer Science: Applied Polymer Symposium*; 1983; Vol. 37, pp 815–827.
- (23) Gharehkhani, S.; Sadeghinezhad, E.; Kazi, S. N.; Yarmand, H.; Badarudin, A.; Safaei, M. R.; Zubir, M. N. M. "Basic Effects of Pulp Refining on Fiber Properties—A Review". *Carbohydr. Polym.* 2015, *115*, 785–803. DOI: 10.1016/j.carbpol.2014.08.047.
- (24) Klemm, D.; Kramer, F.; Moritz, S.; Lindström, T.; Ankerfors, M.; Gray, D.; Dorris, A. "Nanocelluloses: A New Family of Nature-Based Materials". *Angew. Chemie Int. Ed.*

- 2011, 50 (24), 5438–5466. DOI: 10.1002/anie.201001273.
- (25) Teo, H. L.; Wahab, R. A. “Towards an Eco-Friendly Deconstruction of Agro-Industrial Biomass and Preparation of Renewable Cellulose Nanomaterials: A Review”. *Int. J. Biol. Macromol.* 2020, 161, 1414–1430. DOI: 10.1016/j.ijbiomac.2020.08.076.
- (26) Lavoine, N.; Desloges, I.; Dufresne, A.; Bras, J. “Microfibrillated Cellulose – Its Barrier Properties and Applications in Cellulosic Materials : A Review”. *Carbohydr. Polym.* 2012, 90 (2), 735–764. DOI: 10.1016/j.carbpol.2012.05.026.
- (27) Prasad, R.; Kumar, V.; Kumar, M. *Nanotechnology*; Prasad, R., Kumar, V., Kumar, M., Eds.; Springer Singapore: Singapore, 2017. DOI: 10.1007/978-981-10-4678-0.
- (28) Eriksen, Ø.; Syverud, K.; Gregersen, Ø. “The Use of Microfibrillated Cellulose Produced from Kraft Pulp as Strength Enhancer in TMP Paper”. *Nord. Pulp Pap. Res. J.* 2008, 23 (3), 299–304. DOI: 10.3183/npprj-2008-23-03-p299-304.
- (29) Spence, K. L.; Venditti, R. A.; Rojas, O. J.; Habibi, Y.; Pawlak, J. J. “A Comparative Study of Energy Consumption and Physical Properties of Microfibrillated Cellulose Produced by Different Processing Methods”. *Cellulose* 2011, 18 (4), 1097–1111. DOI: 10.1007/s10570-011-9533-z.
- (30) Villalobos-Castillejos, F.; Granillo-Guerrero, V. G.; Leyva-Daniel, D. E.; Alamilla-Beltrán, L.; Gutiérrez-López, G. F.; Monroy-Villagrana, A.; Jafari, S. M. “Fabrication of Nanoemulsions by Microfluidization”. *Nanoemulsions Formul. Appl. Charact.* 2018, No. March 2019, 207–232. DOI: 10.1016/B978-0-12-811838-2.00008-4.
- (31) Karande, V. S.; Bharimalla, A. K.; Hadge, G. B.; Mhaske, S. T.; Vigneshwaran, N. “Nanofibrillation of Cotton Fibers by Disc Refiner and Its Characterization”. *Fibers Polym.* 2011, 12 (3), 399–404. DOI: 10.1007/s12221-011-0399-3.
- (32) Ho, T. T. T.; Abe, K.; Zimmermann, T.; Yano, H. “Nanofibrillation of Pulp Fibers by Twin-Screw Extrusion”. *Cellulose* 2015, 22 (1), 421–433. DOI: 10.1007/s10570-014-0518-6.
- (33) Hietala, M.; Rollo, P.; Kekäläinen, K.; Oksman, K. “Extrusion Processing of Green Biocomposites: Compounding, Fibrillation Efficiency, and Fiber Dispersion”. *J. Appl. Polym. Sci.* 2014, 131 (6), n/a-n/a. DOI: 10.1002/app.39981.
- (34) Dufresne, A.; Dupeyre, D.; Vignon, M. R. “Cellulose Microfibrils from Potato Tuber Cells: Processing and Characterization of Starch-Cellulose Microfibril Composites”. *J. Appl. Polym. Sci.* 2000, 76 (14), 2080–2092. DOI: 10.1002/(SICI)1097-4628(20000628)76:14<2080::AID-APP12>3.0.CO;2-U.
- (35) Dufresne, A.; Cavaille, J.-Y.; Vignon, M. R. “Mechanical Behavior of Sheets Prepared from Sugar Beet Cellulose Microfibrils”. *J. Appl. Polym. Sci.* 1997, 64 (6), 1185–1194. DOI: 10.1002/(SICI)1097-4628(19970509)64:6<1185::AID-APP19>3.0.CO;2-V.
- (36) Chen, W.; Yu, H.; Liu, Y.; Hai, Y.; Zhang, M.; Chen, P. “Isolation and Characterization

- of Cellulose Nanofibers from Four Plant Cellulose Fibers Using a Chemical-Ultrasonic Process”. *Cellulose* 2011, 18 (2), 433–442. DOI: 10.1007/s10570-011-9497-z.
- (37) Chen, W.; Yu, H.; Liu, Y.; Chen, P.; Zhang, M.; Hai, Y. “Individualization of Cellulose Nanofibers from Wood Using High-Intensity Ultrasonication Combined with Chemical Pretreatments”. *Carbohydr. Polym.* 2011, 83 (4), 1804–1811. DOI: 10.1016/j.carbpol.2010.10.040.
- (38) Andresen, M.; Johansson, L.-S. S.; Tanem, B. S.; Stenius, P. “Properties and Characterization of Hydrophobized Microfibrillated Cellulose”. *Cellulose* 2006, 13 (6), 665–677. DOI: 10.1007/s10570-006-9072-1.
- (39) Iwamoto, S.; Nakagaito, A. N. N.; Yano, H.; Nogi, M. “Optically Transparent Composites Reinforced with Plant Fiber-Based Nanofibers”. *Appl. Phys. A* 2005, 81 (6), 1109–1112. DOI: 10.1007/s00339-005-3316-z.
- (40) Zeng, J.; Hu, F.; Cheng, Z.; Wang, B.; Chen, K. “Isolation and Rheological Characterization of Cellulose Nanofibrils (CNFs) Produced by Microfluidic Homogenization, Ball-Milling, Grinding and Refining”. *Cellulose* 2021, 28 (6), 3389–3408. DOI: 10.1007/s10570-021-03702-3.
- (41) Joseleau, J. P.; Chevalier Billosta, V.; Ruel, K. “Interaction between Microfibrillar Cellulose Fines and Fibers: Influence on Pulp Qualities and Paper Sheet Properties”. *Cellulose* 2012, 19 (3), 769–777. DOI: 10.1007/s10570-012-9693-5.
- (42) Nakagaito, A. N.; Yano, H. “Novel High-Strength Biocomposites Based on Microfibrillated Cellulose Having Nano-Order-Unit Web-like Network Structure”. *Appl. Phys. A Mater. Sci. Process.* 2005, 80 (1), 155–159. DOI: 10.1007/s00339-003-2225-2.
- (43) Nakagaito, A. N. N.; Yano, H. “The Effect of Morphological Changes from Pulp Fiber towards Nano-Scale Fibrillated Cellulose on the Mechanical Properties of High-Strength Plant Fiber Based Composites”. *Appl. Phys. A Mater. Sci. Process.* 2004, 78 (4), 547–552. DOI: 10.1007/s00339-003-2453-5.
- (44) Atik, C.; İmamoğlu, S.; Valchev, I. “Determination of Specific Beating Energy-Applied on Certain Pulps in a Valley Beater”. *J. Univ. Chem. Technol. Metall.* 2005, 40 (3), 199–204.
- (45) Chakraborty, A.; Sain, M. M.; Kortschot, M. T.; Ghosh, S. B. “Modeling Energy Consumption for the Generation of Microfibres from Bleached Kraft Pulp Fibres in a PFI Mill”. *BioResources* 2007, 2 (2), 210–222. DOI: 10.15376/biores.210-222.
- (46) Lal, S. S.; Mhaske, S. T. “TEMPO-Oxidized Cellulose Nanofiber/Kafirin Protein Thin Film Crosslinked by Maillard Reaction”. *Cellulose* 2019, 26 (10), 6099–6118. DOI: 10.1007/s10570-019-02509-7.
- (47) Saito, T.; Isogai, A. “Introduction of Aldehyde Groups on Surfaces of Native Cellulose

- Fibers by TEMPO-Mediated Oxidation". *Colloids Surfaces A Physicochem. Eng. Asp.* 2006, 289 (1–3), 219–225. DOI: 10.1016/j.colsurfa.2006.04.038.
- (48) Saito, T.; Okita, Y.; Nge, T. T.; Sugiyama, J.; Isogai, A. "TEMPO-Mediated Oxidation of Native Cellulose: Microscopic Analysis of Fibrous Fractions in the Oxidized Products". *Carbohydr. Polym.* 2006, 65 (4), 435–440. DOI: 10.1016/j.carbpol.2006.01.034.
- (49) Saito, T.; Nishiyama, Y.; Putaux, J.-L.; Vignon, M.; Isogai, A. "Homogeneous Suspensions of Individualized Microfibrils from TEMPO-Catalyzed Oxidation of Native Cellulose". *Biomacromolecules* 2006, 7 (6), 1687–1691. DOI: 10.1021/bm060154s.
- (50) Isogai, T.; Saito, T.; Isogai, A. "Wood Cellulose Nanofibrils Prepared by TEMPO Electro-Mediated Oxidation". *Cellulose* 2011, 18 (2), 421–431. DOI: 10.1007/s10570-010-9484-9.
- (51) Wågberg, L.; Winter, L.; Ödberg, L.; Lindström, T. "On the Charge Stoichiometry upon Adsorption of a Cationic Polyelectrolyte on Cellulosic Materials". *Colloids and Surfaces* 1987, 27 (4), 163–173. DOI: 10.1016/0166-6622(87)80140-3.
- (52) Wågberg, L.; Decher, G.; Norgren, M.; Lindström, T.; Ankerfors, M.; Axnäs, K. "The Build-Up of Polyelectrolyte Multilayers of Microfibrillated Cellulose and Cationic Polyelectrolytes". *Langmuir* 2008, 24 (3), 784–795. DOI: 10.1021/la702481v.
- (53) Aulin, C.; Netrval, J.; Wågberg, L.; Lindström, T. "Aerogels from Nanofibrillated Cellulose with Tunable Oleophobicity". *Soft Matter* 2010, 6 (14), 3298. DOI: 10.1039/c001939a.
- (54) Liimatainen, H.; Visanko, M.; Sirviö, J. A.; Hormi, O. E. O.; Niinimäki, J. "Enhancement of the Nanofibrillation of Wood Cellulose through Sequential Periodate–Chlorite Oxidation". *Biomacromolecules* 2012, 13 (5), 1592–1597. DOI: 10.1021/bm300319m.
- (55) Liimatainen, H.; Visanko, M. "Sulfonated Cellulose Nanofibrils Obtained from Wood Pulp through Regioselective Oxidative Bisulfite Pre-Treatment". 2013, 741–749. DOI: 10.1007/s10570-013-9865-y.
- (56) Song, Y.; Sun, Y.; Zhang, X.; Zhou, J.; Zhang, L. "Homogeneous Quaternization of Cellulose in NaOH/Urea Aqueous Solutions as Gene Carriers". *Biomacromolecules* 2008, 9 (8), 2259–2264. DOI: 10.1021/bm800429a.
- (57) Aulin, C.; Johansson, E.; Wågberg, L.; Lindström, T. "Self-Organized Films from Cellulose I Nanofibrils Using the Layer-by-Layer Technique". *Biomacromolecules* 2010, 11 (4), 872–882. DOI: 10.1021/bm100075e.
- (58) Arvidsson, R.; Nguyen, D.; Svanström, M. "Life Cycle Assessment of Cellulose Nanofibrils Production by Mechanical Treatment and Two Different Pretreatment Processes". *Environ. Sci. Technol.* 2015, 49 (11), 6881–6890. DOI:

10.1021/acs.est.5b00888.

- (59) de Britto, D.; Assis, O. B. G. "Thermal Degradation of Carboxymethylcellulose in Different Salty Forms". *Thermochim. Acta* 2009, 494 (1–2), 115–122. DOI: 10.1016/j.tca.2009.04.028.
- (60) Fukuzumi, H.; Saito, T.; Okita, Y.; Isogai, A. "Thermal Stabilization of TEMPO-Oxidized Cellulose". *Polym. Degrad. Stab.* 2010, 95 (9), 1502–1508. DOI: 10.1016/j.polymdegradstab.2010.06.015.
- (61) Habibi, Y. "Key Advances in the Chemical Modification of Nanocelluloses". *Chem. Soc. Rev.* 2014, 43 (5), 1519–1542. DOI: 10.1039/C3CS60204D.
- (62) Zhu, J. Y.; Sabo, R.; Luo, X. "Integrated Production of Nano-Fibrillated Cellulose and Cellulosic Biofuel (Ethanol) by Enzymatic Fractionation of Wood Fibers". *Green Chem.* 2011, 13 (5), 1339. DOI: 10.1039/c1gc15103g.
- (63) Lynd, L. R.; Weimer, P. J.; Zyl, W. H. Van; Isak, S. "Microbial Cellulose Utilization : Fundamentals and Biotechnology". *Microbiol. Mol. Biol. Rev.* 2002, 66 (3), 506–577. DOI: 10.1128/MMBR.66.3.506.
- (64) Pääkkö, M.; Ankerfors, M.; Kosonen, H.; Nykänen, A.; Ahola, S.; Österberg, M.; Ruokolainen, J.; Laine, J.; Larsson, P. T.; Ikkala, O.; Lindström, T. "Enzymatic Hydrolysis Combined with Mechanical Shearing and High-Pressure Homogenization for Nanoscale Cellulose Fibrils and Strong Gels". *Biomacromolecules* 2007, 8 (6), 1934–1941. DOI: 10.1021/bm061215p.
- (65) Henriksson, M.; Henriksson, G.; Berglund, L. A.; Lindström, T. "An Environmentally Friendly Method for Enzyme-Assisted Preparation of Microfibrillated Cellulose (MFC) Nanofibers". *Eur. Polym. J.* 2007, 43 (8), 3434–3441. DOI: 10.1016/j.eurpolymj.2007.05.038.
- (66) Minor, J. L. "Hornification - Its Origin and Meaning". *Progress Pap. Recycl.* 1994, 3 (2), 93–95.
- (67) Josefsson, G.; Tanem, B. S.; Li, Y.; Vullum, P. E.; Gamstedt, E. K. "Prediction of Elastic Properties of Nanofibrillated Cellulose from Micromechanical Modeling and Nano-Structure Characterization by Transmission Electron Microscopy". *Cellulose* 2013, 20 (2), 761–770. DOI: 10.1007/s10570-013-9868-8.
- (68) Kangas, H.; Lahtinen, P.; Sneek, A.; Saariaho, A.-M.; Laitinen, O.; Hellén, E. "Characterization of Fibrillated Celluloses. A Short Review and Evaluation of Characteristics with a Combination of Methods". *Nord. Pulp Pap. Res. J.* 2014, 29 (1), 129–143. DOI: 10.3183/npprj-2014-29-01-p129-143.
- (69) Mao, Y.; Liu, K.; Zhan, C.; Geng, L.; Chu, B.; Hsiao, B. S. "Characterization of Nanocellulose Using Small-Angle Neutron, X-Ray, and Dynamic Light Scattering Techniques". *J. Phys. Chem. B* 2017, 121 (6), 1340–1351. DOI: 10.1021/acs.jpcc.6b11425.

- (70) Foster, E. J.; Moon, R. J.; Agarwal, U. P.; Bortner, M. J.; Bras, J.; Camarero-Espinosa, S.; Chan, K. J.; Clift, M. J. D.; Cranston, E. D.; Eichhorn, S. J.; Fox, D. M.; Hamad, W. Y.; Heux, L.; Jean, B.; Korey, M.; Nieh, W.; Ong, K. J.; Reid, M. S.; Renneckar, S.; Roberts, R.; Shatkin, J. A.; Simonsen, J.; Stinson-Bagby, K.; Wanasekara, N.; Youngblood, J. "Current Characterization Methods for Cellulose Nanomaterials". *Chem. Soc. Rev.* 2018, 47 (8), 2609–2679. DOI: 10.1039/C6CS00895J.
- (71) Jakubek, Z. J.; Chen, M.; Couillard, M.; Leng, T.; Liu, L.; Zou, S.; Baxa, U.; Clogston, J. D.; Hamad, W. Y.; Johnston, L. J. "Characterization Challenges for a Cellulose Nanocrystal Reference Material: Dispersion and Particle Size Distributions". *J. Nanoparticle Res.* 2018, 20 (4), 98. DOI: 10.1007/s11051-018-4194-6.
- (72) Pinheiro, I. F.; Ferreira, F. V.; Alves, G. F.; Rodolfo, A.; Morales, A. R.; Mei, L. H. I. "Biodegradable PBAT-Based Nanocomposites Reinforced with Functionalized Cellulose Nanocrystals from Pseudobombax Munguba: Rheological, Thermal, Mechanical and Biodegradability Properties". *J. Polym. Environ.* 2019, 27 (4), 757–766. DOI: 10.1007/s10924-019-01389-z.
- (73) Tibolla, H.; Pelissari, F. M.; Martins, J. T.; Vicente, A. A.; Menegalli, F. C. "Cellulose Nanofibers Produced from Banana Peel by Chemical and Mechanical Treatments: Characterization and Cytotoxicity Assessment". *Food Hydrocoll.* 2018, 75, 192–201. DOI: 10.1016/j.foodhyd.2017.08.027.
- (74) Tibolla, H.; Pelissari, F. M.; Rodrigues, M. I.; Menegalli, F. C. "Cellulose Nanofibers Produced from Banana Peel by Enzymatic Treatment: Study of Process Conditions". *Ind. Crops Prod.* 2017, 95, 664–674. DOI: 10.1016/j.indcrop.2016.11.035.
- (75) da Silva, L. C. E.; Cassago, A.; Battirolo, L. C.; Gonçalves, M. do C.; Portugal, R. V. "Specimen Preparation Optimization for Size and Morphology Characterization of Nanocellulose by TEM". *Cellulose* 2020, 27 (9), 5435–5444. DOI: 10.1007/s10570-020-03116-7.
- (76) Yang, X.; Han, F.; Xu, C.; Jiang, S.; Huang, L.; Liu, L.; Xia, Z. "Effects of Preparation Methods on the Morphology and Properties of Nanocellulose (NC) Extracted from Corn Husk". *Ind. Crops Prod.* 2017, 109, 241–247. DOI: 10.1016/j.indcrop.2017.08.032.
- (77) Usov, I.; Nyström, G.; Adamcik, J.; Handschin, S.; Schütz, C.; Fall, A.; Bergström, L.; Mezzenga, R. "Understanding Nanocellulose Chirality and Structure-Properties Relationship at the Single Fibril Level". *Nat. Commun.* 2015, 6 (May). DOI: 10.1038/ncomms8564.
- (78) Nechyporchuk, O.; Pignon, F.; Belgacem, M. N. "Morphological Properties of Nanofibrillated Cellulose Produced Using Wet Grinding as an Ultimate Fibrillation Process". *J. Mater. Sci.* 2015, 50 (2), 531–541. DOI: 10.1007/s10853-014-8609-1.
- (79) Pöhler, T.; Lappalainen, T.; Tammelin, T.; Eronen, P.; Hiekkataipale, P.; Vehniäinen, A.; Koskinen, T. M. "Influence of Fibrillation Method on the Character of Nanofibrillated Cellulose (NFC)". In *International Conference on Nanotechnology for*

the Forest Products Industry 2010; International Conference on Nanotechnology for the Forest Products Industry: Espoo, 2010; pp 437–458.

- (80) Rana, A. K.; Thakur, V. K. “Impact of Physico-chemical Properties of Nanocellulose on Rheology of Aqueous Suspensions and Its Utility in Multiple Fields: A Review”. *J. Vinyl Addit. Technol.* 2023, 29 (4), 617–648. DOI: 10.1002/vnl.22006.
- (81) Nechyporchuk, O.; Belgacem, M. N.; Pignon, F. “Rheological Properties of Micro-/Nanofibrillated Cellulose Suspensions: Wall-Slip and Shear Banding Phenomena”. *Carbohydr. Polym.* 2014, 112, 432–439. DOI: 10.1016/j.carbpol.2014.05.092.
- (82) Cheng, Z.; Li, J.; Wang, B.; Zeng, J.; Xu, J.; Zhu, S.; Duan, C.; Chen, K. “Comparative Study on Properties of Nanocellulose Derived from Sustainable Biomass Resources”. *Cellulose* 2022, 29 (13), 7083–7098. DOI: 10.1007/s10570-022-04717-0.
- (83) Li, M.-C.; Wu, Q.; Song, K.; Lee, S.; Qing, Y.; Wu, Y. “Cellulose Nanoparticles: Structure–Morphology–Rheology Relationships”. *ACS Sustain. Chem. Eng.* 2015, 3 (5), 821–832. DOI: 10.1021/acssuschemeng.5b00144.
- (84) Li, M.; Wu, Q.; Moon, R. J.; Hubbe, M. A.; Bortner, M. J. “Rheological Aspects of Cellulose Nanomaterials: Governing Factors and Emerging Applications”. *Adv. Mater.* 2021, 33 (21), 2006052. DOI: 10.1002/adma.202006052.
- (85) Tortorella, S.; Sambri, L.; Locatelli, E. “Surface-Modified Nanocellulose for Application in Biomedical Engineering and Nanomedicine : A Review”. 2020, 9909–9937.
- (86) Kargarzadeh, H.; Mariano, M.; Gopakumar, D.; Ahmad, I.; Thomas, S.; Dufresne, A.; Huang, J.; Lin, N. “Advances in Cellulose Nanomaterials”. *Cellulose* 2018, 25 (4), 2151–2189. DOI: 10.1007/s10570-018-1723-5.
- (87) Eyley, S.; Thielemans, W. “Surface Modification of Cellulose Nanocrystals”. *Nanoscale* 2014, 6 (14), 7764–7779. DOI: 10.1039/C4NR01756K.
- (88) Beaumont, M.; Jusner, P.; Gierlinger, N.; King, A. W. T.; Potthast, A.; Rojas, O. J.; Rosenau, T. “Unique Reactivity of Nanoporous Cellulosic Materials Mediated by Surface-Confined Water”. *Nat. Commun.* 2021, 12 (1), 1–8. DOI: 10.1038/s41467-021-22682-3.
- (89) Lunardi, V. B.; Soetaredjo, F. E.; Putro, J. N.; Santoso, S. P.; Yuliana, M.; Sunarso, J.; Ju, Y.; Ismadji, S. “Nanocelluloses: Sources, Pretreatment, Isolations, Modification, and Its Application as the Drug Carriers”. *Polymers (Basel)*. 2021, 13 (13), 2052. DOI: 10.3390/polym13132052.
- (90) Afrin, S.; Karim, Z. “Isolation and Surface Modification of Nanocellulose: Necessity of Enzymes over Chemicals”. *ChemBioEng Rev.* 2017, 4 (5), 289–303. DOI: 10.1002/cben.201600001.
- (91) Božič, M.; Liu, P.; Mathew, A. P.; Kokol, V. “Enzymatic Phosphorylation of Cellulose

- Nanofibers to New Highly-Ions Adsorbing, Flame-Retardant and Hydroxyapatite-Growth Induced Natural Nanoparticles". *Cellulose* 2014, 21 (4), 2713–2726. DOI: 10.1007/s10570-014-0281-8.
- (92) Parikka, K.; Leppänen, A.-S.; Xu, C.; Pitkänen, L.; Eronen, P.; Österberg, M.; Brumer, H.; Willför, S.; Tenkanen, M. "Functional and Anionic Cellulose-Interacting Polymers by Selective Chemo-Enzymatic Carboxylation of Galactose-Containing Polysaccharides". *Biomacromolecules* 2012, 13 (8), 2418–2428. DOI: 10.1021/bm300679a.
- (93) Božič, M.; Vivod, V.; Kavčič, S.; Leitgeb, M.; Kokol, V. "New Findings about the Lipase Acetylation of Nanofibrillated Cellulose Using Acetic Anhydride as Acyl Donor". *Carbohydr. Polym.* 2015, 125, 340–351. DOI: 10.1016/j.carbpol.2015.02.061.
- (94) Leung, M. K. M.; Hagemeyer, C. E.; Johnston, A. P. R.; Gonzales, C.; Kamphuis, M. M. J.; Ardipradja, K.; Such, G. K.; Peter, K.; Caruso, F. "Bio-Click Chemistry: Enzymatic Functionalization of PEGylated Capsules for Targeting Applications". *Angew. Chemie* 2012, 124 (29), 7244–7248. DOI: 10.1002/ange.201203612.
- (95) Filpponen, I.; Kontturi, E.; Nummelin, S.; Rosilo, H.; Kolehmainen, E.; Ikkala, O.; Laine, J. "Generic Method for Modular Surface Modification of Cellulosic Materials in Aqueous Medium by Sequential "Click" Reaction and Adsorption". *Biomacromolecules* 2012, 13 (3), 736–742. DOI: 10.1021/bm201661k.
- (96) Grönqvist, S.; Suurnäkki, A.; Niku-Paavola, M.-L.; Kruus, K.; Buchert, J.; Viikari, L. "Lignocellulose Processing with Oxidative Enzymes". In *Applications of Enzymes to Lignocellulosics*; 2003; pp 46–65. DOI: 10.1021/bk-2003-0855.ch003.
- (97) Rabuka, D.; Rush, J. S.; DeHart, G. W.; Wu, P.; Bertozzi, C. R. "Site-Specific Chemical Protein Conjugation Using Genetically Encoded Aldehyde Tags". *Nat. Protoc.* 2012, 7 (6), 1052–1067. DOI: 10.1038/nprot.2012.045.
- (98) Syverud, K.; Xhanari, K.; Chinga-Carrasco, G.; Yu, Y.; Stenius, P. "Films Made of Cellulose Nanofibrils: Surface Modification by Adsorption of a Cationic Surfactant and Characterization by Computer-Assisted Electron Microscopy". *J. Nanoparticle Res.* 2011, 13 (2), 773–782. DOI: 10.1007/s11051-010-0077-1.
- (99) Xhanari, K.; Syverud, K.; Chinga-Carrasco, G.; Paso, K.; Stenius, P. "Reduction of Water Wettability of Nanofibrillated Cellulose by Adsorption of Cationic Surfactants". *Cellulose* 2011, 18 (2), 257–270. DOI: 10.1007/s10570-010-9482-y.
- (100) Bertsch, P.; Fischer, P. "Adsorption and Interfacial Structure of Nanocelluloses at Fluid Interfaces". *Adv. Colloid Interface Sci.* 2020, 276, 102089. DOI: 10.1016/j.cis.2019.102089.
- (101) Gorur, Y. C.; Larsson, P. A.; Wågberg, L. "Self-Fibrillating Cellulose Fibers: Rapid in Situ Nanofibrillation to Prepare Strong, Transparent, and Gas Barrier Nanopapers". *Biomacromolecules* 2020, 21 (4), 1480–1488. DOI: 10.1021/acs.biomac.0c00040.

- (102) Lin, N.; Huang, J.; Dufresne, A. "Preparation, Properties and Applications of Polysaccharide Nanocrystals in Advanced Functional Nanomaterials: A Review". *Nanoscale* 2012, 4 (11), 3274. DOI: 10.1039/c2nr30260h.
- (103) Moon, R. J.; Martini, A.; Nairn, J.; Simonsen, J.; Youngblood, J. "Cellulose Nanomaterials Review: Structure, Properties and Nanocomposites". *Chem. Soc. Rev.* 2011, 40 (7), 3941. DOI: 10.1039/c0cs00108b.
- (104) Mietner, J. B.; Jiang, X.; Edlund, U.; Saake, B.; Navarro, J. R. G. "3D Printing of a Bio-Based Ink Made of Cross-Linked Cellulose Nanofibrils with Various Metal Cations". *Sci. Rep.* 2021, 11 (1), 6461. DOI: 10.1038/s41598-021-85865-4.
- (105) Lizundia, E.; Meaurio, E.; Vilas, J. L. "Grafting of Cellulose Nanocrystals". In *Multifunctional Polymeric Nanocomposites Based on Cellulosic Reinforcements*; Elsevier, 2016; pp 61–113. DOI: 10.1016/B978-0-323-44248-0.00003-1.
- (106) Granville, A. M.; Brittain, W. J. "Recent Advances in Polymer Brush Synthesis". In *Polymer Brushes*; Advincula, R. C., Brittain, W. J., Caster, K. C., Rhe, J., Eds.; Wiley, 2004; pp 33–50. DOI: 10.1002/3527603824.ch1.
- (107) Matyjaszewski, K.; Tsarevsky, N. V. "Nanostructured Functional Materials Prepared by Atom Transfer Radical Polymerization". *Nat. Chem.* 2009, 1 (4), 276–288. DOI: 10.1038/nchem.257.
- (108) G. Banwell, M.; Liu, X.; A. Connal, L.; G. Gardiner, M. "Synthesis of Functionally and Stereochemically Diverse Polymers via Ring-Opening Metathesis Polymerization of Derivatives of the Biomass-Derived Platform Molecule Levoglucosenone Produced at Industrial Scale". *Macromolecules* 2020, 0 (0). DOI: 10.1021/acs.macromol.0c01305.
- (109) Xu, C.; Yu, J.; Fan, Y.; Wang, J.; Chu, F. "Chemical Modification of Nanocellulose via Atom Transfer Radical Polymerization: Strategy, Applications and Challenges". *Huagong Xuebao/CIESC J.* 2022, 73 (3), 1022–1043. DOI: 10.11949/0438-1157.20211451.
- (110) Soeriyadi, A. H.; Boyer, C.; Nystrm, F.; Zetterlund, P. B.; Whittaker, M. R. "High-Order Multiblock Copolymers via Iterative Cu(0)-Mediated Radical Polymerizations (SET-LRP): Toward Biological Precision". *J. Am. Chem. Soc.* 2011, 133 (29), 11128–11131. DOI: 10.1021/ja205080u.
- (111) Bialk, M.; Prucker, O.; Rhe, J. "Grafting of Polymers to Solid Surfaces by Using Immobilized Methacrylates". *Colloids Surfaces A Physicochem. Eng. Asp.* 2002, 198–200, 543–549. DOI: 10.1016/S0927-7757(01)00958-X.
- (112) Amara, C.; El Mahdi, A.; Medimagh, R.; Khwaldia, K. "Nanocellulose-Based Composites for Packaging Applications". *Curr. Opin. Green Sustain. Chem.* 2021, 31, 100512. DOI: 10.1016/j.cogsc.2021.100512.
- (113) Kramer, F.; Klemm, D.; Schumann, D.; Heßler, N.; Wesarg, F.; Fried, W.; Stadermann,

- D. "Nanocellulose Polymer Composites as Innovative Pool for (Bio)Material Development". *Macromol. Symp.* 2006, 244, 136–148. DOI: 10.1002/masy.200651213.
- (114) Zhang, W.; Wang, L.; Mäkilä, E.; Willför, S.; Xu, C. "Ultralight and Porous Cellulose Nanofibers/Polyethyleneimine Composite Aerogels with Exceptional Performance for Selective Anionic Dye Adsorption". *Ind. Crops Prod.* 2022, 177, 114513. DOI: 10.1016/j.indcrop.2021.114513.
- (115) Zhang, L.; Liu, Z.; Cui, G.; Chen, L. "Biomass-Derived Materials for Electrochemical Energy Storages". *Prog. Polym. Sci.* 2015, 43, 136–164. DOI: 10.1016/j.progpolymsci.2014.09.003.
- (116) Rai, R.; Dhar, P. "Biomedical Engineering Aspects of Nanocellulose: A Review". *Nanotechnology* 2022, 33 (36). DOI: 10.1088/1361-6528/ac6fef.
- (117) Yu, H.; Oh, S.; Han, Y.; Lee, S.; Jeong, H. S.; Hong, H.-J. "Modified Cellulose Nanofibril Aerogel: Tunable Catalyst Support for Treatment of 4-Nitrophenol from Wastewater". *Chemosphere* 2021, 285, 131448. DOI: 10.1016/j.chemosphere.2021.131448.
- (118) Percec, V.; Popov, A. V.; Ramirez-Castillo, E.; Monteiro, M.; Barboiu, B.; Weichold, O.; Asandei, A. D.; Mitchell, C. M. "Aqueous Room Temperature Metal-Catalyzed Living Radical Polymerization of Vinyl Chloride". *J. Am. Chem. Soc.* 2002, 124 (18), 4940–4941. DOI: 10.1021/ja0256055.
- (119) Moreno, A.; Liu, T.; Ding, L.; Buzzacchera, I.; Galià, M.; Möller, M.; Wilson, C. J.; Lligadas, G.; Percec, V. "SET-LRP in Biphasic Mixtures of Fluorinated Alcohols with Water". *Polym. Chem.* 2018, 9 (17), 2313–2327. DOI: 10.1039/c8py00062j.
- (120) Guliashvili, T.; Percec, V. "A Comparative Computational Study of the Homolytic and Heterolytic Bond Dissociation Energies Involved in the Activation Step of ATRP and SET-LRP of Vinyl Monomers". *Polym. Sci.* 2007, 45, 1607–1618. DOI: 10.1002/pola.21927.
- (121) Nguyen, N. H.; Levere, M. E.; Percec, V. "TREN versus Me₆-TREN as Ligands in SET-LRP of Methyl Acrylate". *J. Polym. Sci. Part A Polym. Chem.* 2012, 50 (1), 35–46. DOI: 10.1002/pola.24962.
- (122) Navarro, J. R. G.; Rostami, J.; Ahlinder, A.; Mietner, J. B.; Bernin, D.; Saake, B.; Edlund, U. "Surface-Initiated Controlled Radical Polymerization Approach to In Situ Cross-Link Cellulose Nanofibrils with Inorganic Nanoparticles". *Biomacromolecules* 2020, 21 (5), 1952–1961. DOI: 10.1021/acs.biomac.0c00210.
- (123) Rosen, B. M.; Jiang, X.; Wilson, C. J.; Nguyen, N. H.; Monteiro, M. J.; Percec, V. "Synthesis of Dendritic Macromolecules Through Divergent/Iterative Thio-Bromo "Click" Chemistry and SET-LRP". *J. Polym. Sci. Part A Polym. Chem.* 2009, 47 (21), 5606–5628. DOI: 10.1002/pola.23518.

- (124) Majoinen, J.; Walther, A.; McKee, J. R.; Kontturi, E.; Aseyev, V.; Malho, J. M.; Ruokolainen, J.; Ikkala, O. "Polyelectrolyte Brushes Grafted from Cellulose Nanocrystals Using Cu-Mediated Surface-Initiated Controlled Radical Polymerization". *Biomacromolecules* 2011, 12 (8), 2997–3006. DOI: 10.1021/bm200613y.
- (125) Anastasaki, A.; Nikolaou, V.; Simula, A.; Godfrey, J.; Li, M.; Nurumbetov, G.; Wilson, P.; M. Haddleton, D. "Expanding the Scope of the Photoinduced Living Radical Polymerization of Acrylates in the Presence of CuBr₂ and Me₆-Tren". *Macromolecules* 2014, 47 (12), 3852–3859. DOI: 10.1021/ma500787d.
- (126) Geng, J.; Lindqvist, J.; Mantovani, G.; Haddleton, D. M. "Simultaneous Copper(I)-Catalyzed Azide–Alkyne Cycloaddition (CuAAC) and Living Radical Polymerization". *Angew. Chemie Int. Ed.* 2008, 47 (22), 4180–4183. DOI: 10.1002/anie.200800179.
- (127) Zhang, W.; Zhang, W.; Zhang, Z.; Zhu, J.; Zhu, X. "SET-RAFT Polymerization of Progargyl Methacrylate and a One-Pot/One-Step Preparation of Side-Chain Functionalized Polymers via Combination of SET-RAFT and Click Chemistry". *Macromol. Rapid Commun.* 2010, 31 (15), 1354–1358. DOI: 10.1002/marc.201000008.
- (128) Coelho, J. F. J.; Mendonça, P. V.; Popov, A. V.; Percec, V.; Gonçalves, P. M. O. F.; Gil, M. H. "Synthesis of High Glass Transition Temperature Copolymers Based on Poly(Vinyl Chloride) via Single Electron Transfer—Degenerative Chain Transfer Mediated Living Radical Polymerization (SET-DTLRP) of Vinyl Chloride in Water". *J. Polym. Sci. Part A Polym. Chem.* 2009, 47 (24), 7021–7031. DOI: 10.1002/pola.23741.
- (129) Nguyen, N. H.; Rosen, B. M.; Percec, V. "SET-LRP of N,N-Dimethylacrylamide and of n-Isopropylacrylamide at 25 °C in Protic and in Dipolar Aprotic Solvents". *J. Polym. Sci. Part A Polym. Chem.* 2010, 48 (8), 1752–1763. DOI: 10.1002/pola.23940.
- (130) Xie, Z.; Deng, X.; Liu, B.; Huang, S.; Ma, P.; Hou, Z.; Cheng, Z.; Lin, J.; Luan, S. "Construction of Hierarchical Polymer Brushes on Upconversion Nanoparticles via NIR-Light-Initiated RAFT Polymerization". *ACS Appl. Mater. Interfaces* 2017, 9 (36), 30414–30425. DOI: 10.1021/acsami.7b09124.
- (131) Van De Watering, P.; Zuidam, N. J.; Van Steenberghe, M. J.; Van Der Houwen, O. A. G. J.; Underberg, W. J. M.; Hennink, W. E. "A Mechanistic Study of the Hydrolytic Stability of Poly(2-(Dimethylamino)Ethyl Methacrylate)". *Macromolecules* 1998, 31 (23), 8063–8068. DOI: 10.1021/ma980689g.
- (132) Anastasaki, A.; Waldron, C.; Wilson, P.; McHale, R.; Haddleton, D. M. "The Importance of Ligand Reactions in Cu(0)-Mediated Living Radical Polymerisation of Acrylates". *Polym. Chem.* 2013, 4 (9), 2672–2675. DOI: 10.1039/c3py00270e.
- (133) Zhang, N.; Samanta, S. R.; Rosen, B. M.; Percec, V. "Single Electron Transfer in Radical Ion and Radical-Mediated Organic, Materials and Polymer Synthesis". *Chem. Rev.* 2014, 114 (11), 5848–5958. DOI: 10.1021/cr400689s.

- (134) Zhang, Q.; Collins, J.; Anastasaki, A.; Wallis, R.; Mitchell, D. A.; Becer, C. R.; Haddleton, D. M. "Sequence-Controlled Multi-Block Glycopolymers to Inhibit DC-SIGN-Gp120 Binding". *Angew. Chemie Int. Ed.* 2013, 52 (16), 4435–4439. DOI: 10.1002/anie.201300068.
- (135) Samanta, S. R.; Cai, R.; Percec, V. "A Rational Approach to Activated Polyacrylates and Polymethacrylates by Using a Combination of Model Reactions and SET-LRP of Hexafluoroisopropyl Acrylate and Methacrylate". *Polym. Chem.* 2015, 6 (17), 3259–3270. DOI: 10.1039/C5PY00082C.
- (136) Ding, L.; Li, J.; Jiang, R.; Wang, L.; Song, W.; Zhu, L. "Cu(0) Wire-Mediated Single-Electron Transfer-Living Radical Polymerization of Oligo(Ethylene Oxide) Methyl Ether Acrylate by Selecting the Optimal Reaction Conditions". *Chinese J. Polym. Sci.* 2019, 37 (11), 1130–1141. DOI: 10.1007/s10118-019-2263-7.
- (137) Rosen, B. M.; Percec, V. "Implications of Monomer and Initiator Structure on the Dissociative Electron-transfer Step of SET-LRP". *J. Polym. Sci. Part A Polym. Chem.* 2008, 46 (16), 5663–5697. DOI: 10.1002/pola.22888.
- (138) Leng, X.; Nguyen, N. H.; Van Beusekom, B.; Wilson, D. A.; Percec, V. "SET-LRP of 2-Hydroxyethyl Acrylate in Protic and Dipolar Aprotic Solvents". *Polym. Chem.* 2013, 4 (10), 2995–3004. DOI: 10.1039/c3py00048f.
- (139) Nguyen, N. H.; Rosen, B. M.; Percec, V. "SET-LRP of N, N -Dimethylacrylamide and of N -Isopropylacrylamide at 25 °C in Protic and in Dipolar Aprotic Solvents". *J. Polym. Sci. Part A Polym. Chem.* 2010, 48 (8), 1752–1763. DOI: 10.1002/pola.23940.
- (140) Nicol, E.; Derouineau, T.; Puaud, F.; Zaitsev, A. "Synthesis of Double Hydrophilic Poly(Ethylene Oxide)-b-Poly(2-Hydroxyethyl Acrylate) by Single-Electron Transfer-Living Radical Polymerization". *J. Polym. Sci. Part A Polym. Chem.* 2012, 50 (18), 3885–3894. DOI: 10.1002/pola.26185.
- (141) Samanta, S. R.; Nikolaou, V.; Keller, S.; Monteiro, M. J.; Wilson, D. A.; Haddleton, D. M.; Percec, V. "Aqueous SET-LRP Catalyzed with "in Situ" Generated Cu(0) Demonstrates Surface Mediated Activation and Bimolecular Termination". *Polym. Chem.* 2015, 6 (11), 2084–2097. DOI: 10.1039/C4PY01748J.
- (142) Boyer, C.; Atme, A.; Waldron, C.; Anastasaki, A.; Wilson, P.; Zetterlund, P. B.; Haddleton, D.; Whittaker, M. R. "Copper(0)-Mediated Radical Polymerisation in a Self-Generating Biphasic System". *Polym. Chem.* 2013, 4 (1), 106–112. DOI: 10.1039/c2py20560b.
- (143) Soliman, S. M. A.; Nouvel, C.; Babin, J.; Six, J. L. "O-Nitrobenzyl Acrylate Is Polymerizable by Single Electron Transfer-Living Radical Polymerization". *J. Polym. Sci. Part A Polym. Chem.* 2014, 52 (15), 2192–2201. DOI: 10.1002/pola.27232.
- (144) Lligadas, G.; Rosen, B. M.; Monteiro, M. J.; Percec, V. "Solvent Choice Differentiates SET-LRP and Cu-Mediated Radical Polymerization with Non-First-Order Kinetics". *Macromolecules* 2008, 41 (22), 8360–8364. DOI: 10.1021/ma801774d.

- (145) Rosen, B. M.; Lligadas, G.; Hahn, C.; Percec, V. "The Disproportionation of Cu(I)X Mediated by Ligand and Solvent into Cu(0) and Cu(II)X₂ and Its Implications for SET-LRP". *J. Polym. Sci. Part A Polym. Chem.* 2009, 47 (15), 3940–3948. DOI: 10.1002/pola.23518.
- (146) Zhang, Q.; Wilson, P.; Anastasaki, A.; McHale, R.; Haddleton, D. M. "Synthesis and Aggregation of Double Hydrophilic Diblock Glycopolymers via Aqueous SET-LRP". *ACS Macro Lett.* 2014, 3 (5), 491–495. DOI: 10.1021/mz5001724.
- (147) Nguyen, N. H.; Levere, M. E.; Percec, V. "SET-LRP of Methyl Acrylate to Complete Conversion with Zero Termination". *J. Polym. Sci. Part A Polym. Chem.* 2012, 50 (5), 860–873. DOI: 10.1002/pola.25838.
- (148) Hornby, B. D.; West, A. G.; Tom, J. C.; Waterson, C.; Harrisson, S.; Perrier, S. "Copper(0)-Mediated Living Radical Polymerization of Methyl Methacrylate in a Non-Polar Solvent". *Macromol. Rapid Commun.* 2010, 31 (14), 1276–1280. DOI: 10.1002/marc.201000031.
- (149) Nguyen, N. H.; Percec, V. "Disproportionating versus Nondisproportionating Solvent Effect in the SET-LRP of Methyl Acrylate during Catalysis with Nonactivated and Activated Cu(0) Wire". *J. Polym. Sci. Part A Polym. Chem.* 2011, 49 (19), 4227–4240. DOI: 10.1002/pola.24865.
- (150) Jiang, X.; Fleischmann, S.; Nguyen, N. H.; Rosen, B. M.; Percec, V. "Cooperative and Synergistic Solvent Effects in SET-LRP of MA". *J. Polym. Sci. Part A Polym. Chem.* 2009, 47 (21), 5591–5605. DOI: 10.1002/pola.23689.
- (151) Wright, P. M.; Mantovani, G.; Haddleton, D. M. "Polymerization of Methyl Acrylate Mediated by Copper(0)/Me₆-TREN in Hydrophobic Media Enhanced by Phenols; Single Electron Transfer-Living Radical Polymerization". *J. Polym. Sci. Part A Polym. Chem.* 2008, 46 (22), 7376–7385. DOI: 10.1002/pola.23042.
- (152) Levere, M. E.; Nguyen, N. H.; Sun, H.; Percec, V. "Interrupted SET-LRP of Methyl Acrylate Demonstrates Cu(0) Colloidal Particles as Activating Species". *Polym. Chem.* 2013, 4 (3), 686–694. DOI: 10.1039/C2PY20791E.
- (153) Lligadas, G.; Grama, S.; Percec, V. "Single-Electron Transfer Living Radical Polymerization Platform to Practice, Develop, and Invent". *Biomacromolecules* 2017, 18 (10), 2981–3008. DOI: 10.1021/acs.biomac.7b01131.
- (154) Lligadas, G.; Ladislaw, J. S.; Guliashvili, T.; Percec, V. "Functionally Terminated Poly(Methyl Acrylate) by SET-LRP Initiated with CHBr₃ and CHI₃". *J. Polym. Sci. Part A Polym. Chem.* 2008, 46 (1), 278–288. DOI: 10.1002/pola.22379.
- (155) Rosen, B. M.; Percec, V. "Single-Electron Transfer and Single-Electron Transfer Degenerative Chain Transfer Living Radical Polymerization". *Chem. Rev.* 2009, 109 (11), 5069–5119. DOI: 10.1021/cr900024j.
- (156) Lligadas, G.; Rosen, B. M.; Bell, C. A.; Monteiro, M. J.; Percec, V. "Effect of Cu(0)

- Particle Size on the Kinetics of SET-LRP in DMSO and Cu-Mediated Radical Polymerization in MeCN at 25 °C". *Macromolecules* 2008, 41 (22), 8365–8371. DOI: 10.1021/ma8018365.
- (157) Ding, L.; Li, J.; Jiang, R. Y.; Wang, L. F.; Song, W.; Zhu, L. "Cu(0) Wire-Mediated Single-Electron Transfer-Living Radical Polymerization of Oligo(Ethylene Oxide) Methyl Ether Acrylate by Selecting the Optimal Reaction Conditions". *Chinese J. Polym. Sci. (English Ed.)* 2019, 37 (11), 1130–1141. DOI: 10.1007/s10118-019-2263-7.
- (158) Zhai, S.; Song, X.; Yang, D.; Chen, W.; Hu, J.; Lu, G.; Huang, X. "Synthesis of Well-Defined PH-Responsive PPEGMEA- g -P2VP Double Hydrophilic Graft Copolymer via Sequential SET-LRP and ATRP". *J. Polym. Sci. Part A Polym. Chem.* 2011, 49 (18), 4055–4064. DOI: 10.1002/pola.24848.
- (159) Nguyen, N. H.; Rosen, B. M.; Lligadas, G.; Percec, V. "Surface-Dependent Kinetics of Cu(0)-Wire-Catalyzed Single-Electron Transfer Living Radical Polymerization of Methyl Acrylate in DMSO at 25 °C". *Macromolecules* 2009, 42 (7), 2379–2386. DOI: 10.1021/ma8028562.
- (160) Nguyen, N. H.; Kulis, J.; Sun, H.-J.; Jia, Z.; van Beusekom, B.; Levere, M. E.; Wilson, D. A.; Monteiro, M. J.; Percec, V. "A Comparative Study of the SET-LRP of Oligo(Ethylene Oxide) Methyl Ether Acrylate in DMSO and in H₂O". *Polym. Chem.* 2013, 4 (1), 144–155. DOI: 10.1039/C2PY20782F.
- (161) Rosen, B. M.; Percec, V. "A Density Functional Theory Computational Study of the Role of Ligand on the Stability of CuI and CuII Species Associated with ATRP and SET-LRP". *J. Polym. Sci. Part A Polym. Chem.* 2007, 45 (21), 4950–4964. DOI: 10.1002/pola.22328.
- (162) Anastasaki, A.; Nikolaou, V.; Haddleton, D. M. "Cu(0)-Mediated Living Radical Polymerization: Recent Highlights and Applications; a Perspective". *Polym. Chem.* 2016, 7 (5), 1002–1026. DOI: 10.1039/C5PY01916H.
- (163) Whittaker, M. R.; Urbani, C. N.; Monteiro, M. J. "Synthesis of Linear and 4-Arm Star Block Copolymers of Poly(Methyl Acrylate- b -Solketal Acrylate) by SET-LRP at 25 °C". *J. Polym. Sci. Part A Polym. Chem.* 2008, 46 (18), 6346–6357. DOI: 10.1002/pola.22946.
- (164) Voepel, J.; Edlund, U.; Albertsson, A.-C.; Percec, V. "Hemicellulose-Based Multifunctional Macroinitiator for Single-Electron-Transfer Mediated Living Radical Polymerization". *Biomacromolecules* 2011, 12 (1), 253–259. DOI: 10.1021/bm101357k.
- (165) Alizadeh, R.; Ghaemy, M. "PH-Responsive ABC Type Miktoarm Star Terpolymers: Synthesis via Combination of Click Reaction and SET-LRP, Characterization, Self-Assembly, and Controlled Drug Release". *Polymer (Guildf.)* 2015, 66, 179–191. DOI: 10.1016/j.polymer.2015.04.034.
- (166) Zoppe, J. O.; Ataman, N. C.; Mocny, P.; Wang, J.; Moraes, J.; Klok, H.-A. "Surface-

- Initiated Controlled Radical Polymerization: State-of-the-Art, Opportunities, and Challenges in Surface and Interface Engineering with Polymer Brushes”. *Chem. Rev.* 2017, *117* (3), 1105–1318. DOI: 10.1021/acs.chemrev.6b00314.
- (167) Moreno, A.; Grama, S.; Liu, T.; Galià, M.; Lligadas, G.; Percec, V. “Polymer Chemistry Water – Organic Solvent Mixtures Provides the Most Economical and Efficient Process”. *Polym. Chem.* 2017, *8* (0), 7559–7574. DOI: 10.1039/c7py01841j.
- (168) Boyer, C.; Corrigan, N. A.; Jung, K.; Nguyen, D.; Nguyen, T.-K.; Adnan, N. N. M.; Oliver, S.; Shanmugam, S.; Yeow, J. “Copper-Mediated Living Radical Polymerization (Atom Transfer Radical Polymerization and Copper(0) Mediated Polymerization): From Fundamentals to Bioapplications”. *Chem. Rev.* 2016, *116* (4), 1803–1949. DOI: 10.1021/acs.chemrev.5b00396.
- (169) Wang, Q.; Chan, T. R.; Hilgraf, R.; Fokin, V. V.; Sharpless, K. B.; Finn, M. G. “Bioconjugation by Copper(I)-Catalyzed Azide-Alkyne [3 + 2] Cycloaddition”. *J. Am. Chem. Soc.* 2003, *125* (11), 3192–3193. DOI: 10.1021/ja021381e.
- (170) Kloetzel, M. C. “The Diels-Alder Reaction with Maleic Anhydride”. In *Organic Reactions*; Wiley, 2011; pp 1–59. DOI: 10.1002/0471264180.or004.01.
- (171) Inglis, A. J.; Sinnwell, S.; Stenzel, M. H.; Barner-Kowollik, C. “Ultrafast Click Conjugation of Macromolecular Building Blocks at Ambienttemperature”. *Angew. Chemie - Int. Ed.* 2009, *48* (13), 2411–2414. DOI: 10.1002/anie.200805993.
- (172) Nilsson, C.; Simpson, N.; Malkoch, M.; Johansson, M.; Malmström, E. “Synthesis and Thiol-Ene Photopolymerization of Allyl-Ether Functionalized Dendrimers”. *J. Polym. Sci. Part A Polym. Chem.* 2008, *46* (4), 1339–1348. DOI: 10.1002/pola.22474.
- (173) Xiong, L.; Zhan, F.; Liang, H.; Chen, L.; Lan, D. “Chemical Grafting of Nano-TiO₂ onto Carbon Fiber via Thiol–Ene Click Chemistry and Its Effect on the Interfacial and Mechanical Properties of Carbon Fiber/Epoxy Composites”. *J. Mater. Sci.* 2018, *53* (4), 2594–2603. DOI: 10.1007/s10853-017-1739-5.
- (174) Rostovtsev, V. V.; Green, L. G.; Fokin, V. V.; Sharpless, K. B. “A Stepwise Huisgen Cycloaddition Process: Copper(I)-Catalyzed Regioselective “Ligation” of Azides and Terminal Alkynes”. *Angew. Chemie - Int. Ed.* 2002, *41* (14), 2596–2599. DOI: 10.1002/1521-3773(20020715)41:14<2596::AID-ANIE2596>3.0.CO;2-4.
- (175) Tornøe, C. W.; Christensen, C.; Meldal, M. “Peptidotriazoles on Solid Phase: [1,2,3]-Triazoles by Regiospecific Copper(I)-Catalyzed 1,3-Dipolar Cycloadditions of Terminal Alkynes to Azides”. *J. Org. Chem.* 2002, *67* (9), 3057–3064. DOI: 10.1021/jo011148j.
- (176) Himo, F.; Lovell, T.; Hilgraf, R.; Rostovtsev, V. V.; Noodleman, L.; Sharpless, K. B.; Fokin, V. V. “Copper(I)-Catalyzed Synthesis of Azoles. DFT Study Predicts Unprecedented Reactivity and Intermediates”. *J. Am. Chem. Soc.* 2005, *127* (1), 210–216. DOI: 10.1021/ja0471525.

- (177) Kaur, J.; Saxena, M.; Rishi, N. "An Overview of Recent Advances in Biomedical Applications of Click Chemistry". *Bioconjug. Chem.* 2021, 32 (8), 1455–1471. DOI: 10.1021/acs.bioconjchem.1c00247.
- (178) Presolski, S. I.; Hong, V. P.; Finn, M. G. "Copper-Catalyzed Azide–Alkyne Click Chemistry for Bioconjugation". *Curr. Protoc. Chem. Biol.* 2011, 3 (4), 153–162. DOI: 10.1002/9780470559277.ch110148.
- (179) Hein, J. E.; Fokin, V. V. "Copper-Catalyzed Azide-Alkyne Cycloaddition (CuAAC) and beyond: New Reactivity of Copper(i) Acetylides". *Chem. Soc. Rev.* 2010, 39 (4), 1302–1315. DOI: 10.1039/b904091a.
- (180) Song, W.; Xiao, C.; Cui, L.; Tang, Z.; Zhuang, X.; Chen, X. "Facile Construction of Functional Biosurface via SI-ATRP and "Click Glycosylation"". *Colloids Surfaces B Biointerfaces* 2012, 93, 188–194. DOI: 10.1016/j.colsurfb.2012.01.002.
- (181) Ramapanicker, R.; Chauhan, P. "Click Chemistry: Mechanistic and Synthetic Perspectives". *Click React. Org. Synth.* 2016, 1–24. DOI: 10.1002/9783527694174.ch1.
- (182) Akeroyd, N.; Klumperman, B. "The Combination of Living Radical Polymerization and Click Chemistry for the Synthesis of Advanced Macromolecular Architectures". *Eur. Polym. J.* 2011, 47 (6), 1207–1231. DOI: 10.1016/j.eurpolymj.2011.02.003.
- (183) Letcher, T. M. "Introduction to Plastic Waste and Recycling". In *Plastic Waste and Recycling*; Elsevier, 2020; pp 3–12. DOI: 10.1016/B978-0-12-817880-5.00001-3.
- (184) Spagnuolo, L.; D’Orsi, R.; Operamolla, A. "Nanocellulose for Paper and Textile Coating: The Importance of Surface Chemistry". *Chempluschem* 2022, 87 (8). DOI: 10.1002/cplu.202200204.
- (185) Dimic-Misic, K.; Gane, P. A. C.; Paltakari, J. "Micro- and Nanofibrillated Cellulose as a Rheology Modifier Additive in CMC-Containing Pigment-Coating Formulations". *Ind. Eng. Chem. Res.* 2013, 52 (45), 16066–16083. DOI: 10.1021/ie4028878.
- (186) Schwab, A.; Levato, R.; D’Este, M.; Piluso, S.; Eglin, D.; Malda, J.; D’Este, M.; Piluso, S.; Eglin, D.; Malda, J. "Printability and Shape Fidelity of Bioinks in 3D Bioprinting". *Chem. Rev.* 2020, 120 (19), 11028–11055. DOI: 10.1021/acs.chemrev.0c00084.
- (187) Zhou, G.; Li, M.; Liu, C.; Wu, Q.; Mei, C. "3D Printed Ti₃C₂T_x MXene/Cellulose Nanofiber Architectures for Solid-State Supercapacitors: Ink Rheology, 3D Printability, and Electrochemical Performance". *Adv. Funct. Mater.* 2022, 32 (14), 1–11. DOI: 10.1002/adfm.202109593.
- (188) Jain, K.; Wang, Z.; Garma, L. D.; Engel, E.; Ciftci, G. C.; Fager, C.; Larsson, P. A.; Wågberg, L. "3D Printable Composites of Modified Cellulose Fibers and Conductive Polymers and Their Use in Wearable Electronics". *Appl. Mater. Today* 2023, 30 (December 2022). DOI: 10.1016/j.apmt.2022.101703.

- (189) Shin, S.; Hyun, J. "Matrix-Assisted Three-Dimensional Printing of Cellulose Nanofibers for Paper Microfluidics". *ACS Appl. Mater. Interfaces* 2017, 9 (31), 26438–26446. DOI: 10.1021/acsami.7b07609.
- (190) Kulkarni, N.; Rao, P.; Jadhav, G. S.; Kulkarni, B.; Kanakavalli, N.; Kirad, S.; Salunke, S.; Tanpure, V.; Sahu, B. "Emerging Role of Injectable Dipeptide Hydrogels in Biomedical Applications". *ACS Omega* 2023. DOI: 10.1021/acsomega.2c05601.
- (191) Athukoralalage, S. S.; Balu, R.; Dutta, N. K.; Roy Choudhury, N. "3D Bioprinted Nanocellulose-Based Hydrogels for Tissue Engineering Applications: A Brief Review". *Polymers (Basel)*. 2019, 11 (5), 898. DOI: 10.3390/polym11050898.
- (192) Markstedt, K.; Mantas, A.; Tournier, I.; Martínez Ávila, H.; Hägg, D.; Gatenholm, P. "3D Bioprinting Human Chondrocytes with Nanocellulose-Alginate Bioink for Cartilage Tissue Engineering Applications". *Biomacromolecules* 2015, 16 (5), 1489–1496. DOI: 10.1021/acs.biomac.5b00188.
- (193) Maturi, M.; Buratti, V. V.; Casula, G.; Locatelli, E.; Sambri, L.; Bonfiglio, A.; Comes Franchini, M. "Surface-Stabilization of Ultrathin Gold Nanowires for Capacitive Sensors in Flexible Electronics". *ACS Appl. Nano Mater.* 2021. DOI: 10.1021/acsanm.1c01849.
- (194) Zhang, Q.; Chen, C.; Chen, W.; Pastel, G.; Guo, X.; Liu, S.; Wang, Q.; Liu, Y.; Li, J.; Yu, H.; Hu, L. "Nanocellulose-Enabled, All-Nanofiber, High-Performance Supercapacitor". *ACS Appl. Mater. Interfaces* 2019. DOI: 10.1021/acsami.8b17414.
- (195) Kaushik, M.; Moores, A. "Review: Nanocelluloses as Versatile Supports for Metal Nanoparticles and Their Applications in Catalysis". *Green Chem.* 2016, 18 (3), 622–637. DOI: 10.1039/c5gc02500a.
- (196) Sánchez-López, E.; Gomes, D.; Esteruelas, G.; Bonilla, L.; Lopez-Machado, A. L.; Galindo, R.; Cano, A.; Espina, M.; Ettcheto, M.; Camins, A.; Silva, A. M.; Durazzo, A.; Santini, A.; Garcia, M. L.; Souto, E. B. "Metal-Based Nanoparticles as Antimicrobial Agents: An Overview". *Nanomaterials* 2020, 10 (2), 1–39. DOI: 10.3390/nano10020292.
- (197) Chouirfa, H.; Bouloussa, H.; Migonney, V.; Falentin-Daudré, C. "Review of Titanium Surface Modification Techniques and Coatings for Antibacterial Applications". *Acta Biomater.* 2019, 83, 37–54. DOI: 10.1016/j.actbio.2018.10.036.
- (198) Sirelkhatim, A.; Mahmud, S.; Seeni, A.; Kaus, N. H. M.; Ann, L. C.; Bakhori, S. K. M.; Hasan, H.; Mohamad, D. "Review on Zinc Oxide Nanoparticles: Antibacterial Activity and Toxicity Mechanism". *Nano-Micro Lett.* 2015, 7 (3), 219–242. DOI: 10.1007/s40820-015-0040-x.
- (199) Martins, P. M.; Lima, A. C.; Ribeiro, S.; Lanceros-Mendez, S.; Martins, P. "Magnetic Nanoparticles for Biomedical Applications: From the Soul of the Earth to the Deep History of Ourselves". *ACS Appl. Bio Mater.* 2021, acsabm.1c00440. DOI: 10.1021/acsabm.1c00440.

- (200) Liu, C. M.; Guo, L.; Wang, R. M.; Deng, Y.; Xu, H. Bin; Yang, S. "Magnetic Nanochains of Metal Formed by Assembly of Small Nanoparticles". *Chem. Commun.* 2004, No. 23, 2726–2727. DOI: 10.1039/b411311j.
- (201) Rahmatika, A. M.; Toyoda, Y.; Nguyen, T. T.; Goi, Y.; Kitamura, T.; Morita, Y.; Kume, K.; Ogi, T. "Cellulose Nanofiber and Magnetic Nanoparticles as Building Blocks Constructing Biomass-Based Porous Structured Particles and Their Protein Adsorption Performance". *ACS Sustain. Chem. Eng.* 2020, 8 (50), 18686–18695. DOI: 10.1021/acssuschemeng.0c07542.
- (202) Zhang, Q.; Zhang, L.; Wu, W.; Xiao, H. "Methods and Applications of Nanocellulose Loaded with Inorganic Nanomaterials: A Review". *Carbohydr. Polym.* 2020, 229, 115454. DOI: 10.1016/j.carbpol.2019.115454.
- (203) Madivoli, E. S.; Kareru, P. G.; Gachanja, A. N.; Makhanu, D. S.; Mugo, S. M. "Cellulose-Based Hybrid Nanoarchitectonics with Silver Nanoparticles: Characterization and Antimicrobial Potency". *J. Inorg. Organomet. Polym. Mater.* 2022, 32 (3), 854–863. DOI: 10.1007/s10904-021-02212-w.
- (204) Alle, M.; Bandi, R.; Sharma, G.; Dadigala, R.; Lee, S.-H.; Kim, J.-C. "Gold Nanoparticles Spontaneously Grown on Cellulose Nanofibrils as a Reusable Nanozyme for Colorimetric Detection of Cholesterol in Human Serum". *Int. J. Biol. Macromol.* 2022, 201, 686–697. DOI: 10.1016/j.ijbiomac.2022.01.158.
- (205) Farooq, A. A. A.; Patoary, M. K.; Zhang, M.; Mussana, H.; Li, M.; Naeem, M. A.; Mushtaq, M.; Farooq, A. A. A.; Liu, L. "Cellulose from Sources to Nanocellulose and an Overview of Synthesis and Properties of Nanocellulose/Zinc Oxide Nanocomposite Materials". *Int. J. Biol. Macromol.* 2020, 154, 1050–1073. DOI: 10.1016/j.ijbiomac.2020.03.163.
- (206) Zeng, Z.; Mavrona, E.; Sacré, D.; Kummer, N.; Cao, J.; Müller, L. A. E.; Hack, E.; Zolliker, P.; Nyström, G. "Terahertz Birefringent Biomimetic Aerogels Based on Cellulose Nanofibers and Conductive Nanomaterials". *ACS Nano* 2021, 15 (4), 7451–7462. DOI: 10.1021/acsnano.1c00856.
- (207) Oprea, M.; Panaitescu, D. M. "Nanocellulose Hybrids with Metal Oxides Nanoparticles for Biomedical Applications". *Molecules* 2020, 25 (18), 4045. DOI: 10.3390/molecules25184045.
- (208) Saba, N.; Mohammad, F.; Pervaiz, M.; Jawaid, M.; Allothman, O. Y.; Sain, M. "Mechanical, Morphological and Structural Properties of Cellulose Nanofibers Reinforced Epoxy Composites". *Int. J. Biol. Macromol.* 2017, 97, 190–200. DOI: 10.1016/j.ijbiomac.2017.01.029.
- (209) Radakisnin, R.; Abdul Majid, M. S.; Jamir, M. R. M.; Jawaid, M.; Sultan, M. T. H.; Mat Tahir, M. F. "Structural, Morphological and Thermal Properties of Cellulose Nanofibers from Napier Fiber (*Pennisetum Purpureum*)". *Materials (Basel)*. 2020, 13 (18), 4125. DOI: 10.3390/ma13184125.

- (210) Arof, A. K.; Mat Nor, N. A.; Aziz, N.; Kufian, M. Z.; Abdulaziz, A. A.; Mamatkarimov, O. O. "Investigation on Morphology of Composite Poly(Ethylene Oxide)Cellulose Nanofibers". *Mater. Today Proc.* 2019, 17, 388–393. DOI: 10.1016/j.matpr.2019.06.265.
- (211) *Fluorescence SpectraViewer*. ThermoFischer Scientific. https://www.thermofisher.com/order/fluorescence-spectraviewer/?gclid=Cj0KCQjws560BhCuARIsAHMqE0HPMpVI3_C6Vjlg_u_3rBoCmoXcd4vzQk9qqM_52blfQurj4JhGVf4QaAm4jEALw_wcB&ef_id=Cj0KCQjws560BhCuARIsAHMqE0HPMpVI3_C6Vjlg_u_3rBoCmoXcd4vzQk9qqM_52blfQurj4JhGVf4QaAm4jEAL.
- (212) Abbe, H. F. R. M. S. "The Relation of Aperture and Power in the Microscope (Continued) .*". *J. R. Microsc. Soc.* 1882, 2 (4), 460–473. DOI: 10.1111/j.1365-2818.1882.tb04805.x.
- (213) Abbe, E. "Beiträge Zur Theorie Des Mikroskops Und Der Mikroskopischen Wahrnehmung". *Arch. für Mikroskopische Anat.* 1873, 9 (1), 418–440. DOI: 10.1007/BF02956174.
- (214) Huang, B.; Babcock, H.; Zhuang, X. "Breaking the Diffraction Barrier: Super-Resolution Imaging of Cells". *Cell* 2010, 143 (7), 1047–1058. DOI: 10.1016/j.cell.2010.12.002.
- (215) Vicidomini, G.; Bianchini, P.; Diaspro, A. "STED Super-Resolved Microscopy". *Nat. Methods* 2018, 15 (3), 173–182. DOI: 10.1038/nmeth.4593.
- (216) Roobala, C.; Ilanila, I. P.; Basu, J. K. "Applications of STED Fluorescence Nanoscopy in Unravelling Nanoscale Structure and Dynamics of Biological Systems". *J. Biosci.* 2018, 43 (3), 471–484. DOI: 10.1007/s12038-018-9764-3.
- (217) Sezgin, E.; Schneider, F.; Galiani, S.; Urbančič, I.; Waithe, D.; Lagerholm, B. C.; Eggeling, C. "Measuring Nanoscale Diffusion Dynamics in Cellular Membranes with Super-Resolution STED-FCS". *Nat. Protoc.* 2019, 14 (4), 1054–1083. DOI: 10.1038/s41596-019-0127-9.
- (218) Stephan, T.; Roesch, A.; Riedel, D.; Jakobs, S. "Live-Cell STED Nanoscopy of Mitochondrial Cristae". *Sci. Rep.* 2019, 9 (1), 1–6. DOI: 10.1038/s41598-019-48838-2.
- (219) Liu, Y.; Peng, Z.; Peng, X.; Yan, W.; Yang, Z.; Qu, J. "Shedding New Lights Into STED Microscopy: Emerging Nanoprobes for Imaging". *Front. Chem.* 2021, 9 (April), 1–22. DOI: 10.3389/fchem.2021.641330.
- (220) Busko, D.; Baluschev, S.; Crespy, D.; Turshatov, A.; Landfester, K. "New Possibilities for Materials Science with STED Microscopy". *Micron* 2012, 43 (5), 583–588. DOI: 10.1016/j.micron.2011.10.003.
- (221) Friedemann, K.; Turshatov, A.; Landfester, K.; Crespy, D. "Characterization via Two-

- Color STED Microscopy of Nanostructured Materials Synthesized by Colloid Electrospinning". *Langmuir* 2011, 27 (11), 7132–7139. DOI: 10.1021/la104817r.
- (222) Stockhammer, A.; Bottanelli, F. "Appreciating the Small Things in Life: STED Microscopy in Living Cells". *J. Phys. D. Appl. Phys.* 2021, 54 (3), 033001. DOI: 10.1088/1361-6463/abac81.
- (223) Calovi, S.; Soria, F. N.; Tønnesen, J. "Super-Resolution STED Microscopy in Live Brain Tissue". *Neurobiol. Dis.* 2021, 156, 105420. DOI: 10.1016/j.nbd.2021.105420.
- (224) Schermelleh, L.; Heintzmann, R.; Leonhardt, H. "A Guide to Super-Resolution Fluorescence Microscopy". *J. Cell Biol.* 2010, 190 (2), 165–175. DOI: 10.1083/jcb.201002018.
- (225) Urban, N. T.; Willig, K. I.; Hell, S. W.; Nägerl, U. V. "STED Nanoscopy of Actin Dynamics in Synapses Deep inside Living Brain Slices". *Biophys. J.* 2011, 101 (5), 1277–1284. DOI: 10.1016/j.bpj.2011.07.027.
- (226) Guise, C.; Fanguero, R. "Biomedical Applications of Nanocellulose". *RILEM Bookseries* 2016, 12, 155–169. DOI: 10.1007/978-94-017-7515-1_12.
- (227) Edwards, J. V.; Prevost, N.; Sethumadhavan, K.; Ullah, A.; Condon, B. "Peptide Conjugated Cellulose Nanocrystals with Sensitive Human Neutrophil Elastase Sensor Activity". *Cellulose* 2013, 20 (3), 1223–1235. DOI: 10.1007/s10570-013-9901-y.
- (228) Golmohammadi, H.; Morales-Narváez, E.; Naghdi, T.; Merkoçi, A. "Nanocellulose in Sensing and Biosensing". *Chem. Mater.* 2017, 29 (13), 5426–5446. DOI: 10.1021/acs.chemmater.7b01170.
- (229) Zhai, S.; Chen, H.; Zhang, Y.; Li, P.; Wu, W. "Nanocellulose: A Promising Nanomaterial for Fabricating Fluorescent Composites". *Cellulose* 2022, 29 (13), 7011–7035. DOI: 10.1007/s10570-022-04700-9.
- (230) Wu, W.; Song, R.; Xu, Z.; Jing, Y.; Dai, H.; Fang, G. "Fluorescent Cellulose Nanocrystals with Responsiveness to Solvent Polarity and Ionic Strength". *Sensors Actuators, B Chem.* 2018, 275, 490–498. DOI: 10.1016/j.snb.2018.07.085.
- (231) Salari, M.; Bitounis, D.; Bhattacharya, K.; Pyrgiotakis, G.; Zhang, Z.; Purington, E.; Gramlich, W.; Grondin, Y.; Rogers, R.; Bousfield, D.; Demokritou, P. "Development & Characterization of Fluorescently Tagged Nanocellulose for Nanotoxicological Studies". *Environ. Sci. Nano* 2019, 6 (5), 1516–1526. DOI: 10.1039/c8en01381k.
- (232) Ning, L.; You, C.; Zhang, Y.; Li, X.; Wang, F. "Polydopamine Loaded Fluorescent Nanocellulose–Agarose Hydrogel: A PH-Responsive Drug Delivery Carrier for Cancer Therapy". *Compos. Commun.* 2021, 26 (November 2020), 100739. DOI: 10.1016/j.coco.2021.100739.
- (233) Schyrr, B.; Pasche, S.; Voirin, G.; Weder, C.; Simon, Y. C.; Foster, E. J. "Biosensors

Based on Porous Cellulose Nanocrystal-Poly(Vinyl Alcohol) Scaffolds". *ACS Appl. Mater. Interfaces* 2014, 6 (15), 12674–12683. DOI: 10.1021/am502670u.

- (234) Navarro, J. R. G.; Wennmalm, S.; Godfrey, J.; Breitholtz, M.; Edlund, U. "Luminescent Nanocellulose Platform: From Controlled Graft Block Copolymerization to Biomarker Sensing". *Biomacromolecules* 2016, 17 (3), 1101–1109. DOI: 10.1021/acs.biomac.5b01716.
- (235) Goodge, K.; Frey, M. "Biotin-Conjugated Cellulose Nanofibers Prepared via Copper-Catalyzed Alkyne-Azide Cycloaddition (CuAAC) "Click" Chemistry". *Nanomaterials* 2020, 10 (6), 1172. DOI: 10.3390/nano10061172.
- (236) Babi, M.; Fatona, A.; Li, X.; Cerson, C.; Jarvis, V. M.; Abitbol, T.; Moran-Mirabal, J. M. "Efficient Labeling of Nanocellulose for High-Resolution Fluorescence Microscopy Applications". *Biomacromolecules* 2022, 23 (5), 1981–1994. DOI: 10.1021/acs.biomac.1c01698.
- (237) Voronova, M. I.; Lebedeva, T. N.; Radugin, M. V.; Surov, O. V.; Prusov, A. N.; Zakharov, A. G. "Interactions of Water-DMSO Mixtures with Cellulose". *J. Mol. Liq.* 2006, 126 (1–3), 124–129. DOI: 10.1016/j.molliq.2005.12.001.
- (238) Gårdebjer, S.; Bergstrand, A.; Idström, A.; Börstell, C.; Naana, S.; Nordstierna, L.; Larsson, A. "Solid-State NMR to Quantify Surface Coverage and Chain Length of Lactic Acid Modified Cellulose Nanocrystals, Used as Fillers in Biodegradable Composites". *Compos. Sci. Technol.* 2015, 107, 1–9. DOI: 10.1016/j.compscitech.2014.11.014.
- (239) Storms-Miller, W. K.; Pugh, C. "Prop-2-Yn-1-Yl 2-Bromo-2-Methylpropanoate: Identification and Suppression of Side Reactions of a Commonly Used Terminal Alkyne-Functional ATRP Initiator". *Macromolecules* 2015, 48 (12), 3803–3810. DOI: 10.1021/acs.macromol.5b00652.
- (240) Freeman, A. J.; Watson, R. E. "Theoretical Investigation of Some Magnetic and Spectroscopic Properties of Rare-Earth Ions". *Phys. Rev.* 1962, 127 (6), 2058–2075. DOI: 10.1103/PhysRev.127.2058.
- (241) Lotey, G. S.; Verma, N. K. "Magnetoelectric Coupling in Multiferroic Tb-Doped BiFeO₃ Nanoparticles". *Mater. Lett.* 2013, 111, 55–58. DOI: 10.1016/j.matlet.2013.08.022.
- (242) Meng, F.; Zhang, C.; Fan, Z.; Gong, J.; Li, A.; Ding, Z.; Tang, H.; Zhang, M.; Wu, G. "Hydrothermal Synthesis of Hexagonal CeO₂ Nanosheets and Their Room Temperature Ferromagnetism". *J. Alloys Compd.* 2015, 647, 1013–1021. DOI: 10.1016/j.jallcom.2015.06.186.
- (243) Grundmann, M.; Christen, J.; Ledentsov, N. N.; Böhrer, J.; Bimberg, D.; Ruvimov, S. S.; Werner, P.; Richter, U.; Gösele, U.; Heydenreich, J.; Ustinov, V. M.; Egorov, A. Y.; Zhukov, A. E.; Kop'ev, P. S.; Alferov, Z. I. "Ultranarrow Luminescence Lines from Single Quantum Dots". *Phys. Rev. Lett.* 1995, 74 (20), 4043–4046. DOI:

10.1103/PhysRevLett.74.4043.

- (244) Dabbousi, B. O.; Rodriguez-Viejo, J.; Mikulec, F. V.; Heine, J. R.; Mattoussi, H.; Ober, R.; Jensen, K. F.; Bawendi, M. G. "(CdSe)ZnS Core–Shell Quantum Dots: Synthesis and Characterization of a Size Series of Highly Luminescent Nanocrystallites". *J. Phys. Chem. B* 1997, *101* (46), 9463–9475. DOI: 10.1021/jp971091y.
- (245) Liu, Y.; Lu, Y.; Yang, X.; Zheng, X.; Wen, S.; Wang, F.; Vidal, X.; Zhao, J.; Liu, D.; Zhou, Z.; Ma, C.; Zhou, J.; Piper, J. A.; Xi, P.; Jin, D. "Amplified Stimulated Emission in Upconversion Nanoparticles for Super-Resolution Nanoscopy". *Nature* 2017, *543* (7644), 229–233. DOI: 10.1038/nature21366.
- (246) Yang, Y.; Sun, Y.; Cao, T.; Peng, J.; Liu, Y.; Wu, Y.; Feng, W.; Zhang, Y.; Li, F. "Hydrothermal Synthesis of NaLuF₄:153Sm,Yb,Tm Nanoparticles and Their Application in Dual-Modality Upconversion Luminescence and SPECT Bioimaging". *Biomaterials* 2013, *34* (3), 774–783. DOI: 10.1016/j.biomaterials.2012.10.022.
- (247) Sekhar, P. K.; Wilkinson, A. R.; Elliman, R. G.; Kim, T.-H.; Bhansali, S. "Erbium Emission from Nanoengineered Silicon Surface". *J. Phys. Chem. C* 2008, *112* (51), 20109–20113. DOI: 10.1021/jp808462j.
- (248) Ryoo, R.; Kim, J.; Jo, C.; Han, S. W.; Kim, J.-C.; Park, H.; Han, J.; Shin, H. S.; Shin, J. W. "Rare-Earth–Platinum Alloy Nanoparticles in Mesoporous Zeolite for Catalysis". *Nature* 2020, *585* (7824), 221–224. DOI: 10.1038/s41586-020-2671-4.
- (249) Mun, K. R.; Kyhm, J.; Lee, J. Y.; Shin, S.; Zhu, Y.; Kang, G.; Kim, D.; Deng, R.; Jang, H. S. "Elemental-Migration-Assisted Full-Color-Tunable Upconversion Nanoparticles for Video-Rate Three-Dimensional Volumetric Displays". *Nano Lett.* 2023, *23* (7), 3014–3022. DOI: 10.1021/acs.nanolett.3c00397.
- (250) Maurizio, S. L.; Clermont-Paquette, A.; Naccache, R.; Capobianco, J. A. "Covert Information Storage and Encryption Using Temporal Emissions from Lanthanide-Doped LiYF₄ Nanoparticles". *ACS Appl. Nano Mater.* 2023, *6* (23), 21496–21502. DOI: 10.1021/acsanm.3c05134.
- (251) Zheng, B.; Fan, J.; Chen, B.; Qin, X.; Wang, J.; Wang, F.; Deng, R.; Liu, X. "Rare-Earth Doping in Nanostructured Inorganic Materials". *Chem. Rev.* 2022, *122* (6), 5519–5603. DOI: 10.1021/acs.chemrev.1c00644.
- (252) Bloembergen, N. "Solid State Infrared Quantum Counters". *Phys. Rev. Lett.* 1959, *2* (3), 84–85. DOI: 10.1103/PhysRevLett.2.84.
- (253) Auzel, F. "History of Upconversion Discovery and Its Evolution". *J. Lumin.* 2020, *223* (December 2019), 116900. DOI: 10.1016/j.jlumin.2019.116900.
- (254) Esterowitz, L.; Noonan, J.; Bahler, J. "Erratum: Enhancement in a Ho³⁺–Yb³⁺ Quantum Counter by Energy Transfer". *Appl. Phys. Lett.* 1967, *11* (2), 72–72. DOI: 10.1063/1.1755034.

- (255) Zijlmans, H. J. M. A. A.; Bonnet, J.; Burton, J.; Kardos, K.; Vail, T.; Niedbala, R. S.; Tanke, H. J. "Detection of Cell and Tissue Surface Antigens Using Up-Converting Phosphors: A New Reporter Technology". *Anal. Biochem.* 1999, 267 (1), 30–36. DOI: 10.1006/abio.1998.2965.
- (256) Johnson, L. F.; Guggenheim, H. J. "Infrared-Pumped Visible Laser". *Appl. Phys. Lett.* 1971, 19 (2), 44–47. DOI: 10.1063/1.1653816.
- (257) Sun, L.-D. D.; Dong, H.; Zhang, P.-Z. Z.; Yan, C.-H. H. "Upconversion of Rare Earth Nanomaterials". *Annu. Rev. Phys. Chem.* 2015, 66 (1), 619–642. DOI: 10.1146/annurev-physchem-040214-121344.
- (258) Tao, K.; Sun, K. "Upconversion Nanoparticles". In *Photonanotechnology for Therapeutics and Imaging*; Elsevier Inc., 2020; pp 147–176. DOI: 10.1016/b978-0-12-817840-9.00006-0.
- (259) Park, Y. Il; Lee, K. T.; Suh, Y. D.; Hyeon, T. "Upconverting Nanoparticles: A Versatile Platform for Wide-Field Two-Photon Microscopy and Multi-Modal in Vivo Imaging". *Chem. Soc. Rev.* 2015, 44 (6), 1302–1317. DOI: 10.1039/c4cs00173g.
- (260) Kumar, B.; Malhotra, K.; Fuku, R.; Van Houten, J.; Qu, G. Y.; Piunno, P. A. E.; Krull, U. J. "Recent Trends in the Developments of Analytical Probes Based on Lanthanide-Doped Upconversion Nanoparticles". *TrAC - Trends Anal. Chem.* 2021, 139, 116256. DOI: 10.1016/j.trac.2021.116256.
- (261) Zhang, X.; Guo, Z.; Zhang, X.; Gong, L.; Dong, X.; Fu, Y.; Wang, Q.; Gu, Z. "Mass Production of Poly(Ethylene Glycol) Monooleate-Modified Core-Shell Structured Upconversion Nanoparticles for Bio-Imaging and Photodynamic Therapy". *Sci. Rep.* 2019, 9 (1), 1–10. DOI: 10.1038/s41598-019-41482-w.
- (262) Tan, M.; Chen, G. "Rare Earth-Doped Nanoparticles for Advanced In Vivo Near Infrared Imaging". In *Near Infrared-Emitting Nanoparticles for Biomedical Applications*; Springer International Publishing: Cham, 2020; pp 63–81. DOI: 10.1007/978-3-030-32036-2_4.
- (263) Ansari, A. A.; Thakur, V. K.; Chen, G. "Functionalized Upconversion Nanoparticles: New Strategy towards FRET-Based Luminescence Bio-Sensing". *Coord. Chem. Rev.* 2021, 436, 213821. DOI: 10.1016/j.ccr.2021.213821.
- (264) Sun, C.; Gradzielski, M. "Upconversion-Based Nanosystems for Fluorescence Sensing of PH and H₂O₂". *Nanoscale Adv.* 2021, 3 (9), 2538–2546. DOI: 10.1039/D0NA01045F.
- (265) Zhang, L.; Jin, D.; Stenzel, M. H. "Polymer-Functionalized Upconversion Nanoparticles for Light/Imaging-Guided Drug Delivery". *Biomacromolecules* 2021, 22 (8), 3168–3201. DOI: 10.1021/acs.biomac.1c00669.
- (266) Nguyen, T.-D.; Hamad, W. Y.; MacLachlan, M. J. "Near-IR-Sensitive Upconverting Nanostructured Photonic Cellulose Films". *Adv. Opt. Mater.* 2017, 5 (1), 1600514.

DOI: 10.1002/adom.201600514.

- (267) Muhr, V.; Wilhelm, S.; Hirsch, T.; Wolfbeis, O. S. "Upconversion Nanoparticles: From Hydrophobic to Hydrophilic Surfaces". *Acc. Chem. Res.* 2014, *47* (12), 3481–3493. DOI: 10.1021/ar500253g.
- (268) Dong, A.; Ye, X.; Chen, J.; Kang, Y.; Gordon, T.; Kikkawa, J. M.; Murray, C. B. "A Generalized Ligand-Exchange Strategy Enabling Sequential Surface Functionalization of Colloidal Nanocrystals". *J. Am. Chem. Soc.* 2011, *133* (4), 998–1006. DOI: 10.1021/jal08948z.
- (269) Huang, Ching-Hui; Tsourkas, A.; Huang, C.-H.; Tsourkas, A. "Gd-Based Macromolecules and Nanoparticles as Magnetic Resonance Contrast Agents for Molecular Imaging". *Curr. Top. Med. Chem.* 2013, *13* (4), 411–421. DOI: 10.2174/1568026611313040002.
- (270) Huang, R.; Zhou, X.; Chen, G.; Su, L.; Liu, Z.; Zhou, P.; Weng, J.; Min, Y. "Advances of Functional Nanomaterials for Magnetic Resonance Imaging and Biomedical Engineering Applications". *WIREs Nanomedicine and Nanobiotechnology* 2022, *14* (4), 1–32. DOI: 10.1002/wnan.1800.
- (271) Murphy, A.; Ballinger, J. *Relaxation*. Radiopaedia.org. DOI: 10.53347/rID-22554.
- (272) Evanics, F.; Diamente, P. R.; Van Veggel, F. C. J. M.; Stanisz, G. J.; Prosser, R. S. "Water-Soluble GdF₃ and GdF₃/LaF₃ Nanoparticles - Physical Characterization and NMR Relaxation Properties". *Chem. Mater.* 2006, *18* (10), 2499–2505. DOI: 10.1021/cm052299w.
- (273) Yon, M.; Billotey, C.; Marty, J. D. "Gadolinium-Based Contrast Agents: From Gadolinium Complexes to Colloidal Systems". *Int. J. Pharm.* 2019, *569*, 118577. DOI: 10.1016/j.ijpharm.2019.118577.
- (274) Ersoy, H.; Rybicki, F. J. "Biochemical Safety Profiles of Gadolinium-Based Extracellular Contrast Agents and Nephrogenic Systemic Fibrosis". *J. Magn. Reson. Imaging* 2007, *26* (5), 1190–1197. DOI: 10.1002/jmri.21135.
- (275) Bridot, J.-L.; Faure, A.-C.; Laurent, S.; Rivière, C.; Billotey, C.; Hiba, B.; Janier, M.; Josserand, V.; Coll, J.-L.; Vander Elst, L.; Muller, R.; Roux, S.; Perriat, P.; Tillement, O. "Hybrid Gadolinium Oxide Nanoparticles: Multimodal Contrast Agents for in Vivo Imaging". *J. Am. Chem. Soc.* 2007, *129* (16), 5076–5084. DOI: 10.1021/ja068356j.
- (276) Zhu, S.; Wen, C.; Bai, D.; Gao, M. "Diagnostic Efficacy of Intravascular Ultrasound Combined with Gd₂O₃-EPL Contrast Agent for Patients with Atherosclerosis". *Exp. Ther. Med.* 2020, *20* (6), 1–1. DOI: 10.3892/etm.2020.9265.
- (277) Guo, L.; Xin, H.; Luo, X.; Zhang, C. "Phase Evolution, Mechanical Properties and MRI Contrast Behavior of GdPO₄ Doped Hydroxyapatite for Dental Applications". *Mater. Sci. Eng. C* 2020, *111*, 110858. DOI: 10.1016/j.msec.2020.110858.

- (278) Rodriguez-Liviano, S.; Becerro, A. I.; Alcántara, D.; Grazú, V.; de la Fuente, J. M.; Ocaña, M. "Synthesis and Properties of Multifunctional Tetragonal Eu:GdPO₄ Nanocubes for Optical and Magnetic Resonance Imaging Applications". *Inorg. Chem.* 2013, 52 (2), 647–654. DOI: 10.1021/ic3016996.
- (279) Hu, K.-W.; Hsu, K.-C.; Yeh, C.-S. "PH-Dependent Biodegradable Silica Nanotubes Derived from Gd(OH)₃ Nanorods and Their Potential for Oral Drug Delivery and MR Imaging". *Biomaterials* 2010, 31 (26), 6843–6848. DOI: 10.1016/j.biomaterials.2010.05.046.
- (280) Shapoval, O.; Kaman, O.; Hromádková, J.; Vavřík, D.; Jiráček, D.; Machová, D.; Parnica, J.; Horák, D. "Multimodal PSSMA-Functionalized GdF₃:Eu³⁺(Tb³⁺) Nanoparticles for Luminescence Imaging, MRI, and X-Ray Computed Tomography". *Chempluschem* 2019, 84 (8), 1135–1139. DOI: 10.1002/cplu.201900352.
- (281) Polozhentsev, O. E.; Pankin, I. A.; Khodakova, D. V.; Medvedev, P. V.; Goncharova, A. S.; Maksimov, A. Y.; Kit, O. I.; Soldatov, A. V. "Synthesis, Characterization and Biodistribution of GdF₃:Tb³⁺@RB Nanocomposites". *Materials (Basel)*. 2022, 15 (2), 569. DOI: 10.3390/ma15020569.
- (282) Passuello, T.; Pedroni, M.; Piccinelli, F.; Polizzi, S.; Marzola, P.; Tambalo, S.; Conti, G.; Benati, D.; Vetrone, F.; Bettinelli, M.; Speghini, A. "PEG-Capped, Lanthanide Doped GdF₃ Nanoparticles: Luminescent and T₂ Contrast Agents for Optical and MRI Multimodal Imaging". *Nanoscale* 2012, 4 (24), 7682. DOI: 10.1039/c2nr31796f.
- (283) Dong, C.; Korinek, A.; Blasiak, B.; Tomanek, B.; van Veggel, F. C. J. M. "Cation Exchange: A Facile Method To Make NaYF₄:Yb,Tm-NaGdF₄ Core-Shell Nanoparticles with a Thin, Tunable, and Uniform Shell". *Chem. Mater.* 2012, 24 (7), 1297–1305. DOI: 10.1021/cm2036844.
- (284) Du, Q.; Huang, Z.; Wu, Z.; Meng, X.; Yin, G.; Gao, F.; Wang, L. "Facile Preparation and Bifunctional Imaging of Eu-Doped GdPO₄ Nanorods with MRI and Cellular Luminescence". *Dalt. Trans.* 2015, 44 (9), 3934–3940. DOI: 10.1039/C4DT03444A.
- (285) Hifumi, H.; Yamaoka, S.; Tanimoto, A.; Citterio, D.; Suzuki, K. "Gadolinium-Based Hybrid Nanoparticles as a Positive MR Contrast Agent". *J. Am. Chem. Soc.* 2006, 128 (47), 15090–15091. DOI: 10.1021/ja066442d.
- (286) Tian, G.; Gu, Z.; Zhou, L.; Yin, W.; Liu, X.; Yan, L.; Jin, S.; Ren, W.; Xing, G.; Li, S.; Zhao, Y. "Mn²⁺ Dopant-Controlled Synthesis of NaYF₄:Yb/Er Upconversion Nanoparticles for in Vivo Imaging and Drug Delivery". *Adv. Mater.* 2012, 24 (9), 1226–1231. DOI: 10.1002/adma.201104741.
- (287) Li, R.; Ji, Z.; Chang, C. H.; Dunphy, D. R.; Cai, X.; Meng, H.; Zhang, H.; Sun, B.; Wang, X.; Dong, J.; Lin, S.; Wang, M.; Liao, Y.-P.; Brinker, C. J.; Nel, A.; Xia, T. "Surface Interactions with Compartmentalized Cellular Phosphates Explain Rare Earth Oxide Nanoparticle Hazard and Provide Opportunities for Safer Design". *ACS Nano* 2014, 8 (2), 1771–1783. DOI: 10.1021/nn406166n.

- (288) Li, Y.; Beija, M.; Laurent, S.; Elst, L. Vander; Muller, R. N.; Duong, H. T. T.; Lowe, A. B.; Davis, T. P.; Boyer, C. "Macromolecular Ligands for Gadolinium MRI Contrast Agents". *Macromolecules* 2012, 45 (10), 4196–4204. DOI: 10.1021/ma300521c.
- (289) Younis, M.; Darcos, V.; Paniagua, C.; Ronjat, P.; Lemaire, L.; Nottelet, B.; Garric, X.; Bakkour, Y.; El Nakat, J. H.; Coudane, J. "MRI-Visible Polymer Based on Poly(Methyl Methacrylate) for Imaging Applications". *RSC Adv.* 2016, 6 (7), 5754–5760. DOI: 10.1039/C5RA23646K.
- (290) Shapoval, O.; Sulimenko, V.; Klebanovych, A.; Rabyk, M.; Shapoval, P.; Kaman, O.; Rydvalová, E.; Filipová, M.; Dráberová, E.; Dráber, P.; Horák, D. "Multimodal Fluorescently Labeled Polymer-Coated GdF₃nanoparticles Inhibit Degranulation in Mast Cells". *Nanoscale* 2021, 13 (45), 19023–19037. DOI: 10.1039/d1nr06127e.
- (291) Kumar, A.; Durand, H.; Zeno, E.; Balsollier, C.; Watbled, B.; Sillard, C.; Fort, S.; Baussanne, I.; Belgacem, N.; Lee, D.; Hediger, S.; Demeunynck, M.; Bras, J.; De Paëpe, G. "The Surface Chemistry of a Nanocellulose Drug Carrier Unravelling by MAS-DNP". *Chem. Sci.* 2020, 11 (15), 3868–3877. DOI: 10.1039/c9sc06312a.
- (292) Poonguzhali, R.; Khaleel Basha, S.; Sugantha Kumari, V. "Novel Asymmetric Chitosan/PVP/Nanocellulose Wound Dressing: In Vitro and in Vivo Evaluation". *Int. J. Biol. Macromol.* 2018, 112 (2017), 1300–1309. DOI: 10.1016/j.ijbiomac.2018.02.073.
- (293) Rees, A.; Powell, L. C.; Chinga-Carrasco, G.; Gethin, D. T.; Syverud, K.; Hill, K. E.; Thomas, D. W. "3D Bioprinting of Carboxymethylated-Periodate Oxidized Nanocellulose Constructs for Wound Dressing Applications". *Biomed Res. Int.* 2015, 2015. DOI: 10.1155/2015/925757.
- (294) Tudoroiu, E. E.; Dinu-Pîrvu, C. E.; Kaya, M. G. A.; Popa, L.; Anuța, V.; Prisada, R. M.; Ghica, M. V. "An Overview of Cellulose Derivatives-Based Dressings for Wound-Healing Management". *Pharmaceuticals* 2021, 14 (12). DOI: 10.3390/ph14121215.
- (295) Gehlen, D. B.; Jürgens, N.; Omidinia-Anarkoli, A.; Haraszti, T.; George, J.; Walther, A.; Ye, H.; De Laporte, L. "Granular Cellulose Nanofibril Hydrogel Scaffolds for 3D Cell Cultivation". *Macromol. Rapid Commun.* 2020, 41 (18), 1–10. DOI: 10.1002/marc.202000191.
- (296) Hatakeyama, M.; Kitaoka, T. "Surface-Carboxylated Nanocellulose-Based Bioadaptive Scaffolds for Cell Culture". *Cellulose* 2022, 29 (5), 2869–2883. DOI: 10.1007/s10570-021-04154-5.
- (297) Syverud, K. "Tissue Engineering Using Plant-Derived Cellulose Nanofibrils (CNF) as Scaffold Material". *ACS Symp. Ser.* 2017, 1251, 171–189. DOI: 10.1021/bk-2017-1251.ch009.
- (298) Randhawa, A.; Dutta, S. D.; Ganguly, K.; Patil, T. V.; Patel, D. K.; Lim, K. T. "A Review of Properties of Nanocellulose, Its Synthesis, and Potential in Biomedical Applications". *Appl. Sci.* 2022, 12 (14). DOI: 10.3390/app12147090.

- (299) Durand, H.; Smyth, M.; Bras, J. "Nanocellulose: A New Biopolymer for Biomedical Application". In *Biopolymers for Biomedical and Biotechnological Applications*; Wiley, 2021; pp 129–179. DOI: 10.1002/9783527818310.ch5.
- (300) Souza, S. F.; Mariano, M.; Reis, D.; Lombello, C. B.; Ferreira, M.; Sain, M. "Cell Interactions and Cytotoxic Studies of Cellulose Nanofibers from Curauá Natural Fibers". *Carbohydr. Polym.* 2018, *201*, 87–95. DOI: 10.1016/j.carbpol.2018.08.056.
- (301) Ilves, M.; Vilske, S.; Aimonen, K.; Lindberg, H. K.; Pesonen, S.; Wedin, I.; Nuopponen, M.; Vanhala, E.; Højgaard, C.; Winther, J. R.; Willemoës, M.; Vogel, U.; Wolff, H.; Norppa, H.; Savolainen, K.; Alenius, H. "Nanofibrillated Cellulose Causes Acute Pulmonary Inflammation That Subsides within a Month". *Nanotoxicology* 2018, *12* (7), 729–746. DOI: 10.1080/17435390.2018.1472312.
- (302) Kolakovic, R.; Peltonen, L.; Laukkanen, A.; Hirvonen, J.; Laaksonen, T. "Nanofibrillar Cellulose Films for Controlled Drug Delivery". *Eur. J. Pharm. Biopharm.* 2012, *82* (2), 308–315. DOI: 10.1016/j.ejpb.2012.06.011.
- (303) Taher, M. A.; Zahan, K. A.; Rajaie, M. A.; Ring, L. C.; Rashid, S. A.; Mohd Nor Hamin, N. S.; Nee, T. W.; Yenn, T. W. "Nanocellulose as Drug Delivery System for Honey as Antimicrobial Wound Dressing". *Mater. Today Proc.* 2020, *31* (xxxx), 14–17. DOI: 10.1016/j.matpr.2020.01.076.
- (304) Sulthana, R.; Archer, A. C. "Bacteriocin Nanoconjugates: Boon to Medical and Food Industry". *J. Appl. Microbiol.* 2021, *131* (3), 1056–1071. DOI: 10.1111/jam.14982.
- (305) Ng, Z. J.; Zarin, M. A.; Lee, C. K.; Tan, J. S. "Application of Bacteriocins in Food Preservation and Infectious Disease Treatment for Humans and Livestock: A Review". *RSC Adv.* 2020, *10* (64), 38937–38964. DOI: 10.1039/D0RA06161A.
- (306) Eijsink, V. G. H.; Axelsson, L.; Diep, D. B.; Håvarstein, L. S.; Holo, H.; Nes, I. F. "Production of Class II Bacteriocins by Lactic Acid Bacteria; an Example of Biological Warfare and Communication". *Antonie van Leeuwenhoek, Int. J. Gen. Mol. Microbiol.* 2002, *81* (1–4), 639–654. DOI: 10.1023/A:1020582211262.
- (307) Acedo, J. Z.; Chiorean, S.; Vederas, J. C.; van Belkum, M. J. "The Expanding Structural Variety among Bacteriocins from Gram-Positive Bacteria". *FEMS Microbiol. Rev.* 2018, *42* (6), 805–828. DOI: 10.1093/femsre/fuy033.
- (308) Liao, R.; Duan, L.; Lei, C.; Pan, H.; Ding, Y.; Zhang, Q.; Chen, D.; Shen, B.; Yu, Y.; Liu, W. "Thiopeptide Biosynthesis Featuring Ribosomally Synthesized Precursor Peptides and Conserved Posttranslational Modifications". *Chem. Biol.* 2009, *16* (2), 141–147. DOI: 10.1016/j.chembiol.2009.01.007.
- (309) Jiang, X.; Mietner, J. B.; Raveendran, D.; Ovchinnikov, K. V.; Sochor, B.; Mueller, S.; Boehm-Sturm, P.; Lerouge, F.; Chaput, F.; Gurikov, P.; Roth, S. V.; Navarro, J. R. G. "Multifunctional Cellulose Nanofibrils–GdF3 Nanoparticles Hybrid Gel and Its Potential Uses for Drug Delivery and Magnetic Resonance Imaging". *ACS Appl. Nano Mater.* 2023, *6* (22), 21182–21193. DOI: 10.1021/acsanm.3c04272.

- (310) Remmele, J.; Shen, D. E.; Mustonen, T.; Fruehauf, N. "High Performance and Long-Term Stability in Ambiently Fabricated Segmented Solid-State Polymer Electrochromic Displays". *ACS Appl. Mater. Interfaces* 2015, 7 (22), 12001–12008. DOI: 10.1021/acsami.5b02090.
- (311) Recalde, I.; Estebanez, N.; Francés-Soriano, L.; Liras, M.; González-Béjar, M.; Pérez-Prieto, J. "Upconversion Nanoparticles with a Strong Acid-Resistant Capping". *Nanoscale* 2016, 8 (14), 7588–7594. DOI: 10.1039/C5NR06653K.
- (312) Hund, F. "Das Ternäre Fluorid NaYF₄". *Zeitschrift für Anorg. Chemie* 1950, 261 (1–2), 106–115. DOI: 10.1002/zaac.19502610110.
- (313) Janjua, R. A.; Gao, C.; Dai, R.; Sui, Z.; Ahmad Raja, M. A.; Wang, Z.; Zhen, X.; Zhang, Z. "Na⁺-Driven Nucleation of NaYF₄:Yb,Er Nanocrystals and Effect of Temperature on Their Structural Transformations and Luminescent Properties". *J. Phys. Chem. C* 2018, 122 (40), 23242–23250. DOI: 10.1021/acs.jpcc.8b09327.
- (314) Reinke, S. K.; Roth, S. V.; Santoro, G.; Vieira, J.; Heinrich, S.; Palzer, S. "Tracking Structural Changes in Lipid-Based Multicomponent Food Materials Due to Oil Migration by Microfocus Small-Angle X-Ray Scattering". *ACS Appl. Mater. Interfaces* 2015, 7 (18), 9929–9936. DOI: 10.1021/acsami.5b02092.
- (315) Guccini, V.; Yu, S.; Agthe, M.; Gordeyeva, K.; Trushkina, Y.; Fall, A.; Schütz, C.; Salazar-Alvarez, G. "Inducing Nematic Ordering of Cellulose Nanofibers Using Osmotic Dehydration". *Nanoscale* 2018, 10 (48), 23157–23163. DOI: 10.1039/c8nr08194h.
- (316) Hammouda, B. "A New Guinier-Porod Model". *J. Appl. Crystallogr.* 2010, 43 (4), 716–719. DOI: 10.1107/S0021889810015773.
- (317) Evmenenko, G.; Theunissen, E.; Mortensen, K.; Reynaers, H. "SANS Study of Surfactant Ordering in κ -Carrageenan/Cetylpyridinium Chloride Complexes". *Polymer (Guildf)*. 2001, 42 (7), 2907–2913. DOI: 10.1016/S0032-3861(00)00674-1.
- (318) Engström, J.; Jimenez, A. M.; Malmström, E. "Nanoparticle Rearrangement under Stress in Networks of Cellulose Nanofibrils Using in Situ SAXS during Tensile Testing". *Nanoscale* 2020, 12 (11), 6462–6471. DOI: 10.1039/C9NR10964A.
- (319) Brett, C. J.; Forslund, O. K.; Nocerino, E.; Kreuzer, L. P.; Widmann, T.; Porcar, L.; Yamada, N. L.; Matsubara, N.; Månsson, M.; Müller-Buschbaum, P.; Söderberg, L. D.; Roth, S. V. "Humidity-Induced Nanoscale Restructuring in PEDOT:PSS and Cellulose Nanofibrils Reinforced Biobased Organic Electronics". *Adv. Electron. Mater.* 2021, 7 (6), 2100137. DOI: 10.1002/aelm.202100137.
- (320) Brett, C. J.; Mittal, N.; Ohm, W.; Gensch, M.; Kreuzer, L. P.; Körstgens, V.; Månsson, M.; Frielinghaus, H.; Müller-Buschbaum, P.; Söderberg, L. D.; Roth, S. V. "Water-Induced Structural Rearrangements on the Nanoscale in Ultrathin Nanocellulose Films". *Macromolecules* 2019, 52 (12), 4721–4728. DOI: 10.1021/acs.macromol.9b00531.
- (321) Chen, Q.; Brett, C. J.; Chumakov, A.; Gensch, M.; Schwartzkopf, M.; Körstgens, V.;

- Söderberg, L. D.; Plech, A.; Zhang, P.; Müller-Buschbaum, P.; Roth, S. V. "Layer-by-Layer Spray-Coating of Cellulose Nanofibrils and Silver Nanoparticles for Hydrophilic Interfaces". *ACS Appl. Nano Mater.* 2021, 4 (1), 503–513. DOI: 10.1021/acsnm.0c02819.
- (322) Chen, Q.; Betker, M.; Harder, C.; Brett, C. J.; Schwartzkopf, M.; Ulrich, N. M.; Toimil-Molares, M. E.; Trautmann, C.; Söderberg, L. D.; Weindl, C. L.; Körstgens, V.; Müller-Buschbaum, P.; Ma, M.; Roth, S. V. "Biopolymer-Templated Deposition of Ordered and Polymorph Titanium Dioxide Thin Films for Improved Surface-Enhanced Raman Scattering Sensitivity". *Adv. Funct. Mater.* 2022, 32 (6), 2108556. DOI: 10.1002/adfm.202108556.
- (323) Hammouda, B. "A New Guinier–Porod Model". *J. Appl. Crystallogr.* 2010, 43 (4), 716–719. DOI: 10.1107/S0021889810015773.
- (324) Jiang, X.; Mietner, J. B.; Harder, C.; Komban, R.; Chen, S.; Strelow, C.; Sazama, U.; Fröba, M.; Gimmler, C.; Müller-Buschbaum, P.; Roth, S. V.; Navarro, J. R. G. "3D Printable Hybrid Gel Made of Polymer Surface-Modified Cellulose Nanofibrils Prepared by Surface-Initiated Controlled Radical Polymerization (SI-SET-LRP) and Upconversion Luminescent Nanoparticles". *ACS Appl. Mater. Interfaces* 2023, 15 (4), 5687–5700. DOI: 10.1021/acsmi.2c20775.
- (325) Smilgies, D. M. "Scherrer Grain-Size Analysis Adapted to Grazing-Incidence Scattering with Area Detectors". *J. Appl. Crystallogr.* 2009, 42 (6), 1030–1034. DOI: 10.1107/S0021889809040126.
- (326) Halttunen, N.; Lerouge, F.; Chaput, F.; Vandamme, M.; Karpati, S.; Si-Mohamed, S.; Sigovan, M.; Boussel, L.; Chereul, E.; Douek, P.; Parola, S. "Hybrid Nano-GdF₃ Contrast Media Allows Pre-Clinical in Vivo Element-Specific K-Edge Imaging and Quantification". *Sci. Rep.* 2019, 9 (1), 1–8. DOI: 10.1038/s41598-019-48641-z.
- (327) Albornoz-Palma, G.; Betancourt, F.; Mendonça, R. T.; Chinga-Carrasco, G.; Pereira, M. "Relationship between Rheological and Morphological Characteristics of Cellulose Nanofibrils in Dilute Dispersions". *Carbohydr. Polym.* 2020, 230, 115588. DOI: 10.1016/j.carbpol.2019.115588.
- (328) Hu, X.; Yang, Z.; Kang, S.; Jiang, M.; Zhou, Z.; Gou, J.; Hui, D.; He, J. "Cellulose Hydrogel Skeleton by Extrusion 3D Printing of Solution". *Nanotechnol. Rev.* 2020, 9 (1), 345–353. DOI: 10.1515/ntrev-2020-0025.
- (329) Nechyporchuk, O.; Belgacem, M. N.; Pignon, F. "Current Progress in Rheology of Cellulose Nanofibril Suspensions". *Biomacromolecules* 2016, 17 (7), 2311–2320. DOI: 10.1021/acs.biomac.6b00668.
- (330) Ovchinnikov, K. V.; Kranjec, C.; Thorstensen, T.; Carlsen, H.; Diep, D. B. "Successful Development of Bacteriocins into Therapeutic Formulation for Treatment of MRSA Skin Infection in a Murine Model". *Antimicrob. Agents Chemother.* 2020, 64 (12). DOI: 10.1128/AAC.00829-20.

- (331) Ovchinnikov, K. V.; Kranjec, C.; Telke, A.; Kjos, M.; Thorstensen, T.; Scherer, S.; Carlsen, H.; Diep, D. B. "A Strong Synergy Between the Thiopeptide Bacteriocin Micrococcin P1 and Rifampicin Against MRSA in a Murine Skin Infection Model". *Front. Immunol.* 2021, 12 (July), 1–13. DOI: 10.3389/fimmu.2021.676534.
- (332) Karpati, S.; Hubert, V.; Hristovska, I.; Lerouge, F.; Chaput, F.; Bretonnière, Y.; Andraud, C.; Banyasz, A.; Micouin, G.; Monteil, M.; Lecouvey, M.; Mercey-Ressejac, M.; Dey, A. K.; Marche, P. N.; Lindgren, M.; Pascual, O.; Wiart, M.; Parola, S. "Hybrid Multimodal Contrast Agent for Multiscale in Vivo Investigation of Neuroinflammation". *Nanoscale* 2021, 13 (6), 3767–3781. DOI: 10.1039/D0NR07026B.
- (333) Buffet, A.; Rothkirch, A.; Döhrmann, R.; Körstgens, V.; Abul Kashem, M. M.; Perlich, J.; Herzog, G.; Schwartzkopf, M.; Gehrke, R.; Müller-Buschbaum, P.; Roth, S. V. "P03, the Microfocus and Nanofocus X-Ray Scattering (MiNaXS) Beamline of the PETRA III Storage Ring: The Microfocus Endstation". *J. Synchrotron Radiat.* 2012, 19 (4), 647–653. DOI: 10.1107/S0909049512016895.
- (334) Schaeffler, S.; Perry, W.; Jones, D. "Methicillin-Resistant Strains of Staphylococcus Aureus Phage Type 92". *Antimicrob. Agents Chemother.* 1979, 15 (1), 74–80. DOI: 10.1128/AAC.15.1.74.

Table of figures and schemes

| | |
|--|----|
| Figure 1. 1 Structure of cellulose molecule, representing the anhydrocellubiose unit as the repeating structural, showing the non-reducing end and the reversible equilibrium between hemiacetal and aldehyde groups at the reducing end. The numbering system for carbon atoms in anhydroglucose is indicated in red, and the β -1,4 linkage is indicated in blue..... | 8 |
| Figure 1. 2 Inter- and intra-molecular hydrogen bonding network in cellulose. | 9 |
| Figure 1. 3 (a) Cellulose contained in plants or trees has a hierarchical structure from the meter to the nanometer scale; (b) schematic diagram of the reaction between cellulose and strong acid to obtain nanocellulose; (c) bionanocellulose cultured from cellulose-synthesizing bacteria ⁷ . Copyright 2020 Nanomaterials, with permission of MDPI. | 10 |
| Figure 1. 4 Standard terms for cellulose nanomaterials (TAPPI WI 3021) ¹¹ . Copyright 2018 Cellulose, with permission of Springer Nature. This figure is adapted from Mariano <i>et al.</i> ¹² , Copyright 2014 Journal of Polymer Science Part B: Polymer Physics, with permission of John Wiley and Sons. | 11 |
| Figure 1. 5 Schematic illustrations of recent processes to produce CNFs and CNCs from lignocellulosic materials ¹³ . Copyright 2015 Cellulose - Fundamental Aspects and Current Trends, with permission of InTech..... | 13 |
| Figure 1. 6 The crystalline and amorphous structures of cellulose..... | 14 |
| Figure 1. 7 Schematic diagram of CNF production ² . Copyright 2016 Industrial Crops and Products, with permission of Elsevier..... | 15 |
| Figure 1. 8 The most applied mechanical treatment processes used in fabricating CNFs are the homogenizer, the microfluidizer and the grinder ²⁶ . Copyright 2012 Carbohydrate Polymers, with permission of Elsevier..... | 16 |
| Figure 1. 9 (A) Y-type interaction chamber and (B) Z-type interaction chamber ³⁰ . Copyright 2018 Nanoemulsions, with permission of Elsevier. | 17 |
| Figure 1. 10 Schematic illustration of the hydrolysis of amorphous and microcrystalline cellulose by (A) noncomplexed and (B) complexed cellulase systems. The solid squares represent reducing ends, and the open squares represent nonreducing ends ⁶³ . Copyright 1997 Microbiology and molecular biology reviews: MMBR, with permission of American Society for Microbiology..... | 24 |
| Figure 1. 11 Overview microscopic images of NC: (a-c) TEMPO-mediated oxidized w-CNF, (d-f) w-CNC and (g-i) b-CNC samples via AFM (a,d,g) Cryo-SEM (b,e,h) and TEM (c,f,i). All AFM images have the same magnification in order to provide a direct comparison between nanocellulose particles ⁷⁷ . Copyright 2015 Nature Communications, with permission of Springer Nature..... | 29 |

Figure 1. 12 Microscopic images of CNFs with enzymatic pre-treatment (a-e) and with chemical pre-treatment (f-j): (a, b, f, g) optical microscopy; (c, e, j) FE-SEM and (d, h, i) AFM height images. Adapted with permission from ref ⁷⁸. Copyright 2014 Journal of Materials Science, with permission of Springer Nature. 30

Figure 1. 13 Photographs of NC: (a) 1.0 wt% CNC suspension, (b) 10.0 wt% CNC hydrogel, (c) freeze-dried CNC, (d) 2.0 wt% TEMPO-CNF suspension, (e) 10.0 wt% TEMPO-CNF hydrogel, (f) freeze-dried TEMPO-CNF. Adapted from ref ⁸². Copyright 2022 Cellulose, with permission of Springer Nature. 32

Figure 1. 14 Viscoelasticity curves as functions of strain (C) and frequency (D). The black solid lines, red dashed lines and blue dotted lines represent storage (G') and loss (G'') modulus and $\tan \delta$ (G'/G''), respectively. The configuration of the frequency sweep curve varies based on the characteristics of viscoelastic materials. In solid viscoelastic materials, G'' follows a linear trend, while G' remains frequency-independent. Conversely, in gel-like materials, both G' and G'' exhibit frequency independence. On the other hand, for viscoelastic liquids, both G'' and G' gradually rise with increasing frequency. Adapted with permission from ref ⁸⁴. Copyright 2021 Advanced Materials, with permission of John Wiley and Sons. 33

Figure 1. 15 Schematic representation of the most commonly used surface modification routes of nanocellulose⁵. Copyright 2020 Sec. Polymer Chemistry, with permission of Frontiers Chemistry. 36

Figure 1. 16 Common surface covalent chemical modifications of cellulose nanocrystals¹⁰². Red arrows: substitution of hydroxy groups with small molecules; blue arrows: "grafting to" strategy; yellow arrows: "grafting from" approach. Copyright 2012 Nanoscale, with permission of RSC Pub. 38

Figure 1. 17 Surface modification of CNFs through "traditional" chemical reaction¹⁰³. Copyright 2011 Chemical Society reviews, with permission of ROYAL SOCIETY OF CHEMISTRY, ETC. 39

Figure 1. 18 Schematic illustrations of surface modification approaches: (A) the "grafting to", (B) the "grafting from", and (C) the "grafting through"¹⁰⁵. Copyright 2016 Multifunctional Polymeric Nanocomposites Based on Cellulosic Reinforcements, with permission of Elsevier. 41

Figure 1. 19 Cu⁰-mediated SET-LRP of methyl acrylate in binary mixtures of 2,2,2-trifluoroethanol (TFE) and 2,2,3,3-tetrafluoropropanol (TFP) with water in the presence of the ligand Me₆-Tren ¹¹⁹. Adapted with ref ¹¹⁹. Copyright 2018 Polymer Chemistry, with permission of Royal Society of Chemistry. 43

Figure 1. 20 Schematic illustration of SET-LRP reaction mechanism¹²⁰. Copyright 2007 Journal of Polymer Science Part A: Polymer Chemistry, with permission of John Wiley and Sons. 44

Figure 1. 21 Examples of the chemical structure of acrylate monomers suitable for SET-LRP. 46

| | |
|---|----|
| Figure 1. 22 Kinetic models for SET-LRP in the presence and absence of disproportionation. Adapted with permission from ref ¹⁴⁹ . Copyright 2011 Journal of Polymer Science Part A: Polymer Chemistry, with permission of John Wiley and Sons. . | 47 |
| Figure 1. 23 Molecule structures of N-containing ligands: Me ₆ -TREN, TREN, PMDETA. . | 48 |
| Figure 1. 24 Schematic illustrations of several post-modification methods ¹⁶⁸ . Copyright 2015 American Chemical Society..... | 50 |
| Figure 1. 25 An overview of key factors in cellulose nanomaterial rheology and their influence on its emerging applications ⁸⁴ . Copyright 2021 Advanced Materials, with permission of John Wiley and Sons. | 53 |
| Figure 1. 26 Ideal rheological properties of a DIW ink for good printability and shape retention. (A) The interplay of rheological properties in extrusion-based printing. (B) The amplitude sweep for a viscoelastic material is represented as a function of the shear stress, showing the yield point as the limit of the linear viscoelastic range and the flow point where the viscous modulus G'' surpasses the elastic modulus G', indicating the onset of flow. (C) Elastic recovery test, where G' (blue) and G'' (red) are measured under low deformation (white time interval) and high deformation (gray time interval) ¹⁸⁶ . Copyright 2020 American Chemical Society..... | 54 |
| Figure 1. 27 Emerging applications of CNFs as bioink for 3D printing. (A) The fabrication process of Ti ₃ C ₂ T _x MXene/CNF for solid-state supercapacitor device and its electrochemical performance. Adapted with permission from ref ¹⁸⁷ , Copyright 2021 Advanced Functional Materials, with permission of John Wiley and Sons. (B) 3D printed hollow cylinder, a 5-layered serpentine pattern, and serpentine pattern wrapped around a glass rod with glowing LED light using conductive ink out of modified CNFs and conductive polymers. Adapted with permission from ref ¹⁸⁸ , Copyright 2023 Applied Materials Today, with permission of Elsevier. (C) A flexible microfluidic thin film with multilayered channels by matrix-assisted 3D printing in the CNF hydrogel. Different shapes of channel patterns formed in CNF films. Scale bars are 1 cm. Adapted with permission from ref ¹⁸⁹ , Copyright 2017 Applied Materials, with permission of American Chemical Society. (D) 3D printed human ear (left) and sheep meniscus (right) with CNF-Alginate Bioink. Adapted with permission from ref ¹⁹² , Copyright 2015 Biomacromolecules, with permission of American Chemical Society..... | 55 |
| Figure 1. 28 An overview of the applications of nanocellulose-based hybrid materials with inorganic nanoparticles ²⁰² . Copyright 2020 Carbohydrate Polymers, with permission of Elsevier. | 56 |
| Figure 1. 29 Graphical overview of the studies. | 59 |
| Scheme 1. 1 Chemical pre-treatments of CNF productions: (A) TEMPO-mediated oxidation, adapted from ref ⁴⁶ , Copyright 2019 Cellulose, with permission of Springer Nature. (B) carboxymethylation, (C) quaternization. | 20 |
| Figure 2. 1 Graphical overview of the Chapter 2..... | 62 |

Figure 2. 2 Chemical structure and spectral properties of AF 488 and ATTO 633. The spectra are obtained from Fluorescence SpectraViewer, ThermoFischer Scientific²¹¹.... 63

Figure 2. 3 Left: illustration of stimulated emission depletion (STED) microscopy²¹⁴. Copyright 2010 Cell, with permission of Elsevier. Right: comparison of confocal laser scanning microscopy and STED microscopy images of modified cellulose nanofibrils labeled with a fluorescent dye..... 64

Figure 2. 4 SEM images of cellulose from each stage of mechanical disintegration steps: (A) initial kraft pulp, (B) cellulose fibers after grinding, (C)&(D) CFs underwent microfluidizer 2 times with 400 μm and 200 μm chambers, (E)&(F) CFs underwent microfluidizer 2 times with 200 μm and 100 μm chambers, (G)&(H) final CNFs underwent microfluidizer 4 times with 200 μm and 100 μm chambers..... 66

Figure 2. 5 Width- (left row) and length (right row) distribution diagrams of (A) cellulose fibers after grinding, (B) CFs underwent microfluidizer 2 times with 400 μm and 200 μm chambers, (C) CFs underwent microfluidizer 2 times with 200 μm and 100 μm chambers, (D) final CNFs underwent microfluidizer 4 times with 200 μm and 100 μm chambers. * The values of CFs&CNFs may exceed the resolution of FiberLab (length: 50 μm , width: 1 μm). 67

Figure 2. 6 FT-IR spectra of pristine CNF (black), CNF-MI (red) and PSA-CNF (pink)..... 69

Figure 2. 7 (a) ^{13}C CP-MAS spectrum of CNF sample (b) Deconvolution of 50-120 ppm region. The upper black line corresponds to experimental data. The yellow line corresponds to the sum of individual peaks resulting from the spectral deconvolution. Two signals from hemicelluloses are indicated in orange. Deconvolution of C4 region with crystalline forms Cr ($\text{I}\beta$) and Cr ($\text{I}\alpha+\beta$) (black), paracrystalline form (PCr) (grey), accessible fibril surfaces (AS) (green), and inaccessible fibril surface (IAS) (dark green). 71

Figure 2. 8 ^{13}C CP-MAS spectra (blue), ^{13}C multiCP spectra (black) and the difference between these spectra (red) of (a) CNF, (b) CNF-MI and (c) PSA-CNF. 72

Figure 2. 9 Schematic illustration of side reactions of terminal alkynes under radical polymerizations²³⁹. Copyright 2015 Macromolecules, with permission of American Chemical Society..... 75

Figure 2. 10 FT-IR spectra of the pristine CNF (black), CNF-MI (red), DEG-TMSPgA-CNF (protected alkyne, blue), DEG-PgA-CNF (deprotected alkyne, yellow)..... 76

Figure 2. 11 ^{13}C CP-MAS NMR spectra of (a) CNF-MI, (b) DEG-TMSPgA-CNF, (c) DEG-PgA-CNF. 77

Figure 2. 12 Left: UV-Vis spectra of DEG-PgA-CNF (black) and coumarin@DEG-PgA-CNF (red); right: confocal scanning laser microscopy imaging of coumarin derivate labeled on the polymer modified CNFs (fluorescence image obtained at an excitation wavelength of 488 nm, red color)..... 80

| | |
|--|-----|
| Figure 2. 13 Schematic illustration of labeling fluorescent dyes on CNF surfaces and hypothetical morphologies of modified CNFs..... | 83 |
| Figure 2. 14 Deconvolved STED images of modified CNFs: (a) isolated fibril, (b) dispersion state of fibrils, (c) fibril network, (d) fibril bundle, (e) cluster. | 85 |
| Figure 2. 15 (a) FESEM image of fibrils/PVA composite, (b) STED image of fibrils in PVA. | 86 |
| Figure 2. 16 Schematic illustrations of (a) STED imaging of fibrils dried from DMSO, (b) detecting distribution and morphology of modified CNFs within a PVA composite: (i) a model showcasing modified CNFs in PVA, (ii) a concept map overview depicting modified CNFs in PVA with "in-focus" regions highlighted in circles and "out-of-focus" regions in rectangles, (iii) a conceptual image illustrating the focused structure of modified CNFs within the PVA matrix..... | 87 |
| Figure 2. 17 STED images of modified CNFs (0.5 wt%) in PVA (10 wt%): (a) deconvolved confocal image of a cluster of AF 488&ATTO 633@DEG-PgA-CNF, (b) map overview of ATTO 633@DEG-PgA-CNF in PVA matrix, (c) deconvolved STED image of a cluster of ATTO 633@DEG-PgA-CNF, (d) intrafibrillar network, (e) single fibrils from a bundle. .. | 89 |
| Figure 2. 18 ATTO 633@DEG-PgA-CNF in a PVA matrix: (a) STED image, (b) FESEM image. | 90 |
| Scheme 2. 1 Synthesis of the CNF-based macroinitiator (CNF-MI) and PSA-CNF..... | 68 |
| Scheme 2. 2 General chemical strategy for the immobilization of fluorescent dye onto the CNF. (A) di(ethylene glycol) ethyl ether acrylate (DEGEEA) and the protected alkyne acrylate (TMSPgA) grafted onto the CNFs via surface-initiated SET-LRP, followed by the sequential deprotection of trimethylsilyl groups; (B) Cu-catalyzed azide-alkyne cycloaddition between alkyne-induced CNFs and the azido-chromophores..... | 74 |
| Scheme 2. 3 (A) Fluorescence feature of 3-azido-7-hydroxycoumarin, used to investigate reaction conditions before using the expensive biomolecule or cargo reagent(s); (B) CuAAC reaction of DEG-PgA-CNF and 3-azido-7-hydroxycoumarin: (i) DEG-PgA-CNF before the reaction, (ii) after the reaction with the fluorescence of 3-azido-7-hydroxycoumarin. | 79 |
| Scheme 2. 4 Preparation of luminescent cellulose nanofibrils: labeling of the two dyes ATTO 633 and AF 488 onto DEG-PgA-CNF through click chemistry..... | 81 |
| Figure 3. 1 The history, development and application of rare-earth-based nanomaterials ²⁵¹ . Copyright 2022 Chemical Reviews, with permission of American Chemical Society. | 102 |
| Figure 3. 2 Energy-level diagrams and proposed UC energy transfer pathways in the Yb ³⁺ -Er ³⁺ , Yb ³⁺ -Ho ³⁺ , and Yb ³⁺ -Tm ³⁺ pairs. Adapted with permission from ref ²⁵⁷ . Copyright 2015 Annual Review of Physical Chemistry, with permission of Annual Reviews, Inc. | 105 |

| | |
|--|-----|
| Figure 3. 3 Schematic illustration of the ligand-exchange process with NOBF_4 ²⁶⁸ . Copyright 2011 Journal of the American Chemical Society, with permission of American Chemical Society..... | 106 |
| Figure 3. 4 Schematic illustration of synthesis route of CNF-based hybrid gels..... | 108 |
| Figure 3. 5 CNF-based hybrid materials as an innovative pool for biomaterial development ³⁰⁹ | 110 |
| Figure 3. 6 FT-IR spectra of OA@UCNP (black), BF_4 @UCNP (blue), and AMPS@UCNP (red)..... | 112 |
| Figure 3. 7 TGA curve of AMPS@UCNP..... | 113 |
| Figure 3. 8 . FT-IR spectra of dried initial GdF_3 NPs (black) and dried PDA@ GdF_3 (red). | 116 |
| Figure 3. 9 FT-IR spectra of CNF-MI (red), PSA-CNF (pink) and UCNP-PSA-CNF (blue). | 118 |
| Figure 3. 10 (A) Schematic illustration of upconversion mechanism of UCNPs doped with Yb^{3+} - Er^{3+} ; (B) emission spectra of OA@UCNP (grey), AMPS@UCNP (blue) and UCNP- PSA-CNF (red);(C) the corresponding CIE 1931 chromaticity diagram (D) UCNP-PSA- CNF gel under (I) daylight, (II) 980 nm laser diode excitation..... | 120 |
| Figure 3. 11 Left: TGA of PSA-CNF (black), UCNP-PSA-CNF (red); right: XRD patterns of UCNPs as residue from TGA and the standard data of NaYF_4 (PDF#06-0432)..... | 121 |
| Figure 3. 12 TEM images of (A) OA@UCNP, (B) AMPS@UCNP, (C)-(E) UCNP-PSA-CNF. | 122 |
| Figure 3. 13 FT-IR spectra of initial CNF (black), CNF-MI (red), PSA-CNF (pink), and GdF_3 -PSA-CNF (blue). | 123 |
| Figure 3. 14 Thermogravimetric analysis of PSA-CNF (blue), GdF_3 -PSA-CNF (red)..... | 124 |
| Figure 3. 15 SEM images of GdF_3 -PSA-CNF: (A, C, E) freeze dried, (B, D, F) supercritical CO_2 dried..... | 125 |
| Figure 3. 16 Background-corrected 2D-SAXS data of (A) pristine CNF, (B) PSA-CNF-sd (simply dried), (C) PSA-CNF-3D (3D printed), (D) UCNP-PSA-CNF-3D, (E) UCNP-PSA- CNF-sd, (F) original UCNPs on Kapton. White lines indicate the masked areas. The logarithmic intensity scale for all SAXS patterns is displayed on the right side. The reciprocal space coordinate system with a scale bar is presented in (A). | 127 |
| Figure 3. 17 1D-SAXS curves and corresponding fits: (A) the pristine CNF, (B) PSA-CNF- 3D, (C) PSA-CNF-sd. The corresponding fits are presented in red color. Curves are shifted for clarity. | 129 |

| | |
|--|-----|
| Figure 3. 18 1D-SAXS curves and corresponding fits: (A) OA@UCNPs, (B) UCNP-PSA-CNF-sd, (C) UCNP-PSA-CNF-3D. The corresponding fits are presented in red color. Curves are shifted for clarity..... | 130 |
| Figure 3. 19 USAXS data of (A) 3D-printed gel (blue), (B) simply dried sample (orange), and (C) a single layer of 3D-printed gel (green). The fitted lines are black..... | 133 |
| Figure 3. 20 Schematic illustration of stacking and distribution of (A) UCNPs and (B) GdF ₃ NPs within modified CNFs. | 134 |
| Figure 3. 21. WAXS data of (A) 3D-printed gel (blue), (B) simply dried sample (orange), and (C) a single layer of 3D-printed gel (green). The fitting lines are black. | 135 |
| Figure 3. 22 A suspension of dried UCNP-PSA-CNF redispersed in toluene. | 136 |
| Figure 3. 23 Rheology measurements of CNF-based gels: (A) viscoelastic moduli, (B) yield stress, (C) shear-thinning, (D) shear recovery. The blue square represents PSA-CNF, and the orange circle represents UCNP-PSA-CNF; the solid shape refers to the left Y-axis, and the hollow shape refers to the right Y-axis..... | 137 |
| Figure 3. 24 3D models and prints under daylight and 980 nm laser diodes..... | 139 |
| Figure 3. 25 (A) Layout of the custom-built confocal microscope: BS, 90/10 beamsplitter; Obj, an objective lens with a numerical aperture of 0.7; SP filter, short-pass 750 nm filter; M1&M2, (flip) mirror; L1&L2, lenses; CCD, charge-coupled device; SPAD, single-photon avalanche diode; (B) confocal maps at different depths of the sample; scale bar: 10 μm; (C) typical emission spectrum under 980 nm irradiation; scale bars: 10 μm; (D) zoomed-in image at the focus plane Z=58 μm; intensity is scaled between global min-max..... | 140 |
| Figure 3. 26. Rheology measurements of GdF ₃ -PSA-CNF gels: (A) viscoelastic moduli, (B) amplitude sweep, (C) shear-thinning, (D) shear recovery. The solid circle refers to the left Y-axis; the hollow circle refers to the right Y-axis. | 142 |
| Figure 3. 27. 3D models and 3D prints obtained using the GdF ₃ -PSA-CNF gels. | 143 |
| Figure 3. 28 3D prints before (upper) and after (down) supercritical drying. | 144 |
| Figure 3. 29. ¹ H MRI of toluene control (upper row) and GdF ₃ -PSA-CNF suspension in toluene (1 wt%, lower row). | 145 |
| Figure 3. 30. ¹ H MRI of GdF ₃ -CNF suspension in H ₂ O (1 wt%) embedded in control gel (2 wt% agar in 1× phosphate buffered saline). The arrows indicate the gel, which appears hypointense compared to the surrounding agarose control. This hypointensity can be attributed to transverse relaxation enhancement, resulting in a lower T ₂ relaxation time..... | 145 |
| Figure 3. 31 Antimicrobial test against MRSA ATCC 33591-lux in vitro: (A) simply dried print, (B) freeze-dried print, (C) blank sample (negative control). | 147 |

| | |
|---|-----|
| Scheme 3. 1 Two-step ligand exchange of UCNPs..... | 111 |
| Scheme 3. 2 Grafting polymerization and <i>in situ</i> cross-linking of CNF-MI with SA and UCNPs via SET-LRP..... | 117 |
| Scheme 3. 3 (A) Chemical conversion of CNFs to CNF-MI; (B) surface modification of GdF ₃ NPs with PDA; (C) polymerization and <i>in situ</i> cross-linking of CNF-MI with SA and PDA@ GdF ₃ via SET-LRP..... | 122 |
| Scheme 3. 4 Concept: CNF-based hybrid gels serve different purposes..... | 146 |
| Figure 4. 1 Concept of wound dressing made of CNF-based hybrid gels with customizable shapes and dimensions and drug slow-releasing feature. | 159 |
| Figure 4. 2 Schematic illustration of tensile testing of 3D-printed CNF objects with X-ray beam detecting structural changes: (A) force applied perpendicular to the layer interface, (B) stretching along the layer interface..... | 160 |

List of tables

| | |
|---|-----|
| Table 2. 1 Various parameters for the supramolecular organization of CNFs. | 71 |
| Table 3. 1 R_g denotes the Guinier radius, s the shape parameter and m the Porod coefficient. D is the stacking distance of the nanoparticles, calculated as $D = 2\pi q_0$ | 134 |

Journal publications



A combination of surface-initiated controlled radical polymerization (SET-LRP) and click-chemistry for the chemical modification and fluorescent labeling of cellulose nanofibrils: STED super-resolution imaging of a single fibril and a single fibril embedded in a composite

Xuehe Jiang · J. Benedikt Mietner ·
Julien R. G. Navarro

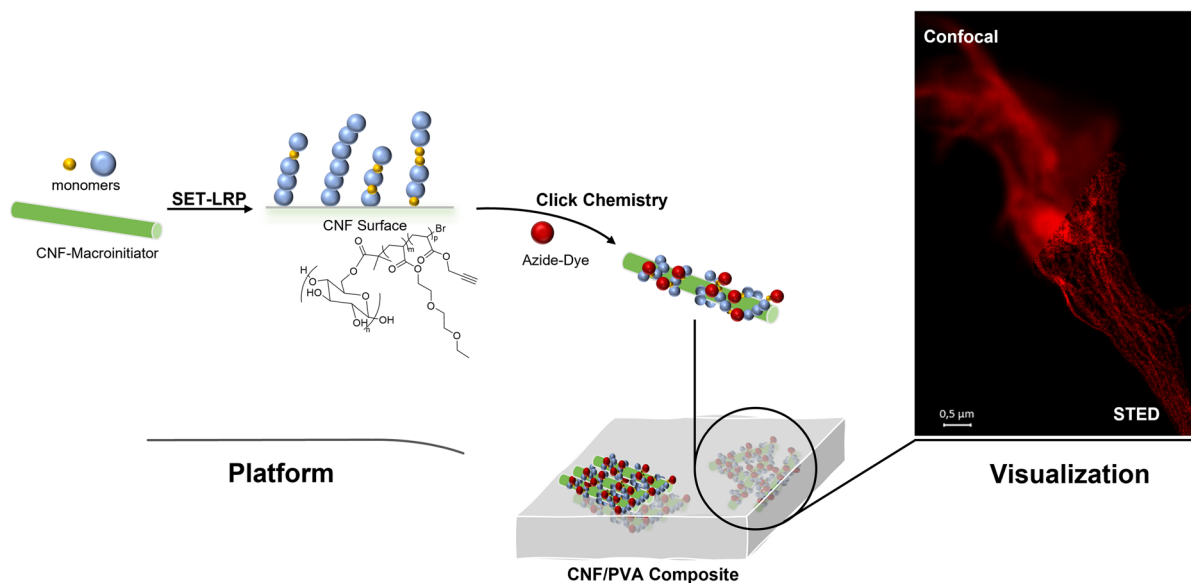
Received: 1 July 2022 / Accepted: 1 December 2022
© The Author(s) 2023

Abstract A strategy is developed to modify cellulose nanofibril (CNF) surfaces with a combination of Cu⁰-mediated radical polymerization (SET-LRP) and Cu^I-catalyzed azide-alkyne click-chemistry (CuAAC). CNFs were grafted with statistical copolymers of di(ethylene glycol) ethyl ether acrylate (DEGEEA) and acrylic acid 3-trimethylsilyl-prop-2-ynyl ester (TMSPgA) that allows labeling of multiple fluorescent dyes, e.g. AF488 and ATTO633,

special dyes for confocal laser scanning microscopy and stimulated emission depletion (STED) microscopy. Through our strategy and these microscopic techniques, we visualized isolated fibrils and fibrils embedded in a PVA composite in a high resolution. This work also provides new insight into the effect of the clickable entity/precursor on the compatibility of modified fibrils with the composite matrix.

X. Jiang · J. B. Mietner · J. R. G. Navarro (✉)
Institute of Wood Science, Universität Hamburg,
Hamburg, Germany
e-mail: Julien.navarro@uni-hamburg.de

Graphical abstract



Keywords Cellulose nanofibrils (CNFs) · Single electron transfer living radical polymerization (SET-LRP) · Grafting-from · Azide-alkyne click chemistry · STED · Bio-based nanocomposite

Abbreviations

| | |
|----------|--|
| CNFs | Cellulose nanofibrils |
| SET-LRP | Single electron transfer living radical polymerization |
| CuAAC | Cu(I)-catalyzed azide-alkyne cycloaddition |
| STED | Stimulated emission depletion microscopy |
| PVA | Poly(vinyl alcohol) |
| DEGEEA | Di(ethylene glycol) ethyl ether acrylate |
| Me6-TREN | Tris[2-(dimethylamino)ethyl]amine |
| CDI | 1,1'-Carbonyldiimidazole |
| TEA | Triethylamine |
| DMSO | Dimethyl sulfoxide |
| NaASC | L-ascorbic acid sodium salt |
| TBAF | Tetrabutylammonium fluoride |
| TMSPgA | Acrylic acid 3-trimethylsilyl-prop-2-ynyl Ester |

Introduction

Nowadays, oil-based materials and resultantly plastic waste and plasticizers have become a significant concern for our planet. Therefore, there is a constantly increasing interest in minimizing the environmental impact of those oil-based products. More and more attention has been given to the utilization of ligno-cellulosic biomass for developing a more sustainable human society. Cellulose is a biodegradable, recyclable, renewable polymer and has already found great interest in numerous fields and potential new applications ranging from a flexible gas sensor, water purification to tissue engineering and drug delivery (Ottenhall et al. 2017; Poonguzhali et al. 2018; Hur et al. 2022).

Cellulose nanofibrils or cellulose nanofibers (CNFs), one of the few nanostructured forms of cellulose, can be assimilated to high aspect ratio wires with an average width of 5–60 nm and several micrometers in length (Klemm et al. 2011). The accurate measurement of the fibril length remains a difficult challenge due to their curved morphologies and

the fibril aggregation behavior. CNFs are generally prepared by pre-treatment and delamination of cellulosic materials through mechanical disintegration (Kalia et al. 2014). CNFs have an abundant number of hydroxy, leading to some drawbacks such as hygroscopic character, instability in many organic solvents, strong inter-fibril hydrogen interactions (leading to fibril aggregation) which ones can drastically limit the use of the CNFs in numerous applications. To avoid those undesirable CNF behaviors, CNFs must be subjected to a surface modification process.

Common chemical surface modification of CNFs includes reactions of hydroxy with small molecules through silylation, (Xhanari et al. 2011) acetylation, (Nogi et al. 2006; Gustavsson et al. 2020) esterification, (Lee et al. 2014; Willberg-Keyriläinen et al. 2017), oxidation, (Liimatainen et al. 2012; Fukuzumi et al. 2014; Zhang and Liu 2018) and click-chemistry (Junka et al. 2014; Hettegger et al. 2016; Beaumont et al. 2018; Aïssa et al. 2019). However, through those mentioned reactions, the substitution degree remains low, limiting the suspendability of the CNFs in numerous organic solvents. Another chemical surface modification approach is the grafting of polymers. Polymerization is an optimal strategy to alter the CNF characteristics and properties as polymerization grows long molecular chains on the CNF backbone, creating, for example, optimal interphase between the CNFs and the surrounding medium such as solvent, host matrix (e.g. polymer) and therefore increasing the CNF stability and processability (e.g. composite production).

Grafting polymerizations can be achieved via three main approaches: “grafting to”, “grafting from”, and “grafting through” (Lizundia et al. 2016). The “grafting to” approach covalently attaches existing, pre-formed polymers onto cellulose surfaces (Tsubokawa et al. 2000). The “grafting from”, also known as surface-initiated polymerization (SIP), involves the immobilization of reactive moieties onto a surface, which therefore initiates the propagation of a monomer. Examples of “grafting from” reactions involve Ring-Opening Polymerization (ROP), (Wang et al. 2007; Lalanne-Tisné et al. 2020) as well as controlled or Living Radical Polymerization (LRP) techniques, (Rosen and Percec 2009) such as Reversible Addition-Fragmentation chain Transfer (RAFT), (Chiefari et al. 1998) Atom Transfer Radical Polymerization (ATRP), (Chiefari et al. 1998) and Single-Electron

Transfer Living Radical Polymerization (SET-LRP) (Zhang et al. 2014a). The “grafting through” strategy can be considered as an intermediate approach between the two strategies described above (Kelly et al. 2021).

Cu⁰-mediated SET-LRP, first introduced by Percec et al. (2006) was described as the “ultrafast synthesis of ultrahigh molecular weight polymers”. The reaction can be performed in the presence of oxygen, non-inert condition, or even in the presence of water while keeping control of the polymer molecular weight (Nguyen et al. 2010, 2012, 2013; Fleischmann and Percec 2010; Nicol et al. 2012; Levere et al. 2013; Samanta et al. 2015). SET-LRP proved to be effective with a large library of hydrophilic or hydrophobic vinyl monomers on CNFs (Majoinen et al. 2011; Samanta et al. 2013; Larsson et al. 2013; Navarro et al. 2020).

“Click Chemistry” is a term describing modular reaction, while offering high yield and in-offensive by-products (Wang et al. 2003). It requires simple synthetic conditions, easy removal of the solvents and simple product isolation. Few reactions already meet these criteria, such as the Diels–Alder cycloaddition (Inglis et al. 2009; Kloetzel 2011) or the thiol–ene reaction (Nilsson et al. 2008; Xiong et al. 2018). In addition, the Cu^I-catalyzed azide-alkyne cycloaddition (CuAAC) can also be classified as a click chemistry reaction. One noticeable fact is that biomolecules can preserve their bioactivity within this simple, efficient reaction, which contributes to the vast array of biomedical applications of click chemistry (Himo et al. 2005; Hein and Fokin 2010; Presolski et al. 2011; Song et al. 2012; Kaur et al. 2021). As its popularity increased over the year, a large library of starting compounds is available, making this reaction very attractive to the scientific community (Akeroyd and Klumperman 2011; Ramapanicker and Chauhan 2016).

The interest in using CNFs as fillers or reinforcing agents in bio-based composites is constantly increasing as CNFs offer many advantages, such as relatively low-cost, it can be extracted from numerous renewable resources, meaning a high abundance and availability all over our planet and high mechanical properties (Moon et al. 2011). Over the last few years many research groups devoted their research interest to wood flour, cellulose fiber or cellulose nanofibrils reinforced composites, aiming to better understand the filler-matrix compatibility, their interaction

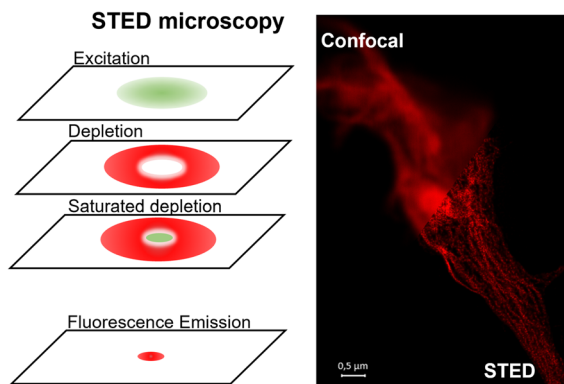


Fig. 1 *Left* Illustration of stimulated emission depletion (STED) Microscopy;(Huang et al. 2010) *Right* comparison of confocal laser scanning microscopy and STED microscopy images of modified cellulose nanofibrils labeled with a fluorescent dye

through their interface and the morphological/dimensional aspect, e.g. homogeneous dispersion and orientation of the filler in the matrix (Saba et al. 2017; Arof et al. 2019; Radakisnin et al. 2020).

The current characterization techniques such as Scanning Electron Microscopy (SEM) or Atomic Force Microscopy (AFM) have been the most widely used tools for imaging and localizing the cellulose fibrils/fiber either alone or in the thermoplastic matrix. Despite the fact that these advanced microscopy techniques have very high resolutions, the elucidation of how CNFs organize themselves when embedded in a polymer matrix remains a challenge, as generally, in composite images, the direct observation of a single buried CNF is significantly harder.

Nakagaito et al. (2004) made detailed scanning electron images of cellulose materials from pulp fiber to CNFs and evaluated the effect of the cellulose morphological changes on the mechanical properties of composites. Fazeli et al. (2018) showed the clear microstructure of individual CNFs with width ranging from 51 to 103 nm via SEM and analyzed the surface roughness of the composite of CNFs reinforced thermoplastic starch via AFM. Frone et al. (2013) discussed CNF dispersion in polylactic acid composites from aspects of the maximum surface height of composites and aggregate sizes of CNFs on the surfaces via advanced AFM. In a bio-based composite material, imaging single cellulose fibrils in the matrix are unfortunately not possible using traditional

microscopy. However, with new technology development such as stimulated emission depletion (STED) microscopy, imaging a luminescent CNF embedded in a polymer matrix could be possible.

Stimulated emission depletion (STED) microscopy is one of super-resolution microscopy techniques that has been developed over decades to overcome the diffraction limit of light microscopy. In STED microscopy, a depletion laser pattern overlaps with the exciting laser and brings excited fluorophores back to the ground state to prevent fluorescence emission in the predefined regions so that it reduces the amount of spontaneous fluorescence emission (Fig. 1) (Huang et al. 2010). As a result, the effective point spread function is lower than the diffraction limit, thus achieving a high resolution down to 20 nm (Vicidomini et al. 2018). STED microscopy has been a versatile tool for biological research (Roo-bala et al. 2018; Stephan et al. 2019; Sezgin et al. 2019) and nanoscale materials (Friedemann et al. 2011; Busko et al. 2012; Liu et al. 2021) as it allows living-cell imaging, (Stockhammer and Bottanelli 2021; Calovi et al. 2021) 3D imaging as well as fast imaging, (Schermelleh et al. 2010) and there is a wide range of commercially available fluorophores suitable for it. Another specialty of STED is deep imaging, by reducing specimen-induced spherical aberration, STED microscopy achieved a resolution of 60–80 nm, 120 μm deep inside scattering biological tissue (Urban et al. 2011). However, to characterize CNFs with STED microscopy, a specific luminescent dye has to be labeled onto the CNFs.

The labeling of cellulose nanomaterials with fluorescent dyes is of interest in biomedical and sensor applications (Edwards et al. 2013; Guise and Fanguero 2016; Golmohammadi et al. 2017; Wu et al. 2018; Zhai et al. 2022). Fluorescently tagged CNFs are also used for the study of, for instance, nanotoxicology and therapeutics. (Salari et al. 2019; Ning et al. 2021) Schyrr et al. (2014) prepared CNF/PVA nanocomposites with a high concentration of fluorescent sensor motifs by thiol-ene click reactions. Navarro et al. (2015) modified CNFs with furan and maleimide groups to enable selective labeling of fluorescent probes through Diels–Alder cycloaddition and thiol-ene click reaction. Goodge et al. (2020) functionalized biotin-CNF membranes with the substitution of alkyne groups, and fluorescently tagged azide-biotin

conjugate via copper-catalyzed alkyne-azide cycloaddition (CuAAC). Recently, a fluorescence-labeling approach on CNFs via a triazine linker and click-chemistry is also reported (Babi et al. 2022). In all these studies, the labeling of CNFs was achieved through specific chemical reactions sequentially inducing certain precursors, followed by one or two click-chemistry reactions.

Our aim, in this paper was to develop a multifunctional platform made of a bio-based polymer nanostructure, the cellulose nanofibrils, that could be easily tunable to adapt to numerous and various applications. To prove our concept idea, we focus this study on labeling the CNFs with specific luminescent dyes and performing single-molecule imaging of isolated fibrils and fibrils embedded in a composite.

We develop a strategy to surface modify the CNFs through Cu⁰-mediated radical polymerization and finally introduce different luminescent dyes via post-modification through Cu^I-catalyzed azide-alkyne click-chemistry. For this purpose, after synthesizing the CNF-based macroinitiators, statistical copolymers were grafted onto the CNFs through Surface Initiated SET-LRP. The monomers comprise a di (ethylene glycol) ethyl ether acrylate (DEGEEA) and a protected alkyne monomer (Acrylic Acid 3-trimethylsilyl-prop-2-ynyl Ester, TMSPgA). DEGEEA was employed to increase the stability of the CNFs in selected solvent (DMSO & H₂O), while it is well known that hydrogen bonding enhanced the inter-fibril interaction yielding aggregation of fibrils automatically. So, this monomer aims to suppress this issue but also to act as a spacer between neighbor luminescent dyes by spacing the reactive clickable monomers. TMSPgA was used to introduce the reactive luminescent dyes on the CNF surface. Unfortunately, this alkyne monomer needed to be protected during the polymerization reaction and later-on deprotected. SET-LRP could not be performed without this protection step. Finally, the morphology of the modified CNFs was investigated through confocal laser scanning microscopy and stimulated emission depletion (STED) microscopy. Within the STED microscopy technique, we could visualize isolated fibrils and fibrils embedded in a composite. Moreover, we could also tune the compatibility of the modified CNFs within the matrix, by simply changing the clickable entity/precursor, and therefore change drastically the adhesion of the CNFs within the composite matrix. Those changes, which could not be observed with traditional electron

microscopy techniques (SEM, AFM), were possible with the STED.

Experimental section

Materials

1,1'-carbonyldiimidazole (CDI, 98%), 3-(Trimethylsilyl)propargyl alcohol (98%) were purchased from abcr. Dimethyl sulfoxide (DMSO, ≥99%), imidazole (≥99%), anhydrous diethyl ether (99%), acryloyl chloride (96%), tris[2-(dimethylamino)ethyl]amine (Me₆-TREN, 98%), copper(II) sulfate pentahydrate (CuSO₄·5H₂O, ≥99%), L-ascorbic acid sodium salt (NaASC, 99%), poly(vinyl alcohol) (PVA, 98–99%), Cu wire (diameter 0.812 mm, 99.9%) were purchased from Alfa Aesar. 2-bromo-2-methylpropionic acid (98%), di(ethylene glycol) ethyl ether acrylate (DEGEEA, 90%), hydroquinone (99%), triethylamine (TEA, 99%), sodium carbonate (Na₂CO₃, 99.5%), hydrogen chloride solution (0.1 M), tetrahydrofuran (THF, 99.9%) and azide fluor 488 (AF488, ≥90%) were purchased from Sigma-Aldrich. Acetone (99.90%) was purchased from BCD-Chemie. Acetic acid (AcOH, 99%) was purchased from Chemsolute. Ethyl 2-bromo-2-methyl propionate (EBiB, 98%) was purchased from Fisher. Tetrabutylammonium fluoride (TBAF, 1 M in THF) and 3-azido-7-hydroxyl-coumarin were purchased from TCI Chemical. ATTO633 was purchased from ATTO-TEC GmbH.

To produce cellulose nanofibrils (CNFs), dried elemental chlorine-free (ECF) bleached kraft pulp (Stendal GmbH, Germany) was used, and the CNF suspension was obtained with the use of a Microfluidizer (M-110EH-30 Microfluidics, Indexcorp).

DI water (0.055 μS/cm) was used for the solvent-exchange procedure and synthesis.

All the monomers for grafting polymerization were passed through a basic alumina column to remove inhibitors.

Production of cellulose nanofibrils

Cellulose nanofibrils were produced as previously described (Mietner et al. 2021). In a general procedure, cellulose pulp suspended in water was firstly ground to 75–80°SR (SR: Schopper-Riegler degrees), then passed through chambers with orifice widths of

400 μm and 200 μm (2 times), 200 μm and 100 μm (4 times) successively under high pressure. The process resulted in a 2% (w/w) CNF aqueous gel. The CNF gel was refrigerated at 5 $^{\circ}\text{C}$.

Solvent exchange procedure

The solvent exchange procedure of the CNF aqueous gel proceeded as previously described (Navarro and Edlund 2017). In general, DMSO was slowly added to the aqueous suspension of CNFs under stirring. Then, the solvent was discarded by centrifugation and replaced with fresh DMSO. The procedure resulted in a 2% (w/w) CNF/DMSO gel.

Synthesis of the CNF-based macroinitiator (CNF-MI)

CNF-based macroinitiator was produced as previously described (Georgouvelas et al. 2020). The suspension of CNFs in DMSO was added with imidazole and degassed via nitrogen purging continuously. Separately, a solution of 2-bromo-2-methyl propionic acid in DMSO was prepared and purged with nitrogen for 10 min; then CDI was slowly added under stirring at room temperature until it was fully dissolved, and no gases were further produced. Finally, the solution was slowly added to the CNF suspension. The reaction proceeded under a nitrogen atmosphere overnight at 55 $^{\circ}\text{C}$. The modified CNFs were purified by sequential washing with DMSO (4 \times 30 ml), centrifugation (4427 rcf for 30 min), and decantation. The process resulted in a 1% (w/w) CNF-MI gel.

Synthesis of acrylic acid 3-trimethylsilyl-prop-2-ynyl ester (TMSPgA)

3-(Trimethylsilyl) propargyl alcohol (5 g, 39 mmol), TEA (7.61 mL, 54.6 mmol), and hydroquinone (30 mg, 0.3 mmol) were dissolved in anhydrous diethyl ether (50 mL) and cooled in an ice–water bath. A solution of acryloyl chloride (3.80 ml) in diethyl ether (20 mL) was added dropwise over 30 min. The reaction was set up in an inert atmosphere under nitrogen; the mixture was stirred in the ice bath for 1 h and then at ambient temperature overnight. The final product was obtained by extraction with Na_2CO_3 solution (1 M aq., 3 \times 100 mL) and rotary evaporation of the collected organic phase.

Synthesis of statistical copolymer of DEGEAA and TMSPgA onto CNFs (DEG-TMSPgA-CNF) via SET-LRP

The copolymerization of statistical copolymer DEG-TMSPgA-CNF (DEGEAA:TMSPgA=6:4) was carried out in one pot. DEGEAA (9.24 mmol) and TMSPgA (6.16 mmol) in DMSO (15 ml) were added into a suspension of CNF-MI (4 g, 1% w/w) in DMSO (30 mL). Separately, a Cu wire (diameter=0.812 mm, length=6 cm) was immersed in a concentrated HCl solution for 10 min, then rinsed with water and acetone and dried prior to use. The suspension with Cu-wire was degassed via nitrogen purging for 10 min and raised to 40 $^{\circ}\text{C}$. The reaction started when the Me6-TREN ligand (200 μL , 10% v/v in DMSO) was added and proceeded overnight under a nitrogen atmosphere. The modified CNFs were purified by sequential washing with DMSO (6 \times 30 ml), centrifugation (4427 rcf for 30 min), and decantation.

Syntheses of statistical polymer DEGEAA and TMSPgA (DEG-TMSPgA, DEGEAA:PgA=6:4) was also carried out according to the description above, except that the ethyl 2-bromo-2-methyl propionate (EBiB) replaced the CNF-MI as a sacrificial initiator at a $[\text{M}]_0/[\text{I}]_0/[\text{L}]_0$ ratio of 100/1/0.2.

Deprotection of trimethyl silyl (TMS) protected polymers

The TMS-protected polymer (TMSPgA induced CNFs, DEG-TMSPgA-CNF 2.9 g, 6.16 mmol TMS groups in theory) was suspended in THF (72 ml) with the addition of acetic acid (0.7 ml, 2 equiv. mol/mol to TMS groups). The suspension was purged with nitrogen and cooled to -20°C . A 1 M solution of TBAF \cdot 3 H_2O in THF (2 equiv. mol/mol to the TMS groups) was slowly added. The mixture was stirred at -20°C for 30 min and then warmed to ambient temperature overnight. The deprotected polymer was purified by sequential washing with THF (4 \times 50 ml), centrifugation (4427 rcf for 30 min), and decantation.

General procedure of CuAAC click reaction

A suspension of an alkyne-containing polymer (TMS-deprotected CNFs, DEG-PgA-CNF 4 mg (dry), 10 μmol alkyne groups in theory) in DMSO (1.6 ml), and a solution of 3-azido-7-hydroxyl-coumarin in

DMSO (5 mM, 2 equiv. mol/mol to alkyne groups) was mixed under an inert atmosphere of nitrogen. Separately, a solution of CuSO_4 (20 M aq., 0.15 equiv. mol/mol to alkyne groups) and sodium ascorbate (100 mM aq., 3 equiv. mol/mol to alkyne groups) in H_2O was deoxygenated and then transferred in the suspension. The resulting suspension was covered by aluminum foil and stirred under nitrogen at room temperature for 24 h. The product was purified by sequential washing with DMSO (4×5 ml), centrifugation (4427 rcf for 30 min), and decantation.

The same procedure was performed for labeling DEG-PgA-CNFs with fluorescent dyes AF 488 and ATTO 633, respectively, except 0.5 mg azide dye was used for 1 g DEG-PgA-CNFs (1% w/w).

Blending of PVA with modified CNFs

Two concentrations of PVA/DMSO solution were prepared: 5–10%. PVA was dissolved in DMSO at 80 °C with constant stirring and cooled down to room temperature. The suspension of modified CNFs with different dyes in DMSO was fully blended into each PVA/DMSO solution, respectively, resulting in the final concentration of all modified CNFs at 0.5% w/w.

Characterization

Fourier transform infrared spectroscopy equipped with an attenuated total reflection (ATR-FTIR) was performed using a Bruker Vector 33 spectrometer. All spectra were obtained as means of 60 scans in the spectral region of $3600\text{--}550\text{ cm}^{-1}$, with a spectral resolution of 4 cm^{-1} .

Ultraviolet–visible (UV–Vis) spectroscopy was carried out with a Lambda 65 UV–vis Spectrometer. Absorption spectra were measured in DMSO from 380 to 900 nm with a resolution of 1 nm in a 10 mm quartz cuvette.

Proton nuclear magnetic resonance ($^1\text{H-NMR}$) experiments were performed on a Bruker Avance-III spectrometer HD 400 MHz operating at 400 MHz at room temperature. Samples were dissolved in chloroform- d and transferred to NMR tubes.

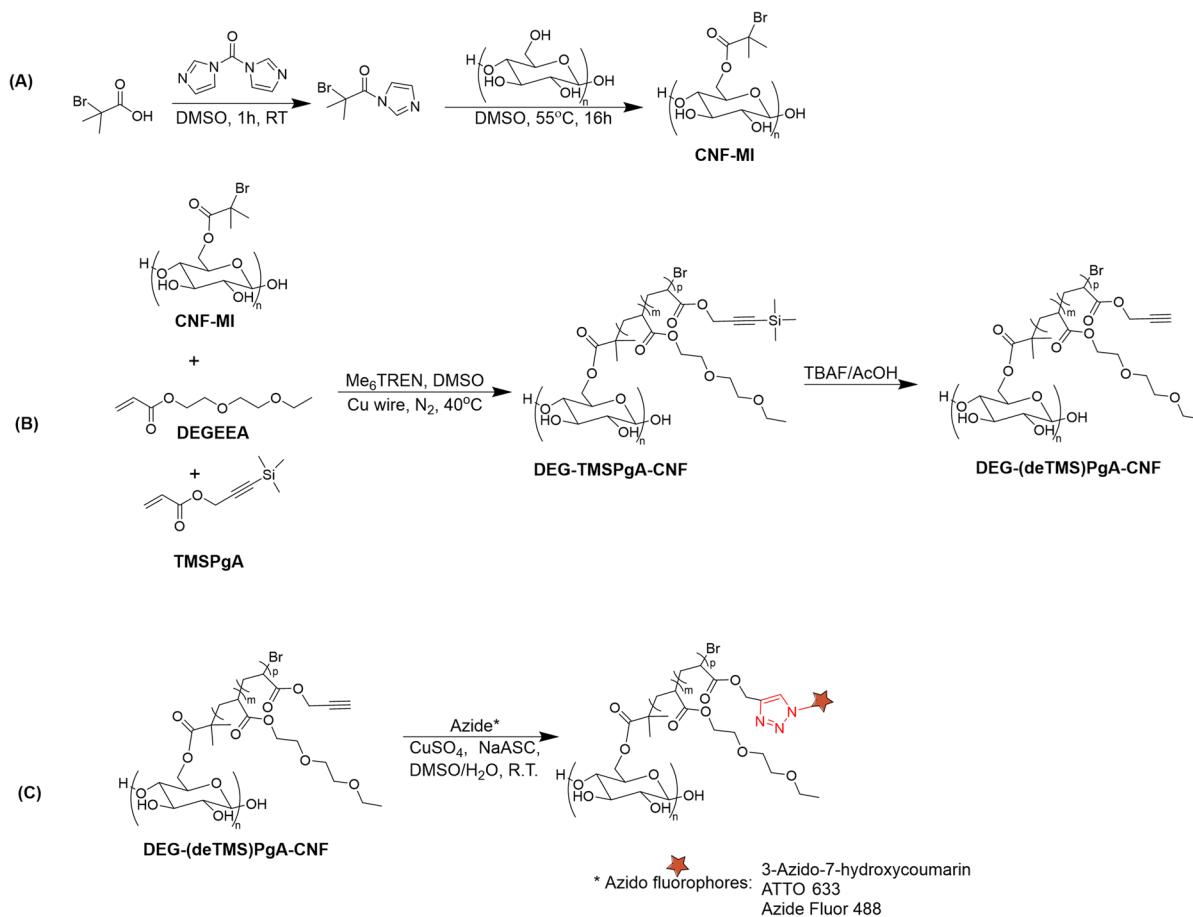
All ^{13}C NMR spectra were acquired with a Bruker 500 Avance III HD spectrometer at Larmor frequencies of 125–500 MHz for ^{13}C and ^1H , respectively.

The samples were packed in 4 mm zirconia rotors to carry out magic angle spinning (MAS) with a spinning rate of 8 kHz. Ramped cross-polarization (CP) ^{13}C MAS NMR spectra were recorded with a ^{13}C nutation frequency of 10 kHz and a contact time of 1.5 ms. All spectra were obtained by Fourier transform of the FIDs, and the chemical shifts were quoted relative to neat tetramethylsilane (TMS).

The morphology of modified CNFs in PVA was observed via ultra-high-resolution field emission scanning electron microscopy (FE-SEM) of the Hitachi S-800. The dried samples were mounted on sample supports using carbon tape and coated with a 5 nm layer of Pd/Pt with a Cressington 208HR under an inert atmosphere.

Stimulated Emission Depletion Microscopy (STED) super-resolution imaging were performed on 1.5H fixed coverslips using a STEDYCON scanner with 488, 561 and 640 nm excitation lasers together with a 775 nm STED laser (all pulsed) (Abberior Instruments GmbH, Göttingen, Germany). The STEDYCON was attached to a Zeiss Axio-imager Z2 with a $100 \times / 1.46$ NA oil immersion Apochromat objective. Depletion power was set to achieve a resolution of 40 nm, the pinhole was set at $50\text{ }\mu\text{m}$, and the sampling rate was fixed at 20 nm/px. The samples were dried on cover glasses under vacuum and mounted on slide glasses with Abberior MOUNT embedding media.

Deconvolution and post-process were used by software Huygens Essential and Zeiss Zen. We used iterative CMLE (Classical Likelihood Estimation) deconvolution with a maximum of 30 iterations to prevent over-deconvolution using the Huygens Professional software package. This algorithm has been validated multiple times and is considered standard in deconvolution. The software package includes a module to estimate the point spread function (PSF) specifically for STEDYCON scanners fitted with a 1.46 NA lens. Moreover, the theoretical PSF was tuned to match the experimental PSF as closely as possible, providing the software with input regarding pixel size (sampling), refractive index mismatch, depth of imaging, wavelength, projected pinhole radius and STED saturation factor.



Scheme 1 General chemical strategy for the polymer grafting onto the cellulose nanofibril (CNF) surface (a) synthesis of the CNF-based macroinitiator (CNF-MI); b Di(ethylene glycol) Ethyl Ether Acrylate (DEGEEA) and the Protected Alkyne

Groups Acrylate (TMSPgA) grafted onto the CNFs via surface initiated SET-LRP, followed by the sequential deprotection of trimethylsilyl groups; c Cu-catalysed azide-alkyne cycloaddition between alkyne-induced CNFs and azido-fluorophore

Results and discussion

Solvent exchange and chemical surface modification of CNFs

Firstly, the unmodified pristine CNFs, initially suspended in water, were solvent exchanged to DMSO. This exchange procedure is an exothermic process due to the water—DMSO interaction and the hydrogen bonding formation between the CNFs and the DMSO. (Voronova et al. 2006) After this, the pristine CNFs, already suspended in DMSO, were surface modified and converted to the CNF-based macroinitiator (CNF-MI) through an esterification reaction between the hydroxy and the 2-bromo-2-methylpropionic acid

(in DMSO). The immobilization of the initiator onto the CNFs, is a one-step process, which will allow us later to directly grow a polymer via the SET-LRP reaction onto the CNF surface using the macroinitiator unit as an anchoring point on the surface. Through this surface-initiated polymerization, the properties of the CNFs can be fully tuned and optimized. The chemical reaction pathway is shown in Scheme 1a.

The correct and successful surface modification was monitored with ATR-FTIR (Fig. 2) and CP-MAS ^{13}C NMR (Fig. 3) spectroscopy. The unmodified CNF spectra show the characteristic bands of the cellulose, with bands localized at 3320 cm^{-1} (O—H), 2950 and 2895 cm^{-1} (C—H), 1430 cm^{-1} (C—H), and 1161 cm^{-1} (C—O—C). In addition to those characteristic bands,

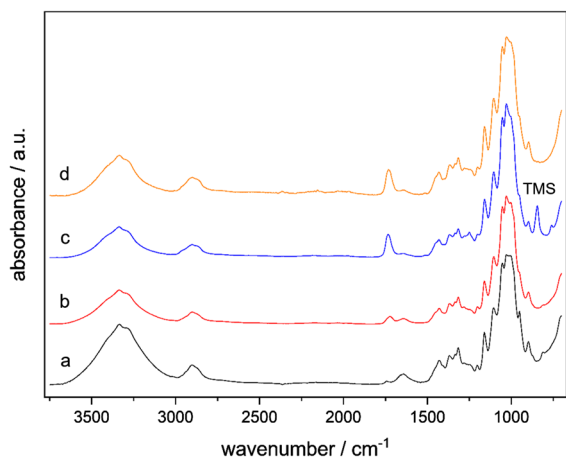


Fig. 2 ATR-FTIR spectra of **a** Pristine CNFs, **b** CNF-MI, **c** DEG-TMSPgA-CNFs and **d** DEG-PgA-CNFs

the spectrum of the CNF-MI shows an absorption band localized at 1733 cm^{-1} ($\text{C}=\text{O}$), which is attributed to the vibration of the carbonyl group of the ester group. The CP-MAS ^{13}C NMR spectra of unmodified CNFs & CNF-MI, along with the peak assignments, are exposed in Fig. 3. The pristine CNFs have the characteristic cellulose NMR peaks located at 105 ppm (C1, glycosidic bonds), 84 ppm (C4), 72 ppm (C2, C3, C5), 62 ppm (C6) for the carbon on surface sites, and at 89 ppm (C4), 76 ppm (C2, C3, C5), 65 ppm (C6) for the crystalline fibril interior (Gårdebjerg et al. 2015). Besides the characteristic signals from pristine CNFs, the spectrum of CNF-MI showed an extra peak at 31 ppm (C9, C10). Although the carbonyl signals were not displayed through the solid-state CP-MAS ^{13}C NMR, the successful conversion of CNFs into CNF-MI can be confirmed by combining the results of both ATR-IR and CP-MAS ^{13}C NMR. Within this strategy, chemically modified CNFs can thus act as a macroinitiator, and initiate the polymerization of two different monomers, for the “grafting from” of polymer chains growing directly on the CNF surface.

Surface initiated SET-LRP: growth of the statistical copolymer DEG-PgA-CNF

The surface-initiated grafting polymerization was carried out in a one-step procedure via SET-LRP. The aim was to initiate the growth of statistical copolymers made of di (ethylene glycol) ethyl ether acrylate

(DEGEEA) (Zhang et al. 2014b; Anastasaki et al. 2014; Bao et al. 2018) and a monomer containing alkyne functions in the presence of the CNF-based macroinitiator. The SET-LRP of the two monomers was proceeded in the presence of a Cu(0) wire and a tetradentate tertiary amine ligand (Me_6TREN).

In our first attempt, we tried to initiate the SET-LRP of the unprotected propargyl acrylate. Unfortunately, the CNFs could not be modified within this approach. Some side reactions of alkyne functions took place during Cu-catalyzed radical polymerizations, as the terminal alkyne groups are prone to oxidative coupling (Glaser coupling) in the presence of Cu^1 and oxidants, (Storms-Miller and Pugh 2015) for example, while air exposure during the post-treatment. Therefore, this work employed a protection/deprotection strategy of the alkyne groups. This strategy allowed us to overcome those unwanted side reactions during copolymerization. Firstly, trimethylsilyl propargyl acrylate (TMSPgA) was synthesized through the esterification reaction of acryloyl chloride and 3-(trimethylsilyl) propargyl alcohol; (Malkoch et al. 2005) after the protection step, both monomers TMSPgA and DEGEEA were copolymerized onto the CNF surface (DEG-TMSPgA-CNFs). In the final step, the trimethylsilyl protecting group was removed using a tetra-*n*-butylammonium fluoride (TBAF) solution in THF and acetic acid (AcOH) as the buffering agent to finally yield the deprotected alkyne group, DEG-PgA-CNFs (Scheme 1b).

The efficiency of the co-grafting polymerization of DEGEEA and TMSPgA onto CNFs was first evaluated with ATR-FTIR (Fig. 2c). Compared to the CNF-MI spectra, the carbonyl band at 1733 cm^{-1} in the DEG-TMSPgA-CNFs and DEG-PgA-CNFs spectrum drastically increase due to the multiplication of the ester group number of the polymer repeating unit. The band localized at 1250 cm^{-1} and 700 cm^{-1} are attributed to trimethylsilyl groups (TMS, $\text{Si}(\text{C}-\text{H}_3)$) of the TMS-protected alkynes. This also confirmed that no cleavage of the trimethylsilyl group from the TMS-protected alkynes occurred during and after the surface-initiated polymerization onto CNFs.

After the deprotection step, and the removal of the trimethylsilyl groups from the CNF surface, the absorption bands located at 1250 cm^{-1} and 700 cm^{-1} disappear from the ATR-FTIR spectra, while the signals from carbonyl remain the same. Unfortunately, the alkyne groups on CNFs are more difficult to

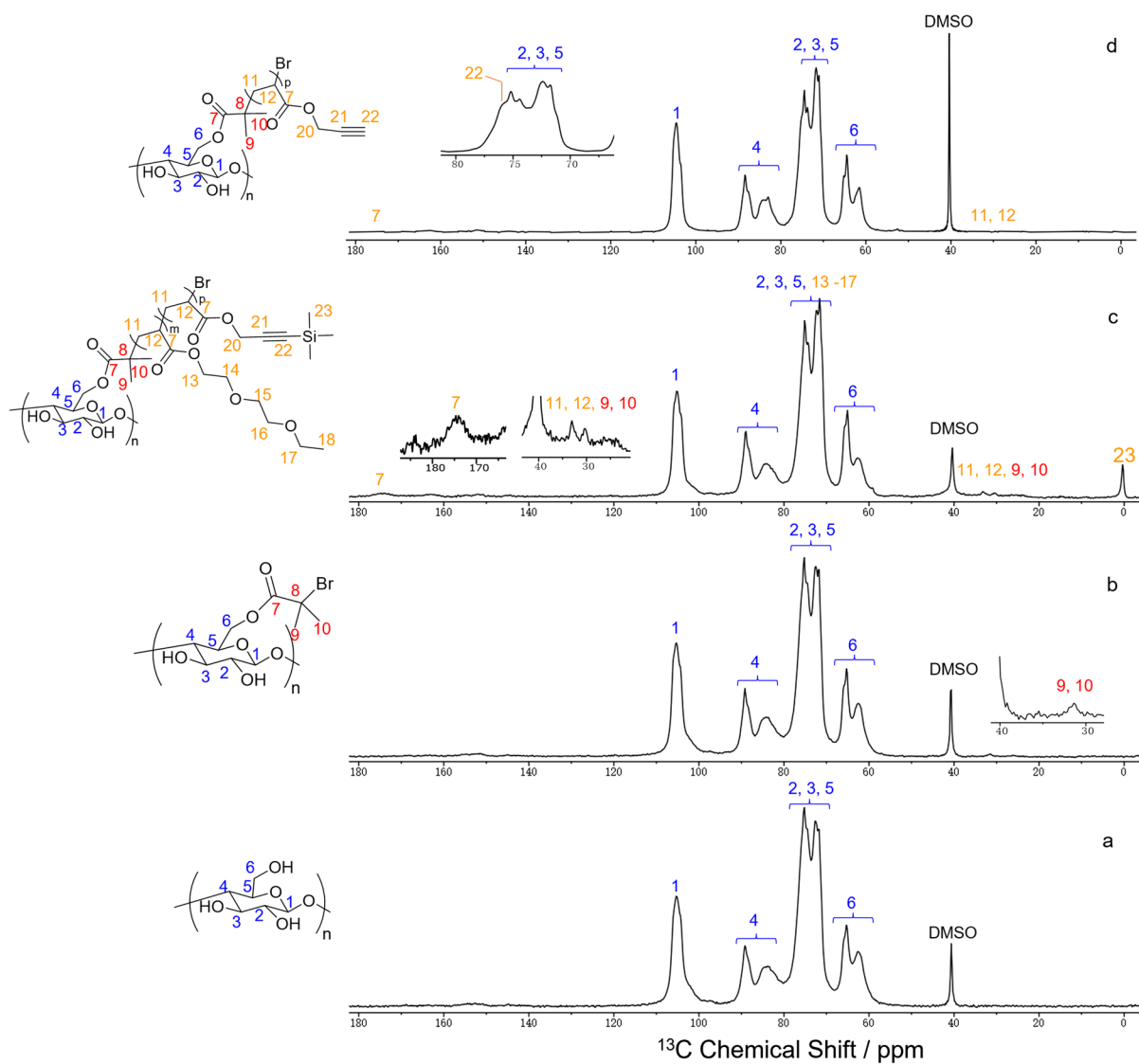


Fig. 3 CP/MAS ^{13}C -NMR spectra of **a** Pristine CNFs, **b** CNF-MI, **c** DEG-TMSPgA-CNF, **d** PgA-CNFs

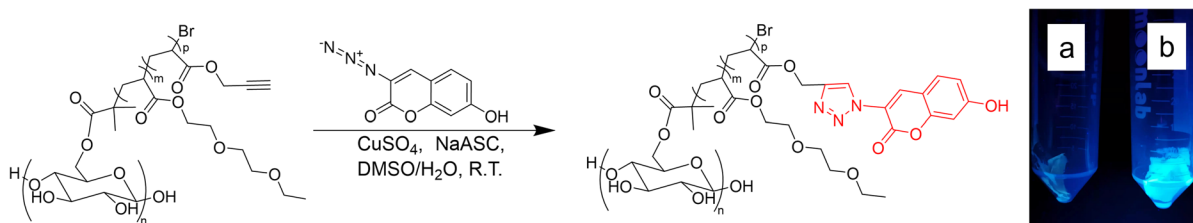


Fig. 4 Click chemistry reaction of DEG-PgA-CNFs and 3-azido-7-hydroxycoumarin: **a** DEG-PgA-CNFs before the reaction, **b** After the reaction with the fluorescence of 3-azido-7-hydroxycoumarin

observe on the spectrum and it remains difficult to distinguish and differentiate them from the background clearly. We further extend the characterization of the product with the solid-state CP-MAS ^{13}C -NMR and the spectra are exposed in Fig. 3. The CP-MAS ^{13}C -NMR results are consistent with the results obtained with the ATR-FTIR. Besides observing, the characteristic CNF peaks, an additional peak located at 175 ppm (C7) appear and is attributed to the carbonyl bonds and the accumulated ester groups of the polymer repeating units. The peak at 0 ppm (C23) is attributed to the trimethylsilyl protecting group. After the deprotection step, besides the disappearance of trimethylsilyl groups, a signal at 76 ppm (C22) is detected from a broad peak overlapped CNFs (C4) and is attributed to the deprotected alkyne groups.

Click chemistry azide-alkyne cycloaddition of alkyne modified CNFs and various fluorescent azides dyes

The proof of the presence of alkyne functions via click chemistry with 3-azido-7-hydroxycoumarin

As mentioned earlier, the surface modification of CNFs through SET-LRP and various monomers was effective; however, the direct presence of the alkyne functions onto CNFs was difficult to observe, and their presence has to be confirmed through the combination

of two characterization techniques. Therefore, to ensure the presence of the alkyne function onto our CNFs, we performed a test click reaction with the DEG-PgA-CNFs and the 3-azido-7-hydroxycoumarin in DMSO/H₂O (Fig. 4). An interesting parameter is the 3-Azido-7-hydroxycoumarin fluorescence properties can only be revealed when the dye reacts with an alkyne function and form 1,2,3-triazole through Cu-catalyzed cycloaddition reactions, otherwise the fluorescence is quenched (Sivakumar et al. 2004). After few minutes, the CNF suspension became highly fluorescent, and after several purification steps, the luminescent CNFs were isolated (Fig. 4).

It should also be stated that this Cu-catalyzed cycloaddition reaction was also performed using unmodified CNFs and CNF-MI (within the same Cu-catalyzed condition). In both cases, the suspensions remained colorless even under UV-light, no reaction occurred since no alkyne function was present (Fig. 4, Picture a). Excessive reagents are unfortunately generally needed to ensure the molecules attachment onto the CNF surface, while the exact amount is still challenging to estimate and even more specifically in our case. In our work, the incorporated reagents for click chemistry were calculated on the free alkyne groups of DEG-PgA-CNFs with 100% chemical conversion of SET-LRP and deprotection (1 μmol alkyne groups in 0.4 mg DEG-PgA-CNFs, dry). 2 equivalents of azide based on alkyne groups were used for

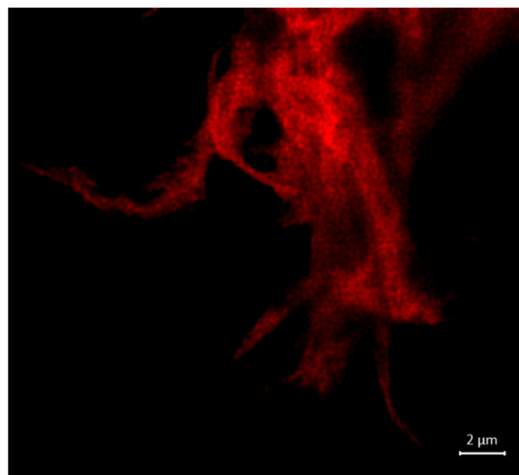
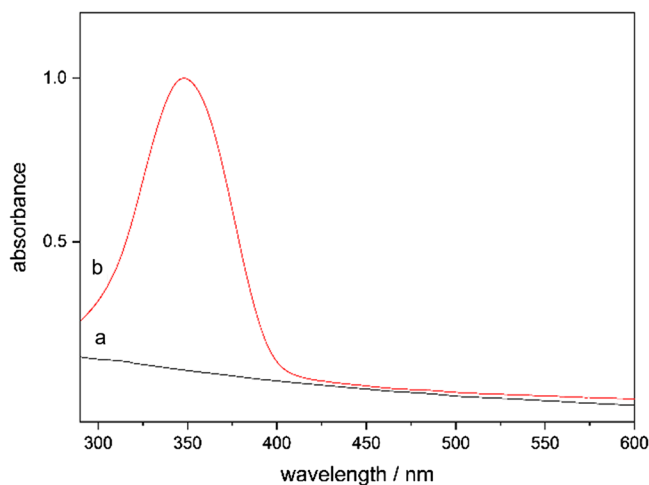
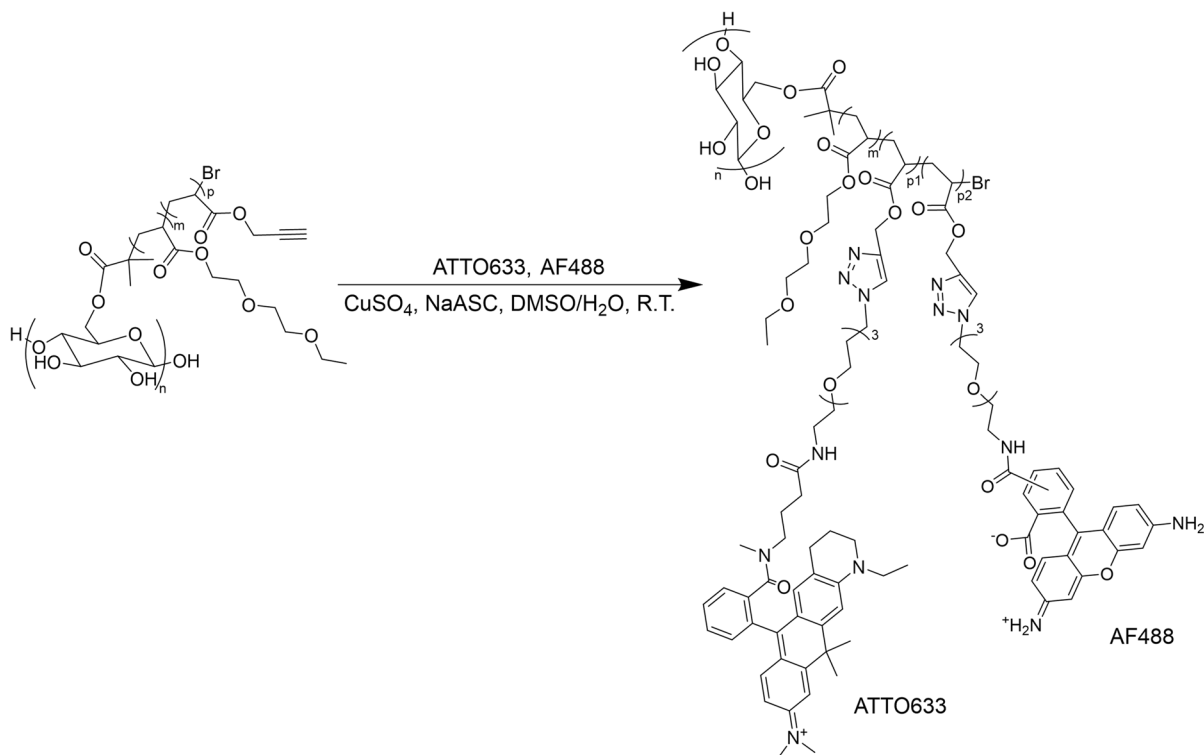


Fig. 5 Left UV-Vis spectra of **a** Pristine CNFs, **b** Coumarin@DEG-PgA-CNFs; Right Confocal scanning laser microscopy imaging of coumarin derivate labelled on the polymer modi-

fied CNFs (Fluorescence image obtained at an excitation wavelength of 488 nm, red color)



Scheme 2 Preparation of the luminescent cellulose nanofibrils: Labeling of the two dyes ATTO633 and AF488 onto the polymer modified CNFs (DEG-PgA-CNF) through click-chemistry

fast reactions and concerning low alkyne contents; the concentration of the Cu catalyst was controlled at $250 \mu\text{M}$ for efficient reactivity. After several purification step, the modified luminescent CNF gel was isolated (Fig. 4, Picture b).

The suspension was first characterized through UV–Vis spectroscopy and the spectra is exposed in Fig. 5. The spectra of the luminescent CNFs show the presence of a strong absorption band at 350 nm , while the spectra of the unmodified CNFs do not show any distinct absorption band. This demonstrates the successful grafting of the coumarin azide dye onto the polymer modified CNFs through a Cu-catalyzed cycloaddition with the alkyne groups (DEG-PgA-CNF). Confocal laser scanning microscopy (CLSM) was used to image the coumarin labeled on the copolymer modified CNFs (Fig. 5, Right). From this CLSM image, it can be seen that fluorescent spots were only observed along the CNFs. Moreover, the fluorescence distribution appears to be homogeneous on the fibril surface.

Click chemistry strategy for STED high-resolution imaging of modified CNFs

As exposed previously, it was possible to label a fluorescent coumarin dye derivative onto the CNFs through a Cu-catalyzed click post-modification reaction. Since the concept worked, our goal was now to label the CNFs with a specific dye and perform STED measurements for single-molecule studies. For this purpose, two dyes the ATTO633 & AF488 were labeled onto the CNFs as exposed in Scheme 2. Both of those dyes have a specific purpose as described in the following.

The AF488 (Abs/Em = $501/525 \text{ nm}$), was initially used to easily localize the CNFs under the microscope. This bright green fluorescent dye is already widely used in confocal microscopy and also has a good spectral separation with the ATTO633. The ATTO633 (Abs/Em = $630/657 \text{ nm}$) fluorescent dye is a red-emitting dye, used especially for the STED microscope due to its photophysical properties, high quantum yield and photo-stability. For

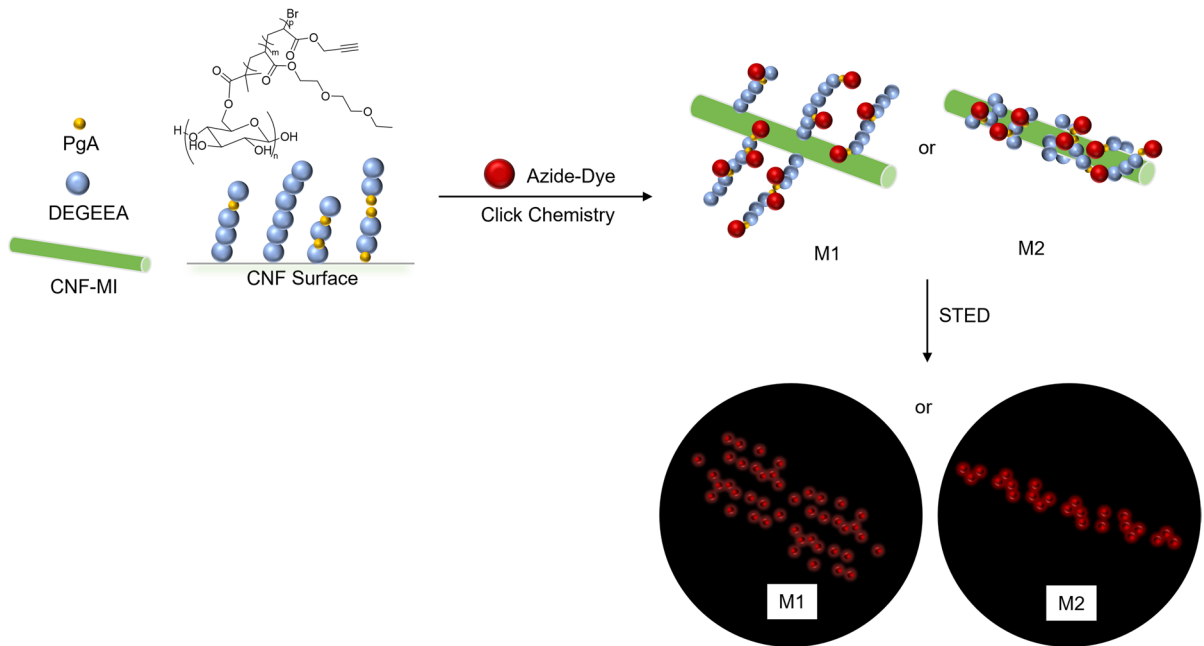
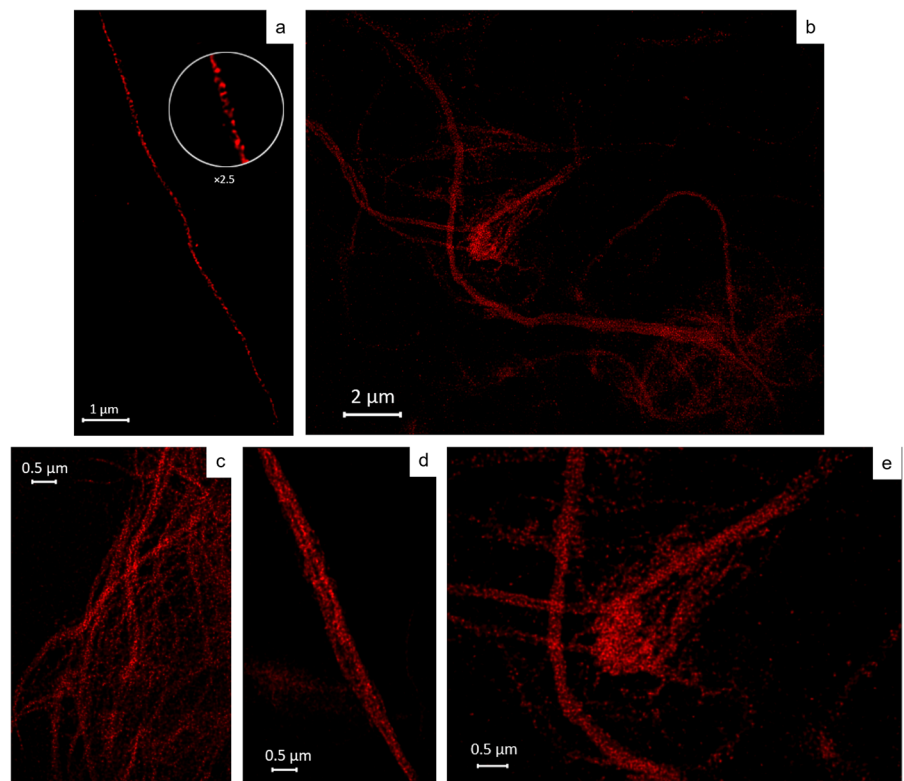


Fig. 6 Schematic illustration of labeling fluorescent dyes on cellulose nanofibril surfaces and hypothetical morphologies of modified CNFs

Fig. 7 Deconvolved STED images of modified cellulose nanofibrils: **a** Isolated fibril, **b** Dispersion state of fibrils, **c** Fibril network, **d** Fibril bundle, **e** Cluster



the purpose of this study, two different batches of fluorescent CNFs were produced, the CNFs labeled with the two dyes AF488 and ATTO633 (AF488&ATTO633@DEG-PgA-CNF) as exposed in scheme 2, and also the CNFs labeled with only the ATTO633 dye (ATTO633@DEG-PgA-CNFs).

As introduced earlier, STED microscopy with the appropriate dyes and the optical scheme can normally achieve a super-high resolution (Fig. 1). For post-processing images, we used deconvolution with a standard algorithm to prevent over-deconvolution, and an experiment specific modelled PSF that was validated measuring 40 nm beads exciting and emitting in the same wavelength ranges as the fibrils.

Therefore, our modified cellulose nanofibrils labeled with special fluorescent dyes as well as in a composite material are ideal objects for investigation with this technique.

STED and high-resolution imaging of modified single CNFs

A suspension of DEG-PgA-CNFs labeled with AF488 and ATTO633 (AF488&ATTO633@DEG-PgA-CNFs) or CNFs only labeled with the ATTO633 (ATTO633@DEG-PgA-CNFs) in DMSO (0.5% w/w) was used for sample preparation to detect isolated modified CNFs and sufficient signals with clean background under the microscope.

We considered hypothetical morphologies of grafted polymer chains stretching away from CNF surfaces (Fig. 6, M1), or wrapping around on CNFs (Fig. 6, M2), which corresponds to fluorescent signals either spreading or wrapping, respectively.

Figure 7 shows a series of deconvolved STED images, in which the fluorophores are represented as red dots and formed into spaghetti-like shapes. For example, in Fig. 7A the fibrils exhibits a fluorescent strip with a width of 56 nm and a length of 9 μm , which match the typical dimension of CNFs produced by mechanical treatments. Interestingly, fluorophores on this strip display a periodical interval (Fig. 7a) with red luminescent dots followed by empty (black) space, which can represent either grafted di(ethylene) glycol chains or unlabeled alkyne function on the CNF surfaces. As mentioned earlier, excess azide dye was employed to ensure the full functionalization of the alkyne groups.

This periodical interval phenomenon was observed among all the CNF images and all our different CNF samples. The study of the morphology of the polymer-modified CNFs revealed that the grafted polymer chains wrap around the CNF surfaces (Fig. 6, M2). In other words, the arrangement of the fluorophores expresses the dimension and morphology of the cellulose nanofibrils and is mostly not influenced by the grafted polymer.

The interactions between several CNF nanostructures were further observed and discussed. Figure 7b provides an overview of the representative CNFs with various inter-fibrillar structures, which could be observed with the STED. The inter-fibrillar nanostructures can be summarized into three types (Fig. 7c–e): homogeneous network, fibril bundle and cluster. The homogeneous network is formed by single fibrils interacting with distances of max. 0.5 μm between them (Fig. 7c); a fibril bundle consists of several aligned fibrils with a thin gap (approx. 50 nm)

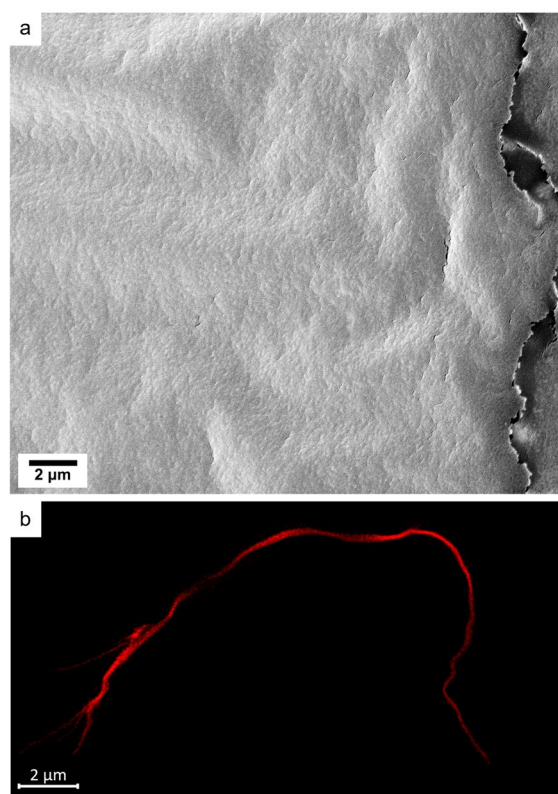


Fig. 8 **a** FESEM image of Fibrils/PVA composite, **b** STED image of fibrils in PVA

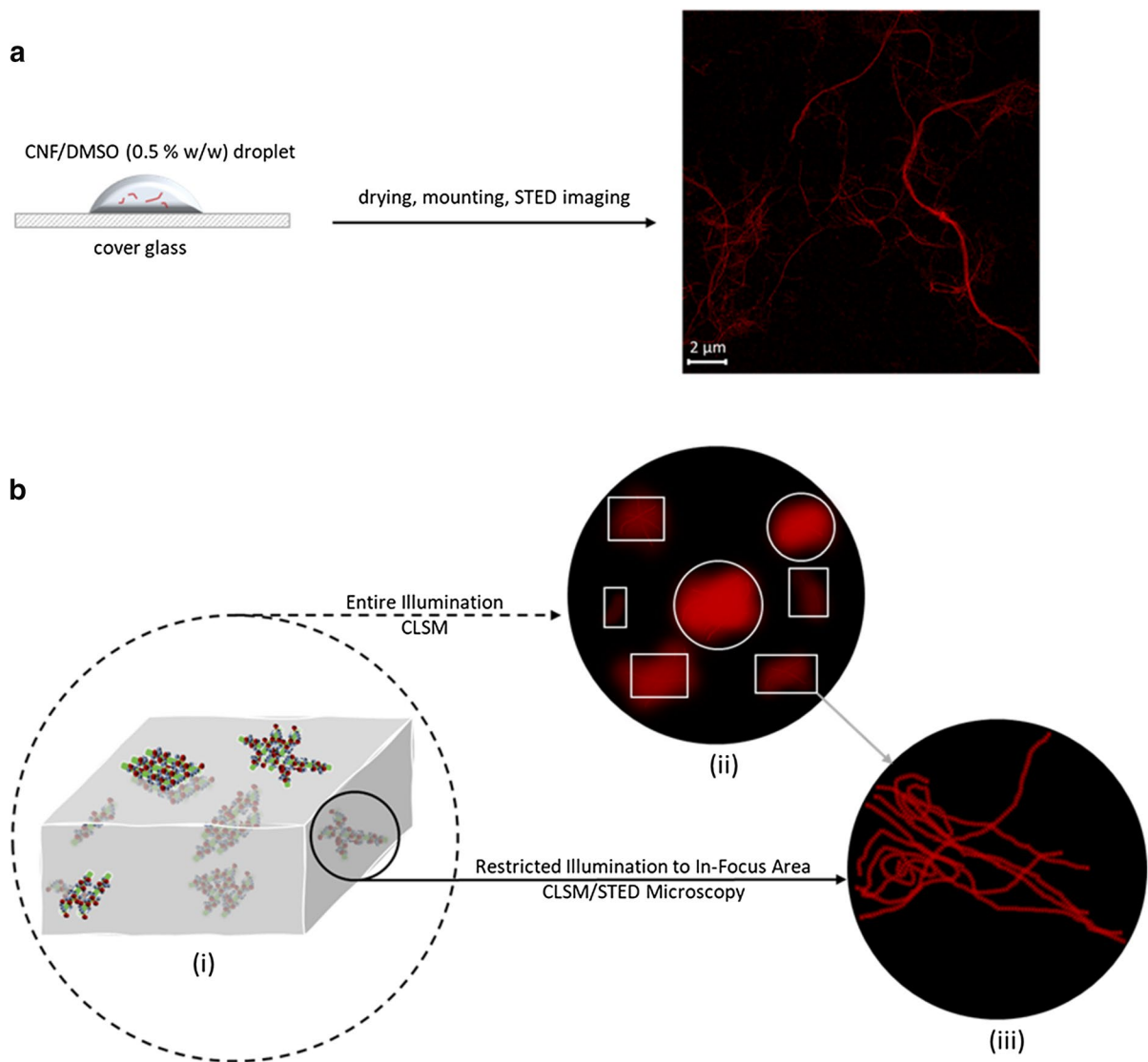


Fig. 9 Schematic illustration of **a** STED imaging of fibrils dried from DMSO, **b** Detecting distribution and morphology of modified CNFs in a PVA composite: (i) Model of modified CNFs in PVA, (ii) Concept map overview of modified CNFs in

PVA: “In-Focus” lights in circle, “Out-of-Focus” lights in rectangle, (iii) Concept image of focused modified CNF structure in PVA

in between (Fig. 7d); a cluster involves all entangled fibrils/bundles with a minimal (below 10 nm) gap (Fig. 7e).

More isolated fibrils or homogeneous networks are desired when dispersing CNFs in a solvent, e.g. DMSO, to form a stable suspension. For this, monomers with more extended hydrophilic groups, such as oligo(ethylene glycol), can be used for modifying the CNF surface, as the long hydrophilic groups interact

effectively with solvent molecules (DMSO&H₂O) and better suppress the inter-fibril interaction.

It should also be noted that for a same chromophore, the brightness of the fluorescent signals is directly proportional to the fluorophore concentration. This concentration effect can, in some cases, indicate an inhomogeneous dispersion of the CNFs, e.g. high density of dye due to large fibril aggregation. This aggregation phenomenon will lead to complete

saturation of the fluorescence signal and STED measurement can therefore not be performed.

STED and high-resolution imaging of modified CNFs in PVA

As previously introduced, the morphology of CNFs in composites is generally studied via microscopic techniques, such as AFM, SEM and TEM. A downside of these techniques is that the distinction between CNFs and the matrix (e.g. PVA) is difficult or not possible. For instance, Fig. 8a shows the surface of a modified CNF/PVA composite detected by FESEM, where the modified CNFs are fully buried. A significant

difference can be obtained by STED microscopy that modified CNFs labeled with fluorescent dyes are illuminated and revealing not only their morphology but also the spatial configuration within a PVA matrix (Fig. 8b).

We here firstly investigated the possibility to image isolated CNF nanostructure through STED microscopy. We now aimed to extend the study and see if the morphology of the modified CNFs embedded in a PVA composite could be investigated through a combination of CSLM and STED microscopy (Fig. 9). CSLM microscopy is a convenient microscopic technique, which can illuminate the entire specimen of interest and localized all the chromophores rapidly

Fig. 10 Microscopic images of modified CNFs (0.5% w/w) in PVA (10% w/w): **a** Deconvolved confocal image of cluster of AF 488&ATTO 633@ DEG-PgA-CNFs, **b**, Map overview of ATTO633@ DEG-PgA-CNFs in PVA Matrix, **c** Deconvolved STED image of cluster of ATTO633@DEG-PgA-CNFs, **d** Intrafibrillar network, **e** Single fibrils from a bundle

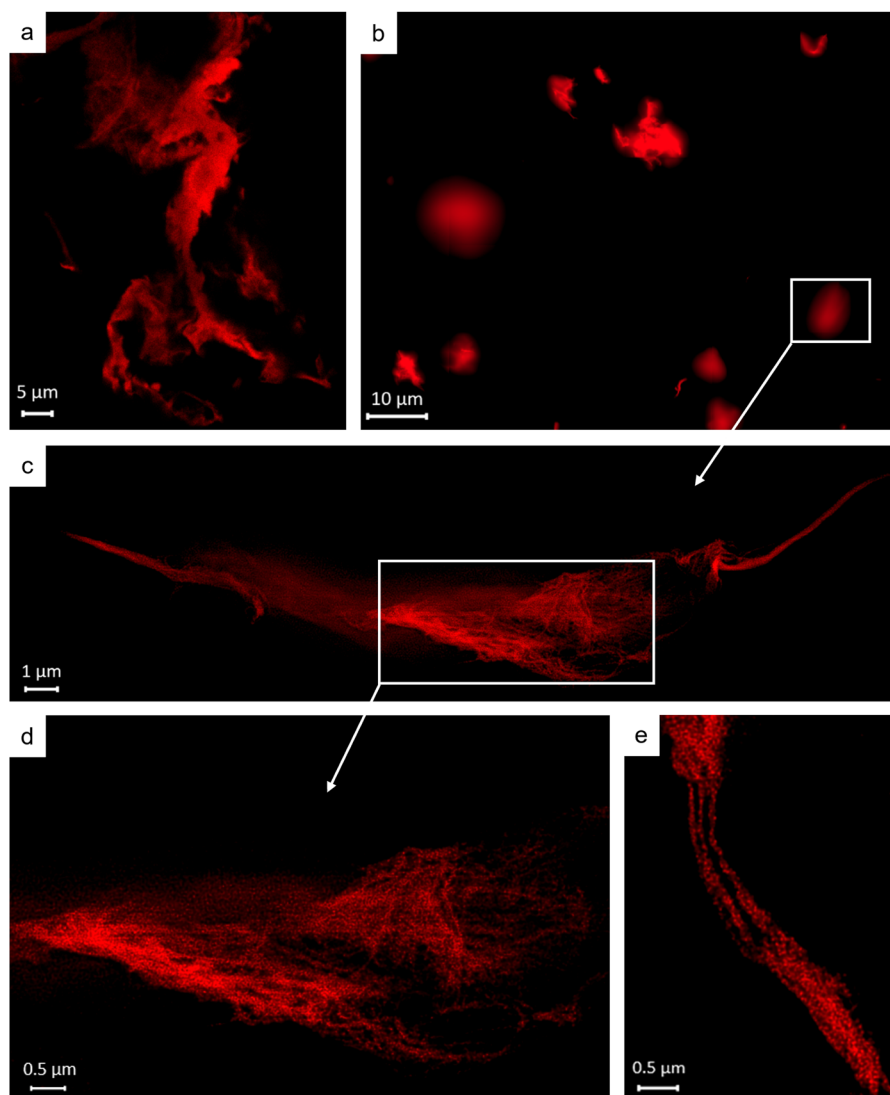
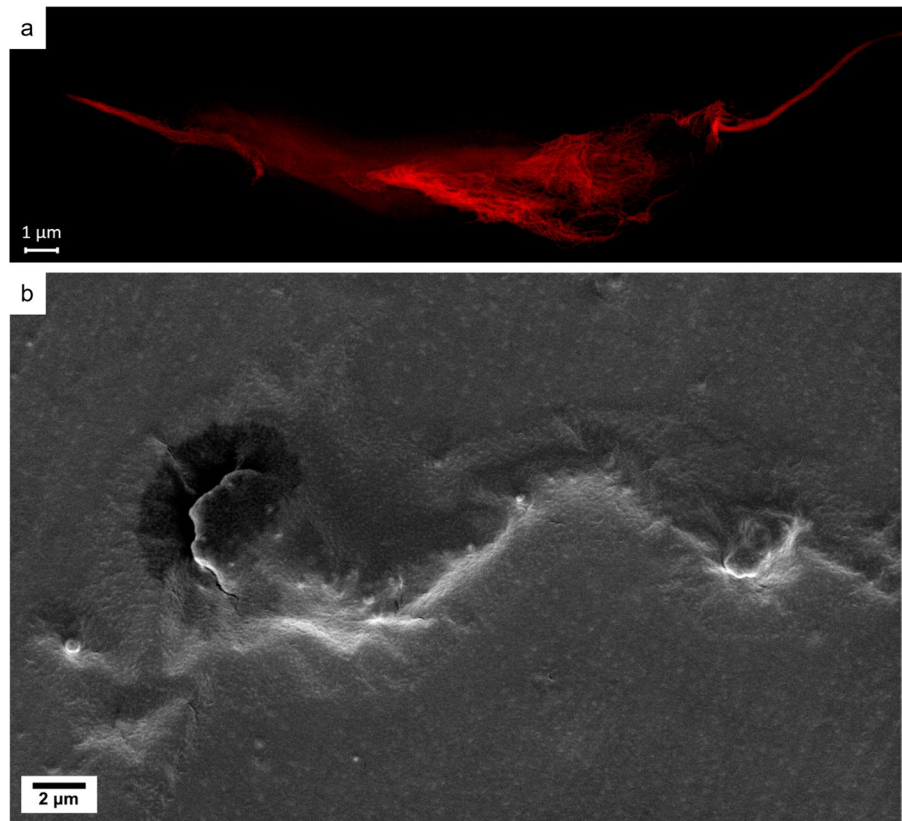


Fig. 11 ATTO633@DEG-PgA-CNFs in a PVA matrix: **a** STED image, **b** FESEM Image



at once. Combining CSLM and STED microscopy, we were able to localize the fluorescently labeled CNFs (AF488&ATTO633@DEG-PgA-CNFs and ATTO633@DEG-PgA-CNFs) and observe their distribution in the three dimensional PVA matrix (Fig. 9b). Despite the fact that both dyes had a specific function in our materials, we rapidly found out that the behavior of those two samples was completely different when mixed with the PVA matrix, and only when mixed.

In the previous STED observation, fibrils were directly deposited on a cover glass through solvent evaporation, and all the fibrils were all on the same focal plane (Fig. 9a). But now, CNFs are distributed in a PVA matrix with a thickness of approx. 10 μm, creating a 3D environment (Fig. 9b). CNFs can either disperse or form aggregates in different locations of the PVA matrix at different heights, and therefore be either on the “in-focus” plane or be observed as blurry spots when CNFs are on a “out-of-focus” plane.

The distribution and the localization of the CNFs in the PVA matrix were firstly observed with the CSLM microscope, so a large overview could be created (Fig. 10a, b). As mentioned previously, both dyes had a specific function in our materials, but their behavior was completely different when mixed with the PVA matrix. In Fig. 10a, the AF488&ATTO633@DEG-PgA-CNF show only large aggregates (between 50–100 μm). Those aggregates could not be studied by STED as the density of chromophore was too substantial, creating a complete saturation of the signal.

Interestingly for the other sample, ATTO633@DEG-PgA-CNFs, much smaller aggregates could be first observed with the CSLM (Fig. 10b). However, when those fibrils were studied with the STED, clear inter-fibrillar structures, fibril networks were observed, with a distinct distance between each fibril.

More detailed structures inside the aggregates of ATTO633@DEG-PgA-CNFs were revealed (Fig. 10c–e). Fibrils still formed a relatively

homogeneous network with a distance of max. 0.2 μm in between; fibril bundles are associated tightly in PVA.

Through STED microscopy, the modified CNFs embedded in a PVA composite are finally exposed. Now we can extrapolate fibrils detected by FESEM. Figure 11b show a classic grey-scale image obtained by FESEM, which shows an aggregate of ATTO633@DEG-PgA-CNFs on the outer face of a PVA matrix, while the deeper structure remains buried. To sum up, STED microscopy manifests its remarkable performance for the fibril morphology study.

Conclusions

We have devised a tunable strategy to surface modify CNFs via a combination of Cu^0 -mediated radical polymerization and Cu^I -catalyzed alkyne-azide cycloaddition. The spectra of ATR-IR and solid-state ^{13}C -NMR demonstrated that CNF-based macroinitiators were synthesized and initiated the growth of statistical copolymers on CNF surfaces via SET-LRP. Furthermore, the effectivity of induced terminal alkyne groups was proven by the restored fluorescence of 3-azido-7-hydroxycoumarin via click chemistry. This versatile strategy could be adapted to modify CNFs with desired properties for applications in a broad scope.

The novelty of our work lies in the morphology study of modified CNFs investigated through laser scanning microscopy and STED microscopy. With these techniques, modified CNFs embedded in a PVA composite were also detected and visualized nondestructively.

In deconvolved STED images, we found out that the grafted polymer chains wrapped around CNFs and thus the dimension of CNFs were outlined. We measured over 30 specimens with widths ranging from 56 to 68 nm and lengths of several micrometers, which match the typical dimension gained by mechanical treatment CNF production. The present study has explored the behaviors of CNFs dried from DMSO, including single fibrils, fibril networks, fibril bundles and clusters. The behavior of CNFs in a DMSO suspension needs to be explored further.

The distribution and morphology of modified CNFs embedded in a PVA composite with a thickness

of approx. 10 μm were revealed through a widefield microscope and CLSM/STED microscopes.

Acknowledgments We thank T. Potsch and Dr. A. Olbrich the Thünen Institute of Wood Research for FESEM imaging. We acknowledge Dr. P. Hernandez-Varas from the Core Facility for Integrated Microscopy, Faculty of Health and Medical Sciences, University of Copenhagen for STED imaging service.

Author contributions All authors: XJ, BM, JN contributed to the study conception and the design of the experiments. The synthesis and materials preparations were performed by XJ. The data collection and analysis were performed by XJ, BM, JN. All authors: XJ, BM, JN contributed to write the first manuscript draft and the submitted version. Participants or animals performed by any of the authors.

Funding Open Access funding enabled and organized by Projekt DEAL. J. Navarro, and all authors thank Fachagentur Nachwachsende Rohstoffe e.V. (FNR/BMEL, Project Holz-Mat3D, number 2220HV024X), for financial support.

Data availability The authors declare that the data supporting the findings of this study are available within the article.

Declarations

Conflict of interest The authors declare no competing financial interests.

Consent for publication All authors agreed with the paper content and all gave explicit consent to submit the paper to Cellulose. Moreover, we obtained consent from the responsible authorities at the institute of wood science where the work has been carried out, before the paper was submitted.

Ethical standard The authors certify that this manuscript is original and has not been published elsewhere and will not be submitted for publication in another journal while being considered by Cellulose. Moreover, this study is not split up into several parts to increase the quantity of submissions and submitted to several journals. This article does not contain any studies with human and/or Animals.

Open Access This article is licensed under a Creative Commons Attribution 4.0 International License, which permits use, sharing, adaptation, distribution and reproduction in any medium or format, as long as you give appropriate credit to the original author(s) and the source, provide a link to the Creative Commons licence, and indicate if changes were made. The images or other third party material in this article are included in the article's Creative Commons licence, unless indicated otherwise in a credit line to the material. If material is not included in the article's Creative Commons licence and your intended use is not permitted by statutory regulation or exceeds the permitted use, you will need to obtain permission directly from the copyright holder. To view a copy of this licence, visit <http://creativecommons.org/licenses/by/4.0/>.

References

- Aïssa K, Karaaslan MA, Renneckar S, Saddler JN (2019) Functionalizing cellulose nanocrystals with click modifiable carbohydrate-binding modules. *Biomacromol* 20:3087–3093. <https://doi.org/10.1021/acs.biomac.9b00646>
- Akeroyd N, Klumperman B (2011) The combination of living radical polymerization and click chemistry for the synthesis of advanced macromolecular architectures. *Eur Polym J* 47:1207–1231. <https://doi.org/10.1016/j.eurpolymj.2011.02.003>
- Anastasaki A, Nikolaou V, Simula A et al (2014) Expanding the scope of the photoinduced living radical polymerization of acrylates in the presence of CuBr₂ and Me₆Tren. *Macromolecules* 47:3852–3859. <https://doi.org/10.1021/ma500787d>
- Arof AK, Mat Nor NA, Aziz N et al (2019) Investigation on morphology of composite poly(ethylene oxide)cellulose nanofibers. *Mater Today Proc* 17:388–393. <https://doi.org/10.1016/j.matpr.2019.06.265>
- Babi M, Fatona A, Li X et al (2022) Efficient labeling of nanocellulose for high-resolution fluorescence Microscopy applications. *Biomacromol* 23:1981–1994. <https://doi.org/10.1021/acs.biomac.1c01698>
- Bao C, Yin Y, Zhang Q (2018) Synthesis and assembly of laccase-polymer giant amphiphiles by self-catalyzed CuAAC click chemistry. *Biomacromol* 19:1539–1551. <https://doi.org/10.1021/acs.biomac.8b00087>
- Beaumont M, Bacher M, Opietnik M et al (2018) A general aqueous silanization protocol to introduce vinyl, mercapto or azido functionalities onto cellulose fibers and nanocelluloses. *Molecules* 23:1427. <https://doi.org/10.3390/molecules23061427>
- Busko D, Balushev S, Crespy D et al (2012) New possibilities for materials science with STED microscopy. *Micron* 43:583–588. <https://doi.org/10.1016/j.micron.2011.10.003>
- Calovi S, Soria FN, Tønnesen J (2021) Super-resolution STED microscopy in live brain tissue. *Neurobiol Dis* 156:105420. <https://doi.org/10.1016/j.nbd.2021.105420>
- Chiefari J, Chong(Bill) YK, Ercole F, Krstina J, Jeffery J, Le TP, Mayadunne RTA, Meijs GF, Moad CL, Moad G, Rizzardo E, Thang SH (1998) Living free-radical polymerization by reversible addition–fragmentation chain transfer: the RAFT process. *Macromolecules* 31(16):5559–5562. <https://doi.org/10.1021/ma9804951>
- Edwards JV, Prevost N, Sethumadhavan K et al (2013) Peptide conjugated cellulose nanocrystals with sensitive human neutrophil elastase sensor activity. *Cellulose* 20:1223–1235. <https://doi.org/10.1007/s10570-013-9901-y>
- Fazeli M, Keley M, Biazar E (2018) Preparation and characterization of starch-based composite films reinforced by cellulose nanofibers. *Int J Biol Macromol* 116:272–280. <https://doi.org/10.1016/j.ijbiomac.2018.04.186>
- Fleischmann S, Percec V (2010) SET-LRP of methyl methacrylate initiated with CCl₄ in the presence and absence of air. *J Polym Sci Part A Polym Chem* 48:2243–2250. <https://doi.org/10.1002/pola.24000>
- Friedemann K, Turshatov A, Landfester K, Crespy D (2011) Characterization via two-color STED microscopy of nanostructured materials synthesized by colloid electrospinning. *Langmuir* 27:7132–7139. <https://doi.org/10.1021/la104817r>
- Frome AN, Berlioz S, Chailan JF, Panaitescu DM (2013) Morphology and thermal properties of PLA-cellulose nanofibers composites. *Carbohydr Polym* 91:377–384. <https://doi.org/10.1016/j.carbpol.2012.08.054>
- Fukuzumi H, Tanaka R, Saito T, Isogai A (2014) Dispersion stability and aggregation behavior of TEMPO-oxidized cellulose nanofibrils in water as a function of salt addition. *Cellulose* 21:1553–1559. <https://doi.org/10.1007/s10570-014-0180-z>
- Gårdebjer S, Bergstrand A, Idström A et al (2015) Solid-state NMR to quantify surface coverage and chain length of lactic acid modified cellulose nanocrystals, used as fillers in biodegradable composites. *Compos Sci Technol* 107:1–9. <https://doi.org/10.1016/j.compscitech.2014.11.014>
- Georgouvelas D, Jalvo B, Valencia L et al (2020) Residual lignin and zwitterionic polymer grafts on cellulose nanocrystals for antifouling and antibacterial applications. *ACS Appl Polym Mater* 2:3060–3071. <https://doi.org/10.1021/acsapm.0c00212>
- Golmohammadi H, Morales-Narváez E, Naghdi T, Merkoçi A (2017) Nanocellulose in sensing and biosensing. *Chem Mater* 29:5426–5446. <https://doi.org/10.1021/acs.chemmater.7b01170>
- Goodge K, Frey M (2020) Biotin-conjugated cellulose nanofibers prepared via copper-catalyzed alkyne-azide cycloaddition (CuAAC) “click” chemistry. *Nanomaterials* 10:1172. <https://doi.org/10.3390/nano10061172>
- Guise, C., & Figueiro, R. (2016). Biomedical applications of nanocellulose. In natural fibres: advances in science and technology towards industrial applications. Springer, Dordrecht, pp (155–169)
- Gustavsson LH, Adolffson KH, Hakkarainen M (2020) Thermoplastic “all-cellulose” composites with covalently attached carbonized cellulose. *Biomacromol* 21(5):1752–1761. <https://doi.org/10.1021/acs.biomac.9b01672>
- Hein JE, Fokin VV (2010) Copper-catalyzed azide-alkyne cycloaddition (CuAAC) and beyond: new reactivity of copper(i) acetylides. *Chem Soc Rev* 39:1302–1315. <https://doi.org/10.1039/b904091a>
- Hettegger H, Beaumont M, Potthast A, Rosenau T (2016) Aqueous modification of nano- and microfibrillar cellulose with a click synthon. *Chemsuschem* 9:75–79. <https://doi.org/10.1002/cssc.201501358>
- Himo F, Lovell T, Hilgraf R et al (2005) Copper(I)-catalyzed synthesis of azoles. DFT study predicts unprecedented reactivity and intermediates. *J Am Chem Soc* 127:210–216. <https://doi.org/10.1021/ja0471525>
- Huang B, Babcock H, Zhuang X (2010) Breaking the diffraction barrier: super-resolution imaging of cells. *Cell* 143:1047–1058. <https://doi.org/10.1016/j.cell.2010.12.002>
- Hur J, Park S, Kim JH et al (2022) ultrasensitive, transparent, flexible, and ecofriendly NO₂ gas sensors enabled by oxidized single-walled carbon nanotube bundles on cellulose with engineered surface roughness. *ACS Sustain Chem Eng* 10:3227–3235. <https://doi.org/10.1021/acssuschemeng.1c07559>

- Inglis AJ, Sinnwell S, Stenzel MH, Barner-Kowollik C (2009) Ultrafast click conjugation of macromolecular building blocks at ambient temperature. *Angew Chemie - Int Ed* 48:2411–2414. <https://doi.org/10.1002/anie.200805993>
- Junka K, Filpponen I, Johansson L-S et al (2014) A method for the heterogeneous modification of nanofibrillar cellulose in aqueous media. *Carbohydr Polym* 100:107–115. <https://doi.org/10.1016/j.carbpol.2012.11.063>
- Kalia S, Boufi S, Celli A, Kango S (2014) Nanofibrillated cellulose: surface modification and potential applications. *Colloid Polym Sci* 292:5–31. <https://doi.org/10.1007/s00396-013-3112-9>
- Kaur J, Saxena M, Rishi N (2021) An overview of recent advances in biomedical applications of click chemistry. *Bioconjug Chem* 32:1455–1471. <https://doi.org/10.1021/acs.bioconjchem.1c00247>
- Kelly PV, Cheng P, Gardner DJ, Gramlich WM (2021) Aqueous polymer modification of cellulose nanofibrils by grafting-through a reactive methacrylate group. *Macromol Rapid Commun* 42:2000531. <https://doi.org/10.1002/marc.202000531>
- Klemm D, Kramer F, Moritz S et al (2011) Nanocelluloses: a new family of nature-based materials. *Angew Chemie Int Ed* 50:5438–5466. <https://doi.org/10.1002/anie.201001273>
- Kloetzel MC (2011) The diels-alder reaction with maleic anhydride. *Org. React.* 1–59
- Lalanne-Tisné M, Mees MA, Eyley S et al (2020) Organocatalyzed ring opening polymerization of lactide from the surface of cellulose nanofibrils. *Carbohydr Polym* 250:1–22. <https://doi.org/10.1016/j.carbpol.2020.116974>
- Larsson E, Sanchez CC, Porsch C et al (2013) Thermo-responsive nanofibrillated cellulose by polyelectrolyte adsorption. *Eur Polym J* 49:2689–2696. <https://doi.org/10.1016/j.eurpolymj.2013.05.023>
- Lee KY, Blaker JJ, Murakami R et al (2014) Phase behavior of medium and high internal phase water-in-oil emulsions stabilized solely by hydrophobized bacterial cellulose nanofibrils. *Langmuir* 30:452–460. <https://doi.org/10.1021/la4032514>
- Levere ME, Nguyen NH, Leng X, Percec V (2013) Visualization of the crucial step in SET-LRP. *Polym Chem* 4:1635–1647. <https://doi.org/10.1039/C2PY21084C>
- Liimatainen H, Visanko M, Sirviö JA et al (2012) Enhancement of the nanofibrillation of wood cellulose through sequential periodate-chlorite oxidation. *Biomacromol* 13:1592–1597. <https://doi.org/10.1021/bm300319m>
- Liu Y, Peng Z, Peng X et al (2021) Shedding new lights into STED microscopy: emerging nanoprobes for imaging. *Front Chem* 9:1–22. <https://doi.org/10.3389/fchem.2021.641330>
- Lizundia E, Meario E, Vilas JL (2016) Grafting of cellulose nanocrystals. In: multifunctional polymeric nanocomposites based on cellulosic reinforcements. Elsevier, 61–113
- Majoinen J, Walther A, McKee JR et al (2011) Polyelectrolyte brushes grafted from cellulose nanocrystals Using Cu-mediated surface-initiated controlled radical polymerization. *Biomacromol* 12:2997–3006. <https://doi.org/10.1021/bm200613y>
- Malkoch M, Thibault RJ, Drockenmuller E et al (2005) Orthogonal approaches to the simultaneous and cascade functionalization of macromolecules using click chemistry. *J Am Chem Soc* 127:14942–14949. <https://doi.org/10.1021/ja0549751>
- Mietner JB, Jiang X, Edlund U et al (2021) 3D printing of a bio-based ink made of cross-linked cellulose nanofibrils with various metal cations. *Sci Rep* 11:1–9. <https://doi.org/10.1038/s41598-021-85865-4>
- Moon RJ, Martini A, Nairn J et al (2011) Cellulose nanomaterials review: structure, properties and nanocomposites. *Chem Soc Rev* 40:3941. <https://doi.org/10.1039/c0cs00108b>
- Nakagaito AN, Yano H (2004) The effect of morphological changes from pulp fiber towards nano-scale fibrillated cellulose on the mechanical properties of high-strength plant fiber based composites. *Appl Phys A Mater Sci Process* 78:547–552. <https://doi.org/10.1007/s00339-003-2453-5>
- Navarro JRG, Edlund U (2017) Surface-initiated controlled radical polymerization approach to enhance nanocomposite integration of cellulose nanofibrils. *Biomacromol* 18:1947–1955. <https://doi.org/10.1021/acs.biomac.7b00398>
- Navarro JRG, Conzatti G, Yu Y et al (2015) Multicolor fluorescent labeling of cellulose nanofibrils by click chemistry. *Biomacromol* 16:1293–1300. <https://doi.org/10.1021/acs.biomac.5b00083>
- Navarro JRG, Rostami J, Ahlinder A et al (2020) Surface-initiated controlled radical polymerization approach to in situ cross-link cellulose nanofibrils with inorganic nanoparticles. *Biomacromol* 21:1952–1961. <https://doi.org/10.1021/acs.biomac.0c00210>
- Nguyen NH, Rosen BM, Percec V (2010) SET-LRP of N, N-dimethylacrylamide and of N-isopropylacrylamide at 25 °C in protic and in dipolar aprotic solvents. *J Polym Sci Part A Polym Chem* 48:1752–1763. <https://doi.org/10.1002/pola.23940>
- Nguyen NH, Levere ME, Percec V (2012) SET-LRP of methyl acrylate to complete conversion with zero termination. *J Polym Sci Part A Polym Chem* 50:860–873. <https://doi.org/10.1002/pola.25838>
- Nguyen NH, Kulis J, Sun H-J et al (2013) A comparative study of the SET-LRP of oligo(ethylene oxide) methyl ether acrylate in DMSO and in H₂O. *Polym Chem* 4:144–155. <https://doi.org/10.1039/C2PY20782F>
- Nicol E, Derouineau T, Puaud F, Zaitsev A (2012) Synthesis of double hydrophilic poly(ethylene oxide)-b-poly(2-hydroxyethyl acrylate) by single-electron transfer-living radical polymerization. *J Polym Sci Part A Polym Chem* 50:3885–3894. <https://doi.org/10.1002/pola.26185>
- Nilsson C, Simpson N, Malkoch M et al (2008) Synthesis and thiol-ene photopolymerization of allyl-ether functionalized dendrimers. *J Polym Sci Part A Polym Chem* 46:1339–1348. <https://doi.org/10.1002/pola.22474>
- Ning L, You C, Zhang Y et al (2021) Polydopamine loaded fluorescent nanocellulose–agarose hydrogel: a pH-responsive drug delivery carrier for cancer therapy. *Compos Commun* 26:100739. <https://doi.org/10.1016/j.coco.2021.100739>
- Nogi M, Abe K, Handa K et al (2006) Property enhancement of optically transparent bionanofiber composites by acetylation. *Appl Phys Lett* 89:233123. <https://doi.org/10.1063/1.2403901>

- Ottenhall A, Illergård J, Ek M (2017) Water purification using functionalized cellulose fibers with nonleaching bacteria adsorbing properties. *Environ Sci Technol* 51:7616–7623. <https://doi.org/10.1021/acs.est.7b01153>
- Percec V, Guliashvili T, Ladislav JS et al (2006) Ultrafast synthesis of ultrahigh molar mass polymers by metal-catalyzed living radical polymerization of acrylates, methacrylates, and vinyl chloride mediated by SET at 25 °C. *J Am Chem Soc* 128:14156–14165. <https://doi.org/10.1021/ja065484z>
- Poonguzhali R, Khaleel Basha S, Sugantha Kumari V (2018) Novel asymmetric chitosan/PVP/nanocellulose wound dressing: in vitro and in vivo evaluation. *Int J Biol Macromol* 112:1300–1309. <https://doi.org/10.1016/j.ijbiomac.2018.02.073>
- Presolski SI, Hong VP, Finn MG (2011) Copper-catalyzed azide-alkyne click chemistry for bioconjugation. *Curr Protoc Chem Biol* 3:153–162. <https://doi.org/10.1002/9780470559277.ch110148>
- Radakisinin R, Abdul Majid MS, Jamir MRM et al (2020) Structural, morphological and thermal properties of cellulose nanofibers from napier fiber (*Pennisetum purpureum*). *Materials (basel)* 13:4125. <https://doi.org/10.3390/ma13184125>
- Ramapanicker R, Chauhan P (2016) Click chemistry: mechanistic and synthetic perspectives. *Click React Org Synth*. <https://doi.org/10.1002/9783527694174.ch1>
- Roobala C, Ilanila IP, Basu JK (2018) Applications of STED fluorescence nanoscopy in unravelling nanoscale structure and dynamics of biological systems. *J Biosci* 43:471–484. <https://doi.org/10.1007/s12038-018-9764-3>
- Rosen BM, Percec V (2009) Single-electron transfer and single-electron transfer degenerative chain transfer living radical polymerization. *Chem Rev* 109:5069–5119. <https://doi.org/10.1021/cr900024j>
- Saba N, Mohammad F, Pervaiz M et al (2017) Mechanical, morphological and structural properties of cellulose nanofibers reinforced epoxy composites. *Int J Biol Macromol* 97:190–200. <https://doi.org/10.1016/j.ijbiomac.2017.01.029>
- Salari M, Bitounis D, Bhattacharya K et al (2019) Development & characterization of fluorescently tagged nanocellulose for nanotoxicological studies. *Environ Sci Nano* 6:1516–1526. <https://doi.org/10.1039/c8en01381k>
- Samanta SR, Levere ME, Percec V (2013) SET-LRP of hydrophobic and hydrophilic acrylates in trifluoroethanol. *Polym Chem* 4:3212–3224. <https://doi.org/10.1039/c3py00289f>
- Samanta SR, Nikolaou V, Keller S et al (2015) Aqueous SET-LRP catalyzed with “in situ” generated Cu(0) demonstrates surface mediated activation and bimolecular termination. *Polym Chem* 6:2084–2097. <https://doi.org/10.1039/C4PY01748J>
- Schermelleh L, Heintzmann R, Leonhardt H (2010) A guide to super-resolution fluorescence microscopy. *J Cell Biol* 190:165–175. <https://doi.org/10.1083/jcb.201002018>
- Schyrer B, Pasche S, Voirin G et al (2014) Biosensors based on porous cellulose nanocrystal-poly(vinyl alcohol) scaffolds. *ACS Appl Mater Interfaces* 6:12674–12683. <https://doi.org/10.1021/am502670u>
- Sezgin E, Schneider F, Galiani S et al (2019) Measuring nanoscale diffusion dynamics in cellular membranes with super-resolution STED-FCS. *Nat Protoc* 14:1054–1083. <https://doi.org/10.1038/s41596-019-0127-9>
- Sivakumar K, Xie F, Cash BM et al (2004) A fluorogenic 1,3-dipolar cycloaddition reaction of 3-azidocoumarins and acetylenes. *Org Lett* 6:4603–4606. <https://doi.org/10.1021/ol047955x>
- Song W, Xiao C, Cui L et al (2012) Facile construction of functional biosurface via SI-ATRP and “click glycosylation.” *Colloids Surf B Biointerfaces* 93:188–194. <https://doi.org/10.1016/j.colsurfb.2012.01.002>
- Stephan T, Roesch A, Riedel D, Jakobs S (2019) Live-cell STED nanoscopy of mitochondrial cristae. *Sci Rep* 9:1–6. <https://doi.org/10.1038/s41598-019-48838-2>
- Stockhammer A, Bottanelli F (2021) Appreciating the small things in life: STED microscopy in living cells. *J Phys D Appl Phys* 54:033001. <https://doi.org/10.1088/1361-6463/abac81>
- Storms-Miller WK, Pugh C (2015) Prop-2-yn-1-yl 2-Bromo-2-methylpropanoate: identification and suppression of side reactions of a commonly used terminal alkyne-functional ATRP initiator. *Macromolecules* 48:3803–3810. <https://doi.org/10.1021/acs.macromol.5b00652>
- Tsubokawa N, Iida T, Takayama T (2000) Modification of cellulose powder surface by grafting of polymers with controlled molecular weight and narrow molecular weight distribution. *J Appl Polym Sci* 75:515–522. [https://doi.org/10.1002/\(SICI\)1097-4628\(20000124\)75:4%3c515::AID-APP6%3e3.0.CO;2-Q](https://doi.org/10.1002/(SICI)1097-4628(20000124)75:4%3c515::AID-APP6%3e3.0.CO;2-Q)
- Urban NT, Willig KI, Hell SW, Nägerl UV (2011) STED nanoscopy of actin dynamics in synapses deep inside living brain slices. *Biophys J* 101:1277–1284. <https://doi.org/10.1016/j.bpj.2011.07.027>
- Vicidomini G, Bianchini P, Diaspro A (2018) STED super-resolved microscopy. *Nat Methods* 15:173–182. <https://doi.org/10.1038/nmeth.4593>
- Voronova MI, Lebedeva TN, Radugin MV et al (2006) Interactions of water-DMSO mixtures with cellulose. *J Mol Liq* 126:124–129. <https://doi.org/10.1016/j.molliq.2005.12.001>
- Wang Q, Chan TR, Hilgraf R et al (2003) Bioconjugation by copper(I)-catalyzed azide-alkyne [3 + 2] cycloaddition. *J Am Chem Soc* 125:3192–3193. <https://doi.org/10.1021/ja021381e>
- Wang K, Li W, Gao C (2007) Poly(ϵ -caprolactone)-functionalized carbon nanofibers by surface-initiated ring-opening polymerization. *J Appl Polym Sci* 105:629–640. <https://doi.org/10.1002/app.26285>
- Willberg-Keyriläinen P, Vartiainen J, Pelto J, Ropponen J (2017) Hydrophobization and smoothing of cellulose nanofibril films by cellulose ester coatings. *Carbohydr Polym* 170:160–165. <https://doi.org/10.1016/j.carbpol.2017.04.082>
- Wu W, Song R, Xu Z et al (2018) Fluorescent cellulose nanocrystals with responsiveness to solvent polarity and ionic strength. *Sens Actuators, B Chem* 275:490–498. <https://doi.org/10.1016/j.snb.2018.07.085>
- Xhanari K, Syverud K, Chinga-Carrasco G et al (2011) Structure of nanofibrillated cellulose layers at the o/w interface.

- J Colloid Interface Sci 356:58–62. <https://doi.org/10.1016/j.jcis.2010.12.083>
- Xiong L, Zhan F, Liang H et al (2018) Chemical grafting of nano-TiO₂ onto carbon fiber via thiol–ene click chemistry and its effect on the interfacial and mechanical properties of carbon fiber/epoxy composites. *J Mater Sci* 53:2594–2603. <https://doi.org/10.1007/s10853-017-1739-5>
- Zhai S, Chen H, Zhang Y et al (2022) Nanocellulose: a promising nanomaterial for fabricating fluorescent composites. *Cellulose* 29:7011–7035. <https://doi.org/10.1007/s10570-022-04700-9>
- Zhang R, Liu Y (2018) High energy oxidation and organo-solv solubilization for high yield isolation of cellulose nanocrystals (CNC) from Eucalyptus hardwood. *Sci Rep* 8:1–11. <https://doi.org/10.1038/s41598-018-34667-2>
- Zhang N, Samanta SR, Rosen BM, Percec V (2014a) Single electron transfer in radical ion and radical-mediated organic, materials and polymer synthesis. *Chem Rev* 114:5848–5958. <https://doi.org/10.1021/cr400689s>
- Zhang Q, Wilson P, Anastasaki A et al (2014b) Synthesis and aggregation of double hydrophilic diblock glycopolymers via aqueous SET-LRP. *ACS Macro Lett* 3:491–495. <https://doi.org/10.1021/mz5001724>

Publisher's Note Springer Nature remains neutral with regard to jurisdictional claims in published maps and institutional affiliations.

3D Printable Hybrid Gel Made of Polymer Surface-Modified Cellulose Nanofibrils Prepared by Surface-Initiated Controlled Radical Polymerization (SI-SET-LRP) and Upconversion Luminescent Nanoparticles

Xuehe Jiang, J. Benedikt Mietner, Constantin Harder, Rajesh Kombar, Shouzheng Chen, Christian Strelow, Uta Sazama, Michael Fröba, Christoph Gimmler, Peter Müller-Buschbaum, Stephan V. Roth, and Julien R. G. Navarro*

Cite This: <https://doi.org/10.1021/acsami.2c20775>

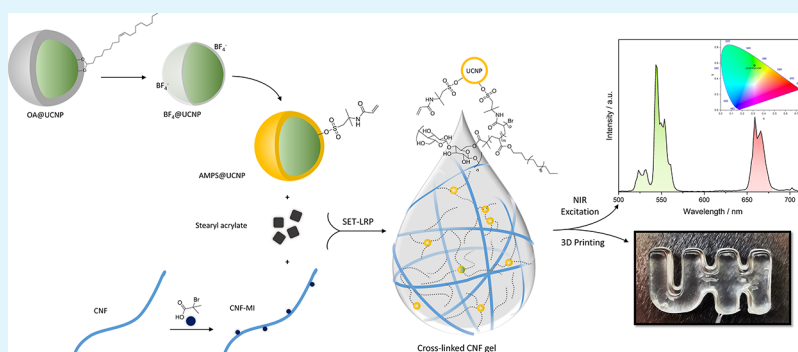
Read Online

ACCESS |

Metrics & More

Article Recommendations

Supporting Information



ABSTRACT: A cellulose nanofibril-based hybrid gel material was developed by grafting the polymerized stearyl acrylate (PSA) and upconversion nanoparticles (UCNPs) onto cellulose nanofibrils (CNFs) via Cu^0 -mediated radical polymerization (SET-LRP) to create a highly cross-linked CNF system. A two-step strategy was exploited to surface-exchange the ligand of the UCNPs from a hydrophobic ligand (oleic acid) to a hydrophilic small-molecule ligand (2-acrylamido-2-methyl-1-propanesulfonic acid, AMPS) and therefore be suitable for SET-LRP. The characteristics and properties of the hybrid material (UCNP-PSA-CNF) were monitored by Fourier transform infrared (FTIR) spectroscopy, thermogravimetric analysis (TGA), rheology, X-ray diffraction (XRD), and microscopic analysis. Those characterization techniques prove the efficient modification of the CNF, with the presence of 1.8% UCNPs. The luminescence measurement was carried out using a homebuilt confocal microscope with a 980 nm laser source. The nanostructure of UCNPs and their incorporated CNF species were measured by small-angle X-ray scattering (SAXS). In addition, this CNF-based hybrid gel has decisive rheological properties, such as good viscoelasticity (loss tangent was below 0.35 for the UCNP-PSA-CNF gel, while the PSA-CNF gel reached the highest value of 0.42), shear-thinning behavior, and shape retention, and was successfully applied to three-dimensional (3D) gel printing throughout various 3D print models.

KEYWORDS: cellulose nanofibrils (CNFs), single electron transfer living radical polymerization (SET-LRP), upconversion nanoparticles (UCNPs), cellulose-based hybrid material, 3D gel printing

INTRODUCTION

Cellulose nanofibrils (CNFs) are well-known biodegradable and renewable materials that are biocompatible, with a high aspect ratio, and can be extracted from lignocellulosic materials through different chemical, mechanical, or enzymatic processes.¹

Typically, CNFs obtained by mechanical processes are in aqueous media, generating viscous dispersion. The abundant numbers of hydroxyl groups on their surface lead to a strong interaction with water molecules and create interfibrillar hydrogen bonds, endowing CNF gels with the morphology

of cross-linked three-dimensional (3D) networks and rheological behaviors, such as viscoelasticity and shear-thinning, that are suitable for gel 3D printing.² Other outstanding intrinsic properties of CNFs, such as a large surface area, high

Received: November 18, 2022

Accepted: January 6, 2023

aspect ratio, high Young's modulus, and good thermal stability,³ render them great potential in additive manufacturing for packaging,⁴ biomedical, and electronic applications.^{5–8}

As a valuable and versatile material, cellulose nanofibrils can also acquire new properties by combining them with inorganic nanoparticles (NPs). Inorganic NPs are different from their bulk counterparts and possess unique characteristics, such as optoelectronic,^{9,10} catalytic,¹¹ antimicrobial,^{12–14} and superparamagnetic characteristics.^{15–17} The functional properties of inorganic NPs can impart to the cellulose-based hybrid materials, where cellulose nanomaterials can support and complement inorganic NPs. The cellulose-based hybrid materials have drawn broad interest as they possess respective features and complementary properties of both constituents. For example, Farooq et al.³ reviewed the recent progress of synthesizing nanocellulose and zinc oxide to produce hybrid nanocomposites with excellent mechanical, UV-barrier, and antibacterial properties, and such nanocomposites could be potentially utilized for food packaging, biochemical applications, and cosmetics. Zeng et al.¹⁸ prepared a series of CNF-based hybrid aerogels where conducting nanomaterials (transition-metal carbide) were embedded in CNFs. The lightweight composites showed good mechanical flexibility, strength, tunable electrical properties, and potential for developing low-cost terahertz devices. Rahmatika et al.¹⁷ developed fine porous particles made of TEMPO-oxidized CNFs and magnetic NPs applied for protein adsorption. The magnetic NPs increased the specific surface area of TEMPO-oxidized CNFs while maintaining their high negative charge on surfaces.¹⁷

However, to extend the use of CNFs in further application, the intrinsic deficiencies of CNFs cannot be neglected. One of the main challenges is brought by the surface hydroxy groups, which leads to poor dispersibility of the CNF in water and most organic solvents and irreversible agglomeration after drying, also known as hornification,¹⁹ due to the strong hydrogen bonds between adjacent cellulose molecules; thereby, the cellulosic fibrillar strands lose their flexibility and conformability. On the other hand, hydroxyl functions are the obvious reactive moieties of CNFs. Therefore, efforts have been made to chemically modify the CNF surface to overcome those deficiencies. A common direct technique is substituting hydroxy with small molecules, including sulfonation,²⁰ acetylation,²¹ esterification,²² silylation,²³ TEMPO-mediated oxidation reaction, etc.²⁴ However, these conventional methods have a relatively low substitution degree and are limited on CNF surfaces. The idea of grafting polymers on CNF surfaces has been a popular strategy as the appended longer molecule chains can act as "spacers", strongly reducing hydrogen-bonding effects, and further extend to the surrounding environment from CNF surfaces, for instance, better interacting with surrounding solvent molecules and thus improve the dispersibility of the CNFs.

Our research group has developed a surface modification pathway in which CNFs were first anchored with initiator groups through the esterification of the hydroxy and then underwent a surface-initiated radical polymerization in the presence of inorganic nanoparticles to tailor their final properties.^{25,26} Cu⁰-mediated radical polymerization, introduced by Percec et al.,²⁷ known as single electron transfer living radical polymerization (SET-LRP), is a robust technique that can be performed in a relatively mild condition and proved to be suitable for a large range of hydrophilic and

hydrophobic vinyl monomers, with full control on the grafted polymeric chain length.

Lanthanide-doped upconversion nanoparticles (UCNPs), as fluorescent nanoparticles, have drawn intense attention in recent decades.²⁸ Their nonlinear optical features, namely, absorbing near-infrared (NIR) photons and emitting visible and ultraviolet (UV) photons, have been widely exploited and triggered their applications in biomedical fields,^{29,30} such as biological imaging,^{31,32} biological detection,^{33,34} and therapeutics.³⁵ Incorporation of luminescent nanoparticles in cellulose as photonic/bio-hybrid is also an active area of research. Earlier, NIR-sensitive upconverting photonic cellulose composite films with a chiral nematic order were demonstrated by coassembled cellulose nanocrystals and UCNPs.³⁶ In addition, UCNPs are chemically stable, potentially possess good biocompatibility, and present high photostability, unperturbed by the laser excitation power and exposure time.²⁹

UCNPs synthesized in organic solvents are typically capped with hydrophobic ligands, such as oleate or oleylamine ligands.³⁷ To proceed further with the SET-LRP, it remains essential that the nanoparticles are surface-modified, and a polymerizable, reactive function is inserted on the surface of nanoparticles. For this reason, the introduction of an acrylate function on the outer-shell surface of the nanoparticles is required. Surface modifications are therefore required prior to subsequent utilization in hydrophilic or aqueous medium. The replacement of the original ligand with another specific species through a ligand exchange procedure is a simple and versatile method, and the distance between the new ligand and the luminescent particle can be well controlled.³⁷ The group of Murray³⁸ reported a generalized strategy for the ligand exchange of nanoparticles using nitrosyl tetrafluoroborate (NOBF₄), which enables sequential surface modification and phase transfer of a wide scope of NPs, such as iron oxide nanoparticles, titanium oxide nanorods, or NaYF₄ nanoplates, to finally functionalize them with a large variety of new protecting ligands.

This paper aims to develop a cellulose nanofibril-based hybrid gel material made of polymer-grafted CNFs, cross-linked with inorganic nanoparticles—here UCNPs, via SET-LRP.^{39–43} Polymers of stearyl acrylate (PSA) grafted on CNF surfaces gave the modified CNF hydrophobic character and reduced the interfibrillar hydrogen bond effect, resulting in modified CNF species that form a highly stable suspension in toluene, which can also be redispersible in toluene from dried status. To evaluate the influence of the fabrication route on the nanostructure of the hybrid materials, we applied small-angle X-ray scattering (SAXS). SAXS allows us to disentangle the changes in the nanostructure of the different materials induced by the composite formation.⁴⁴

We also explored an approach to surface modify UCNPs via a two-step strategy to replace the original oleic ligand with hydrophilic molecules with acrylate functions. The UCNPs with surface ligands can therefore be engaged in the surface-initiated radical polymerization and act as a cross-linking agent, creating networks of modified nanofibrils *in situ*, also incorporating new properties to CNFs, such as improved rheological performance and NIR absorption. We finally investigated the possibility of such a 3D printed CNF-based hybrid material and also investigated if the properties of the nanoparticles remained intact after the 3D printing process, while being embedded in the polymer-modified CNF matrix.

EXPERIMENTAL SECTION

Materials. 1,1'-Carbonyldiimidazole (CDI), 2-bromo-2-methylpropionic acid (98%), imidazole ($\geq 99\%$), stearyl acrylate (SA, 97%), 2-acrylamido-2-methyl-1-propanesulfonic acid (AMPS, 99%), N,N -dimethylformamid (DMF, 99.8%), chloroform ($\geq 99.5\%$), cyclohexane ($\geq 99\%$), nitrosyltetrafluoroborat (NOBF_4 , 95%), isopropanol ($\geq 99.5\%$), ethanol (98%), and toluene were purchased from Sigma-Aldrich. Tris[2-(dimethylamino)ethyl]amine (Me6-TREN) and dimethyl sulfoxide (DMSO, $\geq 99\%$) were purchased from Alfa Aesar. Copper wire (diameter 0.812 mm) was purchased from Fisher. The rare earth-doped upconversion nanoparticles (UCNPs, $\text{NaYF}_4:\text{Yb,Er}/\text{NaYF}_4$) were capped with oleic acid and received as a dispersion (180 mg/mL) in toluene from the Fraunhofer Institute for Applied Polymer Research (IAP)—Center for Applied Nanotechnology (CAN).

For the production of cellulose nanofibrils (CNFs), dried elemental chlorine-free bleached kraft pulp (Stendal GmbH, Germany) was used, and the CNF suspension was obtained using a Microfluidizer (M-110EH-30 Microfluidics, Indecorp). DI water ($0.055 \mu\text{S}/\text{cm}$) was used for all procedures and syntheses.

The monomer used for grafting polymerization was purified by passing through a basic alumina column as a toluene solution to remove inhibitors.

Production of Cellulose Nanofibrils. CNFs were prepared from a previously described procedure.⁴⁵ The dry cellulose source, elemental chlorine-free (ECF) bleached softwood kraft pulp, was purchased from MERCER Stendal GmbH, Germany. The Northern bleached softwood kraft pulp was made of pine (30–60%) and spruce (40–70%), PFI-milled at 23 °C and 50% relative humidity. Briefly, the cellulose pulp was first suspended in water and then ground to obtain a 75–80° SR (SR: Schopper–Riegler degrees, determined using the Schopper–Riegler method (DIN EN ISO 5267–1)). Finally, the ground slurry was defibrillated using a microfluidizer (M-110EH-30, Microfluidizer) under high pressure by passing the slurry several times in different chambers with orifice widths of 400 and 200 μm (2 times, 15,000 psi) and 200 and 100 μm (4 times, 25,000 psi) successively. The collected suspension was concentrated through centrifugation. The process resulted in a 2 wt % CNF aqueous gel.

Solvent Exchange of Cellulose Nanofibrils. The obtained CNF aqueous gel (2 wt %) was solvent-exchanged into DMSO by a described procedure.⁴⁶ For the solvent exchange procedure, the previously obtained CNF aqueous gel (2 wt %) was suspended in water (10 g of gel for 100 mL of water). Then, 100 mL of DMSO was slowly added to the CNF suspension under constant stirring. After stirring for 6 h, the CNF suspension (mixture of DMSO and water) was then centrifuged (4000 rpm/20 min), and the supernatant (DMSO and water) was discarded and replaced with fresh DMSO. The centrifugation tubes were vigorously shaken for 5 min using a vortex and further centrifugated. This procedure was repeated four times. The procedure resulted in a 2 wt % CNF/DMSO gel.

Synthesis of the CNF-Based Macroinitiator (CNF-MI). A CNF-based macroinitiator was synthesized as previously described.⁴⁷ This process resulted in a 1 wt % CNF-MI gel.

Synthesis of $\text{NaYF}_4:\text{Yb,Er}/\text{NaYF}_4$ UCNPs. The synthesis of UCNPs was conducted using an existing Schlenk-line method, which has been reported elsewhere.^{48a,b}

Surface Modification of UCNPs. We used a two-step ligand exchange approach to modify the surface of UCNPs.⁵⁸ More specifically, 55 μL of UCNPs capped with oleic acid (OA@UCNP) in toluene (180 mg/mL) was diluted to 10 mg/mL with cyclohexane; then, 1 mL of DMF was added, resulting in a biphasic system consisting of an upper layer of cyclohexane with OA@UCNP and a lower layer of DMF. Subsequently, 10 mg of nitrosonium tetrafluoroborate (NOBF_4) was added, and the mixture was sonicated for 30 min. It resulted in a phase transfer of UCNPs from cyclohexane to DMF (containing $\text{BF}_4\text{@UCNP}$).

The UCNPs in DMF were collected by adding excessive chloroform (10 mL) and centrifuging at 20,000 rpm for 20 min. Then, the pellet ($\text{BF}_4\text{@UCNP}$) was redispersed in DMF, completed

with chloroform, and centrifuged again. The purification process was repeated three times.

The secondary ligand exchange of UCNPs with 2-acrylamido-2-methyl-1-propanesulfonic acid (AMPS) proceeded straight afterward. The $\text{BF}_4\text{@UCNP}$ was suspended in 1 mL of ethanol and mixed with a solution of AMPS (200 mg) in 4 mL of ethanol. The suspension was heated to 60 °C under vigorous stirring overnight. The resulting mixture was cooled down to room temperature and the surface-modified UCNPs (AMPS@UCNP) were collected and purified three times by centrifugation (15,000 rpm, 20 min) in ethanol.

Procedure for SET-LRP Grafting of CNF and UCNPs (UCNP-PSA-CNF). The CNF-MI (4 g, 1 wt %) and AMPS@UCNP (10 mg) were suspended in DMSO (30 mL), and SA (in 15 mL toluene) was added. A copper wire (diameter = 1 mm, length = 6 cm) was treated with HCl solution (37%) and rinsed with water and acetone prior to use. The HCl-treated Cu wire was added to the suspension, and the system was degassed via nitrogen purging for 10 min and heated up to 40 °C. The reaction started upon the addition of Me6-TREN (200 μL , 10 vol % in DMSO) and proceeded overnight under a nitrogen atmosphere. The resulting solid gel was collected by removing the reaction liquid, dissolved in toluene (15 mL), and consequently precipitated in isopropanol (15 mL). The purification steps were repeated four times through centrifugation (6000 rpm, 1 h) with a toluene/isopropanol (1:1) mixture (30 mL).

Procedure for SET-LRP Grafting of CNF (PSA-CNF). The procedure was the same as described above, except that the AMPS@UCNP was not engaged in the grafting polymerization.

3D Gel Printing of CNF-Based Gels. The 3D printer used in this study was by pneumatic extrusion: a CELLINK INKREDIBLE 3D bioprinter. A disposable syringe was loaded with our printable gel and inserted into the printing cartridge using a female–female Luer lock adapter. Printability has been adjusted by optimizing the inflow air rate through the fixed nozzle to achieve stable and consistent precision of the printing layer. The hybrid gel was printed using a 0.59 mm diameter conical nozzle with an applied pressure of 24 kPa. The 3D models were designed in Tinkercad and converted into g-code via PrusaSlicer.

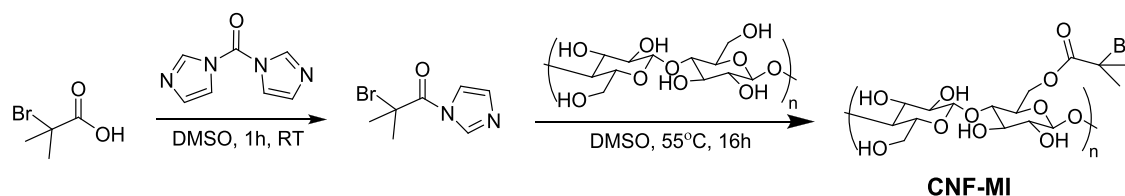
Characterization. Fourier transform infrared spectroscopy with attenuated total reflection (ATR-FTIR) was performed on a Bruker Vector 33 spectrometer. All spectra were obtained as means of 60 scans in the spectral region of 3600–550 cm^{-1} , with a spectral resolution of 4 cm^{-1} .

Thermogravimetric analysis (TGA) and X-ray powder diffraction (XRD) were performed on a Netzsch STA 409 with a TG sample holder. Each sample (approximately 20 mg) was heated, under a nitrogen atmosphere, to 1000 °C at a flow rate of 50 mL/min with a heating rate of 5 °C/min and then held at this temperature for 1 h more. To correct the drift of the balance, blank measurements (without sample) were performed under the same conditions. TGA of UCNP@AMPS was performed in a Netzsch TG 209F1 under a N_2 atmosphere with 20 K/min heating rate.

X-ray diffraction (XRD) analysis was performed in a PANalytical X'PERT Pro diffractometer with a $\text{Cu K}\alpha$ X-ray source (0.154 nm). The samples were prepared on a Si wafer: 50 μL of the obtained stable colloidal dispersion containing nanocrystals was directly dried on a Si wafer.

Rheology tests were monitored using a TA Instrument AR 2000ex with the Advantage Software v5.8.2. All materials were tested with a 40 mm parallel-plate configuration and 500 μm gap distance under room temperature. A shear stress ramp ranging from 0.01 to 1000 Pa was applied, and rotational shear viscosity measurements were performed in flow mode with the shear rate ranging from 0.01 to 1000 s^{-1} . The frequency sweep was between 0.1 and 100 rad/s, and a strain sweep was performed at an angular frequency of 6.28 rad/s to ensure the measurements in the linear viscoelastic region. Rotational recovery measurements were performed to characterize the material recovery behavior by applying a low shear rate of 100 s^{-1} for 200 s, followed by a high shear rate at 1000 s^{-1} for 100 s and a low shear rate of 100 s^{-1} for 200 s.

Scheme 1. Synthesis of a Cellulose Nanofibril-Based Macroinitiator



A JEOL JEM-1011 operating on 100 kV was used for capturing TEM images. Diluted colloidal solution (10 μL) was dried on a carbon-coated copper grid for TEM analysis. A PTI fluorospectrometer, Horiba, coupled with a 980 nm IR laser, was used to obtain emission spectra, and 3 mL of dispersed samples of the initial UCNP and UCNP-PSA-CNF in toluene and AMPS@UCNP in DMSO were taken in quartz cuvettes for the analysis.

The microscopic fluorescence images and spectra were taken with a homebuilt confocal laser scanning setup installed as a combination of optical parts on an optical table. A 980 nm diode laser pointer (15 mW measured at the sample) was used as an excitation source, focused using a Mitutoyo NIR APO 100X HR objective (Obj., 480–1800 nm, N.A.= 0.7) and a 92/8 beam splitter (BS). The laser is focused on the sample positioned on an XYZ piezo stage with 100 μm range in all three dimensions. A short pass 750 nm filter blocks the scattered laser light. The emitted light from the sample is collected from the same objective and coupled to one of two detection units using a moveable mirror (M1): the upconversion signal is focused either by a lens (L1) into a spectrograph equipped with a charge-coupled device (CCD) camera for spectral information or by a second lens (L2) directly onto the 50 μm -sized active area of a single-photon avalanche diode (SPAD) to perform fast and highly sensitive confocal imaging by single photon counting. Note that the small size of the SPAD detector allows abstaining from a pinhole usually installed in confocal microscopes: it effectively acts as a pinhole in front of a large area detector in the same device. Light collected from a sample volume larger than the volume excited by the diffraction-limited laser does not hit the active area of the SPAD in the same way as it cannot pass a pinhole.

Small-angle X-ray scattering (SAXS) measurements were performed at beamline P03, PETRA III, DESY, Hamburg.⁴⁹ A beam size of 25 μm was used with a wavelength of $\lambda = 0.105$ nm and a sample-to-detector distance of SDD = 3901 mm. As a detector, a PILATUS 2M (Decriis, Switzerland) with a pixel size of 172 μm was used. Exposure time per pattern was 10 s. All data were background-corrected. To analyze the data, SASview, v5.0.5, was used together with χ^2 minimization.⁵⁰ Prior to the integration of the 2D SAXS pattern, a mask file was applied.

RESULTS AND DISCUSSION

Esterification of CNFs. The solvent of a CNF aqueous gel was first exchanged to DMSO prior to the chemical conversion to CNF-MI. The esterification occurred between hydroxyl groups of CNFs and the 2-bromo-2-methyl propionic acid in DMSO (Scheme 1).

The IR spectrum of CNF-MI (Figure 1A) shows an additional absorption band at 1733 cm^{-1} (C=O), attributed to the carbonyl group of the ester function, besides the characteristic bands of CNFs localized at 3320 cm^{-1} (O–H), 2950 and 2895 cm^{-1} (C–H), 1430 cm^{-1} (C–H), and 1161 cm^{-1} (C–O–C). This indicates that the alkyl bromide was successfully anchored on the CNF surface through the one-step synthesis and will be able to initiate polymer chains growing from CNFs.

Surface Modification of UCNPs. We used a two-step ligand exchange approach to modify the surface of UCNPs, aiming to attach acrylate functions on UCNP surfaces so that

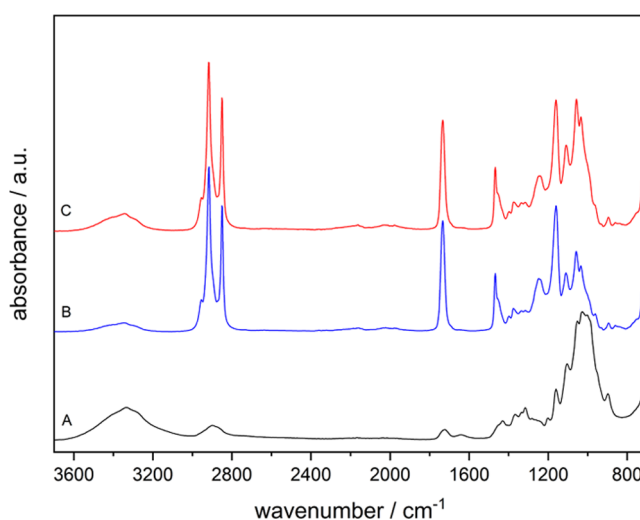


Figure 1. FTIR spectra of (A) CNF-MI, (B) PSA-CNF, and (C) UCNP-PSA-CNF.

they could be engaged in living radical polymerization later on (Scheme 2).

The first step, removing the oleate ligand from UCNP surfaces, was realized by NOBF_4 treatment. The initial UCNPs were capped with oleic acid (OA@UCNP) and can be fully suspended in toluene. The sterically stabilized OA@UCNPs were also fully redispersible in nonpolar solvents, such as cyclohexane. The addition of NOBF_4 led to the phase transfer of UCNPs from cyclohexane to DMF, thus obtaining BF_4 @UCNP, which can also be redispersed in DMF.

The characterization of the nanoparticles through FTIR spectroscopy (Figure 2) confirmed this first step of conversion. The OA capping agent was identified with peaks localized at 2800–3000 cm^{-1} (C–H) and 1500–1600 cm^{-1} (COO). Conversely, those bands were absent in the spectrum of BF_4 @UCNP. In addition, a new band at 1073 cm^{-1} emerged after treatment, which is assigned to BF_4^- . The remaining new band, localized at approximately 1650 cm^{-1} , is due to C=O of the DMF solvent. These results indicate a successful replacement of the OA capping agent with inorganic BF_4^- .

For the second step of ligand exchange, 2-acrylamido-2-methyl-1-propanesulfonic acid (AMPS) was used to functionalize the UCNPs, followed by a modified procedure from a previous report.²⁶ BF_4 @UCNP was suspended in ethanol, and a large excess of ligands AMPS was added to the suspension to replace BF_4^- . The result was monitored with FTIR spectroscopy. The spectrum of AMPS@UCNP (Figure 2C) appears to have bands localized at 1090 cm^{-1} (symmetric stretching S=O), 1190 cm^{-1} (asymmetric stretching S=O), 1556 cm^{-1} (C=C), 1672 cm^{-1} (N–C=O), and 1120 cm^{-1} (C–N). So far, the surface of UCNPs has been successfully functionalized with AMPS and thus can be implemented for further grafting polymerization onto CNFs.

Scheme 2. (A) Surface Modification of UCNPs, (B) Grafting Polymerization and In Situ Cross-Linking of CNF-MI with Stearyl Acrylate (SA) and AMPS@UCNP via SET-LRP

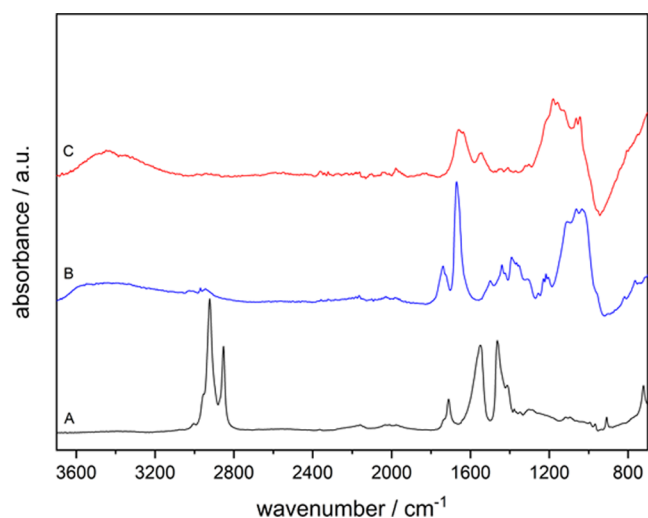
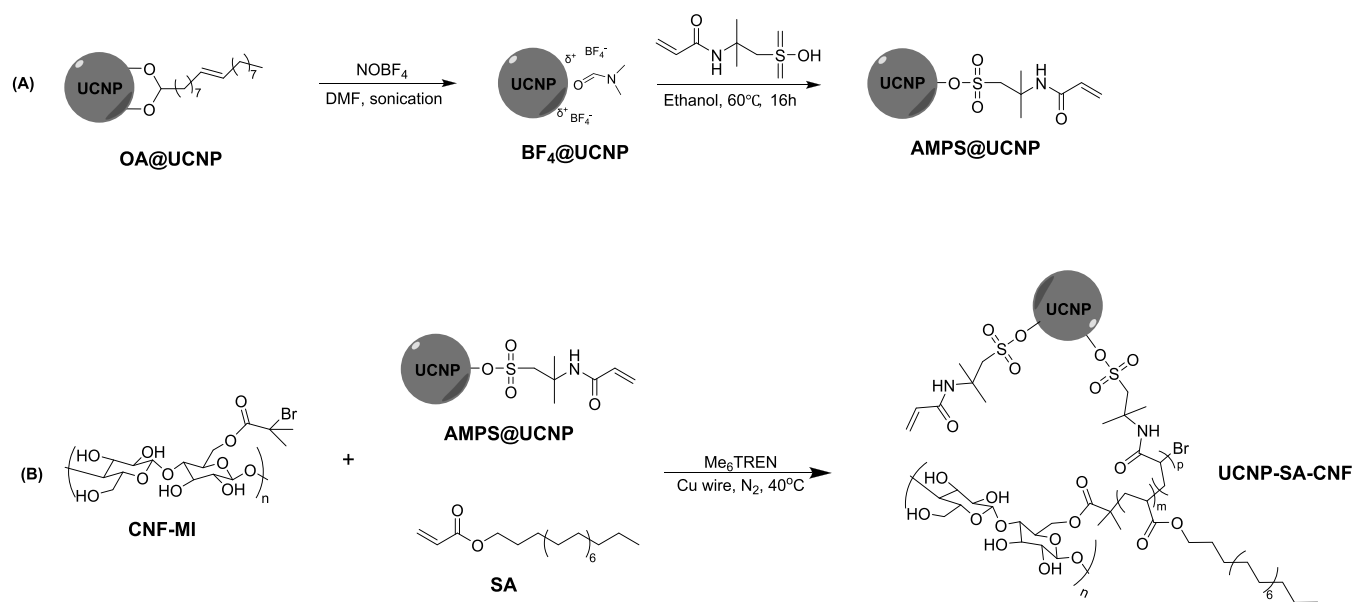


Figure 2. FTIR spectra of (A) OA@UCNP, (B) BF₄@UCNP, and (C) AMPS@UCNP.

The surface-modified UCNP was also characterized with thermogravimetric analysis. Figure 3 shows a two-step weight loss, totaling 5.06% when AMPS@UCNP was heated beyond 500 °C. The first weight loss was due to the evaporation of the absorbed solvent, and the second weight loss of 1.8% corresponded to the surface ligand deposition. The surface coverage (ϕ , molecules/nm²) of AMPS@UCNP was then calculated, and the ligand density of AMPS@UCNP is 0.7 AMPS/nm² (see the Supporting Information (SI) for full details).

Surface-Initiated Radical Polymerization and In Situ Cross-Linking. Finally, we carried out the surface-initiated controlled radical polymerization of stearyl acrylate and AMPS@UCNP with the CNF-based macroinitiator (CNF-MI) yielding the hybrid CNF material (UCNP-PSA-CNF), as illustrated in Scheme 2B. As a comparison, the polymerization without nanoparticle cross-linking was also performed (PSA-CNF).

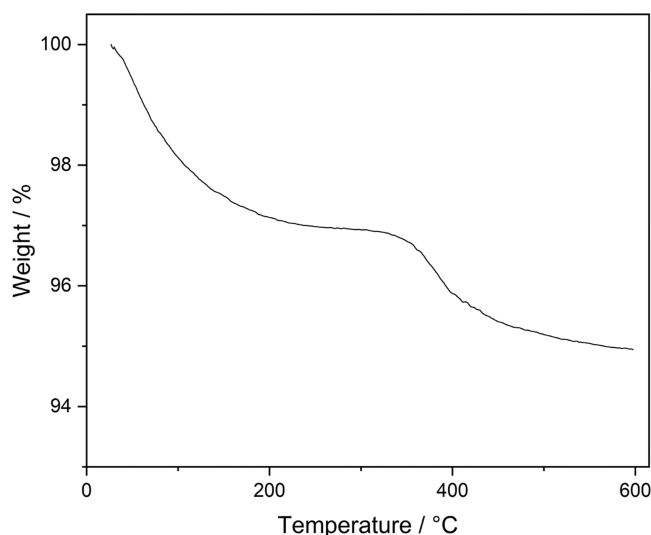


Figure 3. TGA curve of AMPS@UCNP.

The polymerization occurred in a DMSO/toluene mixture to ensure a homogeneous condition as CNF-MI and AMPS@UCNP both were stable in DMSO, while SA was only poorly soluble in DMSO and highly soluble in toluene. As the polymerization proceeded, a large number of white floccules were rapidly formed (in 10 min) due to the low solubility of grafted PSA in the solvent system.

The result of grafting polymerization onto CNF surfaces was analyzed by FTIR spectroscopy (Figure 1) for both samples UCNP-PSA-CNF and PSA-CNF. Besides the characteristic bands from CNFs, both modified CNFs have a high intensity of peaks at 2917 and 2850 cm⁻¹ (C–H), 1733 cm⁻¹ (C=O), 1467 cm⁻¹ (C–H), and 1162 cm⁻¹ (C–O–C), which indicate an abundant number of methylene groups on CNFs. The grafting of PSA on CNFs is thus confirmed. Despite the successful grafting polymerization onto CNFs, it remains difficult to identify UCNPs cross-linked in modified CNFs via FTIR spectroscopy as the characteristic absorption band of

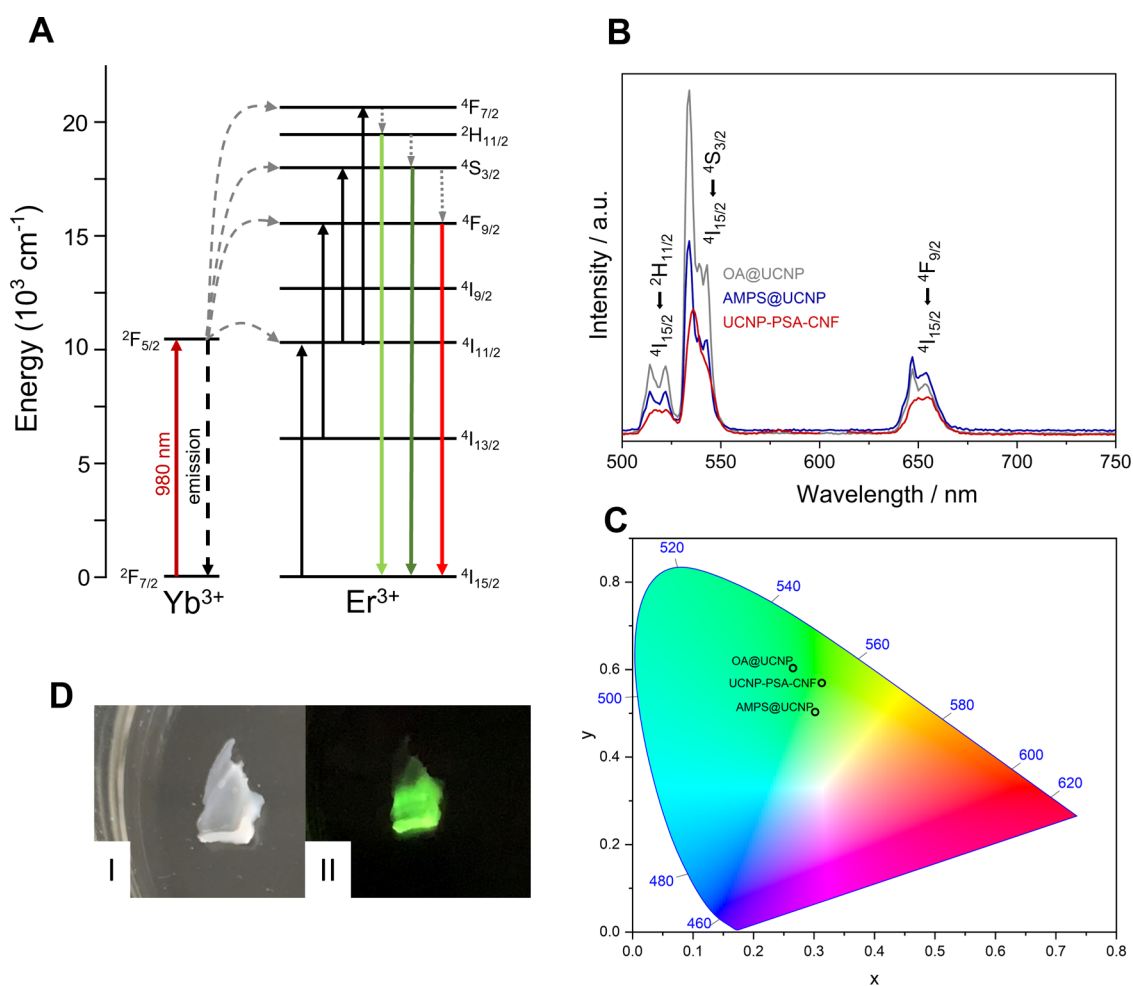


Figure 4. (A) Schematic illustration of the upconversion mechanism of UCNPs doped with Yb^{3+} – Er^{3+} ; (B) emission spectra of OA@UCNP, AMPS@UCNP, and UCNP-PSA-CNF; (C) corresponding CIE 1931 chromaticity diagram of (D) UCNP-PSA-CNF gel under (I) daylight and (II) 980 nm laser diode excitation.

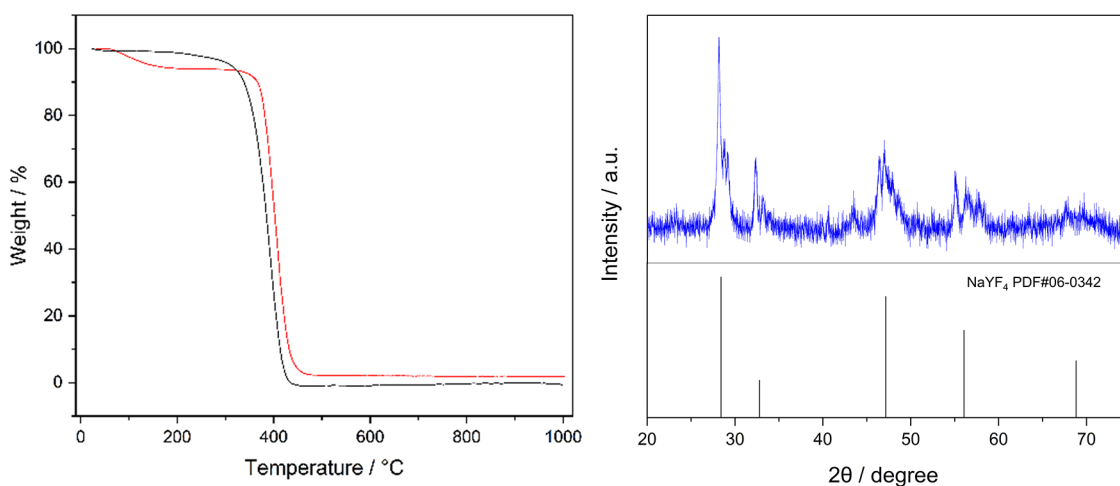


Figure 5. Left: TGA of PSA-CNF (black), UCNP-PSA-CNF (red); right: XRD patterns of UCNPs as residue from TGA and the standard data of $NaYF_4$ (PDF#06-0342).

AMPS@UCNP overlapped with the absorption bands of the PSA and CNF.

As introduced before, lanthanide ions have abundant energy levels and transitions, allowing for unique photophysical properties, such as absorbing NIR light and emitting visible

or ultraviolet light by, for example, using a continuous wave or pulse laser with low power density at room temperature.⁵¹ In our system ($NaYF_4:Yb,Er/NaYF_4$), Er^{3+} acts as an activator owing to its ladder-like intermediate energy levels; codoped Yb^{3+} is the sensitizer, which only possesses a simple energy

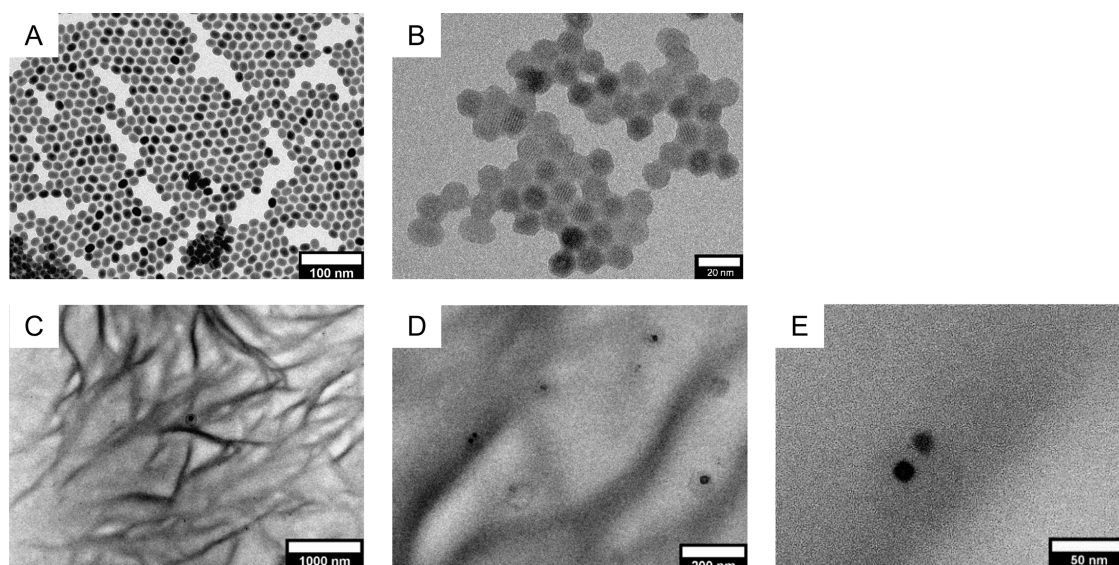


Figure 6. TEM images of (A) OA@UCNP, (B) AMPS@UCNP, and (C–E) UCNP-PSA-CNF.

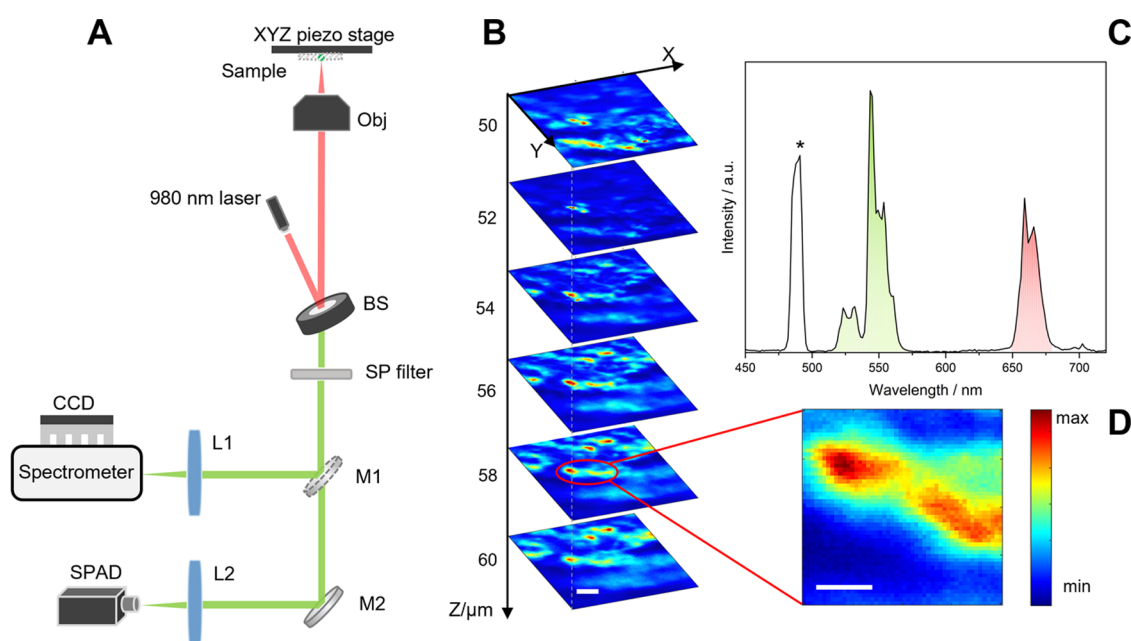


Figure 7. (A) Layout of a homebuilt confocal microscope: BS, 90/10 beam splitter; Obj, objective lens N.A. = 0.7; SP filter, short pass 750 nm filter; M1 & M2, (flip) mirror; L1 & L2, lenses; CCD, charge-coupled device; SPAD, single-photon avalanche diode. (B) Confocal maps at different depths of the sample. Scale bar, 10 μm . (C) Typical emission spectrum under irradiation at 980 nm. Scale bars, 10 μm . (D) Zoom-in image at the focus plane $Z = 58 \mu\text{m}$. Intensity is scaled between global min–max.

transition and higher absorptivity of NIR as well as transfer energy to the neighboring activator (Figure 4A).

Emission spectra of the OA@UCNP, AMPS@UCNP, and UCNP-PSA-CNF in toluene are recorded at $\lambda_{\text{ex}} = 980 \text{ nm}$ and are presented in Figure 4B. Typical emission spectral peaks from Er^{3+} ions are evident in all three spectra. The emission bands at 525 and 545 nm are responsible for the green color emission resulting from ${}^2\text{H}_{11/2}$, ${}^4\text{S}_{3/2} \rightarrow {}^4\text{I}_{15/2}$ transitions, respectively. The peak at 650 nm is attributed to ${}^4\text{F}_{9/2} \rightarrow {}^4\text{I}_{15/2}$. As expected, AMPS@UCNP and its incorporation in the CNF matrix do not change the optical properties of UCNP, as identical fingerprint emission lines from the Er^{3+} are visible in both spectra.

The additive mixture of the spectral colors is displayed in the chromaticity diagram (CIE 1931). All luminescent species, including the UCNP-PSA-CNF gel, were located in the green zone (Figure 4C). The result is in line with the visible green light from the entire area of the UCNP-PSA-CNF gel excited by a 980 nm laser diode (Figure 4D).

To characterize the thermal stability and the amount of UCNP coupled to CNFs, TGA measurement and the sequential XRD of UCNP-PSA-CNF were carried out. The result is provided in Figure 5. The weight loss of UCNP-PSA-CNF from room temperature to 200 $^{\circ}\text{C}$ mainly was due to solvent evaporation. The decomposition of PSA-CNF started at 350 $^{\circ}\text{C}$, while UCNP-PSA-CNF was thermally stable up to

400 °C and left a higher residue content of 4.9% than PSA-CNF due to the presence of UCNPs.

The crystal type of the residue of UCNP-PSA-CNF was examined by XRD (Figure 5). The XRD pattern of the residue is relatively weak, most likely due to the low amount, yet demonstrates crystallinity with characteristic diffraction peaks in agreement with the high temperature cubic phase NaYF_4 mainly (PDF#06-0432).^{52,53}

We used a transmission electron microscope (TEM) and a scanning electron microscope (SEM) to observe the UCNPs, and their cross-linked CNF gels dried at ambient temperature.

TEM images of OA@UCNP, AMPS@UCNP, and UCNP-PSA-CNF are shown in Figure 6. Highly monodisperse individual nanoparticles with an average size of ~ 18 nm and slightly elongated (17 nm \times 20 nm) morphology are shown from the TEM image of OA@UCNP. In Figure 6B, AMPS@UCNP displays the identical dimension and the hexagonal structure, which is in coherence with the result from XRD. Besides, the single crystalline morphology is also shown with a lattice distance of ~ 0.5 nm. The TEM images of UCNP-PSA-CNF (Figure 6C–E) show that modified UCNPs were surrounded by a sphere of AMPS ligand/PSA and coupled on the surface of CNFs through them.

Moreover, as a proof of concept for the UCNPs as fluorescence markers, a 3D printed cube of the UCNP-PSA-CNF gel was investigated using a homebuilt confocal microscope (Figure 7). A small portion of the 3D print was excited by a 980 nm laser diode focusing on a certain sample volume by an objective. The emitted light collected by the objective was filtered by a 750 nm short pass before focusing on detectors. The sample was mounted on an XYZ piezo stage to point-by-point address the desired sample region in all three dimensions during the scan.

Figure 7B shows six confocal slices of different depths within the sample using the SPAD. Strongly localized intensity maxima at different lateral positions were observed at different sample depths. Analyzing the light from these maxima with the spectrometer and the CCD camera, we observed typical spectra as presented in Figure 7C: besides the signal marked with an asterisk (*) representing the second harmonic of the excitation laser, the signals match the typical emission spectra of UCNPs as measured previously. We can therefore attribute these localized intensity maxima to UCNPs coupled to CNFs.

A zoom-in into the slice at $Z = 58 \mu\text{m}$ (Figure 7D) shows strongly localized emission maxima with diameters of a few microns, which indicate small regions of only few UCNPs. These small regions represent the local binding sites of the UCNPs on the individual CNFs. It is important to note that the beam quality of the used laser does not allow formation of a diffraction-limited three-dimensional laser spot. Therefore, the resolution of our setup is limited compared to the resolution of conventional confocal microscopes, and the emission of UCNPs should be localized even stronger. Furthermore, we observed the tendency of the signals to be aligned in wirelike structures reaching from the left to the right side among all confocal slices. Therefore, it is reasonable to assume that this observed distribution in three dimensions can be attributed to the modified CNF.

The measurements principally demonstrate that 3D confocal microscopy of the UCNPs in CNF networks is possible and provide a significant first step toward the identification of the 3D distribution of the UCNPs and individual CNFs inside the network. However, the use of a laser source with a more

defined beam profile would strengthen the possibilities of measurements.

Small-Angle X-ray Scattering (SAXS) Measurements of UCNPs and Modified CNF Species. To deepen the understanding of the structure of UCNP cross-linked modified CNFs, a series of SAXS measurements were performed. SAXS experiments were carried out to characterize the original UCNPs, the pristine CNF, and “simply dried” (annotated as “sd”) and 3D printed (annotated as “3D”) gels of PSA-CNF and UCNP-PSA-CNF. All data were background-corrected as described in the previous section. The two-dimensional SAXS pattern is shown in Figure 8 for the sake of completeness.

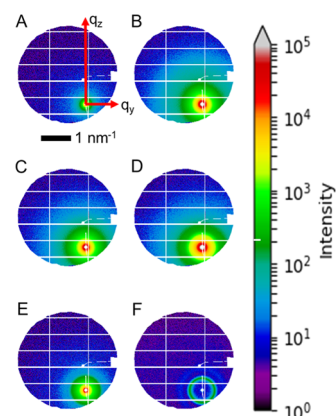


Figure 8. Two-dimensional (2D), background-corrected SAXS data of all (A) pristine CNF, (B) PSA-CNF-sd (simply dried), (C) PSA-CNF-3D (3D printed), (D) UCNP-PSA-CNF-3D, (E) UCNP-PSA-CNF-sd, and (F) original UCNPs on Kapton. The white lines indicate the masked areas. The logarithmic intensity scale for all SAXS patterns is shown on the right. The reciprocal space coordinate system with a scale bar is indicated in panel (A).

SAXS allows for retrieving nanostructural data with high statistical relevance. In detail, Figure 8A–C shows the pristine CNF, the simply dried PSA-CNF composite, and the 3D printed composite. Figure 8F shows the SAXS pattern of the UCNP without the matrix. These four SAXS patterns serve to disentangle the contributions of CNF, PSA, and UCNP in the sd (Figure 8E) and 3D printed (Figure 8D) composites consisting of PSA, CNF, and UCNP. We follow here our route developed in reference⁵⁴ for complex, multicomponent systems. This approach allows for retrieving fabrication-induced changes in the nanostructure and the interaction of the different materials in the full composite. For example, we will show that the PSA component does show a change, which is visible in SAXS.

To analyze the SAXS data of the CNF, we modified the model from Guccini et al.⁵⁵ using the Guinier–Porod model from Hammouda⁵⁶ (see the Supporting Information for full details).

One-dimensional (1D) SAXS curves $I(q)$ were calculated by integrating the full 2D SAXS pattern over the full azimuth (Figures 9 and 10).

The pristine CNF shows a structure with a Guinier radius (R_g) of 149 ± 10 nm with the shape of a sphere ($s = 0$), which is interpreted as large bundles of CNFs. The slope of $m = 3.08$ indicates rough 3D structures. In addition, a correlation length of polymer chains (ξ) of 1.2 ± 0.1 nm shows a short-range correlation length similar to the literature.⁵⁵ The Gaussian in eq. 10 in the SI shows no contribution. The addition of PSA

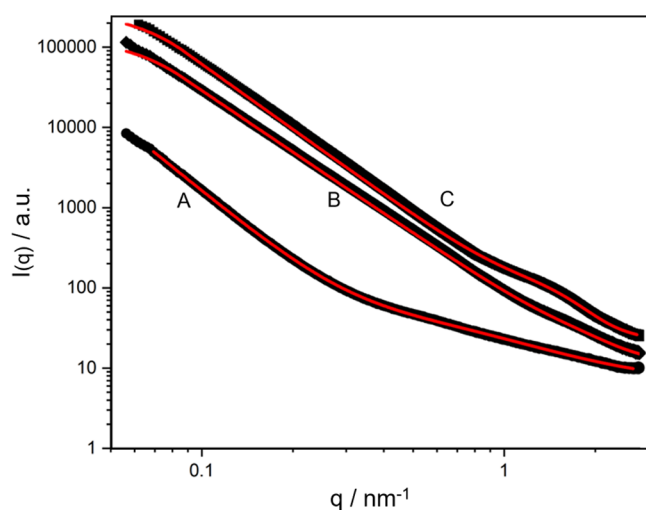


Figure 9. 1D SAXS curves and corresponding fits: (A) pristine CNF, (B) PSA-CNF-3D, and (C) PSA-CNF-sd. The corresponding fits are presented in red color. Curves are shifted for clarity.

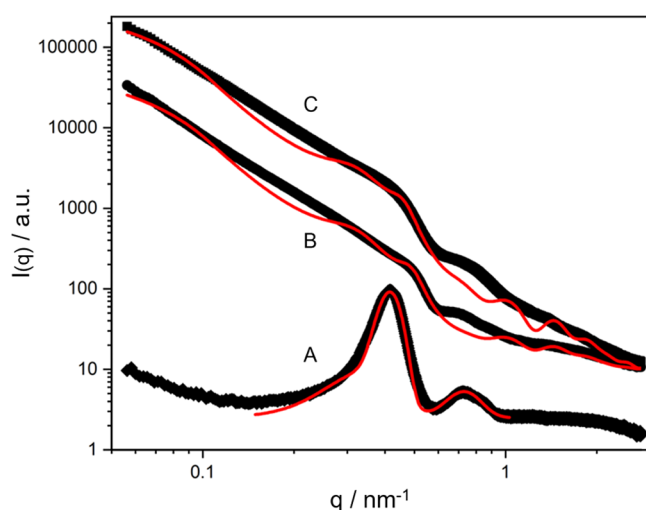


Figure 10. 1D SAXS curves and corresponding fits: (A) OA@UCNPs, (B) UCNP-PSA-CNF-sd, and (C) UCNP-PSA-CNF-3D. The corresponding fits are presented in red color. Curves are shifted for clarity.

shows a clear change in the structure. For both PSA-CNF-sd and PSA-CNF-3D, R_g changes to $R_g = 23 \pm 3$ nm with $s = 2.7$ and $s = 2.55$, showing more oblate structures. The CNF matrix is a porous system. Large values of R_g for pristine CNFs correlate to large bundles or agglomerations of CNFs, as stated above, while smaller values of R_g are consistent with smaller agglomerates⁵⁷ or voids filled by PSA.⁵⁸ Figure 6C–E shows CNF bundles in the same size range.

In addition, the contribution of the Ornstein–Zernike correlation length ξ is vanishing; a new broad structure around 1.1 nm^{-1} (sd) and 1.5 nm^{-1} (3D) represented by a Gaussian appears. This corresponds to real space length scales of around 4–6 nm, interpreted as polymer globules (PSA). In the case of the 3D printed hybrid materials, the contribution of the PSA additive is much reduced by 90%.

In Figure 10, we present the 1D SAXS curves together with the fits based on the simplified, composite model (eqs 10–12 in the SI). This simplified model overall reproduces the curves' progression $I(q)$ and thus allows for disentangling the

contribution of CNFs, UCNPs, and SA polymers. The as-prepared UCNPs sample shows four major structures. The corresponding q -values are 0.35 ± 0.05 , 0.415 ± 0.001 , 0.72 ± 0.02 , and $0.82 \pm 0.04 \text{ nm}^{-1}$, which correspond to distances of 18 ± 3 , 15.13 ± 0.03 , 8.7 ± 0.2 , and 7.7 ± 0.4 nm, respectively. In view of the elongated shape of the UCNPs, the length scales are interpreted as the distance of stacked UCNPs along the long axis, the short axis, and higher orders.

The fraction of the short-axis paracrystalline sublattice in comparison to the long-axis paracrystalline sublattice is $\sim 87\%$ in the case of UCNPs-PSA-CNF-sd and 92% in the case of UCNPs-PSA-CNF-3D. For UCNPs-PSA-CNF-sd, the nearest-neighbor distance is $d_{\text{nn,sd,s}} = 12.6 \pm 0.2$ nm and for UCNPs-PSA-CNF-3D, $d_{\text{nn,3d,s}} = 13.5 \pm 0.2$ nm. It implies a slightly distorted lattice of UCNPs-PSA-CNF-3D. The long-axis sublattice, however, stays constant, $d_{\text{nn,sd,l}} = d_{\text{nn,3d,l}} = 18$ nm and is thus unaffected by the deposition method. Interestingly, for both sublattices, the disorder of the paracrystalline lattices is in both cases 0.3 for the long-axis sublattice $d_{\text{nn,sd}/3d,s}$ and 0.2 for the short-axis sublattice $d_{\text{nn,sd,s}}$.

The UCNPs-PSA-CNF shows two regions (Figure 9). For $q < 0.2 \text{ nm}^{-1}$, the SAXS pattern is dominated by the CNF. For $q > 0.3 \text{ nm}^{-1}$, the SAXS pattern is dominated by the arrangement of the UCNPs. A couple of peaks arise for $q \geq 0.6 \text{ nm}^{-1}$, which are well modeled by the two paracrystalline structure factors and an approximated spherical shape with different radii for the two lattices. Interestingly the influence of PSA structures is much reduced (50%) in the 3D printed case, seen by the steeper slope after 1 nm^{-1} .

The UCNPs-PSA-CNF now shows in both cases (sd, 3D) a structure with $R_g = 23 \pm 3$ nm, $s = 0$, and a Porod constant of $m = 4$. This hints at a rearrangement into more spherical structures, which provides support for recent studies on voids in CNF films.^{58–61} Thus, the cross-linked UCNPs lead to a structural change in the CNF matrix from an oblate structure ($m = 2.7$ for sd and $m = 2.55$ for 3D) to a more spherical structure. This finding is also consistent with the recent results on void filling in CNF films.^{58,59}

Overall, the SAXS results suggest a reduced agglomeration of UCNPs-PSA-CNF. In addition, the UCNPs-PSA-CNF-sd shows a more compact arrangement of UCNPs along the short axis, while the UCNPs-PSA-CNF-3D shows a slightly larger distance. Given these points, the deposition methods (sd and 3D) lead to different phase separations: the 3D printed sample has reduced the agglomeration of polymers. Also, the reduction in polymer agglomerates might be responsible for the increased distance of stacked UCNPs in the 3D printed sample.

Rheology and 3D Printing Performance of the UCNPs Cross-Linked CNF Gel. As mentioned previously, the physical and mechanical properties of CNF gels have been widely studied.^{62,63} Also, in one of our previous study, the physical properties of CNFs and modified CNF gels were evaluated through rheological measurements, proving that the cross-linked network contributed to CNF gels with enhanced yield stress and viscoelasticity.²⁶ Taking this into account, some key rheological parameters were measured, and they were compared with those of the UCNPs cross-linked CNF gel. In the end, we attempted to use the UCNPs cross-linked CNF gel to 3D print models.

It is important to note that both samples, UCNPs-PSA-CNF and PSA-CNF are able to be fully (re)dispersed in toluene (after drying) (Figure 11). So gel samples for rheology measurement had a fixed solid content of 20% prepared by



Figure 11. Suspension of UCNP-PSA-CNF (dried) redispersed in toluene.

redispersing modified CNF species in toluene. The results of the rheology measurements are exposed in Figure 12.

The viscoelastic moduli (Figure 12A) were measured as a function of an oscillatory frequency between 0.1 and 1000 rad/s. It is evident that both CNF gels have consistently larger storage modulus (G') than loss modulus (G''), which means those CNF gels maintained gel-like properties in the applied angular frequency range. The UCNP cross-linked CNF gel had greater values of viscoelastic moduli than the PSA-CNF gel in general. Moreover, the ratio of loss modulus to storage modulus G''/G' , also known as loss tangent, was below 0.35 for the UCNP-PSA-CNF gel, while that for the PSA-CNF gel reached the highest value of 0.42, which indicates that UCNP-PSA-CNF has a better elastic behavior. It can be attributed to the cross-linked UCNP with the surface ligand that endowed a highly entangled network when compared to the uncross-linked CNF gel.

The performed yield stress test showed enhanced physical and mechanical properties (Figure 12B). The viscosity and strain versus shear stress curves visualize the different responses of UCNP-PSA-CNF and PSA-CNF toward the external strength. As shear stress increased, the viscosity of UCNP-PSA-CNF sharply decreased while maintaining better shape retention. This result is consistent with the previous

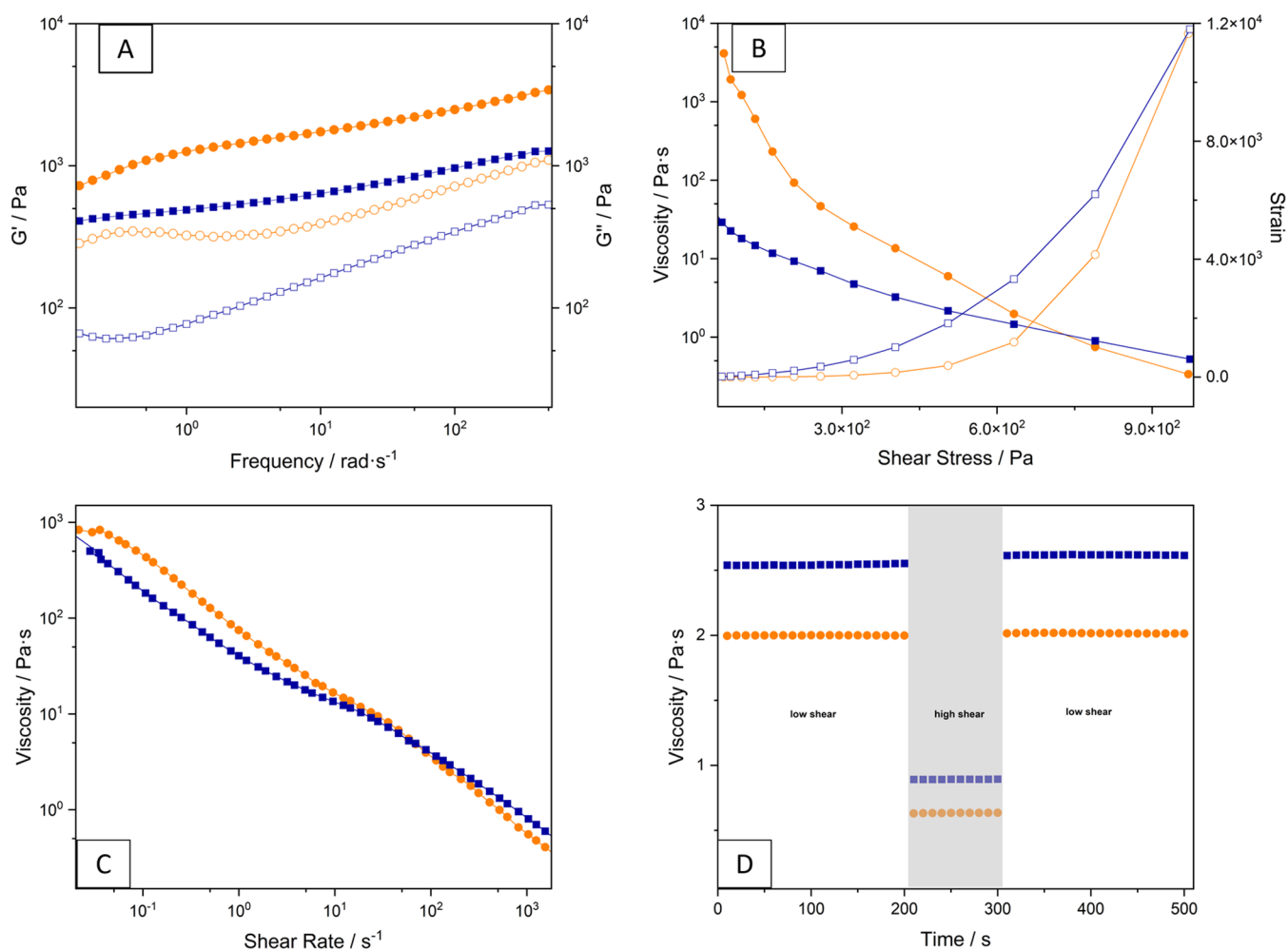


Figure 12. Rheology measurements of CNF-based gels: (A) viscoelastic moduli, (B) yield stress, (C) shear-thinning, and (D) shear recovery. The blue square represents PSA-CNF, the orange circle represents UCNP-PSA-CNF, the solid shape refers to the left Y axis, and the hollow shape refers to the right Y axis.

statement that UCNP-PSA-CNF has enhanced flow, shape retention properties, and, thus, higher yield stress.

Figure 12C represents the shear-thinning behavior of CNF gels. The zero-shear viscosity of UCNP cross-linked CNF gel, which was initially higher, dropped drastically upon the increasing shear rate to the value lower than the value of PSA-CNF. It indicates the ease of extrusion of the UCNP cross-linked CNF gel with good initial shape preservation. The molecular mechanisms behind this behavior might be due to the disentanglement and orientation of grafted polymers and cellulose nanofibrils along the shear flow, also determined by the solvent.⁶⁴

The transition of elastic shape retention and fluid-like flow was monitored by measuring the recovery of the viscosity upon the different magnitudes of shear rate. In Figure 12D, the white area displays the viscosity of CNF gels with a low shear rate at 200 s^{-1} , and the gray area displays the viscosity at a higher shear rate at 1000 s^{-1} . Due to the shear-thinning behavior, UCNP-PSA-CNF had lower viscosity than PSA-CNF, with a shear rate above 100 s^{-1} . UCNP-PSA-CNF and PSA-CNF gels exhibited rapid transition upon time interval and nearly optimal shear recovery. Thus, these CNF gels are promising for 3D gel printing and can achieve a high resolution.

All included, the PSA-CNF gel and UCNP-PSA-CNF gel both have rheological properties suitable for 3D gel printing application. Moreover, the latter has a higher viscosity and enhanced flow and shape retention properties due to the cross-linked UCNP network.

In the final step, the UCNP-PSA-CNF gel ink was processed using 3D printing technologies and several complex structures were obtained. The theoretical models and the 3D prints under daylight or under 980 nm laser diode excitation are shown in Figure 13. With a deposition pressure of 20 kPa, nozzle size of 0.59 mm, and print speed of 10 mm/s, the 3D gel structure was reproducibly printed and closely resembled to the corresponding design model. However, slight deformation

occurred later due to excess solvent evaporation from prints under ambient temperature. Thanks to the unique optical property of UCNP, the 3D prints emitted green light under irradiation with a 980 nm laser diode. It should be noted that the green color is homogeneously distributed all over the 3D printed object.

CONCLUSIONS

We developed a cellulose nanofibril-based hybrid material of CNFs grafted with the polymer of stearyl acrylate and *in situ* cross-linked with upconversion nanoparticles via SET-LRP.

A two-step strategy was exploited to exchange the initial ligand oleic acid of upconversion nanoparticles to a polymerizable small-molecule ligand (AMPS). As exposed previously, the first step of ligand exchange using NOBF_4 achieved phase transfer and full removal of oleic acid as presented with ATR-IR. After the second step exchange, AMPS was successfully attached to UCNPs and allowed sequential coupling on a CNF macroinitiator with stearyl acrylate via SET-LRP, evidenced by TGA, XRD, and microscopic measurements.

In addition, AMPS@UCNP and its incorporation in the CNF matrix kept the optical characteristics of UCNPs as detected by a homebuilt confocal microscope and evidenced by emission spectra in place. The measurement of the confocal microscope preliminarily revealed the 3D distribution of the UCNPs and individual CNFs inside the network.

Further, more interesting aspects emerged from the SAXS analysis. The cross-linked UCNPs led to a structural change in the modified CNF from an oblate structure to a more spherical structure and reduced agglomeration of PSA-grafted CNFs. Also, the 3D printing process has reduced the agglomeration and brought the cross-linked UCNPs to a higher-ordered arrangement.

This cellulose-based hybrid gel has rheological properties suitable for 3D gel printing due to the cross-linked UCNPs with surface ligands rendering an enhanced cross-linked network. With the incorporation of upconversion nanomaterials, this CNF-based hybrid material could have great potential in security inks, additive manufacturing, optical/photonic technologies, and biomedical fields.

ASSOCIATED CONTENT

Supporting Information

The Supporting Information is available free of charge at <https://pubs.acs.org/doi/10.1021/acsami.2c20775>.

Equations and theoretical calculations of TGA (PDF)

AUTHOR INFORMATION

Corresponding Author

Julien R. G. Navarro – Institute of Wood Science, University Hamburg, 21031 Hamburg, Germany; orcid.org/0000-0001-8791-6190; Email: Julien.navarro@uni-hamburg.de

Authors

Xuehe Jiang – Institute of Wood Science, University Hamburg, 21031 Hamburg, Germany; orcid.org/0000-0001-5616-6702

J. Benedikt Mietner – Institute of Wood Science, University Hamburg, 21031 Hamburg, Germany

Constantin Harder – Deutsches Elektronen-Synchrotron DESY, 22607 Hamburg, Germany



Figure 13. 3D models and prints under daylight and 980 nm laser diodes.

Rajesh Komban – Fraunhofer Center for Applied Nanotechnology CAN, D-20146 Hamburg, Germany
Shouzheng Chen – Deutsches Elektronen-Synchrotron DESY, 22607 Hamburg, Germany
Christian Strelow – Department of Chemistry, Institute of Physical Chemistry, University Hamburg, 20146 Hamburg, Germany; orcid.org/0000-0002-5989-1675
Uta Szama – Department of Chemistry, Institute of Inorganic and Applied Chemistry, University Hamburg, 20146 Hamburg, Germany
Michael Fröba – Department of Chemistry, Institute of Inorganic and Applied Chemistry, University Hamburg, 20146 Hamburg, Germany
Christoph Gimmler – Fraunhofer Center for Applied Nanotechnology CAN, D-20146 Hamburg, Germany
Peter Müller-Buschbaum – Physik-Department, Lehrstuhl für Funktionelle Materialien, Technische Universität München, 85748 Garching, Germany; Technical University of Munich, Heinz Maier-Leibnitz Zentrum (MLZ), 85748 Garching, Germany; orcid.org/0000-0002-9566-6088
Stephan V. Roth – Deutsches Elektronen-Synchrotron DESY, 22607 Hamburg, Germany

Complete contact information is available at:
<https://pubs.acs.org/10.1021/acsami.2c20775>

Funding

J.R.G.N., J.B.M., and X.J. thank Fachagentur Nachwachsende Rohstoffe e.V. (FNR/BMEL, Project HolzMat3D, number 2220HV024X), for financial support.

Notes

The authors declare no competing financial interest.

ACKNOWLEDGMENTS

The authors thank R. Schön and S. Werner (University of Hamburg, Institute of Physical Chemistry) for producing TEM images and I. Nevoigt (University of Hamburg, Institute of Inorganic and Applied Chemistry) for XRD measurements. This work benefited from the use of the SasView application, originally developed under NSF award DMR-0520547. SasView also contains code developed with funding from the European Union's Horizon 2020 research and innovation program under the SINE2020 project, grant agreement No 654000.

ABBREVIATIONS

CNF, cellulose nanofibrils
UCNP, upconversion nanoparticle
SET-LRP, single electron transfer living radical polymerization
SA, stearyl acrylate
AMPS, 2-acrylamido-2-methyl-1-propanesulfonic acid

REFERENCES

(1) Moon, R. J.; Martini, A.; Nairn, J.; Simonsen, J.; Youngblood, J. Cellulose Nanomaterials Review: Structure, Properties and Nanocomposites. *Chem. Soc. Rev.* **2011**, *40*, 3941.
(2) Zeng, J.; Hu, F.; Cheng, Z.; Wang, B.; Chen, K. Isolation and Rheological Characterization of Cellulose Nanofibrils (CNFs) Produced by Microfluidic Homogenization, Ball-Milling, Grinding and Refining. *Cellulose* **2021**, *28*, 3389–3408.
(3) Farooq, A. A.; Patoary, M. K.; Zhang, M.; Mussana, H.; Li, M.; Naeem, M. A.; Mushtaq, M.; Farooq, A. A.; Liu, L. Cellulose from Sources to Nanocellulose and an Overview of Synthesis and

Properties of Nanocellulose/Zinc Oxide Nanocomposite Materials. *Int. J. Biol. Macromol.* **2020**, *154*, 1050–1073.

(4) Markstedt, K.; Escalante, A.; Toriz, G.; Gatenholm, P. Biomimetic Inks Based on Cellulose Nanofibrils and Cross-Linkable Xylans for 3D Printing. *ACS Appl. Mater. Interfaces* **2017**, *9*, 40878–40886.

(5) Li, V. C. F.; Mulyadi, A.; Dunn, C. K.; Deng, Y.; Qi, H. J. Direct Ink Write 3D Printed Cellulose Nanofiber Aerogel Structures with Highly Deformable, Shape Recoverable, and Functionalizable Properties. *ACS Sustainable Chem. Eng.* **2018**, *6*, 2011–2022.

(6) Altun, E.; Ekren, N.; Kuruca, S. E.; Gunduz, O. Cell Studies on Electrohydrodynamic (EHD)-3D-Bioprinted Bacterial Cellulose/Polycaprolactone Scaffolds for Tissue Engineering. *Mater. Lett.* **2019**, *234*, 163–167.

(7) Mohan, D.; Khairullah, N. F.; How, Y. P.; Sajab, M. S.; Kaco, H. 3D Printed Laminated CaCO₃-Nanocellulose Films as Controlled-Release 5-Fluorouracil. *Polymers* **2020**, *12*, No. 986.

(8) Mittal, N.; Jansson, R.; Widhe, M.; Benselfelt, T.; Håkansson, K. M. O.; Lundell, F.; Hedhammar, M.; Söderberg, L. D. Ultrastrong and Bioactive Nanostructured Bio-Based Composites. *ACS Nano* **2017**, *11*, 5148–5159.

(9) Maturi, M.; Buratti, V. V.; Casula, G.; Locatelli, E.; Sambri, L.; Bonfiglio, A.; Comes Franchini, M. Surface-Stabilization of Ultrathin Gold Nanowires for Capacitive Sensors in Flexible Electronics. *ACS Appl. Nano Mater.* **2021**, *4*, 8668.

(10) Zhang, Q.; Chen, C.; Chen, W.; Pastel, G.; Guo, X.; Liu, S.; Wang, Q.; Liu, Y.; Li, J.; Yu, H.; Hu, L. Nanocellulose-Enabled, All-Nanofiber, High-Performance Supercapacitor. *ACS Appl. Mater. Interfaces* **2019**, *11*, 5919–5927.

(11) Kaushik, M.; Moores, A. Review: Nanocelluloses as Versatile Supports for Metal Nanoparticles and Their Applications in Catalysis. *Green Chem.* **2016**, *18*, 622–637.

(12) Sánchez-López, E.; Gomes, D.; Esteruelas, G.; Bonilla, L.; Lopez-Machado, A. L.; Galindo, R.; Cano, A.; Espina, M.; Ettchetto, M.; Camins, A.; Silva, A. M.; Durazzo, A.; Santini, A.; Garcia, M. L.; Souto, E. B. Metal-Based Nanoparticles as Antimicrobial Agents: An Overview. *Nanomaterials* **2020**, *10*, No. 292.

(13) Chouirfa, H.; Bouloussa, H.; Mignonney, V.; Falentin-Daudré, C. Review of Titanium Surface Modification Techniques and Coatings for Antibacterial Applications. *Acta Biomater.* **2019**, *83*, 37–54.

(14) Sirelkhatim, A.; Mahmud, S.; Seeni, A.; Kaus, N. H. M.; Ann, L. C.; Bakhori, S. K. M.; Hasan, H.; Mohamad, D. Review on Zinc Oxide Nanoparticles: Antibacterial Activity and Toxicity Mechanism. *Nano-Micro Lett.* **2015**, *7*, 219–242.

(15) Martins, P. M.; Lima, A. C.; Ribeiro, S.; Lanceros-Mendez, S.; Martins, P. Magnetic Nanoparticles for Biomedical Applications: From the Soul of the Earth to the Deep History of Ourselves. *ACS Appl. Bio Mater.* **2021**, *4*, 5839–5870.

(16) Liu, C. M.; Guo, L.; Wang, R. M.; Deng, Y.; Xu, H. B.; Yang, S. Magnetic Nanochains of Metal Formed by Assembly of Small Nanoparticles. *Chem. Commun.* **2004**, *3*, 2726–2727.

(17) Rahmatika, A. M.; Toyoda, Y.; Nguyen, T. T.; Goi, Y.; Kitamura, T.; Morita, Y.; Kume, K.; Ogi, T. Cellulose Nanofiber and Magnetic Nanoparticles as Building Blocks Constructing Biomass-Based Porous Structured Particles and Their Protein Adsorption Performance. *ACS Sustainable Chem. Eng.* **2020**, *8*, 18686–18695.

(18) Zeng, Z.; Mavrona, E.; Sacré, D.; Kummer, N.; Cao, J.; Müller, L. A. E.; Hack, E.; Zolliker, P.; Nyström, G. Terahertz Birefringent Biomimetic Aerogels Based on Cellulose Nanofibers and Conductive Nanomaterials. *ACS Nano* **2021**, *15*, 7451–7462.

(19) Minor, J. L. Hornification -Its Origin and Meaning. *Progress Pap. Recycl.* **1994**, *3*, 93–95.

(20) Pingrey, B.; Hsieh, Y. Lo. Sulfated Cellulose Nanofibrils from Chlorosulfonic Acid Treatment and Their Wet Spinning into High-Strength Fibers. *Biomacromolecules* **2022**, *23*, 1269–1277.

(21) Ren, Q.; Wu, M.; Wang, L.; Zheng, W.; Hikima, Y.; Semba, T.; Ohshima, M. Cellulose Nanofiber Reinforced Poly (Lactic Acid) with Enhanced Rheology, Crystallization and Foaming Ability. *Carbohydr. Polym.* **2022**, *286*, No. 119320.

- (22) Beaumont, M.; Otoni, C. G.; Mattos, B. D.; Koso, T. V.; Abidnejad, R.; Zhao, B.; Kondor, A.; King, A. W. T.; Rojas, O. J. Regioselective and Water-Assisted Surface Esterification of Never-Dried Cellulose: Nanofibers with Adjustable Surface Energy. *Green Chem.* **2021**, *23*, 6966–6974.
- (23) Zhang, X.; Liu, M.; Wang, H.; Yan, N.; Cai, Z.; Yu, Y. Ultralight, Hydrophobic, Anisotropic Bamboo-Derived Cellulose Nanofibrils Aerogels with Excellent Shape Recovery via Freeze-Casting. *Carbohydr. Polym.* **2019**, *208*, 232–240.
- (24) Hatakeyama, M.; Kitaoka, T. Surface-Carboxylated Nanocellulose-Based Bioadaptive Scaffolds for Cell Culture. *Cellulose* **2022**, *29*, 2869–2883.
- (25) Mietner, J. B.; Willruth, S.; Komban, R.; Gimmler, C.; Nehmeh, B.; Navarro, J. R. G. Polymer-Modified Cellulose Nanofibrils Cross-Linked with Cobalt Iron Oxide Nanoparticles as a Gel Ink for 3D Printing Objects with Magnetic and Electrochemical Properties. *Fibers* **2023**, *11*, 2.
- (26) Navarro, J. R. G.; Rostami, J.; Ahlinder, A.; Mietner, J. B.; Bernin, D.; Saake, B.; Edlund, U. Surface-Initiated Controlled Radical Polymerization Approach to In Situ Cross-Link Cellulose Nanofibrils with Inorganic Nanoparticles. *Biomacromolecules* **2020**, *21*, 1952–1961.
- (27) Percec, V.; Popov, A. V.; Ramirez-Castillo, E.; Monteiro, M.; Barboiu, B.; Weichold, O.; Asandei, A. D.; Mitchell, C. M. Aqueous Room Temperature Metal-Catalyzed Living Radical Polymerization of Vinyl Chloride. *J. Am. Chem. Soc.* **2002**, *124*, 4940–4941.
- (28) Sun, L.-D. D.; Dong, H.; Zhang, P.-Z. Z.; Yan, C.-H. H. Upconversion of Rare Earth Nanomaterials. *Annu. Rev. Phys. Chem.* **2015**, *66*, 619–642.
- (29) Tao, K.; Sun, K. Upconversion nanoparticles: a toolbox for biomedical applications. *Photonanotechnol. Ther. Imaging* **2020**, 147–176.
- (30) Kumar, B.; Malhotra, K.; Fuku, R.; Van Houten, J.; Qu, G. Y.; Piunno, P. A. E.; Krull, U. J. Recent Trends in the Developments of Analytical Probes Based on Lanthanide-Doped Upconversion Nanoparticles. *TrAC, Trends Anal. Chem.* **2021**, *139*, No. 116256.
- (31) Benayas, A. *Near Infrared-Emitting Nanoparticles for Biomedical Applications*; 2020. DOI: 10.1007/978-3-030-32036-2.
- (32) Zhang, X.; Guo, Z.; Zhang, X.; Gong, L.; Dong, X.; Fu, Y.; Wang, Q.; Gu, Z. Mass Production of Poly(Ethylene Glycol) Monooleate-Modified Core-Shell Structured Upconversion Nanoparticles for Bio-Imaging and Photodynamic Therapy. *Sci. Rep.* **2019**, *9*, No. 5212.
- (33) Ansari, A. A.; Thakur, V. K.; Chen, G. Functionalized Upconversion Nanoparticles: New Strategy towards FRET-Based Luminescence Bio-Sensing. *Coord. Chem. Rev.* **2021**, *436*, No. 213821.
- (34) Sun, C.; Gradziński, M. Upconversion-Based Nanosystems for Fluorescence Sensing of PH and H₂O₂. *Nanoscale Adv.* **2021**, *3*, 2538–2546.
- (35) Zhang, L.; Jin, D.; Stenzel, M. H. Polymer-Functionalized Upconversion Nanoparticles for Light/Imaging-Guided Drug Delivery. *Biomacromolecules* **2021**, *22*, 3168–3201.
- (36) Nguyen, T.-D.; Hamad, W. Y.; MacLachlan, M. J. Near-IR-Sensitive Upconverting Nanostructured Photonic Cellulose Films. *Adv. Opt. Mater.* **2017**, *5*, No. 1600514.
- (37) Muhr, V.; Wilhelm, S.; Hirsch, T.; Wolfbeis, O. S. Upconversion Nanoparticles: From Hydrophobic to Hydrophilic Surfaces. *Acc. Chem. Res.* **2014**, *47*, 3481–3493.
- (38) Dong, A.; Ye, X.; Chen, J.; Kang, Y.; Gordon, T.; Kikkawa, J. M.; Murray, C. B. A Generalized Ligand-Exchange Strategy Enabling Sequential Surface Functionalization of Colloidal Nanocrystals. *J. Am. Chem. Soc.* **2011**, *133*, 998–1006.
- (39) Kaldéus, T.; Telaretti Leggieri, M. R.; Cobo Sanchez, C.; Malmström, E. All-Aqueous SI-ARGET ATRP from Cellulose Nanofibrils Using Hydrophilic and Hydrophobic Monomers. *Biomacromolecules* **2019**, *20*, 1937–1943.
- (40) Fujisawa, S.; Saito, T.; Kimura, S.; Iwata, T.; Isogai, A. Surface Engineering of Ultrafine Cellulose Nanofibrils toward Polymer Nanocomposite Materials. *Biomacromolecules* **2013**, *14*, 1541–1546.
- (41) Lamm, M. E.; Li, K.; Copenhaver, K.; Kelly, P. V.; Senkum, H.; Tekinalp, H.; Gramlich, W. M.; Ozcan, S. Aqueous-Based Polyimine Functionalization of Cellulose Nanofibrils for Effective Drying and Polymer Composite Reinforcement. *ACS Appl. Polym. Mater.* **2022**, *4*, 7674–7684.
- (42) Dong, H.; Napadensky, E.; Orlicki, J. A.; Snyder, J. F.; Chantawansri, T. L.; Kapllani, A. Cellulose Nanofibrils and Diblock Copolymer Complex: Micelle Formation and Enhanced Dispersibility. *ACS Sustainable Chem. Eng.* **2017**, *5*, 1264–1271.
- (43) Kelly, P. V.; Cheng, P.; Gardner, D. J.; Gramlich, W. M. Aqueous Polymer Modification of Cellulose Nanofibrils by Grafting-Through a Reactive Methacrylate Group. *Macromol. Rapid Commun.* **2021**, *42*, No. 2000531.
- (44) Remmele, J.; Shen, D. E.; Mustonen, T.; Fruehauf, N. High Performance and Long-Term Stability in Ambiently Fabricated Segmented Solid-State Polymer Electrochromic Displays. *ACS Appl. Mater. Interfaces* **2015**, *7*, 12001–12008.
- (45) Mietner, J. B.; Jiang, X.; Edlund, U.; Saake, B.; Navarro, J. R. G. 3D Printing of a Bio-Based Ink Made of Cross-Linked Cellulose Nanofibrils with Various Metal Cations. *Sci. Rep.* **2021**, *11*, No. 6461.
- (46) Navarro, J. R. G.; Edlund, U. Surface-Initiated Controlled Radical Polymerization Approach To Enhance Nanocomposite Integration of Cellulose Nanofibrils. *Biomacromolecules* **2017**, *18*, 1947–1955.
- (47) Georgouvelas, D.; Jalvo, B.; Valencia, L.; Papawassiliou, W.; Pell, A. J.; Edlund, U.; Mathew, A. P. Residual Lignin and Zwitterionic Polymer Grafts on Cellulose Nanocrystals for Antifouling and Antibacterial Applications. *ACS Appl. Polym. Mater.* **2020**, *2*, 3060–3071.
- (48) Komban, R.; Klare, J. P.; Voss, B.; Nordmann, J.; Steinhoff, H. J.; Haase, M. An Electron Paramagnetic Resonance Spectroscopic Investigation on the Growth Mechanism of NaYF₄:Gd Nanocrystals. *Angew. Chem., Int. Ed.* **2012**, *51*, 6506–6510.
- (49) Buffet, A.; Rothkirch, A.; Döhrmann, R.; Körstgens, V.; Abul Kashem, M. M.; Perlich, J.; Herzog, G.; Schwartzkopf, M.; Gehrke, R.; Müller-Buschbaum, P.; Roth, S. V. P03, the Microfocus and Nanofocus X-Ray Scattering (MiNaXS) Beamline of the PETRA III Storage Ring: The Microfocus Endstation. *J. Synchrotron Radiat.* **2012**, *19*, 647–653.
- (50) *the SasView application, Version 5. Released June 3, 2022.* <https://www.sasview.org/>.
- (51) Recalde, I.; Estebanez, N.; Francés-Soriano, L.; Liras, M.; González-Béjar, M.; Pérez-Prieto, J. Upconversion Nanoparticles with a Strong Acid-Resistant Capping. *Nanoscale* **2016**, *8*, 7588–7594.
- (52) Hund, F. Das Ternäre Fluorid NaYF₄. *Z. Anorg. Chem.* **1950**, *261*, 106–115.
- (53) Janjua, R. A.; Gao, C.; Dai, R.; Sui, Z.; Ahmad Raja, M. A.; Wang, Z.; Zhen, X.; Zhang, Z. Na⁺-Driven Nucleation of NaYF₄:Yb,Er Nanocrystals and Effect of Temperature on Their Structural Transformations and Luminescent Properties. *J. Phys. Chem. C* **2018**, *122*, 23242–23250.
- (54) Reinke, S. K.; Roth, S. V.; Santoro, G.; Vieira, J.; Heinrich, S.; Palzer, S. Tracking Structural Changes in Lipid-Based Multi-component Food Materials Due to Oil Migration by Microfocus Small-Angle X-Ray Scattering. *ACS Appl. Mater. Interfaces* **2015**, *7*, 9929–9936.
- (55) Guccini, V.; Yu, S.; Agthe, M.; Gordeyeva, K.; Trushkina, Y.; Fall, A.; Schütz, C.; Salazar-Alvarez, G. Inducing Nematic Ordering of Cellulose Nanofibers Using Osmotic Dehydration. *Nanoscale* **2018**, *10*, 23157–23163.
- (56) Hammouda, B. A New Guinier-Porod Model. *J. Appl. Crystallogr.* **2010**, *43*, 716–719.
- (57) Engström, J.; Jimenez, A. M.; Malmström, E. Nanoparticle Rearrangement under Stress in Networks of Cellulose Nanofibrils Using in Situ SAXS during Tensile Testing. *Nanoscale* **2020**, *12*, 6462–6471.
- (58) Brett, C. J.; Forslund, O. K.; Nocerino, E.; Kreuzer, L. P.; Widmann, T.; Porcar, L.; Yamada, N. L.; Matsubara, N.; Månsson, M.; Müller-Buschbaum, P.; Söderberg, L. D.; Roth, S. V. Humidity-

Induced Nanoscale Restructuring in PEDOT:PSS and Cellulose Nanofibrils Reinforced Biobased Organic Electronics. *Adv. Electron. Mater.* **2021**, *7*, No. 2100137.

(59) Brett, C. J.; Mittal, N.; Ohm, W.; Gensch, M.; Kreuzer, L. P.; Körstgens, V.; Månsson, M.; Frielinghaus, H.; Müller-Buschbaum, P.; Söderberg, L. D.; Roth, S. V. Water-Induced Structural Rearrangements on the Nanoscale in Ultrathin Nanocellulose Films. *Macromolecules* **2019**, *52*, 4721–4728.

(60) Chen, Q.; Brett, C. J.; Chumakov, A.; Gensch, M.; Schwartzkopf, M.; Körstgens, V.; Söderberg, L. D.; Plech, A.; Zhang, P.; Müller-Buschbaum, P.; Roth, S. V. Layer-by-Layer Spray-Coating of Cellulose Nanofibrils and Silver Nanoparticles for Hydrophilic Interfaces. *ACS Appl. Nano Mater.* **2021**, *4*, 503–513.

(61) Chen, Q.; Betker, M.; Harder, C.; Brett, C. J.; Schwartzkopf, M.; Ulrich, N. M.; Toimil-Molaes, M. E.; Trautmann, C.; Söderberg, L. D.; Weindl, C. L.; Körstgens, V.; Müller-Buschbaum, P.; Ma, M.; Roth, S. V. Biopolymer-Templated Deposition of Ordered and Polymorph Titanium Dioxide Thin Films for Improved Surface-Enhanced Raman Scattering Sensitivity. *Adv. Funct. Mater.* **2022**, *32*, No. 2108556.

(62) Albornoz-Palma, G.; Betancourt, F.; Mendonça, R. T.; Chinga-Carrasco, G.; Pereira, M. Relationship between Rheological and Morphological Characteristics of Cellulose Nanofibrils in Dilute Dispersions. *Carbohydr. Polym.* **2020**, *230*, No. 115588.

(63) Hu, X.; Yang, Z.; Kang, S.; Jiang, M.; Zhou, Z.; Gou, J.; Hui, D.; He, J. Cellulose Hydrogel Skeleton by Extrusion 3D Printing of Solution. *Nanotechnol. Rev.* **2020**, *9*, 345–353.

(64) Nechyporchuk, O.; Belgacem, M. N.; Pignon, F. Current Progress in Rheology of Cellulose Nanofibril Suspensions. *Biomacromolecules* **2016**, *17*, 2311–2320.

Multifunctional Cellulose Nanofibrils–GdF₃ Nanoparticles Hybrid Gel and Its Potential Uses for Drug Delivery and Magnetic Resonance Imaging

Xuehe Jiang, J. Benedikt Mietner, Dhanya Raveendran, Kirill V. Ovchinnikov, Benedikt Sochor, Susanne Mueller, Philipp Boehm-Sturm, Frédéric Lerouge, Frédéric Chaput, Pavel Gurikov, Stephan V. Roth, and Julien R. G. Navarro*



Cite This: *ACS Appl. Nano Mater.* 2023, 6, 21182–21193



Read Online

ACCESS |



Metrics & More



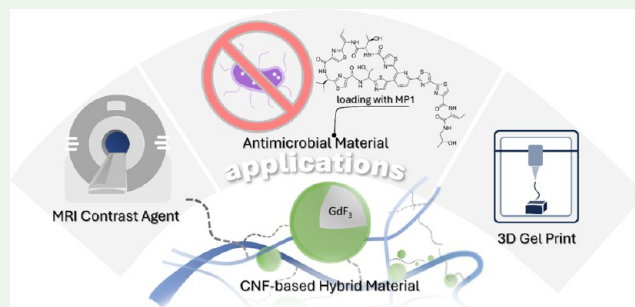
Article Recommendations



Supporting Information

ABSTRACT: A multifunctional hybrid gel based on cellulose nanofibrils (CNFs) was developed by grafting on its surface stearyl acrylate (PSA) and gadolinium(III) fluoride nanoparticles (GdF₃ NPs) *via* Cu⁰-mediated surface-initiated radical polymerization (SET-LRP) while encapsulating antimicrobial peptides in it. GdF₃ NPs were first surface-modified with 11-phosphonoundecyl acrylate (PDA) to participate in the SET-LRP and cross-linked the grafted polymer-modified CNF. Several characterizations of the hybrid material (GdF₃–PSA–CNF) were carried out, such as Fourier transform infrared (FTIR) spectroscopy, thermogravimetric analysis (TGA), rheology, and microscopic analyses. The grafted PSA and cross-linked GdF₃ NPs created sophisticated networks in the CNF-based gel, presenting outstanding rheological properties and promising three-dimensional (3D) printability of this hybrid material (GdF₃–PSA–CNF). The nanostructures of GdF₃ NPs and their incorporated CNF species were characterized *via* small-angle X-ray scattering (SAXS). In addition, due to the unique intrinsic property of the GdF₃ nanoparticles, properties for magnetic resonance imaging (MRI) of GdF₃–PSA–CNF were investigated, showing the potential application as a contrast agent. Finally, the encapsulation of the antimicrobial peptides added another function to the hybrid material, evaluated by an antimicrobial test against methicillin-resistant *Staphylococcus aureus* (MRSA) *in vitro*.

KEYWORDS: cellulose nanofibril (CNF), nanocellulose, single electron transfer living radical polymerization (SET-LRP), cellulose-based hybrid material, gadolinium(III) fluoride nanoparticles, contrast agent, bacteriocins, 3D gel-print, 3D printing



INTRODUCTION

Nanotechnology has been a driving force behind a new industrial revolution, impacting various fields, including nanocomposites, medicine, and biosensing applications.^{1,2} Nanoscale materials, with dimensions of approximately 100 nm in at least one direction, possess unique physicochemical, optical, magnetic, and biological properties compared to those of their bulk materials. In this context, biobased polymeric nanomaterials are being actively pursued as promising alternatives to traditional fossil-based resources.³ These biobased nanomaterials integrate the potentials of nanotechnology with the inherent benefits of renewable sources, such as their plentiful availability, biodegradability, recyclability, biocompatibility, and cost-effectiveness. Therefore, it is possible to develop advanced materials from biobased nanomaterials that not only substitute but also surpass the performance of existing, traditional synthetic materials. Among the various plant-based nanomaterials, cellulose nanomaterials emerge as one of the most extensively studied.^{4–6}

Cellulose nanofibrils (CNFs), a vital component of the cellulose-based nanomaterial category, possess numerous advantageous characteristics,⁷ including high specific surface area, high Young's modulus with remarkable tensile strength, biocompatibility, and lack of toxicity. Due to their high aspect ratio (5–60 nm in width and several micrometers in length)⁸ and specific surface area, CNFs can arrange into two- or three-dimensional (2D or 3D) structures upon the production procedure, such as films, hydrogels or aerogels. Individualized or isolated CNFs can be produced through mechanical disintegration and defibrillation processes of wood cellulosic pulp in aqueous media to form a viscous dispersion. The

Received: September 7, 2023

Revised: October 23, 2023

Accepted: October 23, 2023

Published: November 6, 2023



abundance of the surface hydroxy groups renders the CNF highly hydrophilic and gives rise to interfibrillar interactions due to hydrogen bonds, leading to fibril agglomeration. As a result, CNF gels exhibit a cross-linked 3D network and rheological behaviors, such as viscoelasticity and shear-thinning, which makes CNF gels well suited for 3D gel printing.^{9,10}

Cellulose nanomaterials, as valuable and versatile materials, have drawn broad interest in the field of cellulose-based hybrid materials as cellulose can adapt new properties by combining them with inorganic nanoparticles (NPs). With the complementary association of the cellulose nanomaterials and specific inorganic NPs, the final hybrid systems possess respective properties of both constituents.¹¹ For example, Madivoli et al.¹² developed a TEMPO-oxidized CNF composite that imparted antimicrobial activity by incorporating silver NPs, which could be used as wound dressings and packaging materials, preventing microorganism growth *in vivo*. Alle et al.¹³ reported a spontaneous method for growing gold NPs on CNFs. The hybrid composite was further converted into the paper strip, which served as a biosensor for H₂O₂ and cholesterol detection, suggesting the great potential application in disease diagnosis.¹³ Oprea et al.¹⁴ presented an overview of nanocellulose hybrids with metal oxides (MO) NPs applied in biomedical fields. MONPs, such as ZnO, TiO₂, CuO, MgO, or Fe₃O₄, are mainly used to induce new antibacterial and magnetic functions to CNFs, and CNFs serve as a support material, providing flexibility and a high surface area for MONPs impregnation.¹⁴

In our recent works,^{15–17} we have shown that the CNF surface hydroxyls can be chemically modified to act as a radical polymerization initiator for the Cu⁰-mediated single electron transfer living radical polymerization (SET-LRP), introduced by Percec et al.¹⁸ SET-LRP is a robust polymerization technique as the reaction can be conducted in a relatively mild condition and polymerize vinyl monomers in a broad range, with full control on the grafted polymeric chain length.¹⁸ We employed this powerful technique and demonstrated a series of approaches to cross-link polymer-grafted cellulose nanofibrils with various inorganic nanoparticles based on SET-LRP, therefore creating different CNF-based hybrid materials with enhanced mechanical properties and unique characteristics such as UV-blocking,¹⁵ NIR absorption,¹⁹ and electrochemical properties.²⁰

Gadolinium (Gd) is a rare-earth element from the lanthanide series that is widely utilized as a positive contrast agent (CA) in magnetic resonance imaging (MRI) systems. MRI CAs are used to improve the visibility and image quality of specific tissues or organs during an MRI scan, thereby improving diagnostic accuracy. The primary source of image contrast in MRI comes from the variation in relaxation times of tissues interacting with the CA. Relaxation times are MRI measurements that indicate the rate at which hydrogen nuclei recover following perturbation by using a radiofrequency pulse in the scanner. They are influenced by the molecular environment of the hydrogen atoms within the tissue, primarily associated with tissue water and fat content *in vivo*. Relaxation occurs through two independent processes known as longitudinal (T1) and transverse (T2) relaxation. T1 relaxation time signifies how quickly the net magnetization vector recovers to its ground state along the main static magnetic field direction. On the other hand, T2 relaxation refers to the progressive dephasing of spinning dipoles, resulting in decay in

the magnetization in the transverse plane. The accelerated relaxations are reflected as a signal enhancement on T1-weighted MR images and a signal reduction on T2-weighted MR images.

Chelated complexes of paramagnetic gadolinium(III) ions (Gd³⁺) are widely used as CAs in MRI. However, some conventional Gd-chelates have certain drawbacks, including the lack of diagnostic specificity and the toxicity associated with the unexpected release of free Gd ions.²¹ To address these issues and minimize the release of Gd³⁺ ions *in vivo*, several researchers have proposed an alternative using gadolinium-based nanoparticles. Among the wide range of Gd-based inorganic nanoparticles, such as Gd₂O₃,^{22,23} GdPO₄,^{24,25} and Gd(OH)₃,²⁶ gadolinium fluorides (GdF₃) or GdF₃ NPs doped with luminescent lanthanides, such as Eu, Tb, and Er, have gained significant interest due to their high relaxivity values.^{27–29} In addition, recent studies have highlighted their lack of toxicity and good biocompatibility.²⁷ Notably, GdF₃ NPs offer a distinct advantage over other Gd-based inorganic nanoparticles in terms of chemical stability and versatility, as both cations and anions can easily tailor their surface properties.³⁰

Significant efforts have been directed toward synthesizing Gd NPs with various dimensions and compositions in the past few decades.^{31–34} There is also a growing interest in optimizing the surface properties of Gd NPs through surface modifications, including coating with macromolecules, to achieve enhanced contrast abilities.^{35–37} However, there have been no reports of coupling Gd NPs to cellulose nanomaterials. Therefore, this study attempts to cross-link surface-modified Gd NPs into CNFs using SET-LRP. Our conception is to develop a novel contrast agent that combines the MRI-active magnetic properties of Gd NPs with the biocompatibility of CNFs. Through this approach, we aim to explore new potential applications of cellulose nanomaterials in biomedicine.

In recent years, worldwide focus on the employment of nanocellulose appears in the field of biomedical applications, which includes drug delivery systems,^{4,38–40} wound dressing,^{41–43} scaffolds,^{44–46} etc., along with the assistance of the coupling of multidisciplinary fields such as biology and chemistry.⁴⁷ Durand et al. provided a comprehensive overview of the application and the health and toxicology concerns of nanocellulose in the biomedical field.⁴⁸ In general, CNFs are cytocompatible and mostly not hazardous to human health, especially as they also provide good cell proliferation and migration.^{49,50} A pioneering work of CNFs for drug delivery was reported by Kolakovic et al.⁵¹ A CNF-based film was produced and loaded with drugs up to 20–40% by encapsulation. The drug release studies showed a long-lasting period of up to 3 months with kinetics being dependent on the drug used. The result indicates that CNFs are suitable for controlled release applications and can be processed with poorly water-soluble drugs to give sustained release.⁵¹ In a recent study, Abu et al.⁵² developed nanocellulose composites loaded with honey as an antimicrobial wound dressing. The controlled drug release from the drug delivery system successfully treated chronic wounds.⁵²

Furthermore, the characteristic features of CNFs can be significantly altered by surface modification to create new polymers to adapt to varying requirements of biomedical utilizations. The surface hydroxyls of CNFs are available for numerous chemical modifications. Rai et al.⁵³ provided insight

into the recent advancements in the synthesis, fabrication, and processing of cellulose nanomaterials, with strategic chemical modification routes to tailor their properties for targeted biomedical applications. Bacteriocins, a group of natural antimicrobial peptides, have been selected as alternatives to antibiotics for applications in food preservation and the treatment of infectious diseases in both livestock and humans.^{54,55} Their appeal lies in their minimal toxicity and protein-based nature, addressing the challenges of drug-resistant pathogens. Bacteriocins are produced by bacteria to hinder the growth of other bacterial strains in the competition for nutrients and habitats.⁵⁶ These peptides represent a promising class of natural antibacterial compounds, exhibiting effectiveness against many Gram-positive pathogens.⁵⁷ This efficacy extends to antibiotic-resistant strains, including Methicillin-resistant *Staphylococcus aureus* (MRSA), vancomycin-resistant enterococci, and penicillin-resistant *Streptococcus pneumoniae*.⁵⁸

To conclude, as versatile materials, cellulose nanomaterials can be considered as an innovative pool for biomaterial development. In this study, we present a multifunctional hybrid gel based on CNFs that are suitable for numerous versatile applications. The gel can be used as the ink for 3D gel-printing, exhibit potential as a novel hybrid contrast agent based on MRI-active magnetic GdF₃, and most importantly, serve as an antimicrobial medium by encapsulating bacteriocins.

To achieve this, a surface-initiated radical polymerization (SET-LRP) was employed to graft polymers from CNFs surfaces and cross-link surface-modified GdF₃ *in situ*, in the end, encapsulating bacteriocins. By grafting polymers, specifically stearyl acrylate (PSA), onto the surfaces of CNFs, the interfibrillar hydrogen bond effect in CNFs decreased, and the encapsulation of the hydrophobic biomolecules was facilitated into CNFs.

Additionally, the surface of GdF₃ NPs was modified with the ligand 11-phosphonoundecyl acrylate. NPs could therefore engage in polymerization and act as cross-linking agents, creating sophisticated networks in modified nanofibrils.

EXPERIMENTAL SECTION

Materials. 1,1'-Carbonyldiimidazole (CDI), 2-bromo-2-methylpropionic acid (98%), imidazole (≥99%), stearyl acrylate (SA, 97%), 11-phosphonoundecyl acrylate, isopropanol (≥99.5%), ethanol (98%), and toluene were purchased from Sigma-Aldrich. Tris[2-(dimethylamino)ethyl]amine (Me6-TREN) and dimethyl sulfoxide (DMSO, ≥99%) were purchased from Alfa Aesar. Copper wire (diameter, 1 mm) was purchased from Fisher. The gadolinium(III)-fluoride (Gd_{0.9}Tb_{0.1}F₃) nanoparticles were received as a dispersion (460 mg/mL) in water.

The monomer used for grafting polymerization was purified by passing it through a basic alumina column to remove inhibitors.

Production and Solvent Exchange of Cellulose Nanofibrils. CNFs were prepared from a previously described procedure.⁵⁹ Dried elemental chlorine-free bleached Kraft pulp (Stendal GmbH, Germany) was used. First, the cellulose suspension in water was obtained with a 75–80° SR (SR: Schopper-Riegler degrees were determined using the Schopper-Riegler method (DIN EN ISO 5267–1)). Then, the cellulose pulp was defibrillated by using a microfluidizer (M-110EH-30, Microfluidizer) under high pressure, passing the slurry in different chambers with orifice widths of 400 and 200 μm (2 times, 15,000 psi) and 200 and 100 μm (4 times, 25,000 psi) successively. The collected CNF suspension was concentrated through centrifugation, resulting in a 2 wt % CNF aqueous gel.

Solvent Exchange of Cellulose Nanofibrils. The obtained CNF aqueous gel (2 wt %) was solvent-exchanged into DMSO as previously described.¹⁵ Briefly, 150 mL of DMSO was slowly added to the aqueous suspension of CNFs (10 g of gel in 80 mL of water) under stirring. Then, the solvent was discarded by centrifugation and replaced with fresh DMSO. The procedure resulted in a 2 wt % CNF/DMSO gel.

Synthesis of the CNF-Based Macroinitiator (CNF-MI). CNF-based macroinitiator was synthesized as previously described.⁶⁰ The process resulted in a 1 wt % CNF-MI gel.

Synthesis of GdF₃ Nanoparticles. The synthesis of GdF₃ nanoparticles was conducted following a previously reported, general procedure, easy and applicable to essentially all rare-earth salts.⁶¹ The GdF₃ nanoparticles have an average size of about 10 nm with a slightly elongated spheroidal shape.⁶²

Surface Modification of GdF₃. A mixture of 95:5 (v/v) ethanol/H₂O was used as a solvent for surface modification. 25 mg of 11-phosphonoundecyl acrylate (PDA) was dissolved in 4 mL of solvent and added to a predispersed GdF₃ suspension (50 mg/2.18 mL). The mixture was ultrasonicated at 30–40 °C for 20 min and stirred at 80 °C for 3 h. The surface-modified nanoparticles (PDA@GdF₃) were collected and purified by centrifugation (10,000 rpm, 5 min) in ethanol three times.

Procedure for the SET-LRP Grafting of PDA@GdF₃ and Stearyl Acrylate on CNFs (GdF₃-PSA-CNF). The CNF-MI (4 g, 1 wt %) was suspended in DMSO (30 mL) with the addition of PDA@GdF₃ (10 mg) and SA (in 15 mL toluene). The suspension was degassed *via* nitrogen purging. A Cu wire (diameter = 1 mm, length = 6 cm) was treated with HCl solution (37%) previously and rinsed with water and acetone, then added to the suspension under the nitrogen blanket. The reaction started upon the addition of Me6-TREN (200 μL, 10 vol % in DMSO) and proceeded overnight under a nitrogen atmosphere at 40 °C. The resulting gel was separated from the reaction liquid, purified by dissolving in toluene (15 mL), and then precipitated in isopropanol (15 mL). The purification steps were repeated four times through centrifugation (6000 rpm, 1 h) with a toluene/isopropanol (1:1) mixture.

Procedure for the SET-LRP Grafting of Stearyl Acrylate on CNFs (PSA-CNF). The grafting polymerization was the same as described above, except that the PDA@GdF₃ was not added to the reaction.

Procedure for the SET-LRP Grafting of PDA@GdF₃ on CNFs (GdF₃-CNF). The grafting polymerization was the same as described above except that the stearyl acrylate was not added to the reaction.

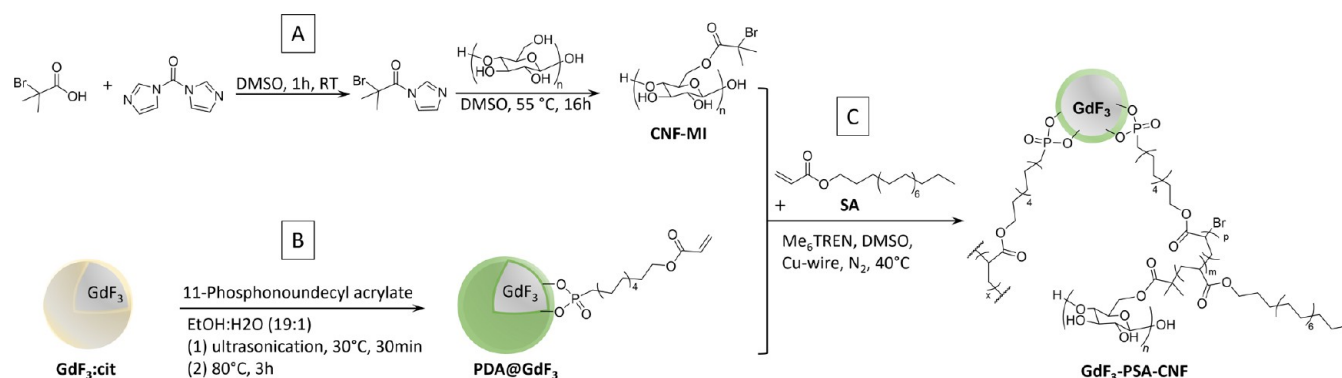
3D Gel Printing of CNF-Based Gels. All CNF-based gels were printed by pneumatic extrusion (INKREDIBLE 3D-Bioprinter, CELLINK) with a nozzle size of 0.45 mm. A disposable syringe was loaded with gels and inserted into the printing cartridge through a female–female Luer Lock adapter. The gel printability was adjusted by optimizing the inflow air rate through the fixed nozzle to achieve stable and consistent precision of the printing layer. The 3D models were designed with Tinkercard and converted into G-code *via* PrusaSlicer.

Procedure for Supercritical CO₂ Drying. Toluene-based sample gels were transferred into a high-pressure autoclave with a volume of 3.9 L and dried with supercritical CO₂ at 40 °C and a pressure of 100 bar for 5 h. The continuous flow of CO₂ was set at 30 g/min. After complete drying, the pressure in the autoclave was decreased at a rate of 2 bar/min.

Bacteriocin Loading on CNF-Based Gels. The thiopeptide bacteriocin micrococcin P1 (MP1) was used in this study. The separation and purification of MP1 were performed as described earlier.⁶³ The 3D-printed cuboids (1 × 1 × 0.5 cm³) of GdF₃-PSA-CNF gel were freeze-dried and dried under ambient temperature separately. 1 mg of MP1 (1 mg/mL) was slowly dropped on the cuboid and dried overnight.

Characterization. Fourier transform infrared spectroscopy equipped with an attenuated total reflection (ATR-FTIR) was performed on a Bruker Vector 33 spectrometer. All spectra were

Scheme 1. (A) Chemical Conversion of CNFs into CNF-Based Macroinitiator (CNF-MI); (B) Surface Modification of GdF₃ NPs with 11-Phosphonoundecyl Acrylate (PDA) as Shell; (C) Grafting Polymerization and *In Situ* Cross-Linking of CNF-MI with Stearyl Acrylate (SA) and PDA@GdF₃ via SET-LRP



obtained through 60 scans in the spectral region 3600–550 cm^{-1} , with a spectral resolution of 4 cm^{-1} .

An ultrahigh-resolution field emission scanning electron microscope (Quanta FEG Type 250, FEI Electron Optics SN: D9122, the Netherlands) was applied for observing modified CNFs at an acceleration voltage of 7 kV and high-vacuum conditions using an Everhart–Thornley detector. Samples were mounted on the stubs using carbon tape and coated with a 5 nm gold layer under an inert atmosphere with a BIORAD SC510 sputtering machine prior to microscopic imaging.

Rheology tests were monitored by a TA Instruments AR 2000ex with Advantage Software v5.8.2. All materials were tested with a 40 mm parallel-plate configuration and a 500 μm gap distance at room temperature. A shear stress ramp ranging from 0.01 to 1000 Pa was applied, and rotational shear-viscosity measurements were performed in flow mode with the shear rate ranging from 0.01 to 1000 s^{-1} . The frequency sweep was between 0.1 and 100 rad/s, and a strain sweep was performed at an angular frequency of 6.28 rad/s to ensure the measurements in the linear viscoelastic region. Rotational recovery measurements were performed to characterize the material recovery behavior by applying a low shear rate of 100 s^{-1} for 200 s, followed by a high shear rate at 1000 s^{-1} for 100 s and a low shear rate of 100 s^{-1} for 200 s.

Thermogravimetric analysis (TGA) was performed with a Netzsch STA409PC Luxx. Each sample (approximately 20 mg) was heated under nitrogen from room temperature to 1000 $^{\circ}\text{C}$ with a heating rate of 10 $^{\circ}\text{C}/\text{min}$ and then held at this temperature for 1 h more.

Magnetic Resonance Imaging (MRI) was performed using a 7T rodent scanner (BioSpec 70/20 USR, Bruker, Germany) running Paravision 6.0.1. software and a 20 mm quadrature volume resonator (RAPID Biomedical GmbH, Rimpar, Germany). To explore their use as MRI contrast agents, GdF₃-CNF suspensions in water (1 wt %) were embedded in 2% agar prepared with phosphate-buffered saline (1 \times PBS). T2-weighted (T2w) and T1-weighted (T1w) MRI was performed with turbo-spin-echo (2D RARE) sequences in either 3 axial or 3 sagittal slices of 1.5 mm with a gap of 1 mm and a field of view (FOV) = 30 mm \times 30 mm and image matrix size (MTX) = 150 \times 150. The T2w image was acquired with repetition time (TR) = 2500 ms, echo time spacing (ΔTE) = 6.9 ms, echo time (TE) = RARE factor = 8, 4 averages, and total acquisition time (TA) = 3:00 min. A short TE was used due to the short T2 of the gels. Scan parameters for the T1w sequence were TR/TE = 1000:10 ms, RARE factor 2, 3 averages, and TA = 2:48 min. For samples that gave a signal, we also determined relaxation times. T2 was measured using multislice multiecho (MSME) T2 mapping with identical geometry as the T2w image and MTX = 100 \times 100, TR = 2000 ms, 30 TEs ranging from 6.5 to 195 ms, TA = 3:12 min. T1 was measured using variable repetition time RARE T1 mapping. A single slice was acquired with identical geometry and resolution as the center slice of the T2 map, 30 TRs ranging from 105 to 12.500 ms, TE = 7 ms, RARE factor 2, TA = 25:30 min. Mean \pm std T2 and T1 were

measured in the gel and in a control substance (pure toluene or agar) using region of interest analysis in ImageJ (<https://imagej.net>).

Ultrasmall- and wide-angle X-ray scattering (USAX, WAXS) were performed at beamline P03, DESY.⁶⁴ The following parameters were used: wavelength $\lambda = 1.048 \text{ \AA}$, beam size $\sim 30 \times 30 \mu\text{m}^2$; sample to detector distance: SDD(USAXS) = 9500 mm and SDD(WAXS) = 211 mm. As detectors, a PILATUS 2 M with a pixel size of 172 μm (Dectris GmbH, Switzerland) for USAXS and a LAMBDA 9 M with a pixel size of 55 μm (X-spectrum GmbH, Germany) were used. The samples were scanned over $2 \times 2 \text{ mm}^2$ with a step size of 0.1 mm and an acquisition time of 1 s to avoid beam damage. All subsequent images were summed up and radially integrated for data analysis to obtain intensity $I(q)$ as a function of wavevector transfer q .

An antimicrobial activity test was performed against MRSA. Multiresistant MRSA strain ATCC 33591-lx (PerkinElmer, Waltham, MA) was grown overnight in brain heart infusion (BHI) broth (Oxoid, U.K.) at 37 $^{\circ}\text{C}$ under aerobic conditions without shaking. The strain was derived from the parental strain *S. aureus* ATCC 33591, a clinical MRSA strain isolated from Elmhurst Hospital in New York, NY.⁶⁵ Agar plate assay and MP1 purification were performed as described earlier.⁶³

RESULTS AND DISCUSSION

Synthesis and Characterization of GdF₃-PSA-CNF.

The global synthesis strategy for the GdF₃-PSA-CNF material is shown in Scheme 1. Surface-modified GdF₃ (PDA@GdF₃) together with a monomer SA was polymerized on the CNF surfaces *via* a surface-initiated controlled radical polymerization, obtaining a hybrid CNF material, namely, GdF₃-PSA-CNF. The polymer of SA hydrophobized CNFs, therefore, reducing their aggregation and inducing a strong hydrophobic network into CNFs. The surface-modified GdF₃ not only enhances the network by cross-linking *in situ* but also brings unique magnetic properties of GdF₃ NPs to expand the utilization of the final product.

The initial GdF₃ NPs were fully dispersed in a citric acid solution. A surface modification with 11-phosphonoundecyl acrylate (PDA) was carried out to introduce acrylic functions in order to engage the NPs in the polymerization. The grafting of PDA at the surface of GdF₃ was monitored by FT-IR measurements (Figure S1). After surface modification, new signals emerged in the spectrum B; the phosphonate groups on GdF₃ NPs were evidenced by the bands at 1058 cm^{-1} (P–O) and 945 cm^{-1} (P–OH), 1225 cm^{-1} (P=O), 1560 cm^{-1} (C=C), 2950 and 2895 cm^{-1} (C–H), and 1733 cm^{-1} (C=O).

On the other hand, CNFs were solvent-exchanged into DMSO and underwent esterification to anchor the alkyl

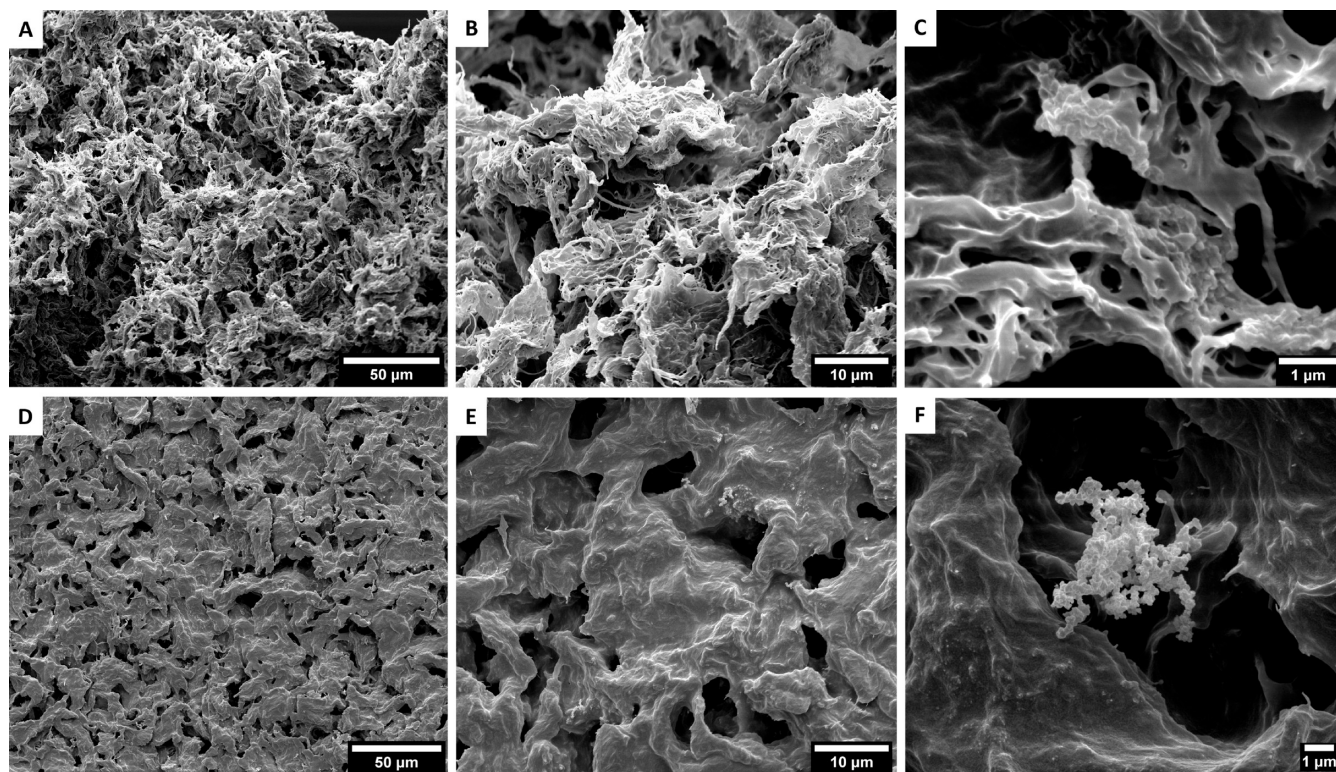


Figure 1. SEM images of GdF₃-PSA-CNF: (A–C) freeze-dried and (D–F) supercritical CO₂ dried.

bromide on their surface to enable monomers grafting from it. The chemical transformation of CNFs into CNF-macroinitiator (CNF-MI) was proved by the IR spectrum (Figure S2A,B), which displays an additional absorption band at 1733 cm⁻¹ (C=O) attributed to the carbonyl group of the ester function, besides the characteristic bands of CNFs (3320 cm⁻¹ O–H, 2950 and 2895 cm⁻¹ C–H, 1430 cm⁻¹ C–H, and 1161 cm⁻¹ C–O–C).

We finally carried out the surface-initiated controlled radical polymerization of SA and PDA@GdF₃ with CNF-MI (GdF₃-PSA-CNF), as illustrated in Scheme 1B. The polymerization occurred in a solvent mixture of DMSO/toluene, as CNF-MI and PDA@GdF₃ are stable in DMSO, while SA is rather highly soluble in toluene. As a comparison, polymerization without PDA@GdF₃ was also performed (PSA-CNF).

The result was analyzed with FT-IR (Figure S2B,C). Besides the characteristic bands from CNF, both modified CNFs have high-intensity peaks at 2917 and 2850 cm⁻¹ (C–H), 1733 cm⁻¹ (C=O), 1467 cm⁻¹ (C–H), and 1162 cm⁻¹ (C–O–C), which indicate an abundant number of methylene groups on CNFs. The grafting of PSA onto CNFs is confirmed. However, it remains challenging to identify the signal from the GdF₃ cross-linked in modified CNF *via* FT-IR as the characteristic absorption band of PSA and CNF overlapped with the PDA@GdF₃ bands.

TGA measurements were carried out to characterize the thermal stability and the amount of GdF₃ nanoparticles coupled to the CNFs. The result is provided in Figure S3. The decomposition of GdF₃-PSA-CNF started at 200 °C, which was slightly lower than PSA-CNF at 225 °C though, and left a higher residue content of 3.4% than PSA-CNF due to the presence of GdF₃ NPs.

We further employed field emission scanning electron microscopy (FE-SEM) for the examination of GdF₃ cross-

linked CNF gel prints. These prints were subjected to freeze-drying and supercritical CO₂ drying separately. As shown in Figure 1A–C, the gel that underwent freeze-drying exhibited a rougher and uneven surface (Figure 1D–F), possibly attributed to structural disruptions caused by the compaction of the gel structure due to solidification of the solvent prior to freeze-drying. On the other hand, the supercritical dried gel displays a smoother surface, which can be attributed to the absence of any phase boundary in supercritical drying, thus providing better preservation of the gel structure. This effect is known for many gel systems.⁶⁶ Moreover, we also found a cluster shown in Figure 1D, which could potentially be aggregates of cross-linked GdF₃ NPs and grafted polymers.

Rheology and 3D-Printing Performance. The study of the gel mechanical properties is essential to estimate its performance for 3D gel-printing. In our previous studies, modified CNF gels with a cross-linked network exhibited enhanced rheological properties, such as viscose flow, yield stress and shape retention properties, making them suitable for 3D gel printing.^{15,19} In this study, we also measured key rheological parameters with the GdF₃-PSA cross-linked CNF gel and attempted to use the gel to create 3D-print models.

For the rheology measurement, the gel sample had a solid content of 10%. The results of the rheology measurements are displayed in Figure 2.

In the oscillatory rheology experiment, the viscoelastic moduli were measured as a function of an oscillatory frequency between 0.1 and 1000 rad/s (Figure 2A). It is worth mentioning that the storage modulus (G') represents the amount of energy elastically stored during deformation and is thus associated with elastic shape retention. The loss modulus (G'') represents the amount of energy dissipated by the gel and therefore is linked to the tendency of a gel to flow. Figure 2A shows that G' was consistently higher than G'' , which means

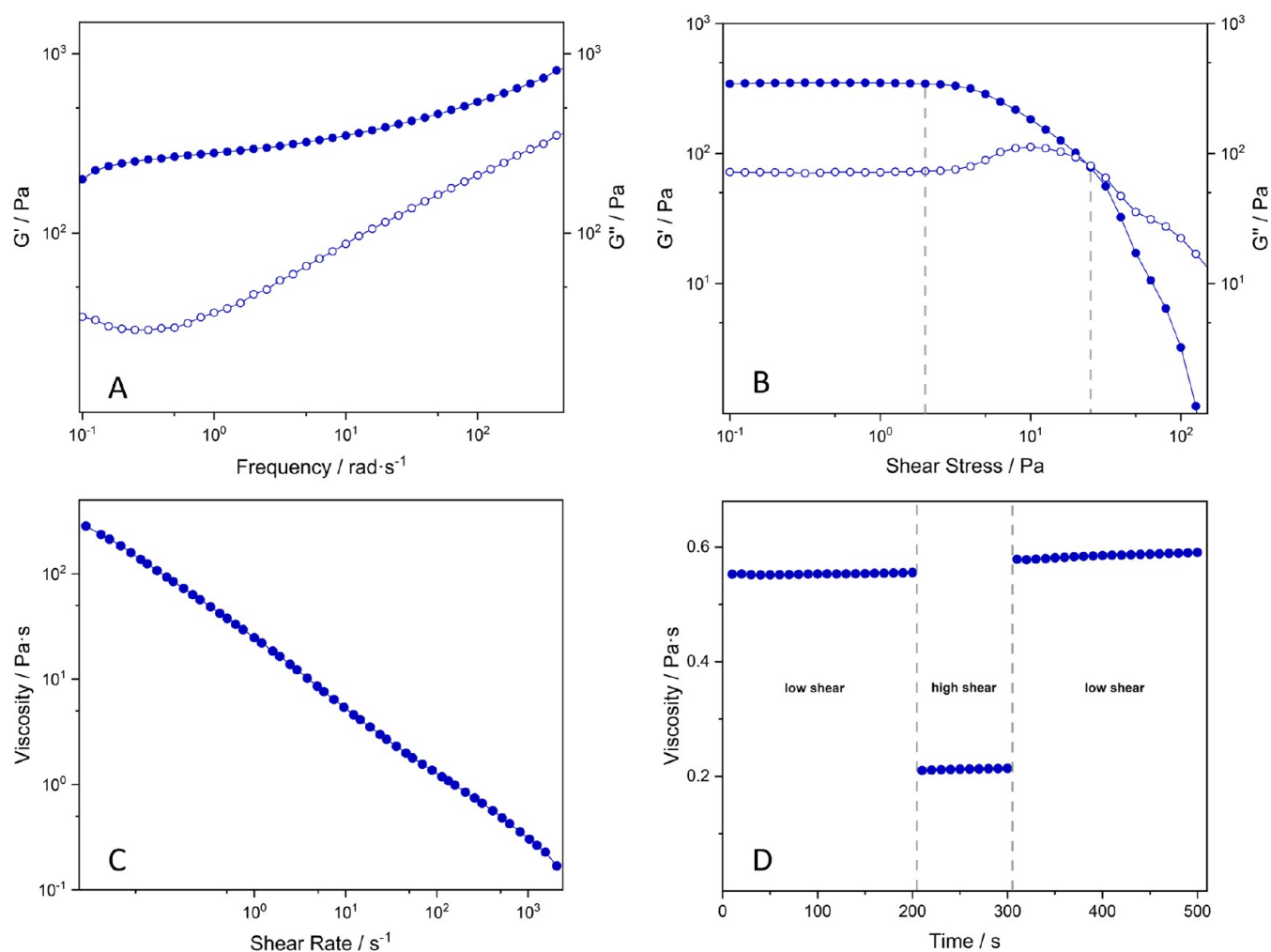


Figure 2. Rheology measurements of GdF₃-PSA-CNF gels: (A) viscoelastic moduli, (B) amplitude sweep, (C) shear-thinning, and (D) shear recovery. The solid circle refers to the left Y axis; the hollow circle refers to the right Y axis.



Figure 3. 3D models and 3D prints obtained using GdF₃-PSA-CNF gels.

the GdF₃-PSA-CNF gel maintained a gel-like behavior in the applied angular frequency range. This indicates that the gel has good shape retention properties.

In another typical experiment (Figure 2B), G' and G'' were measured with respect to oscillatory stress with a fixed angular frequency of 6.28 rad/s. It shows that G' is higher than G'' initially, and this constant plateau indicates a primarily solid-like elastic response of the gel in the lower stress range. At certain deformation amplitudes, the gel reached the limit of the linear viscoelastic range and eventually the flow point, where

G' and G'' cross over, indicating a liquid, viscous-like transition. Interestingly, the G'' curve shows one peak before dropping. The increasing G'' value indicates the increasing deformation energy in the limited range, which might be due to the change in the intramolecular interaction of the gel.

GdF₃-PSA-CNF gel also possesses shear-thinning behavior (Figure 2C). With the increasing shear forces, the viscosity of the GdF₃-PSA-CNF gel drastically drops. This non-Newtonian fluid behavior combined with good initial shape preservation indicates that the gel is suitable for extrusion

printing. After extrusion, a corresponding rise in viscosity is expected with the dropped shear rate to preserve the printed shape. Therefore, the recovery measurement of viscosities upon low/high magnitudes of shear rate was carried out to monitor this process. In Figure 2D, the GdF₃-PSA-CNF gel exhibited a rapid transition of elastic shape retention and fluid-like flow upon time interval and nearly optimal shear recovery.

To conclude, the GdF₃-PSA-CNF gel displays a rheological profile perfectly suited for 3D printability, leading to the design of several 3D-printed objects. All objects were printed with a speed of 10 mm/s through a nozzle with a size of 0.45 mm, and a print flow controlled by a deposition pressure of 20 KPa. All 3D gel structure was reproducibly printed. The theoretical models and 3D prints are shown in Figure 3. The prints in toluene directly underwent supercritical drying and successfully maintained their original shape with minimal observed shrinkage (Figure 4).



Figure 4. 3D prints before (top) and after (bottom) supercritical drying.

Ultra-small- and Wide-Angle X-ray Scattering (USAXS/WAXS) Measurements. We conducted a series of USAXS/WAXS measurements further to investigate the structure of

GdF₃ NPs cross-linked CNFs. The samples used in the study included “simply dried” without 3D printing (annotated as “sd”, as reference), 3D-printed (annotated as “3D/piece”) gels, and a single layer of 3D-printed gel (annotated as “3D/1L”) of GdF₃-PSA-CNF. All data underwent background correction, as explained in the previous section.

In this study, we employed a simplified model compared to our previous work.¹⁹ The model is described by eq 1

$$I(q) = A_1 \cdot F(q) + A_2 \exp\left(-\frac{(q - q_0)^2}{2\sigma^2}\right) + B \quad (1)$$

where A_1 and A_2 denote scale factors, $F(q)$ denotes the Guinier–Porod model from Hammouda,⁶⁷ B denotes the background, and q_0 and σ are the maximum and standard deviation of the Gaussian function, respectively.

The results of the USAXS measurements are presented in Figure 5 (left) and SI-Table 1. It is observed that the stacking distance of NPs is approximately 12 nm, which aligns well with a stacking arrangement along the short axis of the GdF₃ NPs. The shape coefficient (s) is approximately 2, and the Porod coefficient (m) falls in the range of 2.5–3. These values indicate the presence of one-dimensional (1D) structures and ellipsoidal shapes in the Porod region. These findings are consistent with our previous research,¹⁹ suggesting the presence of CNF structures and rough voids. Furthermore, we also identified voids with a Guinier radius of approximately 230–260 nm. Notably, in this study, the influence of NP scattering is reduced.

The GdF₃ NPs cross-linked in modified CNFs exhibit a more chain-like and disordered arrangement compared to our previous work¹⁹ (Figure S4). This is evident from the absence of a second-order peak in the range 0.06–0.1 Å⁻¹. A predominant stacking along the long axis is visible as an NP distance of around 12 nm (Table S1). Using Debye–Scherrer equation,⁶⁸ we estimate the domain size to be $395 \pm 25 \text{ \AA} \approx 40 \pm 3 \text{ nm}$. This indicates that each domain contains only a few NPs.

The WAXS data are listed in Figure 5 (right). For fitting, the following model was used

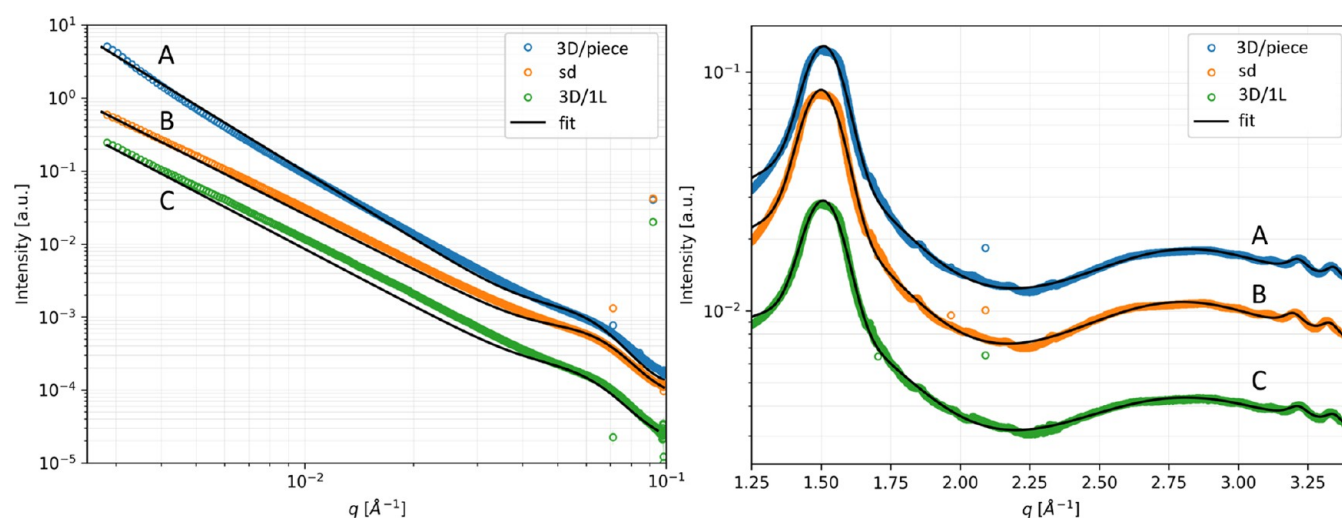
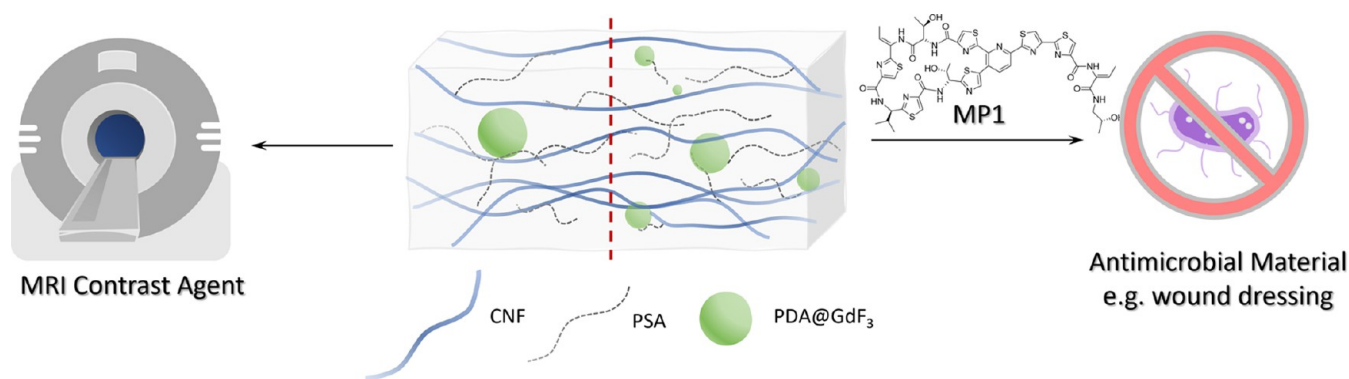


Figure 5. Left: USAXS data; right: WAXS data: (A) 3D-Printed gel (blue), (B) simply dried sample (orange), and (C) single layer of 3D-printed gel (green). Fitted lines are in black.

Scheme 2. Concept: CNF-Based Hybrid Gel with GdF₃ NPs Serves Different Purposes, MRI Contrast Agent, and Antimicrobial Material


$$I(q) = \sum_{j=1}^3 G_j \exp\left(-\frac{(q - q_j)^2}{2\sigma_j^2}\right) + \sum_{j=1}^2 L_j / (1 + ((q - q_j)/(w_j/2))^2) + BG \quad (2)$$

where q_j denotes the peak positions of Gaussian and Lorentzian functions, s_j and w_j are their corresponding standard deviation and widths, BG is the background, and G_j and L_j denote the amplitudes.

All of the curves exhibit a similar pattern (Figure 5, right). The peak observed at around 1.5 \AA^{-1} corresponds to cellulose, while the peak at around 2.75 \AA^{-1} corresponds to amorphous SA polymers. The peaks detected at around 3.25 \AA^{-1} indicate the arrangement of the GdF₃ NPs. They have a Lorentz function width of 0.08 \AA^{-1} , yielding a coherent scattering size of 71 \AA , which aligns well with the GdF₃ NP diameter range. Additionally, the observed peaks correspond to the (131) and (230) peaks, confirming the presence of NPs throughout the sample.

Multifunctional CNF-Based Hybrid Gel—Proof of Concept. As noted previously, our objective is to develop a versatile hybrid gel based on CNFs, which is designed to serve a range of purposes (Scheme 2). Through the utilization of SET-LRP, we successfully cross-linked GdF₃ NPs with CNFs. Our subsequent focus involves assessing the MRI activity conferred to the CNF-based gel by the presence of GdF₃ NPs.

Additionally, we introduced thiopeptide micrococccin P1 (MP1) to the gel to act as an antimicrobial agent. The antimicrobial effectiveness was observed in its activity against MRSA.

Antimicrobial Test. In previous reports, MP1 was shown to be potent against Multiresistant MRSA strain ATCC 33591-lx (PerkinElmer, Waltham, MA).^{63,69} In the present work, we loaded MP1 (1 mg/mL) on the GdF₃-PSA-CNF gel prints to observe its activity against MRSA. Both freeze-dried and simply dried CNF-based gels containing MP1 exhibited effective antimicrobial activity against MRSA strain even after room temperature storage for 7 days. Both groups of samples were subjected to the test 3 times. Same results were obtained as those presented in Figure 6. It places modified CNF-based gels as a promising skin wound dressing candidate for sustained release of hydrophobic drugs within the wound area. Furthermore, the favorable rheology and printability of this gel enable customization of the wound dressing size and

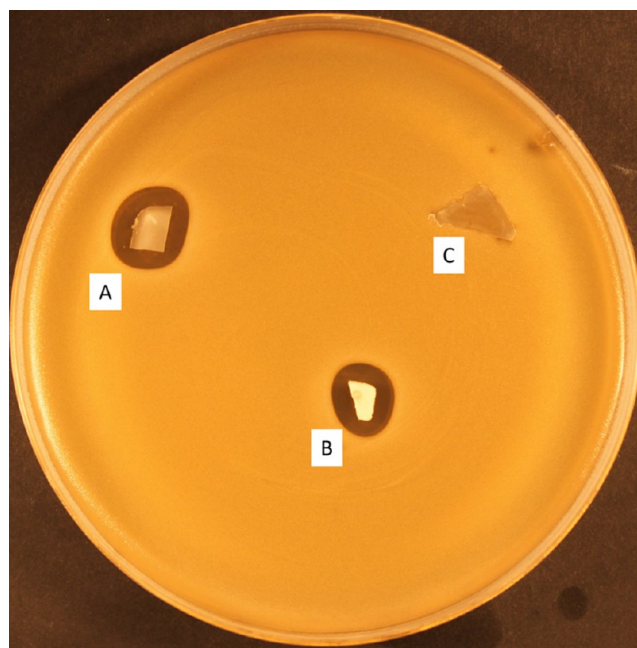


Figure 6. Antimicrobial test against MRSA ATCC 33591-lx *in vitro*: (A) simply dried print, (B) freeze-dried print, and (C) blank sample (negative control).

shape to align with specific dimensions of the wound. Further research is necessary to confirm their antimicrobial activity *in vivo*.

Magnetic Resonance Imaging (MRI). ¹H MRI relaxation time mapping showed significantly decreased T1 and T2 relaxation times, i.e., enhanced relaxivity of GdF₃-PSA-CNF (1 wt % suspension in toluene) compared to toluene control (Figure 7), indicating that GdF₃-PSA-CNF is a contrast agent.

For the agar-embedded GdF₃-CNF suspension in H₂O (1 wt %), a paramagnetic transverse relaxation effect was observed *via* a moderate decrease of T2 from (51.0 ± 0.3) to (18 ± 9) ms. Interestingly, a quite strong decrease of T1 from (2.33 ± 0.02) s to (0.6 ± 0.2) s was seen, indicating that water might be able to directly exchange with the Gd in this sample in addition to long-range paramagnetic relaxation. The gel appeared hypointense due to decreased T2 relaxation time. The GdF₃ seemed to generate a blooming effect, i.e., a paramagnetic effect exceeding that of the sample itself into agarose. A hyperintensity on T1w images would be an indicator of strong water exchange with the Gd atoms, but

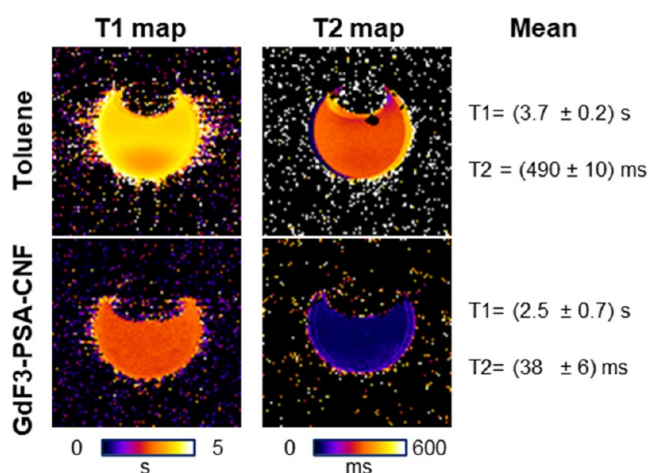


Figure 7. ^1H MRI of toluene control (top row) and GdF_3 -PSA-CNF suspension in toluene (1 wt %, bottom row).

this was not observed with standard MRI scan parameters for T1w imaging (Figure 8).

CONCLUSIONS

The synthesis route and concept of a modified CNF-based hybrid material with antimicrobial activity and MRI-active magnetic properties are demonstrated in this work. The GdF_3 NPs were first surface-modified with ligand 11-Phosphonoundecyl acrylate as presented with FT-IR and successfully engaged in the SET-LRP of CNFs together with the monomer stearyl acrylate. The final material was characterized with FT-IR, TGA, and SEM.

In addition, GdF_3 -PSA-CNF gel (10 wt %) showed favorable rheological properties suitable for 3D gel printing using pneumatic extrusion. We also investigated the structure of those hybrid gels that underwent or without 3D printing process with USAXS/WAXS measurements, further confirming the presence of GdF_3 NPs throughout the sample and their chain-like and disordered arrangement in the modified CNF matrix.

The antimicrobial test verified the effective antimicrobial activity and sustained drug release of the dried GdF_3 -PSA-CNF gel containing MP1 against the MRSA strain, indicating that the gel can also be a potential skin wound dressing candidate with size and shape customization feature. The results from MRI measurements of relaxivities at 7T provide a significant first step toward the potential utilization of this modified CNF-based hybrid gel as a novel MRI contrast agent. Future studies should explore more solvent system alternatives.

ASSOCIATED CONTENT

Supporting Information

The Supporting Information is available free of charge at <https://pubs.acs.org/doi/10.1021/acsnm.3c04272>.

FT-IR spectra for GdF_3 NPs and all CNF species; TGA of PSA-CNF and GdF_3 -PSA-CNF; hypothetical structure of GdF_3 NPs cross-linked modified CNFs; and additional experimental data of USAXS/WAXS measurements (PDF)

AUTHOR INFORMATION

Corresponding Author

Julien R. G. Navarro – Institute of Wood Science, University Hamburg, 21031 Hamburg, Germany; orcid.org/0000-0001-8791-6190; Email: Julien.navarro@uni-hamburg.de

Authors

Xuehe Jiang – Institute of Wood Science, University Hamburg, 21031 Hamburg, Germany; orcid.org/0000-0001-5616-6702

J. Benedikt Mietner – Institute of Wood Science, University Hamburg, 21031 Hamburg, Germany

Dhanya Raveendran – Institute of Wood Science, University Hamburg, 21031 Hamburg, Germany

Kirill V. Ovchinnikov – Faculty of Chemistry, Biotechnology and Food Science, Norwegian University of Life Sciences, 1433 Ås, Norway

Benedikt Sochor – Deutsches Elektronen-Synchrotron DESY, 22607 Hamburg, Germany

Susanne Mueller – Charité 3R | Replace, Reduce, Refine, Charité – Universitätsmedizin Berlin, Corporate Member of Freie Universität Berlin and Humboldt-Universität zu Berlin, 10117 Berlin, Germany; Department of Experimental Neurology and Center for Stroke Research and NeuroCure Cluster of Excellence and Charité Core Facility 7T Experimental MRIs, Charité – Universitätsmedizin Berlin, 10117 Berlin, Germany

Philipp Boehm-Sturm – Charité 3R | Replace, Reduce, Refine, Charité – Universitätsmedizin Berlin, Corporate Member of Freie Universität Berlin and Humboldt-Universität zu Berlin, 10117 Berlin, Germany; Department of Experimental Neurology and Center for Stroke Research and NeuroCure Cluster of Excellence and Charité Core Facility 7T Experimental MRIs, Charité – Universitätsmedizin Berlin, 10117 Berlin, Germany

Frédéric Lerouge – Université de Lyon, Ecole Normale Supérieure de Lyon, CNRS UMR 5182, Université Lyon 1, Laboratoire de Chimie, F69364 Lyon, France; orcid.org/0000-0003-2909-527X

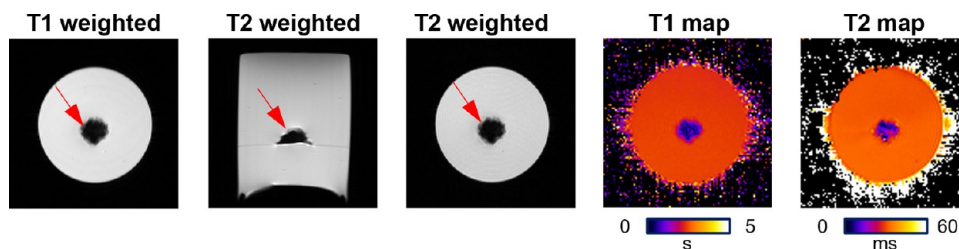


Figure 8. ^1H MRI of GdF_3 -CNF suspension in H_2O (1 wt %) embedded in control gel (2 wt % agar in 1× phosphate-buffered saline). Arrows show the gel, which appears hypointense compared to the surrounding agarose control, which can be explained by transverse relaxation enhancement, i.e., lower T2 relaxation time.

Frédéric Chaput – Université de Lyon, Ecole Normale Supérieure de Lyon, CNRS UMR 5182, Université Lyon 1, Laboratoire de Chimie, F69364 Lyon, France; orcid.org/0000-0002-5315-8675

Pavel Gurikov – Laboratory for Development and Modelling of Novel Nanoporous Materials, Hamburg University of Technology, 21073 Hamburg, Germany

Stephan V. Roth – Deutsches Elektronen-Synchrotron DESY, 22607 Hamburg, Germany; KTH Royal Institute of Technology, Department of Fibre and Polymer Technology, 10044 Stockholm, Sweden

Complete contact information is available at:
<https://pubs.acs.org/10.1021/acsnm.3c04272>

Funding

J.R.G.N., J.B.M., and X.J. thank Fachagentur Nachwachsende Rohstoffe e.V. (FNR/BMEL, Project HolzMat3D, number 2220HV024X) for financial support.

Notes

The authors declare no competing financial interest.

ACKNOWLEDGMENTS

Funding to S.M. and P.B.S. was provided by the German Federal Ministry of Education and Research (BMBF) under the ERA-NET NEURON scheme (01EW2305) and the German Research Foundation (DFG, Project BO 4484/2-1 and EXC-2049-390688087 NeuroCure). *In vitro* MRI experiments were supported by Charité 3^R Replace - Reduce - Refine. The authors acknowledge the inspiration and support by the late Dr. Dzung B. Diep in the antimicrobial part of this paper.

ABBREVIATIONS

CNF, cellulose nanofibrils
SET-LRP, single electron transfer living radical polymerization
MRI, magnetic resonance imaging
MP1, micrococccin P1
MRSA, methicillin-resistant *S. aureus*
SA, stearyl acylate
PDA, 11-phosphonoundecyl acrylate
T1w, T1-weighted MRI
T2w, T2-weighted MRI
USAX&WAXS, Ultrasmall- and wide-angle X-ray scattering

REFERENCES

- (1) Prasad, R.; Kumar, V.; Kumar, M. *Nanotechnology*; Prasad, R.; Kumar, V.; Kumar, M., Eds.; Springer Singapore: Singapore, 2017. DOI: 10.1007/978-981-10-4678-0.
- (2) Athanasiou, V.; Stavroulaki, D.; Arfara, F.; Kampras, D.; Kleideris, I.; Roumelioti, N.; Fragouli, P. G.; Patias, G.; Haddleton, D.; Iatrou, H. Gold Nanoparticles and Nanoshells Embedded as Core–Shell Architectures in Hybrid Poly(l-Histidine)-Containing Polymers for Photothermal Therapies. *ACS Appl. Nano Mater.* **2021**, *4* (12), 14217–14230.
- (3) Josefsson, L.; Ye, X.; Brett, C. J.; Meijer, J.; Olsson, C.; Sjögren, A.; Sundlöf, J.; Davydok, A.; Langton, M.; Emmer, Å.; Lendel, C. Potato Protein Nanofibrils Produced from a Starch Industry Sidestream. *ACS Sustainable Chem. Eng.* **2020**, *8* (2), 1058–1067.
- (4) Lunardi, V. B.; Soetaredjo, F. E.; Putro, J. N.; Santoso, S. P.; Yuliana, M.; Sunarso, J.; Ju, Y.; Ismadij, S. Nanocelluloses: Sources, Pretreatment, Isolations, Modification, and Its Application as the Drug Carriers. *Polymers* **2021**, *13* (13), No. 2052.

- (5) Patel, D. K.; Dutta, S. D.; Lim, K. T. Nanocellulose-Based Polymer Hybrids and Their Emerging Applications in Biomedical Engineering and Water Purification. *RSC Adv.* **2019**, 19143–19162, DOI: 10.1039/c9ra03261d.

- (6) Trache, D.; Tarchoun, A. F.; Derradji, M.; Hamidon, T. S.; Masruchin, N.; Brosse, N.; Hussin, M. H. Nanocellulose: From Fundamentals to Advanced Applications. *Front. Chem.* **2020**, *8*, No. 392, DOI: 10.3389/fchem.2020.00392.

- (7) Mittal, N.; Jansson, R.; Widhe, M.; Benselfelt, T.; Håkansson, K. M. O.; Lundell, F.; Hedhammar, M.; Söderberg, L. D. Ultrastrong and Bioactive Nanostructured Bio-Based Composites. *ACS Nano* **2017**, *11* (5), 5148–5159.

- (8) Klemm, D.; Kramer, F.; Moritz, S.; Lindström, T.; Ankerfors, M.; Gray, D.; Dorris, A. Nanocelluloses: A New Family of Nature-Based Materials. *Angew. Chem., Int. Ed.* **2011**, *50* (24), 5438–5466.

- (9) Shin, S.; Hyun, J. Rheological Properties of Cellulose Nanofiber Hydrogel for High-Fidelity 3D Printing. *Carbohydr. Polym.* **2021**, *263*, No. 117976.

- (10) Jayakumar, A.; Ambekar, R. S.; Mahapatra, P. L.; Singh, A. K.; Kundu, T. K.; P R, S.; Nair, R. R.; Tiwary, C. S. Energy Harvesting Using High-Strength and Flexible 3D-Printed Cellulose/Hexagonal Boron Nitride Nanosheet Composites. *ACS Appl. Nano Mater.* **2023**, *6* (15), 14278–14288.

- (11) Brett, C. J.; Ohm, W.; Fricke, B.; Alexakis, A. E.; Laermann, T.; Körtgens, V.; Müller-Buschbaum, P.; Söderberg, L. D.; Roth, S. V. Nanocellulose-Assisted Thermally Induced Growth of Silver Nanoparticles for Optical Applications. *ACS Appl. Mater. Interfaces* **2021**, *13* (23), 27696–27704.

- (12) Madivoli, E. S.; Kareru, P. G.; Gachanja, A. N.; Makhanu, D. S.; Mugo, S. M. Cellulose-Based Hybrid Nanoarchitectonics with Silver Nanoparticles: Characterization and Antimicrobial Potency. *J. Inorg. Organomet. Polym. Mater.* **2022**, *32* (3), 854–863.

- (13) Alle, M.; Bandi, R.; Sharma, G.; Dadigala, R.; Lee, S.-H.; Kim, J.-C. Gold Nanoparticles Spontaneously Grown on Cellulose Nanofibrils as a Reusable Nanozyme for Colorimetric Detection of Cholesterol in Human Serum. *Int. J. Biol. Macromol.* **2022**, *201*, 686–697.

- (14) Oprea, M.; Panaitescu, D. M. Nanocellulose Hybrids with Metal Oxides Nanoparticles for Biomedical Applications. *Molecules* **2020**, *25* (18), No. 4045.

- (15) Navarro, J. R. G.; Rostami, J.; Ahlinder, A.; Mietner, J. B.; Bernin, D.; Saake, B.; Edlund, U. Surface-Initiated Controlled Radical Polymerization Approach to In Situ Cross-Link Cellulose Nanofibrils with Inorganic Nanoparticles. *Biomacromolecules* **2020**, *21* (5), 1952–1961.

- (16) Dalloul, F.; Mietner, J. B.; Navarro, J. R. G. Three-Dimensional Printing of a Tough Polymer Composite Gel Ink Reinforced with Chemically Modified Cellulose Nanofibrils Showing Self-Healing Behavior. *ACS Appl. Polym. Mater.* **2023**, *5* (5), 3256–3269.

- (17) Jiang, X.; Mietner, J. B.; Navarro, J. R. G. A Combination of Surface-Initiated Controlled Radical Polymerization (SET-LRP) and Click-Chemistry for the Chemical Modification and Fluorescent Labeling of Cellulose Nanofibrils: STED Super-Resolution Imaging of a Single Fibril and a Single Fibril Embedded in a Composite. *Cellulose* **2023**, *30*, 2929–2950.

- (18) Percec, V.; Popov, A. V.; Ramirez-Castillo, E.; Monteiro, M.; Barboiu, B.; Weichold, O.; Asandei, A. D.; Mitchell, C. M. Aqueous Room Temperature Metal-Catalyzed Living Radical Polymerization of Vinyl Chloride. *J. Am. Chem. Soc.* **2002**, *124* (18), 4940–4941.

- (19) Jiang, X.; Mietner, J. B.; Harder, C.; Komban, R.; Chen, S.; Strelow, C.; Sazama, U.; Fröba, M.; Gimmler, C.; Müller-Buschbaum, P.; Roth, S. V.; Navarro, J. R. G. 3D Printable Hybrid Gel Made of Polymer Surface-Modified Cellulose Nanofibrils Prepared by Surface-Initiated Controlled Radical Polymerization (SI-SET-LRP) and Upconversion Luminescent Nanoparticles. *ACS Appl. Mater. Interfaces* **2023**, *15* (4), 5687–5700.

- (20) Mietner, J. B.; Willruth, S.; Komban, R.; Gimmler, C.; Nehmeh, B.; Navarro, J. R. G. Polymer-Modified Cellulose Nanofibrils Cross-Linked with Cobalt Iron Oxide Nanoparticles as a Gel Ink for 3D

- Printing Objects with Magnetic and Electrochemical Properties. *Fibers* **2023**, *11* (1), No. 2.
- (21) Ersoy, H.; Rybicki, F. J. Biochemical Safety Profiles of Gadolinium-Based Extracellular Contrast Agents and Nephrogenic Systemic Fibrosis. *J. Magn. Reson. Imaging* **2007**, *26* (5), 1190–1197.
- (22) Bridot, J.-L.; Faure, A.-C.; Laurent, S.; Rivière, C.; Billotey, C.; Hiba, B.; Janier, M.; Jossierand, V.; Coll, J.-L.; Elst, L. V.; Muller, R.; Roux, S.; Perriat, P.; Tillement, O. Hybrid Gadolinium Oxide Nanoparticles: Multimodal Contrast Agents for in Vivo Imaging. *J. Am. Chem. Soc.* **2007**, *129* (16), 5076–5084.
- (23) Zhu, S.; Wen, C.; Bai, D.; Gao, M. Diagnostic Efficacy of Intravascular Ultrasound Combined with Gd₂O₃-EPL Contrast Agent for Patients with Atherosclerosis. *Exp. Ther. Med.* **2020**, *20* (6), No. 136.
- (24) Guo, L.; Xin, H.; Luo, X.; Zhang, C. Phase Evolution, Mechanical Properties and MRI Contrast Behavior of GdPO₄ Doped Hydroxyapatite for Dental Applications. *Mater. Sci. Eng., C* **2020**, *111*, No. 110858.
- (25) Rodriguez-Liviano, S.; Becerro, A. I.; Alcántara, D.; Gráz, V.; de la Fuente, J. M.; Ocaña, M. Synthesis and Properties of Multifunctional Tetragonal Eu:GdPO₄ Nanocubes for Optical and Magnetic Resonance Imaging Applications. *Inorg. Chem.* **2013**, *52* (2), 647–654.
- (26) Hu, K.-W.; Hsu, K.-C.; Yeh, C.-S. PH-Dependent Biodegradable Silica Nanotubes Derived from Gd(OH)₃ Nanorods and Their Potential for Oral Drug Delivery and MR Imaging. *Biomaterials* **2010**, *31* (27), 6843–6848.
- (27) Passuello, T.; Pedroni, M.; Piccinelli, F.; Polizzi, S.; Marzola, P.; Tambalo, S.; Conti, G.; Benati, D.; Vetrone, F.; Bettinelli, M.; Speghini, A. PEG-Capped, Lanthanide Doped GdF₃ Nanoparticles: Luminescent and T₂ Contrast Agents for Optical and MRI Multimodal Imaging. *Nanoscale* **2012**, *4* (24), 7682–7689.
- (28) Evanics, F.; Diamente, P. R.; van Veggel, F. C. J. M.; Stanis, G. J.; Prosser, R. S. Water-Soluble GdF₃ and GdF₃/LaF₃ Nanoparticles: Physical Characterization and NMR Relaxation Properties. *Chem. Mater.* **2006**, *18* (10), 2499–2505.
- (29) Yon, M.; Billotey, C.; Marty, J. D. Gadolinium-Based Contrast Agents: From Gadolinium Complexes to Colloidal Systems. *Int. J. Pharm.* **2019**, *569*, No. 118577.
- (30) Dong, C.; Korinek, A.; Blasiak, B.; Tomanek, B.; van Veggel, F. C. J. M. Cation Exchange: A Facile Method To Make NaYF₄:Yb,Tm-NaGdF₄ Core-Shell Nanoparticles with a Thin, Tunable, and Uniform Shell. *Chem. Mater.* **2012**, *24* (7), 1297–1305.
- (31) Du, Q.; Huang, Z.; Wu, Z.; Meng, X.; Yin, G.; Gao, F.; Wang, L. Facile Preparation and Bifunctional Imaging of Eu-Doped GdPO₄ Nanorods with MRI and Cellular Luminescence. *Dalton Trans.* **2015**, *44* (9), 3934–3940.
- (32) Hifumi, H.; Yamaoka, S.; Tanimoto, A.; Citterio, D.; Suzuki, K. Gadolinium-Based Hybrid Nanoparticles as a Positive MR Contrast Agent. *J. Am. Chem. Soc.* **2006**, *128* (47), 15090–15091.
- (33) Tian, G.; Gu, Z.; Zhou, L.; Yin, W.; Liu, X.; Yan, L.; Jin, S.; Ren, W.; Xing, G.; Li, S.; Zhao, Y. Mn²⁺ Dopant-Controlled Synthesis of NaYF₄:Yb/Er Upconversion Nanoparticles for in Vivo Imaging and Drug Delivery. *Adv. Mater.* **2012**, *24* (9), 1226–1231.
- (34) Li, R.; Ji, Z.; Chang, C. H.; Dunphy, D. R.; Cai, X.; Meng, H.; Zhang, H.; Sun, B.; Wang, X.; Dong, J.; Lin, S.; Wang, M.; Liao, Y.-P.; Brinker, C. J.; Nel, A.; Xia, T. Surface Interactions with Compartmentalized Cellular Phosphates Explain Rare Earth Oxide Nanoparticle Hazard and Provide Opportunities for Safer Design. *ACS Nano* **2014**, *8* (2), 1771–1783.
- (35) Li, Y.; Beija, M.; Laurent, S.; Elst, L. V.; Muller, R. N.; Duong, H. T. T.; Lowe, A. B.; Davis, T. P.; Boyer, C. Macromolecular Ligands for Gadolinium MRI Contrast Agents. *Macromolecules* **2012**, *45* (10), 4196–4204.
- (36) Younis, M.; Darcos, V.; Paniagua, C.; Ronjat, P.; Lemaire, L.; Nottelet, B.; Garric, X.; Bakkour, Y.; El Nakat, J. H.; Coudane, J. MRI-Visible Polymer Based on Poly(Methyl Methacrylate) for Imaging Applications. *RSC Adv.* **2016**, *6* (7), 5754–5760.
- (37) Shapoval, O.; Sulimenko, V.; Klebanovych, A.; Rabyk, M.; Shapoval, P.; Kaman, O.; Rydvalová, E.; Filipová, M.; Dráberová, E.; Dráber, P.; Horák, D. Multimodal Fluorescently Labeled Polymer-Coated GdF₃nanoparticles Inhibit Degranulation in Mast Cells. *Nanoscale* **2021**, *13* (45), 19023–19037.
- (38) Kumar, A.; Durand, H.; Zeno, E.; Balsollier, C.; Watbled, B.; Sillard, C.; Fort, S.; Baussanne, I.; Belgacem, N.; Lee, D.; Hediger, S.; Demeunynck, M.; Bras, J.; De Paëpe, G. The Surface Chemistry of a Nanocellulose Drug Carrier Unravelling by MAS-DNP. *Chem. Sci.* **2020**, *11* (15), 3868–3877.
- (39) Ning, L.; You, C.; Zhang, Y.; Li, X.; Wang, F. Polydopamine Loaded Fluorescent Nanocellulose–Agarose Hydrogel: A PH-Responsive Drug Delivery Carrier for Cancer Therapy. *Compos. Commun.* **2021**, *26*, No. 100739.
- (40) Carvalho, J. P. F.; Teixeira, M. C.; Lameirinhas, N. S.; Matos, F. S.; Luís, J. L.; Pires, L.; Oliveira, H.; Oliveira, M.; Silvestre, A. J. D.; Vilela, C.; Freire, C. S. R. Hydrogel Bioinks of Alginate and Curcumin-Loaded Cellulose Ester-Based Particles for the Biofabrication of Drug-Releasing Living Tissue Analogs. *ACS Appl. Mater. Interfaces* **2023**, *15*, 40898–40912.
- (41) Poonguzhali, R.; Basha, S. K.; Kumari, V. S. Novel Asymmetric Chitosan/PVP/Nanocellulose Wound Dressing: In Vitro and in Vivo Evaluation. *Int. J. Biol. Macromol.* **2018**, *112* (2017), 1300–1309.
- (42) Rees, A.; Powell, L. C.; Chinga-Carrasco, G.; Gethin, D. T.; Syverud, K.; Hill, K. E.; Thomas, D. W. 3D Bioprinting of Carboxymethylated-Periodate Oxidized Nanocellulose Constructs for Wound Dressing Applications. *Biomed. Res. Int.* **2015**, *2015*, No. 925757.
- (43) Tudoroiu, E. E.; Dinu-Pirvu, C. E.; Kaya, M. G. A.; Popa, L.; Anuța, V.; Prisada, R. M.; Ghica, M. V. An Overview of Cellulose Derivatives-Based Dressings for Wound-Healing Management. *Pharmaceuticals* **2021**, *14* (12), No. 1215, DOI: 10.3390/ph14121215.
- (44) Gehlen, D. B.; Jürgens, N.; Omidinia-Anarkoli, A.; Haraszti, T.; George, J.; Walther, A.; Ye, H.; De Laporte, L. Granular Cellulose Nanofibril Hydrogel Scaffolds for 3D Cell Cultivation. *Macromol. Rapid Commun.* **2020**, *41* (18), No. 2000191.
- (45) Hatakeyama, M.; Kitaoka, T. Surface-Carboxylated Nanocellulose-Based Bioadaptive Scaffolds for Cell Culture. *Cellulose* **2022**, *29* (5), 2869–2883.
- (46) Syverud, K. Tissue Engineering Using Plant-Derived Cellulose Nanofibrils (CNF) as Scaffold Material. In *Nanocelluloses: Their Preparation, Properties, and Applications*; ACS Publications, 2017; Vol. 1251, pp 171–189.
- (47) Randhawa, A.; Dutta, S. D.; Ganguly, K.; Patil, T. V.; Patel, D. K.; Lim, K. T. A Review of Properties of Nanocellulose, Its Synthesis, and Potential in Biomedical Applications. *Appl. Sci.* **2022**, *12* (14), No. 7090.
- (48) Durand, H.; Smyth, M.; Bras, J. Nanocellulose: A New Biopolymer for Biomedical Application. In *Biopolymers for Biomedical and Biotechnological Applications*; Wiley, 2021; pp 129–179.
- (49) Souza, S. F.; Mariano, M.; Reis, D.; Lombello, C. B.; Ferreira, M.; Sain, M. Cell Interactions and Cytotoxic Studies of Cellulose Nanofibers from Curauá Natural Fibers. *Carbohydr. Polym.* **2018**, *201*, 87–95.
- (50) Ilves, M.; Vilske, S.; Aimonen, K.; Lindberg, H. K.; Pesonen, S.; Wedin, I.; Nuopponen, M.; Vanhala, E.; Højgaard, C.; Winther, J. R.; Willemoës, M.; Vogel, U.; Wolff, H.; Norppa, H.; Savolainen, K.; Alenius, H. Nanofibrillated Cellulose Causes Acute Pulmonary Inflammation That Subsides within a Month. *Nanotoxicology* **2018**, *12* (7), 729–746.
- (51) Kolakovic, R.; Peltonen, L.; Laukkanen, A.; Hirvonen, J.; Laaksonen, T. Nanofibrillar Cellulose Films for Controlled Drug Delivery. *Eur. J. Pharm. Biopharm.* **2012**, *82* (2), 308–315.
- (52) Abu, T. M.; Zahan, K. A.; Rajaie, M. A.; Ring, L. C.; Rashid, S. A.; Hamin, N. S. M. N.; Nee, T. W.; Yenn, T. W. Nanocellulose as Drug Delivery System for Honey as Antimicrobial Wound Dressing. *Mater. Today: Proc.* **2020**, *31*, 14–17.

- (53) Rai, R.; Dhar, P. Biomedical Engineering Aspects of Nanocellulose: A Review. *Nanotechnology* **2022**, *33* (36), No. 362001.
- (54) Sulthana, R.; Archer, A. C. Bacteriocin Nanoconjugates: Boon to Medical and Food Industry. *J. Appl. Microbiol.* **2021**, *131* (3), 1056–1071.
- (55) Ng, Z. J.; Zarin, M. A.; Lee, C. K.; Tan, J. S. Application of Bacteriocins in Food Preservation and Infectious Disease Treatment for Humans and Livestock: A Review. *RSC Adv.* **2020**, *10* (64), 38937–38964.
- (56) Eijsink, V. G. H.; Axelsson, L.; Diep, D. B.; Håvarstein, L. S.; Holo, H.; Nes, I. F. Production of Class II Bacteriocins by Lactic Acid Bacteria; an Example of Biological Warfare and Communication. *Antonie van Leeuwenhoek* **2002**, *81* (1–4), 639–654.
- (57) Acedo, J. Z.; Chiorean, S.; Vederas, J. C.; van Belkum, M. J. The Expanding Structural Variety among Bacteriocins from Gram-Positive Bacteria. *FEMS Microbiol. Rev.* **2018**, *42* (6), 805–828.
- (58) Liao, R.; Duan, L.; Lei, C.; Pan, H.; Ding, Y.; Zhang, Q.; Chen, D.; Shen, B.; Yu, Y.; Liu, W. Thiopeptide Biosynthesis Featuring Ribosomally Synthesized Precursor Peptides and Conserved Post-translational Modifications. *Chem. Biol.* **2009**, *16* (2), 141–147.
- (59) Mietner, J. B.; Jiang, X.; Edlund, U.; Saake, B.; Navarro, J. R. G. 3D Printing of a Bio-Based Ink Made of Cross-Linked Cellulose Nanofibrils with Various Metal Cations. *Sci. Rep.* **2021**, *11* (1), No. 6461.
- (60) Georgouvelas, D.; Jalvo, B.; Valencia, L.; Papawassiliou, W.; Pell, A. J.; Edlund, U.; Mathew, A. P. Residual Lignin and Zwitterionic Polymer Grafts on Cellulose Nanocrystals for Antifouling and Antibacterial Applications. *ACS Appl. Polym. Mater.* **2020**, *2* (8), 3060–3071.
- (61) Chaput, F.; Lerouge, F.; Tusseau-Nenez, S.; Coulon, P. E.; Dujardin, C.; Denis-Quanquin, S.; Mpambani, F.; Parola, S. Rare Earth Fluoride Nanoparticles Obtained Using Charge Transfer Complexes: A Versatile and Efficient Route toward Colloidal Suspensions and Monolithic Transparent Xerogels. *Langmuir* **2011**, *27* (9), 5555–5561.
- (62) Karpati, S.; Hubert, V.; Hristovska, I.; Lerouge, F.; Chaput, F.; Bretonnière, Y.; Andraud, C.; Banyasz, A.; Micouin, G.; Monteil, M.; Lecouvey, M.; Mercey-Ressejac, M.; Dey, A. K.; Marche, P. N.; Lindgren, M.; Pascual, O.; Wiart, M.; Parola, S. Hybrid Multimodal Contrast Agent for Multiscale in Vivo Investigation of Neuroinflammation. *Nanoscale* **2021**, *13* (6), 3767–3781.
- (63) Ovchinnikov, K. V.; Kranjec, C.; Telke, A.; Kjos, M.; Thorstensen, T.; Scherer, S.; Carlsen, H.; Diep, D. B. A Strong Synergy Between the Thiopeptide Bacteriocin Micrococcin P1 and Rifampicin Against MRSA in a Murine Skin Infection Model. *Front. Immunol.* **2021**, *12*, No. 676534.
- (64) Buffet, A.; Rothkirch, A.; Döhrmann, R.; Körstgens, V.; Kashem, M. M. A.; Perlich, J.; Herzog, G.; Schwartzkopf, M.; Gehrke, R.; Müller-Buschbaum, P.; Roth, S. V. P03, the Microfocus and Nanofocus X-Ray Scattering (MiNaXS) Beamline of the PETRA III Storage Ring: The Microfocus Endstation. *J. Synchrotron Radiat.* **2012**, *19* (4), 647–653.
- (65) Schaeffler, S.; Perry, W.; Jones, D. Methicillin-Resistant Strains of Staphylococcus Aureus Phage Type 92. *Antimicrob. Agents Chemother.* **1979**, *15* (1), 74–80.
- (66) Ratke, L.; Gurikov, P. *The Chemistry and Physics of Aerogels: Synthesis, Processing, and Properties*; Cambridge University Press, 2021.
- (67) Hammouda, B. A New Guinier–Porod Model. *J. Appl. Crystallogr.* **2010**, *43* (4), 716–719.
- (68) Smilgies, D. M. Scherrer Grain-Size Analysis Adapted to Grazing-Incidence Scattering with Area Detectors. *J. Appl. Crystallogr.* **2009**, *42* (6), 1030–1034.
- (69) Ovchinnikov, K. V.; Kranjec, C.; Thorstensen, T.; Carlsen, H.; Diep, D. B. Successful Development of Bacteriocins into Therapeutic Formulation for Treatment of MRSA Skin Infection in a Murine Model. *Antimicrob. Agents Chemother.* **2020**, *64* (12), No. 10-1128, DOI: 10.1128/AAC.00829-20.